Resonances in Interacting Floquet Systems and Dynamic Transport Phenomena

Christoph Dauer

Dissertation

2022

Resonances in Interacting Floquet Systems and Dynamic Transport Phenomena

Dissertation

Christoph Dauer

Dem Fachbereich Physik der Technischen Universität Kaiserslautern zur Erlangung des akademischen Grades „Doktor der Naturwissenschaften“ eingereichte Dissertation

Betreuer: Prof. Dr. Sebastian Eggert

Datum des Antrages auf Eröffnung des Promotionsverfahrens:
14.04.2022

Abstract

This thesis studies resonant behavior in periodically driven ultracold quantum gases and optical waveguide arrays. Motivated by resonance phenomena from classical mechanics and the wealth of exotic physics that has been found in periodically driven systems, the goal of this thesis is to investigate intriguing resonance-induced behavior in these physical systems. In order to reach this goal, each of the three main parts of this thesis discusses a different type of resonance in a suitable physical model.

For the theoretical description of the time-periodic systems we use Floquet theory. In particular, Floquet theory generalizes the concept of an eigenbasis to time-periodically driven Hamilton operators. Floquet eigenstates, which are also named Floquet steady states, have properties that are tunable by the periodic drive.

In the first part we show with the methods of Floquet scattering theory that the periodic driving of a short range potential between ultracold atoms induces Feshbach resonances. We develop the Floquet-Feshbach resonance theory which is capable of calculating the properties of the driving-induced Feshbach resonances. As a result, highly tunable resonance properties are found. The real part of the scattering length can be adjusted to large positive and negative values, while the imaginary part of the scattering length, describing atom loss, stays relatively small. In an ultracold gas experiment, a time-dependent interatomic potential can be achieved by modulating a magnetic field in the vicinity of a magnetic Feshbach resonance. In this thesis, we model this case by a multichannel description of atom scattering with time-periodic parameters. We find that the periodic drive both engineers the parameters of the magnetic Feshbach resonance, that already exists in the static case, and induces new resonances. The Floquet-Feshbach resonance theory also predicts in this model that the properties of the resonances can be tuned by the periodic drive.

The second part remains in the realm of ultracold quantum gases, and investigates resonant behavior in interacting quantum many-body systems. In such systems, nontrivial correlations are present due to the interaction and entanglement between the particles. In one dimension, the Tomonaga-Luttinger liquid serves as a universal low-energy description of a wide class of quantum many-body systems. In this thesis, we formulate a Floquet-Bogoliubov theory which yields Floquet steady states of time-periodic Hamiltonians that are quadratic in bosonic operators. The Floquet-Bogoliubov theory can be applied to a plurality of physical models, in particular to the periodically driven Tomonaga-Luttinger liquid. However, Floquet solutions turn out to only exist in certain parameter regions. The absence of a Floquet solution is traced back to the phenomenon of parametric resonance and is seen as a divergence in certain expectation values. A finite lifetime in the Tomonaga-Luttinger description regularizes these divergences to peaks with finite maximum and enables us to find a Floquet steady state of a periodically driven quantum many-body system. Combining all the results, we predict a standing density-wave pattern for a one-dimensional Bose gas subject to a time-periodic modulation of the interaction strength.

In the last part we stay in one dimension and introduce time-dependent dissipation as a direction-dependent filter for a Hamiltonian quantum ratchet. Based on the details of a surface plasmon-polariton waveguide array experiment, we investigate dynamic transport phenomena in a periodically driven Su-Schrieffer-Heeger ratchet model. Directed transport with the velocity of one unit cell per driving period is found at certain resonant frequencies in this model. A Floquet-Bloch analysis relates these transport properties to a nontrivial topology. However, the direction and the magnitude of the current depends on the initial state. The direction-dependent filter circumvents this issue by breaking the time-reversal symmetry. The filter absorbs states that move in a certain direction while leaving the states moving in the other direction unimpaired. The properties of the Filter are analyzed with a Floquet S-matrix theory, which we derive for the case of a non-hermitian, time-periodic impurity operator and a time-periodic bulk. Our findings agree with the results of the waveguide experiment.

Zusammenfassung

Diese Arbeit untersucht resonantes Verhalten in periodisch modulierten ultrakalten Quantengasen und optischen Wellenleitern. Motiviert durch bekannte Resonanzphänomene der klassischen Mechanik und die Fülle von exotischer Physik, die in periodisch getriebenen Systemen gefunden wurde, ist das Ziel dieser Arbeit faszinierende, durch Resonanzen induzierte Systemeigenschaften in diesen physikalischen Systemen zu untersuchen. Um dieses Ziel zu erreichen diskutiert jeder Hauptteil eine spezielle Art der Resonanz in einem geeigneten physikalischen Modell.

Periodisch modulierte Systeme werden mithilfe der Floquet-Theorie beschrieben. Das zentrale Element ist hierbei, dass die Floquet-Theorie das Konzept der Eigenbasis auf zeitperiodische Hamiltonoperatoren verallgemeinert. Die Eigenschaften der Floquet-Eigenzustände sind durch das periodische Treiben kontrollierbar.

In dem ersten Teil wird mithilfe der Floquet-Streutheorie gezeigt, dass das periodische Treiben eines kurzreichweitigen Potentials zwischen ultrakalten Atomen Feshbach-Resonanzen erzeugt. Die in dieser Arbeit entwickelte Floquet-Feshbach-Resonanztheorie ermöglicht das Berechnen der Eigenschaften dieser Resonanzen, mit dem Ergebnis, dass die Resonanzeigenschaften durch die periodische Modulation stark verändert werden können. Der Realteil der Streulänge kann auf große positive und negative Werte eingestellt werden, gleichzeitig ist der Imaginärteil der Streulänge, welcher Verlust von Atomen beschreibt, vergleichsweise gering. Ein zeitabhängiges inter-atomares Potential kann in ultrakalten Quantengasen durch ein zeitlich veränderliches Magnetfeld in der Nähe einer magnetischen Feshbach-Resonanz erzeugt werden. Hier wird dieser Fall durch ein Vielkanalmodell der interatomaren Streuung mit periodisch modulierten Parametern beschrieben. Als Ergebnis erhalten wir, dass die periodische Modulation sowohl die bereits existierende magnetische Feshbach-Resonanz verändert, als auch neue Resonanzen induziert. Die Floquet-Feshbach-Resonanztheorie findet auch in diesem Modell Resonanzeigenschaften, die durch die periodische Modulation verändert werden können.

Der zweite Teil ist ebenfalls im Gebiet der ultrakalten Quantengase angesiedelt und betrachtet die resonante Modulation eines wechselwirkenden Quanten-Vielteilchensystems. Diese Systeme haben durch die Verschränkung und Wechselwirkung zwischen den Teilchen eine nichttriviale Korrelation. Die niedrigenergetischen Zustände einer großen Klasse von eindimensionalen Vielteilchensystemen können durch ein universelles Modell, der Tomonaga-Luttinger Flüssigkeit, beschrieben werden. In dieser Arbeit wird eine Floquet-Bogoliubov Theorie formuliert, mit welcher Floquet-Eigenzustände von periodisch modulierten Hamiltonoperatoren, die quadratisch von bosonischen Operatoren abhängen, berechnet werden können. Die Floquet-Bogoliubov Theorie kann auf eine Vielzahl von physikalischen Modellen angewendet werden, im speziellen auch auf die periodisch getriebene Tomonaga-Luttinger Flüssigkeit. Allerdings existieren diese Floquet-Lösungen nur in einem bestimmten Parameterbereich, während deren Abwesenheit auf das Phänomen der parametrischen Resonanz zurückgeführt und durch eine Divergenz bestimmter Erwartungswerte angezeigt wird. Die Einführung einer endlichen Lebensdauer in der Tomonaga-Luttinger Flüssigkeit regularisiert diese Divergenzen zu Spitzen mit endlicher Höhe und ermöglicht es, einen Floquet Eigenzustand eines periodisch getriebenen Quanten-Vielteilchensystems zu finden. Mit der Kombination aller Ergebnisse kann die Aussage getroffen werden, dass eine periodisch modulierte Wechselwirkungsstärke in einem eindimensionalen bosonischen Gas stehende Dichtewellen erzeugt.

Der letzte Teil bleibt in einer Dimension und untersucht, wie zeitabhängige Dissipation als richtungsabhängiger Filter in einer hamiltonschen Ratsche agieren kann. Dazu werden zuerst dynamische Transportphänomene in einem periodisch moduliertem Su-Schrieffer-Heeger Ratschenmodell, welches die Gegebenheiten eines Wellenleiterexperiments mit Oberflächen Plasmon-Polaritonen beschreibt, betrachtet. Dieses Modell ermöglicht bei speziellen Resonanzfrequenzen gerichteten Transport mit einer Geschwindigkeit von einer Einheitszelle pro Treibperiode. Eine Analyse mithilfe der Floquet-Bloch-Theorie verknüpft die Eigenschaften des Teilchentransports mit einer nichttrivialen Topologie. Nichtsdestotrotz hängt sowohl die Richtung als auch die Stärke des Teilchenstromes von dem Anfangszustand ab. Der richtungsabhängige Filter unterdrückt diese Abhängigkeit vom Anfangszustand durch das Brechen der Zeitumkehrinvarianz. Der Filter absorbiert Zustände, die sich in eine bestimmte Richtung bewegen, während Zustände, die sich in die andere Richtung bewegen, unverändert den Filter passieren können. Die Eigenschaften des Filters werden mit einer Floquet S-Matrix Theorie analysiert, welche speziell für den Fall einer nicht-hermitschen, zeitperiodischen Verunreinigung und einem zeitperiodischen Hauptteil des Systems hergeleitet wird. Die Ergebnisse stimmen mit den Resultaten des Wellenleiterexperimentes überein.

Contents

1. Introduction **1**
1.1. Resonances in Time-Periodically Driven Classical Systems 2
1.2. Ultracold Quantum Gases 5
1.3. Photonic Waveguide Arrays 7
1.4. Outline of the Thesis 8

2. Floquet Theory **11**
2.1. Introduction to Floquet Theory in Quantum Mechanics 11
2.1.1. Transformation to Time-Independent Frame and Introduction of Floquet States 11
2.1.2. Time-Evolution Operator 13
2.1.3. Floquet Engineering in the High-Frequency Limit 14
2.2. Floquet Equation 15
2.2.1. Floquet Equation as Time-Independent Eigenvalue Equation 15
2.2.2. Floquet Theory in Floquet Hilbert Space 17
2.2.3. Properties of Floquet Modes and Expectation Values 20
2.2.4. Calculation of Transformation and Effective Hamiltonian 21

3. Floquet-Feshbach Resonance Theory **23**
3.1. Relation of Interaction Strength and Scattering Length in Ultracold Quantum Gases . 25
3.2. Theory of Quantum Scattering 26
3.2.1. The Key Concepts of Quantum Scattering Theory 26
3.2.2. Partial Wave Expansion 27
3.2.3. Scattering Length 29
3.2.4. The Pseudo Potential 30
3.3. Feshbach Resonances 32
3.3.1. Introduction into Feshbach Resonances 32
3.3.2. Short-Range Model of a Feshbach Resonance 34
3.4. Feshbach Resonances in Ultracold Gases 36
3.4.1. Magnetic Feshbach Resonances 37
3.4.2. Optical Feshbach Resonances 42
3.4.3. Radio-Frequency and Microwave Feshbach Resonances 43
3.4.4. Floquet-Feshbach Resonances 44
3.5. Floquet Scattering Theory 44
3.5.1. General Properties of Floquet Scattering 45
3.5.2. Floquet Partial Wave Expansion 47

3.6. Scattering Resonances in a Harmonically Driven Pseudo Potential 48
  3.6.1. Recursion Relation for Floquet Scattering States 49
  3.6.2. Continued Fraction Solution 51
  3.6.3. Tunability of the Scattering Length by the Drive 53
3.7. Floquet-Feshbach Resonance Theory for a Harmonically Driven Pseudo Potential . . . 55
  3.7.1. Floquet-Feshbach Resonance Theory 56
  3.7.2. Solving the Bound State Equations 61
  3.7.3. Position and Width of Floquet-Feshbach Resonances 67
  3.7.4. Recursion Coefficients at Resonance Positions 73
  3.7.5. Inelastic Scattering 74
3.8. Floquet-Feshbach Resonances for the Pseudo Potential with a Higher Harmonic Drive 75
  3.8.1. Numerical Calculation of the Floquet Scattering Problem 76
  3.8.2. Floquet-Feshbach Resonance Theory 76
  3.8.3. Losses and Asymmetries as an Influence of a Higher Harmonic Drive 80
  3.8.4. Results of the Floquet-Feshbach Resonance Theory for a Higher Harmonic Drive 83
3.9. Frequency Scales of the Model 85
3.10. Multi-Channel Model of a Feshbach Resonance with Periodically Driven Parameters . 86
  3.10.1. Periodically Driven Multi-Channel Model 87
  3.10.2. Investigation of the Periodically Driven Two-Level System 89
  3.10.3. Numerical Floquet Scattering Solution of the Driven Multi-Channel Model . . 92
  3.10.4. Floquet-Feshbach Resonances 93
  3.10.5. Analysis with the Floquet-Feshbach Resonance Theory 96
  3.10.6. Periodic Driving of a Low-Field Magnetic Feshbach Resonance 105
3.11. Conclusion and Outlook 108

4. Floquet-Bogoliubov Steady States **113**
4.1. Introduction into the Tomonaga-Luttinger Liquid Theory 115
4.2. Time-Independent Single Mode Bogoliubov Transformation 118
4.3. Floquet Single Mode Bogoliubov Transformation 121
  4.3.1. Floquet-Bogoliubov Transformation in Heisenberg Picture 121
  4.3.2. Finding Floquet States with the Floquet-Bogoliubov Transformation 124
  4.3.3. Floquet Vacuum State 126
4.4. Solution Method of the Floquet-Bogoliubov Equations: Stability and Instability Regions 128
4.5. Expectation Values and Stability Charts 131
4.6. Regularization of Diverging Expectation Values by a Finite Lifetime 138
4.7. Floquet-Steady States of the Tomonaga-Luttinger Liquid 144
  4.7.1. Floquet-Bogoliubov Solution and Transformation to Floquet Frame 145
  4.7.2. Results of the Floquet Analysis 146
4.8. Conclusion and Outlook 151

5. Dissipation Engineered Direction-Dependent Filter for Hamiltonian Quantum Ratchets **155**
5.1. Introduction to Waveguide Experiments 157
  5.1.1. Simulation of Schrödinger Equation with Waveguide Arrays 157
  5.1.2. Surface Plasmon-Polariton Waveguide Array Experiment 159

5.2. Hamiltonian Quantum Ratchet 160
  5.2.1. Lattice Model 160
  5.2.2. Floquet-Bloch Analysis 164
  5.2.3. Discrete Symmetries of the Ratchet Model 168
  5.2.4. Rectification of Transport in a Hamiltonian Quantum Ratchet 170
  5.2.5. Helical Bands and Relation to Topology 174
  5.2.6. Analysis of the Experimentally Motivated Driving Scheme 179
5.3. Introducing a Direction-Dependent Filter 183
5.4. Floquet S-Matrix Theory 187
  5.4.1. Floquet Lippmann-Schwinger Equation 187
  5.4.2. Møller Wave Operators and Floquet S Matrix for a Non-Hermitian Impurity . 191
  5.4.3. Finding Transmission and Reflection Coefficients with the Floquet S Matrix . 194
  5.4.4. Numerical Method for Calculating the Floquet T Matrix 196
5.5. Analysis of the Direction-Dependent Filter 197
  5.5.1. Understanding the Direction-Dependent Filter within Floquet S-Matrix Theory 197
  5.5.2. Floquet S-Matrix Analysis of the Direction-Dependent Filter 200
  5.5.3. Direction-Dependent Reflection 204
5.6. Results of the Waveguide Experiment 206
5.7. Conclusion and Outlook 208

6. Conclusion of the Thesis and Outlook 211

Bibliography 213

Appendices 233

A. Relating a Recursion Relation to a Continued Fraction 235

B. Floquet-Feshbach Resonance Theory for Multi-Channel Models 237

C. Non-Hermitian Floquet Theory 239

D. Inductive Generation of the Floquet-Bogoliubov Spectrum 241

E. Transformation to Rotating Frame in Floquet-Bogoliubov Transformation 243

1. Introduction

Periodic driving can drastically change the behavior of a physical system. One important consequence of an external drive is the phenomenon of resonance which can be seen in everyday life: If one turns up the volume of a radio, the sound waves can make objects to vibrate resonantly. In science, resonances have a prominent impact to various research topics. For example, in the construction of bridges resonances typically have to be avoided in order to prevent a collapse, and in medicine resonances are used in the commonly known magnetic resonance imagining method. The pattern formation in a fluid by a shaken receptacle is explained by a resonance that is related with the intrinsic properties of the fluid [1, 2]. In this thesis, we specialize to investigate resonant behavior in the realm of ultracold quantum gases and photonic waveguide arrays. Both systems offer a high tunability and accessibility which is in favor of investigating the effects of periodic driving. In ultracold gas experiments, atoms are cooled to very low temperatures such that their quantum nature is of relevance. The atoms can be trapped in various geometries with the use of external fields, even the interaction strength between the atoms is tunable. This makes ultracold gas experiments a seminal way of simulating and probing a wealth of concepts of theoretical physics [3]. Photonic waveguide arrays are used as a simulator of quantum wave mechanics. The fabrication process offers to create arrays in various geometries which is for the benefit of experimentally realizing periodically driven systems with intriguing properties [4].

In this thesis, we investigate the effect of periodic driving with the methods of theoretical physics. Here, the silver bullet is to use Floquet theory since it is in particular capable of generalizing the celebrated concept of an eigenbasis to time-periodic Hamilton operators. These Floquet eigenstates, which are called Floquet steady states, can have fascinating properties that are tunable by the periodic drive. The Floquet theory predicts that the nature of a periodically driven system significantly depends on the frequency of the drive. One path of research considers driving frequencies that are much larger than the natural energy scale of the system. Here, no resonances occur and the system follows the dynamics of an effective model. For example, artificial gauge fields for ultracold neutral atoms can emerge as a consequence of such a drive [5]. We, however, are especially interested in what happens if the driving frequency matches with the energy scale of the system. In this case, resonances emerge, that have intriguing physical consequences. For instance, in a resonantly driven ultracold quantum gas standing density wave patterns [2, 6] and the collective emission of matter-wave jets [7] have been observed. In order to get an impression on the influence of resonances on periodically driven systems, the reader is introduced in Sec. 1.1 to resonant behavior in classical mechanics. Section 1.2 gives an overview on ultracold quantum gases, while in Sec. 1.3 photonic waveguide arrays are briefly discussed. Section 1.4 is devoted to an outline of the thesis.

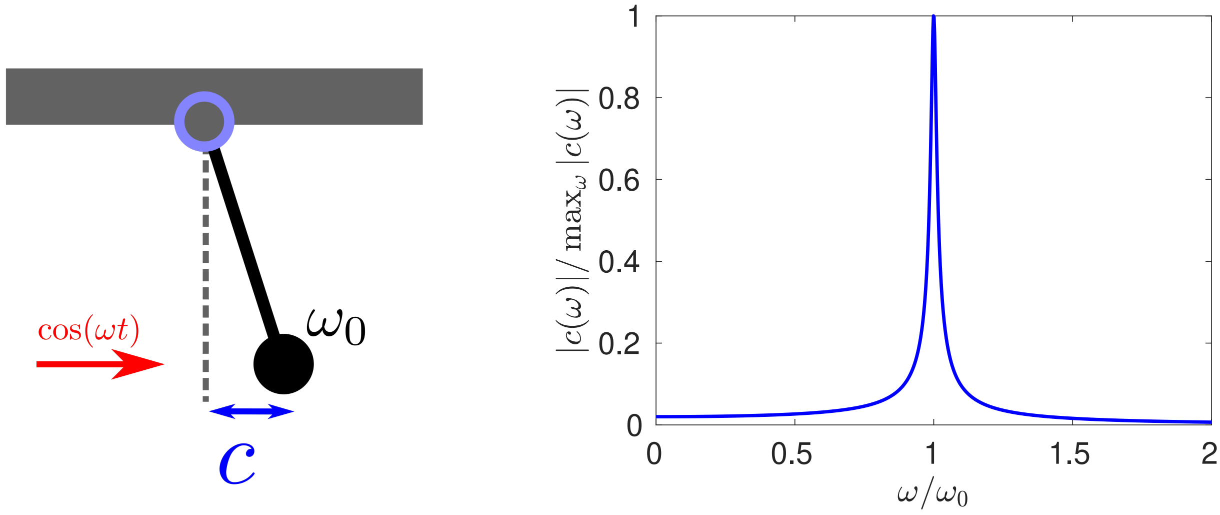

(a) **(b)**

Figure 1.1.: (a) Sketch of an externally forced mathematical pendulum, (b) amplitude $c(\omega)$ of the long-time behavior of the oscillator, that is induced by the external drive, in dependence of the driving frequency with finite damping.

1.1. Resonances in Time-Periodically Driven Classical Systems

Let us begin with one of the simplest systems possible: The harmonic oscillator subject to a time-periodic force. As sketched in Fig. 1.1 (a), a possible setup consists of a pendulum with eigenfrequency ω_0 that is periodically forced by an external drive with frequency ω. Since small but finite friction is assumed, the transient motion decays in a finite time. In the long-time limit the system oscillates with the frequency ω of the external drive. It is well-known from classical mechanics [8] that the response of the oscillator shows a prominent peak that is centered around the eigenfrequency ω_0, which is exemplary shown in Fig. 1.1 (b). This is the prototypical example of a resonance, which in general can be defined as an enhanced response induced by an external influence [9]. The frequency, where the response is maximal, is called as resonance frequency. The resonance frequencies are closely related to the eigenfrequencies of the system, as it can be seen in Fig. 1.1 (b) for the driven harmonic oscillator. A small difference of the resonance frequency and the eigenfrequency ω_0, which is hard to see in Fig. 1.1, comes due to the finite damping. At last, we emphasize that the resonance peak shown in Fig. 1.1 (b) is, in a good approximation, symmetric in the close vicinity of the resonance frequency.

Next, we increase the complexity and consider two coupled harmonic oscillators as sketched in Fig. 1.2 (a). Following Refs. [9, 10], both oscillators have a different eigenfrequency, as example we consider the case of $\omega_2 = 1.2\,\omega_1$, while solely oscillator 1 is subject to the external monochromatic drive. Figures 1.2 (b), (c) display amplitudes of the long-time behavior of both oscillators as a function of the driving frequency. The amplitude of oscillator 1 shows a broad resonance peak near

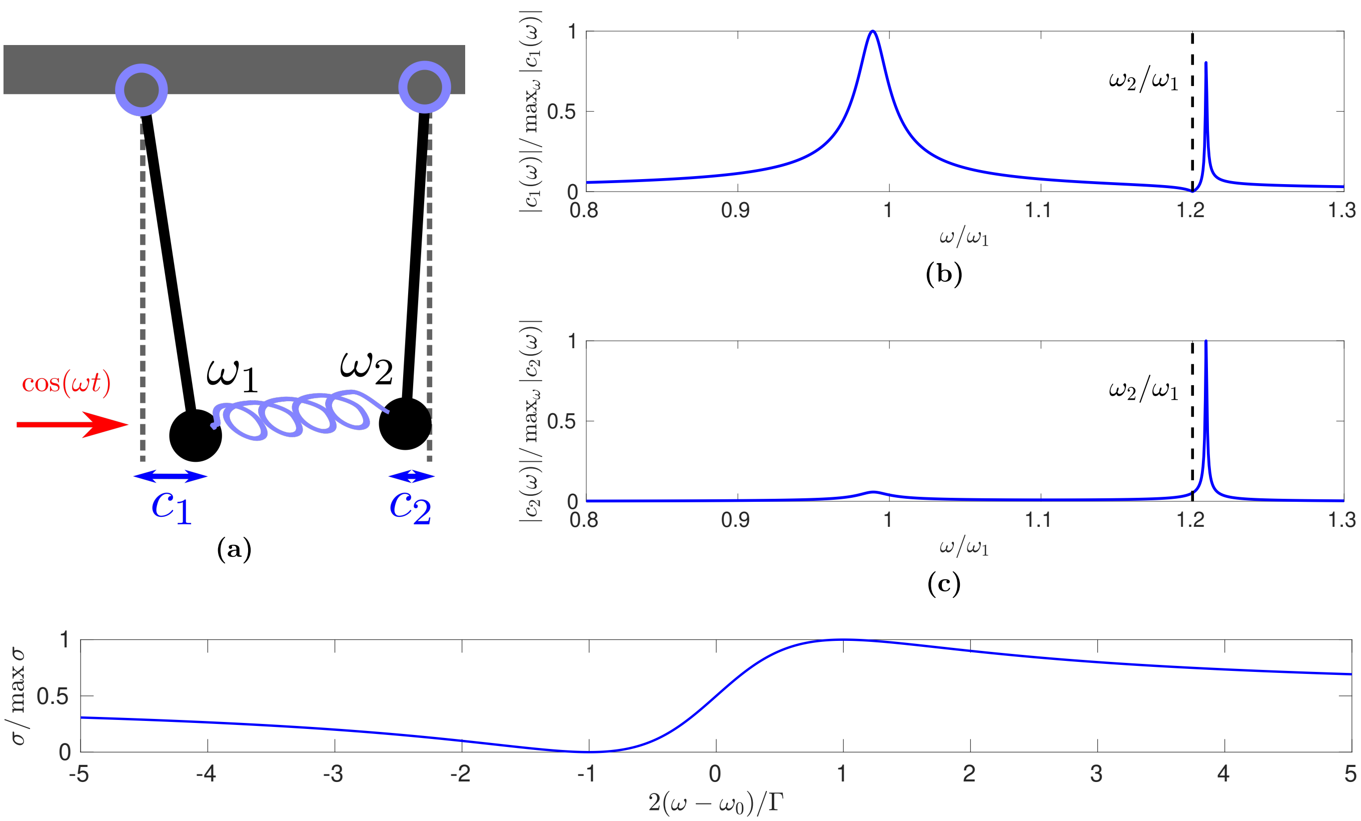

(a)

(b)

(c)

(d)

Figure 1.2.: (a) Sketch of two harmonic oscillators which are coupled by a spring. The external drive acts on oscillator 1, following Ref. [10]. (b), (c): Blue lines shown the amplitudes $c_i(\omega)$, $i = 1, 2$, of the long-time behavior induced by the external monochromatic drive. The black dashed line marks the eigenfrequency ω_2. (d) Plot of the Fano formula $\sigma = (x + q)^2/(x^2 + 1)$ with $x = 2(\omega - \omega_0)/\Gamma$ and $q = 1$ [9, 10]. Here, ω_0 is the resonant frequency and Γ corresponds to the width of the resonance state, for details see Ref. [9].

the eigenfrequency ω_1 while the amplitude of oscillator 2 is enhanced near $\omega_2 = 1.2\ \omega_1$. Again, the lineshapes of those peaks are, in a good approximation, symmetric in the vicinity of the resonance frequencies. Near ω_2, however, the response of oscillator 1 differs from what we have learned so far, since the near resonant maximum the response gets zero, which adds asymmetry in the shape of this peak. It is the combination of the external forcing and the motion of the second oscillator that forces the first oscillator to the zero amplitude [10]. This intriguing behavior is related to the so called Fano resonances [9, 10] named after U. Fano, who derived a theory that explains asymmetric lineshapes found in spectroscopy experiments. His seminal work [11] considered the photoionization of an atom. He assumed that this process can be achieved via two paths: A direct process and a process involving an autoionized state [9, 11]. U. Fano found that the interference of the two paths leads to an asymmetric lineshape in a cross section [9, 11–13], which is exemplarily shown in Fig. 1.2 (d). Fano's theory further describes an asymmetric response near a resonance in a wide class of physical systems [9, 11, 12], including nuclear physics [14], spectroscopy experiments [15, 16], waveguide arrays [9, 10, 17] and atomic physics [18].

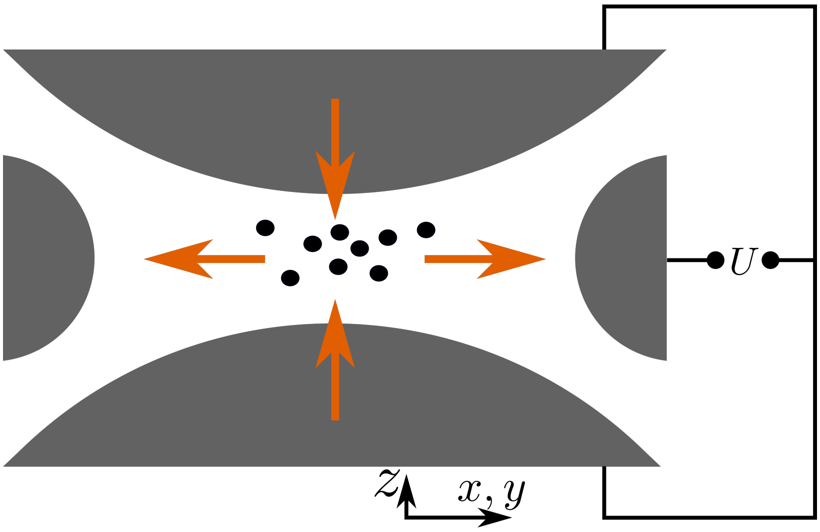

Figure 1.3.: Sketch of a cut through a quadrupole ion trap, based on Ref. [20]. Bottom right is a coordinate system. On top and bottom the end-cap electrodes are sketched in gray, left and right the hyperbolic ring in gray. A voltage U is applied between ring and end caps. Black dots mark charged particles in the center of the trap. The orange arrows exemplarily sketch the direction of the force on the particles that is induced by the electric field. For the shown configuration the particles are pushed outside the trap in radial direction, while the force acts towards the center in z-direction. The periodic driving of the voltage U can lead to a configuration where in average the particles are forced towards the center in all directions.

Now we discuss the quadrupole ion trap which hosts a third class of resonance that is of relevance to this thesis. Since the trap has been invented by W. Paul it is also known as Paul trap. For the invention of the trap W. Paul was awarded by the shared Physics Nobel prize of the year 1989 [19,20]. A possible setup of a Paul trap is sketched in Fig. 1.3. It consists of a hyperbolic ring combined with two end-cap electrodes facing each other on bottom and top [20]. An electric potential is applied between the ring and the end-cap electrodes, such that the motion of charged particles in the center of the trap is generated by a quadratic electric potential [20]. As a consequence of Gauss law, this potential either can be attractive in z-direction or in radial direction, but it cannot be attractive in both directions at the same time [19, 20]. In the static case, the Paul trap does not work as a trap, since charged particles are always pushed to the outside. This issue is resolved with the aid of time-periodic driving. The voltage between ring and end-cap electrodes is varied sinusoidally around an offset. As a result, the periodic drive stabilizes for carefully chosen parameters the motion of charged particles such that they remain inside the trap. On a phenomenological level, the drive induces an effective potential that acts on average attractive on the charged particles such that it traps the particles in the center. Mathematically, this behavior can be understood by showing that the Newton equations of motion for a charged particle in the time-dependent electric potential can be mapped onto the dynamic equations of an undamped parametric oscillator [19].

A parametric oscillator is a harmonic oscillator with a time-dependent eigenfrequency. In the undriven case, this system oscillates with its eigenfrequency, but, at finite driving, a parametric resonance can occur. If the undamped parametric oscillator is driven with twice its eigenfrequency, its amplitude grows exponentially in time. This behavior can be made visible by the physics of a swing, which serves as an everyday-life example of a parametric oscillator. Here, the case of parametric resonance occurs if a person swings and thus periodically imparts energy into the motion of the swing. For driving frequencies away from the condition of a parametric resonance, the motion remains bounded. If, for example, a swing is rocked with a too low frequency, the amplitude of the oscillation stays at small values. The absence of parametric resonance is desired for a Paul trap, since in this case the motion of charged particles is stable in all directions [19,20], as a result the particles remain in the center of the trap. This demonstrates that the Paul trap with a time-dependent electric voltage is able to trap charged particles.

In a different configuration, the Paul trap operates as a mass spectrometer [19, 20]. Here, the parametric resonance turns into an advantage, since it is used to selectively stabilize the motion of particles in a certain mass interval, while the trajectories for particles with masses outside this interval leave the trap. If the relative width of this interval is small, this can be used in order to determine the mass of the particles with a good accuracy [20].

Each classical system that is discussed above gives host to a different type of resonance. These resonances are of relevance to the main discussion of this thesis. In the following we give an introduction to ultracold quantum gases and photonic waveguide arrays, which are the physical platforms that are considered during this work.

1.2. Ultracold Quantum Gases

When atomic gases are cooled to ultracold temperatures, the quantum nature of matter becomes of particular relevance. For bosonic particles a quantum-statistical phase transition to a Bose-Einstein condensate occurs. The Bose-condensed phase is allocated with a macroscopic occupation of the lowest energy state. In order to experimentally obtain a Bose-Einstein condensate in a dilute gas, the gas has typically to be cooled to the micro- or nanokelvin regime by a combination of laser cooling and evaporative cooling while it is trapped by magnetic or optical fields [18, 21–23].

The theory of Bose-Einstein condensation goes back on a work of S. N. Bose from the year 1924 [24]. Based on this work, A. Einstein predicted the phase transition to a Bose-Einstein condensate in 1925 [25]. Although the theoretical discovery of Bose-Einstein condensation was in the 1920s, it took until 1995 for its first observation in an experiment. This has been achieved by the team of C. E. Wieman and E. A. Cornell with rubidium [26] and by the team of W. Ketterle with sodium atoms [27]. The experimental realization was awarded by the Nobel prize in Physics of the year 2001.

A key feature of ultracold quantum gases is the possibility to tune the interaction strength via a Feshbach resonance. This tunability is given by the fact that the interaction strength in ultracold gas systems is determined by atomic collisions. The scattering of atoms at ultracold temperatures is fully characterized by the scattering length a which corresponds in a rough approximation to the radius of the scattering cross sections of the atoms. The Born approximation of quantum scattering finds that the scattering length is proportional to the interaction strength [28]. Using a magnetic Feshbach resonance the scattering length, and thus the interaction strength, can be tuned to almost arbitrary positive and negative values by controlling an external magnetic field [14,18,29]. Feshbach resonances have a pronounced impact on the research with ultracold atoms: There are atomic species where the intrinsic scattering length does not allow for the attainment of a Bose-Einstein condensate, such as ^{85}Rb, ^{133}Cs and ^{39}K [18,30]. Optimal conditions for the attainment of a Bose-Einstein condensate are reached if the scattering length is positive and not too large or too small [18]. A Feshbach resonance can tune the scattering length into the desired interval and thus enables to produce a considerably large Bose-Einstein condensate at all [18,31–33]. Furthermore, Feshbach resonances are used to obtain noninteracting condensates [18,32], in which dipolar effects can be dominant [34].

A few years after the first experimental realizations of a Bose-Einstein condensate, the investigation of degenerate Fermi gases gained interest [18,28,35–37]. Also in these systems the interaction is controllable by the use of Feshbach resonances. A major research topic in the area of degenerate Fermi gases is the investigation of the crossover between the Bardeen-Cooper-Schrieffer superfluid of fermionic atoms and Bose-Einstein condensate of fermionic molecules (BEC-BCS crossover) [28,37–39]. The Feshbach tuning of the scattering length is key for the experimental observation of the BEC-BCS crossover [18,39].

One of the most prominent research directions in the field of ultracold quantum gases are the optical lattices for ultracold atoms [3,40]. These lattices are typically created by a standing wave pattern of counter-propagating laser beams. Depending on the spatial configuration of these laser beams, various types of lattice structures such as cubic, hexagonal and Kagome have been realized [41]. The combination of an optical lattice and a Feshbach resonance leads to a high controllability of the ultracold gas system. Thus, these optical-lattice systems are predestinated for the investigation of quantum many-body physics that is described by well-known theoretical models, such as the Bose-Hubbard or the Fermi-Hubbard model [3]. In addition, ultracold gases are accessible due to powerful detection techniques, for example the time-of-flight method [3,42]. In this method the quantum gas is released from the trapping potential, such that it expands freely, provided that the interactions between the atoms are negligible at this stage. After a finite time the density distribution is measured. Correlation functions of the quantum many-body state are obtained out of the experimental data [3,42]. Further measurement techniques include single-atom detection, which is used to measure density distributions and correlation functions [41,43,44]. A famous result of ultracold gas experiments with optical lattices is the measurement of the quantum phase transition from a superfluid to a Mott insulator for bosonic atoms [3,45–49]. In order to achieve this, Ref. [46] loaded ultracold ^{87}Rb atoms into a three-dimensional optical lattice. The above mentioned quantum phase transition has been observed by ramping the depth of the lattice, which changes the hopping amplitude relative to the interaction strength in the Bose-Hubbard model. Correlations have been measured using the time-of-flight method. There is a plethora of further studies that involve an optical lattice, such as optical lattice clocks [50], Talbot interferometry [51], the realization of the Hofstadter model [5], the moving and merging of Dirac cones in a honeycomb lattice [52] and the experimental realization of a

Mott insulator of fermionic atoms [53]. By a strong confinement in certain spatial directions one- and two-dimensional systems can be realized. In the 1D case, the strongly correlated quantum physics, that is predicted by the theoretical models, is observed [3, 40, 54–61]. These studies demonstrate the impact of optical lattices to the understanding of quantum many-body systems and show their ability to simulate a wide class of models that appear in condensed matter physics. For example, the vision of Ref. [53] is to use the knowledge found in the ultracold gas experiment for the deeper understanding of superconductivity at high temperatures.

The high tunability of ultracold quantum gases enables for time-periodic driving. A famous effect that is related to a periodic drive is called dynamic localization [62–64]. The periodic shaking of an optical lattice with a driving frequency that is larger than the width of the quasienergy band can be described by an effective time-independent model within the tight-binding approximation. The time-periodic drive renormalizes the coupling strength of this effective model [63]. Ref. [64] shows that the ballistic spreading of an ultracold atomic cloud follows the predictions of the effective model. For carefully chosen driving parameters the effective coupling strength vanishes, such that the atom cloud is localized due to the time-periodic driving of the lattice. Other seminal works continued this idea and observed the quantum phase transition between a superfluid and a Mott insulator just by tuning the parameters of the drive [65–67]. This is possible, since the renormalized coupling constant can be tuned relative to the interaction strength of the particles by the periodic driving. Further prominent examples of exotic Floquet effects are the photon-assisted tunneling [68, 69], the creation of artificial gauge fields for neutral atoms [5, 70] and the realization of topologically nontrivial phases [4, 71–74]. Time-periodic driving can also be used in order to induce resonant behavior. Ref. [75] applies a time-dependent magnetic field in the vicinity of a Feshbach resonance and observes the excitation of collective modes of a Bose-Einstein condensate. Further, Faraday waves, which are related to a parametric resonance, have been observed in ultracold gas experiments with periodic driving [2, 76–78], and the collective emission of matter-wave jets of a periodically driven Bose-Einstein condensate has been reported in Ref. [7]. Periodically driven interacting quantum many-body systems suffer from heating at long timescales, since the periodic drive imparts energy into the system [79–82]. Reference [83] found with the use of an exact space-time mapping that heating can be completely suppressed for driving parameters, at which the periodically driven system can be mapped to a static one. The absence of heating is related to Fano resonances that appear in the heating rate [83].

1.3. Photonic Waveguide Arrays

Another promising research direction is given by photonic waveguide arrays. Light can be guided in optical fibers which then act as waveguides. If multiple photonic waveguides are arranged in an array or a lattice structure, they allow for the investigation of various effects of fundamental research. Prominent examples are the observation of Fano resonances [9] and the field of topological photonics, where topological effects are harnessed in order to suppress unwanted scattering in photonic structures [84]. In this thesis, we focus on the dielectric and plasmonic waveguide arrays which either operate with light at an optical wavelength or surface plasmon polaritons, a collective excitation of electromagnetic waves and conduction electrons at the interface of a metal and a dielectric. Both system are highly accessible in an experiment and are used to simulate the dynamics in Schrödinger wave mechanics with time-dependent Hamiltonians [85]. This is possible by the quantum-optical analog, which relates the time-evolution of Schrödinger equation to the propagation of light in the waveguides, which is governed by the paraxial Helmholtz equation. Time-periodic Hamiltonians are realized by a periodic change of the waveguide geometry along the propagation direction. These properties have led to the implementation of artificial gauge fields for photons by a periodically bending of the waveguide center [86–88] as well as the observation of dynamic localization in a waveguide system [88, 89]. Further, Floquet topological insulators have been realized in waveguide arrays [4, 90] and the stability of edge states to time-periodic perturbations has been tested [87, 91, 92]. In optics, an imaginary refractive index leads to a spatially decaying electric field, a fact that is known as Beer-Lambert law. This effect implies that with optical waveguide arrays non-hermitian dynamics can be implemented [93, 94], with a plethora of interesting phenomena such as exceptional points [95], the non-hermitian skin effect [96], non-hermitian transparency [97] and the realization of a fast, dissipative Thouless pump [98].

1.4. Outline of the Thesis

The main part of the thesis is structured into three chapters. As prelude, Chapter 2 gives a comprehensive review of Floquet theory formulated in the language of quantum mechanics. This chapter is at the heart of the thesis, since all three main chapters are based on the Floquet theory. The review starts by introducing a time-dependent transformation to the Floquet frame that enables to generalize the concept of eigenstates to time-periodically driven systems. In this course, Floquet Engineering within the high-frequency approximation is discussed. At last, a full theory that allows for the calculation and analysis of Floquet eigenstates is introduced.

Chapter 3 contains the Floquet-Feshbach resonance theory. In ultracold gas experiments, the scattering length is highly tunable with the use of Feshbach resonances, which are closely related to the concept of Fano resonance discussed in sec. 1.1 [9]. Since the scattering length dictates the interaction strength in ultracold gas systems, this implies a high controllability of the inter-particle interaction. A common way to achieve this in an experiment is the use of a magnetic Feshbach resonance, where the scattering length is adjustable by an external static magnetic field. However, the properties of a magnetic Feshbach resonance, such as position and width, are not variable. An optical Feshbach resonance overcomes these limitations, in this method the resonances are highly tunable, but a large atom loss limits their applicability. In this thesis, we consider an alternative approach proposed in Ref. [99]. The idea is to apply a time-periodic magnetic field in the vicinity of a magnetic Feshbach resonance. As a result, the periodic drive induces new resonances. In this chapter we derive the Floquet-Feshbach resonance theory which relates these driving-induced scattering resonances to the well-known concept of a Feshbach resonance. Furthermore, the theory yields an analytic formula that describes the scattering length in the vicinity of a resonance. Results are found for the harmonically driven pseudo potential, which serves as a simple model that captures all the relevant physics. For this model, driving-induced scattering resonances tune the scattering length to arbitrary positive and negative values. The Floquet-Feshbach resonance theory finds that both position and width of these resonances are controllable by the parameters of the periodic drive. Furthermore, our theory proves that atom loss due to inelastic collisions is minimal, which is beneficial for an experimental realization. The Floquet-Feshbach resonance theory generalizes to driving schemes that include higher harmonics. In this case, resonant atom loss is present. However, the lineshape of the loss coefficient is asymmetric. This asymmetry is connected to the Fano physics in the Floquet structure of the Hilbert space and leads to a smaller atom loss as compared to an optical Feshbach resonance. The last part contains a multi-channel model of a magnetic Feshbach resonance under the influence of a time-periodic magnetic field. This model goes beyond the description of a simple pseudo potential and allows for a more accurate description of a possible experimental realization. In this case, the periodic drive influences the system in two ways: It induces new resonances with properties that depend on the details of the drive and it engineers already existing Feshbach resonances. An analysis of these resonances is performed with the use of the Floquet-Feshbach resonance theory. We report that many of the advantageous resonance properties found for the driven contact potential are also present in the multi-channel model.

Chapter 4 is devoted to the Floquet-Bogoliubov transformation. This theory generalizes the concept of a Bogoliubov transformation to the periodically driven case. In order to find results for a concrete physical model, we specialize to the Lieb-Liniger model that describes a bosonic gas in 1D with a short range interatomic potential. Again, a time-periodic modulation of the interaction strength is assumed. In contrast to investigation of Floquet-Feshbach resonances within scattering theory, here the many-body nature of the system is of relevance. Due to the entanglement and interactions between the particles nontrivial correlations can appear in a quantum many-body system. The low-energy excitations of the Lieb-Liniger model are determined by the Tomonaga-Luttinger Liquid theory which in turn can be solved via a Bogoliubov transformation. The Floquet steady state solution of the periodically driven model is found by introducing a Floquet-Bogoliubov transformation. The Floquet-Bogoliubov transformation distinguishes two cases: In the stability regions this method finds the quasienergy spectrum and the Floquet steady states of a time-periodic Hamiltonian that is quadratic in bosonic operators. In the instability regions, however, no such Floquet solution is possible. Instead, the periodic drive induces a parametric resonance, a concept that is introduced in Sec. 1.1 with the Paul trap. Using the Floquet-Bogoliubov transformation, stability charts and selected expectation values are discussed. As a central result we find that the average number of excitations diverges in the instability regions, signaling the presence of a parametric resonance. By introducing a finite lifetime of the bosons these divergences regularize to finite maxima. This knowledge is finally applied to the periodically driven Tomonaga-Luttinger Liquid using which correlation functions are calculated. The Floquet-Bogoliubov theory predicts that the periodic driving of the interacting one-dimensional bosonic gas induces standing density wave patterns at a wavelength that is determined by the condition of a parametric resonance.

A direction-dependent filter for a Hamiltonian quantum ratchet is discussed in Chapter 5, where we remain in the case of one dimension and discuss dynamic transport phenomena in the ratchet model as well as the scattering by a time-periodic, dissipative impurity. The details of the model are designed to fit with the conditions of the experimental realization of the ratchet and the filter within a surface plasmon-polariton waveguide experiment. The first part of the chapter contains a ratchet model that is based on a time-periodically driven Su-Schriffer-Heeger Hamiltonian. If the driving frequency is on resonance with the sublattice oscillations that appear in this model, directed transport with the velocity of one unit cell per driving period is possible. An analysis of the quasienergy spectrum with the use of Floquet-Bloch theory finds out that maximal transport is related to a nontrivial topology. Further, the rectification of transport by the ratchet scheme is analyzed in detail using a symmetry analysis of the model. We find that both magnitude and direction of the rectified current depend on the initial state. This is unfortunate for systems where an experimentalist has little control over the initial state, since in this case a directed current might not be observed. The direction-dependent filter is designed to circumvent this issue. The filter absorbs states that move in a certain direction while the states that move in the other direction pass the filter almost unimpaired. The working principle of the filter is elaborated. In the mathematical description, this filter is introduced as a time-periodic, non-hermitian impurity operator. For calculating transmission coefficients, we derive a Floquet S-matrix theory in the case of a time-periodic, non-hermitian impurity. Asymmetric transmission coefficients, that characterize the quality of the filter, are a central result. Using the Floquet S-matrix method we analyze the properties of this filter theoretically. Our findings agree with the results of the waveguide experiment.

2. Floquet Theory

Floquet theory plays a central role in this thesis. It allows a structured analysis of the time-dependent Schrödinger equation with a Hamiltonian periodic in time. In Sec. 2.1 we introduce Floquet theory to quantum mechanics and show that Floquet theory generalizes the concept of eigenstates to periodically driven systems. It is briefly mentioned how properties of a quantum system can be tailored by time-periodic driving in the sense of "Floquet Engineering". Sec. 2.2 deals with the Floquet equation which is an eigenvalue equation for finding the Floquet steady states of the time-periodic Hamiltonian.

2.1. Introduction to Floquet Theory in Quantum Mechanics

The goal of the Floquet description of quantum systems is to analyze and solve the time-dependent Schrödinger equation

$$i\hbar\partial_t|\psi(t)\rangle = H(t)|\psi(t)\rangle, \tag{2.1}$$

where the Hamiltonian $H(t)$ is time-periodic with period T, obeying $H(t) = H(t+T)$. The corresponding driving frequency is fixed via the relation $\omega = 2\pi/T$. A quantum system with time-periodic Hamiltonian $H(t)$ is called Floquet system or periodically driven quantum system [63,100]. The periodic driving of Hamiltonian $H(t)$ introduces an energy scale given by $\hbar\omega$ named as drive quantum.

2.1.1. Transformation to Time-Independent Frame and Introduction of Floquet States

Floquet theory was introduced by the French mathematician Gaston Floquet in the year 1883 as a theory for solving systems of coupled linear ordinary differential equations with periodic coefficients [101]. Floquet theory applied to Schrödinger equation (2.1) states the formal existence of a time-periodic unitary transformation $U_\mathrm{P}(t) = U_\mathrm{P}(t+T)$, that transforms equation (2.1) to a Schrödinger equation with a time-independent Hamiltonian [63,102–104]

$$i\hbar\partial_t|\tilde{\psi}(t)\rangle = \tilde{H}_\mathrm{eff}|\tilde{\psi}(t)\rangle. \tag{2.2}$$

Here the transformed state is given by $|\tilde{\psi}(t)\rangle = U_\mathrm{P}^\dagger(t)|\psi(t)\rangle$, and the time-independent effective Hamiltonian reads

$$\tilde{H}_\mathrm{eff} = U_\mathrm{P}^\dagger(t)H(t)U_\mathrm{P}(t) - i\hbar U_\mathrm{P}^\dagger(t)\frac{\partial}{\partial t}U_\mathrm{P}(t). \tag{2.3}$$

Note, that these statements are proven for finite-dimensional Hilbert spaces, in case of an infinite-dimensional space the transformation $U_{\mathrm{P}}(t)$ might not exist [63, 100, 105]. If a transformation $U_{\mathrm{P}}(t)$ exists, it is not unique [63]. Indeed, if $U_{\mathrm{P}}(t)$ is multiplied by a time-independent unitary matrix Q, the corresponding unitary transformation $U'_{\mathrm{P}}(t) = U_{\mathrm{P}}(t)Q$ also transforms the Schrödinger equation (2.1) to a time-independent frame $|\tilde{\psi}'(t)\rangle = U'^{\dagger}_{\mathrm{P}}|\psi(t)\rangle$ with the effective Hamiltonian

$$\tilde{H}'_{\mathrm{eff}} = U'^{\dagger}_{\mathrm{P}}(t)H(t)U'_{\mathrm{P}}(t) - i\hbar U'^{\dagger}_{\mathrm{P}}(t)\frac{\partial}{\partial t}U'_{\mathrm{P}}(t) = Q^{\dagger}\tilde{H}_{\mathrm{eff}}Q. \tag{2.4}$$

The choice of Q solely alters the description in the Floquet frame. However, we will see that the physics stays unchanged.

The time-independent effective Hamiltonian (2.3) allows to generalize the concept of eigenstates to the time-dependent Floquet setting. Consider therefore the eigenvalue equation of the effective Hamiltonian [63, 104]

$$\tilde{H}_{\mathrm{eff}}|\tilde{\phi}_{\alpha}\rangle = \epsilon_{\alpha}|\tilde{\phi}_{\alpha}\rangle. \tag{2.5}$$

Here the quasienergy ϵ_{α} is introduced and labeled by the quantum number α. The so called Floquet modes are defined by mapping the eigenstates of the effective Hamiltonian back to the original frame [63, 104]

$$|\phi_{\alpha}(t)\rangle = U_{\mathrm{P}}(t)|\tilde{\phi}_{\alpha}\rangle. \tag{2.6}$$

The Floquet modes (2.6) are time-periodic with period T and form a basis at each time. Based on the Floquet modes (2.6) the Floquet states are defined as [63, 100, 106]

$$|\psi_{\alpha}(t)\rangle = e^{-i\epsilon_{\alpha}(t-t_0)/\hbar}|\phi_{\alpha}(t)\rangle. \tag{2.7}$$

The Floquet states (2.7) solve the time-dependent Schrödinger equation (2.1) and are thus regarded as the steady states of the time-dependent Hamiltonian $H(t)$. Here, the above formalism is used in order to define quasienergies and Floquet modes and not for calculating them explicitly. Reference [104] goes beyond this and finds a time-dependent transformation that enables to solve a Floquet problem for quasienergies and Floquet modes (2.6). We present this transformation in Subsec. 4.7.1.

It is important to mention that there is an ambiguity in defining the quasienergies ϵ_{α} and the Floquet modes $|\phi_{\alpha}(t)\rangle$. The quasienergies can be shifted by an integer multiple of $\hbar\omega$, while the Floquet modes are multiplied by a corresponding factor

$$\begin{aligned} \epsilon_{\alpha} \quad &\rightarrow \quad \epsilon_{\alpha,m} = \epsilon_{\alpha} + m\hbar\omega, && \text{(2.8a)} \\ |\phi_{\alpha}(t)\rangle \quad &\rightarrow \quad |\phi_{\alpha,m}(t)\rangle = e^{im\omega t}|\phi_{\alpha}(t)\rangle. && \text{(2.8b)} \end{aligned}$$

with $m \in \mathbb{Z}$ [100]. Substitution (2.8) is chosen such that the factor $m\hbar\omega$ cancels out in the definition of the Floquet states (2.7). We will see that also the time-evolution operator is unimpaired by substitution (2.8). It follows that m can be chosen such that all quasienergies lie in an interval of length $\hbar\omega$, while the solutions for different m are physically equivalent. A common choice is to locate the quasienergies in the so called first Floquet Brillouin zone $[-\hbar\omega/2, \hbar\omega/2[$ by defining $\epsilon_{\alpha,m=0} \in [-\hbar\omega/2, \hbar\omega/2[$. In order to keep the notation simple, in the following the index m is dropped for quantities in the first Floquet Brillouin zone, such as $\epsilon_{\alpha} = \epsilon_{\alpha,m=0}$.

2.1.2. Time-Evolution Operator

The time-evolution operator of a Floquet system can be constructed by using the properties of the Floquet modes (2.6): As the Floquet modes (2.6) form a basis at each time, any arbitrary state $|\psi\rangle$ can be expanded into them $|\psi\rangle = \sum_\alpha |\phi_\alpha(t_0)\rangle\langle\phi_\alpha(t_0)|\psi\rangle$. Thus, only the time-evolution of the Floquet modes is important, which is easily found with the use of Eq. (2.7), yielding the time-evolution operator in the form

$$U(t,t_0) = \sum_\alpha e^{-i\epsilon_\alpha(t-t_0)/\hbar}|\phi_\alpha(t)\rangle\langle\phi_\alpha(t_0)|. \tag{2.9}$$

At first, note the conceptual similarity of Eq. (2.9) to the time-evolution operator of a time-independent quantum system. Instead of eigenenergies, the quasienergies ϵ_α appear in Eq. (2.9) as dynamical phase, instead of the eigenfunctions the Floquet modes (2.6) show up. In summary, the time evolution of a time-periodic quantum system can be seen as a time-dependent coherent superposition of its Floquet steady states, where the amplitude of each steady state is determined at initial time. A more compact expression of the time-evolution operator (2.9) is found by

$$U(t,t_0) = U_{\mathrm{P2}}(t,t_0)\exp\left[-\frac{i}{\hbar}H_{\mathrm{eff}}(t-t_0)\right], \tag{2.10}$$

with the two-point micromotion operator $U_{\mathrm{P2}}(t,t_0) = \sum_\alpha |\phi_\alpha(t)\rangle\langle\phi_\alpha(t_0)| = U_{\mathrm{P}}(t)U_{\mathrm{P}}^\dagger(t_0)$ and the effective Hamiltonian in the original frame $H_{\mathrm{eff}} = \sum_\alpha \epsilon_\alpha|\phi_\alpha(t_0)\rangle\langle\phi_\alpha(t_0)| = U_{\mathrm{P}}(t_0)\tilde{H}_{\mathrm{eff}}U_{\mathrm{P}}^\dagger(t_0)$ [63]. With Eq. (2.10) it directly follows that the time-evolution operator for a single period is fully determined by the effective Hamiltonian

$$U(t_0+T,t_0) = e^{-iH_{\mathrm{eff}}T/\hbar}. \tag{2.11}$$

Equation (2.11) is of interest as it allows for calculating the quasienergies and Floquet modes at initial time by solving the eigenvalue problem of the time evolution operator

$$U(t_0+T,t_0)|\phi_\alpha(t_0)\rangle = e^{-i\epsilon_\alpha T/\hbar}|\phi_\alpha(t_0)\rangle. \tag{2.12}$$

If the time-evolution operator is known, Eq. (2.12) is a common method for finding the quasienergy spectrum [72, 100, 107], but it only yields the Floquet modes at initial time and not the full time dependence. However, with the knowledge of $U(t_0+T,t_0)$ the time-evolution operator at integer multiples of the driving period T, i.e. the stroboscopic time evolution, can be found by

$$U(t_0+nT,t_0) = U(t_0+T,t_0)^n,\ n\in\mathbb{N}. \tag{2.13}$$

This shows together with Eq. (2.11) the key result that the stroboscopic time evolution of a Floquet system is fully determined by the effective Hamiltonian in the original frame H_{eff} and emphasizes the importance of H_{eff} in Floquet physics [108].

A further expression of the time-evolution operator $U(t,t_0)$ that is found in common literature [63, 102, 109] is given by:

$$U(t,t_0) = U_{\mathrm{P}}(t)\exp\left[-\frac{i}{\hbar}\tilde{H}_{\mathrm{eff}}(t-t_0)\right]U_{\mathrm{P}}^\dagger(t_0). \tag{2.14}$$

The merit of equation (2.14) is that it divides the time-evolution into three descriptive steps. At initial time, the system undergoes a "kick" [102] described by the transformation matrix to the Floquet frame $U_\mathrm{P}^\dagger(t_0)$. Afterwards it is evolved by the effective Hamiltonian $\tilde{H}_\mathrm{eff}$ from initial to final time while at final time a second kick $U_\mathrm{P}(t)$ appears.

At last, note that the time-evolution operator of a Floquet system is independent on the choice of the Floquet Brillouin zone. This is seen most easily with Eq. (2.9) where any additional factor introduced by Eq. (2.8) cancels out. Also the choice of multiplying the transformation $U_\mathrm{P}(t)$ by any time-independent unitary matrix Q does not have an effect on the time-evolution, as with Eqns. (2.4) and (2.14) is is directly verified that an additional unitary Q cancels out.

2.1.3. Floquet Engineering in the High-Frequency Limit

Equation (2.14) shows that the time-evolution of a Floquet system is fully determined by the effective Hamiltonian $\tilde{H}_\mathrm{eff}$ and the transformation $U_\mathrm{P}(t)$. In short, the Floquet time-evolution Eq. (2.14) allows to simulate the time evolution with the time-independent effective Hamiltonian (2.3). Here the term "Floquet engineering" enters the game, where the key is to tailor the time-periodic drive of $H(t)$ in such a way that a desired effective Hamiltonian is achieved, which in turn can show features that are not accessible without the drive [63]. Famous examples of Floquet engineering in quantum systems are the dynamic localization of a matter wave [62,64], the creation of artificial gauge fields in ultracold quantum gases [5,70] and the realization of Floquet topological phases [4,71–74]. Often, and especially for quantum many body systems, it is demanding to calculate the effective Hamiltonian exactly. In case when the drive quantum $\hbar\omega$ is larger than the energy scale of the system, $\tilde{H}_\mathrm{eff}$ and $U_\mathrm{P}(t)$ can be approximated by a high-frequency expansion [63]

$$\begin{aligned}\tilde{H}_\mathrm{eff} &= H^{(0)} - \sum_{\substack{n=-\infty\\ n\neq 0}}^{\infty} \frac{H^{(n)}H^{(-n)}}{n\hbar\omega} \\ &\quad + \sum_{\substack{n=-\infty\\ n\neq 0}}^{\infty} \left[\frac{[H^{(n)},[H^{(0)},H^{(-n)}]]}{2(n\hbar\omega)^2} + \sum_{\substack{l=-\infty\\ l\neq 0,n}}^{\infty} \frac{[H^{(l)},[H^{(n-l)},H^{(-n)}]]}{3nl(\hbar\omega)^2} \right] + \mathcal{O}\left[\frac{1}{(\hbar\omega)^3}\right] \end{aligned} \tag{2.15a}$$

$$\begin{aligned}U_\mathrm{P}(t) &= e^{G(t)},\ G(t) = \sum_{\substack{n=-\infty\\ n\neq 0}}^{\infty} \frac{e^{-in\omega t}H^{(n)}}{n\hbar\omega} \\ &\quad + \sum_{\substack{n=-\infty\\ n\neq 0}}^{\infty} \left[\frac{e^{-in\omega t}[H^{(0)},H^{(n)}]}{(n\hbar\omega)^2} + \sum_{\substack{l=-\infty\\ l\neq 0,n}}^{\infty} \frac{e^{-i(n-l)\omega t}[H^{(-l)},H^{(n)}]}{2n(n-l)(\hbar\omega)^2} \right] + \mathcal{O}\left[\frac{1}{(\hbar\omega)^3}\right]. \end{aligned} \tag{2.15b}$$

Here $H^{(n)} = 1/T \int_0^T dt\ e^{in\omega t} H(t)$ are the Fourier components of the Hamiltonian $H(t)$. Equation (2.15a) visualizes that in leading order the effects of the Floquet drive on the effective Hamiltonian is induced by products and commutators of the Fourier components of the Hamilton operator. Physically, these terms allow to engineer the effective Hamiltonian such that it has the properties of interests, e.g. induces the aforementioned artificial gauge fields. Equation (2.15) allows for the perturbation analysis of certain effects related to time-periodic driving. A more detailed overview of Floquet engineering is found in Refs. [63, 102]. In this thesis we go beyond the high-frequency approximation and present in the next section a method that is capable of finding quasienergies and Floquet states at an arbitrary driving frequency ω.

2.2. Floquet Equation

In this section the Floquet equation is introduced, which serves as an complementary approach to the unitary transformation introduced in Subsec. 2.1.1. The Floquet equation is an eigenvalue equation that allows for the calculation of quasienergies and Floquet modes of almost arbitrary time-periodic Hamiltonians and is derived by inserting the Floquet states (2.7) into the Schrödinger equation (2.1). It reads

$$[H(t) - i\hbar\partial_t]|\phi_{\alpha,m}(t)\rangle = \epsilon_{\alpha,m}|\phi_{\alpha,m}(t)\rangle. \tag{2.16}$$

Equation (2.16) is set up in the so called Floquet space $\mathcal{F} = \mathcal{R} \bigotimes \mathcal{T}$ being the product of configuration space $\mathcal{R}$, i.e. the Hilbert space where $H(t)$ acts on, and the space $\mathcal{T}$ of bounded time-periodic functions with period T [108, 110, 111]. With the introduction of Floquet space, time t is promoted from a parameter to a coordinate [111]. Since $\mathcal{F}$ is larger than configuration space $\mathcal{R}$, the spectrum of eigenvalue equation (2.16) contains all Floquet Brillouin zones, such state the eigenfunctions $|\phi_{\alpha,m}(t)\rangle$ are labeled by both α and Floquet Brillouin zone index m. This statement can be shown by the fact that if there is a solution of Eq. (2.16) for some certain $m \in \mathbb{Z}$, it can be extended to all other Floquet Brillouin zones with the aid of Eq. (2.8).

2.2.1. Floquet Equation as Time-Independent Eigenvalue Equation

The Floquet equation (2.16) can be written as a time-independent eigenvalue equation by introducing the Fourier decomposition of Floquet modes and Hamiltonian

$$|\phi_{\alpha,m}(t)\rangle = \sum_{n=-\infty}^{\infty} e^{-in\omega t}|\phi_{\alpha,m}^{(n)}\rangle, \tag{2.17a}$$

$$H(t) = \sum_{n=-\infty}^{\infty} e^{-in\omega t}H^{(n)}. \tag{2.17b}$$

Inserting Eq. (2.17) into Eq. (2.16), the Floquet equation becomes a time-independent eigenvalue equation for the Fourier-components $|\phi_{\alpha,m}^{(n)}\rangle$ of the Floquet modes (2.6):

$$\sum_{l=-\infty}^{\infty} (H^{(n-l)} - l\hbar\omega\delta_{n,l})|\phi_{\alpha,m}^{(l)}\rangle = \epsilon_{\alpha,m}|\phi_{\alpha,m}^{(n)}\rangle. \tag{2.18}$$

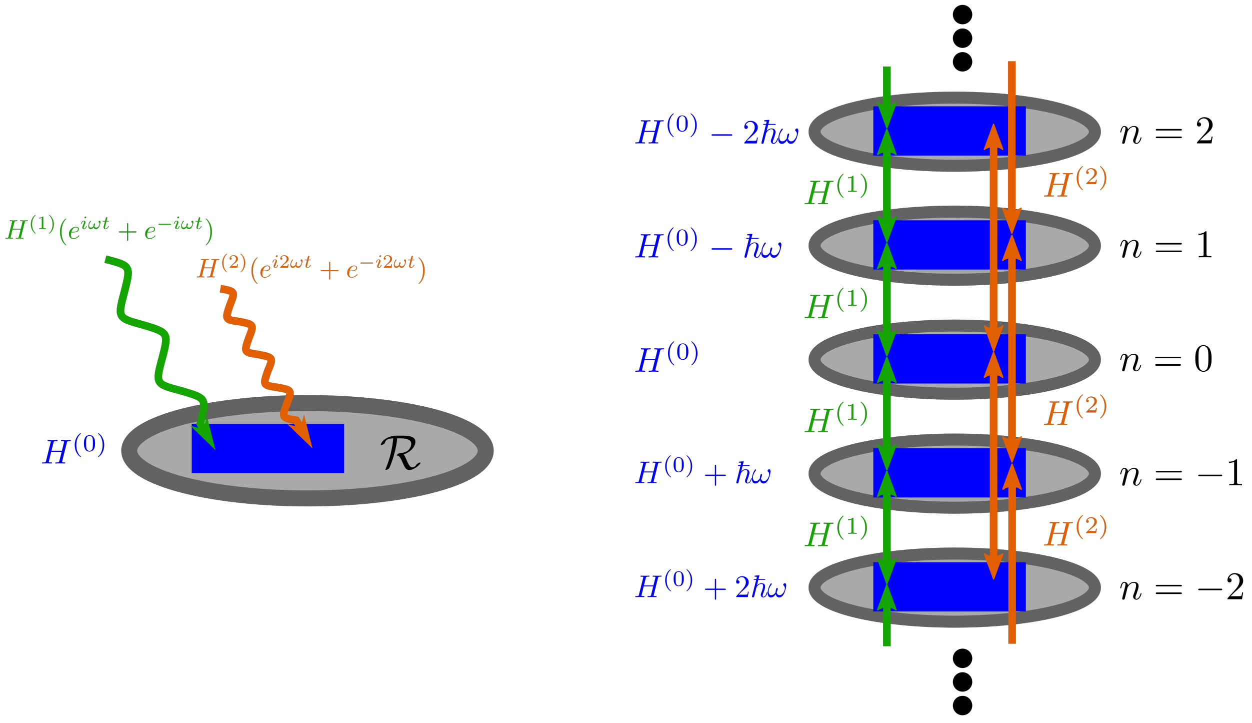

(a) **(b)**

Figure 2.1.: (a) Sketch of a physical system (blue) subject to a time-periodic drive of different harmonics (green and orange). The configuration space $\mathcal{R}$ is depicted by a grey sphere. (b) Corresponding picture in Fourier representation. Here infinitely many copies of the original Hilbert space labeled by channel number n with an additional offset potential $-n\hbar\omega$ are depicted. The periodic drive couples these distinct Hilbert spaces, where $H^{(1)}$ couples neighbors and $H^{(2)}$ next-nearest neighbors, as sketched by colored arrows.

Equation (2.18) is a major result of this section, since it formulates the Floquet equation in a time-independent way and thus maps a time-dependent problem to a time-independent one. The price to pay is the enhanced complexity of the Floquet Hilbert space in comparison to the original Hilbert space $\mathcal{R}$. This is incorporated in Equation (2.18) by an additional multi-channel structure labeled by the Fourier index n. Eq. (2.18) can be seen as an eigenvalue equation of an infinite dimensional matrix

$$\mathcal{H}=\begin{pmatrix} \ddots & \ddots & \ddots & \ddots & \ddots \\ \dots & H^{(0)}-(n-1)\hbar\omega & H^{(-1)} & H^{(-2)} & \dots \\ \dots & H^{(1)} & H^{(0)}-n\hbar\omega & H^{(-1)} & \dots \\ \dots & H^{(2)} & H^{(1)} & H^{(0)}-(n+1)\hbar\omega & \dots \\ \ddots & \ddots & \ddots & \ddots & \ddots \end{pmatrix}. \tag{2.19}$$

Figure 2.1 visualizes this representation. The Floquet matrix (2.19) is partitioned into multiple subspaces labeled by the channel number n, where each channel has an energy offset $-n\hbar\omega$. From a physical point of view, each channel is associated with a certain number of drive quanta $\hbar\omega$. This is now visualized further. Consider an atom interacting with a monochromatic quantized field. The Floquet description of this system treats the field classically. Nevertheless, the energy offset $-n\hbar\omega$ allows to associate the nth Floquet channel to contain states with $N_0 - n$ photons in the field, where N_0 is a large natural number [109]. This means that the Fourier index n can be related to the number of photons the atom has absorbed or emitted, or generally speaking to the number of drive quanta the system absorbed or emitted. While the time-averaged part of the Hamiltonian $H^{(0)}$ acts on each subspace, the dynamical part of the Hamiltonian $H^{(n)}$, $n \neq 0$, couples different channels. The couplings introduced by $H^{(n)}$, $n \neq 0$ correspond to n-drive quanta processes, e.g. $H^{(\pm 1)}$ couples neighboring channels and corresponds to one drive quantum processes, $H^{(\pm 2)}$ couples next nearest neighbors by a two-drive quanta process and so on. At this point we again emphasize that there is no time-dependence in Eq. (2.18), the above mentioned processes determine the Fourier coefficients $|\phi^{(n)}_{\alpha,m}\rangle$ of the Floquet steady states.

Equation (2.18) can be solved numerically. A numerical scheme, that will be commonly used within this thesis, introduces a cutoff $m_\mathrm{c} \in \mathbb{N}$ in Eq. (2.18) such that $|\phi^{(n)}_{\alpha,m}\rangle = 0, \ \forall |n| > m_\mathrm{c}$. This is equivalent to truncating the Floquet matrix (2.19) to a finite size. The resulting finite-dimensional eigenvalue equation is then solved by exact diagonalisation. In order to ensure that the numerics yield accurate results, the cutoff m_c has to be chosen large enough to guarantee that the Floquet modes in a single Floquet Brillouin zone have converged, i.e. the Fourier coefficients near the cutoff are close to zero in a numerical sense $|\phi^{(n)}_{\alpha,m}\rangle \to 0$ for $|n| \lesssim m_\mathrm{c}$.

If the quasienergies and Floquet modes are found by solving the Floquet equation, the time-evolution operator can be constructed with Eq. (2.9), so the whole information of our Floquet system is encoded in the quasienergies and Floquet modes. This motivates the importance of the Floquet equation for solving and analyzing time-periodic quantum systems.

2.2.2. Floquet Theory in Floquet Hilbert Space

The findings of the above subsection can be further formalized. In the following we provide a rigorous theory of the eigenvalue equations (2.16) and (2.18) in Floquet space. The introduction of this theory offers benefits which are used later in this thesis. For example, the theory helps for a better understanding of the structure of Floquet space and allows to express theories in Floquet space in a concise but complete way. We follow the considerations of Ref. [110]. At first, the following scalar products on the different Hilbert spaces are defined [108]:

$$\langle f, g\rangle = \int dx\ f^*(x)g(x),\ f(x), g(x) \in \mathcal{R}, \tag{2.20a}$$

$$(f, g) = \frac{1}{T}\int_0^T dt\ f^*(t)g(t),\ f(t), g(t) \in \mathcal{T}, \tag{2.20b}$$

$$\langle\langle f, g\rangle\rangle = \frac{1}{T}\int_0^T dt\ \langle f(t), g(t)\rangle,\ f(x,t), g(x,t) \in \mathcal{F}. \tag{2.20c}$$

In Eq. (2.20a) we assumed that configuration space $\mathcal{R}$ is the space of square-integrate functions. Of course, instead of position x the coordinate of the configuration space can also be assumed to be a spin quantum number, number of lattice site, or others. Equation (2.20a) must then be changed accordingly.

Let us now focus on a subtle point: It is desired to express the functions in $\mathcal{T}$ in a bra-ket notation. Similar to the introduction of the basis $|x\rangle$ of position space [112], the basis states $|t)$ with $t \in [0, T[$ are introduced [110]. The $|t)$ states are spanning the space $\mathcal{T}$ and obey the orthonormality relation

$$(t'|t) = T\delta(t - t'), \tag{2.21}$$

where $\delta(x)$ denotes the Dirac delta function. The completeness relation reads

$$\mathbb{I}_{\mathcal{T}} = \frac{1}{T}\int_0^T dt\ |t)(t|. \tag{2.22}$$

Here and elsewhere $\mathbb{I}_{\mathcal{Y}}$ denotes the identity on Hilbert space $\mathcal{Y}$. With this new basis of $\mathcal{T}$, time-periodic wave functions $|\phi(t)\rangle \in \mathcal{R}$ are defined in Floquet space by [110]

$$|\phi\rangle\rangle = \frac{1}{T}\int_0^T dt|\phi(t)\rangle|t). \tag{2.23}$$

Equation (2.23) is similar to expressing a wave function in the position basis $|\psi\rangle = \int dx\ \psi(x)|x\rangle$ and manifests the role of the time t as a coordinate of the Floquet Hilbert space. The double-ket notation $|\phi\rangle\rangle$ is used in this thesis to denote states of the Floquet space $\mathcal{F}$. Conversely to (2.23), the time-dependent wave function can be obtained by performing with Eq. (2.21) the projection

$$(t|\phi\rangle\rangle = |\phi(t)\rangle. \tag{2.24}$$

A time-dependent operator $A(t)$ obeying $A(t+T) = A(t)$, such as the Hamiltonian $H(t)$, is defined in Floquet space similar to Eq. (2.23) as

$$\hat{A} = \frac{1}{T}\int_0^T dt|t)A(t)(t|. \tag{2.25}$$

Here and elsewhere the hat marks that $\hat{A}$ is acting on Floquet space. The action of $\hat{A}$ on an element $|\phi\rangle\rangle$ of Floquet space is given by $\hat{A}|\phi\rangle\rangle = 1/T \int_0^T dt\ A(t)|\phi(t)\rangle|t)$, i.e. as expected, at each time t the operator $A(t)$ acts on state $|\phi(t)\rangle$. In contrast, the time-derivative operator does not follow definition (2.25), since it acts nontrivially on the space $\mathcal{T}$. It is defined via its action on an element of Floquet space:

$$\hat{\partial}_t|\phi\rangle\rangle = \frac{1}{T}\int_0^T dt\ [\partial_t|\phi(t)\rangle]|t). \tag{2.26}$$

Due to the periodic boundary conditions of elements of $\mathcal{T}$ the operator $i\hat{\partial}_t$ is hermitian. With Eqns. (2.25) and (2.26) there is everything together in order to write down Floquet equation (2.16) in Floquet space

$$\hat{\mathcal{H}}|\phi_{\alpha,m}\rangle\rangle = \epsilon_{\alpha,m}|\phi_{\alpha,m}\rangle\rangle, \tag{2.27}$$

with the so called Floquet Hamiltonian

$$\hat{\mathcal{H}} = \hat{H} - i\hbar\hat{\partial}_t. \tag{2.28}$$

Like in Eq. (2.16), the eigenfunctions of (2.27) are labeled by α and m. The Floquet Hamiltonian (2.28) inherits hermiticity from $H(t)$. Equation (2.27) is an important result, since it allows a shorthand notation and reads like a time-independent Schrödinger equation in the Floquet Hilbert space.

But how to include the Floquet matrix (2.19) into this theory? This is done by introducing a Fourier basis $|n)$ with $n \in \mathbb{Z}$ by a temporal Fourier transform of the $|t)$ states [110]

$$|n) = \frac{1}{T}\int_0^T dt\ e^{-in\omega t}|t),\ \ n \in \mathbb{Z}. \tag{2.29}$$

Note that Eq. (2.29) is similar to introducing a momentum basis in common quantum mechanics [112]. By projecting on $(t|$ the temporal form of the Fourier basis states is revealed to be

$$(t|n) = e^{-in\omega t}, \tag{2.30}$$

which is a monochromatic complex exponential function being commonly used for Fourier transformation. The Fourier basis is orthonormal $(n|m) = \delta_{n,m}$ and complete [110]

$$\mathbb{I}_{\mathcal{T}} = \sum_{n=-\infty}^{\infty} |n)(n|. \tag{2.31}$$

The introduction of the Fourier states $|n)$ allows to express an abstract Floquet state $|\phi\rangle\rangle \in \mathcal{F}$ in different representations. The definition (2.23) can be interpreted as a "time-representation" of an state $|\phi\rangle\rangle$. Similarly, a Fourier representation of $|\phi\rangle\rangle$ can be found with the use of Eq. (2.31) by

$$|\phi\rangle\rangle = \sum_{n=-\infty}^{\infty} |\phi^{(n)}\rangle|n). \tag{2.32}$$

Here the Fourier components

$$|\phi^{(n)}\rangle = \frac{1}{T}\int_0^T dt\ e^{in\omega t}|\phi(t)\rangle \tag{2.33}$$

are introduced, Eq. (2.33) fits with the definition of the inverse transformation (2.17a). A Fourier representation of an operator $\hat{A}$, which is defined via Eq. (2.25), is found with

$$\hat{A} = \sum_{n,m=-\infty}^{\infty} |n)A^{(n-m)}(m|, \tag{2.34}$$

where the Fourier components read

$$A^{(n)} = \frac{1}{T}\int_0^T dt\ e^{in\omega t}A(t). \tag{2.35}$$

Also Eq. (2.35) fits with the inverse transformation (2.17b). The Fourier representation of the time-derivative operator (2.26) is found using the definition of the Fourier basis (2.29) and the Fourier components Eq. (2.33) by its action on a state

$$\hat{\partial}_t|\phi\rangle\rangle = \sum_{n=-\infty}^{\infty} (-in\omega)|\phi^{(n)}\rangle|n). \tag{2.36}$$

Thus, the time-derivative operator reads in the Fourier basis

$$\hat{\partial}_t = \mathbb{I}_{\mathcal{R}} \otimes \sum_{n=-\infty}^{\infty} (-in\omega)|n)(n|. \tag{2.37}$$

This gives us the possibility to write the Floquet Hamiltonian in Fourier representation

$$\hat{\mathcal{H}} = \sum_{n,m=-\infty}^{\infty} \left[|n)(H^{(n-m)} - \delta_{n,m} n\hbar\omega)(m|\right]. \tag{2.38}$$

Equation (2.38) is an elegant shorthand notation of the Floquet matrix (2.19), the eigenvalue problem of (2.38) is equivalent to Eq. (2.18). This demonstrates that Eqns. (2.16) and (2.18) are "time" and Fourier representations of an abstract Floquet equation (2.27).

2.2.3. Properties of Floquet Modes and Expectation Values

In this subsection the orthonormality and completeness conditions of the Floquet modes are presented and expectation values on Floquet space are defined. As eigenfunctions of a hermitian operator the Floquet modes form a basis and fulfill the orthonormality relation [108]

$$\langle\langle\phi_{\alpha,n}|\phi_{\beta,m}\rangle\rangle = \delta_{\alpha,\beta}\delta_{n,m}. \tag{2.39}$$

Note that solutions of different Floquet Brillouin zones are orthogonal to each other. With Eqns. (2.8) and (2.39) the Fourier components of solutions in different Floquet Brillouin zones are related by

$$|\phi^{(n)}_{\alpha,m}\rangle = |\phi^{(n+m)}_{\alpha,0}\rangle. \tag{2.40}$$

With (2.40) it follows that the Floquet modes from one Floquet Brillouin zone are orthogonal at each time

$$\langle\phi_{\alpha,0}(t)|\phi_{\beta,0}(t)\rangle = \delta_{\alpha,\beta}. \tag{2.41}$$

The completeness relation in Floquet space reads [108]

$$\mathbb{I}_{\mathcal{F}} = \sum_{\alpha,m} |\phi_{\alpha,m}\rangle\rangle\langle\langle\phi_{\alpha,m}|, \tag{2.42}$$

where the sum in Eq. (2.42) includes all Floquet Brillouin zones. With the identity $\delta(x) = \frac{1}{2\pi}\sum_m e^{imx}$ a completeness relation on $\mathcal{R}$ is extracted from Eq. (2.42):

$$\mathbb{I}_{\mathcal{R}} = \sum_{\alpha} |\phi_{\alpha,0}(t)\rangle\langle\phi_{\alpha,0}(t)|. \tag{2.43}$$

Here the summation runs only within one Floquet Brillouin zone.

At last, we provide a short hand notation for a time-averaged expectation value of a time-periodic operator $A(t)$, if the system is in a Floquet state

$$\langle\langle \hat{A} \rangle\rangle_{\alpha,m} = \langle\langle \phi_{\alpha,m} | \hat{A} | \phi_{\alpha,m} \rangle\rangle. \tag{2.44}$$

If it is clear in which state the system is, the indices α, m are often dropped and it is simply written as $\langle\langle \hat{A} \rangle\rangle$. In the time- and Fourier representation the expectation value reads

$$\langle\langle \hat{A} \rangle\rangle_{\alpha,m} = \frac{1}{T} \int_0^T dt \langle \phi_{\alpha,m}(t) | A(t) | \phi_{\alpha,m} \rangle = \sum_{n,s=-\infty}^{\infty} \langle \phi_{\alpha,m}^{(n+s)} | A^{(s)} | \phi_{\alpha,m}^{(n)} \rangle. \tag{2.45}$$

The time-representation of $\langle\langle \hat{A} \rangle\rangle_{\alpha,m}$ in Eq. (2.45) shows why we use the term "time-averaged expectation value". Equation (2.45) is further useful to generalize observables from the time-independent to the Floquet case.

2.2.4. Calculation of Transformation and Effective Hamiltonian

Here we connect to Subsec. 2.1.1 and give formulas for the unitary transformation $U_\mathrm{P}(t)$ and the effective Hamiltonian $\tilde{H}_\mathrm{eff}$ in terms of quasienergies $\epsilon_{\alpha,m}$ and Floquet modes $|\phi_{\alpha,m}(t)\rangle$. If the quasienergies and Floquet modes are known, e.g. by the solving of the Floquet equation Eq. (2.27), these formulas can be used to calculate $U_\mathrm{P}(t)$ and $\tilde{H}_\mathrm{eff}$ explicitly. As a prerequisite, we need a time-independent, orthonormal basis $|\alpha\rangle$ of the configuration space $\mathcal{R}$. For example, the Floquet modes at any time, with indices out of the first Floquet Brillouin zone, $|\phi_{\alpha,0}(t)\rangle$ are such a basis, see Eqns. (2.41) and (2.43). With the basis $|\alpha\rangle$ and Eq. 2.6 a unitary transformation to a Floquet picture is found by

$$U_\mathrm{P}(t) = \sum_\alpha |\phi_{\alpha,m}\rangle\langle\alpha|, \tag{2.46}$$

while with Eq. 2.5 the effective Hamiltonian reads

$$\tilde{H}_\mathrm{eff} = \sum_\alpha \epsilon_{\alpha,0} |\alpha\rangle\langle\alpha|. \tag{2.47}$$

Note, that the choice of the basis $|\alpha\rangle$ is equivalent to multiplying $U_\mathrm{P}(t)$ by a time-independent, unitary matrix Q as discussed in Eq. (2.4) and that the $|\alpha\rangle$ states correspond to the $|\tilde{\phi}_\alpha\rangle$ states defined in Subsec. 2.1.1.

3. Floquet-Feshbach Resonance Theory

The study of ultracold quantum gases generated knowledge on a wealth of phenomena that are related to quantum many-body physics. Famous examples are the crossover between the Bardeen-Cooper-Schrieffer superfluid of fermionic atoms and Bose-Einstein condensate of fermionic molecules [28, 37–39] and the observation of the quantum phase transition between a superfluid and a Mott-insulating state [3, 45–49]. For all of these studies, the high tunability and accessibility of ultracold gas experiments is the key. One of the quantities over which the experimentalist have control is the interaction strength between the atoms. Using a Feshbach resonance, the interaction strength can be tuned to almost arbitrary positive or negative values. Feshbach resonances are a concept from scattering theory [113, 114] and allow for a tuning of the scattering length. The scattering length in turn determines the interaction strength, which are linearly related in the Born approximation [28]. A common way to realize such a tuning of the scattering length in an ultracold gas experiment is to use a magnetic Feshbach resonance [18]. In this method, the scattering length can be adjusted to almost arbitrary positive and negative values by choosing the strength of a magnetic field. Magnetic Feshbach resonances only exist at predetermined magnetic field strengths for given atomic species while also the width is preset, which means that magnetic Feshbach resonances are not intrinsically tunable. These limitations can be overcome by optical Feshbach resonances. In this method a ground state atom is coupled to an excited electronic state by a laser beam [115], as a result a Feshbach resonance is induced. The benefit of the optical Feshbach resonance is the tunability of both resonance frequency and width by the optical drive. However, optical Feshbach resonances suffer from a strong drawback: Typically, the excited electronic state that the laser couples to, has a finite lifetime due to the spontaneous emission of photons. As a result, both the range of tunability of the scattering length is limited to finite values and inelastic collisions are enhanced. This is commonly not of favor for ultracold gas experiments, since the inelastic collisions introduce a decay into the dynamics of the ultracold gas.

A promising proposal that resolves this issue has been made in Ref. [99], which investigates the periodic modulation of a magnetic field in the vicinity of a Feshbach resonance. As a result, the drive induces new scattering resonances that tune the scattering length to almost arbitrary positive and negative values, while resonance position and width depend on the parameters of the drive. What is really remarkable is that in combination with this high tunability the inelastic collisions are relatively low [116]. This makes this method more favorable compared to optical Feshbach resonances. An interesting point from the theory side is that the description of these driving-induced scattering resonances includes the case of strong driving, such that the use of Floquet theory is necessary. However, the relation of these recently found driving-induced resonances to the well-known concept of Feshbach resonances is still unclear. While Ref. [116] states that such a relation would only hold at weak driving, Ref. [117] qualitatively found a connection between these new resonances and Fano-Feshbach physics in the Floquet picture. However, a full theory that rigorously provides this connection and systematically calculates parameters such as resonance position and width is still lacking. In this chapter, we will resolve this issue and derive a theory of Feshbach resonances in the Floquet Hilbert space. A remarkable thing is that this theory enables a full qualitative understanding of the physics of these driving-induced Floquet-Feshbach resonances in a relatively simple picture. Further, we are able to quantitatively calculate both resonance position and width in the whole parameter range. As a major result will find out that these resonance properties are highly tunable by the parameters of the periodic drive. In the following, we give an outline of this chapter.

In Sec. 3.1 a relation between the scattering length and the interaction strength in the ultracold gas description, that is of central importance to this chapter, is provided Section 3.2 introduces the reader into the theory of quantum scattering. Here we define the pseudo potential which is singular at the origin, and resembles the scattering properties of an actual inter-atomic potential in the limit of low energies. At the same time, the mathematical description of the scattering by a pseudo potential is kept simple. Section 3.3 is devoted to the theory of Feshbach resonances. It starts with a brief introduction and provides a simple but nontrivial theoretical model of a Feshbach resonance. In Sec. 3.4, commonly used realizations of Feshbach resonances in ultracold gases are discussed. We continue with our Feshbach resonance model by applying it to a multi-channel description of a magnetic Feshbach resonance. A brief summary of the Floquet scattering theory is presented in Sec. 3.5.

The scattering properties of the sinusoidally driven pseudo potential are calculated in Sec. 3.6. This model is explicitly suited in order to describe the scattering of ultracold atoms. The Floquet equation is solved with continued fractions, as a result driving-induced Floquet-Feshbach resonances are reported.

Motivated by these findings, we formulate the Floquet-Feshbach resonance theory in Sec. 3.7. As an ultimate goal we derive a simple formula that describes the scattering length of a resonance. Further, the theory gives mathematical expressions for the position and the width of the resonance, which allows for quantitative predictions. A systematic analysis of both position and width found by the Floquet-Feshbach resonance theory is performed. The section is rounded off by showing that inelastic scattering is not resonantly enhanced for these resonances. Section 3.8 introduces higher harmonics into the drive. Also, for this case a Floquet-Feshbach resonance theory is derived that approximates the actual scattering length accurately. We discuss the influence of this higher harmonic drive on the Floquet-Feshbach resonances, as a key result we find that resonant inelastic scattering is induced which is asymmetric around the resonance. This asymmetry is related to the special structure of the Floquet Hilbert space. Section 3.9 gives actual values of length and frequency scales that are relevant to an experimental application of this theory.

The pseudo potential describes resonant scattering in the vicinity of a magnetic Feshbach resonance. However, there are magnetic Feshbach resonances where this approximation is only valid in a small magnetic field range. In Sec. 3.10 we overcome this limitation and bring in periodic driving in the multi-channel description of a magnetic Feshbach resonance, which yields for an investigation of Floquet-Feshbach resonances on a much wider magnetic field range. For a simple mathematical description that still captures the relevant physics we come back to the multi-channel Feshbach model that is introduced in Sec. 3.3, but this time we assume time-periodic parameters. The scattering length is extracted from the numerical Floquet scattering solution of the periodically driven multi-channel model. As a result, the periodic drive both induces new resonances and engineers already existing ones. The Floquet-Feshbach resonance theory provides a detailed analysis how these resonances are influenced by the drive. We propose to realize this model in low-field magnetic Feshbach resonances. This has the advantage, that lower driving frequencies and smaller magnetic field amplitudes can be used in order to reach the strongly driven limit. We specialize our model to the broad magnetic Feshbach resonance of ^{133}Cs at a magnetic field strength of 30 G that is reported in Ref. [30]. Here, effects that are related to the strong Floquet driving are clearly visible. We point out that the multi-channel model obtains more accurate results compared to the plain periodically driven pseudo potential.

We conclude with Sec. 3.11.

3.1. Relation of Interaction Strength and Scattering Length in Ultracold Quantum Gases

The goal of this section is to relate scattering theory to the many-body physics of ultracold quantum gases. Here, a connection of the two areas of physics is exemplary shown for the well-known Gross-Pitaevskii mean-field description of a Bose-Einstein condensate. In this theory the relevant quantity is the order parameter of the condensate $\psi(\mathbf{r}, t)$ which is for low enough temperatures and a dilute gas connected to the condensate density by $n(r, t) = |\psi(\mathbf{r}, t)|^2$. In this regime the dynamics of the order parameter is given by the well-known Gross-Pitaevskii equation [21, 28]

$$i\hbar \frac{\partial}{\partial t}\psi(\mathbf{r}, t) = \left[-\frac{\hbar^2 \Delta}{2m} + V(\mathbf{r}, t) + g|\psi(\mathbf{r}, t)|^2\right] \psi(\mathbf{r}, t). \tag{3.1}$$

In Eq. (3.1), Δ is the Laplace operator, m the boson mass, $V(\mathbf{r}, t)$ an external potential and g the interaction strength. The Gross-Pitaevskii equation (3.1) has the form of a Schrödinger equation with an additional non-linear term that comes in due to inter-particle interactions. In Eq. (3.1) short range interactions are assumed. In the so called Born-Oppenheimer approximation the actual inter-atomic potential is approximated by the scattering length. The scattering length in turn, is accessible via the scattering theory and gives, in a rough approximation, the radius of the cross section of the atoms. Within the Born-Oppenheimer approximation the interaction strength g is found to be proportional to the scattering length a [28]:

$$g = \frac{4\pi\hbar^2 a}{m}. \tag{3.2}$$

Equation (3.2) is of central relevance to this thesis, since it connects the interaction strength to the scattering length which can be calculated with the use of scattering theory. In Sec. 1.2 we discussed that the tuning of the scattering length with the use of a Feshbach resonance lead to various breakthroughs in the field of ultracold quantum gases. In the following sections Feshbach resonances are introduced in a rigorous way, as a starting point we review scattering theory in the next section.

3.2. Theory of Quantum Scattering

Scattering theory is the cornerstone to investigate the scattering of particles and waves in a vast amount of physical scenarios. Traditionally, the theory has been used in order to calculate cross sections which could be compared to the outcome of a scattering experiment [113]. Here, the interest in scattering theory comes due to its importance for ultracold quantum gases, where we saw in Eq. (3.2) that the scattering length is proportional to the interaction strength in the quantum many-body description. We give in Subsec. 3.2.1 a brief introduction to the most relevant concepts of scattering theory, which is based on the knowledge of Refs. [113, 118, 119]. Subsection 3.2.2 contains the partial wave expansion which is a method that is used later for finding the scattering properties of given model systems. In Subsec. 3.2.3 the scattering length is introduced. Subsection 3.2.4 discusses the short-range pseudo potential, that is of central relevance to this chapter.

3.2.1. The Key Concepts of Quantum Scattering Theory

Here we give an introduction to prominent definitions of the scattering theory of quantum particles. For the sake of simplicity we assume here two particles with no internal structure. The Hamiltonian describing this process in the center-of-mass frame of reference reads

$$H(\mathbf{r}) = -\frac{\hbar^2}{2\mu}\Delta + V(\mathbf{r}). \tag{3.3}$$

In Eq. (3.3) $\mu = (m_1 m_2)/(m_1 + m_2)$ denotes the reduced mass, which depends on the individual masses m_i of the two particles, Δ represents the Laplace operator in three dimensions and $V(\mathbf{r})$ is the inter-particle potential depending solely on the particle separation $\mathbf{r}$. For the following theory to work it is assumed that the potential $V(\mathbf{r})$ converges faster to zero than $1/r^2$ [113], where r is the modulus of $\mathbf{r}$. For example, the commonly known Lennard-Jones potential or the hard sphere potential fulfill this condition. Although a realistic scattering process is always time-dependent, a time-independent analysis of (3.3) allows accurate predictions of measurable quantities [113]. Here a plane wave with momentum k along the z-direction and energy $E = \hbar^2 k^2/(2\mu)$ is assumed. At asymptotically large distances $r \to \infty$ the wave function that describes the scattering process can be written as a sum of the plane wave and an outgoing spherical wave [113, 119]

$$\psi(\mathbf{r}) = e^{i\mathbf{k}\mathbf{r}} + f(\Omega)\frac{e^{ikr}}{r}, \text{ for } r \to \infty. \tag{3.4}$$

The outgoing spherical wave is induced by the scattering process while the scattering amplitude $f(\Omega)$ characterizes the strength of this scattering process. The scattering amplitude depends on the solid angle Ω and is related to the differential cross section $\frac{d\sigma}{d\Omega}$, a quantity that can be measured in an experiment. Note that the solid angle $\Omega = (\theta, \phi)$ is characterized by the polar angle θ and the azimuthal angle ϕ. The differential cross section is defined as the flux of the scattered wave probability current $\mathbf{j}_{\text{scatt}}\mathbf{dA}$ through an infinitesimal area $dA = r^2 d\Omega$ at asymptotically large r, divided by $d\Omega$ and incident current density $\mathbf{j}_{\text{in}}$ [113]

$$|\mathbf{j}_{\text{in}}| \frac{d\sigma}{d\Omega} d\Omega = \mathbf{j}_{\text{scatt}} \mathbf{e}_{\text{r}} r^2 d\Omega. \tag{3.5}$$

Here $\mathbf{e}_{\text{r}}$ is the unit vector pointing in radial direction. With the probability current density for a given wave function $\mathbf{j} = \hbar[\psi^*(\mathbf{r})\nabla\psi(\mathbf{r}) - \psi(\mathbf{r})\nabla\psi^*(\mathbf{r})]/(2i\mu)$ it holds with Eq. (3.4) that $\mathbf{j}_{\text{in}} = \hbar\mathbf{k}/\mu$, while the current density of the scattered wave is given by $\mathbf{j}_{\text{scatt}} = \hbar k |f(\Omega)|^2 \mathbf{e}_{\text{r}}/(\mu r^2) + \mathcal{O}(1/r^3)$. Thus the differential cross section is simply given by the modulus squared of the scattering amplitude

$$\frac{d\sigma}{d\Omega} = |f(\Omega)|^2. \tag{3.6}$$

The total cross section is defined as the integral of Eq. (3.6) over the full solid angle

$$\sigma = \int_{\Omega} d\Omega |f(\Omega)|^2 \tag{3.7}$$

and characterizes the total amount of scattered particle flux. At last, we present the optical theorem [113, 119]

$$\sigma = \frac{4\pi}{k^2} \text{imag} f(\theta = 0, \phi), \tag{3.8}$$

which comes from the fact that the interference of the plane and the spherical wave in forward direction $\theta = 0$ is related to the total amount of scattered probability current [113, 119].

3.2.2. Partial Wave Expansion

If the scattering potential is radial symmetric, i.e. $V(\mathbf{r}) = V(r)$, the partial wave expansion can be used in order to analyze and solve the scattering problem. As a starting point we note that $V(r)$ commutes with the angular momentum operator $\mathbf{L} = -i\hbar\mathbf{r} \times \boldsymbol{\nabla}$, so that the wave function can be expanded in spherical harmonics $Y_{l,m}(\Omega)$, which are the eigenfunctions of L^2 and L_z [112]. Here l denotes the angular momentum quantum number and m the magnetic quantum number. For a wave-vector of the incoming plane wave that points in z-direction $\mathbf{k} = k\mathbf{e}_z$ the problem becomes cylindrical symmetric around the z-axis. It is thus sufficient to expand the wave function in solutions with $m = 0$, which are proportional to the Legendre-polynomials $P_l(x)$ [120]. Thus the partial wave expansion of the wave function reads

$$\psi(r, \theta, \phi) = \sum_{l=0}^{\infty} R_l(r) P_l(\cos(\theta)). \tag{3.9}$$

Here $R_l(r)$ is called radial wave function, l denotes the angular momentum quantum number. The wave function with $l = 0$ is called the s-wave part, $l = 1$ the p-wave part and so on. Inserting

(3.9) into the Schrödinger equation and separating the different l, the radial Schrödinger equation is derived

$$[\Delta_r + k^2 - v_{\text{eff}}]R_l(r) = 0. \tag{3.10}$$

Here $\Delta_r = r^{-2}\partial_r r^2 \partial_r$ is the radial Laplacian, and $v_{\text{eff}}(r) = V(r)2\mu/\hbar^2 + l(l+1)/r^2$ is the effective potential involving a centrifugal term. Note that in Eq. (3.10) we divided by $\hbar^2/(2\mu)$ such that the energy of the scattered wave is encoded by the term k^2. In order to characterize the influence of the scattering potential on the radial wave function, Eq. (3.10) is first solved in the absence of the potential $V(r) = 0$. In this case Eq. (3.10) corresponds to the Schrödinger equation of a free particle in three dimensions. For each angular momentum l two linear independent solutions are found

$$R_l^{\text{reg}}(r) = j_l(kr), \;\; R_l^{\text{irr}}(r) = y_l(kr), \tag{3.11}$$

where $j_l(x)$ and $y_l(x)$ are the spherical Bessel functions of first and second kind, respectively. Their explicit expressions are given by [120]

$$j_l(x) = (-x)^l \left(\frac{1}{x}\frac{d}{dx}\right)^l \frac{\sin(x)}{x}, \;\; y_l(x) = -(-x)^l \left(\frac{1}{x}\frac{d}{dx}\right)^l \frac{\cos(x)}{x}. \tag{3.12}$$

The superscript "reg" denotes the fact that $R_l^{\text{reg}}(r)$ remains regular as $r \to 0$, while $R_l^{\text{irr}}(r)$ becomes irregular in this limit. This behavior is easily verified using Eq. (3.12). The plane wave can be expanded into spherical waves by [113, 119]

$$e^{i\mathbf{kr}} = e^{ikr\cos(\theta)} = \sum_{l=0}^{\infty}(2l+1)i^l j_l(kr)P_l(\cos(\theta)). \tag{3.13}$$

This shows that without the presence of a scattering potential, only the regular solutions $j_l(kr)$ are present. Now we take a look at the situation for a non-vanishing scattering potential $V(r)$. At low radii, where $V(r)$ has a notable impact, the actual form of the radial wave function $R_l(r)$ can become quite complex and has to found for each problem separately. But at large radii, we can make a statement that is generic for all admissible potentials $V(r)$. In order to do so, the asymptotic behavior of of the spherical Bessel functions is of importance [113]

$$j_l(x) \approx \frac{\sin(x - l\frac{\pi}{2})}{x}, \;\; y_l(x) \approx \frac{\cos(x - l\frac{\pi}{2})}{x}, \;\; \text{as } x \to \infty. \tag{3.14}$$

Any solution of the scattering problem with non-vanishing $V(r)$ can be written at large radii by a superposition of the asymptotic forms (3.14) [18, 113, 119]:

$$R_l(r) \propto \frac{\sin(kr - l\frac{\pi}{2} + \delta_l(k))}{kr}, \tag{3.15}$$

where the mixing of the two solutions is parameterized by the momentum-dependent scattering phase shift $\delta_l(k)$. Eq. (3.15) is the key result of this subsection, since it shows that the influence of the scattering process can be described by a single quantity for each l, namly the scattering phase shift $\delta_l(k)$. As indicated by the name "scattering phase shift", the potential $V(r)$ shifts the phase of the wave function at large distances by the amount of $\delta_l(k)$ compared to the case of $V(r) = 0$. The knowledge of the δ_l allows to calculate the scattering amplitude

$$f(\theta) = \sum_{l=0}^{\infty} f_{(l)} P_l[\cos(\theta)], \text{ with } f_{(l)} = \frac{2l+1}{k} e^{i\delta_l(k)} \sin(\delta_l(k)), \tag{3.16}$$

where $f_{(l)}$ are called partial-wave scattering amplitudes [113]. Eq. (3.16) is found by comparing Eq. (3.4) to Eqns. (3.13) and (3.15) [119]. The total cross section is found with the properties of the Legendre polynomials to be [113, 118, 119, 121]

$$\sigma = \sum_{l=0}^{\infty} \sigma_{(l)}, \text{ with } \sigma_{(l)} = \frac{4\pi}{k^2}(2l+1)\sin^2(\delta_l(k)). \tag{3.17}$$

Note that the scattering cross section can be calculated if all scattering phase shifts are known. This demonstrates the importance of the scattering phase shifts: They allow for an intuitive introduction on the level of the radial wave function and enable for calculating important scattering quantities such as the total cross section (3.17). The scattering phase shifts in turn have to be determined by the actual solution of each scattering problem.

For indistinguishable particles the overall scattering wave function has to be symmetrized in the case of bosons and antisymmetrized in the case of fermions. This implies that the cross section for each partial wave is multiplied by a factor g_l [18, 115, 119]:

$$\sigma_{(l)} = g_l \frac{4\pi}{k^2}(2l+1)\sin^2(\delta_l(k)), \tag{3.18}$$

where $g_l = (1 \pm (-1)^l)$, with the plus sign standing for bosons and the minus sign standing for fermions. As a result, bosons only scatter in partial wave with even l, while fermions scattering is restricted to odd l. For the case of s-wave scattering, which is of central relevance to this thesis, we have $g_0 = 2$ for bosons and $g_0 = 0$ for fermions, such that the cross section for bosons is doubled compared to the case of distinguishable particles, while the s-wave cross section for fermions vanishes.

3.2.3. Scattering Length

In the limit of vanishing energy $E \to 0$ the description of scattering becomes very simple. In order to perform the limit $E, k \to 0$ the following expression of the scattering amplitude Eq. (3.16) is of importance

$$-\frac{1}{f_{(l)}} = \frac{1}{2l+1}\left(-\frac{k}{\tan[\delta_l(k)]} + ik\right). \tag{3.19}$$

In the limit $k \to 0$ the tangent of the scattering length depends in the form of a power law on the momentum $\tan(\delta_l(k)) \propto k^{2l+1}$ With Eq. (3.19) it follows that the terms with small l dominate the scattering physics in this limit [113, 118]. For the case of s-wave scattering, which is most relevant to this thesis, the scattering length a_{scatt} is defined as the proportionality factor of this power law behavior [113, 118]

$$-\lim_{k\to 0} k^{-1}\tan(\delta_0(k)) = a_{\mathrm{scatt}}. \tag{3.20}$$

The s-wave scattering length Eq. (3.20) does not depend on the angles θ, ϕ. Thus, s-wave scattering is isotropic and the total cross section reads $\sigma_0 = 4\pi|a_{\mathrm{scatt}}|^2$. Note that the scattering length Eq. (3.20) does not depend on the momentum k. The interesting point is that all scattering properties, such as differential and total cross section, are determined by the scattering length a_{scatt}, if only s-wave scattering is of relevance. This case readily applies to the scattering of bosons in an ultracold gas experiment.

It is useful to generalize the scattering length to finite energies E by introducing the energy-dependent scattering length a_{E} as [122]:

$$a_{\mathrm{E}}(k) = -\frac{\tan(\delta_0(k))}{k}. \tag{3.21}$$

With Eq. (3.19) we have $-f_{(0)}^{-1} = a_{\mathrm{E}}^{-1} + ik$. The true scattering length (3.20) is then found by $\lim_{k\to 0} a_{\mathrm{E}}(k) = a_{\mathrm{scatt}}$.

3.2.4. The Pseudo Potential

For realistic scattering potentials the calculation of the scattering amplitudes may be involved. In this subsection the so called pseudo potential is introduced, which allows to find all scattering properties within a simple calculation. The pseudo potential is defined by the operator

$$V_a^{\mathrm{pseudo}}(r) = \lim_{s\to 0^+} \frac{\hbar^2}{2\mu}\frac{a}{s^2}\delta(r-s)\frac{\partial}{\partial r}r, \tag{3.22}$$

and its strength is parameterized by the length a [123, 124]. The operator $\partial_r r$ acts on a radial wave function that is to the right of the potential. In a later part of this thesis matrix elements of the pseudo potential have to be calculated. In this case Eq. (3.22) is genrealized, such that $\partial_r r$ acts to wave functions that are both to the left and to the right of the potential [123, 124]:

$$V_a^{\mathrm{pseudo}}(r) = \lim_{s\to 0^+} \frac{\hbar^2}{2\mu}\frac{a}{s^2}\delta(r-s)\overleftrightarrow{\frac{\partial}{\partial r}}r, \tag{3.23}$$

The double arrow notation that is defined by the action of the pseudo potential on the radial wave functions $\psi(r)$, $\phi(r)$:

$$\psi(r)\left[\lim_{s\to 0^+} \frac{\hbar^2}{2\mu}\frac{a}{s^2}\delta(r-s)\overleftrightarrow{\frac{\partial}{\partial r}}r\right]\phi(r) = \lim_{s\to 0^+}\left[\frac{\partial}{\partial r}r\psi(r)\right]\frac{\hbar^2}{2\mu}\frac{a}{s^2}\delta(r-s)\left[\frac{\partial}{\partial r}r\phi(r)\right], \tag{3.24}$$

i.e as already discussed, the operator $\frac{\partial}{\partial r}r$ acts on both the radial wave function to the left $\psi(r)$ and the right $\phi(r)$. In the case that $\psi(r) = 1$ Eq. (3.22) is recovered. In the forms (3.22) and (3.23) the pseudo potential is restricted to s-wave scattering at low energies. For a higher partial wave index l and finite energies E extensions of Eq. (3.23) exist [123,124], which are not of relevance to this thesis.

In order to understand the physical meaning of the pseudo potential, we give a brief introduction. A detailed derivation is found in Refs. [117,121]. Initially, the pseudo potential was designed to absorb a hard sphere potential, i.e. the boundary condition $R(r) = 0$, $\forall r < a_0$, with a_0 as an arbitrary length, onto a boundary condition for the radial wave function at the origin [124,125]. In order to do so, the wave function outside the potential $r > a_0$ is extended to regions inside. For small k, the s-wave scattering phase shift of the hard sphere is given by $\delta_0 \approx -ka_0$, while the pseudo potential with $a = a_0$ leads to identically the same behavior. This is the main point: If we are interested in describing the scattering phase shift we can replace the actual potential by the pseudo potential with the length parameter a given by the appropriate s-wave scattering length. This approximation is valid, if the wavelength $\lambda = 2\pi/k$ is longer than the range of the actual potential.

Before the scattering properties of the pseudo potential are calculated, the pseudo potential is compared to a bare delta function. Consider therefore the regular and irregular solution of the free radial Schrödinger equation in the case of s-wave scattering: $R^{\mathrm{reg}}(r) = \sin(kr)/(kr)$ and $R^{\mathrm{irr}}(r) = \cos(kr)/(kr)$. We perform the following integrals

$$\textstyle\int_0^\infty dr\ r^2 \lim_{s\to0^+} \frac{\delta(r-s)}{s^2} R^{\mathrm{reg}}(r) = 1, \qquad \displaystyle\int_0^\infty dr\ r^2 \lim_{s\to0^+} \frac{\delta(r-s)}{s^2} R^{\mathrm{irr}}(r) \to \infty, \tag{3.25a}$$

$$\textstyle\int_0^\infty dr\ r^2 v_a^{\mathrm{pseudo}}(r) R^{\mathrm{reg}}(r) = a, \qquad \displaystyle\int_0^\infty dr\ r^2 v_a^{\mathrm{pseudo}}(r) R^{\mathrm{irr}}(r) = 0, \tag{3.25b}$$

with $v_a^{\mathrm{pseudo}}(r) = V_a^{\mathrm{pseudo}}(r) 2\mu/\hbar^2$. The divergence appearing when evaluating the bare Dirac delta function is turning to zero when we are dealing with the pseudo potential. The result for the regular solution remains, however, unchanged. Thus, the radial derivative inside the pseudo potential is used for regularization issues since it projects the $1/r$ divergences out which come in by evaluating the pseudo potential with the irregular solution $R^{\mathrm{irr}}(r)$ at the origin. Since a general radial wave function can always be written as a superposition of regular and irregular solution, no divergences of the type of Eq. (3.25) appear when we consider the pseudo potential instead of a bare delta function.

We are now able to calculate scattering properties of the pseudo potential, for example the scattering amplitude f. An ansatz is chosen to be

$$R(r) = \frac{\sin(kr)}{kr} + f\frac{e^{ikr}}{r}, \tag{3.26}$$

where the first term stems from the s-wave part of the partial wave expansion of the plane wave (3.13). For calculating the scattering amplitude f the radial Schrödinger equation (3.10) is integrated on a sphere of radius r_ϵ with center $\mathbf{r} = \mathbf{0}$ [117]. There are two relevant steps for this calculation. The integral over the kinetic energy is evaluated using the divergence theorem [117]

$$\frac{1}{4\pi}\int_{B_{r_\epsilon}(0)} d^3r\ \Delta R(r) = r^2 \frac{\partial}{\partial r} R(r)|_{r=r_\epsilon}, \tag{3.27}$$

while $R(r)$ is assumed to be a function with zero angular momentum obeying $\Delta R(r) = \Delta_r R(r)$. The other relevant part is the integral over the pseudo potential, which leads to

$$\frac{1}{4\pi}\int_{B_{r_\epsilon}(0)} drr^2 d\Omega\ v_a^{\text{pseudo}}(r)R(r) = a\frac{\partial}{\partial r}u(r)|_{r=r_\epsilon}, \tag{3.28}$$

with the notation $R(r) = u(r)/r$. By taking the limit $r_\epsilon \to 0$ the scattering amplitude reads

$$f = \frac{-1}{\frac{1}{a} + ik}. \tag{3.29}$$

This shows that here the scattering length is of canonical form (3.19) with an energy-dependent scattering length of $a_{\text{E}}(k) = -\tan(\delta_0)/k = a$. In addition to scattering states also bound states can be present. For $a > 0$ the pseudo potential possesses a bound state with the wave function

$$R(r) = C\frac{e^{-\kappa r}}{r}. \tag{3.30}$$

Inserting (3.30) into the radial Schrödinger equation and performing the integration techniques discussed in Eqns. (3.27) and (3.28) determines the decay rate as $\kappa = 1/a$. The bound state energy is thus $E = -E_{\text{D}}$ with the so called dimer energy

$$E_{\text{D}} = \frac{\hbar^2}{2\mu}\frac{1}{a^2}. \tag{3.31}$$

The name dimer energy stems from the fact that state Eq. (3.30) is associated with a weakly bound dimer in ultracold gas experiments [18, 99].

3.3. Feshbach Resonances

In this section we introduce the reader into Feshbach resonances. While Subsec. 3.3.1 is devoted to a general overview, a simple model that describes the essential of a Feshbach resonance is introduced in Subsec. 3.3.2.

3.3.1. Introduction into Feshbach Resonances

A resonance in quantum mechanical scattering can be interpreted as an almost bound state [113, 117]. As the state is not truly bound, it can couple to a continuum of scattering states and induce a rapid jump of the scattering phase shift $\delta_l(k)$ [113]. Two prominent types of scattering resonances are distinguished [113, 117]. A shape resonances occurs if a state trapped behind a barrier potential is able to decay to a continuum outside the potential. The second type, Feshbach resonances occur in multichannel systems, where a bound state in closed channels is coupled by inter-channel coupling to continua in open channels [14, 18, 113, 114]. A rigorous theory of resonant scattering originates

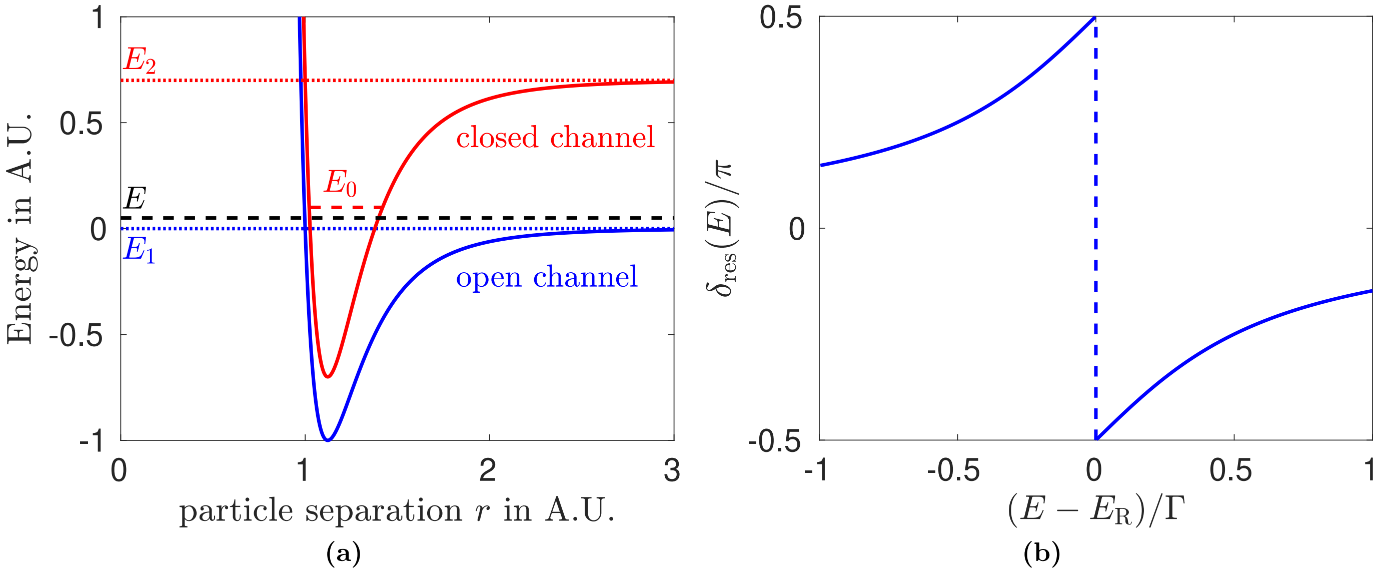

Figure 3.1.: (a) Sketch of a Feshbach resonance. A scattering state of energy E is assumed in the open channel whose potential is displayed in blue, while the potential of the closed channel marked in red possesses a bound state with energy E_0. The channel thresholds are drawn by dotted colored lines. If the channels are coupled, a Feshbach resonance occurs if the energy of the scattering state E matches with the energy of the bound state E_0. (b) resonant phase shift Eq. (3.34) over normalized energy, the resonance position is marked by a dashed line.

from Feshbach [14, 114] and Fano [11–13], who independently derived a theory of resonances using different methods [18]. In the following we introduce the concept of Feshbach resonances in quantum mechanical scattering, based on Refs. [18,113]. A model including two channels is assumed, for which the radial Schrödinger equation reads

$$-\frac{\hbar^2}{2\mu}\Delta_r\psi_\nu(r) + \sum_\eta V_{\nu,\eta}(r)\psi_\eta(r) = E\psi_\nu(r), \;\; \nu = 1, 2. \tag{3.32}$$

In Eq. (3.32) s-wave scattering is assumed. Compared to single channel scattering the wave function in Eq. (3.32) has an additional channel index ν, which is related to internal degrees of freedom, as it will be thoroughly discussed in Subsec. 3.4.1 for the case of a magnetic Feshbach resonance. Further, the radial potential $V_{\nu,\eta}(r)$ has a matrix form. It is assumed that at asymptotically large distances the channels decouple

$$\lim_{r\to\infty} V_{\nu,\eta}(r) = E_\nu\delta_{\nu,\eta}. \tag{3.33}$$

The quantity E_ν is named as channel threshold. The channel $\nu = 1$ is assumed to be open, which means that $E_1 < E$ such that free solutions are possible for given energy E in this channel. Channel $\nu = 2$ is closed, that implies the condition $E < E_2$ such that a solution with energy E remains bound. If an open channel contains an incoming plane wave it is named as entrance channel [18]. This configuration implies $E_1 < E < E_2$. In the uncoupled case, i.e. $V_{\nu,\eta\neq\nu}(r) = 0$ the closed channel possesses (at least) one bound state, whose eigenenergy is denoted by E_0. A Feshbach resonance occurs if the energy E of the scattering state is tuned to the vicinity of the bound state E_0, see Fig. 3.1 (a). In this case the scattering phase shift is the sum of a background scattering phase shift δ_{bg} induced by the potential of the open channel $V_{1,1}(r)$ and a resonant phase δ_{res} given by [11,14,18,113]

$$\tan \delta_{\mathrm{res}}(E) = -\frac{\Gamma/2}{E - E_{\mathrm{R}}}. \tag{3.34}$$

Here $E_{\mathrm{R}} = E_0 + \delta E$ is the position of the resonance which equals the energy of the bound state plus an additional shift δE, see Ref. [113]. The width of the resonance is described by the parameter Γ. In Fig. (3.1) (b) the resonant scattering phase shift Eq. (3.34) is displayed, where the scattering resonance is seen as a sudden jump of the phase shift of π.

3.3.2. Short-Range Model of a Feshbach Resonance

After the brief introduction, in the following a deeper understanding of Feshbach resonances is provided. In order to grasp the underlying physics while keeping the math simple we choose, following Ref. [117], the concrete form of the multi-channel potential to be the short range pseudo potential given by Eq. (3.23):

$$v_{\nu,\eta}(r) = v^{\mathrm{pseudo}}_{a_{\nu,\eta}}(r) + \delta_{\nu,\eta}\delta_{\nu,2}E_2. \tag{3.35a}$$

Note that in Eq. (3.35a) and further throughout this subsection we measure all energies in the units of a squared inverse length, as described by the rescaling $E \to E\ 2\mu/\hbar^2$. The threshold of the second channel is given by the parameter E_2, while the one for the first is set to zero. The strength of the multi-channel version of the pseudo potential is parameterized by the matrix-valued length $a_{\nu,\eta}$. In order to sustain hermiticity, the $a_{\nu,\eta}$ matrix must be symmetric. As the pseudo potential vanishes for $r \neq 0$, the ansatz for the wave function reads

$$\psi_1(r) = \frac{\sin(kr)}{kr} + f\frac{e^{ikr}}{r}, \tag{3.36a}$$

$$\psi_2(r) = f_2\frac{e^{ik_2 r}}{r}, \tag{3.36b}$$

where f is the scattering amplitude. The dispersion relation is given by $E = k^2$. If the second channel is closed, the wave vector $k_2 = \sqrt{E - E_2}$ is purely imaginary. By performing the integration technique from Eqns. (3.27) and (3.28) the following equations are derived:

$$(1 + a_{1,1}ik)f + a_{1,2}ik_2 f_2 = -a_{1,1}, \tag{3.37a}$$

$$(1 + a_{2,2}ik_2)f_2 + a_{2,1}ikf = -a_{2,1}. \tag{3.37b}$$

Equation (3.37) can be solved for f and f_2. Let us first discuss the uncoupled case where $a_{1,2} = a_{2,1} = 0$. Here the scatting amplitude is given by the potential strength of the open channel $-f^{-1} = a_{1,1}^{-1} + ik$, while the second channel possesses a bound state with energy $E_0 = E_2 - 1/a_{2,2}^2$. No resonances occur

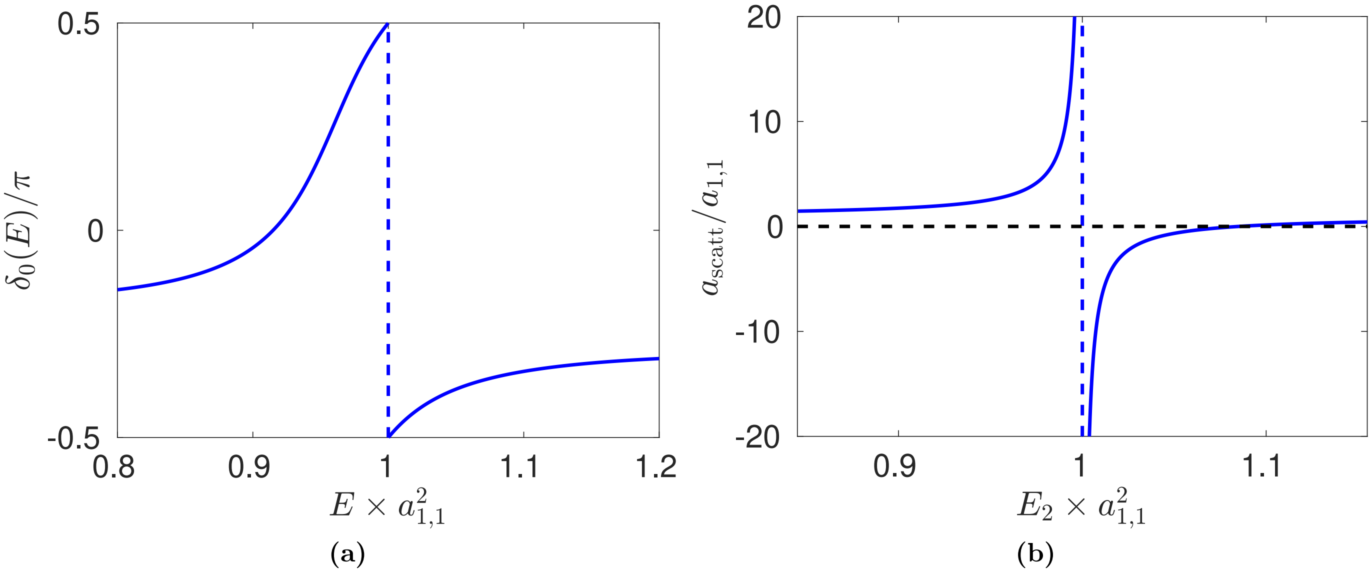

Figure 3.2.: (a) Scattering phase shift in dependence on the energy for $E_2 \times a_{1,1}^2 = 1$. (b) Scattering length in dependence on the channel threshold E_2, the black dashed line at $y = 0$. Both plots use the parameters $a_{2,2} = a_{1,1}$ and $a_{1,2} = a_{2,1} = 0.2a_{1,1}$. The position of the resonance is indicated by a blue dashed line.

in this limit. With finite coupling the states in the channels mix and the scattering amplitude reads $-f^{-1} = a_E^{-1} + ik$ with the energy-dependent scattering length

$$a_E(k) = a_{1,1} - \frac{a_{1,2}a_{2,1}ik_2}{1 + ik_2a_{2,2}}. \tag{3.38}$$

As displayed in Fig. 3.2 (a), the scattering phase shift described by Eq. (3.38) shows a phase jump of π which is a typical feature of a Feshbach resonance as shown in Fig. 3.1. In fact, for the parameters used in Fig. 3.2 (a), the bound state energy is $E_0 = 1 \times a_{1,1}^2$, and coincides with the location of a Feshbach resonance. This demonstrates the basic principle of a Feshbach resonance: The interaction of a bound state with a scattering state leads to resonant behavior in the scattering phase shift at energies near the energy of the bound state E_0. Note that there is no shift δE in this case as the jump in $\delta_0(E)$ appears directly at E_0.

We have just investigated a Feshbach resonance while tuning the energy E, but we could also alter the bound state energy E_0 in order to observe resonant features. For ultracold quantum gases, as described in later sections, it is due to the low temperatures common to consider inter-atomic collisions at vanishing energy [18]. In this case the central quantity is the s-wave scattering length a_{scatt}. The bound state energy E_0 can be tuned by changing the channel threshold E_2, the resulting scattering length a_{scatt} is shown in Fig. 3.2 (b). The resonance appears as a pole in the scattering length. The position of the resonance $E_2^{(0)}$ can be found by setting denominator in Eq. (3.38) to zero:

$$E_2^{(0)} = \frac{1}{a_{2,2}^2} + E, \tag{3.39}$$

This again shows that a Feshbach resonance appears if the energy of the bound state equals the energy of the scattering state.

Equation (3.38) can be brought to a simple form the is known in common literature [18, 126, 127]. Starting point is to expand the wave vector $-ik_2 = \kappa = \sqrt{E_2 - E}$ around the resonance position

$$\sqrt{E_2 - E} = \frac{1}{a_{2,2}} + \frac{a_{2,2}}{2}(E_2 - E_2^{(0)}) + \mathcal{O}[(E_2 - E_2^{(0)})^2]. \tag{3.40}$$

Inserting the first order expansion into the scattering amplitude (3.38), the scattering length can be approximated by the formula [117]

$$a_{\mathrm{scatt}} = a_{\mathrm{bg}} \left[1 - \frac{\Delta}{E_2 - E_2^{(0)}} \right]. \tag{3.41}$$

Besides the resonance position $E_2^{(0)}$ the parameters in Eq. (3.41) are the background scattering length

$$a_{\mathrm{bg}} = a_{1,1} \left(1 - \frac{a_{1,2}a_{2,1}}{a_{1,1}a_{2,2}} \right) \tag{3.42}$$

and the resonance width

$$\Delta = \frac{2a_{1,2}a_{2,1}}{a_{2,2}^3 a_{\mathrm{bg}}}. \tag{3.43}$$

Equation (3.41) is a generic form parameterizing a Feshbach resonance [18, 122], that will show up many times in this chapter. As already said, at resonance position $E_2^{(0)}$ the scattering length has a pole, while the background scattering length a_{bg} determines the value of the scattering length away from the resonance. Here a_{bg} consists of the bare scattering length of the first channel plus a dressing stemming from the interaction with the closed channel. The parameter Δ determines the width of the resonance. The larger Δ, the broader the resonance appears. This is supported by the fact that a_{scatt} has a zero at $E_2 = E_2^{(0)} + \Delta$, the width Δ is exactly the difference between the zero and the pole of the resonant scattering length (3.41). The width Δ grows with increasing coupling of the channels, it further depends on the parameter $a_{2,2}$ and the background scattering length a_{bg}. Note, that the pole in Eq. (3.41) only appears in the limit $E = 0$. In any experiment, the energy E of the colliding particles is finite, such that due to $-f_{(0)}^{-1} = a_{\mathrm{E}}^{-1} + ik$ a structure with finite amplitude, that depends of E, is seen instead of a true pole. After having understood the concept of Feshbach resonances in a simple case, the next subsection is about Feshbach resonances in ultracold quantum gases, where the model of Subsec. 3.3.2 is explicitly applied for describing a magnetic Feshbach resonance.

3.4. Feshbach Resonances in Ultracold Gases

The tuning of the interaction strength in ultracold quantum gases by the use of Feshbach resonances is of importance to the field [18]. Prominent findings related to Feshbach tuned interactions are the controlled collapse of a condensate at negative a_{scatt} [18, 128, 129] as well as the creation of noninteracting condensates using the zero crossing of a_{scatt} near a Feshbach resonance [18, 32, 130], which can show dipolar effects [34, 131]. Furthermore the investigation of many-body systems that have been realized with optical lattices, strongly benefits from the adaptable interactions [3]. This high tunability of the interaction strength allows for the experimental realization of a plethora of well-known models of condensed matter theory, as mentioned in Sec. 1. In the following common methods of creating Feshbach resonances in ultracold quantum gases are introduced. Subsection 3.4.1 contains the magnetic Feshbach resonances. We introduce a model of a magnetic Feshbach resonance that is based on the considerations of Subsec. 3.3.2 and will be of further relevance to this chapter. Optical Feshbach resonances are introduced in Subsec. 3.4.2, while Subsec. 3.4.3 is devoted to radio-frequency and microwave Feshbach resonances. In Subsec. 3.4.4 we introduce the driving-induced Feshbach resonances, which can be realized by applying a time-periodic magnetic field in the vicinity of a Feshbach resonance [99]. The further part of this chapter is devoted to research on these driving-induced Feshbach resonances.

3.4.1. Magnetic Feshbach Resonances

After the first experimental realization of a magnetic Feshbach resonance in the year 1998 [29, 132], they became a common tool for tuning the interaction strength in ultracold quantum gases [18]. In order to understand the physical origin of a magnetic Feshbach resonance, we briefly recap the internal structure of atoms in ultracold gas experiments. Typically, for these atoms the electron orbital angular momentum $\mathbf{L}_i$ is coupled with the electron total spin $\mathbf{S}_i$ to the angular momentum $\mathbf{j}_i$, and $\mathbf{j}_i$ couples with the nuclear spin $\mathbf{I}_i$ to the total angular momentum of one atom $\mathbf{f}_i$ [18, 133]. Here $i = 1, 2$ labels the two colliding atoms. Good quantum numbers are in this case the total angular momentum f_i and its projection to the z-axis m_i. At the presence of a finite magnetic field $\mathbf{B}$ the quantity m_i remains a good quantum number, while states with different f_i mix [18]. Nevertheless, a state at finite $\mathbf{B}$ can be labeled by that f_i to which it is adiabatically connected when lowering the $\mathbf{B}$ field up to $\mathbf{B} = \mathbf{0}$, for details see Ref. [18]. Due to this rich internal structure the scattering of two atoms becomes a multi-channel problem with the channel multiindex $\alpha = (f_1, m_1, f_2, m_2, l, m_l)$ [18], where l and m_l are the quantum numbers of the angular motion of the colliding atoms. At short distances those channels are coupled by a non-vanishing inter channel potential [18]. The scattering state and the bound state that are involved in the Feshbach resonance reside in different channels with different quantum numbers f_i, m_i, such that the magnetic moments of the colliding atoms μ_{atoms} and the bound state μ_{bound} differ. By varying the magnetic field strength B the difference of the Zeeman energies can be tuned. This results in a change of the bound state energy of the closed channel relative to the energy E of the scattering state [18]

$$E_0 = \delta\mu(B - B_{\mathrm{c}}), \tag{3.44}$$

where $\delta\mu = \mu_{\mathrm{atoms}} - \mu_{\mathrm{bound}}$ and B_{c} is a critical field strength. If both energies E and E_0 are tuned close to each other by the magnetic field, a Feshbach resonance occurs. In the zero energy limit of Eq. (3.34) the scattering length for fields around the magnetic Feshbach resonance is found to be [18, 29, 126, 127]

$$a_{\mathrm{scatt}} = a_{\mathrm{bg}} \left(1 - \frac{\Delta B}{B - B_0}\right). \tag{3.45}$$

Here $\Delta B = \lim_{k\to 0} \Gamma/(2a_{\mathrm{bg}} k \delta\mu)$ and $B_0 = B_{\mathrm{c}} - \delta E/\delta\mu$ with Γ and δE as defined in Eq. (3.34) [18]. Formula (3.45) is of the same form as Eq. (3.42): Here, the resonance position is given by B_0, while ΔB denotes its width. The effect of the background scattering is parameterized by the background scattering length a_{bg}. As a divergence appears in Eq. (3.45), the scattering length can theoretically be tuned to arbitrary positive and negative values by changing the magnetic field strength B, only a finite scattering energy E restricts to finite values. This leads with Eq. (3.2) to a highly tunable interaction strength for ultracold gas systems. However, the value of the parameters B_0 and ΔB cannot be tuned by the magnetic field $\mathbf{B}$ and are fixed to values that are preset by the properties of the respective atoms. There are Feshbach resonances with considerably large ΔB, which are called broad Feshbach resonances, and narrow resonances with relatively small ΔB [18]. If one is interested in tuning the interaction strength by the Feshbach resonance in an experiment, it is of favor to have a broad one.

In Fig. 3.3 the scattering length of a magnetic Feshbach resonance is shown for the case of a model that will be derived in subsection 3.4.1. A pole in the scattering length is clearly visible, and the approximation with Eq. (3.45) works well in the vicinity of the resonance. In Fig. 3.3 also the binding energy E_{b} of the bound state that induces the resonance in the coupled channel description is shown. The value of E_{b} grows linearly with the slope $\delta\mu$ away from the resonance, while it reaches the threshold of the entrance channel at B_0. Near the position of the Feshbach resonance this bound state becomes a weakly bound molecular state [18]. In this regime the wave-functions of both channels mix and the bound state energy is given by [18, 126]

$$E_{\mathrm{b}} = \frac{\hbar^2}{2\mu} \frac{1}{a^2_{\mathrm{scatt}}(B)}. \tag{3.46}$$

This behavior is clearly visible in Fig. 3.3 (b), since $a_{\mathrm{scatt}} \propto (B - B_0)^{-1}$ in the vicinity of the resonance, here the bound state depends quadratically on $B - B_0$. The range of magnetic field strengths where E_{b} depends quadratically on $B - B_0$ has universal properties, here bound state and resonance scattering can be described by the pseudo potential $V^{\mathrm{pseudo}}_{a_{\mathrm{scatt}}(B)}(r)$ [18]. In Fig. 3.3 (a) this range of universal behavior is too small to be observed. Depending on the size of the universal region Feshbach resonances can be classified in entrance channel dominated or closed channel dominated resonances [18, 134]. In entrance channel dominated resonances, bound states and threshold scattering are determined to a high degree by the properties of the entrance channel, the area of universal behavior extends a vast range of the interval $B_0 + [-\Delta B, \Delta B]$, as seen in Fig. 3.3 (b) [134]. In closed channel dominated resonances the physics of the Feshbach resonance is determined by the closed channels, the region with universal behavior is tiny [134]. Figure 3.3 (a) displays such a case. Here a coupled channel description is necessary in order to grasp the relevant physics of the resonance [18].

Two-Channel Model of a Magnetic Feshbach Resonance

After the general introduction to magnetic Feshbach resonances we introduce a model that will be relevant in a later section. The derivation is motivated by the considerations of Refs. [126, 127]. A scattering process with two relevant channels is assumed. This is achieved for example with alkali atoms, which possess a $^2S_{1/2}$ ground state [18]. In this situation the physics is mainly determined by the spins S_i of the valence electrons. At first, we assume a magnetic field B large enough in order to neglect the interaction of the electron spins with the nuclear magnetic moment I_i. In this case the spins S_i can couple with either triplet or singlet configuration. In the triplet configuration the two valence electrons act as indistinguishable particles, which lowers the probability that the atoms are close to each other. In the singlet case the two electrons are in principle allowed to be on the same position in space. This is leading to a Born-Oppenheimer potential for the singlets that is much deeper than the triplet one [18, 126]. For realistic magnetic fields the hyperfine interaction V_{HF} is not negligible and is able to flip an electronic spin such that the system can perform transitions between triplet and singlet configuration [127]. Following Ref. [126], we describe the scattering physics of such a system by the following two-channel model

$$\left[-\Delta_R + \begin{pmatrix} v_1(r) & C \\ C & v_2(r)+\delta \end{pmatrix}\right] \begin{pmatrix} R_1(r) \\ R_2(r) \end{pmatrix} = E \begin{pmatrix} R_1(r) \\ R_2(r) \end{pmatrix}, \tag{3.47}$$

where $C = V_{\mathrm{HF}}\ 2\mu/\hbar^2$ is the coupling of triplet and singlet channel induced by the hyperfine interaction V_{HF}, $v_1(r)$ / $v_2(r)$ is the potential in triplet / singlet channel, and

$$\delta = \delta\mu\ B\ 2\mu/\hbar^2 \tag{3.48}$$

describes the relative detuning of the channel thresholds by the magnetic field B, with $\delta\mu$ as the difference of the magnetic moments of triplet and singlet channel [126]. In order to differentiate the channel detuning δ from the scattering phase shift $\delta_l(k)$, note, that we always write the scattering phase shift as an either momentum or energy dependent function, while the detuning is in all cases given without an argument. Further, we have rescaled in Eq. (3.47) and throughout this calculation all energies by $E \to E\ 2\mu/\hbar^2$. In the following the pseudo potential is assumed as concrete form of both triplet and single channel potential:

$$v_1(r) = v_{a_{\mathrm{e}}}^{\mathrm{pseudo}}(r),\ v_2(r) = v_{a_{\mathrm{c}}}^{\mathrm{pseudo}}(r), \tag{3.49}$$

with a_{e} / a_{c} as a channel dependent scattering length. Here, the "e" stands for entrance channel, the "c" for closed channel, since in the uncoupled case $C = 0$ the first channel is the entrance channel and the second is closed. The form (3.49) allows for a simple calculation without loosing the essential physics. In the following it is assumed that $\delta > 0$. In model (3.47) the channels are not decoupled at large radii r as demanded by Eq. (3.33). The first step is thus to restore Eq. (3.33) by diagonalizing the internal Hamiltonian

$$H_{\mathrm{int}} = \begin{pmatrix} 0 & C \\ C & \delta \end{pmatrix}. \tag{3.50}$$

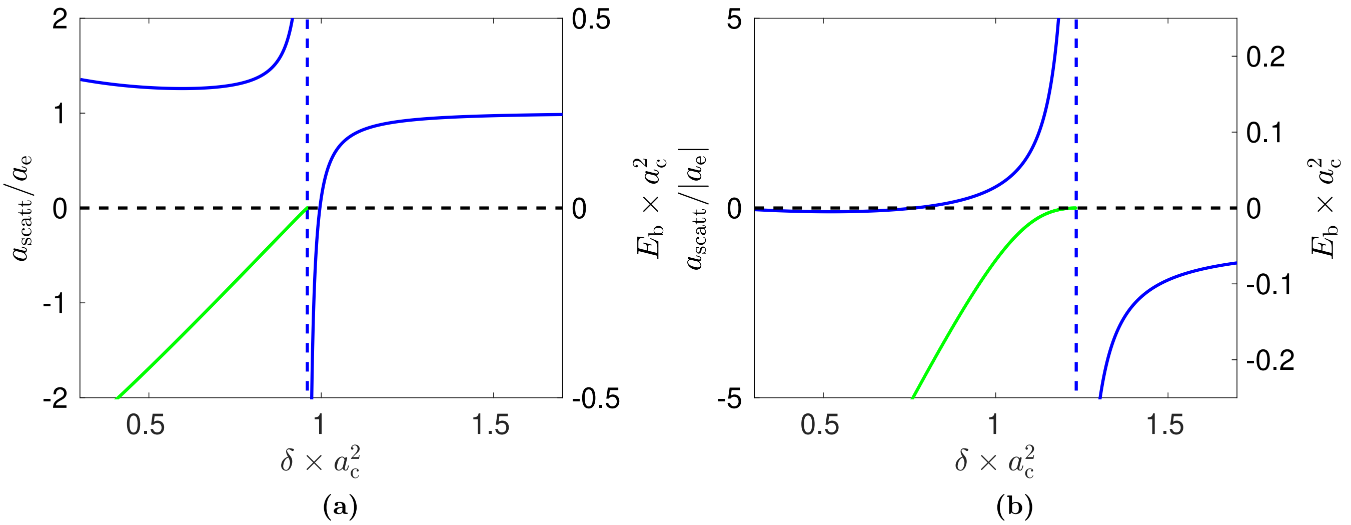

Figure 3.3.: Magnetic Feshbach resonance of model (3.47). Left axis: Scattering length in blue. Right axis: Binding energy E_{b} that is calculated by Eq. (3.57) in green. (a) with parameters $a_{\mathrm{e}} = 0.5\, a_{\mathrm{c}}$, $C \times a_{\mathrm{c}}^2 = 0.2$, (b) with parameters $a_{\mathrm{e}} = -4 a_{\mathrm{c}}$, $C \times a_{\mathrm{c}}^2 = 0.2$.

This is achived by the transformation $Q^\dagger H_{\mathrm{int}} Q = E_{\mathrm{int}}$, with

$$Q = \begin{pmatrix} \cos(\theta) & \sin(\theta) \\ -\sin(\theta) & \cos(\theta) \end{pmatrix}, \ \tan(2\theta) = \frac{2C}{\delta}, \tag{3.51a}$$

$$E_{\mathrm{int}} = \begin{pmatrix} E_- & 0 \\ 0 & E_+ \end{pmatrix}, \ E_\pm = \frac{\delta}{2} \pm \sqrt{\left(\frac{\delta}{2}\right)^2 + C^2}. \tag{3.51b}$$

Physically the transformation Q changes the triplet/singlet channels to become hyperfine channels [126], which are asymptotically decoupled. Measuring all energies relative to the threshold of the first channel E_-, Eq. (3.47) transforms to a potential of the form (3.35a) with matrix valued scattering length

$$\underline{\underline{a}} = Q^\dagger \begin{pmatrix} a_{\mathrm{e}} & 0 \\ 0 & a_{\mathrm{c}} \end{pmatrix} Q \tag{3.52}$$

and closed channel threshold $E_2 = E_+ - E_-$. The hyperfine channel with the lower energy is the entrance channel, in our case this is the first channel. The second channel is closed. Thus we are exactly in the situation of Subsec. 3.3.2, where with formula (3.38) the energy-dependent scattering length is found.

Since it is aimed to describe ultracold collisions, we again restrict to low energy scattering that is described by the limit $E \to 0$. Figure 3.3 shows the resulting scattering length at zero energy and is serving as a prototype example of a magnetic Feshbach resonance. A pole is visible near $\delta \approx 1/a_{\mathrm{c}}^2$, where the energy of bound state and scattering state are on resonance. We can go even further and calculate position and width with the deliberations of Sec. 3.3.2. The resonance position $\delta^{(0)}$ is calculated by applying condition (3.39) to the δ dependent parameters of the model (3.47).

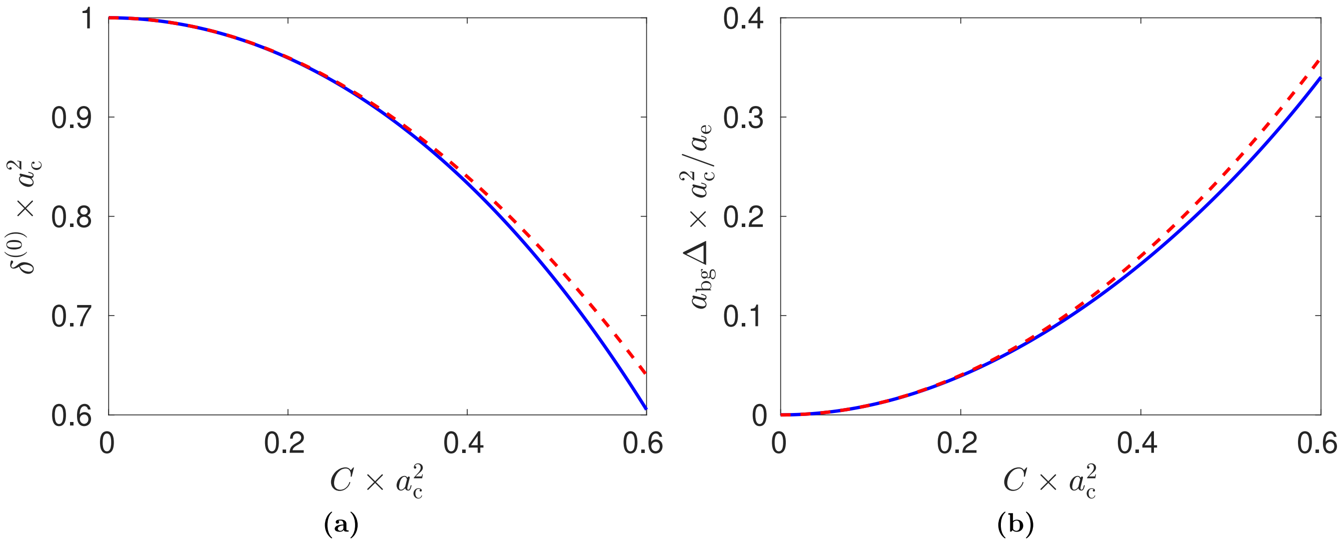

Figure 3.4.: (a) Resonance position, (b) product of resonance width and background scattering length over the coupling strength C. In blue numerically calculated quantities using Eq (3.53) and a generalization of Eq. (3.43), in red analytic approximations Eqns. (3.54) and (3.55). Both plots are made with $a_\mathrm{e} = a_\mathrm{c}/2$.

Using $\sin^2(\arctan(x/2)) = (\sqrt{x^2+1}-1)/2$, $\cos^2(\arctan(x/2)) = [(x^2+1)^{-1/2}+1]/2$, and $x = 2C/\delta$, Eq. (3.39) reads in case of the magnetic Feshbach resonance model as

$$\delta\sqrt{1+x^2} = \frac{1}{\left[a_\mathrm{e}\left(\frac{\sqrt{x^2+1}-1}{2}\right) + \frac{a_\mathrm{c}}{2}\left(\frac{1}{\sqrt{x^2+1}}+1\right)\right]^2}. \tag{3.53}$$

Equation (3.53) can be solved numerically for general parameters, in the following a perturbative result is derived for small x. With $(a+x)^b = a^b + bxa^{b-1} + (b-1)bx^2a^{b-2}/2 + \mathcal{O}(x^3)$ the resonance position is calculated up to second order in x to be

$$\delta^{(0)} = \frac{1}{a_\mathrm{c}^2} - 2a_\mathrm{e}a_\mathrm{c}C^2. \tag{3.54}$$

In the limit of vanishing coupling C the resonance position is indeed given by that detuning δ where bound state and scattering state are at resonance. For finite C both channels mix, which results in a shift of the resonance position as indicated by Eq. (3.54) and shown in Fig. 3.4 (a). Eq. (3.54) states that the direction of the shift to either positive or negative δ depends on the sign of a_e. For small C, the deviation of the resonance position from the uncoupled limit depends quadratically on C. In fact, for the examined parameter range there is a good agreement between numeric and analytic results. The width of the resonance can be calculated with the method of Subsec. 3.3.2. Since in this case all parameters are δ dependent, the derivation is more involved compared to the derivation of Eq. (3.41). Performing again an expansion up to second order in C one arrives at

$$a_\mathrm{bg}\Delta = 2a_\mathrm{c}(a_\mathrm{e}-a_\mathrm{c})^2C^2. \tag{3.55}$$

Here and in Fig. 3.4 (b) the product $a_\mathrm{bg}\Delta$ is investigated. This is done, as due to the δ dependence of the system parameters the background scattering length calculated by the theory as in Eq. (3.42) can differ from the naively assumed background scattering length given by $a_{\mathrm{bg}} = \lim_{\delta\to\infty} a_{\mathrm{scatt}}(\delta)$. Similar considerations are discussed in Ref. [122] in detail. In order to calculate the resonances width Δ as in Eq. (3.42) one has to know or define a value of a_{bg}. However, our theory is able to predict an unique value for the product of background scattering length and width. This can be seen in Eq. (3.43), where it is divided by a_{bg}, but this is only done in order to be able to factor out a_{bg} in Eq. (3.41). In order to avoid ambiguities we therefore choose to investigate the unique quantity $a_{\mathrm{bg}}\Delta$ which is shown in Fig. 3.4 (b). For small C the resonance width is narrow, while it increases quadratically in C. This behavior is considered as typical for a Feshbach resonance [11, 18], but in fact only holds for small couplings C. The deviation of the numerically calculated resonance width from the quadratic behavior is explained by the non-linearities of the cosine and sine functions that appear in the transformed inter-channel potential.

In addition to the scattering solutions of Eq. (3.47) also bound state solutions of the full coupled channel equations exist, which are calculated in the following. These solutions should not be confused with the bound states in the closed channels. The wave function is found by the ansatz

$$\begin{pmatrix} R_1(r) \\ R_2(r) \end{pmatrix} = Q \begin{pmatrix} D_1 e^{-\kappa_1 r}/(\kappa_1 r) \\ D_2 e^{-\kappa_2 r}/(\kappa_2 r) \end{pmatrix}. \tag{3.56}$$

The dispersion relation reads $\kappa_1 = \sqrt{-E_{\mathrm{b}}}$ and $\kappa_2 = \sqrt{E_+ - E_- - E_{\mathrm{b}}}$, where E_{b} is the binding energy of the bound state. Integrating around the origin with Eqns. (3.27) and (3.28) yields

$$\left[\begin{pmatrix} 1/\kappa_1 & 0 \\ 0 & 1/\kappa_2 \end{pmatrix} - Q^\dagger \begin{pmatrix} a_{\mathrm{e}} & 0 \\ 0 & a_{\mathrm{c}} \end{pmatrix} Q\right] \begin{pmatrix} D_1 \\ D_2 \end{pmatrix} = 0. \tag{3.57}$$

As the coefficients $D_i,\ i = 1, 2$, should not vanish, the determinant of the matrix must be zero. The resulting equation can be solved numerically for the binding energy E_{b}. As seen in Fig. 3.3 it turns out that for $a_{\mathrm{e}} > 0$ the region of universal behavior is narrow, while for $a_{\mathrm{e}} < 0$ the universal region is clearly visible.

3.4.2. Optical Feshbach Resonances

Optical Feshbach resonances are achieved by coupling the colliding atoms with a bound state in an exited electronic level [18, 115, 135]. This can induce a resonance in the scattering length, which can be parameterized by the form [18]

$$a_{\mathrm{scatt}} = a_{\mathrm{bg}} \left[1 + \frac{\Gamma_0(I)}{\hbar[\omega - \omega_{\mathrm{v}} - \delta\omega(I)] + i\gamma/2}\right]. \tag{3.58}$$

Here $\Gamma_0(I)$ is the resonance width, ω_{v} is the frequency of the unshifted transition, $\delta\omega(I)$ is the optical induced shift and γ the decay rate of the bound state e.g. due to spontaneous transmission. The resonance position $\omega_0(I) = \omega_{\mathrm{v}} + \delta\omega(I)$ and resonance width $\Gamma(I)$ of an optical Feshbach resonance can be tuned by the intensity of the laser [18]. This tunability of the resonance parameters is a great advantage compared to magnetic Feshbach resonances, where the properties of the resonance such

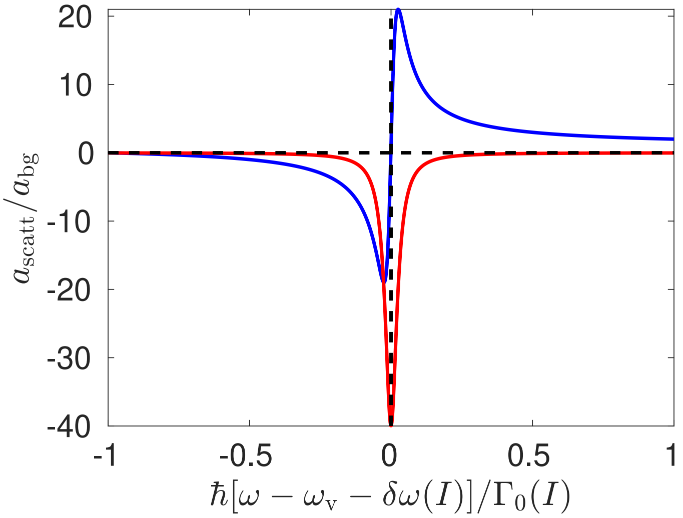

Figure 3.5.: Real (blue) and imaginary (red) part of an optical Feshbach resonance for $\gamma = 0.05\Gamma_0$.

as position and width cannot be controlled by external parameters. The large drawback of optical Feshbach resonances is the presence of a finite decay parameter γ. This implies that the scattering length becomes a complex number. The real part

$$\mathrm{Re}\; a_{\mathrm{scatt}} = a_{\mathrm{bg}} \left(1 + \frac{\Gamma_0(I)\hbar[\omega-\omega_{\mathrm{v}}-\delta\omega(I)]}{\hbar^2[\omega-\omega_{\mathrm{v}}-\delta\omega(I)]^2+\gamma^2/4}\right) \tag{3.59}$$

quantifies the elastic scattering, while the imaginary part

$$\mathrm{Im}\; a_{\mathrm{scatt}} = -\frac{a_{\mathrm{bg}}\Gamma_0(I)\gamma/2}{\hbar^2[\omega-\omega_{\mathrm{v}}-\delta\omega(I)]^2+\gamma^2/4} \tag{3.60}$$

is related to atom loss by a relation with the inelastic rate coefficient $K_{\mathrm{inel}} = -4\pi \mathrm{Im}\; a_{\mathrm{scatt}}/\mu$. As shown in Fig. 3.5 the maximum of the real part of the scattering length is finite, reducing the tunability of the resonance. In addition, loss is present that is often undesired. The loss can be minimized in the case of $\gamma \ll \Gamma_0(I)$ with a large detuning from the actual resonance position [18]. In addition to the scheme described above various extensions of optical Feshbach resonances have been created. For example Ref. [136] adds additional laser fields in order to achieve a situation similar to a Raman-transition, Ref. [137] realizes an optical Feshbach resonance coupling to a Rydberg molecule.

3.4.3. Radio-Frequency and Microwave Feshbach Resonances

In Refs. [138–145] it has been shown that Feshbach resonances can be influenced and induced by radio frequency (rf) or microwave (mw) fields. The fields couple the scattering state to a bound state [138, 141, 142], allowing for a high controllability of the resonance parameters by the external field. The width of the resonance is determined by the magnetic dipole element. Although the magnetic dipole coupling is generically weaker than the electric one, which is used in the case of optical Feshbach resonances, there can be no particle loss induced by spontaneous emission when working with rf or mv fields [141]. Alternatively the properties of an existing magnetic Feshbach resonance can be influenced by mw or rf fields [142,143,145]. Ref. [145] proposed a combination of a magnetic Feshbach resonance and a rf drive in order to provide independent control of the scattering lengths in a multi-component ultracold gas.

3.4.4. Floquet-Feshbach Resonances

This chapter is devoted to the so called Floquet-Feshbach resonances. Here, the idea is to induce Feshbach resonances by a time-periodic modulation of the inter-atomic potential, i.e. by periodically changing the depth of a potential well. The term "Floquet-Feshbach resonance" is motivated by the case of strong driving, where Floquet physics becomes relevant.

Reference [99] suggests to realize a time dependent inter-atomic potential by a sinusoidal driving of a magnetic field, that is polarized along the spin-quantization axis, in the vicinity of a magnetic Feshbach resonance. In this case, atom scattering is described by a pseudo potential with periodically driven interaction strength [18, 99]. Reference [99] found out that this procedure induces a resonance at magnetic fields away from the location of the undriven Feshbach resonance, which the author named as "Modulated Magnetic Feshbach Resonance". Both position and width of this resonance can be tuned by the drive. This resonance is created by coupling the scattering state to the dimer molecule of the Feshbach resonance, where much lower driving frequencies and larger drive amplitudes are possible compared to rf- or mw resonances. Ref. [116] performed a more detailed analysis of this effect and emphasized that due to the possible large driving amplitudes Floquet physics becomes relevant in this case.

In this thesis we develop the field by relating this driving-induced resonances to Feshbach resonances in Floquet space in a rigorous way. This strengthens our choice of the name "Floquet-Feshbach resonance". In Sec. 3.7 we will derive a theory that qualitatively predicts both the resonance position and the width of the Floquet-Feshbach resonances. As a prerequisite, a short wrap up of Floquet scattering theory is done in the next section.

3.5. Floquet Scattering Theory

This chapter introduces basic concepts of Floquet scattering theory, a theory which generalizes the scattering theory to time-periodically driven systems. At first, in Sec. 3.5.1 the basic ideas of Floquet scattering are introduced, while Sec. 3.5.2 summarizes the Floquet partial wave expansion.

3.5.1. General Properties of Floquet Scattering

This section deals with the scattering of two quantum particles by a time-periodic potential in three spatial dimensions. This process can be described in the center-of-mass frame of reference by the Hamiltonian

$$H(\mathbf{r},t) = -\frac{\hbar^2}{2\mu}\Delta + V(\mathbf{r},t), \tag{3.61}$$

where $V(\mathbf{r},t)$ describes the time-periodic interaction potential depending on the position $\mathbf{r}$ relative to the center-of-mass, $\mu = (m_1 m_2)/(m_1+m_2)$ denotes the reduced mass and Δ the Laplace operator in three dimensions. Similar to the time-independent case described in Sec. 3.2, the potential $V(\mathbf{r},t)$ is assumed to drop off faster than $1/r^2$ for large radii. As the Hamiltonian (3.61) is periodic in time, we can write down Floquet equation (2.16) using the Floquet modes $\phi_\epsilon(\mathbf{r},t)$. The Floquet equation is expressed using the Fourier components of the Floquet modes (2.33) and scattering potential (2.35)

$$\sum_{m=-\infty}^{\infty}\left[-\frac{\hbar^2}{2\mu}\Delta + V^{(n-m)}(\mathbf{r}) - n\hbar\omega\delta_{n,m}\right]\phi_\epsilon^{(m)}(\mathbf{r}) = \epsilon\phi_\epsilon^{(n)}(\mathbf{r}). \tag{3.62}$$

Like in chapter 2, the originally time-dependent problem is transformed into a static multi-channel problem, where each channel is labeled by the Fourier index n. This is an important result, since for a static multi-channel scattering problem various solution methods exist [113]. We name the channels emerging due to the structure of the Floquet Hilbert space as "Floquet channels". At this point we compare to a time-independent multi-channel model, such as Eq. (3.47). There the channels correspond to internal degrees of freedom, such as different hyperfine states of ultracold atoms, and the model contains a finite number of channels. In Eq. (3.62) an infinite number of channels is present, which have a special structure that is governed by the structure of Floquet theory. In the Floquet channel with index n the Fourier component $\phi_\epsilon^{(n)}(\mathbf{r})$ of the wave function resides, which has the a dynamic phase of $e^{-i(\epsilon/\hbar+n\omega)t}$. This visualizes that each Floquet channel contains a wave function with a different energy [116].

In the Floquet induced multi-channel problem (3.62), it is natural to assume an incoming plane wave to be localized solely in a single Floquet channel. The dynamic part of the potential induces scattering to other channels, so outgoing spherical waves appear in all Floquet channels. These arguments can be formulated mathematically: In analogy to static scattering theory it can be shown that in the limit of large r eq. (3.62) has the asymptotic solution

$$\phi_{\epsilon,n}(\mathbf{r}) = e^{i\mathbf{kr}}\delta_{n,0} + f_n(\Omega)\frac{e^{ik_n r}}{r}. \tag{3.63}$$

Without loss of generality, the incoming plane wave is assumed in the Floquet channel with channel index $n = 0$. The scattering amplitudes $f_n(\Omega)$ depend in general on the solid angle Ω. At asymptotic large distances r the scattering potential vanishes, implying that the dispersion relation is given by

$$\frac{\hbar^2}{2\mu}k_n^2 = \epsilon + n\hbar\omega. \tag{3.64}$$

We denote $\mathbf{k} = \mathbf{k}_0$. Evaluating Eq. (3.64) at $n = 0$ determines the quasienergy as the energy of the incoming plane wave $\epsilon = \hbar^2k^2/(2\mu)$. As typical for a scattering problem, we can choose ϵ to be any positive real number, which determines the energy of the incoming particles. For given ϵ, Eq. (3.64) is then used in order to calculate the momenta k_n in all Floquet channels. As previously discussed, the Floquet channel with index n host a wave functions with an energy of $\epsilon + n\hbar\omega$. There exists a critical index $n_c = \lceil -\frac{\epsilon}{\hbar\omega} \rceil$ where k_n is real if $n \geq n_\mathrm{c}$ while for $n < n_\mathrm{c}$ the wave vectors k_n are purely imaginary. Note that $\lceil x \rceil$ denotes the ceiling of a real valued x [120]. A real wave vector corresponds to a scattering state with the ability to propagate a finite probability current, so the channels with $n \geq n_\mathrm{c}$ are called open. A spherical wave with purely imaginary wave vector has a vanishing probability current, so the channels with $n < n_\mathrm{c}$ are closed channels. This structure is important for the calculation of observables, where we assume that the measuring process is faster than the driving frequency, such that a time average can be taken. The time-averaged differential cross section is given by [117]

$$\langle\langle \frac{d\sigma}{d\omega} \rangle\rangle = \sum_{n \geq n_c} \frac{d\sigma_n}{d\Omega}, \ \frac{d\sigma_n}{d\Omega} = |f_n|^2 \frac{k_n}{k_0}, \tag{3.65}$$

where $\frac{d\sigma_n}{d\Omega}$ denotes the differential cross section in the nth Floquet channel. Note that the sum in Eq. (3.65) only extends over the open Floquet channels. In order to derive Eq. (3.65) one basically follows the idea of Sec. 3.2 with a time-dependent probability current, while the factor k_n/k_0 comes from the different group velocities in the Floquet channels. The time-averaged total cross section is found by integration over the solid angle

$$\langle\langle \sigma \rangle\rangle = \sum_{n \geq n_\mathrm{c}} \sigma_n, \ \sigma_n \int_\Omega d\Omega |f_n(\Omega)|^2 \frac{k_n}{k_0}. \tag{3.66}$$

The elastic cross section is defined as the cross section in the channel $n = 0$ containing the incoming wave $\langle\langle \sigma_\mathrm{el} \rangle\rangle = \sigma_0$, while the elastic scattering amplitude is given by f_0. Scattering inside the $n = 0$ Floquet channel is considered as elastic, since the outgoing wave has the same energy as the incoming. Things are different if transitions between channels occur. In this case the energy of an outgoing wave is $E_n = \hbar^2 k_n^2/(2\mu) = \epsilon + n\hbar\omega$, where n "quanta" from the drive have been emitted or absorbed. Thus scatting to Floquet channels with $n \neq 0$ is inelastic. We name the Floquet channels with $n \geq n_\mathrm{c}, n \neq 0$ inelastic Floquet channels. The magnitude of inelastic scattering can be characterized by the inelastic rate coefficient [18],

$$K_\mathrm{inel} = \frac{\hbar k}{\mu} \langle\langle \sigma_\mathrm{inel} \rangle\rangle, \ \langle\langle \sigma_\mathrm{inel} \rangle\rangle = \sum_{\substack{n \geq n_\mathrm{c} \\ n \neq 0}} \sigma_n, \tag{3.67}$$

being defined as velocity $v = \hbar k/\mu$ times inelastic cross section $\langle\langle \sigma_\mathrm{inel} \rangle\rangle$. Similar to time-independent scattering there exists a Floquet optical theorem

$$\langle\langle \sigma \rangle\rangle = 4\pi \frac{\mathrm{Im}\ f_0(\theta = 0)}{k_0}, \tag{3.68}$$

that relates the time-averaged total cross section to the imaginary part of f_0 in forward direction $\theta = 0$ [116, 117].

3.5.2. Floquet Partial Wave Expansion

Like in the time-independent case a partial wave expansion can be performed if a spherical symmetric potential $V(r,t)$ is assumed. The following section provides a brief summary, while details are found in Ref. [117]. The partial wave expansion of the Fourier-components of the Floquet modes reads

$$\phi_{\epsilon,n}(\mathbf{r}) = \sum_{l=0}^{\infty} R_{l,n}(r) P_l(\cos\theta), \tag{3.69}$$

where l denotes the total angular momentum quantum number and $P_l(\cos\theta)$ the lth Legendre polynomial depending on the polar angle θ. We assume $\mathbf{k} = k\mathbf{e}_\mathrm{z}$. Similar to the time-independent case Eq. (3.10) the radial Floquet equation can be derived [117]

$$\left[\Delta_r + k_n^2 - \frac{l(l+1)}{r^2}\right] R_{l,n}(r) - \sum_{m=-\infty}^{\infty} v_m(r) R_{l,n-m}(r) = 0, \tag{3.70}$$

where the Fourier components of the potential are given by $v_n(r) = \frac{2\mu}{\hbar^2 T}\int_0^T dt e^{in\omega t} V(r,t)$. An asymptotic solution for large r of the Floquet partial wave equation (3.70) can be found by [117]

$$R_{l,n}(r) = \frac{2l+1}{2} i^l \delta_{n,0} i \frac{e^{-i(k_n r - \frac{\pi}{2} l)}}{k_n r} - B_{l,n} i \frac{e^{i(k_n r - \frac{\pi}{2} l)}}{k_n r}. \tag{3.71}$$

The mathematical structure stems from the large argument limit of the spherical Hankel functions $h_l^\pm(x)$, which are related to the spherical Bessel functions by $h_l^\pm(x) = j_l(x) \pm i y_l(x)$ [146]. The coefficients in front of the incoming waves are determined by the partial wave expansion of the plane wave (3.13), for details see Ref. [117]. The $B_{l,n}$ coefficients determine the strength of the scattering: Unlike to the static single channel calculation they do not only differ by a phase from the coefficients of the incoming wave, but they can also differ in magnitude. Thus they are related to a complex scattering phase shift $\delta^{(l,n)}$ according to $B_{l,n} = \frac{2l+1}{2} i^l e^{2i\delta^{(l,n)}}$ [117]. The $B_{l,n}$ coefficients are used to calculate the scattering amplitudes by [117]

$$f_n = \sum_{l=0}^{\infty} f_{l,n} P_l(\cos(\theta)),\ f_{l,n} = \frac{(-i)^{l+1}}{k_n}\left[B_{l,n} - \frac{2l+1}{2} i^l \delta_{n,0}\right]. \tag{3.72}$$

With Eq. (3.72) other observables such as the cross section can be calculated. In the case of s-wave scattering a Floquet-scattering length in the nth channel a_n^{Fl} is defined as $a_n^{\mathrm{Fl}} = -\lim_{\epsilon\to 0} f_n$ [117], while the effective scattering length is given by [99]

$$a_{\mathrm{scatt}} = a_{n=0}^{\mathrm{Fl}}. \tag{3.73}$$

Like in the time-independent case the scattering length a_{scatt} does neither depend on energy ϵ nor on the angles θ and ϕ. Thus Floquet s-wave scattering at low energies is isotropic. With Eq. (3.73) the elastic cross section reduces to [116]

$$\langle\langle \sigma_{\mathrm{el}} \rangle\rangle = 4\pi |a_{\mathrm{scatt}}|^2, \tag{3.74}$$

which is similar to the result of the time-independent case. Using Eqs. (3.65) and (3.68) for $\epsilon \to 0$ under the assumption that a_{scatt} is regular, the imaginary part of a_{scatt} can be related to inelastic scattering in Floquet channels with $n \neq 0$ according to Im $a_{\text{scatt}} = -\sum_{n \geq n_c,\ n \neq 0} |a_n^{\text{Fl}}|^2 k_n$. First, this shows that the imaginary part Im a_{scatt} is always negative. Second, the inelastic rate coefficient Eq. (3.67) is related to the imaginary part of the scattering length by

$$K_{\text{inel}} = -4\pi\hbar \ \text{Im}\ a_{\text{scatt}}/\mu. \tag{3.75}$$

The condition Im $a_{\text{scatt}} \leq 0$ gives rise to a positive K_{inel} describing the loss of particles. Microscopically, the particles leave the entrance channel by the Floquet scattering to the inelastic channels.

3.6. Scattering Resonances in a Harmonically Driven Pseudo Potential

In this section we discuss the driving-induced Floquet-Feshbach resonances in a harmonically driven pseudo potential. The pseudo potential describes the resonant scattering in the vicinity of a magnetic Feshbach resonance in the limit of low energy collisions [18] and thus explicitly describes scattering in an ultracold quantum gas. A time-periodic drive of the magnetic field in the vicinity of the Feshbach resonance leads to a time-periodic scattering length in the pseudo potential description. This is possible, since a low enough temperature of the ultracold atoms leads to wavelengths in the scattering solution which are much longer than the range of the actual inter-atomic potential. In this case, the range of the potential is negligible and the pseudo potential is a valid model for describing the inter-atomic scattering [18, 116, 117]. This is remarkable, since in combination with the simple mathematical structure of the pseudo potential we will be able to find interesting physics without an overhead of notation from scattering theory. The considered radial Hamiltonian reads

$$H(r,t) = -\Delta_R + \lim_{s \to 0^+} \frac{a(t)}{s^2} \delta(r-s) \overleftrightarrow{\frac{\partial}{\partial r}} r, \tag{3.76}$$

with $\Delta_R = \frac{1}{r^2}\frac{\partial}{\partial r} r^2 \frac{\partial}{\partial r}$ as the radial Laplacian and the harmonically driven scattering length

$$a(t) = \bar{a} + 2a_1 \cos(\omega t). \tag{3.77}$$

Equation (3.77) involves the driving frequency ω, the average scattering length $\bar{a}$ and the driving strength a_1, which is formulated in terms of Fourier components. With this the total amplitude of the AC-part of the drive is given by $a_{\text{AC}} = 2a_1$. Note that in Eq. (3.76) we already divided by $\hbar^2/(2\mu)$, where μ is the reduced mass. Further, in Eq. (3.76) the case of s-wave scattering is considered where no angular momenta with $l > 0$ are involved.

We start in Subsec. 3.6.1 by mapping the Floquet scattering problem to a recursion relation in the Fourier index. This recursion is solved analytically with the continued fraction method in Subsec. 3.6.2. As a result, driving-induced resonances are reported in Subsec. 3.6.3. These resonances tune the real part of the scattering length to arbitrary positive and negative values while losses due to inelastic collisions are not resonantly enhanced. It is indicated that both position and width of these resonances depend on the parameters of the periodic drive.

At this place we point out the different solution strategies of Eq. (3.76), that will be discussed in the following. In this section we introduce exact solution methods, which are a continued fraction approach and a numerical method, that truncates the Floquet scattering equations to a finite linear system. It will turn out that these exact methods are rather hard to interpret physically. The Floquet-Feshbach resonance theory, that will be derived in Sec. 3.7, yields, as a second method, an approximate solution of Eq. (3.76). However, the Floquet-Feshbach resonance theory makes a physical interpretation and a detailed analysis of the resonance parameters possible.

3.6.1. Recursion Relation for Floquet Scattering States

We aim to solve the radial Floquet equation

$$\left[H(r,t) - i\hbar\frac{\partial}{\partial t}\right] R(r,t) = \epsilon R(r,t) \tag{3.78}$$

with the Hamiltonian (3.76) and the Floquet mode

$$R(r,t) = \sum_n e^{-in\omega t} R_n(r) \tag{3.79}$$

with quasienergy ϵ. We are interested in the scattering problem, for which we can write down the radial wave function explicitly. We can always choose to write the wave function in terms of spherical Hankel functions [117]

$$R_n(r) = \frac{i}{2}\delta_{n,0}\frac{e^{-ik_n r}}{k_n r} - D_n i \frac{e^{ik_n r}}{k_n r}, \tag{3.80}$$

where the coefficients D_n are yet unknown. Ansatz (3.80) solves Eq. (3.78) trivially at each $r \neq 0$ with the dispersion relation Eq. (3.64). Again, we identify the quasienergy ϵ as the energy of the incoming particle, which is assumed to be in the $n = 0$ channel. Since we are generally interested in low-energy scattering the condition $\epsilon < \omega$ is assumed. This leads to evanescent waves with $k_n^2 < 0$ for all $n < 0$, which do not contribute to the scattering. All channels with $n \geq 0$ have free solutions with $k_n^2 \geq 0$ that lead to outgoing spherical waves. With Eq. (3.72) the corresponding scattering amplitudes can be calculated by the D_n coefficients with

$$f_n = -\frac{i}{k_n}\left(D_n - \frac{1}{2}\delta_{n,0}\right). \tag{3.81}$$

A recursion relation for the D_n coefficients is derived by integrating Eq. (3.78) with Hamiltonian Eq. (3.76) on a sphere with radius r_ϵ that is centered at the origin. Using Eqns. (3.27) and (3.28) we arrive at the following recursion relation [117]:

$$\left(\frac{i}{k_n} - \bar{a}\right) D_n - a_1 \left(D_{n+1} + D_{n-1}\right) = h_n, \tag{3.82}$$

with the right-hand side

$$h_n = \left(\frac{i}{k_n} + \bar{a}\right)\frac{\delta_{n,0}}{2} + a_1\left(\frac{\delta_{n+1,0}}{2} + \frac{\delta_{n-1,0}}{2}\right). \tag{3.83}$$

In order to be able to normalize the Floquet scattering state, the D_n coefficients should converge to zero fast enough at large absolute values of n [116]. This results in the following boundary condition for the coefficients

$$\lim_{n\to\pm\infty} D_n = 0. \tag{3.84}$$

Before solving recursion (3.82), we discuss two important issues. First, note that the recursion relation has a scale invariance such that we can measure all lengths and momenta in units of $|\bar{a}|$:

$$\tilde{a}_1 = \frac{a_1}{|\bar{a}|},\ \tilde{k}_n = k_n|\bar{a}|. \tag{3.85}$$

This implies that all energies, which appear inside $k_n = \sqrt{(\epsilon + n\hbar\omega)2\mu/\hbar^2}$ are measured in units of the so called dimer energy $E_\mathrm{D} = \hbar^2/(2\mu\bar{a}^2)$:

$$\tilde{\epsilon} = \frac{\epsilon}{E_\mathrm{D}},\ \tilde{\omega} = \frac{\hbar\omega}{E_\mathrm{D}}. \tag{3.86}$$

The physical relevance of the dimer energy is motivated by the static limit of $a_1 = 0$, where the Hamiltonian (3.76) possesses a bound state with an energy of $-E_\mathrm{D}$ in the case of positive $\bar{a}$, see Eq. (3.31). In dimensionless units the recursion relation Eq. (3.82) reads

$$\left(\frac{i}{\tilde{k}_n} - \mathrm{sign}(\bar{a})\right) D_n - \tilde{a}_1\left(D_{n+1} + D_{n-1}\right) = \tilde{h}_n, \tag{3.87}$$

with the inhomogeneity

$$\tilde{h}_n = \left(\frac{i}{\tilde{k}_n} + \mathrm{sign}(\bar{a})\right)\frac{\delta_{n,0}}{2} + \tilde{a}_1\left(\frac{\delta_{n+1,0}}{2} + \frac{\delta_{n-1,0}}{2}\right). \tag{3.88}$$

Second, if one would like to find a solution of the recursion (3.82) for the relevant case of $\epsilon = 0$, one would have to divide by zero in order to calculate the $n = 0$ scattering amplitude (3.81). We will see that this subtlety can be circumvented with our analytical solution found in the next subsection, but if the D_n are calculated numerically, this issue gets problematic. In this case it is favorable to insert Eq. (3.81) into recursion (3.87) and (3.88) and write down the recursion in terms of the scattering amplitudes [116, 117]

$$-(1 + \tilde{k}_n)\tilde{f}_n - i\tilde{a}_1(\tilde{k}_{n+1}\tilde{f}_{n+1} + \tilde{k}_{n-1}\tilde{f}_{n-1}) = \delta_{n,0} + \tilde{a}_1(\delta_{n,1} + \delta_{n,-1}), \tag{3.89}$$

where $\tilde{f}_n = f_n/|\bar{a}|$. For solving Eq. (3.89) numerically, one first needs to introduce a cutoff m with $\tilde{f}_n = 0$ for $|n| > m$. For the resulting finite scattering amplitudes $\tilde{f}_n$, $-m \leq n \leq m$ the recursion (3.89) transforms to a linear system which is uniquely solvable with common numerical methods. The cutoff m has to be chosen large enough such that $\tilde{f}_n$ is numerically small for indices near $-m$ and m. Instead of following this common numerical solution method [99, 117], we go beyond and derive an analytical solution of recursion (3.82) via continued fractions.

3.6.2. Continued Fraction Solution

In the following we derive an analytic solution of the scattering amplitude with the use of continued fractions. As a starting point we look at the recursion relation Eq. (3.87) for indices n where the homogeneity $\tilde{h}_n$ is nonzero, where we make the definition $L_n = \tilde{a}_1/(i/\tilde{k}_n - \mathrm{sign}(\bar{a}))$:

$$\begin{aligned} D_{\pm 1} - L_{\pm 1}(D_0 + D_{\pm 2}) &= \frac{L_{\pm 1}}{2}, && (3.90a)\\ \left(\frac{i}{\tilde{k}_0} - \mathrm{sign}(\bar{a})\right) D_0 - \tilde{a}_1(D_1 + D_{-1}) &= \frac{1}{2}\left(\frac{i}{\tilde{k}_0} + \mathrm{sign}(\bar{a})\right). && (3.90b)\end{aligned}$$

Eqns. (3.90) would be a solvable, closed set of equations, if the ratio of $D_{\pm 2}/D_{\pm 1}$ is explicitly known. At this point the continued fractions become relevant [147, 148]. With the ratio of neighboring recursion coefficients

$$q_n^{\pm} = \frac{D_{\pm(n-1)}}{D_{\pm n}}, \tag{3.91}$$

recursion (3.87) can be rewritten for the remaining indices with $|n| \geq 2$ to

$$q_n^{\pm} = \frac{1}{L_{\pm n}} - \frac{1}{q_{n+1}^{\pm}}. \tag{3.92}$$

For calculating the desired $(q_2^{\pm})^{-1} = D_{\pm 2}/D_{\pm 1}$, we can now apply Eq. (3.92) recursively. It is shown in Appendix A that the procedure of recursively inserting the $q_n^{\pm}$ into each other is equivalent to express $q_2^{\pm}$ by a continued fraction

$$q_2^{\pm} = \frac{1}{L_{\pm 2}} - \cfrac{1}{\frac{1}{L_{\pm 3}} - \cfrac{1}{\frac{1}{L_{\pm 4}} - \cfrac{1}{\ddots}}} = \frac{1}{L_{\pm 2}} - \cfrac{L_{\pm 3}}{1 - \cfrac{L_{\pm 3}L_{\pm 4}}{1 - \cfrac{L_{\pm 4}L_{\pm 5}}{\ddots}}}. \tag{3.93}$$

The identity of the last two expressions is found by an equivalence transformation [149], i.e by expanding each fraction line of the continued fraction by $L_{\pm n}$ such that they cancel out the $1/L_{\pm n}$ terms. Inserting the result (3.93) into Eq. (3.90a) we can relate D_0 and $D_{\pm 1}$ by

$$D_{\pm 1} = L_{\pm 1}\left(D_0 + \frac{1}{2}\right)\mathrm{cf}^{\pm} \tag{3.94}$$

with the continued fraction

$$\mathrm{cf}^{\pm} = \cfrac{1}{1 - \cfrac{L_{\pm 1}L_{\pm 2}}{1 - \cfrac{L_{\pm 2}L_{\pm 3}}{\ddots}}}. \tag{3.95}$$

This expresses D_0 and the elastic scattering amplitude $\tilde{f}_0 = -i/\tilde{k}_0(D_0 - 1/2)$ by an analytic formula

$$\tilde{f}_0 = \frac{-1}{\frac{1}{\tilde{a}^{\epsilon}} + i\tilde{k}_0}, \tag{3.96}$$

where the energy-dependent scattering length is expressed analytically with the use of continued fractions

$$\tilde{a}^{\epsilon} = \mathrm{sign}(\bar{a}) + \tilde{a}_1 L_1 \mathrm{cf}^{+} + \tilde{a}_1 L_{-1}\mathrm{cf}^{-}. \tag{3.97}$$

Eq. (3.96) is a remarkable result, as it allows us to express the elastic scattering amplitude f_0 of a Floquet problem in an analytical expression and even has the same mathematical structure as the solution of the corresponding static problem [117]. In the limit of vanishing energy, the experimentally relevant Floquet s-wave scattering length is given by

$$\tilde{a}_{\text{scatt}} = \lim_{\epsilon\to 0} \tilde{a}^{\epsilon}. \tag{3.98}$$

From Eq. (3.97) we can see that there are three contributions to the Floquet s-wave scattering length. First, there is the bare static scattering length, which equals $\text{sign}(\bar{a})$ in normalized units. Second, there is the contribution of the open Floquet channels which involves the continued fraction cf^{+}. Although the closed channels do not appear explicitly in formulas for the scattering cross section etc., they contribute in a third term involving cf^{-} to the scattering amplitude. In Sec. 3.7 we find out that it is exactly this term that induces the scattering resonances.

Before the scattering resonances are discussed in Subsec. 3.6.3, we now take a look at the convergence of recursion coefficients (3.82). For doing so it is instructive to write down the recursion (3.82) in the limit of large $|n|$:

$$\text{sign}(\bar{a})D_n - \tilde{a}_1(D_{n+1} + D_{n-1}) = 0. \tag{3.99}$$

Equation (3.99) is solved by $D_n = \Lambda_{\pm}^{|n|}$ with

$$\Lambda_{\pm} = \frac{-\text{sign}(\bar{a}) \pm \sqrt{1-4\tilde{a}_1^2}}{2\tilde{a}_1}. \tag{3.100}$$

It holds that $\Lambda_{+}\Lambda_{-} = 1$ and $\Lambda_{\text{sign}(a)} < 1$ if $\tilde{a}_1 < 1/2$. For $1/2 \geq \tilde{a}_1$ we get $|\Lambda_{\pm}| = 1$. This implies, that if the AC-part of the drive is smaller than the modulus of the average scattering length $a_{\text{AC}} = 2a_1 < |\bar{a}|$, the recursion converges to zero for large $|n|$ since one solution $\Lambda_{\pm}$ is smaller than one. In this case condition (3.84) can be fulfilled. In the other case, where $\tilde{a}_{\text{AC}} = 2\tilde{a}_1 \geq 1$, the recursion does not converge, as both solutions $\Lambda_{\pm}$ are of modulus one. Hence recursion coefficients D_n and thus the Fourier components of the wave function $R_n(r)$ with arbitrary large index n have a non-zero value. This implies that neither the steady state wave-function is normalizable nor its energy expectation value exists. Thus, the steady state is unphysical and cannot be reached experimentally in a finite time [116]. Due to this reasons we restrict in the following to the case $\tilde{a}_1 < 1/2$.

In the following the limits of high and low driving frequency are investigated, in each the scattering length is of a simple form. In the limit of an infinitely high driving frequency $\tilde{\omega} \to \infty$ it holds that $\tilde{k}_n \to \infty$ for $|n| \leq 1$. Thus, the scattering length is given by a regular continued fraction with constant partial numerators

$$\tilde{a}_{\text{scatt}}(\omega \to \infty) = \text{sign}(\bar{a})(1 + 2\cfrac{\tilde{a}_1^2}{1-\cfrac{\tilde{a}_1^2}{1-\cfrac{\tilde{a}_1}{\ddots}}}). \tag{3.101}$$

Eq. (3.101) can be explicitly evaluated using the relation [150]

$$\cfrac{\tilde{a}_1^2}{1-\cfrac{\tilde{a}_1^2}{1-\cfrac{\tilde{a}_1}{\ddots}}} = \sqrt{\frac{1}{4} - \tilde{a}_1^2} - \frac{1}{2}. \tag{3.102}$$

Finally we find a simple equation for the scattering length at infinite large driving frequency

$$\tilde{a}_{\text{scatt}}(\omega \to \infty) = \operatorname{sign}(\bar{a})\sqrt{1 - 4\tilde{a}_1^2}. \tag{3.103}$$

This is remarkable, since Eq. (3.103) shows that still at infinite high frequencies $\tilde{\omega}$ the scattering length is influenced by the driving strength $\tilde{a}_1$, and does not equal the average $\bar{a}$ as expected from a naive application of a high-frequency expansion, such as Eq. (2.15a). Mathematically this comes from the non-linear operations when calculating the effective scattering length (3.97) and shows that despite the high driving frequencies nontrivial Floquet scattering is possible. We further emphasize that Eq. (3.103) has no imaginary part.

In the opposite limit of low driving frequencies $\hbar\omega/E_{\text{D}} \ll 1$ Eq. (3.89) reduces for vanishing energy to

$$-\lim_{\epsilon \to 0} \tilde{f}_n = \delta_{n,0} + \tilde{a}_1(\delta_{n,1} + \delta_{n,-1}) \tag{3.104}$$

As a result we find that the Floquet scattering length adiabatically follows the course of $a(t)$ in this limit.

In the next subsection we do not restrict to either high or low driving frequencies and observe the occurrence of scattering resonances.

3.6.3. Tunability of the Scattering Length by the Drive

In the common description of ultracold quantum gases with a Gross-Pitaevskii mean field equation the inter-particle interaction is proportional to the s-wave scattering length a_{scatt}, c.f. Eq. (3.2). Here we are interested to analyze this case and investigate the effective s-wave scattering length Eq. (3.98) at zero energy of the model Eq. (3.76). The absolute value of the real part of the effective scattering Re $\tilde{a}_{\text{scatt}}$ length characterizes the strength of the inter-particle interaction while its sign determines if the interaction is attractive or repulsive [18]. The imaginary part Im $\tilde{a}_{\text{scatt}}$ is negative and characterizes particle loss from the Bose-Einstein condensate which is often wanted to be minimal [18]. In terms of the Floquet scattering theory, the absolute value of $\tilde{a}_{\text{scatt}}$ corresponds to the magnitude of the elastic cross section $\langle\langle\sigma_{\text{el}}\rangle\rangle = 4\pi|a_{\text{scatt}}|^2$, while the imaginary part is associated with inelastic scattering to higher Floquet channels with $n > 0$, c.f. the inelastic rate coefficient Eq. (3.75). In summary, it is often desired to control the real part Re $\tilde{a}_{\text{scatt}}$ while keeping the imaginary part Im $\tilde{a}_{\text{scatt}}$ small.

Figure 3.6 shows both real and imaginary part of the scattering length a_{scatt} of model (3.76). We clearly see resonances in the real part of the Floquet scattering length $\tilde{a}_{\text{scatt}}$ while the imaginary part is kept relatively small. This enables to tune the scattering length $\tilde{a}_{\text{scatt}}$ to arbitrary positive and negative values by choosing a desired driving frequency $\tilde{\omega}$ at a given driving strength $\tilde{a}_1$. Since the resonances are induced by the time-periodic drive the are named as driving-induced scattering resonances [117]. It turns out that for each $\tilde{a}_1 < 1/2$ all resonances lie below a certain driving frequency ω. This allows us to label the resonances from high to low resonant frequencies, where the

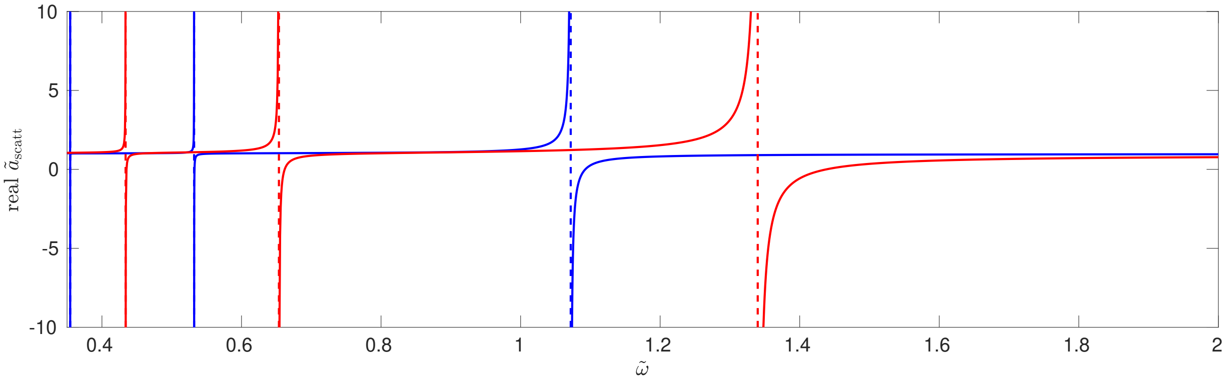

(a)

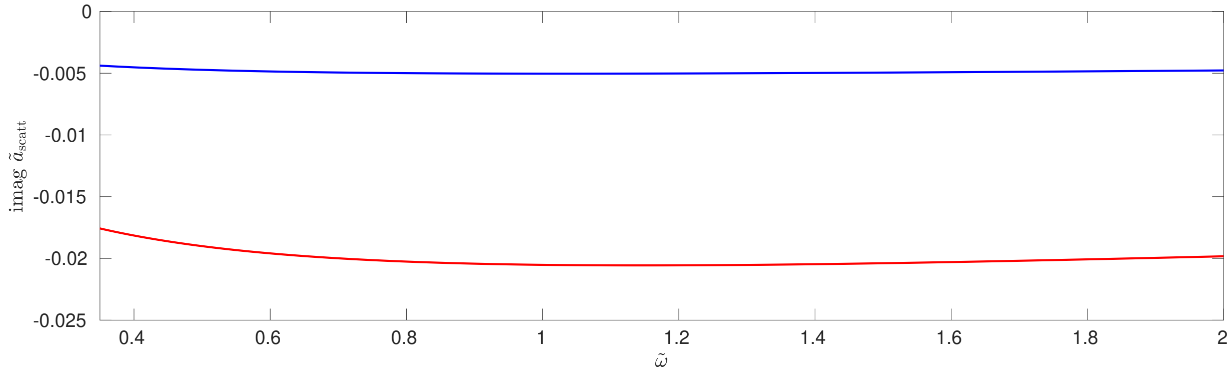

(b)

Figure 3.6.: Real part (a) and imaginary part (b) of the Floquet s-wave scattering length $\tilde{a}_{\rm scatt}$ for $\tilde{a}_1 = 0.1$ (blue) and $\tilde{a}_1 = 0.2$ (red) for positive $\bar{a}$. The resonance positions are marked with dashed lines in (a).

highest frequency corresponds to the first resonance. There are infinitely many resonances [117] and the smaller the frequency ω, at which a resonance appears, the narrower it is. Furthermore the resonance parameters are highly tunable. Both position and width change in dependence on the driving strength $\tilde{a}_1$. As it is seen in Fig. 3.6 (a), the resonance positions shift to higher frequencies $\tilde{\omega}$ if the driving strength $\tilde{a}_1$ increases while the resonances get wider for larger $\tilde{a}_1$. This allows one to choose the coveted resonance position and width by adjusting the driving strength $\tilde{a}_1$. The imaginary part of $\tilde{a}_{\rm scatt}$ is roughly two orders of magnitude smaller than the average scattering length $\bar{a}$ and does not peak near a resonance as it is usual for optical Feshbach resonances. Thus we find that for the driving-induced scattering resonance the losses are comparably small.

Fig. 3.7 (a) shows how the scattering length can also be tuned in the high-frequency limit as described by Eq. (3.103). Here no resonances are seen, but the periodic drive lowers the Floquet scattering length $\tilde{a}_{\rm scatt}$ below the corresponding static value $\bar{a}$. The scattering length even reaches zero for the case of maximal $2\tilde{a}_1 = \tilde{a}_{\rm AC} = 1$. In Fig. 3.7 we show the Floquet scattering length $\tilde{a}_{\rm scatt}$ for negative $\bar{a}$ in the same frequency range as in Fig. 3.6. Here clearly no resonances are visible, an examination of a wider parameter range shows that in general no resonances are found for negative $\bar{a}$ [117].

In this subsection we reported driving-induced scattering resonances in the sinusoidally driven pseudo

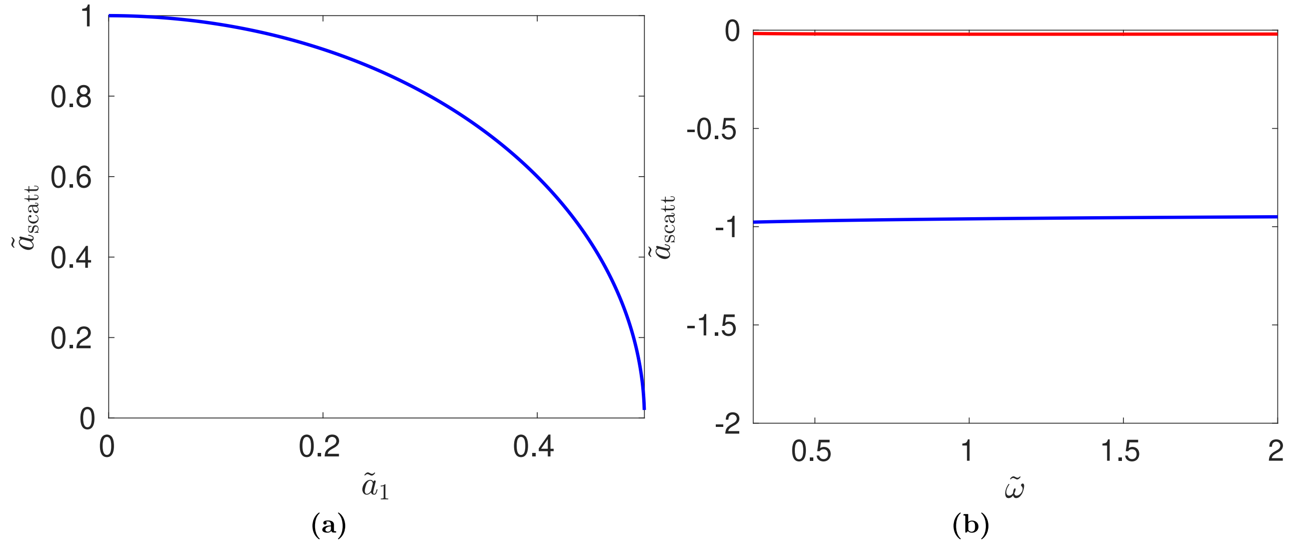

Figure 3.7.: (a): Floquet scattering length $\tilde{a}_{\rm scatt}$ over the driving strength $\tilde{a}_1$ in the limit of $\tilde{\omega} \to \infty$, (b): real (blue) and imaginary (red) part of the Floquet scattering length $\tilde{a}_{\rm scatt}$ for $\tilde{a}_1 = 0.2$ and $\bar{a} < 0$.

potential. However, the physical origin of these resonances is still elusive. In order to resolve this, the Floquet-Feshbach resonance theory is introduced in the next section. Further, using the Floquet-Feshbach resonance theory we calculate the resonance properties. This especially allows to discuss the limit $2\tilde{a}_1 \to 1$, where we expect with Eq. (3.100) that a large number of Floquet channels become relevant.

3.7. Floquet-Feshbach Resonance Theory for a Harmonically Driven Pseudo Potential

This section is the heart of this chapter. It gives host to the Floquet-Feshbach resonance theory which yields a quantitative understanding of the driving-induced scattering resonances. In order to have an elegant theory without loosing the essential train of thought we directly formulate the Floquet-Feshbach resonance theory for the case of the driven contact interaction in Subsec. 3.7.1. The Floquet-Feshbach resonance theory can be seen as a further solution method of Eq. (3.76) to the exact solutions found in Subsec. 3.6. As a prerequisite of the discussion of the resonance properties, Floquet bound states are calculated in Subsec. 3.7.2. Subsection. 3.7.3 contains the discussion of resonance position and width using the Floquet-Feshbach resonance theory. This discussion includes both numerical and analytical calculations of the resonance parameters. In Subsec. 3.7.4 recursion coefficients that characterize the Floquet bound state wave functions are presented, while Subsec. 3.7.5 is devoted to the inelastic scattering.

3.7.1. Floquet-Feshbach Resonance Theory

In this subsection the Floquet-Feshbach resonance theory is derived. The heart of the theory lies in the description of the scattering process in the Floquet Hilbert space, in which the time-periodic problem can be formulated as a static multi-channel scattering problem, c.f. Eq. (3.62). As discussed in Sec. 3.5, in Floquet space there are open and closed channels which are coupled by the periodic drive. This setting is similar to the one of a Feshbach resonance [14, 18, 113, 114]. As discussed in Sec. 3.3, a coupling of an open and closed channel induces a Feshbach resonance if the energy of a bound state in the closed channel equals the energy of a scattering state in the open channel. In our case we have instead of one channel infinitely many closed Floquet channels hosting possible bound states. Since these closed channels are coupled with each other by the periodic drive, possible bound states are expected to reside in multiple closed channels. These bound states couple with scattering states in the elastic Floquet channel ($n = 0$) and thus induce resonances in the elastic scattering amplitude as seen in the previous section. Compared to the static case discussed in Sec. 3.3 the Floquet scattering is more involved, since the elastic Floquet channel is also coupled to the inelastic channels with $n > 0$, which can influence the whole scattering problem. However, as seen in Fig. 3.6 (b) by the relatively small Im $\tilde{a}_{\text{scatt}}$, it will turn out with Eqns. (3.67) and (3.75) that the effect of the inelastic channels is rather small.

With these thoughts in mind we begin the derivation of the Floquet-Feshbach resonance theory by writing down the Floquet Hamiltonian $\mathcal{H} = H(t) - i\hbar\partial_t$ in Fourier space, see Subsec. 2.2.2 for the notation:

$$\mathcal{H}_{n,n} = -\frac{\hbar^2}{2\mu}\Delta_R - n\hbar\omega + \lim_{s\to 0^+}\frac{\hbar^2}{2\mu}\frac{\bar{a}}{s^2}\delta(r-s)\overleftrightarrow{\frac{\partial}{\partial r}}r, \tag{3.105a}$$

$$\mathcal{H}_{n,n\pm1} = \frac{\hbar^2}{2\mu}\frac{a_1}{s^2}\delta(r-s)\overleftrightarrow{\frac{\partial}{\partial r}}r, \tag{3.105b}$$

where all other $\mathcal{H}_{n,m} = (n|\hat{\mathcal{H}}|m)$ are zero. In Eq. (3.105) the diagonal part involves the radial Laplacian Δ_R, the threshold for each Floquet channel $-n\hbar\omega$ and the static part of the pseudo potential. The off-diagonal part of the tridiagonal matrix $\mathcal{H}_{n,m}$ is given by the AC-part of the driven interaction. For the following discussion it is of central relevance to separate into the elastic channel $n = 0$, the inelastic channels $n > 0$ and closed channels $n < 0$. This configuration implies $\epsilon < \hbar\omega$, which is valid in our range of interest $\epsilon \to 0$.

Similar to Feshbach's theory [14, 113, 114] we assume that there are bound states $|\phi_{\mathrm{B}}^{\alpha}\rangle\rangle$ in the closed channels, if the closed channels are decoupled from the open ones. As already discussed in Sec. 3.3.1, the energies of these bound states determine the position of the Feshbach resonance. Since we interested in finding the resonance position and further resonance properties, the bound states have to be discussed first. In the following, the index α labels different bound state solutions. The bound states fulfill the eigenvalue equation

$$\mathcal{H}_{n<0,n<0}|\phi_{\mathrm{B}}^{\alpha}\rangle\rangle = E_{\alpha}|\phi_{\mathrm{B}}^{\alpha}\rangle\rangle, \tag{3.106}$$

where E_α denotes their energy, and the notation from Subsec. 2.2.2 is used. The bound states are an element of Floquet space, where the bound state wave functions are defined by $(n|\phi^\alpha_{\mathrm{B}}\rangle\rangle = |\phi^\alpha_{n,\mathrm{B}}\rangle$ and $\langle r|\phi^\alpha_{n,\mathrm{B}}\rangle = \phi^\alpha_{n,\mathrm{B}}(r)$. In order to be bound states, they have to fulfill in addition to Eq. (3.106) the boundary condition

$$\lim_{r\to\infty} \phi^\alpha_{n,\mathrm{B}}(r) = 0,\ \forall n. \tag{3.107}$$

For the explicit form of the bound state wave functions we can always choose

$$\phi^\alpha_{n,\mathrm{B}}(r) = -D^\alpha_n \frac{e^{-\tilde{\kappa}_n r}}{\tilde{\kappa}_n r}, \tag{3.108}$$

with $\tilde{\kappa}^\alpha_n = \sqrt{-\tilde{E}_\alpha - n\tilde{\omega}}$. We insert Eq. (3.108) into Eq. (3.106). Using Eqns. (3.27) and (3.28) a recursion relation is derived

$$\left(\frac{1}{\tilde{\kappa}^\alpha_n} - \mathrm{sign}(\bar{a})\right) D^\alpha_n - \tilde{a}_1(D^\alpha_{n-1} + D^\alpha_{n+1}) = 0, \forall n < 0, \tag{3.109}$$

with the boundary conditions

$$D^\alpha_0 = 0,\ \lim_{n\to-\infty} D^\alpha_n = 0. \tag{3.110}$$

Furthermore we require the bound states to be normalized to one in Floquet space $\langle\langle\phi^\alpha_{\mathrm{B}}|\phi^\alpha_{\mathrm{B}}\rangle\rangle = 1$ which reads in terms of the coefficients

$$1 = \sum_{n<0} \frac{|D^\alpha_n|^2}{2(\tilde{\kappa}^\alpha_n)^3}. \tag{3.111}$$

Since besides of D^α_n also the energy E_α has to be determined, Eqns. (3.109) and (3.111) are considered as a set of non-linear equations and will be solved in Subsec. 3.7.2. Here it is assumed that all solutions D^α_n and E_α are known.

The next step in this derivation is to calculate the influence of the bound states defined in Eq. (3.106) on the scattering amplitude $\tilde{f}_0$. For doing so we introduce the full radial wave function in Floquet space $|R\rangle\rangle$. For an accessible mathematical description we define the notation $|R_{n=0}\rangle\rangle$ for the $n = 0$ Fourier component $(n = 0|R\rangle\rangle = |R_{n=0}\rangle\rangle$, and $|R_{n<0}\rangle\rangle$ for all Fourier components in the closed channels $|R_{n<0}\rangle\rangle = \sum_{n<0}(n|R\rangle\rangle|n)$, and so on. We aim to solve the Floquet equation

$$\mathcal{H}|R\rangle\rangle = \epsilon|R\rangle\rangle, \tag{3.112}$$

with $\mathcal{H}$ as defined in (3.105). The wave function in the $n = 0$ is given by

$$R_0(r) = \frac{\sin(kr)}{kr} + f_0\frac{e^{ikr}}{r}. \tag{3.113}$$

In Eq. (3.113) the first term is the s-wave part of the incoming plane wave, while the second denotes an outgoing spherical wave with elastic scattering amplitude f_0. The quasienergy ϵ is related to momentum by $\epsilon = \hbar^2 k^2/(2\mu)$ and thus denotes the energy of the incoming particle. Reference [117] found that $f_0 = i/k$ and $f_n = 0\ \forall n > 0$ holds at the resonance position. This implies for recursion (3.87) that the $n = 0$ part and the closed channels decouple. As a result Eq. (3.109) holds for the

$n < 0$ part of the solution of the full recursion (3.87) in this case [117]. This is of relevance to our theory, since it implies that exactly at resonance the wave function in the closed channels is equal to one bound state wave function fulfilling Eq. (3.109). This consideration further strengthens the argument of Sec. 3.3.1 and Refs. [14, 113], that we can approximate the wave function in the closed channels by a superposition of the Floquet bound states found with Eq. 3.106:

$$|R_{n<0}\rangle\rangle \approx \sum_{\alpha} A_\alpha |\phi_{\mathrm{B}}^{\alpha}\rangle\rangle. \tag{3.114}$$

In Eq. (3.114), the coefficients A_α have to be determined.

Having the final goal of finding an closed formula for $\tilde{f}_0$, the Floquet equation (3.112) is now evaluated for the closed channels. Using the eigenvalue equation (3.106) we find

$$\sum_{\alpha} (E_\alpha A_\alpha |\phi_{\mathrm{B}}^{\alpha}\rangle\rangle) + \mathcal{H}_{n<0,0}|R_0\rangle\rangle = \epsilon \sum_{\alpha} A_\alpha |\phi_{\mathrm{B}}^{\alpha}\rangle\rangle. \tag{3.115}$$

Projecting with $\langle\langle\phi_{\mathrm{B}}^{\beta}|$ and using the orthonormality $\langle\langle\phi_{\mathrm{B}}^{\beta}|\phi_{\mathrm{B}}^{\alpha}\rangle\rangle = \delta_{\alpha,\beta}$ yields

$$(E_\beta - \epsilon)A_\beta = -\langle\langle\phi_{\mathrm{B}}^{\beta}|\mathcal{H}_{n<0,0}|R_0\rangle\rangle = -\langle\phi_{-1,\mathrm{B}}^{\beta}|\mathcal{H}_{-1,0}|R_0\rangle. \tag{3.116}$$

For the last equality we use the tridiagonal structure of Floquet Hamiltonian (3.105). The matrix element can be explicitely evaluated with the expression of the Hamiltonian (3.105) and both wavefunctions (3.108) and (3.113) to

$$(\tilde{E}_\beta - \tilde{\epsilon})A_\beta = -D_{-1}^{\beta}\tilde{a}_1(1 + i\tilde{k}\tilde{f}_0). \tag{3.117}$$

This equation relates the A_β coefficients to the elastic scattering amplitude $\tilde{f}_0$. Now we turn to the inelastic channels $n > 0$. Here we assume the wave function $|R_{n>0}\rangle\rangle$ is given by the ansatz (3.80). For $n = 1$ we obtain by an integration around the origin using (3.27) and (3.28) the equation

$$-\frac{i}{\tilde{k}_1}D_1 + \mathrm{sign}(\bar{a})D_1 + \tilde{a}_1(1 + i\tilde{k}\tilde{f}_0) + \tilde{a}_1 D_2 = 0. \tag{3.118}$$

Recursion (3.87) holds for $n \geq 2$, such that we can relate $D_1 = q_2^+ D_2$ where q_2^+ is given by the continued fraction (3.93). Inserting $D_1 = q_2^+ D_2$ into (3.118) relates D_1 with the scattering amplitude $\tilde{f}_0$.

$$D_1 = L_1 \mathrm{cf}^+(1 + i\tilde{k}\tilde{f}_0), \tag{3.119}$$

where cf^+ is given by Eq. (3.95). At last we look for an equation for $n = 0$ with the common integration of the Floquet equation around the origin

$$(1 + i\ \mathrm{sign}(a)\tilde{k})\tilde{f}_0 + \mathrm{sign}(a) + \tilde{a}_1 \sum_{\alpha} D_{-1}^{\alpha} A_\alpha + \tilde{a}_1 D_1 = 0. \tag{3.120}$$

Now we do the last step by solving Eq. (3.117) for A_α, insert the result and Eq. (3.119) into Eq. (3.120) and finally solve Eq. (3.120) for the elastic scattering amplitude $\tilde{f}_0$. The scattering amplitude has the form

$$\tilde{f}_0 = \frac{-1}{\frac{1}{\tilde{a}^\epsilon} + i\tilde{k}}, \tag{3.121}$$

where the energy-dependent scattering length is given by

$$\tilde{a}^{\epsilon} = \text{sign}(\bar{a}) + \tilde{a}^{\epsilon}_{\text{res}} + \tilde{a}^{\epsilon}_{\text{inel}}. \tag{3.122}$$

Similar to Eq. (3.97), which we found by the direct continued fraction solution of the Floquet scattering problem Eq. (3.78), the energy-dependent scattering length consists of three terms: The bare scattering length $\bar{a}$, the resonant term given by

$$\tilde{a}^{\epsilon}_{\text{res}} = -\sum_{\alpha} \frac{\tilde{a}_1^2 |D^{\alpha}_{-1}|^2}{\tilde{E}_{\alpha} - \epsilon}. \tag{3.123}$$

and the inelastic scattering length

$$\tilde{a}^{\epsilon}_{\text{inel}} = \tilde{a}_1 L_1 \text{cf}^{+}. \tag{3.124}$$

The pronounced difference of Eq. (3.122) to (3.97) lies in the contribution of the closed channels. In this respect (3.123) yields a better physical interpretation as compared to (3.97), since it enables us to explain the driving-induced scattering resonance by a Feshbach theory in Floquet space. Equation (3.123) says that the contribution of the closed channels can be split into single terms, where each term is related to a single bound state and its contribution leads to a divergence the Floquet scattering length if the corresponding bound state energy $\tilde{E}_{\alpha}$ is on resonance with the energy $\tilde{\epsilon}$ of the scattering state. Thus we finally reached our goal of a rigorous understanding of the driving-induced scattering resonances: Our theory relates them to Feshbach physics in the Floquet Hilbert space. Based on this knowledge we name the driving-induced scattering resonances found in Subsec. 3.6.3 as Floquet-Feshbach resonances. Compared to the static model of a Feshbach resonance that is discussed in subsec. (3.3.2), the bound states in the Floquet-Feshbach resonance theory can be influenced by the time-periodic drive. Thus, $\tilde{E}_{\alpha}$ is interpreted as the energy of a state that is dressed by the periodic driving, in comparison to Subsec. (3.3.2) where no such dressing is possible. This leads to the interpretation that a Floquet-Feshbach resonance is as a Feshbach resonance that couples to the bound state being dressed by the periodic drive. Further, it is remarkable that the contributions of the inelastic channels can be elegantly solved by means of a continued fraction. We will see that for more complicated models such a simple continued fraction solution is no more possible.

Apart from this qualitative understanding, the Floquet-Feshbach resonance theory enables us to precisely define and calculate resonance positions and widths. For doing so we investigate how the scattering length $\tilde{a}_{\text{scatt}}$ at vanishing energy ϵ depends on the driving frequent ω. Performing the limit $\tilde{\epsilon} \to 0$ in Eq. (3.122) yields

$$\tilde{a}_{\text{scatt}}(\omega) = \text{sign}(\bar{a}) - \sum_{\alpha} \frac{\tilde{a}_1^2 |D^{\alpha}_{-1}|^2}{\tilde{E}_{\alpha}} + \tilde{a}_{\text{inel}}. \tag{3.125}$$

with $\tilde{a}_{\text{inel}} = \lim_{\epsilon \to 0} \tilde{a}^{\epsilon}_{\text{inel}}$. At first, we are interested if Eq. (3.125) recovers the known formula (3.103) for $\omega \to \infty$. In this case the channel thresholds $-n\hbar\omega$ are the largest energy scale in the Floquet Hamiltonian (3.105) for given $\tilde{a}_1$. This determines that the quasienergies E_{α} tend to infinity as $\omega \to \infty$. With this result the limit of infinite large frequencies follows as

$$\tilde{a}_{\text{scatt}}(\omega \to \infty) = \text{sign}(\bar{a}) \left(\frac{1}{2} + \sqrt{\frac{1}{4} - \tilde{a}_1^2} \right), \tag{3.126}$$

which obviously differs from the previous result Eq. (3.103). This demonstrates that the Floquet-Feshbach resonance theory does not yield the correct value of the scattering length away from the resonances. In the following we resolve this issue by renormalizing the scattering length, which is based on the subsequent argumentation. In Eq. (3.114) we assumed that the wave function in the closed channels is a superposition of bound states and neglected the contribution of the free states in the closed channels

$$|\phi^{\mathrm{free}}_{n<0}\rangle\rangle = \int_{\omega}^{\infty} d\tilde{E} A_{\tilde{E}} |\phi^{\tilde{E}}_{n<0}\rangle\rangle. \tag{3.127}$$

The states $|\phi^{\tilde{E}}_{n<0}\rangle\rangle$ are eigenstates of Eq. (3.106) which do not fulfill the boundary condition (3.107) and thus form the continuous spectrum of $\mathcal{H}_{n<0,n<0}$. Since the minimal threshold of all closed channels is $\tilde{\omega}$, free states must have energies above this value. The states $|\phi^{\tilde{E}}_{n<0}\rangle\rangle$ are an orthogonal set in Floquet space and are also orthogonal to the bound states $|\phi^{\alpha}_{n,\mathrm{B}}\rangle\rangle$. The exact wave-function in the closed channels with corrections reads $|R_{n<0}\rangle\rangle = \sum_\alpha A_\alpha |\phi^\alpha_{\mathrm{B}}\rangle\rangle + |\phi^{\mathrm{free}}_{n<0}\rangle\rangle$. Performing the steps (3.115)–(3.117) with $|\phi^{\mathrm{free}}_{n<0}\rangle\rangle$ leads to a new term $a_{\mathrm{free-corr}}$ in the scattering length

$$\tilde{a}^{\epsilon} = \mathrm{sign}(\bar{a}) + \tilde{a}^{\epsilon}_{\mathrm{res}} + \tilde{a}^{\epsilon}_{\mathrm{inel}} + \tilde{a}_{\mathrm{free-corr}}. \tag{3.128}$$

The calculation of the $A_{\tilde{E}}$ is not necessary, since we will see in the next section that it is an excellent approximation if we use the term $\tilde{a}_{\mathrm{free-corr}}$ in order to renormalize the non-resonant scattering length such that it fits to the limit (3.103). This renormalization is introduced by

$$\mathrm{sign}(\bar{a}) + \tilde{a}^{\epsilon}_{\mathrm{inel}} + \tilde{a}_{\mathrm{free-corr}} \approx \tilde{a}_{\mathrm{bg}} + \tilde{a}_{\mathrm{non-res}}, \tag{3.129}$$

where we define the background scattering length to fit to Eq. (3.103) by

$$\tilde{a}_{\mathrm{bg}} = \lim_{\omega\to\infty} \tilde{a}_{\mathrm{scatt}} = \mathrm{sign}(\bar{a})\sqrt{1-4\tilde{a}_1^2}. \tag{3.130}$$

The non-resonant part of the scattering length is defined to have a vanishing limit $\omega \to \infty$:

$$\tilde{a}_{\mathrm{non-res}} = \tilde{a}_{\mathrm{inel}} - \lim_{\omega\to\infty} \tilde{a}_{\mathrm{inel}}. \tag{3.131}$$

In order to further simplify Eq. (3.125), we note that the quasienergies of the bound states depend on the system parameters $E_\alpha = E_\alpha(\omega, \tilde{a}_1)$. It will turn out that each energy has a single zero which is named $\tilde{\omega}_\alpha$

$$\tilde{E}_\alpha(\tilde{\omega}_\alpha(\tilde{a}_1), \tilde{a}_1) = 0, \tag{3.132}$$

and depends in turn on the driving strength $\tilde{a}_1$. For parameters near $\tilde{\omega}_\alpha$ the resonant contribution of the α-th term in Eq. (3.125) dominates, otherwise its contribution is minimal. Thus we truncate the full functional form of $\tilde{E}_\alpha(\tilde{\omega}_\alpha, \tilde{a}_1)$ by a first-order Taylor expansion

$$\tilde{E}_\alpha(\tilde{\omega}_\alpha, \tilde{a}_1) \approx \frac{\partial \tilde{E}_\alpha}{\partial \tilde{\omega}}|_{\tilde{\omega}=\tilde{\omega}_\alpha} \times (\tilde{\omega} - \tilde{\omega}_\alpha). \tag{3.133}$$

With this we arrive at the final result

$$\tilde{a}_{\mathrm{scatt}}(\tilde{\omega}) = \tilde{a}_{\mathrm{res}} + \tilde{a}_{\mathrm{non-res}}, \tag{3.134}$$

with the resonant part of the scattering length given by

$$\tilde{a}_{\text{res}} = \tilde{a}_{\text{bg}} \left(1 - \sum_{\alpha} \frac{\tilde{\Delta}_\alpha}{\tilde{\omega} - \tilde{\omega}_\alpha} \right). \tag{3.135}$$

Here the resonant frequencies $\tilde{\omega}_\alpha$ are defined by (3.132) and the widths are given by

$$\tilde{\Delta}_\alpha = \frac{\tilde{a}_1^2 |D_{-1}^\alpha|^2}{\tilde{a}_{\text{bg}} \frac{\partial \tilde{E}_\alpha}{\partial \tilde{\omega}}|_{\tilde{\omega}=\tilde{\omega}_\alpha}}. \tag{3.136}$$

Equation (3.135) is the main result of this investigation. It does not only allow to qualitatively understand the origin of the driving-induced scattering resonances as Feshbach resonances in Floquet space, in combination with equations (3.132) and (3.136) we are even able to quantitatively calculate the resonance properties such as position and width. This result goes beyond recent the literature [99,116,117]. In particular, our theory exceeds the work of those references by the rigorous connection of the driving-induced scattering resonances to the physics of a Feshbach resonance. In contrast to Ref. [117], we are not restricted to a fitting procedure, since our theory proves with Eqns. (3.134) and (3.135) that the shape of a Floquet-Feshbach resonance is described by a simple formula and gives with Eqns. (3.132) and (3.136) expressions for calculating both position and width of the resonances. In particular, the resonant part Eq. (3.135) of a Floquet-Feshbach resonance is given by a similar formula as the scattering length of a magnetic Feshbach resonance Eq. (3.45). However, in Eq. (3.134) an additional non-resonant contribution stemming from inelastic scattering is present. As seen in Fig. 3.6 it turns out that effect of this non-resonant term is rather small as compared to the resonant enhancement of Re $\tilde{a}_{\text{scatt}}$. In particular, this shows that the imaginary part of the scattering length and thus atom loss is comparably small. In the next subsections we will use this theory in order to calculate how both position and width of the Floquet-Feshbach resonances depend on the driving strength $\tilde{a}_1$. As a prerequisite, we calculate the Floquet bound states in the next subsection.

3.7.2. Solving the Bound State Equations

In this subsection we find the energies and the wave functions of the eigenvalue equation (3.106) in the closed channels. Concretely, this subsection is about to solve the non-linear eigenvalue equation (3.109) together with the normalization condition (3.111). In the following we provide a full numerical solution in combination with analytical results for small and large driving strength $\tilde{a}_1$. With the resulting energies and wave functions of the Floquet bound states we can finally calculate position and width of the Floquet-Feshbach resonances in Subsec. 3.7.3.

Solving the Non-Linear System Numerically

For general $\tilde{a}_1$, the bound state energies and wave functions are calculated numerically by solving a non-linear set of equations, which we aim to write down in the general form

$$\mathbf{F}(\mathbf{q}) = \mathbf{0}. \tag{3.137}$$

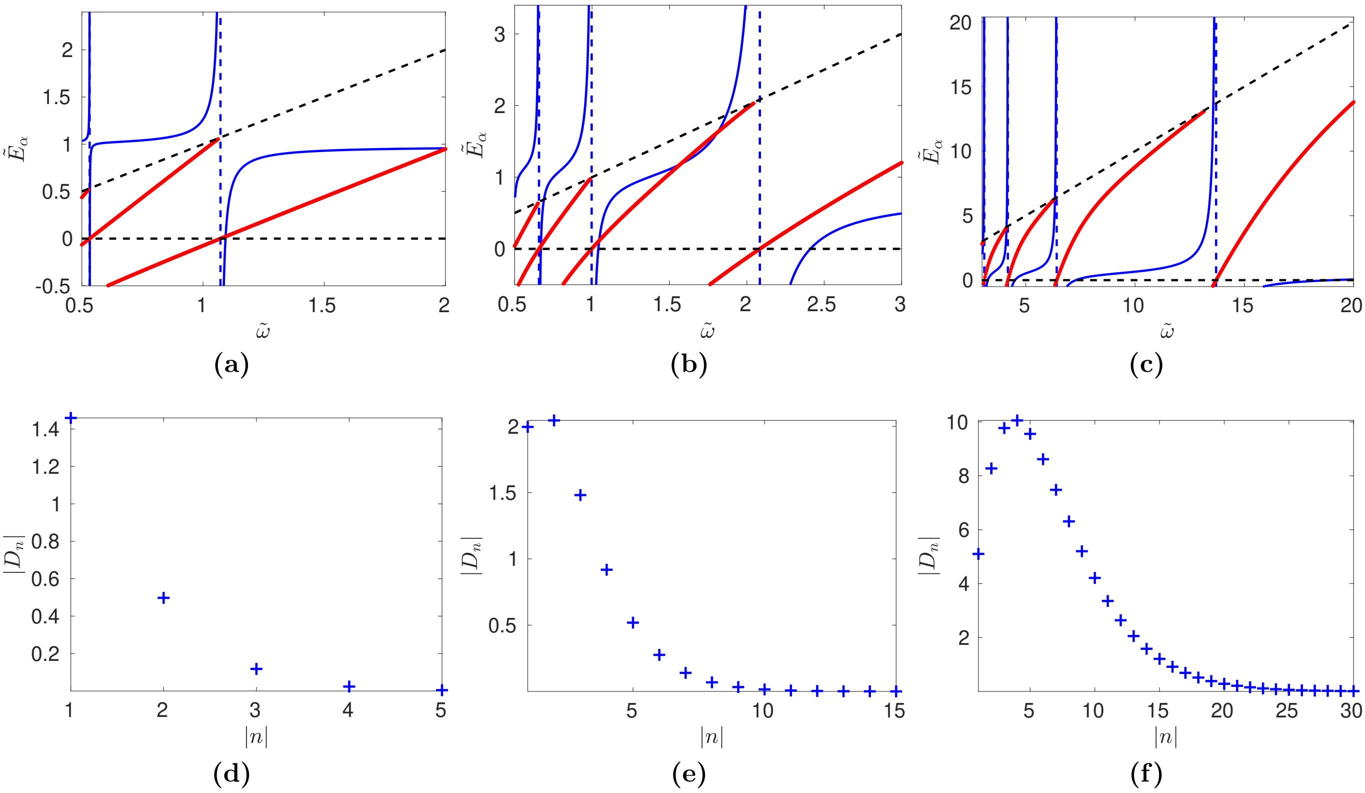

Figure 3.8.: (a-c): Bound state energies $\tilde{E}_\alpha$ (red), scattering length $\tilde{a}_{\text{scatt}}$ at $\epsilon = 0$ (blue), for the parameter $\tilde{a}_1 = 0.1$ (a), $\tilde{a}_1 = 0.3$ (b) and $\tilde{a}_1 = 0.45$ (c). Black dashed lines defined by equations $\tilde{E} = 0$ and $\tilde{E} = \tilde{\omega}$. The resonance position is marked by a blue dashed line. (d-f): Absolute value of recursion coefficients $|D_n|$ for the parameters $\tilde{a}_1 = 0.1$, $\tilde{\omega} = 1.071$ (d) and $\tilde{a}_1 = 0.3$, $\tilde{\omega} = 2.083$ (e) and $\tilde{a}_1 = 0.45$, $\tilde{\omega} = 13.72$ (f). The frequencies correspond to the larges zero of a bound state energy in the corresponding panel. In all panels we used as cutoff $n_{\text{c}} = 60$.

In order to make the vector function $\mathbf{F}$ finite dimensional, a cutoff in the Fourier index n_{c} is introduced. The cutoff has to be chosen such that the absolute value of the numerical solution is below a numerically small threshold for indices near n_{c} . For example, in Fig. 3.8 the absolute value of the coefficients D_n^α converged to a small value even for indices below the chosen $n_{\text{c}} = 60$. We emphasize that our numerical procedure automatically checks if n_{c} is large enough. With this the recursion relation (3.109) can be written as a homogeneous linear system

$$\underline{\underline{A}}(\lambda)\mathbf{D} = \mathbf{0}, \tag{3.138}$$

where $A_{n,n} = 1/\sqrt{-\lambda + n\tilde{\omega}}$ and $A_{n,n\pm1} = \tilde{a}_1$ while all other matrix elements are zero. For a solution of Eq. (3.138) it holds that $\mathbf{D}_n = D_{-n}^\alpha$ and $\lambda = \tilde{E}_\alpha$. The normalisation condition (3.111) is written as

$$\mathbf{D}^T\underline{\underline{V}}(\lambda)\mathbf{D} - 1 = 0, \tag{3.139}$$

where $V_{n,n} = 1/[2(-\lambda + n\tilde{\omega})^{3/2}]$ is a diagonal matrix. With this at hand we define the vector

$$\mathbf{q} = \begin{pmatrix} \mathbf{D} \\ \lambda \end{pmatrix} \tag{3.140}$$

and the function

$$\mathbf{F}(\mathbf{q}) = \begin{pmatrix} \underline{\underline{A}}(\lambda)\mathbf{D} \\ \mathbf{D}^T \underline{\underline{V}}(\lambda)\mathbf{x} - 1 \end{pmatrix} \tag{3.141}$$

in order to write our equation in the form (3.137). The non-linear equation is solved numerically.

In Fig. 3.8 (a-c) the numerically calculated bound state energies $\tilde{E}_\alpha$ are shown in red. One sees that there are multiple ones which increase in energy for larger driving frequencies $\tilde{\omega}$. The larger the driving strength, the more curvature the lines $E_\alpha(\tilde{\omega})$ have. As predicted by the Floquet-Feshbach resonance theory, we see in Fig. 3.8 that the zeros of the bound state energies $\tilde{E}_\alpha$ coincide with the locations of the resonances, i.e. the frequency at which the scattering amplitude diverges. Thus we label the bound states similar to the resonances from right to left along the frequency line, such that the first bound state causes the resonance with the largest resonant frequency, and so on. In Fig. 3.8 (a-c) the parameters are chosen such that the first resonance is always shown on the right. With larger driving strength the bound state energies $\tilde{E}_\alpha$ shift to negative values such that the zeros of the bound states $\tilde{E}_\alpha(\tilde{\omega})$ and thus the resonance positions move to the right. This shift is solely due to the periodic drive and thus a manifestation of Floquet physics. In Fig. 3.8 (d-f) we plot the recursion coefficients D_n^α of solutions of Eq. (3.109) over the absolute value of the index $|n|$ at the position of the first resonance. We see that with increasing driving strength more indices $|n|$ get populated, starting from about 5 at $\tilde{a}_1 = 0.1$ up to about 30 at $\tilde{a}_1 = 0.45$. This is indicating, that at large driving the coupling between the Floquet channels dominates, leading to a broad distribution of the recursion coefficient D_n^α. With the full numerical solution at hand we provide in the following analytical solutions for weak and strong driving.

Expansion with respect to the Driving Strength

In the case of weak driving, i.e. small $\tilde{a}_1$, we perform a perturbative analysis of Eqns. (3.109) and (3.111) by expanding both bound state energies and recursion coefficients in orders of $\tilde{a}_1$

$$D_n^\alpha = \sum_{l=0}^{\infty} D_n^{(l),\alpha}, \tag{3.142a}$$

$$\tilde{E}_\alpha = \sum_{l=0}^{\infty} \tilde{E}_\alpha^{(l)}. \tag{3.142b}$$

In Eq. (3.142), each coefficient indexed by l is assumed to be of order $\tilde{a}_1^l$. For the further analysis of Eqns. (3.109) and (3.111), the Taylor expansion of κ_n^{-s} with $s = 1,\ s = 3$ is important

$$\frac{1}{(\sqrt{a+x})^s} = \frac{1}{(\sqrt{a})^s} - \frac{sx}{2a^{(s+2)/2}} + \frac{s(s+1)x^2}{8a^{(s+4)/2}} + \mathcal{O}(x^3/a^{(s+6)/2}). \tag{3.143}$$

Applied to our case we have $a = -\tilde{E}_\alpha^{(0)} + |n|\tilde{\omega}$ and $x = \sum_{l>0} E_\alpha^{(l)}$. Expanding Eq. (3.109) in zeroth order $\tilde{a}_1$ we find the unperturbed bound states by the equation

$$\left(\frac{1}{\sqrt{-\tilde{E}_\alpha^{(0)} + |n|\tilde{\omega}}} - \operatorname{sign}(\bar{a}) \right) D_n^{(0),\alpha} = 0. \tag{3.144}$$

In the case of $\bar{a} > 0$ there are infinitely many solutions of Eq. (3.144) labeled by $\alpha \in \mathbb{N}$

$$D_n^{(0),\alpha} = N_\alpha \delta_{-\alpha,n}. \tag{3.145}$$

The energies of these bound states are given by

$$\tilde{E}_\alpha^{(0)} = -1 + \alpha\tilde{\omega}. \tag{3.146}$$

Equation (3.146) is an analytic formula for the bound state energies in the limit of small driving strength $\tilde{a}_1$. In this limit a Floquet-Feshbach resonance occurs if $\tilde{E}_\alpha^{(0)}$ is equal to the energy of the incoming particle ϵ. With Eq. (3.146) we interpret that in the case of small $\tilde{a}_1$ resonances occur if the bound dimer state of the pseudo potential with energy $-\tilde{E}_\mathrm{D} = -1$ is brought to energetic resonance with the scattering state at energy $\tilde{\epsilon}$ by α quanta of the drive. At last, note, that the normalization of the bound state recursion coefficients is given in the zeroth order of $\tilde{a}_1$ with Eq. (3.111) by

$$D_{-\alpha}^{(0),\alpha} = \sqrt{2}. \tag{3.147}$$

As seen in Eq. (3.136), the correctly normalized recursion coefficients are important for calculating the resonance width.

In the case of negative $\bar{a}$ Eq. (3.144) has no solutions. We conclude that no bound states are present in this case. Physically, this result comes from the fact that the static pseudo potential hosts no bound state in the case of negative $\bar{a}$. Since there is no bound state to couple to, no resonances occur in this case. Due to this we restrict ourselves to $\bar{a} > 0$ in the following.

We continue with $\mathcal{O}(\tilde{a}_1)$. Due to the structure of the recursion only the nearest neighbors of a solution Eq. (3.144) with quantum number $\alpha \geq 2$ are unequal from one. The recursion relation Eq. (3.109) implies the following equations

$$-\alpha \quad : \quad \frac{\tilde{E}_\alpha^{(1)}}{2} D_{-\alpha}^{(0),\alpha} = \tilde{a}_1 \sum_{\pm} D_{-\alpha\pm 1}^{(0),\alpha}, \tag{3.148a}$$

$$-\alpha \pm 1 \quad : \quad \left(\frac{1}{\sqrt{1 \pm \tilde{\omega}}} - 1 \right) D_{-\alpha\pm 1}^{(1),\alpha} = \tilde{a}_1 D_{-\alpha}^{(0),\alpha}. \tag{3.148b}$$

With (3.148a) it follows $\tilde{E}_\alpha^{(1)} = 0$ and with (3.148b) one gets

$$D_{-\alpha\pm 1}^{(1),\alpha} = \sqrt{2} \frac{\tilde{a}_1}{\frac{1}{\sqrt{1\pm\tilde{\omega}}} - 1}. \tag{3.149}$$

The $\mathcal{O}(\tilde{a}_1)$-part of the normalization equation (3.111) yields

$$\sum_{n<0} \frac{D_n^{(0),\alpha} D_n^{(1),\alpha}}{(-\tilde{E}_\alpha^{(0)} + |n|\tilde{\omega})^{3/2}} + \frac{|D_n^{(0),\alpha}|^2}{2} \frac{3\tilde{E}_\alpha^{(1)}}{2(-\tilde{E}_\alpha^{(0)} + |n|\tilde{\omega})^{5/2}} = 0. \tag{3.150}$$

Inserting the known values from the recursion relation into Eq. (3.150), we get $D_{-\alpha}^{(0),\alpha} D_{-\alpha}^{(1),\alpha}/2 = 0$ which implies $D_{-\alpha}^{(1),\alpha} = 0$. For $\alpha + n$ with $|n| > 1$ it holds that $D_{-\alpha+n}^{(1),\alpha} = 0$, since only the nearest neighbors of α are coupled to $D_{-\alpha}^{(0),\alpha}$ at this stage.

We now elaborate $\mathcal{O}(\tilde{a}_1^2)$, assuming $\alpha \geq 3$. The parts of the recursion relation (3.109) containing a second order of $\tilde{a}_1$ are

$$-\alpha \quad : \quad \frac{\tilde{E}_\alpha^{(2)}}{2} D_{-\alpha}^{(0),\alpha} = \tilde{a}_1 \sum_{\pm} D_{-\alpha\pm 1}^{(\alpha),1}, \tag{3.151a}$$

$$-\alpha \pm 1 \quad : \quad \left(\frac{1}{\sqrt{1 \pm \tilde{\omega}}} - 1 \right) D_{-\alpha\pm 1}^{(2),\alpha} = \tilde{a}_1 D_{-\alpha}^{(1),\alpha}, \tag{3.151b}$$

$$-\alpha \pm 2 \quad : \quad \left(\frac{1}{\sqrt{1 \pm 2\tilde{\omega}}} - 1 \right) D_{-\alpha\pm 2}^{(2),\alpha} = \tilde{a}_1 D_{-\alpha\pm 1}^{(1),\alpha}. \tag{3.151c}$$

The second order energy correction calculates with Eqns. (3.147), (3.149) and (3.151a)

$$\tilde{E}_\alpha^{(2)} = 2\tilde{a}_1^2 \sum_{\pm} \frac{1}{\frac{1}{\sqrt{1\pm\tilde{\omega}}} - 1}, \tag{3.152}$$

which is smaller than zero. Note that Eq. (3.152) also holds for $\alpha = 2$, while for $\alpha = 1$ only the "+"-term appears. Eq. (3.151b) implies $D_{-\alpha\pm 1}^{(2),\alpha} = 0$ and (3.151c) yields

$$D_{-\alpha\pm 2}^{(2),\alpha} = \frac{\tilde{a}_1}{\frac{1}{\sqrt{1\pm 2\tilde{\omega}}} - 1} D_{-\alpha\pm 1}^{(1),\alpha}. \tag{3.153}$$

This result can be generalized by a recursive argument to higher orders of $\tilde{a}_1$ for the outermost non-vanishing coefficient $D_{-\alpha\pm n}^{(n),\alpha}$:

$$D_{-\alpha\pm n}^{(n),\alpha} = \sqrt{2} \frac{\tilde{a}_1^n}{\Pi_{j=1}^n \left(\frac{1}{\sqrt{1\pm j\tilde{\omega}}} - 1 \right)}, \tag{3.154}$$

while $D_{-\alpha\pm n}^{(j),\alpha} = 0 \; \forall j < n$. For the energies $\tilde{E}_\alpha^{(n)}$ no such recursive argument is possible. These results are enough to calculate position and width of the resonances in Subsec. 3.7.3. In the following we discuss the Floquet bound states in the case of large driving strength $\tilde{a}_1$.

Continuum Theory for Large Driving Amplitudes

Fig. 3.8 (d-f) shows that the distribution of the D_n^α indices gets broad for large $\tilde{a}_1$. Due to this observation we assume that it might be fruitful to derive a theory by performing a continuum limit for the recursion coefficients D_n^α for strong driving. As seen in Fig. 3.8 (a-c), the resonant frequency shifts to larger values if the driving strength increases. Therefore we construct the continuum limit in the case of $\tilde{\omega} \to \infty$. Following Ref. [116], a unitary transformation in Floquet space is done

$$\mathcal{D}_n = (-1)^n D_{-n}, \tag{3.155}$$

which flips the sign in the $\tilde{a}_1$ term and changes the sign in the index n. This is necessary in order to have an attractive potential in the continuum theory. At second, we define the continuous variable $x = n/\tilde{\omega}$. With this it follows that $\tilde{\kappa}_n = \sqrt{n\tilde{\omega} - \tilde{E}_\alpha} = \sqrt{x - y_\alpha}\tilde{\omega}$ with the dimensionless energy y_α defined by $\tilde{E}_\alpha = y_\alpha \omega^2$. Using these definitions, the normalization equation (3.111) reads

$$\sum_{n>0} \Delta n \frac{|\mathcal{D}_{x\omega}|^2}{2(x - y_\alpha^{3/2})\tilde{\omega}^3} = 1, \tag{3.156}$$

with $dx = \Delta n/\tilde{\omega}$, $\Delta n = 1$ and the definition of the continuous field

$$\mathcal{D}(x) = \frac{\mathcal{D}_{x\omega}}{\tilde{\omega}}. \tag{3.157}$$

Definition (3.157) is such that the normalization becomes independent of the driving frequency

$$\int_0^\infty dx \ \frac{|\mathcal{D}(x)|^2}{2(x - y_\alpha)^{3/2}} = 1. \tag{3.158}$$

From recursion relation (3.109) an equation for the field $\mathcal{D}(x)$ can be derived by multiplying with $1/\tilde{a}_1$ and using $0 = 2\mathcal{D}_n - 2\mathcal{D}_n$:

$$\frac{1}{\tilde{a}_1}\left(\frac{1}{\sqrt{x - y\tilde{\omega}}} - 1\right)\mathcal{D}(x) + \mathcal{D}_{(x+\frac{1}{\omega})\omega} + D_{(x-\frac{1}{\omega})\omega} - 2\mathcal{D}_{x\omega} + 2\mathcal{D}_{x\omega} = 0. \tag{3.159}$$

With $dx = 1/\omega$ a second derivative with respect to x is introduced by

$$\mathcal{D}_{(x+\frac{1}{\omega})\omega} + D_{(x-\frac{1}{\omega})\omega} - 2\mathcal{D}_{x\omega} = \frac{1}{\omega}\frac{\partial^2}{\partial x^2}\mathcal{D}(x). \tag{3.160}$$

Now we arrive at the continuous version of the recursion relation

$$\left(-\frac{\tilde{\omega}}{\tilde{a}_1\sqrt{x - y_\alpha}} - \frac{\partial^2}{\partial x^2}\right)\mathcal{D}(x) = 2\omega^2\left(1 - \frac{1}{2\tilde{a}_1}\right)\mathcal{D}(x). \tag{3.161}$$

This relation can be mapped to a one-dimensional Schrödinger equation of an attractive inverse square root potential

$$\left(-\frac{1}{A}\frac{1}{\sqrt{x - y}} - \frac{\partial^2}{\partial x^2}\right)\phi(x) = E\phi(x), \tag{3.162}$$

if we set

$$A = \tilde{a}_1/\tilde{\omega} > 0,\ E = 2\tilde{\omega}^2(1 - 1/(2\tilde{a}_1)),\ \ y = y_\alpha \text{ and } \phi(x) = \mathcal{D}(x). \tag{3.163}$$

In order to have a non-singular potential, $y_\alpha \leq 0$ is assumed. Ref. [116] finds a similar result having $y = 0$, where a solution in terms of confluent-hypergeometric functions can be found [151]. Here we go beyond and find a quasi-analytic formula for the eigenenergy E of Eq. (3.162) at general $y \leq 0$. We therefore apply the transformation $x = cz$ and $y = cz_0$ to Eq. (3.162) and choose c such that in Eq. (3.162) the same coefficients stand in front of both potential and kinetic term. The transformed equation reads

$$\left(-\frac{1}{A\sqrt{c}} \frac{1}{\sqrt{z - z_0}} - \frac{1}{c^2} \frac{\partial^2}{\partial z^2} \right) \tilde{\phi}(z) = E \tilde{\phi}(z), \tag{3.164}$$

where $\tilde{\phi}(z) = \phi(cz)$. Both terms have the same prefactor $A^{4/3}$, provided that $c = A^{2/3}$. Multiplying by $A^{4/3}$ we have factored out the A dependence and absorb it into the definition of the eigenenergies

$$\left(\frac{-1}{\sqrt{z - z_0}} - \frac{\partial^2}{\partial z^2} \right) \tilde{\phi}(z) = E^{\bullet} \tilde{\phi}(z), \tag{3.165}$$

where $E^{\bullet} = A^{4/3} E$. With this result a quasi-analytic expression for the eigenenergies is derived

$$E(z_0, A) = E^{\bullet}(z_0) A^{-4/3}. \tag{3.166}$$

It is termed quasi-analytic, since only the dependence on A can be expressed analytically, while the z_0 dependence $E^{\bullet}(z_0)$ has to be calculated numerically. The different solutions of Eq. (3.165) are in the following labeled by the index α. It is know that the attractive inverse square root potential hosts countable many bound states [151], which are labeled with ascending energy starting at the ground state with $\alpha = 1$. This definition relates these labels with the labeling of the Floquet-Feshbach resonances.

The quasienergies $\tilde{E}_\alpha$ for the Floquet bound states are finally calculated by looking at Eq. (3.166), while assuming $A(\tilde{a}_1, \tilde{\omega}) = \tilde{a}_1/\omega$ and $E(\tilde{a}_1, \tilde{\omega}) = 2\omega^2(1 - 1/(2\tilde{a}_1))$ for our concrete physical problem. Using $y = A^{2/3} z_0$, Eq. (3.166) is solved for y by the inverse function of $E^{\bullet}_{\alpha}$, which we denote as $g_\alpha = E^{\bullet}{}^{-1}_{\alpha}$ and obeys $g_\alpha(E^{\bullet}_{\alpha}(z_0)) = z_0$:

$$y = y_\alpha = A(\tilde{a}_1, \tilde{\omega})^{2/3} g_\alpha[A(\tilde{a}_1, \tilde{\omega})^{4/3} E(\tilde{a}_1, \tilde{\omega})]. \tag{3.167}$$

Using $\tilde{E}_\alpha = \tilde{\omega}^2 y_\alpha$ we can express the quasienergy as

$$\tilde{E}_\alpha = \tilde{\omega}^2 A(\tilde{a}_1, \tilde{\omega})^{2/3} g_\alpha[A(\tilde{a}_1, \tilde{\omega})^{4/3} E(\tilde{a}_1, \tilde{\omega})]. \tag{3.168}$$

We will use Eq. (3.168) and the further results found in this subsection in order to calculate the position and width of the Floquet-Feshbach resonances with the use of Eqns. (3.132) and (3.136) found within the Floquet-Feshbach resonance theory.

3.7.3. Position and Width of Floquet-Feshbach Resonances

In this subsection position and width of the resonances are calculated, based on equations (3.132) and (3.136). We combine an full numerical solution with analytical approximations found for small and large driving strength.

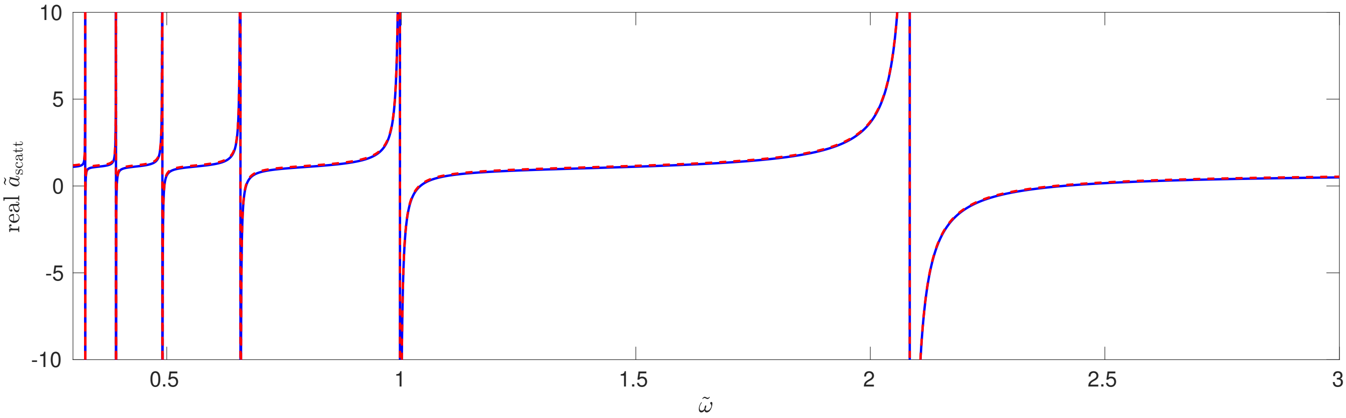

Figure 3.9.: Real part of the effective scattering length $\tilde{a}_{\mathrm{scatt}}$ in dependence on the driving frequency $\tilde{\omega}$ for $\tilde{a}_1 = 0.3$. Blue solid the exact solution of the full Floquet scattering problem Eq. (3.87) with $\epsilon = 0$, red dashed the results of the Floquet-Feshbach resonance theory Eq. (3.134). The resonance positions are marked with dashed lines.

The following calculation of position and width is based on the knowledge of the bound state wave functions and energies, that is gained in the previous subsection. Again, we are interested in the limit of vanishing energy $\epsilon \to 0$, which is relevant for ultracold quantum gases. With our numerical method we are able to calculate the bound state energies $\tilde{E}_\alpha(\tilde{\omega})$ and numerically determine its zero and the coefficients D_n^α at the zero. In fact, it turns out that it is computationally much faster to directly calculate the resonant frequencies by setting $\epsilon = 0$ in the recursion (3.109) and the normalization condition (3.111), and solving a non-linear system similar to Eq. (3.141) with

$$\mathbf{F}(\mathbf{q}) = \begin{pmatrix} \underline{\underline{A}}(\lambda = 0, \tilde{\omega})\mathbf{D} \\ \mathbf{D}^T \underline{\underline{V}}(\lambda = 0, \tilde{\omega})\mathbf{D} - 1. \end{pmatrix} \tag{3.169}$$

Here $q = (\mathbf{D}^T, \tilde{\omega})^T$ and $\underline{\underline{V}}$, $\underline{\underline{A}}$ as defined for (3.141). In Fig. 3.9 we compare the Floquet-Feshbach resonance theory (3.134) against the full solution of the Floquet scattering equation Eq. (3.87) for $\tilde{\epsilon} = 0$ and $\tilde{a}_1 = 0.3$. Both curves have a good agreement, especially in the vicinity of a resonance. For example, at $\tilde{\omega} = 1.5$ the two curves have a relative deviation of $\approx 4\%$. As indicated by the overlapping vertical lines, the Floquet-Feshbach resonance theory excellently predicts the position of the driving-induced scattering resonances. All in all, the Floquet-Feshbach resonance theory does not only explain the physical origin of the Floquet-Feshbach resonances, but also predicts the course of the effective scattering length with a quite high accuracy, even for a relatively large driving strength of $\tilde{a}_1 = 0.3$. With this at hand we now calculate resonance position and width using the Floquet-Feshbach resonance theory. Our numerical solution provides us directly with the resonance frequencies $\tilde{\omega}_\alpha$ for a given $\tilde{a}_1$, the corresponding recursion coefficients D_n^α and the numerical derivative $\frac{\partial \tilde{E}_\alpha}{\partial \tilde{\omega}}|_{\tilde{\omega}=\tilde{\omega}_\alpha}$, with which the resonance width $\tilde{\Delta}_\alpha$ can be calculated according to Eq. (3.136).

In Fig. 3.10 we show the numerically calculated position and width of the first eight resonances by colored lines. One recognizes that all resonances shift to higher frequencies as the driving strength increases, while simultaneously the width increases. Another feature is that with higher resonance number α the resonance width decreases which fits to the interpretation of higher resonances as a

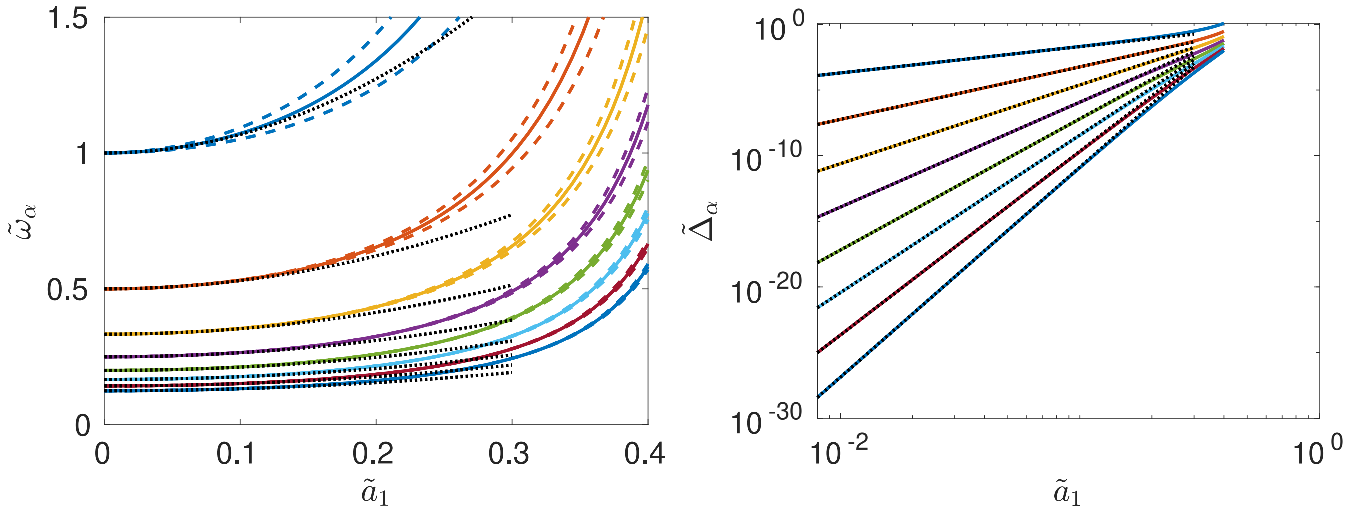

(a) **(b)**

Figure 3.10.: (a) Resonance position $\tilde{\omega}_\alpha$ of the first eight resonances $\alpha = 1, ..., 8$ from top to bottom (solid lines), addition and subtraction of position and width $\tilde{\omega}_\alpha \pm \tilde{\Delta}_\alpha$ (dashed lines), approximation of the resonance frequency in second order $\tilde{a}_1$ with Eq. (3.171a) (black dotted lines). (b) resonance width $\tilde{\Delta}_\alpha$ of the first eight resonances $\alpha = 1, .., 8$ from top to bottom (solid lines), approximation of the width with Eq. (3.172), (3.172) resp. (black dashed lines).

multi-photon process. Figure 3.10 displays the central result of this section. It demonstrates how both position and width can be tuned by the driving strength $\tilde{a}_1$. In combination with the shape of a Floquet-Feshbach resonance given by Eq. (3.135), Fig. 3.10 contains all the relevant information that one needs in order to tune the scattering length to any desired value. In particular, it is worth to mention that the width of the Floquet-Feshbach resonances can be influenced by the periodic drive, while in contrast the width of a magnetic Feshbach resonance is fixed to a predetermined value. This feature of the Floquet-Feshbach resonances might be of interest for the experimental realization, where a large resonance width is often desired.

In addition to the numerical analysis we gain additional qualitative knowledge about the resonances with the analytic solutions of the bound state equations found in subsection 3.7.2. Using them we are able to write down explicit formulas for position $\tilde{\omega}_\alpha$ and width $\tilde{\Delta}_\alpha$ in the case of weak and strong driving. For infinitely small $\tilde{a}_1$, Eq. (3.132) is solved with the expression for the bound state energies in zeroth order $\tilde{a}_1$, Eq. (3.146), to

$$\tilde{\omega}_\alpha = \frac{1}{\alpha}. \tag{3.170}$$

This can be spotted at the y-axis in Fig. 3.10. Equation (3.170) indicates the known result that for an infinitesimally small driving the resonant frequency $\tilde{\omega}_\alpha$ has to fit α times into the energetic difference of the scattering state at zero energy $\tilde{\epsilon} = 0$ and the energy of the bound dimer state $-E_\text{D}$. This result further indicates that there are infinitely many Floquet-Feshbach resonances. For the next order $\mathcal{O}(\tilde{a}_1^2)$ the ansatz $\tilde{\omega} = 1/\alpha + \delta\tilde{\omega}_\alpha$ is inserted into the second-order expansion of $\tilde{E}_\alpha$, Eq. (3.152). Solving Eq. (3.152) up to order $\tilde{a}_1^2$ yields

$$\delta\tilde{\omega}_1 = 2\tilde{a}_1^2(2+\sqrt{2}),\ \alpha = 1, \tag{3.171a}$$

$$\delta\tilde{\omega}_\alpha = \frac{2}{\alpha}\sum_{\pm}\frac{\tilde{a}_1^2}{1-\frac{1}{\sqrt{1\pm\frac{1}{\alpha}}}},\ \alpha > 1. \tag{3.171b}$$

These results are shown as black dotted lines in Fig. 3.10 which agree with the numerical results for small $\tilde{a}_1$, as expected. Since the bound state energies are shifted to below for increasing driving strength $\tilde{a}_1$, also the second order frequency shift (3.171a) is positive. The larger the resonant number α, the smaller both the resonant frequency $\tilde{\omega}_\alpha \propto 1/\alpha$ and the shift $\delta\tilde{\omega} \propto 1/\alpha$ get. The shift of the resonant frequencies with $\tilde{a}_1$ is interpreted as a dressing of the bound state energy by the periodic drive.

Now we come to the perturbative calculation of the resonance width. For the first resonance one gets in zeroth order $\tilde{a}_1$ that $D_{-1}^{\alpha} = \sqrt{2}$. With $\tilde{a}_{\mathrm{bg}} = 1 + \mathcal{O}(\tilde{a}_1^2)$, and $\frac{\partial \tilde{E}_\alpha^{(0)}}{\partial\omega}(\omega_\alpha) \approx 1$ it follows with Eq. (3.136) that

$$\tilde{\Delta}_1 = 2\tilde{a}_1^2 + \mathcal{O}(\tilde{a}_1^4). \tag{3.172}$$

In order to get a non-vanishing result for the resonance width $\tilde{\Delta}_\alpha$, we have to use that order in $\tilde{a}_1$ which is leading first to a non-zero coupling to the scattering states. The zeroth order approximation of the bound state energies $\tilde{E}_\alpha = -1 + \alpha\tilde{\omega}$ is sufficient, it leads to $\frac{\tilde{\partial} E_\alpha}{\partial\omega}(\tilde{\omega}_\alpha) = \alpha$. But for the states, Eq. (3.154) has to be used, which gives selected, but relevant, recursion coefficients in αth order. The width of the αth resonance is calculated with Eq. (3.136) to

$$\tilde{\Delta}_\alpha = C_\alpha \tilde{a}_1^{2\alpha} + \mathcal{O}(\tilde{a}_1^{2\alpha+1}), \tag{3.173}$$

where C_α is a constant given by

$$C_\alpha = \frac{2}{\alpha \times \Pi_{j=1}^{(\alpha-1)}\left(\frac{1}{\sqrt{1-j\tilde{\omega}_\alpha}}-1\right)^2}. \tag{3.174}$$

Fig. 3.10 shows a good agreement between Eq. (3.173) and the numerical calculation and yields that the widths are given by a characteristic power law in $\tilde{a}_1$. The interpretation of the decrease of the width $\tilde{\Delta}_\alpha$ with the resonance number α as multi-photon resonances is emphasized by the α dependence of the power law Eq. (3.173) and by the fact that we have to use α couplings of neighboring Floquet channels in order to obtain Eq. (3.154).

After discussing the result for small driving we now focus on an analytic approximation of position and width in the case of strong driving, i.e. $\tilde{a}_{\mathrm{AC}} = 2\tilde{a}_1 \approx 1$. The case $\tilde{\epsilon} = 0$ is given within the continuum theory for large driving amplitudes by $y = 0$, so we can write Eq. (3.166) with definitions (3.163) to [116]

$$2\tilde{\omega}_\alpha^2\left(1-\frac{1}{2\tilde{a}_1}\right) = E = E_\alpha^\bullet(z_0=0)A^{-4/3} = E_\alpha^\bullet(z_0=0)\left(\frac{\tilde{a}_1}{\tilde{\omega}_\alpha}\right)^{-4/3}. \tag{3.175}$$

The quantity $E_\alpha^\bullet(z_0=0)$ is found numerically by solving the inverse square root potential (3.165) with unit strength. Each eigenvalue $E_\alpha^\bullet(z_0=0) = E_\alpha^\bullet$ found by the numerics corresponds to a different

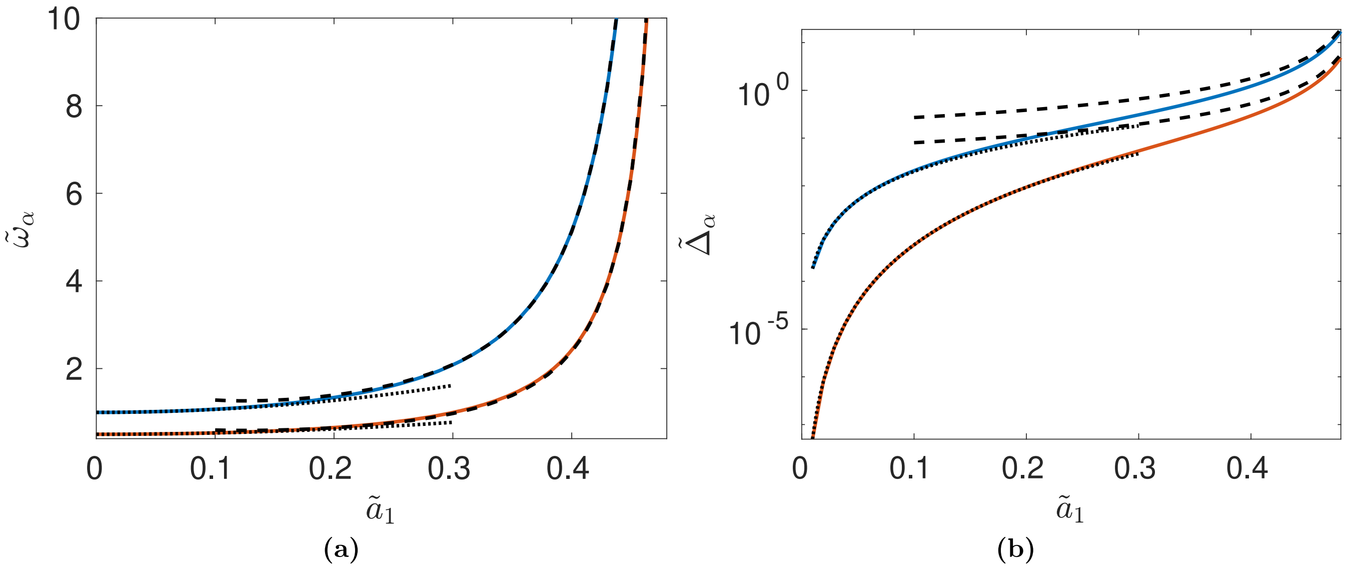

Figure 3.11.: Numerically calculated position (a) and width (b) of first (blue) and second (red) resonance, perturbative results for small $\tilde{a}_1$ (black dotted), perturbative results for large $\tilde{\omega}$ (black dashed).

resonance $\tilde{\omega}_\alpha$, if (3.175) is solved for $\tilde{\omega}_\alpha$. The five smallest values of $E^\bullet_\alpha$ correspond to the five first resonances and read $E^\bullet_\alpha = -0.4380, -0.2632, -0.1976, -0.1617, -0.1386$. Finally, Eq. (3.175) is solved for $\tilde{\omega}_\alpha$:

$$\tilde{\omega}_\alpha = \frac{|E^\bullet_\alpha|^{3/2}}{2^{2/3}\tilde{a}_1^2}\left|1 - \frac{1}{2\tilde{a}_1}\right|^{-3/2}. \tag{3.176}$$

Equation (3.176) gives an approximation for the resonance frequency in the limit of large driving. Fig. 3.11 shows for the first two resonances that Eq. (3.176) coincides with the analytic solution for $\tilde{a}_1$ larger than 0.2. In combination with the expansion for small $\tilde{a}_1$ in Eq. (3.171a) we can find in the whole $\tilde{\omega}$-$\tilde{a}_1$ plane an approximate analytic formula which describes the course of the resonant frequencies. This is an remarkable result. Another prominent feature of Eq. (3.176) is that it finally shows that the resonant frequencies diverge for $2\tilde{a}_1 \to 1$. Its asymptotic behavior is given by a power law $x^{-3/2}$, where $x = |1 - 1/(2\tilde{a}_1)|$ is the difference of the inverted AC-part of the scattering length $\tilde{a}_{\mathrm{AC}} = 2\tilde{a}_1$ and its minimal value $(1/a_{\mathrm{AC}})_{\min} = 1$. The divergence of $\tilde{\omega}_\alpha$ for $2\tilde{a}_1 \to 1$ shows that physically the strength of the dressing of the Flouqet bound states approaches infinity in this limit. Thus, the physics is governed by the coupling of the Floquet channels leading to the large shift of bound state energy and thus the driving frequency.

Now we come to an analytic formula approximating the resonance width $\tilde{\Delta}_\alpha$ in the limit of strong driving. In Eq. (3.136) only the quantities D^α_{-1} and $\frac{\partial \tilde{E}_\alpha}{\partial \tilde{\omega}}|_{\partial\tilde{\omega}=\tilde{\omega}_\alpha}$ are unknown, so we have to find a formula for them. Following a consideration described in Ref. [116], we find D^α_{-1} without explicitly solving the high-frequency continuum limit Eq. (3.161). We start by performing a partial derivative of the Schrödinger equation with the inverse square root potential Eq. (3.162) with $y = 0$. Multiplying this result with the complex conjugate of the field $\phi^*(x)$ yields

$$\frac{1}{A}\int_0^\infty dx \frac{|\phi(x)|^2}{2x^{3/2}} = \int_0^\infty dx \phi^*(x)\phi'''(x) + \int_0^\infty dx \left(\frac{1}{A\sqrt{x}} - E\right)\phi^*(x)\phi'(x), \tag{3.177}$$

where $'$ denotes the derivative with respect to x. Using the normalization equation (3.158), it can be shown that the integral on the left side of the equal sign equals 1. Using two times an integration by parts with the boundary conditions $\phi(0) = 0$ and $\lim_{x\to\infty}\phi(x) = 0$ one finds that

$$\int_0^\infty dx \phi^*(x)\phi'''(x) = -|\phi'(x)|^2|_0^\infty - \int_0^\infty dx \phi^{*\prime\prime}(x)\phi'(x). \tag{3.178}$$

With $\lim_{x\to\infty}\phi(x) = 0$ and $\lim_{x\to\infty}\phi'(x) = 0$ the intermediate step

$$\frac{1}{A} = |\phi'(x)|^2|_{x=0} + \int_0^\infty dx \left[-\left(\frac{-1}{A\sqrt{x}} - \frac{\partial^2}{\partial x^2}\right)\phi^*(x) - E\phi^*(x)\right]\phi'(x) \tag{3.179}$$

is derived. Since also $\phi^*(x)$ fulfills Eq. (3.162), the integral in Eq. (3.179) vanishes and we are left with the simple result

$$\frac{1}{A} = |\phi'(x)|^2|_{x=0}. \tag{3.180}$$

But how does that relate to $|D^\alpha_{-1}|^2$? First, note that with the special case $A = \tilde{a}_1/\omega$ and $E = \omega^2(2 - 1/\tilde{a}_1)$ it holds that $\mathcal{D}^\alpha(x) = \phi(x)$. Second, the boundary condition $D^\alpha_0 = 0$ implies

$$D^\alpha_{-1} - D^\alpha_0 = -\mathcal{D}^\alpha_1 - \mathcal{D}^\alpha_0 = -\frac{1}{\omega}\frac{\mathcal{D}^\alpha_{x\omega} - \mathcal{D}^\alpha_{0\omega}}{\frac{1}{\omega}}. \tag{3.181}$$

Inserting the continuum theory for large frequencies $\mathcal{D}^\alpha_{x\omega} = \omega\mathcal{D}^\alpha(x)$ and performing the limit $\omega \to \infty$ in the numerical derivative yields

$$D^\alpha_{-1} = -\frac{\partial\mathcal{D}^\alpha}{\partial x}(x)|_{x=0}. \tag{3.182}$$

In summary, we conclude that

$$|D^\alpha_{-1}|^2 = \frac{\tilde{\omega}}{\tilde{a}_1}. \tag{3.183}$$

Now $\frac{\partial\tilde{E}_\alpha}{\partial\tilde{\omega}}$ is calculated by performing a partial derivative with respect to $\tilde{\omega}$ on the bound state energies derived from the high-frequency theory in Eq. (3.168). As we want to get the expression at $\epsilon = 0$, we set $z_0 = 0$:

$$\frac{\partial\tilde{E}_\alpha}{\partial\tilde{\omega}}|_{z_0=0} = \frac{\partial}{\partial\tilde{\omega}}(\tilde{\omega}^2 A^{2/3})g_\alpha(E^\bullet(z_0))|_{z_0=0} + \tilde{\omega}^2 A^{2/3}\frac{\partial g_\alpha}{\partial E^\bullet_\alpha}|_{z_0=0}\frac{\partial}{\partial\tilde{\omega}}(E(\tilde{a}_1,\tilde{\omega})A(\tilde{a}_1,\tilde{\omega}^{4/3}))|_{\tilde{\omega}=\tilde{\omega}_\alpha}. \tag{3.184}$$

Since it holds that $g(E^\bullet_\alpha(z_0)) = z_0$, the first term in Eq. (3.184) vanishes at $z_0 = 0$. In the second term of Eq. (3.184) we substituted $E^\bullet_\alpha(z_0) = E(\tilde{a}_1,\tilde{\omega})A(\tilde{a}_1,\tilde{\omega})^{4/3}$ in the inner derivative, whose derivative can be exactly evaluated. The derivative $\frac{g_\alpha}{\partial E^\bullet_\alpha}|_{z_0=0}$ is found by numerically calculating the derivative of $E^\bullet_\alpha$ with respect to z_0:

$$F_\alpha = \frac{\partial g_\alpha}{\partial E^\bullet_\alpha}|_{z_0=0} = \left(\frac{\partial E^\bullet_\alpha}{\partial z_0}|_{z_0=0}\right)^{-1}. \tag{3.185}$$

The first five values read $F_\alpha = -7.087, -23.89, -47.96, -78.28, -114.25$. In summary we find an analytic formula for the partial derivative

$$\frac{\partial \tilde{E}_\alpha}{\partial \tilde{\omega}} = \frac{4}{3}\tilde{a}_1^2 F_\alpha \left(1 - \frac{1}{2\tilde{a}_1}\right)\tilde{\omega}_\alpha. \tag{3.186}$$

Using that $\tilde{a}_{\text{bg}} = \sqrt{1-4\tilde{a}_1^2} = 2\tilde{a}_1\sqrt{[1/(2\tilde{a}_1)+1][1/(2\tilde{a}_1)-1]}$ and by inserting all necessary expressions into the definition of the width (3.136) we finally arrive at an approximate formula of the width with our high frequency theory

$$\tilde{\Delta}_\alpha = \frac{3}{8\tilde{a}_1^2|F_\alpha|\sqrt{\frac{1}{2\tilde{a}_1}+1}}\left|1 - \frac{1}{2\tilde{a}_1}\right|^{-3/2}. \tag{3.187}$$

Equation (3.187) is the central result of this calculation, since it is an analytic formula for the resonance width at large driving strength $\tilde{a}_1$. Equation (3.187) shows that the width diverges by a power law if the driving strength converges to its maximum value $2\tilde{a}_1 = a_{\text{AC}} \to 1$. In Fig. 3.11 (b) one sees that the high-frequency approximation of the width (3.187) converges at large driving strengths $\tilde{a}_1$ to the numerically calculated values. The ratio of resonant position and width

$$\frac{\tilde{\omega}_\alpha}{\tilde{\Delta}_\alpha} = \frac{2^{7/3}}{3}|E^{\bullet}_\alpha||F_\alpha|\sqrt{\frac{1}{2\tilde{a}_1}+1} \tag{3.188}$$

turns out to be always larger than one for the first five resonances. This means that the resonance can be always resolved, since its width is smaller than the physically available frequency range. The fact, that the width is smaller than the resonant frequency can be seen with Eq. (3.188), since it holds $E'_\alpha F_\alpha > 1$ for the first five resonances and the remaining part of Eq. (3.188) is also larger than one. For the first five resonances the ratio (3.188) increases with α, so we extrapolate that this ratio is larger than one for general α.

3.7.4. Recursion Coefficients at Resonance Positions

The absolute value of the numerically found recursion coefficients D_n^α is shown in Fig. 3.12. For small $\tilde{a}_1$ each resonance is located at a single index n, namely the one which corresponds to the resonance number, as predicted by Eq. (3.145). The first coefficient D_{-1}^α, which enters the equation for the width Eq. (3.136), increases with the driving strength. This explains the ascent of the width with $\tilde{a}_1$. Also with rising $\tilde{a}_1$ more recursion coefficients gain a relevant weight and, thus, indicate that Floquet physics becomes more relevant for larger $\tilde{a}_1$. The smearing out of the coefficients over a vast range of indices further shows that by performing the continuum limit we can describe the physics in the case of strong driving in an accurate way. The general increase of the coefficient values for large indices is related to the normalization (3.111) of the recursion coefficients. Further, an interesting feature is that the higher-order resonances show knots of a low value of $|D_n^\alpha|$ in the density profile, corresponding to the order of resonance. With larger $\tilde{a}_1$ the knots wander to larger indices $|n|$, but the number remains constant. At last, note that the numerics adaptively chooses a cutoff in Floquet space. The white regions mark the indices which are above this cutoff and are set to zero when plotting this Fig. 3.12. Note, that the cutoff is always chosen large enough in order to cover the relevant physics, in order to show the relevant behavior we restricted to values $|n| < 40$.

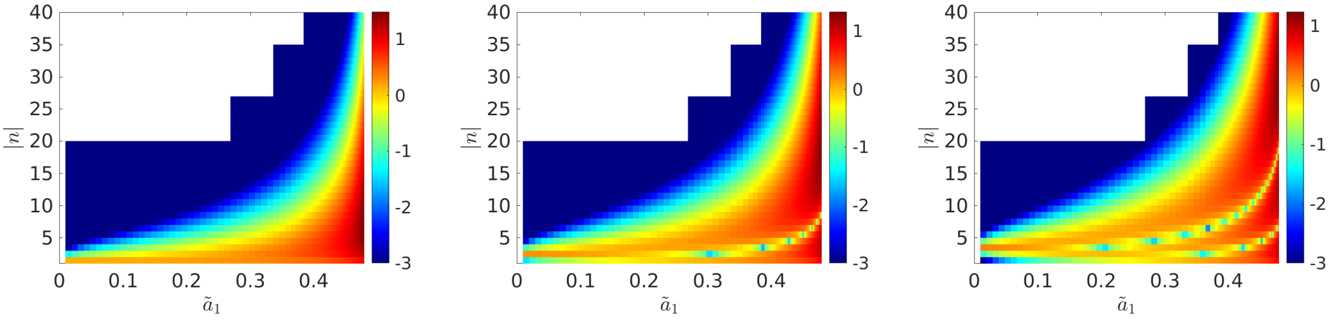

(a) **(b)** **(c)**

Figure 3.12.: In color code the decade logarithm of the absolute value of the recursion coefficients $\log_{10}\,|D_n^\alpha|$ for the indices $|n| \leq 40$ over the driving strength $\tilde{a}_1$ for: (a) first resonance, (b) second resonance, (c) third resonance.

3.7.5. Inelastic Scattering

As we discussed in Subsec. 3.7.3, the real part of the effective scattering length Eq. (3.134) shows interesting resonant behavior which is described by the Floquet-Feshbach resonance theory. But in the derivation of Eq. (3.134) also a non-resonant contribution appears, giving rise to an imaginary part in the effective scattering length. As previously discussed, this imaginary part describes the inelastic scattering to Floquet channels with positive index. In our full continued fraction solution Eq. (3.97) it turns out that only the "+"-part stemming from the inelastic Floquet channels is responsible for the imaginary part. In the effective scattering length of our Floquet-Feshbach resonance theory Eq. (3.134), exactly the same term enters through the inelastic scattering length (3.124). Thus the imaginary part of the full continued fraction solution (3.97) and the Floquet-Feshbach resonance theory (3.134) are the same, showing that inelastic scattering is correctly incorporated in the resonance theory.

In Fig. 3.13 the imaginary part of the effective scattering length Im $\tilde{a}_{\text{scatt}}$, which is negative in the whole parameter range, is shown in the $\tilde{\omega}$-$\tilde{a}_1$ plane. This reflects the fact, that due to inelastic scattering only losses and no gain can be induced. But its maximum value is found to be 17 % of the average scattering length $\bar{a}$, such that inelastic processes can be much weaker than elastic scattering, which is resonantly enhanced by the Floquet-Feshbach resonances. For small $\tilde{a}_1$ the inelastic scattering is much weaker than for large ones. At fixed $\tilde{a}_1$ the imaginary part first increases up to $\tilde{\omega} \approx 1$, while it then decreases down to zero at infinite $\tilde{\omega}$.

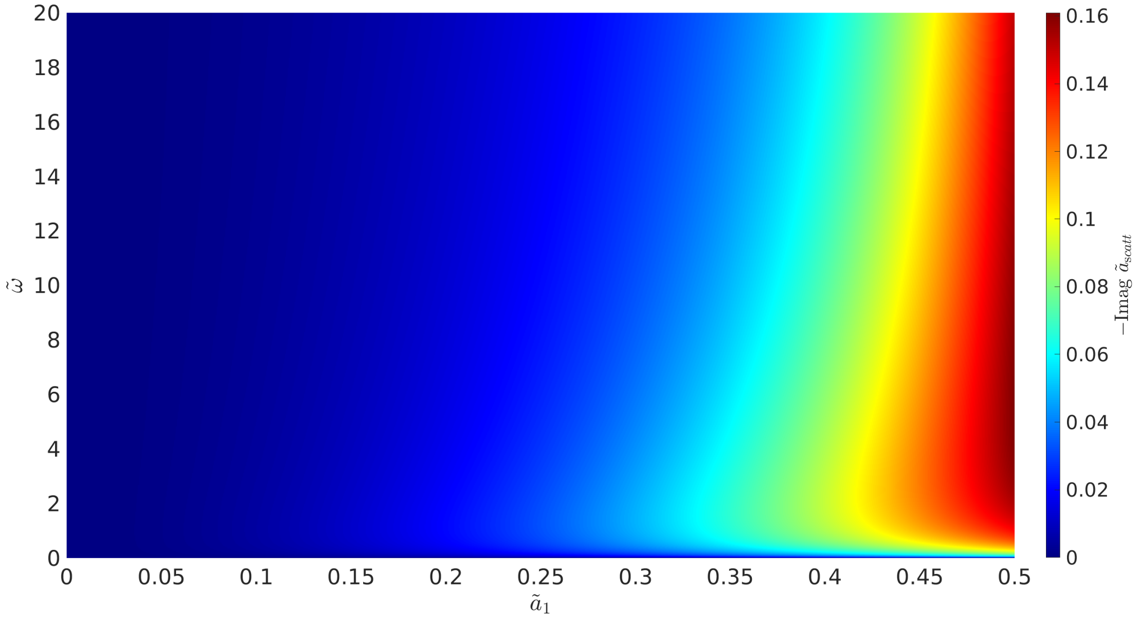

Figure 3.13.: Negative imaginary part of the effective scattering length $\tilde{a}_{\mathrm{scatt}}$ in dependence on the driving strength $\tilde{a}_1$ and driving frequency $\tilde{\omega}$.

3.8. Floquet-Feshbach Resonances for the Pseudo Potential with a Higher Harmonic Drive

The harmonically driven contact interaction is the simplest model where Floquet-Feshbach resonances occur. The next complicated setup is to assume a general time-periodic drive of the form

$$a(t) = \sum_{n=-\infty}^{\infty} e^{-in\omega t} a_n, \tag{3.189}$$

with $a^*_{-n} = a_n$ to ensure a real valued $a(t)$. We will see that a drive of the form (3.189) induces resonances that have different properties as in the harmonically driven case. The Hamiltonian in Floquet space reads

$$\mathcal{H}_{n,m} = \left(-\frac{\hbar^2}{2\mu}\Delta_R - n\hbar\omega\right)\delta_{n,m} + \lim_{s\to 0^+} a_{n-m}\frac{\hbar^2}{2\mu}\frac{\delta(r-s)}{s^2}\overleftrightarrow{\frac{\partial}{\partial r}} r. \tag{3.190}$$

The harmonic driving of a magnetic field $B(t) = B_1 + B_{\mathrm{AC}}\cos(\omega t)$ that is close to the position B_0 of a magnetic Feshbach resonance in fact induces such higher harmonics in the drive, since the scattering length is a non-linear function of the magnetic field

$$a(t) = a_{\mathrm{BG}}\left[1 - \frac{\Delta B}{B(t) - B_0}\right]. \tag{3.191}$$

In the region of universal behavior close to B_0 the scattering is described by a contact interaction with Eq. (3.191) as time-dependent interaction strength. Equation (3.191) corresponds to a driving scheme involving higher harmonics $a_n \neq 0$ for all $n \in \mathbb{Z}$.

This section is structured as follows. In Subsec. 3.8.1 the scattering length is extracted from the Floquet scattering solution. The Floquet-Feshbach resonance theory for a driven pseudo potential including higher harmonics is discussed in Subsec. 3.8.2. We emphasize in Subsec. 3.8.3 that the higher harmonic drive induces a peak in the imaginary part of the scattering length that has an asymmetric lineshape. This asymmetry is related to the Floquet structure of the Hilbert space. An analysis of the resonance properties using the Floquet-Feshbach resonance theory is provided in Subsec. 3.8.4.

3.8.1. Numerical Calculation of the Floquet Scattering Problem

For calculating the scattering amplitude, ansatz (3.80) still holds in the case that $a(t)$ is of the general form (3.189). Like in the harmonically driven case, we measure in the following all length scales by $|a_0|$ and energy scales by $E_\mathrm{D} = \hbar^2/(2\mu|a_0|^2)$ by denoting $\tilde{a} = a/|a_0|$, $\tilde{E} = E/E_\mathrm{D}$ and $\tilde{\omega} = \hbar\omega/E_\mathrm{D}$. A recursion relation similar to Eq. (3.82) is derived:

$$\sum_{m=-\infty}^{\infty} \left(\frac{i}{\tilde{k}_m} \delta_{n,m} - \tilde{a}_{n-m} \right) D_m = \frac{i}{2\tilde{k}_n} \delta_{n,0} + \frac{\tilde{a}_n}{2}. \tag{3.192}$$

Equation (3.192) can also be expressed in terms of the scattering amplitudes (3.81):

$$\sum_{m=-\infty}^{\infty} (\delta_{n,m} + i\tilde{k}_m \tilde{a}_{n-m}) \tilde{f}_m = -\tilde{a}_n. \tag{3.193}$$

Equation (3.193) is solved numerically by truncating the sum to indices smaller than a cutoff, i.e. $|n|, |m| \leq m_\mathrm{c}$, the resulting finite linear system is inverted numerically in an efficient manner. The scattering length is extracted according to $\tilde{a}_\mathrm{scatt} = -\tilde{f}_0(\tilde{k} = 0)$. Also here, the goal is to further understand the Floquet-Feshbach resonances by introducing a Feshbach theory in Floquet space, which is worked out in the next subsection.

3.8.2. Floquet-Feshbach Resonance Theory

A Floquet-Feshbach resonance theory is derived in case of a driven pseudo potential including higher harmonics. Low-energy scattering is assumed, i.e. we have $\tilde{\epsilon} < \tilde{\omega}$, where the channels with $n < 0$ are closed. The wave function of the scattering state that solves the Floquet equation (3.112) is given in analogy to Subsec. 3.7.1. In the closed channels a superposition of bound states according to Eq. (3.114) is assumed, where the radial wave function of the bound states is given by Eq. (3.108). In the $n = 0$ channel we assume Eq. (3.113), for the channels with $n > 0$ we use the ansatz Eq. (3.80). The eigenvalue equation for the bound states $\tilde{\mathcal{H}}_{n<0,n<0} |\phi_\mathrm{B}^\alpha\rangle\rangle = \tilde{E}_\alpha |\phi_\mathrm{B}^\alpha\rangle\rangle$ reads in terms of the coefficients

$$\sum_{m<0}\left(\frac{1}{\tilde{\kappa}_m^\alpha}\delta_{n,m}-\tilde{a}_{n-m}\right)D_m^\alpha=0,\ \text{for } n<0, \tag{3.194}$$

where $\tilde{\kappa}_n^\alpha=\sqrt{-\tilde{E}_\alpha-n\tilde{\omega}}$. Equation (3.194) shows that the higher harmonic drive induces higher-order couplings between the bound state recursion coefficients D_n^α. The normalization condition (3.111) still holds. We solve Eqns. (3.194) and (3.111) numerically for the bound state energies $\tilde{E}_\alpha$ and recursion coefficients D_n^α. These quantities are needed for calculating the properties of the resonant scattering amplitude. Evaluating the Floquet equation (3.112) for the closed channels and projecting by $\langle\langle\phi_{\mathrm{B}}^\alpha|$ we arrive at

$$(\tilde{E}_\alpha-\tilde{\epsilon})A_\alpha=-\langle\langle\phi_{\mathrm{B}}^\alpha|\tilde{\mathcal{H}}_{<,0}|R_0\rangle\rangle-\langle\langle\phi_{\mathrm{B}}^\alpha|\tilde{\mathcal{H}}_{<,>}|R_{n>0}\rangle\rangle, \tag{3.195}$$

while we use the notation of Subsec. 2.2.2. Inserting the actual form of the wave functions and evaluating the pseudo potential, Eq. (3.195) transforms to

$$(\tilde{E}_\alpha-\tilde{\epsilon})A_\alpha=-\sum_{n<0}D_n^\alpha\tilde{a}_n(1+i\tilde{k}\tilde{f}_0)-\sum_{\substack{n<0\\m>0}}D_n^\alpha\tilde{a}_{n-m}D_m. \tag{3.196}$$

In comparison to the result for the harmonically driven case (3.117), additional couplings to the inelastic channels with $n>0$ arise. By the integration techniques Eqns. (3.27) and (3.28) we obtain the equations for $n=0$

$$\tilde{a}_0+(1+ik\tilde{a}_0)\tilde{f}_0+\sum_{n>0}\tilde{a}_{-n}D_n+\sum_{n<0}\tilde{a}_{-n}D_n=0 \tag{3.197}$$

and $n>0$

$$-\frac{i}{\tilde{k}_n}D_n+\sum_{m>0}\tilde{a}_{n-m}D_m+\tilde{a}_n(1+i\tilde{k}\tilde{f}_0)+\sum_{m<0}\tilde{a}_{n-m}D_m=0. \tag{3.198}$$

The above equations are written such that they separate processes which couple the three different sectors of the Floquet space. Like in discussion of the harmonically driven potential in Sec. 3.7, these sectors are: The closed channels incorporating the bound states, the the entrance channel, and the channels with indices $n>0$ introducing the inelastic processes.

In the following, we aim to find a formula for the scattering length which is similar to Eq. (3.135). The starting point is to solve Eq. (3.198) for the coefficients D_n

$$D_n=\sum_{m>0}\Lambda_{n,m}\left[\tilde{a}_m(1+i\tilde{k}\tilde{f}_0)+\sum_{m'<0}\tilde{a}_{m-m'}D_{m'}\right], \tag{3.199}$$

where the the matrix $\Lambda_{n,m}$, which is in general complex while the indices are restricted to strictly positive values $n,m>0$, is uniquely defined by

$$\sum_{l>0}\Lambda_{n,l}\left(\frac{i}{\tilde{k}_l}\delta_{l,m}-\tilde{a}_{l-m}\right)=\delta_{n,m}. \tag{3.200}$$

Using the $\Lambda_{n,m}$ matrix the prefactors before the coefficients D_m in (3.198) are inverted. The matrix $\Lambda_{n,m}$ describes the scattering within the inelastic channels. In the case that there is a low amplitude in the $n>0$ channels, the scattering between those channels can be neglected. A condition for that to occur is $|\tilde{a}_n| \ll 1$ for $|n| \geq 1$. The $\Lambda_{n,m}$ matrix in this case is of a simple diagonal form

$$\Lambda_{n,m} \approx \delta_{n,m} \frac{1}{\frac{i}{\tilde{k}_n} - \tilde{a}_0}, \ n, m > 0. \tag{3.201}$$

Now result (3.199) is inserted into Eq. (3.196) while assuming that close to resonance α in the sum $D_{n<0} \approx \sum_\alpha A_\alpha D^\alpha_{n<0}$ only the αth coefficient is important. This yields

$$(\tilde{E}_\alpha - \tilde{\epsilon} + \delta\tilde{E}_\alpha + i\tilde{\gamma}_\alpha)A_\alpha = -w_\alpha(1 + i\tilde{k}\tilde{f}_0), \tag{3.202}$$

with

$$\delta\tilde{E}_\alpha + i\tilde{\gamma}_\alpha \ = \ \sum_{\substack{n<0\\m>0\\m'>0\\m''<0}} D^\alpha_n \tilde{a}_{n-m}\Lambda_{m,m'}\tilde{a}_{m'-m''}D^\alpha_{m''}, \ \delta\tilde{E}_\alpha, \tilde{\gamma}_\alpha \in \mathbb{R}, \tag{3.203a}$$

$$w_\alpha \ = \ \left(\sum_{n<0} D^\alpha_n \tilde{a}_n + \sum_{\substack{n<0\\m>0\\m'>0}} D^\alpha_n \tilde{a}_{n-m}\Lambda_{m,m'}\tilde{a}_{m'} \right). \tag{3.203b}$$

In contrast to the harmonically driven pseudo potential, here the resonances shift in energy by $\delta\tilde{E}_\alpha$, while losses are introduced by a non-vanishing $\tilde{\gamma}_\alpha$. Both quantities describe the real and the imaginary part of Eq. (3.203a), which describes the following process: A bound state scatters into the inelastic channels, then possibly involves multiple scattering processes within the inelastic channels, and finally comes back to the bound state. The parameter w_α determines the strength of the effective coupling of the bound states to the elastic channel $n=0$. It consists of the direct coupling of closed channels and elastic channel, which is also present in the harmonically driven case as given by Eq. (3.117), and an additional term involving a coupling of closed channels and the elastic channel via the inelastic channels. Equation (3.202) is inserted together with $D_{n<0} \approx \sum_\alpha A_\alpha D^\alpha_n$ into Eq. (3.198) which is used for solving (3.197). Using $D_{n<0} \approx \sum_\alpha A_\alpha D^\alpha_n$ in Eqns. (3.198) and (3.197), an explicit form of the scattering amplitude is found by $-f_0^{-1} = \tilde{a}_{\mathrm{E}}^{-1} + ik$, with

$$\tilde{a}_{\mathrm{E}} = \tilde{a}_0 + \tilde{a}_{\mathrm{non-res}} - \sum_\alpha \left(\sum_{\substack{n>0\\m>0\\m'<0}} \tilde{a}_{-n}\Lambda_{n,m}\tilde{a}_{m-m'}D^\alpha_{m'} + \sum_{n<0} \tilde{a}_{-n}D^\alpha_n \right) \frac{w_\alpha}{\tilde{E}_\alpha + \delta\tilde{E}_\alpha - \tilde{\epsilon} + i\tilde{\gamma}_\alpha} \tag{3.204}$$

and

$$\tilde{a}_{\mathrm{non-res}} = \sum_{\substack{n>0\\m>0}} \tilde{a}_{-n}\Lambda_{n,m}\tilde{a}_m. \tag{3.205}$$

Let us discuss Eq. (3.204). The first term describes the background scattering length $\tilde{a}_0$, while the second is a non-resonant part given by Eq. (3.205). The third term is the most relevant, since it shows a resonant peak provided that the energies of the scattering state and the Floquet bound state plus additional energy shift match: $\tilde{\epsilon} = \tilde{E}_\alpha + \delta\tilde{E}_\alpha$. In comparison to the theory of the sinusoidally driven pseudo potential Eq. (3.122), an imaginary part $\tilde{\gamma}_\alpha$ is present in Eq. (3.204). Further, the width of the resonance will involve terms that include the matrix $\Lambda_{n,m}$ that describes the scattering in the inelastic channels.

Again, we are interested in the case of low-energy scattering that is relevant for ultracold gases and assume in the following $\tilde{\epsilon} \to 0$. In particular, the dependence of the scattering length $\tilde{a}_{\mathrm{scatt}}$ on the driving frequency $\tilde{\omega}$ is of interest. The resonance frequency $\tilde{\omega}_\alpha$ is defined as the frequency where the real part of the denominator in Eq. W(3.204) vanishes

$$\tilde{E}_\alpha(\tilde{\omega}_\alpha) + \delta\tilde{E}_\alpha(\tilde{\omega}_\alpha) = 0. \tag{3.206}$$

Similar to the harmonic case Eq. (3.132), only a single resonance per quantum number α occurs. But in Eq. (3.206) there is an energy shift $\delta\tilde{E}_\alpha$, which additional alters the position of the resonance. As described by Eq. (3.203a), this energy shift stems from the coupling of the bound state to the inelastic channels with $n > 0$.

The three variables $\tilde{\omega}_\alpha$ and D_n^α and $\tilde{E}_\alpha$ at resonance condition (3.206) are found by numerically solving simultaneously Eqns. (3.111), (3.194) and (3.206). For finding the resonance width $\tilde{\Delta}_\alpha$ we renormalize the background scattering length by demanding $\tilde{a}_{\mathrm{bg}} = \lim_{\omega\to\infty} \tilde{a}_{\mathrm{scatt}}$, where $\tilde{a}_{\mathrm{scatt}}$ is calculated by solving Eq. (3.193) numerically, and perform in analogy to Eq. (3.133) the approximation $E_\alpha(\tilde{\omega}) + \delta\tilde{E}_\alpha(\tilde{\omega}) \approx [\partial_{\tilde{\omega}} E_\alpha(\tilde{\omega}) + \partial_{\tilde{\omega}} \delta\tilde{E}_\alpha(\tilde{\omega})]_{\omega=\omega_\alpha} \times (\tilde{\omega} - \tilde{\omega}_\alpha)$. The resulting scattering length reads

$$\tilde{a}_{\mathrm{scatt}} = \tilde{a}_{\mathrm{bg}} \left(1 - \sum_\alpha \frac{\tilde{\Delta}_\alpha}{\tilde{\omega} - \tilde{\omega}_\alpha + i\tilde{\gamma}_\alpha}\right) + \tilde{a}_{\mathrm{non-res}}(\tilde{\epsilon} = 0), \tag{3.207}$$

while the resonance width is given by

$$\begin{aligned} \tilde{\Delta}_\alpha = & \left(\sum_{n<0} D_n^\alpha \tilde{a}_n + \sum_{\substack{n<0\\ m>0\\ m'>0}} D_n^\alpha \tilde{a}_{n-m} \Lambda_{m,m'} \tilde{a}_{m'}\right) \\ & \times \left(\sum_{\substack{n>0\\ m>0\\ m'<0}} \tilde{a}_{-n} \Lambda_{n,m} \tilde{a}_{m-m'} D_{m'}^\alpha + \sum_{n<0} \tilde{a}_{-n} D_n^\alpha\right) \frac{1}{\tilde{a}_{\mathrm{bg}}[\partial_{\tilde{\omega}} E_\alpha(\tilde{\omega}) + \partial_{\tilde{\omega}} \delta\tilde{E}_\alpha(\tilde{\omega})]_{\omega=\omega_\alpha}}. \end{aligned} \tag{3.208}$$

Equation (3.207) looks similar to Eq. (3.134), that has been derived for the harmonically driven case. However, there are two mayor differences. First, the coupling to the inelastic channels by the higher harmonics of the drive induces an imaginary part $\tilde{\gamma}_\alpha$ given by Eq. (3.203a), which leads to a finite maximum of the real part of $\tilde{a}_{\mathrm{scatt}}$ and a resonant imaginary part of $\tilde{a}_{\mathrm{scatt}}$. Second, Eq. (3.208) shows that the width has, in addition to a contribution form a direct coupling of the bound states to the scattering state in the elastic $n = 0$ channel, a contribution involving scattering from the closed channels over inelastic channels to the elastic channel. These additional terms involve the

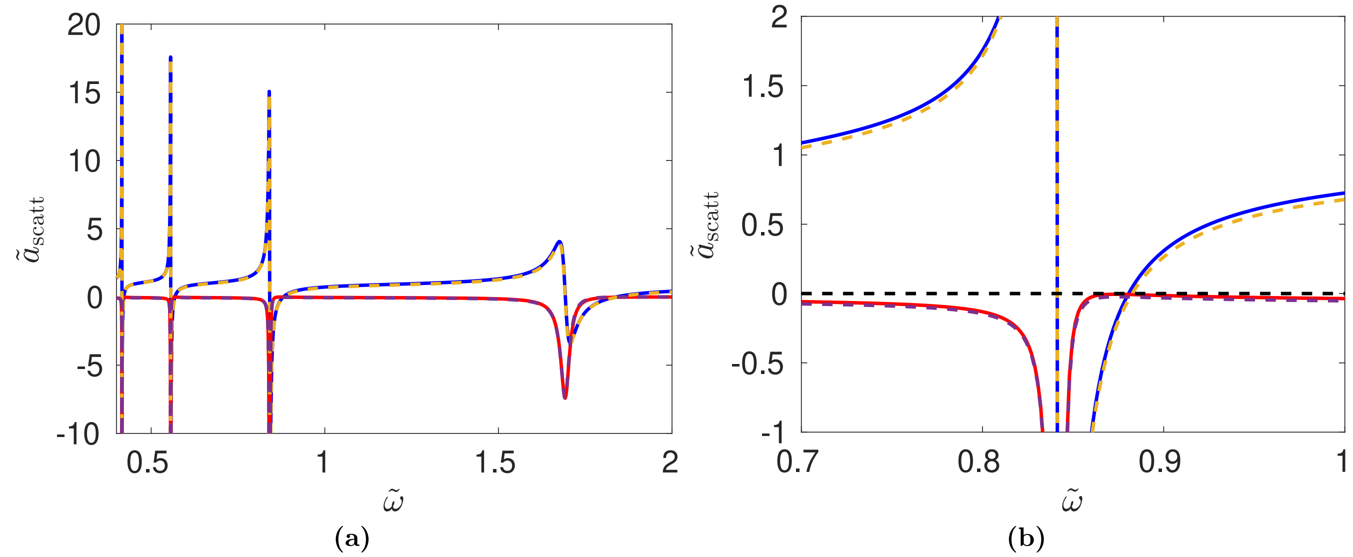

(a) **(b)**

Figure 3.14.: Real part (blue solid) and imaginary part (red solid) of the scattering length $\tilde{a}_{\text{scatt}}$ calculated numerically with Eq. (3.193). Real part (yellow dashed) and imaginary part (purple dashed) of the scattering length calculated by the Floquet-Feshbach resonance theory with Eq. (3.207). The parameters are $\tilde{a}_0 = 1, \tilde{a}_1 = 0.3, \tilde{a}_2 = 0.1$. (a) Overview plot of the resonances $\alpha = 1, ..., 4$ (from right to left), (b) zoom of (a), highlighting the 2nd resonance.

matrix $\Lambda_{n,m}$. For a vanishing higher harmonic driving, $\tilde{a}_n = 0,\ n > 1$, Eq. (3.136) valid for a sinusoidal driving is recovered. This is visible, since all terms involving a $\Lambda_{n,m}$ as well as the term $\partial_{\tilde{\omega}} \delta \tilde{E}_\alpha(\tilde{\omega})|_{\omega=\omega_\alpha}$ vanish. Since the matrix $\Lambda_{n,m}$ is complex, the resonance width Eq. (3.208) becomes complex in the presence of a higher-harmonic driving. This induces interesting behavior which is discussed in the next subsection.

3.8.3. Losses and Asymmetries as an Influence of a Higher Harmonic Drive

We now evaluate the scattering length Eq. (3.207) found with the Floquet-Feshbach resonance theory and discuss the relevant features. In Fig. 3.14 the result of the Floquet-Feshbach resonance theory Eq. (3.207) is compared with the the numerically calculated scattering length and a good agreement is found. This shows that the theory incorporates the relevant physics. Similar to the sinusoidally driven case displayed in Fig. 3.9, multiple resonances occur, which are labeled from high to low driving frequencies starting at $\alpha = 1$ at the highest frequency. In difference to the harmonically driven case, the resonances in Fig. 3.14 have a real part with finite extrema. In addition, the imaginary part peaks at the resonance position. This shows that the resonances have losses, as with Eq. (3.75) the imaginary part of the scattering length is associated with loss into inelastic channels. These losses originate from the direct coupling of the bound states to the inelastic channels, through which the bound states can decay into the inelastic channels. In Fig. 3.14 (b) a zoomed plot of the resonance

$\alpha = 2$ is shown, where an asymmetry in the imaginary part of the scattering length can be observed. The outstanding effect of this asymmetry is to shape a minimum of $|\mathrm{Im}\ \tilde{a}_{\mathrm{res}}|$ which suppresses the losses to a minimal value. It allows a tuning of the elastic scattering while keeping the losses small, a setup that is often desired in ultracold gas experiments [18].

For the further understanding of the aforementioned features, we discuss the mathematical properties of the resonant part of Eq. (3.207), which reads

$$\tilde{a}_{\mathrm{res}} = \tilde{a}_{\mathrm{bg}} \left(1 - \frac{\tilde{\Delta}}{\tilde{x} + i\gamma} \right), \tag{3.209}$$

with $\tilde{x} = \tilde{\omega} - \tilde{\omega}_\alpha$. It can be split in real and imaginary part by

$$\begin{aligned} \mathrm{Re}\ \tilde{a}_{\mathrm{res}} &= \tilde{a}_{\mathrm{bg}} \left(1 - \frac{\tilde{\Delta}_0 \tilde{x} + \tilde{\tau}\tilde{\gamma}}{\tilde{x}^2 + \tilde{\gamma}^2} \right), & (3.210\text{a}) \\ \mathrm{Im}\ \tilde{a}_{\mathrm{res}} &= \tilde{a}_{\mathrm{bg}} \frac{\tilde{\tau}\tilde{x} - \tilde{\gamma}\tilde{\Delta}_0}{\tilde{x}^2 + \tilde{\gamma}^2}, & (3.210\text{b}) \end{aligned}$$

where $\tilde{\Delta} = \tilde{\Delta}_0 + i\tilde{\tau}$. The imaginary part of the width $\tilde{\tau}$ mixes the the original behavior of real and imaginary part of the scattering length. While for $\tilde{\tau} = 0$ the imaginary part is of Lorentzian form, a non-vanishing $\tilde{\tau}$ adds an additional dispersive behavior. A finite $\tilde{\tau}$ adds a Lorentzian behavior to the real part. The extremal values of Re $\tilde{a}_{\mathrm{res}}$ are $\tilde{x}^{\mathrm{Re}}_{\pm} = \tilde{\gamma}\tilde{\tau}/\tilde{\Delta}_0 \pm |\tilde{\gamma}|\sqrt{1 + (\tilde{\tau}/\tilde{\Delta}_0)^2}$. These correspond to the maximum and the minimum the function Re a_{res} has in the vicinity of the resonance. For $\tilde{\tau} = 0$ we find $\tilde{x}^{\mathrm{Re}}_{\pm} = \pm|\tilde{\gamma}|$ and $\mathrm{Re}\ \tilde{a}_{\mathrm{res}}(\tilde{x}^{\mathrm{Re}}_{\pm}) = a_{\mathrm{bg}}(1 \pm \tilde{\Delta}_0/(2\tilde{\gamma}))$. This shows that in the presence of a finite decay rate $\tilde{\gamma}$ the maximal enhancement of the real part Re $\tilde{a}_{\mathrm{res}}$ is finite, and it decreases with increasing $\tilde{\gamma}$. The imaginary part has two extrema at

$$\tilde{x}^{\mathrm{Im}}_{\pm} = \frac{\tilde{\gamma}\tilde{\Delta}_0}{\tilde{\tau}} \pm |\tilde{\gamma}| \sqrt{1 + \frac{\tilde{\Delta}_0^2}{\tilde{\tau}^2}}. \tag{3.211}$$

The quantity $x^{\mathrm{Im}}_{\mathrm{sign}(\tilde{\gamma}\tilde{\Delta}_0/\tilde{\tau})\mp}$ corresponds to the central peak of Im a_{res}. In the limit of $\tilde{\tau} \to 0$ the approximation $x^{\mathrm{Im}}_{\mathrm{sign}(\tilde{\gamma}\tilde{\Delta}_0/\tilde{\tau})\mp} \approx 0$ holds and we find that $\mathrm{Im}\ a_{\mathrm{res}}(\tilde{x} = 0) \approx -\tilde{a}_{\mathrm{bg}}\tilde{\Delta}_0/\tilde{\gamma}$. Thus the maximum of the imaginary part also diverges with $\mathrm{Im}\ \tilde{a}_{\mathrm{res}}(x^{\mathrm{Im}}_{\mathrm{sign}(\tilde{\gamma}\tilde{\Delta}_0/\tilde{\tau})\mp}) \propto -1/\tilde{\gamma}$ for vanishing $\tilde{\gamma}$. The other extremum $x^{\mathrm{Im}}_{\mathrm{sign}(\tilde{\gamma}\tilde{\Delta}_0/\tilde{\tau})\pm}$ corresponds to the maximum of the imaginary part, i.e. the position where it is closest to zero. In the limit $\tilde{\tau} \to 0$ the location of this extremum diverges to $x^{\mathrm{Im}}_{\mathrm{sign}(\tilde{\gamma}\tilde{\Delta}_0/\tilde{\tau})\pm} \to \pm\infty$. Thus the presence of a non-vanishing $\tilde{\tau}$ is related to a finite value of $x^{\mathrm{Im}}_{\mathrm{sign}(\tilde{\gamma}\tilde{\Delta}_0/\tilde{\tau})\pm}$, which can lie to the left or to the right the resonance position, depending on the value of $\mathrm{sign}(\tilde{\gamma}\tilde{\Delta}_0/\tilde{\tau})$. The closer $x^{\mathrm{Im}}_{\mathrm{sign}(\tilde{\gamma}\tilde{\Delta}_0/\tilde{\tau})\pm}$ is to the resonance position $x^{\mathrm{Im}}_{\mathrm{sign}(\tilde{\gamma}\tilde{\Delta}_0/\tilde{\tau})\mp}$, the more asymmetric the resonance shape becomes. Therefore we can take the value of $x^{\mathrm{Im}}_{\mathrm{sign}(\tilde{\gamma}\tilde{\Delta}_0/\tilde{\tau})\mp}$ as a measure for the asymmetry of the resonance.

The minimum of the imaginary part reached at $x^{\mathrm{Im}}_{\mathrm{sign}(\tilde{\gamma}\tilde{\Delta}_0/\tilde{\tau})\pm}$ can be of practical importance if one

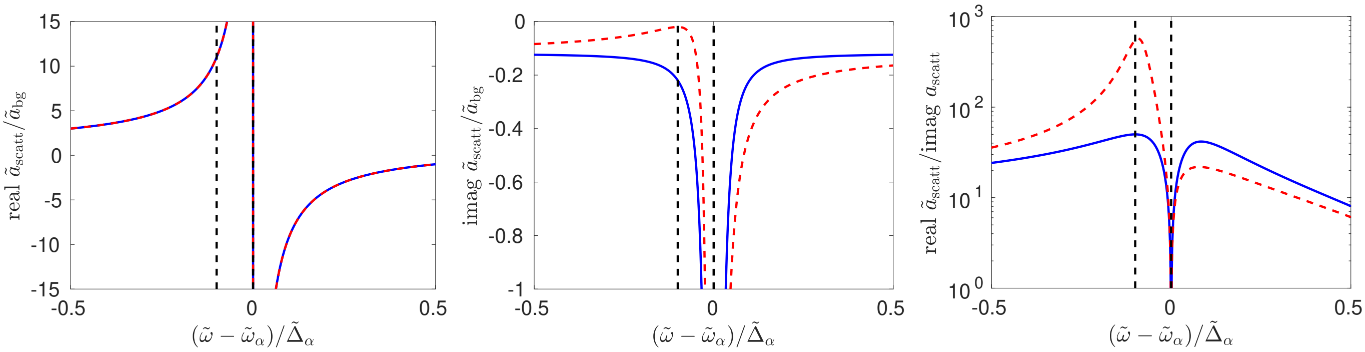

(a) **(b)** **(c)**

Figure 3.15.: The quantity $\tilde{a}_{\rm scatt} = \tilde{a}_{\rm res} + a_{\rm non-res}$ is shown exemplarily with $\tilde{a}_{\rm res}$ as in Eq. (3.209) and $a_{\rm non-res}(\tilde{\omega}) = \mathit{const} = -0.12\tilde{a}_{\rm bg}$. The parameters are $\tilde{\gamma} = -10^{-3}$ and $\tilde{\tau} = 0$ for the blue solid curves, $\tilde{\gamma} = -10^{-3}$, $\tilde{\tau} = 2 \times 10^{-2}$ for the red dashed curves. The left black dashed line marks $\tilde{x} = 0$, the right dashed line the position of minimal $|\mathrm{Im}\ \tilde{a}_{\rm res}|$. In (a) the real part is shown, in (b) the imaginary part. (c) displays the ratio Re $\tilde{a}_{\rm scatt}/\mathrm{Im}\ \tilde{a}_{\rm scatt}$.

is interested in maximizing the real part of $\tilde{a}_{\rm scatt}$, which controls e.g. the interaction strength in an ultracold gas experiment, while keeping the atom loss at a minimum. Fig. 3.15 exemplarily shows two resonant curves, one with $\tilde{\tau} = 0$ and the other with $\tilde{\tau} = 2 \times 10^{-2}$. While the real part is barely influenced by a finite $\tilde{\tau}$, the imaginary parts of the two configurations notably differ and the asymmetry of the plot for $\tilde{\tau} = 2 \times 10^{-2}$ is clearly visible. The minimum of $|\mathrm{Im}\ \tilde{a}_{\rm scatt}|$ lies on the left side of the resonance. As shown in Fig. 3.15 (c), this results in an enlarged ratio of Re $\tilde{a}_{\rm scatt}/\mathrm{Im}\ \tilde{a}_{\rm scatt}$ near the position of minimal $|\mathrm{Im}\ \tilde{a}_{\rm scatt}|$, compared to the case with vanishing $\tilde{\tau}$, which is for example given in case of an optical Feshbach resonance [18, 115]. This enhancement of the ratio Re $\tilde{a}_{\rm scatt}/\mathrm{Im}\ \tilde{a}_{\rm scatt}$ is an advantage of the Floquet-Feshbach resonances compared to optical ones.

We interpret the physical origin of this asymmetry as a Fano resonance suppressing the population of the inelastic channels, similar to the results of U. Fano in Ref. [11]. There, the author considered the decay of a bound state into a continuum in the presence of an autoionization level. The bound state can do a direct transition to the continuum or decay via the autoionization level into the continuum. It turns out that both paths interfere, enabling the possibility that the matrix element for the transition vanishes [11]. In our case we conjecture that similar processes happen for the inelastic channels. The Floquet scattering theory ensures by $\mathrm{Im}\ a_{\rm scatt} = -\sum_{n \geq n_{\rm c},\ n \neq 0} |a_n^{\rm Fl}|^2 k_n$ that the imaginary part of the scattering length is related to the population of the inelastic channels. In the following we make it visible that the minimum population of the inelastic channels may come from a Fano resonance. Here the two interfering paths are the following: One is the direct excitation of inelastic channels via the higher Fourier components, e.g. with $\tilde{a}_2$ from $n = -1$ to $n = 1$, the other is the sequenced hopping to the next higher channel with $\tilde{a}_1$, e.g. from $n = -1$ over $n = 0$ to $n = 1$. Since the driving frequency $\tilde{\omega}$ enters into the parameters of the Floquet-Feshbach resonance theory, it also depends on the driving frequency how these paths interfere. This explains that the minimal $|\mathrm{Im}\ \tilde{a}_{\rm scatt}|$ can be reached while tuning $\tilde{\omega}$. The Floquet Hilbert space contains more complexity than the aforementioned prototype process of a Fano resonance. This makes it visible that in most cases there is no complete destructive interference and thus no complete suppression of losses.

Mathematically we can make the statement that without the direct coupling of closed to inelastic Floquet channels there is a vanishing loss parameter $\tilde{\gamma}_\alpha$ and a vanishing imaginary part of the width $\tilde{\tau}_\alpha$. Refs. [122, 152, 153] found that the presence of inelastic scattering induces a formula for the scattering length of a similar shape as Eq. (3.209). With this we conclude that the asymmetry of the imaginary part is related to inelastic multi-channel scattering. In our case these channels are the Floquet channels, therefore the asymmetry is an effect that is related to Floquet physics. This is a remarkable result, since it allows to directly proof the presence of Floquet physics by measuring asymmetries in the imaginary part $\operatorname{Im} \tilde{a}_{\mathrm{scatt}}$, that are tunable by the parameters of the drive. In an ultracold gas experiment, this may be achieved by measuring the two-body losses with inelastic loss spectroscopy [18, 29].

3.8.4. Results of the Floquet-Feshbach Resonance Theory for a Higher Harmonic Drive

After having discussed the central properties of the Floquet-Feshbach resonances in case of a higher harmonic drive, we analyze the behavior of the resonance parameters in dependence on the driving strength $\tilde{a}_n$. In Fig. 3.16 several parameters of the Floquet-Feshbach resonance formula Eq. (3.207) are shown for $\tilde{a}_0 = 1, \tilde{a}_1 = 0.25$ with $\tilde{a}_n = \tilde{a}_{-n}$ for $|n| \leq 2$ and $\tilde{a}_n = 0$ for $|n| > 2$. This means we start at a given harmonic driving scheme and increase the second Fourier component $\tilde{a}_2$.

As seen in Fig. 3.16 (a), all resonant frequencies $\tilde{\omega}_\alpha$ shift to lower values for small $\tilde{a}_2$ while they increase for larger $\tilde{a}_2$. In addition, the resonance width shows an interesting behavior. While the width of the first resonance drops and the width of the third resonance stagnates, the second resonance gets broader. This behavior becomes clear if one thinks of the interpolation between a drive with $\tilde{a}_1 \neq 0,\ \tilde{a}_2 = 0$ and $\tilde{a}_1 = 0,\ \tilde{a}_2 \neq 0$, rather than a pure increase of $\tilde{a}_2$. In the case $\tilde{a}_2 = 0$ the pseudo potential is harmonically driven and resonances occur for each $\alpha \in \mathbb{N}$. If $\tilde{a}_1 = 0$, the drive is as well harmonic, but with frequency $2\tilde{\omega}$. Odd and even Floquet channels are decoupled from each other, thus only the resonances with even α appear in this case. The odd resonances disappear, which means that their width becomes zero. The road towards this scenario is exactly what is displayed in Fig. 3.16 (b), while Fig. 3.16 (c) shows that the imaginary parts of Δ_α increase with $\tilde{a}_2$. The behavior of the loss parameter $\tilde{\gamma}_\alpha$ shown in Fig. 3.16 (d) can be explained similarly to discussion of Fig. 3.16 (b). The loss parameters for the first and third resonance increase, while $\tilde{\gamma}_{\alpha=2}$ stagnates at large $\tilde{a}_2$. In this parameter region the resonances $\alpha = 1, 3$ are stronger damped than the resonance $\alpha = 2$. Overall the first resonance suffers substantially more loss than the others, since a mayor population of the bound state is directly coupled with $\tilde{a}_2$ to the inelastic channels. For small $\tilde{a}_2$ it holds the smaller the resonance number α, the smaller the loss parameter $\tilde{\gamma}_\alpha$. In Fig. 3.16 (e) the maximal enhancement of the real part of the scattering length is shown. For small $\tilde{a}_2$ values larger than 10^4 are possible, while for the first and second resonance it decreases permanently. For the second resonance there is after the initial decrease an additional increase, which can be understood with the interpolation argument from the discussion above. Fig. 3.16 (f) displays the position of the

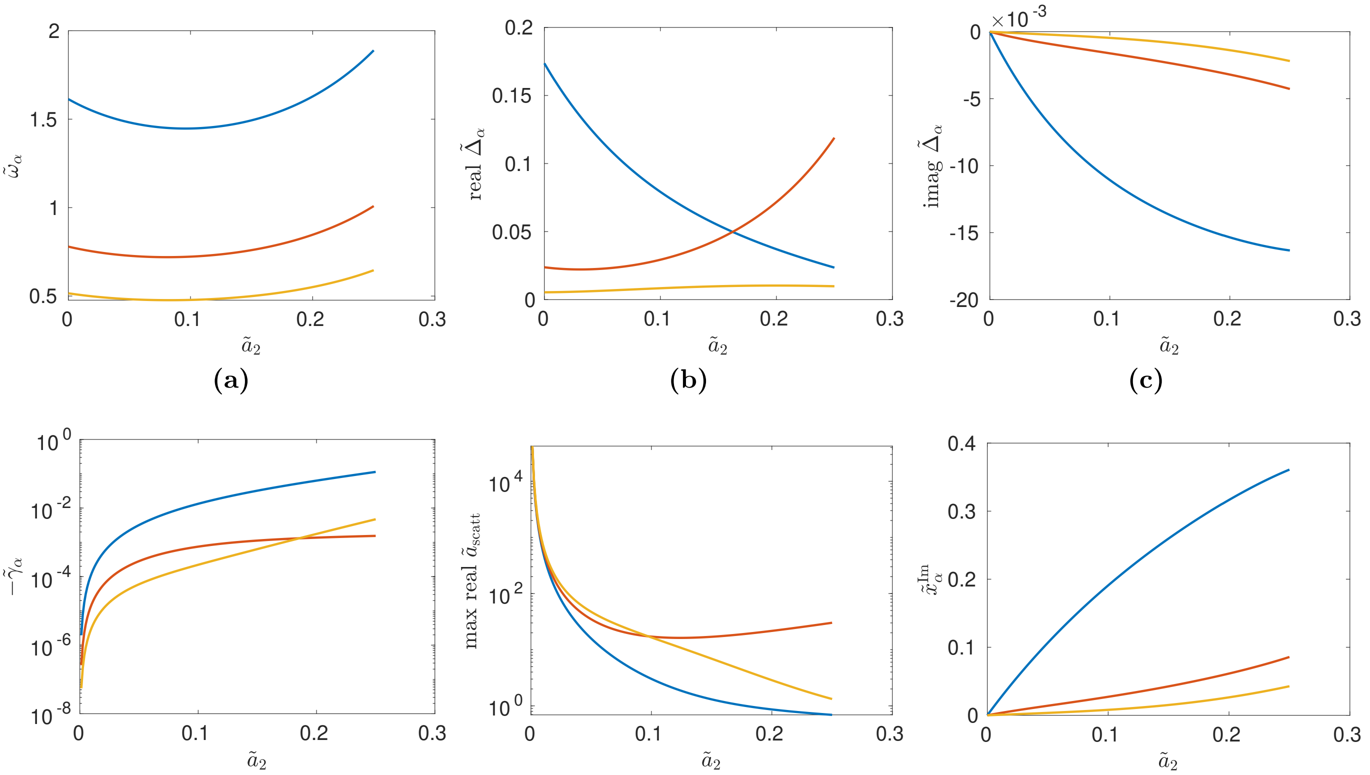

(a) **(b)** **(c)**

(d) **(e)** **(f)**

Figure 3.16.: Resonance parameters for resonances with numbers $\alpha = 1$ (blue), $\alpha = 2$ (red), $\alpha = 3$ (yellow) with $\tilde{a}_0 = 1$ and $\tilde{a}_1 = \tilde{a}_{-1} = 0.25$ in dependence on $\tilde{a}_2 = \tilde{a}_{-2}$. max real $\tilde{a}_{\text{scatt}}$ in (e) is calculated with max real $\tilde{a}_{\text{scatt}} = \tilde{a}_{\text{res}}(\tilde{\omega}_\alpha + \tilde{x}_-^{\text{Re}}) + \tilde{a}_{\text{non-res}}(\tilde{\omega}_\alpha + \tilde{x}_-^{\text{Re}})$, $\tilde{x}_\alpha^{\text{Im}}$ in panel (f) is calculated by $\tilde{x}_\alpha^{\text{Im}} = x^{\text{Im}}_{\text{sign}(\tilde{\gamma}\tilde{\Delta}_0/\tilde{\tau})\mp}$.

minimal imaginary part, which represents our measure for the asymmetry of the resonance curves. For small $\tilde{a}_2$ the value of $x^{\text{Im}}_{\text{sign}(\tilde{\gamma}\tilde{\Delta}_0/\tilde{\tau})\mp}$ is close to zero due to the fact that $\tilde{\gamma}_\alpha$ is smaller than the imaginary part of the width. Indeed, the resonance shapes show for small $\tilde{a}_2$ the most prominent asymmetry. With increasing $\tilde{a}_2$ there is a rise of $x^{\text{Im}}_{\text{sign}(\tilde{\gamma}\tilde{\Delta}_0/\tilde{\tau})\mp}$, thus the resonance curves appear more symmetric. The slope of the increase is slower, the larger the resonance number is.

In summary, we conclude that a higher-harmonic drive induces losses to the Floquet-Feshbach resonances that come in due to the presence of inelastic scattering, which is unfortunate to most applications in ultracold quantum gases. However, we find that for certain parameters these losses are highly asymmetric. This allows, in comparison to optical Feshbach resonances, for a larger ratio of real to imaginary part.

As an outlook we mention that by tuning the relative phase of the first and second harmonic the imaginary part $\tilde{\gamma}_\alpha$ can be reduced. A further calculation might quantify this argument.

3.9. Frequency Scales of the Model

In this section we give the frequency scales that are of relevance for the experimental realization of a Floquet-Feshbach resonance. We refer to the proposal of Ref. [99] of applying a time-periodic magnetic field in the vicinity of a magnetic Feshbach resonance. We assume to be in the range of universal behavior close to the position of the magnetic Feshbach resonance, such that resonant scattering is described by the pseudo potential. The relevant energy scale for this is the dimer energy Eq. (3.46) with scattering length Eq. (3.45). With this the dependence of the dimer energy on the magnetic field is given by

$$E_\mathrm{D} = hf_\mathrm{D}\left(\frac{B-B_0}{B-B_0-\Delta}\right)^2 \approx hf_\mathrm{D}\left(\frac{B-B_0}{\Delta}\right)^2, \tag{3.212}$$

where the maximal dimer frequency

$$f_\mathrm{D} = \frac{\hbar}{4\pi\mu}\frac{1}{a_\mathrm{bg}^2} \tag{3.213}$$

yields the relevant frequency scale. In Eq. (3.212), the approximation holds for $|B - B_0| < |\Delta|$. As described by Eq. (3.213), the dimer frequency depends on the reduced mass of the atom and the background scattering length of the magnetic Feshbach resonance around which the periodic magnetic field is applied.

The other relevant frequency scale is related to the range of the actual potential. Following Ref. [18] we assume a van der Waals potential for the scattering of ultracold atoms, whose length scale is given by the quantity r_vdW, which can explicitely calculated with the properties of each inter-atomic potential. The approximation of the actual van der Walls potential by the pseudo potential is valid if the condition $r_\mathrm{vdW}k_1 \ll 1$ holds [116, 117]. This can also be expressed as

$$f \ll f_\mathrm{vdW} \tag{3.214}$$

with the van der Waals frequency given by

$$f_\mathrm{vdW} = \frac{\hbar}{4\pi\mu}\frac{1}{r_\mathrm{vdW}^2}. \tag{3.215}$$

In Table 3.1 numbers are shown for selected isotopes and Feshbach resonances. All frequencies lie in the kHz and MHz regime. For all cases shown, the dimer frequency is smaller than the van der Waals frequency. This is signaling that condition (3.214) is valid for all relevant magnetic field strengths. Note, that by choosing the time-averaged magnetic field to be close to the field strength of the magnetic Feshbach resonance, the frequency scale of the actual dimer energy can be decreased by orders of magnitude.

At last, we present the Fourier coefficients that correspond to a sinusoidal drive of the magnetic field. The time-dependent scattering length is given by Eq. (3.191) with a time-periodic magnetic field of the form $B(t) = B_1 + B_\mathrm{AC}\cos(\omega t)$. With the residue theorem the Fourier components are

Table 3.1.: Table showing the dimer frequency f_D and the van der Waals frequency f_vdW for different isotopes at a Feshbach resonance with magnetic field strength B_0. The values are taken from [18]. Here, $a_\mathrm{Bohr} = 5.29 \times 10^{-11}$ m denotes the Bohr radius.

Isotope	$\mathbf{B_0}$	$\mathbf{a}_\mathrm{bg}$	$\mathbf{f}_\mathrm{D}$	$\mathbf{f}_\mathrm{vdW}$
^{6}Li	843 G	$-1405\ a_\mathrm{Bohr}$	304 kHz	641 MHz
^{87}Rb	1007.4 G	$443\ a_\mathrm{Bohr}$	4.15 MHz	6.07 MHz
^{133}Cs	800 G	$1940\ a_\mathrm{Bohr}$	7.21 kHz	2.66 MHz

found under the assuption that $|B_\mathrm{AC}| < |B_1 - B_0|$ to be [117]

$$a_n = a_\mathrm{BG}\left[\delta_{n,0} - \frac{\Delta}{(B_1 - B_0)\sqrt{1-y^2}}\left(\frac{\sqrt{1-y^2}-1}{y}\right)^{|n|}\right], \tag{3.216}$$

where $y = B_\mathrm{AC}/(B_1 - B_0)$. Using Eq. (3.216) the Fourier coefficients of $a(t)$ can be calculated for any desired situation. For the opposite case $|B_\mathrm{AC}| > |B_1 - B_0|$ the Fourier coefficients Eq. (3.216) do not converge. In this case a Floquet solution is not possible. Note, that for driving the magnetic field by a driving scheme including higher harmonics, the Fourier components a_n can be tuned to values other than Eq. (3.216).

3.10. Multi-Channel Model of a Feshbach Resonance with Periodically Driven Parameters

Reference [99] found that the periodic driving of a magnetic field in the vicinity of a Feshbach resonance induces new resonances. If the strength of the applied magnetic field lies in the range of universal behavior, a pseudo potential with a time-dependent strength describes the scattering physics. This situation is thoroughly discussed in Secs. 3.6 - 3.8. However, this description has several limitations. First, there are Feshbach resonances where this range of universal behavior is narrow, as discussed in Subsec. 3.4.1. Thus, it is of high interest to find a theory that exceeds this limited range. Second, if the AC-part of the magnetic field is larger than the difference of the average magnetic field to the position of the magnetic Feshbach resonance, the Floquet solution of the driven pseudo potential does not converge, c.f. Eq. (3.216). However, both above mentioned cases can be reached in an experimental setup. These limitations motivate us to find a model that is capable of describing the effects of a time-periodic magnetic field on the scattering properties for a much wider parameter range.

The multi-channel description of a Feshbach resonance, introduced in Subsec. 3.4, resolves the above raised issues. Since we like to keep the mathematical description simple, we specialize to the two-channel magnetic Feshbach resonance model Eq. (3.47) with a pseudo potential as inter-particle interaction. A periodic modulation of the magnetic field leads to time-dependent parameters in this model. Using the multi-channel model we are able to analyze the Floquet-Feshbach resonances for a vast range of magnetic field strengths. In particular, this discussion includes the above mentioned cases where the simple pseudo potential model fails for a description of the Floquet-Feshbach resonances.

The periodically driven multi-channel model is introduced in Subsec. 3.10.1. In order to understand the Floquet scattering solution, it is key to discuss the Floquet modes of a time-periodically driven two-level system, which is done in Subsec. 3.10.2. The numerical Floquet scattering solution is derived in Subsec. 3.10.3. We report in Subsec. 3.10.4 that the periodic drive both induces new resonances and engineers Feshbach resonances that already exist in the static case. Subsec. 3.10.5 is devoted to the analysis of these resonances using a combination of the Floquet-Feshbach resonance theory and analytical approximations of the Floquet scattering problem. In Subsec. 3.10.6 we apply the model to a low-field magnetic Feshbach resonance with experimentally inspired parameters.

3.10.1. Periodically Driven Multi-Channel Model

The goal of this subsection is to find a Floquet scattering solution of the two-channel model Eq. (3.47) with time-periodic parameters $C(t) = C(t+T)$, $\delta(t) = \delta(t+T)$:

$$H = -\Delta_r + \begin{pmatrix} 0 & C(t) \\ C(t) & \delta(t) \end{pmatrix} + \begin{pmatrix} a_\mathrm{e} & 0 \\ 0 & a_\mathrm{c} \end{pmatrix} \lim_{s\to 0^+} \frac{\delta(r-s)}{s^2} \frac{\overleftrightarrow{\partial}}{\partial r} r. \tag{3.217}$$

In Eq. (3.217), Δ_r denotes the radial Laplacian while the multi-channel structure is encoded in the matrix-valued potentials. The upper component corresponds to the the entrance channel, the lower will host a bound state that is needed for the Feshbach resonance. The scattering potential is assumed to be a matrix valued pseudo potential, with a_e / a_c parametrizing the strength. Both the detuning of the channel thresholds $\delta(t)$ and the coupling $C(t)$ between the channels are time periodic, as it is discussed later. These quantities are expressed in a general Fourier series

$$C(t) = \sum_n e^{-in\omega t} C_n, \tag{3.218a}$$

$$\delta(t) = \sum_n e^{-in\omega t} \delta_n. \tag{3.218b}$$

Let us discuss the parameters of Eq. (3.217) for the case of a magnetic Feshbach resonance. As described in Sec. 3.4, the nature of the two channels is determined for alkali atoms by the spins of the valence electron, which can be either in triplet or in singlet configuration. The coupling between those channels is given by the hyperfine interaction $C = V_\mathrm{HF}\ 2\mu/\hbar^2$ while the detuning describes a Zeeman term $\delta = \delta\mu\ B\ 2\mu/\hbar^2$. A time-periodic magnetic field along the quantization direction can thus be modeled with a time-dependent detuning $\delta(t)$ [99, 144]. In addition, a time-dependent coupling constant $C(t)$ may be induced by a time-dependent electromagnetic field that allows for electric or magnetic dipole (multipole) transitions in the electronic states that serve as definitions for the channels [138, 141, 144]. For example, a magnetic field polarized perpendicular to the quantization axis can in principle induce such couplings [99, 138, 143]. In the static case, a Feshbach resonance occurs if the energy of the scattering state is near a bound state of the van-der Waals potential in a closed channel. Here we reduce the complexity of finding these bound states drastically by assuming a pseudo potential in the closed channel. In this case is holds that this channel posses a bound state for $a_\mathrm{c} > 0$ and the energy of this bound state is known explicitly by Eq. (3.31). Since we are interested in describing scattering in ultracold quantum gases, the low-energy limit is of relevance. In this limit it will be a good approximation to substitute the actual scattering potential in the entrance channel by the pseudo potential with the interaction strength parameterized by the scattering length a_e, as done in model (3.217).

If a two-channel model with realistic inter-atomic potentials is given, we can at least qualitatively describe the physics with the pseudo potential model Eq. (3.217) by the following considerations. We can choose a_e to equal the background scattering length in the entrance channel, while a_c is chosen such that the energy of the bound state in the pseudo potential model coincides with the value of the realistic potential. The coupling C can be determined with the results of Fig. (3.4) (b), if the width of the actual Feshbach resonance is known.

In order to find the Floquet scattering solution, Hamiltonian (3.217) is expressed in the notation of Floquet Hilbert space, c.f. sec. 2.2.2. The Floquet equation reads

$$\left(-\Delta_r + \hat{H}_\mathrm{int} + \hat{A} \lim_{s\to 0^+} \frac{\delta(r-s)}{s^2}\frac{\partial}{\partial r} r\right) |\phi\rangle\rangle = \epsilon |\phi\rangle\rangle. \tag{3.219}$$

Here $\hat{A} = A \otimes I_\mathcal{T}$, with

$$A = \begin{pmatrix} a_\mathrm{e} & 0 \\ 0 & a_\mathrm{c} \end{pmatrix}, \tag{3.220}$$

and $\otimes$ as the Kronecker product and $I_\mathcal{T}$ the identity matrix in the space of time-periodic functions. Note that in Eq. (3.219) we divided by $\hbar^2/(2\mu)$. We will measure in this section all energies in units of a squared inverse length, based on the rescaling $\epsilon \to \epsilon\, 2\mu/\hbar^2$. The internal Hamiltonian in Floquet space $\hat{H}_\mathrm{int}$ is given by

$$(m|\hat{H}_\mathrm{int}|n) = \begin{pmatrix} 0 & C_{m-n} \\ C_{m-n} & \delta_{m-n} \end{pmatrix} - \delta_{n,m} n\hbar\omega \begin{pmatrix} 1 & 0 \\ 0 & 1 \end{pmatrix}. \tag{3.221}$$

Similar to the static calculation described in Sec. 3.4, the first step of finding the scattering solution is to determine the asymptotic channels by diagonalizing Hamiltonian (3.221) in Floquet space

$$\hat{H}_\mathrm{int}|\mu, m\rangle\rangle = E_{\mu,m}|\mu, m\rangle\rangle. \tag{3.222}$$

Here $\mu = 1, 2$ labels the two eigenstates within one Floquet Brillouin zone and m denotes the Floquet Brillouin zone in which the solution resides. It holds that $E_{\mu,m} = E_{\mu,0} + m\hbar\omega$.

In order to clarify the discussion of the following subsections, we will point out the three solution methods of the Floquet scattering equations (3.219) that are used during this section. We can always solve the Floquet scattering equations (3.219) numerically. This method yields exact results, however, it is not descriptive for a physical interpretation. As a second approach we will perform rotating-wave approximations, which yield an analytical discussion of the physics for certain parameter values. The rotating-wave approximations are especially valid for weak driving. Since the numerical solution shows effects that are beyond the rotating-wave approximations, we apply as a third approach the Floquet-Feshbach resonance theory to the periodically driven multi-channel model. The Floquet-Feshbach resonance theory allows for a deeper understanding of the resonances compared to above two methods, and with it we are able to calculate the resonance parameters for a wide range of system parameters, including the case of strong driving.

Due to the relevance to all above mentioned methods, we will discuss the physics of the periodically driven two-level system Eq. (3.221) in the following subsection.

3.10.2. Investigation of the Periodically Driven Two-Level System

In order to understand the Floquet scattering solution of Eq. (3.219), it is key to know about the physics of the periodically driven two-level system Eq. (3.222). We discuss the numerical solution of the periodically driven two-level system, and further explain the results within rotating-wave approximations. Of mayor interest is the dependence of the parameters on the static part of the detuning δ_0, since this case describes the dependence on the magnetic field, which is typically investigated in magnetic Feshbach resonances.

In order to solve Eq. (3.222) numerically, we truncate it in Floquet space to a matrix of finite size, as described in Subsec. 2.2.1. In order to find an accurate Floquet solution, the cutoff m_{co} must fulfill the condition $\delta_0 < m_{\mathrm{co}}\hbar\omega$ such that the Floquet Brillouin zone containing the solution of the corresponding time-independent system can be reached with the numerical solution. We verified that this condition is always fulfilled in our calculations. In Fig. 3.17 the quasienergies $E_{\mu,m}$ are shown in the case of a sinusoidally driven coupling constant $C(t)$. The quasienergies undergo multiple avoided crossings. The avoided crossing near $\delta_0 = 0$ is largest for the chosen parameters and also present in the static two-level solution, as shown by Eq. (3.51). The avoided crossings near $\delta_0/(\hbar\omega) = \pm 1$ correspond to the case where the driving frequency ω matches the level spacing δ_0, such that the two levels are resonantly coupled. Near $\delta_0/(\hbar\omega) = \pm 2, \pm 3, ...$ higher-order resonances occur. However, they are so weak that no avoided crossing is directly visible on the scales used in Fig. 3.17 (a). In Fig. 3.17 (b) the coupling strength is reduced as compared to panel (a), here each avoided crossing is isolated from the others.

In order to get an even better understanding of the physics, we will discuss in the following how each avoided crossing can be described by a rotating wave approximation. Further, we will later find that with these rotating wave approximations we can get an effective description of the Floquet scattering problem Eq. (3.219). Near $\delta_0 = 0$, we neglect any time-dependence of $C(t)$ and use Eq. (3.51) in order to describe the physics. Near $\delta_0/(\hbar\omega) = \pm 1$ only the term oscillating with $e^{\mp i\omega t}$ is of relevance, in the rotating wave approximation all other terms are considered as rotating too fast and are thus neglected. As a result, a system driven by $C(t) = C_0 + 2C_1 \cos(\omega t)$ is approximately described for

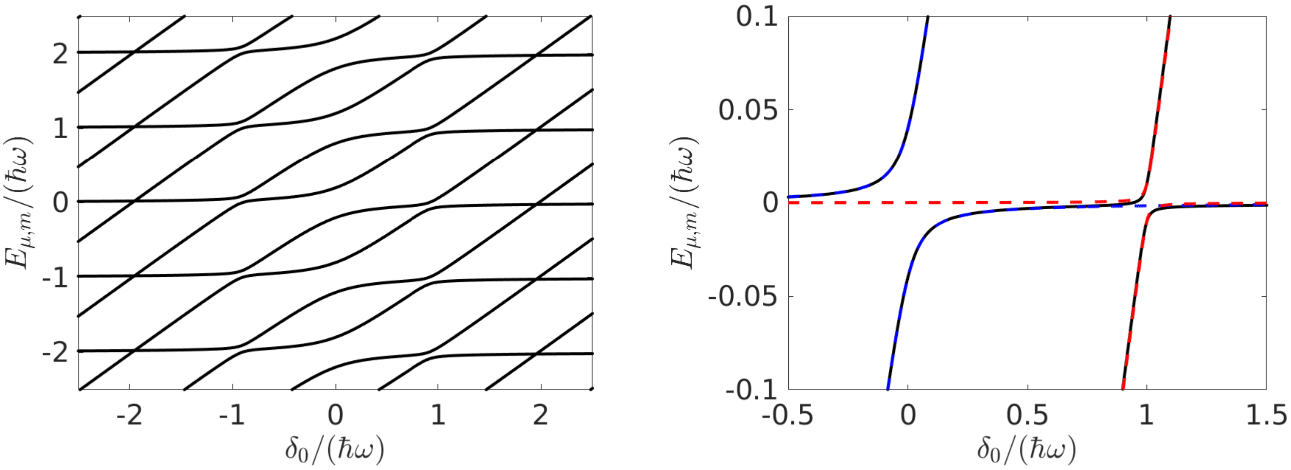

(a) **(b)**

Figure 3.17.: Quasienergies of the time periodically driven two-level system Eq. (3.222). (a) drive of the form $\delta(t) = \delta_0$, $C(t)/(\hbar\omega) = 0.2 + 0.1 \times \cos(\omega t)$, (b) drive of the form $\delta(t) = \delta_0$, $C(t)/(\hbar\omega) = 0.04 + 0.02 \times \cos(\omega t)$. Black the numerical solution of the Floquet equation, blue / red the rotating wave approximation with zero / one drive quantum.

$\delta_0 \approx \pm\hbar\omega$ by the following static Hamiltonian

$$H_{\text{int}}^{\text{RWA}-\text{C}} = \begin{pmatrix} 0 & C_1 \\ C_1 & \delta_0 \mp \omega \end{pmatrix}. \tag{3.223}$$

Figure 3.17 (b) shows that for weak coupling the rotating wave approximation fits well to the actual Floquet solution.

In the case of a sinusoidal modulation of the detuning $\delta(t) = \delta_0 + 2\delta_1 \cos(\omega t)$, a rotating wave approximation includes a gauge transformation that leads to nontrivial Floquet effects, as discussed below. In Fig. 3.18 (a) the quasienergies of the two-level system Eq. (3.222) with sinusoidally driven $\delta(t)$ are shown, also here avoided crossings are present. Assuming that all resonances are well enough isolated from each other we aim to find an approximate Floquet solution near $\delta_0 \approx -n_{\text{rwa}}\hbar\omega$, with n_{rwa} as an integer number. For doing so, we start with writing down the Schrödinger equation of the time-dependent internal Hamiltonian (3.221):

$$i\hbar\partial_t c_1 = C_0 c_2, \tag{3.224a}$$

$$i\hbar\partial_t c_2 = C_0 c_1 + [\delta_0 + 2\delta_1 \cos(\omega t)]c_2 \tag{3.224b}$$

Here it is directly visible that the drive acts as a time-dependent on-site potential on the level 2. In order to get a better description it is useful to perform a gauge transformation that is quite common in Floquet physics [63]: $c_1 = \tilde{c}_1$, $c_2 = \tilde{c}_2 \exp[-i2\delta_1 \sin(\omega t)/(\hbar\omega)]$. This brings Eq. (3.224) to the form

$$i\hbar\partial_t \tilde{c}_1 = C_0 \exp[-i2\delta_0 \sin(\omega t)/(\hbar\omega)]\tilde{c}_2, \tag{3.225a}$$

$$i\hbar\partial_t \tilde{c}_2 = \delta_0 \tilde{c}_2 + C_0 \exp[i2\delta_0 \sin(\omega t)/(\hbar\omega)]\tilde{c}_1 \tag{3.225b}$$

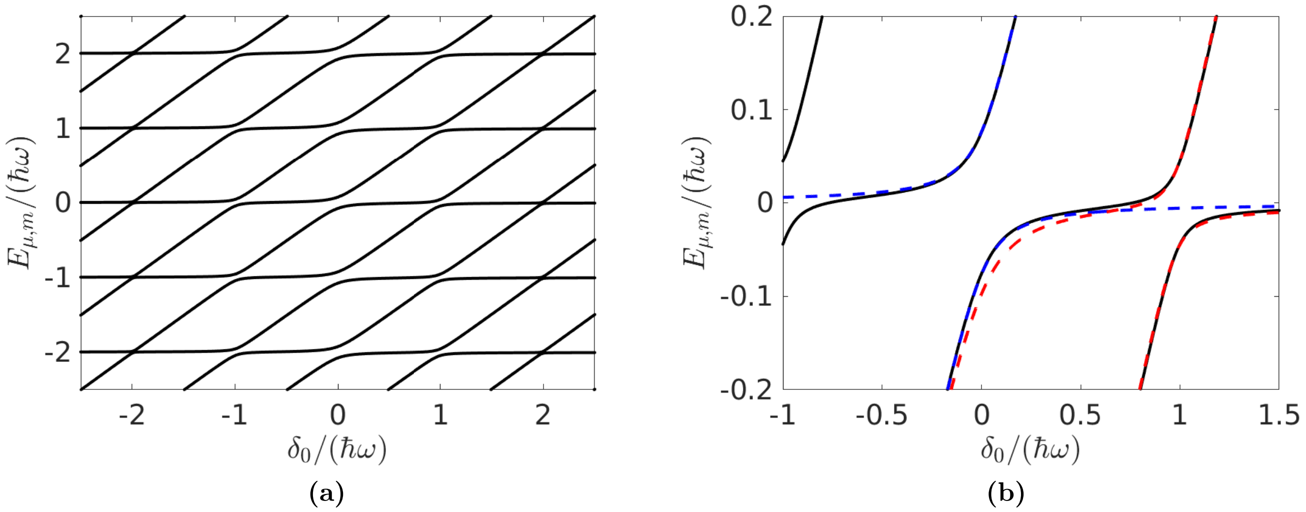

Figure 3.18.: Quasienergies of the time-periodically driven two-level system Eq. (3.222) with a drive of the form $\delta(t) = \delta_0 + 0.25/(\hbar\omega)\cos(\omega t)$, $C(t)/(\hbar\omega) = 0.1$ (a),(b): Black the numerical solution of the Floquet equation. (b): blue / red the Floquet-gauge rotating wave approximation with zero / one drive quantum.

In order to perform a rotating-wave approximation the Jacobi-Anger expansion [120]

$$\exp[iz\sin(\theta)] = \sum_{n=-\infty}^{\infty} \mathcal{J}_n(z)e^{in\theta}, \tag{3.226}$$

with $\mathcal{J}_n(x)$ denoting the Bessel functions of the first kind, is used in order to express the time-dependent coupling constants of Eq. (3.225) in a Fourier series. Now the transformation $\tilde{c}_1 = \bar{c}_1$, $\tilde{c}_2 = e^{in_{\rm rwa}\omega t}\bar{c}_2$ is introduced, where $n_{\rm rwa} \in \mathbb{Z}$ represents the number of drive quanta that is involved in the considered avoided crossing. The label of $n_{\rm rwa}$ suggest that we perform a rotating wave approximation while assuming $\delta_0 \approx -n_{\rm rwa}\hbar\omega$. In this case all terms oscillating with $e^{\pm i\omega t}$ or corresponding higher harmonics are assumed to oscillate so fast that their contribution averages to zero. In this rotating-wave approximation the dynamics of the coefficients $\bar{c}_i,\ i = 1, 2$, is given by the time-independent Hamiltonian

$$H_{\rm int}^{\rm RWA-\Delta} = \begin{pmatrix} 0 & C_0\mathcal{J}_{n_{\rm rwa}}(2\delta_1/(\hbar\omega)) \\ C_0\mathcal{J}_{n_{\rm rwa}}(2\delta_1/(\hbar\omega)) & \delta_0 + n_{\rm rwa}\hbar\omega \end{pmatrix}. \tag{3.227}$$

Although we performed a rotating-wave approximation, Eq. (3.227) still shows nontrivial Floquet behavior, which is indicated by the appearance of the Bessel functions. Since these Bessel functions enter into Eq. (3.227) by a gauge transformation, we name this method "Floquet-gauge rotating wave approximation". The quasienergies found by solving Eq. (3.227) are shown with blue / red dashed lines for $n_{\rm rwa} = 0$ / $n_{\rm rwa} = 1$ in Fig. 3.18 (b), so we conclude that Eq. (3.227) provides a good description of the involved avoided crossings.

Note that a finite coupling in Eq. (3.227) is only possible if both static coupling C_0 and AC-drive

δ_1 are non-vanishing. In contrast, if the coupling $C(t)$ itself is harmonically modulated, avoided crossings are also possible if $C_0 = 0$.

In this section we discussed the solution methods for the periodically driven two-level model Eq. (3.222). A numerical solution with the methods of Subsec. 2.2.1 is always possible. However, we also find analytical solutions by using a combination of gauge transformation and rotating wave approximation. Using both the numerical result and the rotating-wave approximation, we are able to discuss the physics of the periodically driven two-level system.

3.10.3. Numerical Floquet Scattering Solution of the Driven Multi-Channel Model

With the numerical solution of the periodically driven two-level Hamiltonian Eq. (3.221), we can find a numerical solution of the Floquet-scattering problem Eq. (3.219). The Floquet states $|\mu, m\rangle\rangle$ are found by numerically solving the Floquet equation of the two-level Hamiltonian Eq. (3.221) as described in Subsec. 2.2.1 and define Floquet channels that are decoupled at asymptotically large distances $r \to \infty$. Due to this it is beneficial to express the Floquet mode in the basis of the $|\mu, m\rangle\rangle$ states:

$$\langle r|\phi\rangle\rangle = \sum_{\mu,m} |\mu, m\rangle\rangle \phi_{\mu,m}(r), \tag{3.228}$$

where $\phi_{\mu,m}(r)$ is the wave function in the Floquet channel with label (μ, m). In order to understand Eq. (3.228) further, it is useful to compare it to the reasoning of Sec. 3.5, where no internal multi-channel structure is present. We therefor refer to the setting of Sec. 3.5 as single-channel Floquet scattering and name Eq. (3.76) as periodically driven single-channel channel pseudo potential. In this case, the Floquet channels are introduced by a simple Fourier transform, which can be expressed in Floquet space by $\langle r|\phi\rangle\rangle = \sum_n |n)\phi_n(r)$ with $|n)$ as defined in Eq. (2.29). For the periodically driven multi-channel model Eq. (3.219), such a simple Fourier transform would not lead to decoupled channels at asymptotic distances $r \to \infty$, since it does not account for the nontrivial structure of the internal Hamiltonian. Thus, it is necessary to use the Floquet modes of the internal Hamiltonian (3.222) in order to find the correct asymptotically decoupled channels and an equation for the wave function as in Eq. (3.228).

In order to solve the Floquet scattering problem, we insert Floquet mode (3.228) into (3.219) and project with $\langle\langle \sigma, n|$. As a result, Eq. (3.219) is expressed in the $|\mu, m\rangle\rangle$ basis

$$(-\Delta_r + E_{\sigma,n})\phi_{\sigma,n}(r) + \sum_{\mu,m} \langle\langle \sigma, n|\hat{A}|\mu, m\rangle\rangle \lim_{s\to 0^+} \frac{\delta(r-s)}{s^2} \frac{\partial}{\partial r} r\phi_{\mu,m}(r) = \epsilon\phi_{\sigma,n}(r). \tag{3.229}$$

Since the pseudo potential only acts at the origin $r = 0$, the following ansatz can always be assumed

$$\phi_{\sigma,n}(r) = \delta_{\sigma,\sigma_0}\delta_{n,n_0} \frac{\sin(k_{\sigma,n}r)}{k_{\sigma,n}r} + f_{\sigma,n}\frac{e^{ik_{\sigma,n}r}}{r}. \tag{3.230}$$

Here (σ_0, n_0) denotes the entrance channel in which an incoming s-wave part of a plane wave is located. The scattering amplitude in the channel (σ, n) is given by $f_{\sigma,n}$. In the following we describe how the multi-index (σ_0, n_0) of the entrance channel is determined. In the static case of Eq. (3.47), the atoms are assumed to be initially in the internal state with the minimal energy, i.e. the lowest hyperfine state. In the Floquet calculation, such an argument cannot be made, since the Floquet spectrum does not allow to define a state with lowest quasienergy, c.f. Eq. (2.8). Here, we instead calculate the overlap of the two Floquet states in the first Floquet Brillouin zone at initial time and the two eigenstates of the corresponding static problem Eq. (3.51). The Floquet state with the higher overlap to the static ground state is considered to define the entrance channel of the Floquet scattering problem. We label this channel with $(\sigma_0, n_0) = (1, 0)$.

For the further calculation a shift of the quasienergies by $-E_{\sigma_0,n_0}$ is provided, since this results in a vanishing threshold for the entrance channel. By inserting Eq. (3.230) into Eq. (3.219) at $r \neq 0$ the dispersion relation is found to be

$$k_{\sigma,n}^2 + E_{\sigma,n} - E_{\sigma_0,n_0} = \epsilon. \tag{3.231}$$

For the entrance channel we have $k_{\sigma_0,n_0}^2 = \epsilon$, thus ϵ denotes the energy of the incoming particle relative to the threshold E_{σ_0,n_0}.

A linear system for the scattering amplitudes $f_{\sigma,n}$ is found by inserting Eq. (3.230) into Eq. (3.219) and by integrating around the origin with Eqns. (3.27) and (3.28):

$$f_{\sigma,n} + \sum_{\mu,m} \langle\langle \sigma, n | A | \mu, m \rangle\rangle f_{\mu,m} i k_{\mu,m} = -\langle\langle \sigma, n | A | \sigma_0, n_0 \rangle\rangle. \tag{3.232}$$

In order to write down Eq. (3.232) in a compact form, we define the unitary matrix in Floquet space $\hat{Q} = \big((|\mu, m\rangle\rangle)_{(\mu,m)}\big)$, where each column consist of an Floquet mode $|\mu, m\rangle\rangle$, the diagonal matrix $\hat{K}$ with $\hat{K}_{(\mu,m),(\mu,m)} = k_{\mu,m}$ and the vector $\mathbf{f} = (f_{\mu,m})_{(\mu,m)}$. With these definitions Eq. (3.232) can be written as

$$(\hat{\mathbb{I}} + \hat{Q}^\dagger \hat{A} \hat{Q} i \hat{K})\mathbf{f} = -\hat{Q}^\dagger \hat{A} |\sigma_0, n_0\rangle\rangle. \tag{3.233}$$

Equation (3.233) is a key result since it enables to write down a linear system that determines the Floquet scattering amplitudes in a concise form and is used in order to calculate the exact results using the numerics. In order to obtain the scattering amplitudes, Eq. (3.233) is first truncated to a finite size and then solved numerically. The cutoff is chosen large enough such that the solution has converged.

3.10.4. Floquet-Feshbach Resonances

We also find in the periodically driven two-channel model Floquet-Feshbach resonances. Similar to the calculation in Sec. 3.6 we are primarily interested in the time-averaged scattering length in the entrance channel

$$a_{\text{scatt}} = -\lim_{k\to 0} f_{\sigma_0,n_0}(k). \tag{3.234}$$

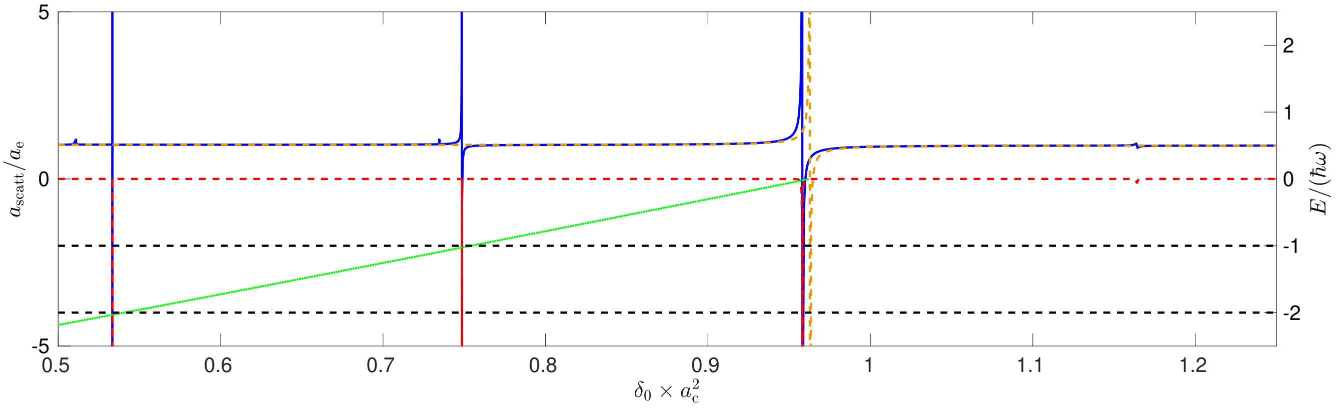

Figure 3.19.: Axis on the left: Real (blue) and imaginary (red) part of the scattering length a_{scatt} with time-periodic driving, yellow the scattering length for the corresponding time-independent model Eq. (3.47). Axis on the right: Energy of the bound state (green) calculated with Eq. (3.57), black dashed lines at $-\hbar\omega$ and $-2\hbar\omega$. The parameters are $a_{\mathrm{e}} = a_{\mathrm{c}}/\sqrt{1.5}$, $C(t) \times a_{\mathrm{c}}^2 = 0.15 + 0.075 \times \cos(\omega t)$, $\delta(t) = \delta_0$, $\hbar\omega \times a_{\mathrm{c}}^2 = 0.2$ and $\epsilon = 0$. The corresponding time-independent model uses $C \times a_{\mathrm{c}}^2 = 0.15$.

Following Ref. [126], the scattering length as defined in Eq. (3.234) is related to the inter-atomic interaction g. The elastic cross section is given by $\langle\langle\sigma_{\mathrm{el}}\rangle\rangle = 4\pi|a_{\mathrm{scatt}}|^2$, while the inelastic rate coefficient reads $K_{\mathrm{inel}} = -4\pi\hbar \mathrm{Im}\ a_{\mathrm{scatt}}/\mu$ for multi-channel Floquet scattering [18, 115]. Since the quasienergies $E_{\sigma,n}$ have the Floquet sideband structure given by Eq. (2.8), Eq. (3.231) dictates that there are open channels with $k_{\sigma,n}^2 \geq 0$ and closed channels with $k_{\sigma,n}^2 < 0$. The structure of these channels is discussed later. The important point is that the closed channels can host Floquet bound states that are able to induce Floquet-Feshbach resonances.

In Fig. 3.19 the scattering length is shown in dependence on the time-average of the detuning δ_0 for a sinusoidal driving of the coupling constant $C(t)$. In order to understand the results of the Floquet scattering calculation it is important to know the corresponding static model. The position of the static resonance is shifted to a value below $\delta_0 \times a_{\mathrm{c}}^2 = 1$, as described by Eq. (3.54). For δ_0 smaller than the position of the resonance there exists a bound state in the coupled channel description that is calculated by Eq. (3.57) and shown in green in Fig. 3.19. The bound state energy has a linear dependence on δ_0 in a large parameter region. Near the resonance there is a strong hybridization of the two channels and the bound state follows an universal behavior given by Eq. (3.46). However, this region of universal behavior is too small to be visible on the parameter scale of Fig. 3.19.

In the periodically driven multi channel model Eq. (3.217) the time-periodic driving is able to engineer already existing Feshbach resonances and to induce new ones. This is seen in Fig. 3.19, where the time-periodic drive is shifts the static resonance to a lower value of δ_0. The resonances at $\delta_0 \times a_{\mathrm{c}}^2 < 0.9$ are induced by the time-periodic driving and do not exist in the static case. In a good approximation, the position of these resonances is given by

$$E_{\mathrm{b}} + \alpha\hbar\omega = 0,\ \alpha \in \mathbb{N}, \tag{3.235}$$

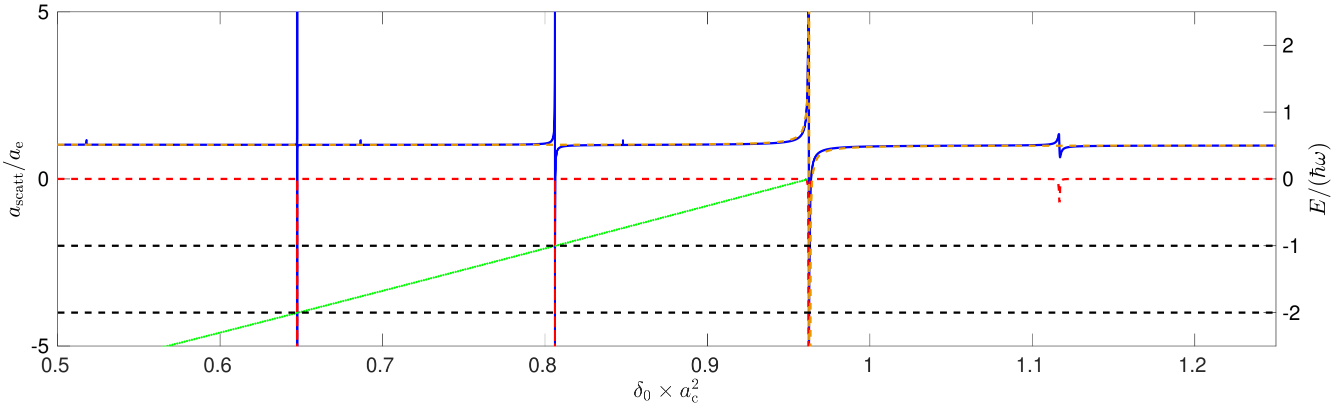

Figure 3.20.: Axis on the left: Real (blue) and imaginary (red) part of the scattering length a_{scatt} with time-periodic driving, yellow the scattering length for the corresponding time-independent model Eq. (3.47). Axis on the right: Energy of the bound state (green) calculated with Eq. (3.57), black dashed lines at $-\hbar\omega$ and $-2\hbar\omega$. The parameters are $a_{\mathrm{e}} = a_{\mathrm{c}}/\sqrt{1.5}$, $C(t) \times a_{\mathrm{c}}^2 = 0.15$, $\delta(t) = \delta_0 + 0.12\cos(\omega t)/a_{\mathrm{c}}^2$, $\hbar\omega \times a_{\mathrm{c}}^2 = 0.15$ and $\epsilon = 0$. The corresponding time-independent model uses $C \times a_{\mathrm{c}}^2 = 0.15$.

where the bound state energy E_{b} is determined by Eq. (3.57) and α is an integer number. For the parameters of Fig. 3.19, the resonance near $\delta_0 \times a_{\mathrm{c}}^2 \approx 0.75$ corresponds to $\alpha = 1$, the one near $\delta_0 \times a_{\mathrm{c}}^2 = 0.52$ to $\alpha = 2$. Equation (3.235) provides the interpretation that the drive induces resonances if the scattering state with energy $\epsilon = 0$ is coupled to the bound state of the coupled channel description by α drive quanta. A similar condition is found by Eq. (3.146) for the periodically driven single channel pseudo potential. By looking closely to Fig. 3.19 it is visible that these resonances are slightly shifted away from condition (3.235). This effect is interpreted as a Floquet dressing of the bound state which is able to shift the quasienergy compared to the static case, in analogy to the results of Sec. 3.7. The resonances for $\delta_0 \times a_{\mathrm{c}}^2 < 0.9$ allow for a tuning of the real part of the scattering length to large positive and negative values. At the same time losses due to a finite imaginary part are present, but they do not dominate the physics. At $\delta_0 \times a_{\mathrm{c}}^2 \approx 1.18$ a resonance with strong damping is visible. This resonance does not allow to tune the real part of the scattering length far from its background value, while the losses given by the imaginary part are comparably large. Thus this resonance is not useful for a tuning of the scattering length. It turns out, that this resonance is induced by coupling to a state that intrinsically decays to the open channels which is giving this state a comparably short lifetime. At last, note that there are small kinks in the scattering length near $\delta_0 \times a_{\mathrm{c}}^2 \approx 0.73$ and $\delta_0 \times a_{\mathrm{c}}^2 \approx 0.52$. It turns out that these kinks are related to a change of the entrance channel due to avoided crossings in the quasienergies of the periodically driven two-level system.

In Fig. 3.20 the scattering length is shown for the case that the detuning δ is modulated sinusoidally. Here, a similar picture as in Fig. 3.19 emerges, the periodic drive engineers existing and to induces new resonances. However, there is one key difference: The drive only weakly shifts the position of the resonance that also exist in the static case. Further, the location of the Floquet-Feshbach resonances is with a high accuracy given by Eq. (3.235) also in the case of stronger driving.

We have now seen that the time-periodic driving of the parameters of the two-channel model (3.217) induces and engineers resonances in the scattering length. In the next subsection we systematically analyze these resonances by a Floquet-Feshbach resonance theory for the time-periodically driven multi-channel model.

3.10.5. Analysis with the Floquet-Feshbach Resonance Theory

We apply the Floquet-Feshbach resonance theory to the periodically driven multi-channel model in order to analyze the properties of the Floquet-Feshbach resonances. Due to the mathematical complexity of this theory, the resonance parameters can only be calculated numerically. If possible, we therefore compare the results of the Floquet-Feshbach resonance theory to analytical findings within a rotating-wave approximation.

The Floquet-Feshbach resonance theory of the driven multi-channel model is derived similar to the case of the pseudo potential with a time-periodic drive that involves higher harmonics, c.f. Subsec. 3.8.2. We therefore skip this derivation here, and present it in App. B. The theory finds the following scattering length, which is defined in the multi-channel description according to Eq. (3.234), in the vicinity of a resonance:

$$a_{\text{scatt}} = a_{\text{bg}} \left(1 - \frac{\Delta_\alpha}{\delta_0 - \delta_\alpha^{\text{res}} + i\gamma_\alpha} \right) + a_{\text{non-res}}. \tag{3.236}$$

Equation (3.236) is an important finding, the formula has the same mathematical structure as Eq. (3.207) that is found for the single-channel pseudo potential with higher harmonic drive. In the following we will explain all quantities involved in Eq. (3.236). First, α is used in order to label different resonances, a labeling of a_{scatt} as in Eq. (3.236) with α is implicitly assumed. As visible in Fig. 3.23 (a) the resonance that corresponds to the static Feshbach resonance is labeled with $\alpha = 0$ while resonances that are located at larger detuning δ_0 than the static resonance are labeled with negative integer, the ones with a lower are labeled by a positive integer. As introduced in Eq. (3.218b), δ_0 denotes the time-average of the time dependent $\delta(t)$. The position of the resonance is denoted by δ_α, while $\Delta_\alpha \in \mathbb{C}$ represents the resonance width and γ_α stands for the strength of possible losses. Also in Eq. (3.236) a non-resonant part of the scattering length $a_{\text{non-res}}$ appears which shows no singularities. The mathematical expressions used for calculating the parameters of Eq. (3.236) are found in Appendix B. In the following we give a heuristic understanding of the involved physics.

Similar to Eq. (3.206), the resonance position is found by the condition that the dressed energy of a Floquet bound state has to be equal to the energy of the scattering state. The resonance width Δ_α is mainly determined by the coupling of the closed channels to the entrance channel. Even if $\hat{Q}$ is of tridiagonal form in Floquet space, the matrix $\hat{Q}^\dagger \hat{A} \hat{Q}$, that induces the coupling in Eq. (3.233), couples channels that are next-nearest neighbors. Similar to Eq. (3.208), the resonance width also contains a part that stems from this higher harmonic coupling to the inelastic channels. As a result the width can become complex $\Delta_\alpha \in \mathbb{C}$. Due to similar reasons as discussed below Eq. (3.55), we can here only calculate the product $a_{\mathrm{bg}}\Delta_\alpha$ with our theory. The decay rate γ_α is determined by the direct coupling of closed and inelastic channels.

Formula (3.236) gives the form of the Floquet-Feshbach resonances in the periodically driven multi-channel model, which is the same form that is found for the single-channel pseudo potential including a higher-harmonic drive in Subsec. (3.8.2). We thus point out the analogies and the differences of single-channel and multi-channel Floquet-Feshbach resonances. In both cases we couple a scattering state to a bound state that resides in the closed channels and whose energy can be tuned by the periodic drive. We find in both cases a Feshbach resonance if the energies of scattering state and bound state are close to each other. Further general features are that the coupling of closed channels and the entrance channel determines the size of the width Δ_α, while resonant losses, that are described by the parameter γ_α, are induced by coupling the closed to the inelastic channels. We emphasize that in both theories the width can become complex. These analogies show, that the on a qualitative level the Floquet-Feshbach resonances in both single- and multi-channel model are given by the same physics. Differences come in, when looking quantitatively on the two theories, since the resonance parameters of Eq. (3.207) and Eq. (3.236) are given by different formulas. This is visualized by the fact that for the static single-channel calculation the bound state lies in the same channel as in the scattering state, but in the static multi-channel model Eq. (3.57) the bound state can also reside in both channels. A further difference is that Eq. (3.207) depends on the driving frequency, while Eq. (3.236) depends on the static detuning δ_0.

The parameters of Eq. (3.236) are found for each resonance by a numerical method that works similar to the one discussed in Sec. 3.7. In Fig. 3.21 the results of the Floquet-Feshbach resonance theory is compared to the numerical solution of Eq. (3.233), where an excellent agreement between both curves can be spotted. This shows the strength of the Floquet-Feshbach resonance theory. We see in Fig. 3.21 (b-d) a zoomed plot into three resonances of Fig. 3.21 (a), which show a behavior, that is well described by Eq. (3.236). The real part of the scattering length shows a dispersive behavior, while the imaginary part peaks in the vicinity of the resonance. This imaginary part is unfortunate for experiments, where atom loss, which is induced by an imaginary scattering length, is often desired to be minimal. In order to still get a relatively large real part in combination with a small imaginary part, one has to go slightly away from the resonance position. The widths of the resonances $\alpha = 1, 0, -1$ are $a_{\mathrm{bg}}\Delta_\alpha \times a_{\mathrm{c}}^2/a_{\mathrm{e}} \approx 5.4 \times 10^{-4} + i\ 5.2 \times 10^{-8},\ 3.4 \times 10^{-3} + i\ 6.2 \times 10^{-7},\ 5.4 \times 10^{-4} + i\ 4.6 \times 10^{-7}$. This shows that the width of the $\alpha = 0$ resonance is largest, as it is seen in Fig. 3.21 (a). The imaginary part of the width is orders of magnitudes smaller as compared to the real part. The decay rate γ_α is given for these resonances by $-\gamma_\alpha \times a_{\mathrm{c}}^2 \approx 3.9 \times 10^{-6},\ 1.3 \times 10^{-4},\ 9.8\ \times 10^{-4}$. This shows that the $\alpha = 1$ resonance has the lowest decay rate, while the $\alpha = -1$ resonance is strongest damped.

In order to understand this behavior further using the multi-channel Floquet-Feshbach resonance theory, it is important to understand which channels are open and which are closed. Equation (3.231) implies that a channel with label $(\mu = 1, n)$ is closed if $\epsilon < n\hbar\omega$. Thus, in the limit of $\epsilon \to 0$ we can consider all channels $(\mu = 1, n > 0)$ to be closed. In order to find a rough estimate for the channels with $\mu = 2$, the case of weak coupling $|C| \ll \delta$ is considered. Here, the static solution of the two-level system Eq. (3.51b) suggests the approximation $E_{\mu=2,n} - E_{\mu=1,n} \approx \delta_0$. This approximation finds that

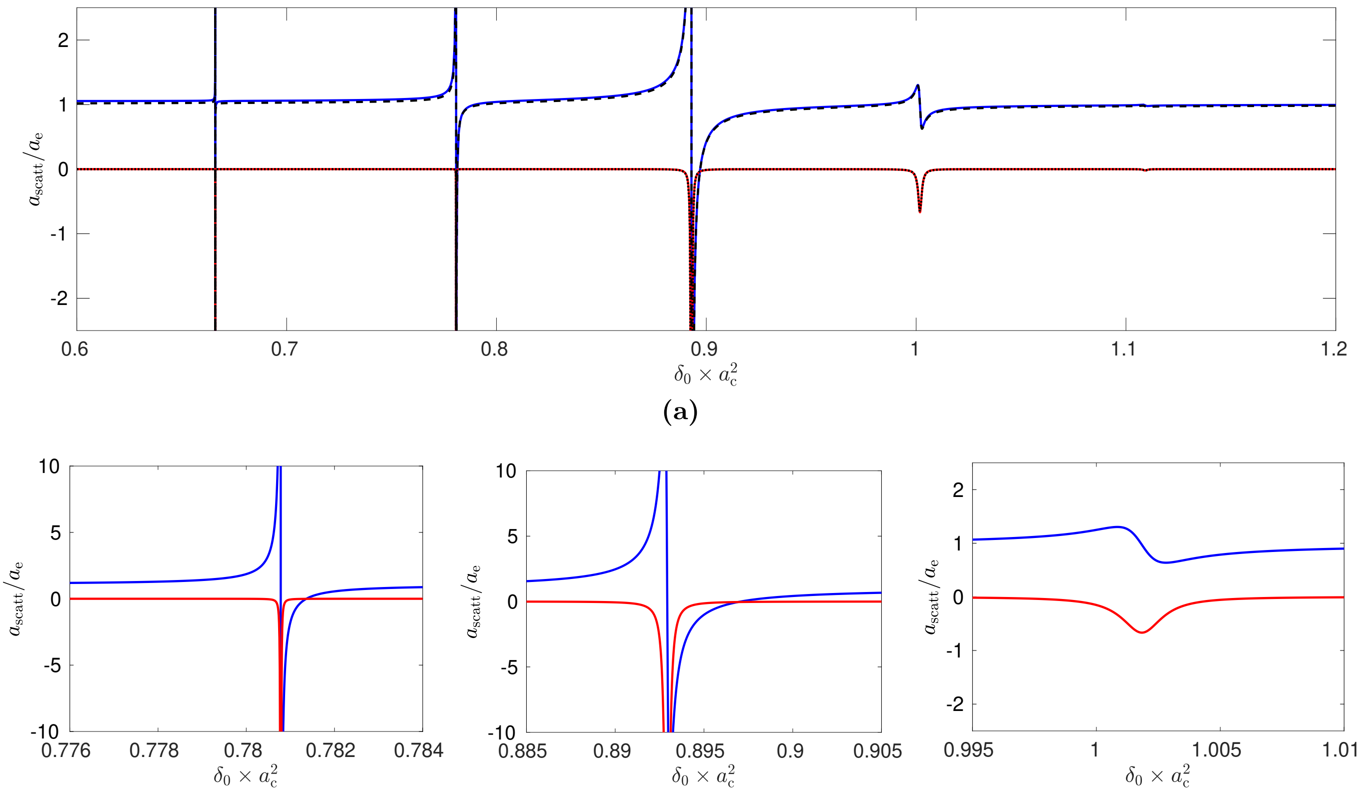

(a)

(b) (c) (d)

Figure 3.21.: (a) Real (blue) and imaginary part (red) of the scattering length found with the numeric solution of Eq. (3.233). Real (black dashed) and imaginary part (black dotted) found by the Floquet-Feshbach resonance theory. The parameters are $a_{\mathrm{e}} = a_{\mathrm{c}}/\sqrt{1.5}$, $C(t) \times a_{\mathrm{c}}^2 = 0.25$, $\delta(t) = \delta_0 + 0.8\hbar\omega\cos(\omega t)$, $\hbar\omega \times a_{\mathrm{c}}^2 = 0.1$ and $\epsilon = 0$. (b,c,d): Zoomed Plots from the data of (a).

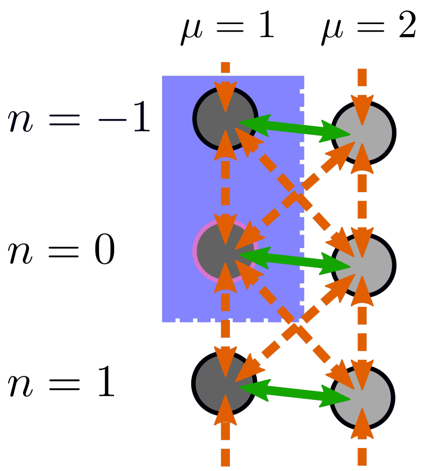

Figure 3.22.: Sketch of the channel structure of the Floquet multi-channel model in the case of $\omega < \delta_0$. The left column shows the channels with $\mu = 1$, the right column the ones with $\mu = 2$. Each pair of approximately equal height corresponds to one Floquet-Brillouin zone index n. The light blue rectangle includes the open channels, all other displayed channels are closed. The entrance channel is marked by a pink circle. In the static case only the channels with the same index n zone are coupled, these couplings are indicated by green arrows. The Floquet drive allows to couple channels with different n, a coupling of neighboring channels in Floquet space is drawn by orange arrows.

a channel $(\mu = 2, n)$ is closed if the condition $\epsilon - \delta_0 < n\hbar\omega$ holds. Here, an additional shift by $-\delta_0$ is present as compared to the $\mu = 1$ channels. Thus, for $\epsilon = 0$ all channels with $-n\hbar\omega < \delta_0$ are closed. For $\hbar\omega \ll \delta_0$, all channels $n = \mathcal{O}(1)$ are closed. This situation is visualized in Fig. 3.22, where the channel $(\mu = 1, n = 1)$ is closed, the same hold for the channels $(\mu = 2, n = 0, \pm 1)$. All other channels in Fig. 3.22 are open. This situation motivates the following rule of thumb: For Floquet indices $n > 0$, both channels $(\mu = 1, 2\ , n)$ are closed while for $n \leq 0$ at least one channel is open.

The position of the resonances in the limit of vanishing driving amplitude can be found by calculating the energies of possible Floquet bound states in the closed channels, in analogy to the considerations of Sec. 3.7.2. For the multichannel problem, this can be done by solving an equation that similar to Eq. (3.57). Unfortunately, there is no accessible solution of Eq. (3.57). In order to still get an analytic understanding of the physics, we perform the approximation $k^2_{\mu=2,n\geq 0} \approx -1/a_{\mathrm{c}}^2$, which is valid in the weakly driven limit $C_0 \to 0$. Using the dispersion relation Eq. (3.231) an approximate formula of the bound state energy is found by $E_\alpha = -1/a_{\mathrm{c}}^2 + \delta_0 + \alpha\hbar\omega$, where we again made the approximation $E_{\mu=2,0} - E_{\mu=1,0} \approx \delta_0$. At low energies $\epsilon \to 0$ a resonance occurs if $E_\alpha = 0$ is fulfilled, yielding an approximation of the resonance position according to

$$\delta_\alpha^{\mathrm{res}} \approx \frac{1}{a_{\mathrm{c}}^2} - \alpha\hbar\omega. \tag{3.237}$$

Equation (3.237) connects the resonances, as shown in Figs. 3.19 and 3.20, to the structure of the Floquet space by making the statement that the resonance with number α is induced by a bound state that resides in a closed channel with Floquet index $n = \alpha$. Note, that in the weak coupling

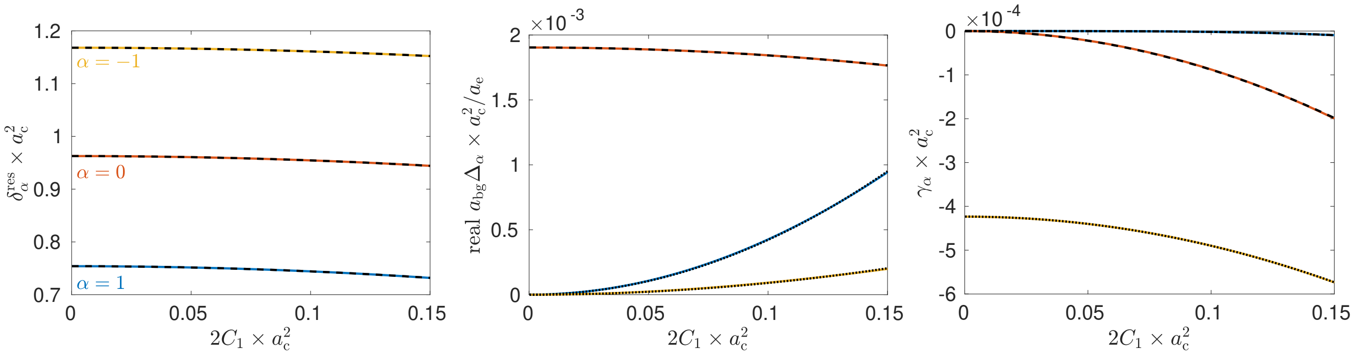

(a) **(b)** **(c)**

Figure 3.23.: Parameters of Eq. (3.236) for $a_{\rm e} = a_{\rm c}/\sqrt{1.5}$ and a drive of the form $C(t) = C_0 + 2C_1\cos(\omega t)$, $\delta(t) = \delta_0$ with $C_0 \times a_{\rm c}^2 = 0.15$ and $\hbar\omega \times a_{\rm c}^2 = 0.2$. In color the results of the Floquet-Feshbach Resonance theory, blue for $\alpha = -1$, red for $\alpha = 0$ and yellow for $\alpha = 1$. (a) Resonance position δ_α, (b) Resonance width Re Δ_α, (c) loss parameter γ_α. Black dashed line fit with the curve $y = a + b\ C_1^2$, black dotted line fit with $y = b\ C_1^2$ and black dash-dotted line fit with $y = c\ C_1^4$. The fit parameters are presented in Table 3.2 (a).

regime Eq. (3.237) coincides with the heuristically found Eq. (3.235). After having now set the stage, we will in the following use the Floquet-Feshbach resonance theory in order to analyze the parameters of the resonances appearing in the periodically driven multi-channel model.

Sinusiodal Drive of the Coupling C

In Fig. 3.23 the parameters of Eq. (3.236) are shown for the case of a sinusoidally driven coupling constant

$$C(t) = C_0 + 2C_1\cos(\omega t). \tag{3.238}$$

These parameters are calculated using the Floquet-Feshbach resonance theory that is discussed in Appendix B. At $C_1 \approx 0$ Eq. (3.237) roughly predicts the position of the resonances, but in Fig. 3.23 there are notable deviations to this equation, which are related to two effects. One effect is that at finite static coupling C_0 the resonance position is shifted to lower values as described by Eq. (3.54). For the parameters of Fig. 3.23 this effect fully explains the position of the $\alpha = 0$ resonance. The second effect is seen by the fact that the spacing of neighboring resonance is not exactly given by $\hbar\omega$, c.f. table 3.2. This is related to small non-linearities of the δ_0 dependence of the bound state energy $E_{\rm b}$ that imply with Eq. (3.235) a shift in the resonance position $\delta_\alpha^{\rm res}$ from the naively expected behavior.

Figures 3.23 (a) and (b) show that both position $\delta_\alpha^{\rm res}$ and width Δ_α have a quadratic dependence on the driving strength C_1. For the resonances $\alpha = \pm 1$, this can be qualitatively understood within the rotating-wave approximation, which approximates the internal Floquet Hamiltonian by the static two-level system Eq. (3.223). In combination with Eqns. (3.54) and (3.55), we expect a quadratic behavior

$$\delta_\alpha^{\mathrm{res}} \approx a_\alpha + b_\alpha\ C_1^2 \tag{3.239}$$

and

$$\Delta_\alpha \approx a_0 \delta_{\alpha,0} + b_\alpha\ C_1^2. \tag{3.240}$$

The black lines in Figs. 3.23 (a) and (b) follow exactly such a power law that was fitted on the numerical data. The results of the fitting procedure are shown in Table 3.2. The implication of this is that a rotating-wave approximation describes the behavior of the resonances even at strong driving amplitudes.

However, we still find physics that is beyond the rotating wave approximation. The width of the resonance with $\alpha = 1$ grows faster that the width of the $\alpha = -1$ resonance, while a rotating wave approximation expects that both widths would be the same. Thus, we relate this effect to the Floquet physics that is involved. We also find that the resonances have a finite loss parameter γ_α. As discussed in Sec. 3.5, this loss is given due to the presence of inelastic scattering. The Floquet-Feshbach resonance theory predicts that the parameter γ_α grows quadradically with the coupling of a bound state, that has its major weight in the channel (μ_α, n_α), to the inelastic channels. An approximate form is given by

$$\gamma_\alpha \approx \sum_{(\mu,n),\ k_{\mu,n}^2 > 0} |\langle\langle \mu_\alpha, n_\alpha | \hat{A} | \mu, n \rangle\rangle|^2. \tag{3.241}$$

In the following, we will derive with the use of Eq. (3.241) and Fig. 3.22 the correct power law behavior of the parameter γ_α for the three resonances displayed in Fig.3.23. The bound state that induces the resonance with $\alpha = -1$ resides at low driving in the channel $(\mu_{\alpha=-1} = 2, n_{\alpha=-1} = -1)$. This channel is directly coupled to the inelastic channel $(\mu = 1, n = 1)$ with a static coupling $\langle\langle(\mu = 1, n = -1)|\hat{A}|(\mu_{\alpha=-1} = 2, n_{\alpha=-1} = -1)\rangle\rangle$, which corresponds to the green arrow in Fig. 3.22. This implies strong losses, which result in a behavior of the form

$$\gamma_{\alpha=-1} = a + b\ C_1^2, \tag{3.242}$$

where we took into account that the next higher order scales with C_1^2, as it is suggested from the discussion below. The resonance $\alpha = 0$ is induced by the bound state in the $(\mu_{\alpha=0} = 2, n_{\alpha=0} = 0)$ channel. It is coupled by a dynamic coupling of first order $\langle\langle(\mu = 2, n = 0)|\hat{A}|(\mu = 1, n = -1)\rangle\rangle$ to the inelastic channel, this displayed with orange lines in Fig. 3.22. With a perturbation theory argument one can easily see that these dynamic couplings are proportional to the driving strength $\langle\langle(\mu = 2, n = 0)|\hat{A}|(\mu = 1, n = -1)\rangle\rangle \propto C_1$. With Eq. (3.241) it follows that

$$\gamma_{\alpha=0} \propto C_1^2. \tag{3.243}$$

For the resonance $\alpha = 1$ either two dynamic couplings or a next-nearest neighbor coupling are needed in order to connect the corresponding bound state to the inelastic channels, as it is sketched in Fig. 3.22. As a result, the loss coefficient goes with

$$\gamma_{\alpha=1} \propto C_1^4. \tag{3.244}$$

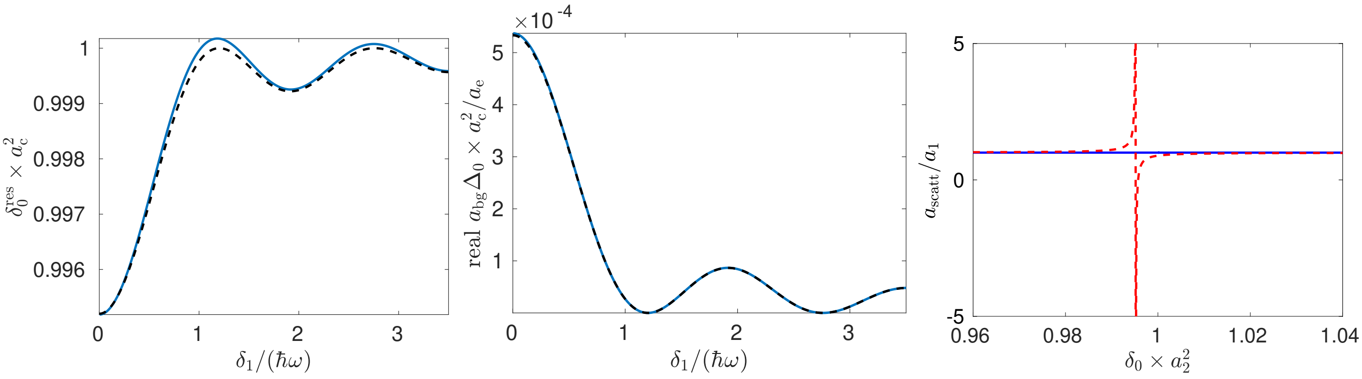

(a) **(b)** **(c)**

Figure 3.24.: Parameters of Eq. (3.236) for $a_\mathrm{e} = a_\mathrm{c}/\sqrt{1.5}$ and a drive of the form $\delta(t) = \delta_0 + 2\delta_1 \cos(\omega t)$, $C(t) \times a_\mathrm{c}^2 = 0.04$ and $\hbar\omega \times a_\mathrm{c}^2 = 3$. In blue the results of the Floquet-Feshbach resonance theory, black dashed Eqns. (3.246), respectively. (a) resonance position, δ_0^{res} (b) resonance width real Δ_α, (c) scattering length in dependence on the detuning δ_0 for the above parameters and $\delta_1 = 0$ (red), $\delta_1 = 1.212\ \hbar\omega$ (blue), which corresponds to the first zero of the Bessel function.

It is seen in Fig. 3.23 (c) that these power laws describe the actual course of the parameter γ_α very well. It is important to emphasize, that a finite γ_α leads to a maximum value of Re $a_{\mathrm{scatt}} \approx a_{\mathrm{bg}}\mathrm{Re}\ \Delta_\alpha/(2\gamma_\alpha)$, while the imaginary part scales as Im $a_{\mathrm{scatt}} \approx a_{\mathrm{bg}}\mathrm{Re}\ \Delta_\alpha/\gamma_\alpha$. If we insert the above found power-law behaviors, we find that the $\alpha = -1$ resonance is strongly damped Re $a_{\mathrm{scatt}} \propto C_1^2$. This corresponds to the findings of Fig. 3.19 and 3.21. For the $\alpha = 0$ resonance the behavior of Re a_{scatt} is found by Re $a_{\mathrm{scatt}} \approx b + aC_1^{-2}$. This shows that for $C_1 \to 0$ the maximal enhancement of the scattering length goes to infinity, while at finite C_1 it decays to a finite value. For the $\alpha = 1$ resonance a behavior similar to $\alpha = 0$ is found. This short calculation demonstrates that using the $\alpha = 0, 1$ resonances a large enhancement of Re a_{scatt} is possible.

Sinusoidal Drive of the Detuning δ

A sinusoidal driving of the detuning

$$\delta(t) = \delta_0 + 2\delta_1 \cos(\omega t) \tag{3.245}$$

is considered in the following, while the coupling is assumed to be constant $C(t) = C_0$. We start in the limit of weak coupling $C_0 \times a_\mathrm{c}^2 \ll 1$ and large driving frequencies $\delta_0 \ll \hbar\omega$ and aim for the description of the resonance near $\delta_0 \times a_\mathrm{c}^2 \approx 1$. In this case, the effective dynamics of the internal Hamiltonian is found by the Floquet-Gauge rotating-wave approximation Eq. (3.227). As a result, the resonance can be described with the static model (3.47), but with a renormalized coupling constant $C \to C_0\mathcal{J}_0[2\delta_1/(\hbar\omega)]$. Since the limit of weak coupling $C_0 \times a_\mathrm{c}^2 \ll 1$ is assumed, Eqns. (3.54) and (3.55) can be used in order to describe resonance position and width. Adapted to the renormalized coupling strength, these equations read

$$\begin{aligned} \delta_0^{\mathrm{res}} &= \frac{1}{a_{\mathrm{c}}^2} - 2a_{\mathrm{e}}a_{\mathrm{c}}C_0^2\mathcal{J}_0^2[2\delta_1/(\hbar\omega)], && (3.246\mathrm{a}) \\ a_{\mathrm{bg}}\Delta_0 &= 2a_{\mathrm{c}}(a_{\mathrm{e}}-a_{\mathrm{c}})^2C_0^2\mathcal{J}_0^2[2\delta_1/(\hbar\omega)]. && (3.246\mathrm{b}) \end{aligned}$$

Equation (3.246) is the key result of this part, since it shows in shorthand analytic formulas that the sinusoidal high-frequency drive changes the position and the width of the resonance by effectively renormalizing the coupling strength by a Bessel function. We saw in Subsec. 3.10.2 that this Bessel function is related to a gauge transformation that is applied to the internal Hamiltonian and is interpreted as an effect of Floquet physics. Since in Eqns. (3.54) and (3.55) the coupling strength enters quadratically, Eq. (3.246) shows a quadratic dependence on the Bessel function.

In Fig. 3.24 (a,b) resonance position and width are displayed, here Eqns. (3.246) show an excellent agreement with the results of the Floquet-Feshbach resonance theory. It can be seen that the high frequency drive engineers the Feshbach resonance, since both position and width are tunable by the drive. Figure 3.24 displays that it is possible to shift the position over wider distances compared to its width. The course of both position and width is governed by the oscillating behavior of the Bessel function $\mathcal{J}_0(x)$. If the drive is tuned to a zero of the Bessel function, we can even let the resonance disappear. This case is shown in Fig. 3.24 (c), where a Feshbach resonance, that is present in the static case, is tuned to zero width by the periodic drive by choosing a driving strength that corresponds to the first zero of a Bessel function. For the parameters of Fig. 3.24 we find that $\gamma_\alpha \times a_{\mathrm{c}}^2 \approx 10^{-6}$ and Im $a_{\mathrm{bg}}\Delta_\alpha \times a_{\mathrm{c}}^2/a_{\mathrm{e}} \approx 10^{-9}$, such that they only become relevant if the width is close to zero.

In Fig. 3.25 the resonance parameters are shown at a lower driving frequency and stronger coupling C_0 sas compared to Fig. 3.24. Although we are not in the high frequency and weakly coupled limit, the behavior of the resonance width can still be described by a Bessel function

$$a_{\mathrm{bg}}\Delta_\alpha = a_\alpha\mathcal{J}_{|\alpha|}^2[2b_\alpha\delta_1/(\hbar\omega)], \tag{3.247}$$

which even holds for general resonances $\alpha = 0, \pm1, \ldots$. Equation (3.247) shows that the appearance of Bessel functions in the resonance width is quite universal for the two-channel model with sinusoidally modulated detuning, as it is suggested by the Hamiltonian of the Floquet-gauge rotating-wave approximation Eq. (3.227). The parameters a_α and b_α differ from the result of the rotating wave approximation and are found via fitting Eq. (3.247) to the data found by the Floquet-Feshbach resonance theory, see table. 3.2 (b). The fitting parameters describe a renormalization of the parameters in Eq. (3.246b) that is induced by strong couplings in the Floquet channel structure. For example, $b_{\alpha=\pm1}$ is slightly below one, such that a higher driving strength δ_1 is needed in order to reach the maximum width as compared to Eq. (3.246b).

The sinusoidal driving of the detuning δ also induces a shift of the resonance position towards lower values. The physics of the loss parameter γ_α for small values of δ_1 is similar to the case of a sinusoidal modulation of $C(t)$. While the $\alpha = -1$ resonance suffers strong losses $\gamma_{\alpha=-1} = \mathcal{O}(1)$, the loss parameter for the $\alpha = 0$ resonance follows $\gamma_{\alpha=0} \propto \delta_1^2$ and for the $\alpha = 1$ resonance we again have $\gamma_{\alpha=1} \propto \delta_1^4$. As seen in Fig. 3.25 (c), the loss parameters γ_α differ at large driving strength δ_1 from the power law behavior.

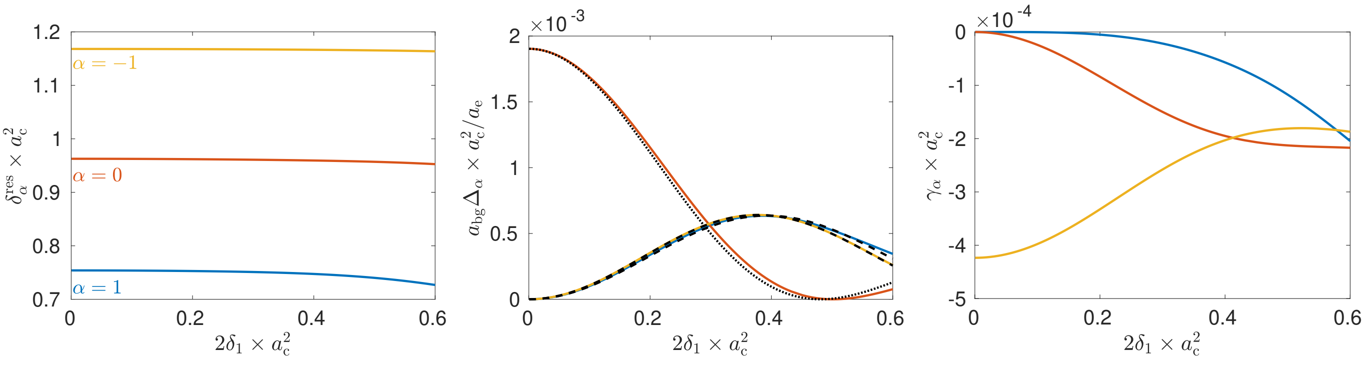

(a) **(b)** **(c)**

Figure 3.25.: Parameters of Eq. (3.236) for $a_\mathrm{e} = a_\mathrm{c}/\sqrt{1.5}$ and a drive of the form $C(t) = C_0$, $\delta(t) = \delta_0 + 2\delta_1 \cos(\omega t)$ with $C_0 \times a_\mathrm{c}^2 = 0.15$ and $\hbar\omega \times a_\mathrm{c}^2 = 0.2$. In color the results of the Floquet-Feshbach resonance theory, blue for $\alpha = -1$, red for $\alpha = 0$ and yellow for $\alpha = 1$. (a) Resonance position δ_α, (b) Resonance width Re Δ_α, (c) loss parameter γ_α. Black dashed lines fit with the curve $y = a\mathcal{J}_1^2[2b\delta_1/(\hbar\omega)]$, black dotted line fits with $y = a\mathcal{J}_0^2[2\delta_1/(\hbar\omega)]$. The fit parameters are presented in table 3.2 (b).

Table 3.2.: (a) Parameters for the fit curves in Fig. 3.23. A dash marks a variable that is not used for the fit of the corresponding quantity. (b) Parameters for the fit curves used in Fig. 3.25. The curve $\alpha = 0$ is found exactly with $y = a\mathcal{J}_0^2(2\delta_1/\omega)$, where $a = \Delta_{\alpha=0}(\delta_1 = 0)$.

Resonances in Fig. 3.23	**Fit Formula**	**a**	**b**	**c**
(a), $\alpha = -1$	$y = a + bC_1^2$	0.754	3.936	-
(a), $\alpha = 0$	$y = a + bC_1^2$	0.963	3.288	-
(a), $\alpha = 1$	$y = a + bC_1^2$	1.168	2.809	-
(b), $\alpha = -1$	$y = bC_1^2$	-	0.138	-
(b), $\alpha = 0$	$y = a + bC_1^2$	1.5×10^{-3}	-0.02	-
(b), $\alpha = 1$	$y = bC_1^2$	-	0.03	-
(c), $\alpha = -1$	$y = cC_1^4$	-	-	-0.297
(c), $\alpha = 0$	$y = bC_1^2$	-	-0.035	-
(c), $\alpha = 1$	$y = a + bC_1^2$	-0.027	4.2×10^{-4}	-

(a)

Resonances in Fig. 3.25	**Fit Formula**	**a**	**b**
(b), $\alpha = -1$	$y = a\mathcal{J}_1^2(2b\delta_1/(\hbar\omega))$	1.5×10^{-3}	0.938
(b), $\alpha = 0$ (no fit)	$y = a\mathcal{J}_0^2(2\delta_1/(\hbar\omega))$	0.019	-
(b), $\alpha = 1$	$y = a\mathcal{J}_1^2(2b\delta_1/(\hbar\omega))$	1.5×10^{-3}	0.974

(b)

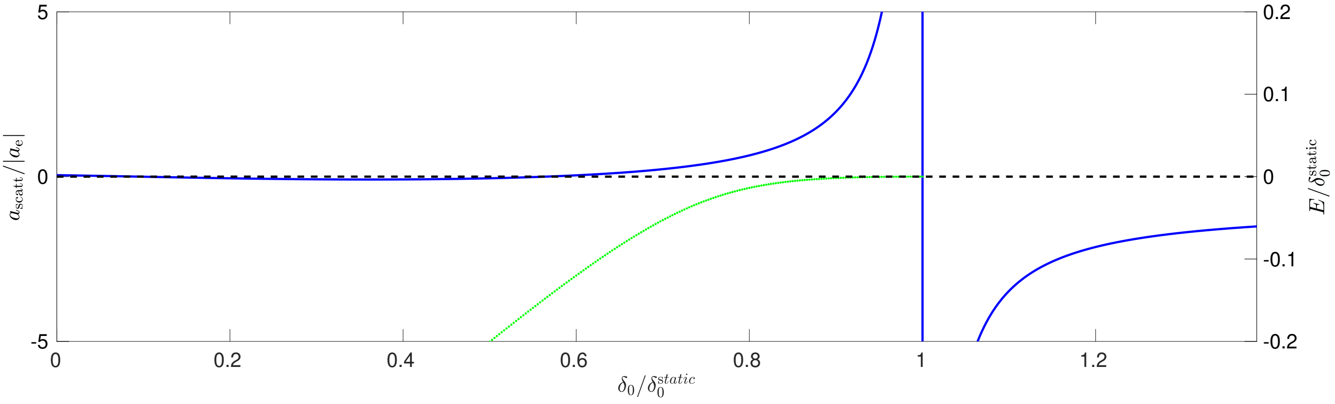

Figure 3.26.: Axis on the left: Scattering length a_{scatt} in blue, Axis on the right: Bound state energy E_{b} in green for a time-independent model with the parameters $a_{\mathrm{e}} = -10a_{\mathrm{c}}$, $C_0 \times a_{\mathrm{c}}^2 = 0.19$ such that $\delta_0^{\mathrm{static}} \times a_{\mathrm{c}}^2 = 1.44$. The model parameters resemble the low-field resonance discussed in Ref. [30].

3.10.6. Periodic Driving of a Low-Field Magnetic Feshbach Resonance

After having discussed the resonances of the periodically driven two-channel model within the Floquet-Feshbach resonance theory, we now go for model parameters that are motivated by an experimentally observed Feshbach resonance. Typically, magnetic Feshbach resonances reside at magnetic field strengths of several hundreds of Gauss, which corresponds to a frequency of $f = \mu_{\mathrm{B}} B_0/h$ in the low Gigahertz regime. Here, μ_{B} denotes the Bohr magneton and h the Planck constant. In order to observe the physics that is discussed in the previous section for such a magnetic resonance, the magnetic field has to oscillate with frequencies in the Gigahertz regime. This, however, is hard to realize in an experiment due to eddy currents in the coils that produce the time-dependent magnetic field [99, 154]. We therefore suggest to use a low-field magnetic Feshbach resonance in order to probe the Floquet physics that is predicted by our theory and give in the following numbers for low-field resonances that have been observed experimentally. Ref. [155] found Feshbach resonances in Rb-Cs collisions at a magnetic field of $B_0 \approx 0.5$ G which corresponds to a frequency of $f \approx 700$ kHz. Ref. [156] observed Feshbach resonances in Dysprosium at $B \approx 10$ G which leads to $f \approx 14$ MHz. Here, we specialize to the parameters of Ref. [30], who measured with ^{133}Cs in the $F = 3, m_{\mathrm{F}} = 3$ hyperfine state a Feshbach resonance at $B_0 = 30$ G with a width of $\Delta = 13$ G. We choose model parameters that resemble the course of the magnetic Feshbach resonance, the resulting scattering length is shown in Fig. 3.26. Here, the value $\delta_0^{\mathrm{static}}$ corresponds to the resonance at $B_0 = \delta_0^{\mathrm{static}}\hbar^2/(2\mu\delta\mu) = 30$ G. The zero crossing is with our parameters at $\delta_0 \approx 0.54\delta_0^{\mathrm{static}}$, which is close to the value of $(B_0 - \Delta)/B_0 = 17/30 \approx 0.56$ found in the experiment.

The background scattering length of this Cesium hyperfine state is negative. This is known to suppress the formation of a large condensate [18, 30]. Thus, a Feshbach tuning of the scattering length to positive values is necessary in order to achieve a Bose-Einstein condensate with a considerable large number of particles at all [30]. As seen in Fig. 3.26, the low-field magnetic Feshbach resonance allows for a positive scattering length in a certain parameter range. If the magnetic field is varied sinusoidally with a frequency that is larger than the width, new Floquet-Feshbach resonances appear that tune the scattering length to positive values. Thus, the periodic drive allows to attain a condensate at a magnetic field strength where in the static case the scattering length is negative and thus an attainment of a Bose-Einstein condensate would not be possible.

With a periodically driven low-field magnetic Feshbach resonance, the Floquet physics, that is discussed in the Subsec. 3.10.5, can be observed. Here we specialize to investigate the Floquet-Feshbach resonances for low driving frequencies $\hbar\omega/\delta_0^{\mathrm{static}} \ll 1$. For this discussion it is important to note that the bound state E_{b} obeys a quadratic behavior near the resonance position $\delta_0^{\mathrm{static}}$, which can clearly be seen in Fig. 3.26. The course of this bound state is directly related to the position on the Floquet-Feshbach resonances by the resonance condition Eq. (3.235), see Fig. 3.27 (a) where a resonance occurs if E_{b} matches with integer multiples of $\hbar\omega$. As a key result, we find that the non-linear behavior of E_{b} has the intriguing consequence that the difference of neighboring resonances is not given by $\delta_{\alpha+1}^{\mathrm{res}} - \delta_{\alpha}^{\mathrm{res}} = \hbar\omega$, as naively expected, but is notably different to it. Note, that the course of E_{b} as given by Fig. 3.26 is made with the model (3.217) and the assumption $a_{\mathrm{e}} = -10a_{\mathrm{c}}$, the result of a realistic description of the Born-Oppenheimer potentials might result in a quantitatively different course.

The Floquet-Feshbach resonances shown in Fig. 3.27 (a) tune the elastic scattering length Re a_{scatt} to large values without suffering too strong losses. For example, the resonance near $\delta_0/\delta_0^{\mathrm{static}} \approx 0.8$ in Fig. 3.27 (a) enhances the scattering length by a factor of max Re $a_{\mathrm{scatt}}/a_{\mathrm{bg}} \approx 120$. In order to visualize the effect of the driving strength δ_1 of the Floquet-Feshbach resonances, Fig. 3.27 (b) shows the scattering length for a driving amplitude δ_1 that is larger compared to one used in Fig. 3.27 (a). As expected, the width of the Floquet-Feshbach resonances increases with δ_1. In addition, in Fig. 3.27 (b) the resonances are shifted notably from condition Eq. (3.235). We interpret this as a result of a dressing of the bound state by the time-periodic drive, in analogy to the discussion of Sec. 3.7. In both Fig. 3.27 (a) and (b) it is seen that the drive induces a peak in the imaginary part at the resonance frequency, as it is described by a finite γ_α in the Floquet Feshbach formula Eq. (3.236). For the resonances with $\delta_\alpha < \delta_0^{\mathrm{static}}$, however, the imaginary part is asymmetric due to the presence of a complex resonance width. As discussed in Subsec. 3.8.3, this asymmetry has two important consequences. First, as a remnant of the Floquet Hilbert space, it signals that Floquet theory is needed in order to describe the physics. Second, an implication of this asymmetry is that in a certain range of detuning δ_0 the imaginary part of the scattering length and thus atom loss is comparably small. As sketched in Fig. 3.15, this tunes the ratio of real to imaginary part of the scattering length to a much higher value than it would be possible without this asymmetry.

At last, we qualitatively compare the multi-channel description with the single-channel calculation of Sec. 3.6. In the region where the bound state energy E_{b} in the static two-channel model, which is calculated with Eq. (3.57), obeys a quadratic behavior, the resonant scattering can be described by a pseudo potential [18,99]. A time-dependent magnetic field leads to a time-dependent potential strength, such that this case can be described with the results of Sec. 3.6, where we discussed the single-channel Floquet scattering by a periodically driven pseudo potential. In order to compare the results of the Floquet single-channel and the Floquet multi-channel calculation, we refer to the limit of weak driving. In this case, the resonances of the driven multi-channel model are given by

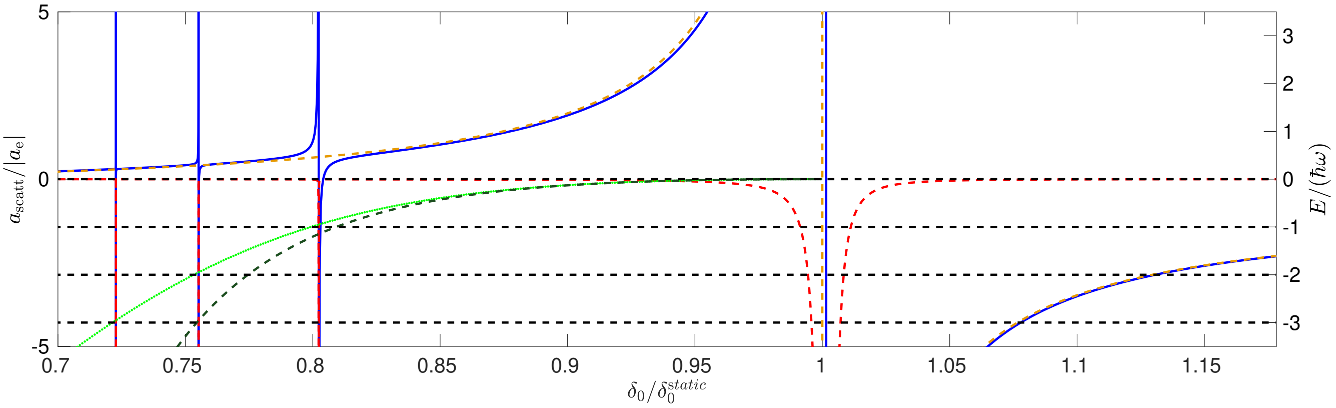

(a)

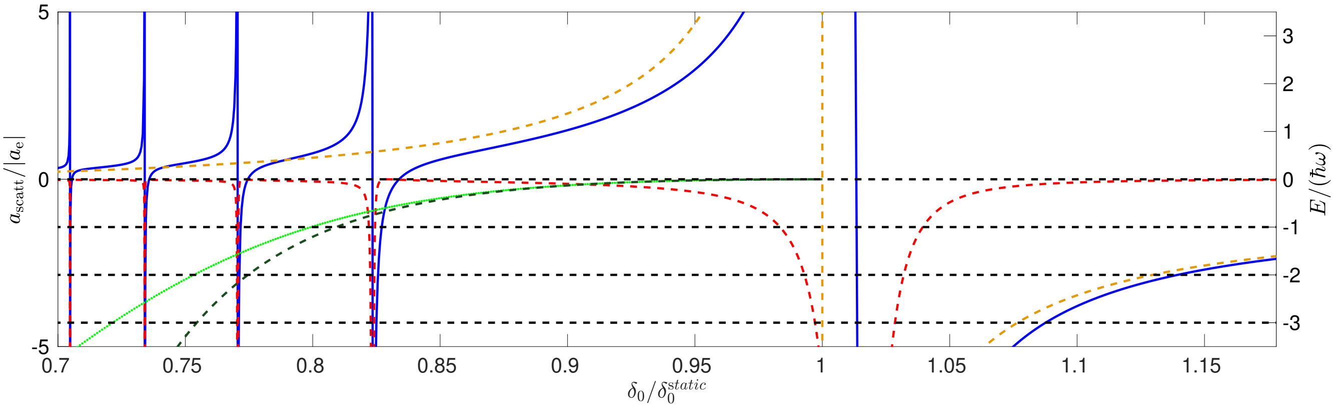

(b)

Figure 3.27.: Axis on the left: Real (blue) and imaginary (red) part of the scattering length a_{scatt} with time-periodic driving, yellow the scattering length for the corresponding time-independent model Eq. (3.47). Axis on the right: Energy of the bound state (green) calculated with Eq. (3.57), dimer energy (dashed, dark green), black dashed lines at $-n\hbar\omega$. The parameters are $a_{\mathrm{e}} = -10\ a_{\mathrm{c}}$, $C(t) \times a_{\mathrm{c}}^2 = 0.19$, $\delta(t) = \delta_0 + 2\delta_1 \cos(\omega t)\ \hbar\omega \times a_{\mathrm{c}}^2 = 0.02$ and $\epsilon = 0$, which implies $\delta_0^{\mathrm{static}} \times a_{\mathrm{c}}^2 = 1.44$. (a) $\delta_1 = \hbar\omega$, (b) $\delta_1 = 3\hbar\omega$.

Eq. (3.235), while in the driven single-channel calculation, resonances appear if the scattering state is coupled via multiple drive quanta to the so-called dimer state. In order to investigate if both approaches agree, the energy of the dimer state, which depends quadratically on the inverse of the scattering length as given by Eq. (3.31), is compared in Fig. 3.27 to the value of the bound state E_{b} of the static multi-channel calculation. For a detuning δ_0 near $\delta_0^{\mathrm{static}}$ the dimer energy and the multi-channel bound state energy E_{b} coincide. This is the region with universal properties where we expect that the Floquet-Feshbach resonances are described by the findings of Sec. 3.7 and that the periodically driven single- and multi-channel calculations agree. However, for the parameters used in Fig. 3.27 the dimer energy and multi-channel bound state energy E_{b} notably differ at the resonance positions. Thus, a Floquet single-channel calculation cannot find the correct position of the Floquet-Feshbach resonances for the given driving frequency ω even at small driving strengths δ_1. This finding points out a significant advantage of the multi-channel description to the single-channel model of a Feshbach resonance, the multi-channel model is considered as more realistic. At this point we further emphasize that the engineering of the Feshbach resonance with $\alpha = 0$ cannot be predicted in the Floquet single-channel calculation. This is due to the fact that in this case the condition $\delta_1 < |\delta_0 - \delta_0^{\mathrm{static}}|$ is not fulfilled, which is necessary in order to find a converging Floquet solution in the single-channel Floquet scattering. In summary, this discussion demonstrates our motivation for investigating the periodically driven multi-channel description of a Feshbach resonance.

3.11. Conclusion and Outlook

In this chapter, the time-periodic driving of a scattering potential is investigated. As a relevant model that leads to interesting physics, the harmonically driven pseudo potential is chosen, where a previously unknown solution of the Floquet equation with the use of continuous fractions is found. As a key result, resonances in the s-wave scattering length are reported. These resonances tune the scattering length to arbitrary positive and negative values while keeping the atom loss due to inelastic collisions relatively small. Further, both position and width of these resonances are controllable by the drive.

In this thesis we relate these driving-induced resonances to the concept of a Feshbach resonance in Floquet Hilbert space. The Floquet-Feshbach resonance theory predicts a universal formula that describes the scattering length of a resonance. Important parameters of this formula are the resonance position and width, where both numerical and analytical calculations show that they are tunable by the drive. Finally, the combination of the Floquet-Feshbach resonance theory and the continued fraction solution proofs the absence of resonantly enhanced inelastic collisions in the vicinity of a resonance. This feature makes the Floquet-Feshbach resonance favorable compared to an optical Feshbach resonance, which suffers from strong atom loss.

The Floquet-Feshbach resonance theory also describes resonances for a driving scheme involving higher harmonics. In this case the Floquet-Feshbach resonances suffer from atom loss due to inelastic collisions, which is often undesired in ultracold quantum gases. However, this atom loss turns into an advantage since asymmetries appear in the resonant peak of the imaginary part of the scattering length for well-tuned driving parameters. These asymmetries are directly related to the structure of the Floquet Hilbert space, and thus serve as a probe showing that Floquet physics emerges.

The Floquet-Feshbach resonances are proposed to be observed in an experiment by applying a time-periodic magnetic field near a Feshbach resonance [99]. We introduce a multi-channel model of a Feshbach resonance in order to analyze the influence of a periodically driven magnetic field for a wide range of magnetic field strengths. The numerical solution of the Floquet scattering equations of the multi-channel model predicts that the periodic drive induces new resonances, and in addition is able to engineer the properties of resonances that already exist in the static case. However, such a full numerical solution does not lead to a descriptive physical interpretation. Thus, we generalize the Floquet-Feshbach resonance theory to the multi-channel model and again find a formula that describes the scattering length of a resonance. The Floquet-Feshbach resonance theory gives a deeper understanding of the physics of the resonances. We find that position and width of these Floquet-Feshbach resonances are tunable by the drive. The results of the Floquet-Feshbach resonance theory are compared to analytical results found by calculations within a rotating-wave approximation. As a prominent result we report that for a sinusoidal driving of the detuning $\delta(t)$ the dependence of both position and width on the driving strength involves a Bessel function, which can be used to engineer desired resonance properties. We propose to observe these effects at a low-field magnetic Feshbach resonance, where all frequency scales are smaller than for common Feshbach resonances. Thus, the case of strong driving, where the Floquet physics is expected, can be observed with comparably lower driving frequencies and lower fields. We exemplarily show results for a low-field Feshbach resonance for ^{133}Rb at 30 G that is found in Ref. [30].

In summary, we found Floquet-Feshbach resonances in two distinct model systems and understood that the physical origin is always the same: If we couple a scattering state to a bound state in the closed Floquet channels, a Floquet-Feshbach resonance appears if the energy of the bound state comes close to the energy of the scattering state. The bound state energy can be dressed by the periodic drive which leads to tunable resonance properties. In the following we point out the advantages of the Floquet-Feshbach resonances to common realizations of Feshbach resonances in ultracold gases. Both magnetic and Floquet-Feshbach resonances tune the scattering length to almost arbitrary positive and negative values. Position and width of the Floquet-Feshbach resonances can be adapted by the periodic drive. This is an advantage over a magnetic Feshbach resonance, where the resonance parameters are in principle not tunable. In the case of a harmonically driven pseudo potential, the Floquet-Feshbach resonances obtain a high tunability of the real part of the scattering length while keeping the atom loss comparably small. This situation is often desired in ultracold gas experiments and is showing that Floquet-Feshbach resonances are superior to optical Feshbach resonances, where strong atom loss is present due to the optical decay of the bound state. The periodic driving of the multi-channel model induces resonances which always suffer from a small, but finite loss rate which looks at first view similar to the one of optical Feshbach resonances. In fact, we found that the imaginary part of a Floquet-Feshbach resonance can show a slight asymmetry. This asymmetry in turn implies a larger ratio of real to imaginary part of the scattering length compared to an optical Feshbach resonance.

The Floquet-Feshbach resonance theory can be easily formulated for general radial symmetric scat-

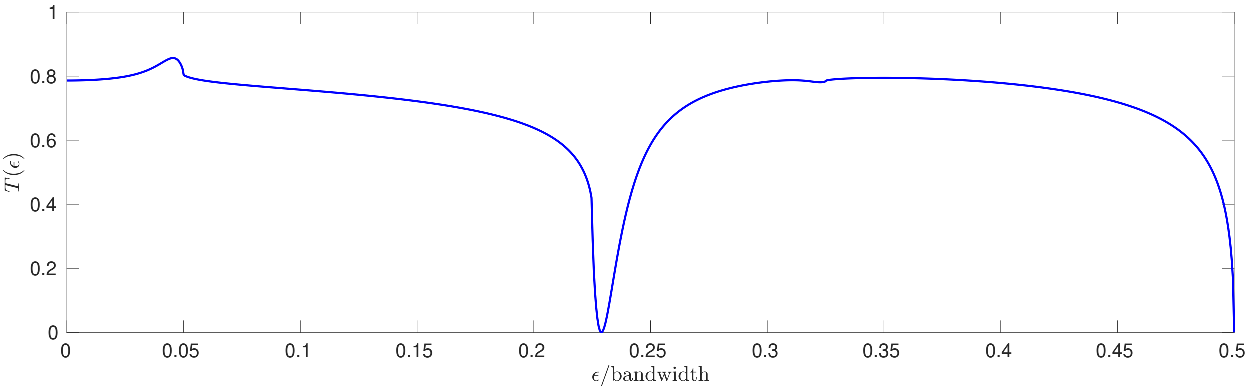

Figure 3.28.: Transmission through a periodically driven impurity in one dimension. As model system a tight-binding lattice is used where at a single site the on-site potential is periodically modulated, for details see Ref. [159].

tering potentials that are beyond a simple pseudo potential [157]. Also in this case, the theory is introduced as a Feshbach resonance theory in Floquet space. Similar to Eq. (3.132), a resonance occurs if the energy of a Floquet bound state is close to the energy of a scattering state. Since the radial Floquet equation cannot be mapped to a simple recursion relation, the calculation of the bound states will be much more involved as compared to the case of a pseudo potential. The Floquet-Feshbach resonance theory predicts in the case of a general scattering potential a formula of the resonant scattering length similar to the form of Eq. (3.134). The parameters of this formula are, however, much more involved to calculate as compared to the case of pseudo potential. In order to write down explicit equations for the parameters, a plethora of definitions from scattering theory has to be known. This makes Floquet-Feshbach resonance theory for general radial symmetric potential less accessible compared to the theory formulated for the pseudo potential. In the case of a general scattering potential, the influence of the inelastic channels can only be treated perturbatively.

Future investigations may apply the Floquet-Feshbach resonance theory in order to get accurate descriptions of the resonant scattering length in the case of a realistic interatomic potential such as the van der Waals potential. In the periodically driven multi channel model we assumed a pseudo potential as inter-atomic potential. This has the limitation, that the pseudo potential might oversimplify nontrivial Franck-Condon factors of the bound state wave function and the scattering state. Further, the pseudo potential allows for at most one bound state in each channel, while in realistic potentials a multitude of states are expected [18]. In order to qualitatively compare to experiments, it is useful to extend the multi-channel description to realistic interatomic potentials.

The Floquet-Feshbach resonance theory can be further generalized to dimensions other than three [158]. Ref. [159] investigates the tunneling through a periodically modulated barrier in a one-dimensional tight-binding lattice. The transmission coefficient T of this model is exemplarily shown in Fig. 3.28. Here it can be seen that the transmission coefficient drops to zero at certain energy ϵ. This intriguing behavior is linked to the Fano-Feshbach resonances we saw for the case of scattering in three dimensions. Since for $T = 0$ the scattering is maximal, it turns out that an analogy of the Floquet-Feshbach resonance theory can be formulated in 1D. Here, however, it would be rather named Floquet-Fano resonance theory, since the outcome of this theory is a formula for the transmission coefficient that has a Fano-like line shape and is valid in the vicinity of a resonance. The position of a resonance, i.e. the energy at which the transmission coefficients obtains a zero, is determined by the properties of bound states which reside in a coupled channel description in Floquet picture. Similar to the 3D case we find that a resonance occurs if the scattering state shares the same energy as a bound state of the closed Floquet channels. In analogy, the resonance width is given by an overlap of bound and scattering state. Ref. [160] discusses a periodically driven impurity in a Fermi-Hubbard model. Fermion pairs are forming in this model for strong attractive interactions. Since the pair tunneling obeys different laws than the single particle tunneling, the driven impurity can be used to create a pair or a single particle filter [160]. It is of interest, if also in this quantum many-body system resonances exist that can be related to the Fano-Feshbach physics of this thesis. As ultimate goal we see a Floquet-Fano resonance theory for the tunneling in the quantum many-body model with periodically driven impurity.

Optical Feshbach resonances change the real part of the scattering length only in a finite interval, c.f. Eq. (3.59). This behavior is due to a finite lifetime of the bound state in a closed channel. It is still an open question, if the time-periodic driving of an optical Feshbach resonance induces new Floquet-Feshbach resonances, that tune the scattering length to higher values than the original optical Feshbach resonance. One promising idea is to couple the scattering state to a bound state in the Born-Oppenheimer potential of the entrance channel by a Raman-type transition via the bound state in a closed channel [136]. This Ramam coupling can be implemented with the driven multichannel model Eq. (3.217). In Ref. [136] the multi-color Raman drive is experimentally realized by an acusto-optical modulator. However, Ref. [136] found with a calculation within the rotating-wave approximation that despite the Raman coupling the real part of the scattering length cannot be enhanced to larger values compared to the case of the original optical Feshbach resonance. Thus, if we want to get an enlarged real part of the scattering length, we have to search for effects in the Floquet description that goes beyond the rotating-wave approximation. It is an interesting further project if there exists a driving scheme which allows, in the presence of decay, for an enhancement of the real part of the scattering length beyond what is possible with common optical Feshbach resonances.

Further, the periodically driven multi-channel model Eq. (3.217) can be generalized to more than two internal degrees of freedom. This includes more parameters and thus a large space for possibly interesting physics. Such a model can be applied to the experiment described in Ref. [155], which found a low-field magnetic Feshbach resonance in Rb-Cs scattering.

The multi-channel model Eq. (3.47) can give host to two bound states. Combined with periodic driving, this can be used in order to investigate interesting phenomena, such as interfering resonances [113, 161].

4. Floquet-Bogoliubov Steady States

In the previous chapter it was investigated how a time-periodic modulation of the inter-particle interaction leads to a renormalization of the effective scattering length for ultracold gas systems. In detail, it is found out that by choosing a suitable driving strength and frequency, the effective scattering length can be tuned to arbitrary positive and negative values, an effect that we fully understood by introducing the Floquet-Feshbach resonance theory.

In this chapter we go beyond the two-body problem, as it is considered in scattering theory, and look at the time-periodic modulation of an interacting quantum many-body system. Here, the Hilbert space is much larger as compared to single or two-particle physics, such that due to the inter-particle interaction and entanglement strong correlations can arise. The quantum phase transition from a superfluid to a Mott insulator is a prominent example where quantum many-body physics is of relevance [45,162]. This phase transition has been observed in ultracold gas experiments [46], which serve as a highly tunable and accessible platform for investigating strongly correlated quantum many-body physics [3], c.f. Sec. 1.2. This high tunability of ultracold gas experiments can be used to realize one-dimensional quantum many-body systems [54, 56, 61], in which the effect of the inter-particle interaction is in particular pronounced. This can be understood by the fact that particles in 1D are confined to move on a line where they cannot avoid each other, which is notably different to the higher dimensional case [163].

Since the effects of inter-particle interaction are strongest pronounced in 1D [56, 163], we aim to investigate the resonant driving of a one-dimensional interacting quantum many-body system, while having an experimental realization within an ultracold gas experiment in mind. For this task we choose the Lieb-Liniger model [57, 58] describing a non-relativistic bosonic gas with a Dirac delta function as inter-particle interaction. As we saw in Ch. 3, the short range interaction in the Lieb-Liniger model serves a valid approximation for the inter-particle interaction in an ultracold gas experiment. A periodic time-dependence can be introduced by modulating a magnetic field in the vicinity of a Feshbach resonance [6, 7, 75]. Compared to the previous chapter, driving frequencies which are much lower than the dimer energy given by Eq. (3.31) are considered. These frequencies are typically in the regime of a few hundreds of Hz or at low kHz [6,75]. As suggested by Eq. (3.104) and observed in Refs. [6, 7, 75] such a drive does not renormalize the effective scattering length, but induces a time-dependent interaction strength in the quantum many-body Hamiltonian. This chapter finds as a prominent result that the time-periodic drive of the Lieb-Liniger model induces resonances that will completely change the physical behavior. These resonances will not be of the Fano-Feshbach type as in the previous chapter, but they are connected to the phenomenon of parametric resonance, which we introduced by the Paul trap in Ch. 1. During this chapter we will find out that resonant driving allows to parametrically excite density waves in the quantum many-body system.

The speciality of one-dimensional quantum many-body physics is that the low energy excitations of a wide class of models is described by the Tomonaga-Luttinger liquid theory [56, 163, 164]. On these grounds it is not the goal to find a Floquet solution of the Lieb-Liniger model in particular, but to analyze the time-periodically driven Tomonaga-Luttinger liquid Hamiltonian. For a time-dependent Tomonaga-Luttinger liquid the time-evolution of a given initial state has been studied in Refs. [165–170]. In this thesis we go beyond simple time evolution and investigate the properties of the possible Floquet steady state solutions of the periodically driven Tomonaga-Luttinger liquid. In order to achieve this on a technical level, the Tomonaga-Luttinger Hamiltonian is written in terms of bosonic operators where it acquires a quadratic form. In the static case such a Hamiltonian can be solved by a Bogoliubov transformation [171–173] which was originally introduced by N. N. Bogoliubov himself in order to analyze the behavior of superfluids [171,172]. In today's physics, Bogoliubov transformations are used for solving and analyzing a wide class of physical models. Prominent examples are the theories of superfluids and superconductors, where a Bogoliubov transformation allows to define quasiparticles whose properties are connected to the superfluidity or a superconducting phase [171, 172, 174]. Further, a Bogoliubov transformation finds a description of certain magnetic excitations in antiferro- and ferrimagnets [175–177]. In the mean-field theory of Bose-Einstein condensates [21, 28] the speed of sound is predicted by a Bogoliubov dispersion [172, 178, 179]. The transformation is even used in the field of astrophysics, for example by S. W. Hawkings paper of "particle creation by black holes" [180]. Having this great impact of Bogoliubov transformations on theoretical physics in mind, we generalize our goal even further and aim to find a Floquet version of a Bogoliubov transformation.

This chapter is structured as follows: We start in Sec. 4.1 with the introduction of the Tomonaga-Luttinger liquid theory, which we concretely apply to the Lieb-Liniger model. We further motivate in detail how the Tomonaga-Luttinger Liquid theory is related to a Hamiltonian that can be solved via a Bogoliubov transformation. In Sec. 4.2 the static Bogoliubov transformation is recapitulated while Sec. 4.3 discusses the Floquet-Bogoliubov solution of a time-periodic Hamiltonian that is quadratic in operators of a single bosonic mode. We derive an eigenvalue equation that is used in order to find the quasienergies of the Floquet-Bogoliubov particles and the parameters of the transformation. Section 4.4 discusses a procedure for numerically solving the Floquet-Bogoliubov eigenvalue equation. It turns our that there exist stability regions, where a Floquet solution is possible, and instability regions with no solution. In Sec. 4.5 physically relevant expectation values are calculated and stability charts for various system parameters are presented. We further relate the occurrence of instability regions to the physics of a parametric resonance. Section 4.6 contains the regularization of diverging excitation values by introducing a finite lifetime of the bosons. Finally, in Sec. 4.1 we discuss the result in the context of the Tomonaga-Luttinger liquid description of a periodically driven Lieb-Liniger model. It turns out that the parametric resonances lead to the pattern formation in the Lieb-Liniger gas. Section 4.8 is devoted to concluding remarks and an outlook.

At this point we note that the results of the work of this chapter has been published in Ref. [104]. The project was a collaboration with the authors of Ref. [104] and the bachelor student A. Becker [181].

4.1. Introduction into the Tomonaga-Luttinger Liquid Theory

The Tomonaga-Luttinger liquid model is an effective field theory that serves as a low energy description of a wide class of one-dimensional quantum systems [56, 163, 164]. In particular, following Ref. [104], we are interested in the Lieb-Liniger model [57, 58], which falls in the class of models where the Tomonaga-Luttinger liquid is applicable. The Hamiltonian of the Lieb-Liniger model reads [57, 58]:

$$H = -\frac{\hbar^2}{2m}\sum_{i=1}^{n}\frac{\partial^2}{\partial x_i^2} + g\sum_{\substack{i,j\\ i<j}}\delta(x_i - x_j). \tag{4.1}$$

The model (4.1) describes interacting bosons with mass m and position x_i in one dimension. The inter-particle interaction is given by a Dirac delta function with g as interaction strength. The model (4.1) can be realized with ultracold quantum gas experiments, where an effective one-dimensional system is achieved by a cigar shaped harmonic trap with two directions strongly confined, so that motion is possible in the remaining direction only [3, 54, 61, 182, 183]. In an ultracold gas experiment, the interaction strength is given by [3, 56, 184]

$$g = \frac{2a_0\hbar^2}{ma_\perp(a_\perp - 1.03\ a_0)}. \tag{4.2}$$

Here, a_0 is the three dimensional scattering length while $a_\perp$ is called confinement length that is related to the lateral confinement of the gas. Both a_0 and $a_\perp$ can be tuned in an experiment [3, 56].

Hamiltonian (4.1) falls into the wide class of models whose low-energy excitations are described by the Tomonaga-Luttinger liquid theory using the bosonization method [55, 56, 163, 164, 185–187]. For interacting one-dimensional systems, these low energy excitations are the collective excitations of a multitude of particles [56, 163, 185]. These collective excitations are described by a density field $\rho(x,t)$ and a phase $\theta(x,t)$, using which a bosonic field operator $\psi^\dagger(x,t)$ can be written as [188]

$$\psi^\dagger(x,t) = [\rho(x,t)]^{1/2}e^{-i\theta(x,t)}. \tag{4.3}$$

Density and phase obey the canonic commutation relation [56]

$$[\rho(x,t), \theta(x',t)] = i\delta(x - x'). \tag{4.4}$$

For a translational invariant system the ground state has a constant density $\langle\rho(x,t)\rangle = \rho_0$, at small excitation energies the system is expected to be close to this value [56]. Refs. [56, 188] introduce the smooth field $\phi(x,t)$ which approximately describes the density field by [56, 163]

$$\rho(x,t) \approx \rho_0 - \frac{1}{\pi}\partial_x\phi(x,t). \tag{4.5}$$

Corrections to Eq. (4.5) in terms of a harmonic series in the variable $\pi x\rho_0 - \phi(x,t)$ are discussed in Ref. [56]. Using the two fields $\phi(x,t)$ and $\theta(x,t)$, the low energy excitations can be described by the Tomonaga-Luttinger liquid Hamiltonian [56, 163, 164, 188]:

$$H = \frac{\hbar}{2\pi}\int dx\ \left[vK[\partial_x\theta(x,t)]^2 + \frac{v}{K}[\partial_x\phi(x,t)]^2\right]. \tag{4.6}$$

Hamiltonian (4.6) solely depends on the two model parameters v and K, where K is known as Luttinger-liquid parameter. The two parameters v and K in turn depend on the microscopic details of each model and can be related to ground state properties [56]. Methods for calculating the parameters v and K include the numerical or analytical solution of the underlying microscopic model, an overview is given in Refs. [56, 188]. In the following we exemplarily show results in the case of the Lieb-Liniger model, which can be solved by the Bethe ansatz [57, 58]. The solution of the Bethe ansatz determines the parameters v and K [56]. With $v_\mathrm{F} = \pi\rho_0/m$ it holds that $v_\mathrm{F} = vK$ and $K > 1$ in the Lieb-Liniger model [104, 188]. The Luttinger-liquid parameter only depends on the dimensionless interaction strength $\gamma = mg/(\hbar^2\rho_0)$ [104, 188]. Ref. [188] found useful approximations for v and K for $\gamma \ll 1$:

$$K \approx \frac{\pi}{\sqrt{\gamma}}\left(1 - \frac{\sqrt{\gamma}}{2\pi}\right)^{-1/2}, \quad \frac{v}{K} \approx v_\mathrm{F}\left(\frac{\gamma}{\pi^2}\right)\left(1 - \frac{\sqrt{\gamma}}{2\pi}\right) \tag{4.7}$$

and for $\gamma \gg 1$

$$K \approx \left(1 + \frac{4}{\gamma}\right), \quad \frac{v}{K} \approx v_\mathrm{F}\left(1 - \frac{8}{\gamma}\right). \tag{4.8}$$

Within the Tomonaga-Luttinger liquid theory various expectation values can be calculated. Refs. [56, 164] show for a ground state calculation with periodic boundary conditions and in the thermodynamic limit that the asymptotic behavior of the correlation function for $x \to \infty$ yields

$$\langle \psi^\dagger(x)\psi(0)\rangle \approx A_0\rho_0\left(\frac{1}{\rho_0|x|}\right)^{\frac{1}{2K}} + \mathcal{O}\left[\left(\frac{1}{|x|}\right)^{2K}\right]. \tag{4.9}$$

Here A_0 is a model dependent constant. Eq. (4.9) displays the famous result that the correlation function in interacting 1D models at asymptotic distances $|x| \to \infty$ is given by a power law with an exponent that only depends on the Luttinger parameter K. The asymptotic density-density correlation is given by [56, 163, 164]

$$\langle \rho(x)\rho(0)\rangle = \rho_0^2\left[1 - \frac{K}{2\pi^2}\left(\frac{1}{\rho_0|x|}\right)^2\right] + \mathcal{O}\left[\left(\frac{1}{|x|}\right)^{2K}\right]. \tag{4.10}$$

Here the Luttinger parameter appears as a prefactor and not in the exponent of the power law. At finite distances the correlation functions (4.9) and (4.10) are corrected by terms oscillating with a wavenumber of ρ_0 or corresponding higher harmonics, for details see Ref. [56].

In order to relate the Tomonaga-Luttinger liquid Hamiltonian (4.6) to a Hamiltonian that is quadratic in bosonic operators, the following definitions are useful [104, 163]

$$vK = v_\mathrm{F}(1 + g_4 - g_2), \tag{4.11a}$$

$$\frac{v}{K} = v_\mathrm{F}(1 + g_4 + g_2). \tag{4.11b}$$

In the Lieb-Liniger model it follows with $v_\mathrm{F} = vK$ and Eq. (4.11) that $g_2 = g_4 = (1/K^2 - 1)/2$ and further $-1/2 < g_2 = g_4 < 0$. The auxiliary fields $\phi_\mathrm{L}(x,t) = [\phi(x,t) + \theta(x,t)]/\sqrt{2}$ and $\phi_\mathrm{R}(x,t) =$

$[\theta(x,t)-\phi(x,t)]/\sqrt{2}$ are defined. They are expanded in bosonic operators

$$\phi_{L/R}(x,t) \propto \sum_{q>0} \frac{e^{\alpha q/2}}{\sqrt{q}} [e^{\mp iqx} b_{q,\mathrm{L/R}} + e^{\pm iqx} b^{\dagger}_{q,\mathrm{L/R}}]. \tag{4.12}$$

In Eq. (4.12) the upper sign stands for L while the lower is related to R. The operator $b_{q,\mathrm{L}}$ is related to a left moving density wave, $b_{q,\mathrm{R}}$ to a right moving density wave, as it can be read of by the plane wave exponents in Eq. (4.12). The operators $b_{q,\chi}$ obey the bosonic commutation relations $[b_{q,\chi}, b^{\dagger}_{q',\chi'}] = \delta_{q,q'}\delta_{\chi,\chi'}$, while all other canonic commutators are zero. The variable α is used as a cutoff. The mode expansion (4.12) is similar to a Fourier expansion, but with the difference that q is restricted to strictly positive values. With the mode expansion (4.12) the Tomonaga-Luttinger liquid Hamiltonian (4.6) can be written as

$$H = \sum_{q>0} H_q + H_0, \tag{4.13}$$

with

$$H_q = \hbar v_{\mathrm{F}} q(1+g_4)(b^{\dagger}_{q,\mathrm{R}} b_{q,\mathrm{R}} + b^{\dagger}_{q,\mathrm{L}} b_{q,\mathrm{L}}) + \hbar q v_{\mathrm{F}} g_2 (b_{q,\mathrm{L}} b_{q,\mathrm{R}} + b^{\dagger}_{q,L} b^{\dagger}_{q,\mathrm{R}}) \tag{4.14}$$

and H_0 as energy offset that is not of relevance for the following discussion. We bring Hamiltonian (4.14) to a even more generic form by the canonic transformation

$$b_{q,\pm} = \frac{1}{\sqrt{2}}(b_{q,\mathrm{L}} \pm b_{q,\mathrm{R}}) \tag{4.15}$$

Thus, Hamiltonian (4.14) transforms to

$$H_q = \sum_{\pm} \left[A_q b^{\dagger}_{q,\pm} b_{q,\pm} \pm \frac{B_q}{2}(b_{q,\pm} b_{q,\pm} + b^{\dagger}_{q,\pm} b^{\dagger}_{q,\pm}) \right], \tag{4.16}$$

with

$$A_q = \hbar v_{\mathrm{F}} q(1+g_4), \tag{4.17a}$$
$$B_q = \hbar q v_{\mathrm{F}} g_2. \tag{4.17b}$$

In Eq. (4.16) the two bosonic modes are separated. This serves as a prototypical example of a Hamiltonian that can be solved by a Bogoliubov transformation.

Time-periodic driving of the parameters of Hamiltonians (4.14) and (4.16) can be realized in an ultracold gas experiment by the time-periodic modulation of the length scales a_0 and $a_\perp$. The modulation of a magnetic field in the vicinity of a Feshbach resonance changes the three dimensional scattering length a_0 [6, 18, 75] while the confinement length $a_\perp$ depends on the strength of the potential that generates the transverse confinement [61]. The time periodic modulation of a_0 and $a_\perp$ leads to time-dependent parameters $g_2(t) = g_4(t)$ in Hamiltonian (4.14). The time-periodic drive of the parameters of the Tomonaga-Luttinger description of the Lieb-Liniger model recasts into time dependent parameters $A_q(t)$, $B_q(t)$. For the discussion of this chapter is useful to express the time-periodic parameters $A(t),\ B(t)$ by a Fourier series

$$A(t) = \sum_{n=-\infty}^{\infty} e^{-in\omega t} A_n, \tag{4.18a}$$

$$B(t) = \sum_{n=-\infty}^{\infty} e^{-in\omega t} B_n. \tag{4.18b}$$

In the following sections we will derive a Floquet version of a Bogoliubov transformation for Hamiltonian that is quadratic in operators of a single bosonic mode. Before we actually write down this time-dependent transformation, it is key to understand the corresponding static model.

4.2. Time-Independent Single Mode Bogoliubov Transformation

In this section the relevant points of a time-independent Bogoliubov transformation are discussed. Motivated by Eq. (4.16), we assume a generic Hamilton operator that is quadratic in bosonic creation / annihilation operators b / $b^\dagger$:

$$H = Ab^\dagger b + \frac{B}{2}(b^\dagger b^\dagger + bb), \tag{4.19}$$

the coefficients A, B are chosen to be real such that H is hermitian. The bosonic operators obey the canonic commutation relations $[b, b^\dagger] = 1$. We aim to solve Hamiltonian (4.19) by the Bogoliubov transformation

$$\beta = ub + vb^\dagger. \tag{4.20}$$

The new operators should obey bosonic commutation relations $[\beta, \beta^\dagger] = 1$, which implies the condition

$$|u|^2 - |v|^2 = 1. \tag{4.21}$$

With the Bogoliubov transformation (4.20) we are in the position to solve the Hamiltonian Eq. (4.19) which will finally determines the coefficients u and v.

In this thesis we present an approach that finds the Bogoliubov transformation in Heisenberg picture. For a given operator A in Schrödinger picture, the corresponding operator in Heisenberg picture reads $A_\mathrm{H}(t) = U(t, t_0)^\dagger A U(t, t_0)$, where $U(t, t_0)$ is the time-evolution operator, t_0 is an arbitrary initial time [189]. In the Heisenberg picture, the time-evolution of the β operator is given by

$$i\hbar\frac{d}{dt}\beta_\mathrm{H} = [\beta_\mathrm{H}, H_\mathrm{H}], \tag{4.22}$$

where the Hamiltonian in Heisenberg picture reads $H_\mathrm{H} = Ab_\mathrm{H}^\dagger b_\mathrm{H} + B(b_\mathrm{H}^\dagger b_\mathrm{H}^\dagger + b_\mathrm{H} b_\mathrm{H})/2$. In order to find the spectrum of Eq. (4.19) by a Bogoliubov transformation, we require that the time evolution of the new operator (4.20) is the one of a non-interacting quantum particle $i\hbar\frac{d}{dt}\beta_\mathrm{H} = \epsilon\beta_\mathrm{H}$, where

ϵ is the energy of the Bogoliubov quasiparticle. The operators $\beta^\dagger$ / β are interpreted as creation / annihilation operators for the Bogoliobov quasiparticles. Combining the trivial time evolution $i\hbar\frac{d}{dt}\beta_{\mathrm{H}} = \epsilon\beta_{\mathrm{H}}$ together with Eq. (4.22) leads to a relation of the operators β which is valid in both Heisenberg and Schrödinger picture

$$[H, \beta] = -\epsilon\beta. \tag{4.23}$$

Equation (4.23) can be evaluated by inserting the explicit form of Hamiltonian (4.19) and comparing coefficients in front of b and $b^\dagger$. This gives an eigenvalue equation for the energy ϵ of the Bogoliubov particles

$$\begin{pmatrix} -A & B \\ -B & A \end{pmatrix} \begin{pmatrix} u \\ v \end{pmatrix} = -\epsilon \begin{pmatrix} u \\ v \end{pmatrix}. \tag{4.24}$$

Note, that due to the bosonic commutation relations the eigenvalue problem Eq. (4.24) is non-hermitian. The eigenvalues of Eq. (4.24) are given by $\epsilon_\pm = \pm\sqrt{A^2 - B^2}$. In the following we restrict ourselves to the case $|A| > |B|$, such that $\epsilon_\pm$ is real valued. The corresponding coefficients are $u_+ = \cosh(\lambda),\ v_+ = \sinh(\lambda)$ and $u_- = \sinh(\lambda),\ v_- = \cosh(\lambda)$, respectively, with

$$\tanh(2\lambda) = \frac{B}{A}. \tag{4.25}$$

The parametrization of the coefficients is such that $|u_\pm|^2 - |v_\pm|^2 = \pm 1$. As we require the canonic constraint Eq. (4.21) to be fulfilled, the solution labeled with minus is dropped. As as result the coefficients in Eq. (4.20) are, up to a global phase, uniquely determined by $u = \cosh(\lambda),\ v = \sinh(\lambda)$ and the energy of a Bogoliubov quasiparticle reads

$$\epsilon = \sqrt{A^2 - B^2}. \tag{4.26}$$

The behavior of Eq. (4.26) in dependence of the ratio B/A is shown in Fig. 4.1 (a), the energy ϵ drops in the form of a quadrant with increasing B/A. In total, the $\beta^\dagger$ / β operators are now fully determined and an expression for the energy of the Bogoliubov quasiparticles is found.

After having found the correct parameters of the transformation it is key to determine the eigenstates of our system. Using the commutator (4.23) all eigenstates of Hamiltonian (4.19) can be constructed inductively, based on the assumption that the vacuum state of the Bogoliubov particles $|\tilde{0}\rangle$ exists [112]. The vacuum state of the Bogoliubov quasiparticles is defined by the equation

$$\beta|\tilde{0}\rangle = 0. \tag{4.27}$$

It can be shown that the state

$$|\tilde{0}\rangle = \frac{1}{\sqrt{|u|}} \exp\left[-\frac{v}{2u}(b^\dagger)^2\right] |0\rangle \tag{4.28}$$

solves Eq. (4.27) [190, 191], where $|0\rangle$ as the vacuum of the b operators obeying $b|0\rangle = 0$. Using $\sum_{n=0}^{\infty}(z/4)^n(2n)!/(n!)^2 = 1/\sqrt{1-z}$ for $|z| \leq 1$ [190] and Eq. (4.21) one can show that the state (4.28) is normalized to one. The eigenstate containing n Bogoliubov particles is given by

$$|\tilde{n}\rangle = \frac{(\beta^\dagger)^n}{\sqrt{n!}}|\tilde{0}\rangle,\ n \in \mathbb{N}_0. \tag{4.29}$$

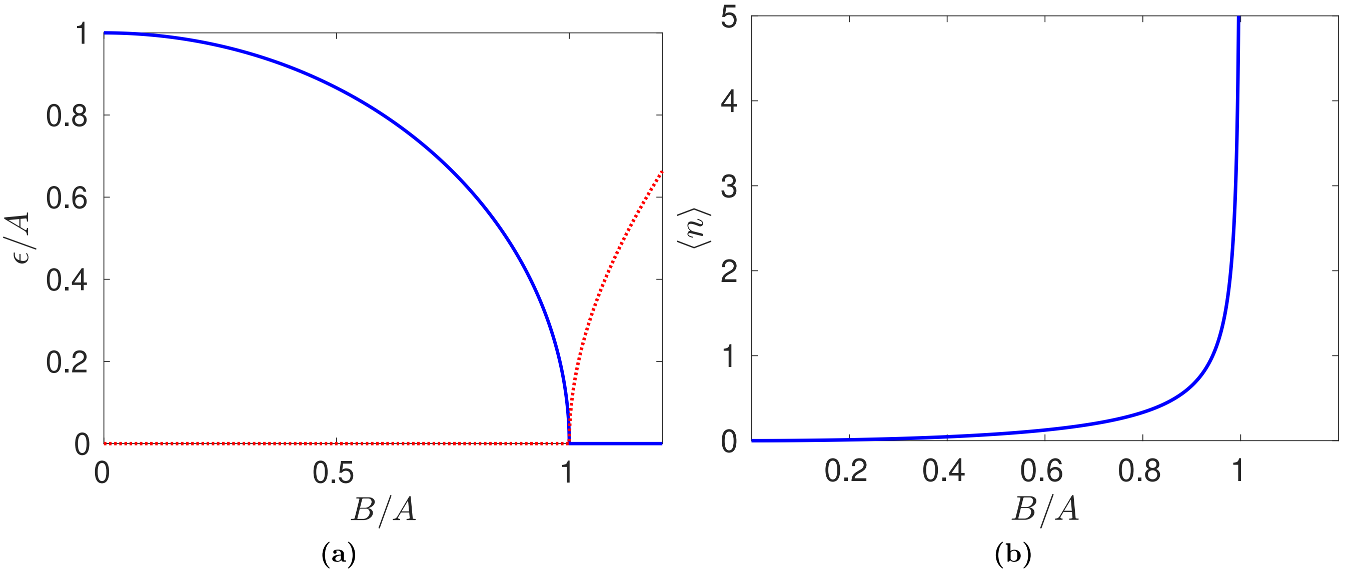

Figure 4.1.: (a) Energy ϵ of the Bogoliubov quasiparticles in dependence of the ratio B/A, real part in blue, imaginary part in red. (b) Expectation value $\langle n \rangle$ of the number of excitations in dependence of the ratio B/A.

In order to verify that the states Eq. (4.29) are eigenstates of Hamiltonian (4.19), we use the inverse of the Bogoliubov transformation

$$b = u\beta - v\beta^\dagger \tag{4.30}$$

in order to finally express the Hamiltonian (4.19) in terms of the β operators:

$$H = \epsilon\beta^\dagger\beta + \frac{\epsilon - A}{2}. \tag{4.31}$$

Thus the state $|\tilde{n}\rangle$ is an eigenstate of Hamiltonian (4.19) with an eigenenergy of $\epsilon_n = n\epsilon + (\epsilon - A)/2$. As a result a complete set of eigenstates of Hamiltonian (4.19) is found.

At last, it is discussed why we above restricted ourselves to $|A| > |B|$. For the opposite case the eigenenergy of the Bogoliubov particles becomes purely imaginary $\epsilon = \pm i\sqrt{B^2 - A^2}$, here the system becomes dynamically unstable [192]. Mathematically, these imaginary eigenvalues come due to the non-hermiticity of Eq. (4.24), that is related to the bosonic nature of the operators. For $|A| < |B|$ it holds that $|u|^2 - |v|^2 = |u|^2[1 - |A - \epsilon|/(B)] = 0$, such that $|u| = |v|$. It follows that the β operators do not obey Bosonic commutation rules in this case while the norm of the vacuum state does not converge [190]. As a result, the Bogoliubov transformation fails to diagonalize Hamiltonian (4.19) for $|A| < |B|$. This is related to the fact that for $|A| < |B|$ the Hamiltonian Eq. (4.19) is unbounded from below. In order to see this argument we introduce artificial position and momentum operators by $b = (X + iP)/\sqrt{2}$, using which Hamiltonian (4.19) reads $H = P^2(A - B)/2 + X^2(A + B)/2$. If $|A| < |B|$, either the quadratic dispersion or the parabolic potential is inverted, it is easily verified that this leads to a Hamiltonian that is unbounded from below.

In order to understand this behavior even further the expectation value of the number of excitations in the vacuum state of the Bogoliubov particles $\langle n\rangle = \langle\tilde{0}|b^\dagger b|\tilde{0}\rangle$ is considered. With Eqns. (4.30) and (4.25) it is calculated to

$$\langle n\rangle = \frac{1-\sqrt{1-(B/A)^2}}{2\sqrt{1-(B/A)^2}}. \tag{4.32}$$

In Fig. 4.1 (b) this expectation value is shown. For $B/A = 0$ it yields $\langle n\rangle = 0$. This is expected, since in this case the Bogoliubov vacuum state $|\tilde{0}\rangle$ equals to the original vacuum state $|0\rangle$, which of course contains no excitations. With increasing ratio B/A the value of $\langle n\rangle$ slightly increases until it diverges for $B/A \to 1$ with a power law $\langle n\rangle \approx [1-(B/A)^2]^{-1/2}$. This is signaling the breakdown of the Bogoliubov solution for $B > A$, since in the limit of $B = A$ the ground state would contain an infinite number of excitations. We will see that a similar behavior is also present in the time-periodically driven case.

4.3. Floquet Single Mode Bogoliubov Transformation

In this section we derive a method that is able to find quasiparticle operators in the case of a Hamiltonian that is quadratic in bosonic operators with time-periodic parameters $A(t) = A(t+T)$, $B(t) = B(t+T)$:

$$H(t) = A(t)b^\dagger b + \frac{B(t)}{2}(b^\dagger b^\dagger + bb). \tag{4.33}$$

Here $H(t) = H(t+T)$, the corresponding driving frequency is fixed via $\omega = 2\pi/T$. The parameters $A(t)$, $B(t)$ are real valued for each time t. This section is structured as follows: In Subsec. 4.3.1 the Floquet Bogoliubov transformation is introduced in the Heisenberg picture. This method allows to define Bogoliubov quasiparticles also for the time-periodically driven case. We note that the basic thoughts of Subsec. 4.3.1 have been formulated in collaboration, especially with S. Fazzini and A. Becker. In Subsec. 4.3.2 the results of the Floquet-Bogoliubov transformation are used in order to find out the nature of possible Floquet steady states. Subsec. 4.3.3 gives an explicit form of the vacuum state of the Floquet-Bogoliubov quasiparticles.

4.3.1. Floquet-Bogoliubov Transformation in Heisenberg Picture

The Floquet-Bogoliubov transformation aims to solve the time-periodic Hamiltonian (4.33), and is introduced in analogy to the static case in Eq. (4.20), by

$$\beta(t) = u(t)b + v(t)b^\dagger. \tag{4.34}$$

In Eq. (4.34), however, the parameters $u(t), v(t)$ are time-dependent. We derive the Floquet-Bogoliubov theory in Heisenberg picture. This approach gains, in combination with the following subsections, a complete understanding of the mathematical and physical structure of the Floquet-Bogoliubov solution. The focus is on the Heisenberg equations of motion for the new operators

$$i\hbar\frac{d}{dt}\beta_{\mathrm{H}}(t) = i\hbar\frac{\partial\beta_{\mathrm{H}}(t)}{\partial t} + [\beta_{\mathrm{H}}(t), H_{\mathrm{H}}(t)], \tag{4.35}$$

with the transformation $\beta_{\mathrm{H}}(t) = u(t) b_{\mathrm{H}}(t) + v(t) b_{\mathrm{H}}^\dagger(t)$ and Hamiltonian $H_{\mathrm{H}}(t) = A(t) b_{\mathrm{H}}^\dagger(t) b_{\mathrm{H}}(t) + \frac{B(t)}{2}[b_{\mathrm{H}}^\dagger(t) b_{\mathrm{H}}^\dagger(t) + b_{\mathrm{H}}(t) b_{\mathrm{H}}(t)]$ in Heisenberg picture. In comparison to the static case, Eq. (4.35) additionally contains a partial time-derivative of the β_{H} operator. This partial derivative is defined via the corresponding operator in the Schrödinger picture $\frac{\partial \beta_{\mathrm{H}}(t)}{\partial t} = U(t,t_0) \frac{\partial \beta(t)}{\partial t} U^\dagger(t,t_0)$ and reads

$$\frac{\partial \beta_{\mathrm{H}}(t)}{\partial t} = \dot{u}(t) b_{\mathrm{H}}(t) + \dot{v}(t) b_{\mathrm{H}}^\dagger(t). \tag{4.36}$$

In Eq. (4.36) the dot denotes the derivative with respect to time.

In the following we derive an eigenvalue equation similar to Eq. (4.23) for the time-dependent case. For doing so the time-evolution of the Floquet-Bogoliubov operator is required to be of the form of an operator describing a quasiparticle $i\hbar \frac{d}{dt} \beta_{\mathrm{H}}(t) = \epsilon \beta_{\mathrm{H}}(t)$. Here ϵ is the yet unknown quasienergy of the possible Floquet-Bogoliubov quasiparticles. Combining the trivial time-evolution $i\hbar \frac{d}{dt} \beta_{\mathrm{H}}(t) = \epsilon \beta_{\mathrm{H}}(t)$ with the Heisenberg equation Eq. (4.35), the following relation for the the operator β_{H} is derived

$$[H_{\mathrm{H}}(t), \beta_{\mathrm{H}}] - i\hbar \frac{\partial \beta_{\mathrm{H}}(t)}{\partial t} = -\epsilon \beta_{\mathrm{H}}(t), \tag{4.37}$$

which generalizes Eq. (4.23) to the time-dependent case. Equation (4.37) is explicitly evaluated with the use of Eq. (4.36). Comparing the coefficients in front of the b_{H} / $b_{\mathrm{H}}^\dagger$ operators, an eigenvalue equation is found

$$\left[\begin{pmatrix} -A(t) & B(t) \\ -B(t) & A(t) \end{pmatrix} - i\hbar \frac{\partial}{\partial t} \right] \begin{pmatrix} u(t) \\ v(t) \end{pmatrix} = -\epsilon \begin{pmatrix} u(t) \\ v(t) \end{pmatrix}. \tag{4.38}$$

Equation (4.38) is a central to this chapter and serves as defining equation for the Floquet-Bogoliubov transformation and the quasienergy ϵ. Since we assume time-periodic coefficients $A(t) = A(t+T)$ and $B(t) = B(t+T)$, Eq. (4.38) can be solved using Floquet theory [98,193]. Equation (4.38) is non-hermitian, in analogy to Eq. (4.24), see App. C for a Floquet theory of non-hermitian Hamiltonians. The Floquet solution yields time-periodic transformation parameters $u(t) = u(t+T)$ and $v(t) = v(t+T)$ and in general complex quasienergies ϵ. The β_{H} operators obey bosonic commuatation relations $[\beta_{\mathrm{H}}, \beta_{\mathrm{H}}^\dagger] = 1$ if

$$|u(t)|^2 - |v(t)|^2 = 1 \tag{4.39}$$

holds for all times t. We will show in Sec. 4.4 that the solutions of Eq. (4.38) can be split into two classes: The stable solutions and the unstable ones. For a stable solution the quasienergies are real. Since we deal with a 2×2 matrix, in each Floquet Brillouin zone there are two quasienergies $\epsilon_\pm$. The corresponding solutions can be normalized to obey $|u_\pm(t)|^2 - |v_\pm(t)|^2 = \pm 1$ for all times. We choose the +-solution, that fulfills Eq. (4.39) with $\epsilon \in [0, \omega[$. This procedure determines the parameters $u(t)$, $v(t)$, up to a global phase, and ϵ uniquely. In the unstable case the quasienergies become complex and $|u(t)|^2 - |v(t)|^2 = 0$. Therefore, the β_{H} operators do not fulfill bosonic commutation relations and can not be interpreted as quasiparticles. We will see that in this case the Floquet-Bogoliubov eigenstates do not exist.

At this point we note, that in the stability regions the β_{H} operator have a time dependence of the form $\beta_{\mathrm{H}}(t) = e^{-i\epsilon t/\hbar} \beta_{\mathrm{H}}^{(0)}$, where $\beta_{\mathrm{H}}^{(0)}$ a time independent operator that is determined at initial time $t_0 = 0$. The b_{H} / $b_{\mathrm{H}}^\dagger$ obey a nontrivial time dependence given by the inverse transformation

$$b_{\mathrm{H}}(t) = u^*(t) \beta_{\mathrm{H}}(t) - v(t) \beta_{\mathrm{H}}^\dagger(t), \tag{4.40}$$

or the corresponding hermitian conjugate equation, respectively.

In the following, we deepen the argument that the $\beta_{\mathrm{H}}(t)$ operators describe quasiparticles by relating the quasienergy spectrum of Hamiltonian (4.33) to the one of a static harmonic oscillator in Heisenberg picture. We assume to be in a stability region. Concretely, we ask the question if a time-independent Hamiltonian $\mathcal{H}$ can be found that generates the Heisenberg equations of motion in the following way

$$i\hbar\frac{d}{dt}\beta_{\mathrm{H}}(t) = [\beta_{\mathrm{H}}(t), \mathcal{H}]. \tag{4.41}$$

The trivial time evolution of the Floquet-Bogoliubov operators $\beta_{\mathrm{H}}(t) = e^{-i\epsilon t/\hbar}\beta_{\mathrm{H}}^{(0)}$ leads to the condition

$$[\mathcal{H}, \beta_{\mathrm{H}}^{(0)}] = -\epsilon\beta_{\mathrm{H}}^{(0)}. \tag{4.42}$$

Since the $\beta_{\mathrm{H}}^{(0)}$ operators obey canonical commutation relations, artificial position and momentum operators can be defined via

$$\beta_{\mathrm{H}}^{(0)} = \frac{1}{\sqrt{2}}(\hat{X} + i\hat{P}). \tag{4.43}$$

The wave function $\langle x|\tilde{0}\rangle = (4\pi)^{-1/4}\exp(-x^2/4)$ fulfills the equation

$$\beta_{\mathrm{H}}^{(0)}|\tilde{0}\rangle = 0. \tag{4.44}$$

Equations (4.42), (4.44) and the bosonic commutation relation $[\beta_{\mathrm{H}}^{(0)}, (\beta_{\mathrm{H}}^{(0)})^\dagger] = 1$ are sufficient to show that the states $|\tilde{n}\rangle = [(\beta_{\mathrm{H}}^{(0)})^\dagger]^n|\tilde{0}\rangle/\sqrt{n!}$ exist which obey the eigenvalue equation

$$\mathcal{H}|\tilde{n}\rangle = (n\epsilon + E_0)|\tilde{n}\rangle. \tag{4.45}$$

With these findings we are left with a harmonic oscillator and are able to write down an expression for the time-independent Hamiltonian $\mathcal{H}$ by

$$\mathcal{H} = \epsilon(\beta_{\mathrm{H}}^{(0)})^\dagger\beta_{\mathrm{H}}^{(0)} + E_0. \tag{4.46}$$

Here E_0 is the quasienergy of the vacuum state of the Bogoliubov quasiparticles that is not yet determined, but it is also not of relevance for calculating the expectation values in the Heisenberg picture. Equation (4.46) finally shows that the time-independent Hamiltonian $\mathcal{H}$ has a diagonal form in terms of the Floquet-Bogoliubov operators β_{H}. This enables, similar to the static case, to interpret $|\tilde{0}\rangle$ as the vacuum state of the Floquet-Bogoliubov particles, while the state $|\tilde{n}\rangle$ contains n Floquet-Bogoliubov quasiparticles. We will see that these definitions allow to calculate expectation values of Floquet-steady states within the Heisenberg picture.

In this subsection a Floquet-Bogoliubov transformation for a periodically driven Hamiltonian that is quadratic in bosonic operators is found. The method is able to calculate the quasienergies and to define states with a certain number of quasiparticles. In the next subsection the eigenstates of $\mathcal{H}$ are connected to Floquet states in Schrödinger picture.

4.3.2. Finding Floquet States with the Floquet-Bogoliubov Transformation

In this subsection we discuss how the Floquet-Bogoliubov transformation generates the full basis of Floquet steady states of the time-dependent Hamiltonian (4.33). In the following it is again assumed to be in a stability region. Similar to the discussion of the quantum harmonic oscillator, an induction argument finds the Floquet steady state basis [112].

For this induction argument the following relation is central [104]

$$[H(t) - i\hbar\frac{\partial}{\partial t}, \beta(t)] = -\epsilon\beta(t). \tag{4.47}$$

Equation (4.47) is derived from Eq. (4.37) while using that

$$[i\hbar\frac{\partial}{\partial t}, \beta(t)]|\psi(t)\rangle = i\hbar\left(\frac{\partial\beta(t)}{\partial t}\right)|\psi(t)\rangle \tag{4.48}$$

holds for an arbitrary time-dependent state $|\psi(t)\rangle$. Equation (4.47) generalizes Eq. (4.23) to the Floquet case and is formulated in Schrödinger picture. The operators β / $\beta^\dagger$ inherit the canonic commutation relations from the Heisenberg picture. In the following we will use Eq. (4.47) in order to inductively generate the whole Floquet spectrum of Hamiltonian (4.33). As base case, it is assumed that a Floquet mode $|\phi_0(t)\rangle$ exists, which solves the Floquet equation

$$\left[H(t) - i\hbar\frac{\partial}{\partial t}\right]|\phi_0(t)\rangle = E_0|\phi_0(t)\rangle, \tag{4.49}$$

with $H(t)$ given by Eq. (4.33). The quasienergy of this state is denoted by E_0. Further, it is assumed that $|\phi_0(t)\rangle$ is the Floquet vacuum state of the Floquet-Bogoliubov particles obeying

$$\beta(t)|\phi_0(t)\rangle = 0, \ \forall t. \tag{4.50}$$

In Subsec. 4.3.3 we show that this state exists and give an explicit expression for both $|\phi_0(t)\rangle$ and E_0. In the following it is demonstrated that the state $|\phi_1(t)\rangle = \beta^\dagger(t)|\phi_0(t)\rangle$ is also a Floquet solution of Hamiltonian (4.33), provided that Eqns. (4.47) and (4.49) hold:

$$\left[H(t) - i\hbar\frac{\partial}{\partial t}\right]\beta^\dagger(t)|\phi(t)\rangle = [H(t) - i\hbar\frac{\partial}{\partial t}, \beta^\dagger(t)]|\phi(t)\rangle + \beta^\dagger(t)\left[H(t) - i\hbar\frac{\partial}{\partial t}\right]|\phi(t)\rangle. \tag{4.51}$$

Using Eqns. (4.47) and (4.49) we finally arrive at

$$\left[H(t) - i\hbar\frac{\partial}{\partial t}\right]|\phi_1(t)\rangle = (E_0 + \epsilon)|\phi_1(t)\rangle. \tag{4.52}$$

Equation (4.52) indeed says that $|\phi_1(t)\rangle$ is a Floquet state with quasienergy $\epsilon_1 = \epsilon + E_0$. In App. D it is shown via mathematical induction that the whole spectrum is given by the quasienergies

$$\epsilon_n = n\epsilon + E_0, \tag{4.53}$$

while the corresponding Floquet modes read

$$|\phi_n(t)\rangle = \frac{[\beta^\dagger(t)]^n}{\sqrt{n!}}|\phi_0(t)\rangle. \tag{4.54}$$

The Floquet modes fulfill the orthonormality condition

$$\langle\phi_n(t)|\phi_m(t)\rangle = \delta_{n,m}. \tag{4.55}$$

In the following, the Floquet states (4.54) are mapped to the eigenstates $|\tilde{n}\rangle$ of the Hamiltonian $\mathcal{H}$ defined in Heisenberg picture. In the Heisenberg picture, the states $|\psi_\mathrm{H}\rangle$ are time independent and related to a state $|\psi(t)\rangle$ in Schrödinger picture by $|\psi(t)\rangle = U(t,t_0)|\psi_\mathrm{H}\rangle$, where $U(t,t_0)$ is the time-evolution operator. This allows to relate the Floquet states corresponding to Eq. (4.54) to the static eigenbasis $|\tilde{n}\rangle$ found in Heisenberg picture by

$$|\psi_n(t)\rangle = U(t,t_0)|\tilde{n}\rangle. \tag{4.56}$$

As $U(t_0,t_0) = \mathbb{I}$, with $\mathbb{I}$ as identity matrix, Eq. (4.56) directly implies that the Floquet modes at initial time are related to the eigenstates found in Heisenberg picture $|\phi_n(t_0)\rangle = |\tilde{n}\rangle$. Using the definition $|\tilde{n}\rangle = [(\beta_\mathrm{H}^{(0)})^\dagger]^n|\tilde{0}\rangle/\sqrt{n!}$, and the relations $U(t,t_0)\beta_\mathrm{H}^{(0)}U^\dagger(t,t_0) = e^{-i\epsilon(t-t_0)}\beta(t)$ and $|\psi_0(t)\rangle = e^{-iE_0(t-t_0)}|\phi_0(t)\rangle = U(t,t_0)|\tilde{0}\rangle$ we can reexpress Eq. (4.56) by

$$|\psi_n(t)\rangle = e^{-i(n\epsilon+E_0)(t-t_0)/\hbar}\frac{[\beta^\dagger(t)]^n}{\sqrt{n!}}|\phi_0(t)\rangle. \tag{4.57}$$

Equation (4.57) is consistent with Eq. (4.54), this verifies that Eq. (4.56) correctly relates the Floquet states to the static eigenbasis $|\tilde{n}\rangle$ in Heisenberg picture. In a similar way the defining equation of the Floquet vacuum state Eq. (4.50) can be related to Eq. (4.44).

With the knowledge of the Floquet states a family of transformations to the Floquet frame, as introduced by Eq. (2.3), can be written down. Note, that there is the choice of multiplying a time-independent unitary matrix Q to a given $U_\mathrm{P}(t)$. The first choice of the unitary transformation, that is considered in this subsection, is given by

$$U_\mathrm{P}^{(1)}(t) = \sum_{n=0}^{\infty}|\phi_n(t)\rangle\langle n|, \tag{4.58}$$

where $|n\rangle$ is the eigenbasis given by $|n\rangle = (b^\dagger)^n|0\rangle/\sqrt{n!}$. Using Eq. (2.3), the effective Hamiltonian in the transformed frame can be calculated. With Eq. (4.58) this calculation yields

$$\tilde{H}_\mathrm{eff}^{(1)} = \sum_{n=0}^{\infty}\epsilon_n|n\rangle\langle n|. \tag{4.59}$$

An equation similar to Eq. (4.59) has been found in Ref. [104]. The Hamiltonian (4.59) is the one of a single harmonic oscillator $\tilde{H}_\mathrm{eff}^{(1)} = \epsilon b^\dagger b + E_0$. This result shows the advantage of the Floquet description, since it maps a nontrivial time-dependent problem to a time-dependent diagonal one.

The second transformation to a Floquet frame, that is considered here, is given by

$$U_{\mathrm{P}}^{(2)}(t) = \sum_{n=0}^{\infty} |\phi_n(t)\rangle\langle\phi_n(0)|, \tag{4.60}$$

which leads with Eq. (4.59) to the following effective Hamiltonian

$$\tilde{H}_{\mathrm{eff}}^{(2)} = \sum_{n=0}^{\infty} \epsilon_n |\phi_n(0)\rangle\langle\phi_n(0)|. \tag{4.61}$$

Defining the operator $\beta_{\mathrm{eff}} = u(0)b_{\mathrm{S}} + v(0)b_{\mathrm{S}}^{\dagger}$, Eq. (4.61) can be brought in combination with Eq. (4.54) to the form

$$\tilde{H}_{\mathrm{eff}}^{(2)} = \epsilon\beta_{\mathrm{eff}}^{\dagger}\beta_{\mathrm{eff}} + E_0. \tag{4.62}$$

With the relation $|\phi_n(t_0)\rangle = |\tilde{n}\rangle$ and Eqns. (4.46) and (4.62) it follows that the $\beta_{\mathrm{H}}^{(0)}$ operator in Heisenberg picture equals the above defined effective quasiparticle annihilation operator

$$\beta_{\mathrm{H}}^{(0)} = \beta_{\mathrm{eff}}. \tag{4.63}$$

We furthermore are able to relate the effective Hamiltonian (4.61) to the static Hamiltonian $\mathcal{H}$ found in Heisenberg picture

$$\tilde{H}_{\mathrm{eff}}^{(2)} = \mathcal{H}. \tag{4.64}$$

This is a remarkable result, as it allows for a better interpretation of the quasiparticle eigenstates in Heisenberg picture. With Eqns. (4.63) and (4.64) we can interpret them as quasiparticles eigenstates of the effective Hamiltonian in a Floquet frame. This interesting fact comes due to the relation of Schrödinger and Heisenberg picture by the time-evolution operator. Note that with the time-evolution operator alone no transformation $U_{\mathrm{P}}(t)$ to Floquet frame can be calculated.

We discussed the general structure of the Bogoliubov transformation in Floquet picture, but one thing is still missing, namely to prove the existence of the Floquet vacuum state $|\phi_0(t)\rangle$. This proof is shown in the following subsection.

4.3.3. Floquet Vacuum State

In the previous subsection it was shown that the whole quasienergy spectrum can be generated inductively using the Floquet-Bogoliubov transformation, if the Floquet vacuum state is known as a base case. However, the existence of such a Floquet vacuum state remained as open question. In this section we proof that the Floquet vacuum state is given by the explicit wave function

$$|\psi_0(t)\rangle = \frac{e^{i\varphi(t)}}{\sqrt{|u(t)|}} \exp\left[-\frac{v(t)}{2u(t)}b^{\dagger}b^{\dagger}\right]|0\rangle. \tag{4.65}$$

Here $|0\rangle$ is the vacuum of the b operators and $\varphi(t)$ is a time-dependent phase that is not yet determined. At first, it is shown that state (4.65) fulfills the condition of a vacuum state at each time:

$$\beta(t)|\psi_0(t)\rangle = 0,\ \forall t. \tag{4.66}$$

This can be done by writing the state (4.65) as

$$|\psi_0(t)\rangle = \frac{e^{i\varphi(t)}}{\sqrt{|u(t)|}} \sum_{n=0}^{\infty} \left[-\frac{v(t)}{2u(t)}\right]^n \frac{\sqrt{2n!}}{n!}|2n\rangle, \tag{4.67}$$

with $|n\rangle = (b^\dagger)^n|0\rangle/\sqrt{n!}$. Using Eq. (4.67), Eq. (4.66) is evaluated as

$$\beta(t)|\psi_0(t)\rangle = \frac{e^{i\varphi(t)}}{\sqrt{|u(t)|}} \sum_{n=0}^{\infty} \left[-\frac{v(t)}{2u(t)}\right]^n \frac{\sqrt{2n!}}{n!}\sqrt{2n+1}\left[-\frac{v(t)}{2u(t)}2u(t)+v(t)\right]|2n+1\rangle. \tag{4.68}$$

The bracket on the right in Eq. (4.68) vanishes trivially for each $n \in \mathbb{N}$, it follows that Eq. (4.66) holds for each time t. Thus, state Eq. (4.65) follows the definition of a time-dependent vacuum state.

Similar to the static case it can be shown that the Floquet vacuum state can be normalized to one for each time $\langle\psi_0(t)|\psi_0(t)\rangle = 1$, if condition Eq. (4.39) holds. In the instability regions, however, it holds that $|u(t)| = |v(t)|$, where similar to the time-independent consideration the norm of the state (4.65) diverges. In this case the vacuum state (4.65) does not exist and a solution with a Floquet-Bogoliubov transformation is not possible. In the following we assume that state Eq. (4.65) exists.

At this point it is left to show that state (4.65) solves the Schrödinger equation with respect to Hamiltonian (4.33):

$$[H(t) - i\hbar\partial_t]|\psi_0(t)\rangle = 0, \tag{4.69}$$

and is of the form of a Floquet state given by Eq. (2.7). A necessary condition for this is that the time-dependent phase is of the form

$$\varphi(t) = -E_0 t/\hbar + \phi(t), \tag{4.70}$$

where E_0 denotes the quasienergy of the Floquet vacuum state and $\phi(t)$ is a time-periodic function with the same period T as the Hamiltonian. With the explicit form of state (4.65) and Hamiltonian (4.33), the Schrödinger equation (4.69) can be evaluated as

$$\begin{aligned} &\left\{-\frac{B(t)v(t)}{2u(t)} + \hbar\dot{\varphi}(t) + \frac{i\hbar}{4}\left[\frac{\dot{u}(t)}{u(t)} + \frac{\dot{u}(t)^*}{u(t)^*}\right]\right\}|\psi_0(t)\rangle \\ &+ \left[i\hbar\frac{\dot{v}(t)u(t) - \dot{u}(t)v(t)}{2u^2(t)} - \frac{A(t)v(t)}{u(t)} + \frac{Bv^2(t)}{2u^2(t)} + \frac{B}{2}\right] b^\dagger b^\dagger|\psi_0(t)\rangle = 0, \end{aligned} \tag{4.71}$$

where a dot denotes a derivative with respect to time. With the Floquet-Bogoliubov equation (4.38) it can be directly shown that the bracket in the second line of Eq. (4.71) vanishes, which is a requirement for the state (4.65) to solve the Schrödinger equation. Assuming that also the bracket in the first line of Eq. (4.71) vanishes, a condition for the time derivative of the phase $\varphi(t)$ can be found

$$-\dot{\varphi}(t) = \frac{\epsilon - A(t)}{2\hbar} + \frac{1}{2}\frac{d}{dt}\text{Im }\log[u(t)] \tag{4.72}$$

Using Eq. (4.70) the quasienergy is found by time averaging $E_0 = (\hbar/T)\int_0^T dt\ (-\dot{\varphi}(t))$. With the explicit expression (4.72) it reads

$$E_0 = \frac{\epsilon - \frac{1}{T}\int_0^T dt\ A(t)}{2} + \frac{\hbar\omega}{2}Q, \tag{4.73}$$

where the quantity Q gives a topological contribution to the quasienergy in the form of an integral of the time-derivative of the complex phase $\theta(t) = \text{Im }\log u(t)$:

$$Q = \frac{1}{2\pi}\int_0^T dt\ \frac{d}{dt}\theta(t). \tag{4.74}$$

Note that there are similarities between Eq. (4.73) and the corresponding time-independent result Eq. (4.31). Since $u(t)$ is time periodic, it follows that $\theta(T) = \theta(0) + m2\pi$ with $m \in \mathbb{Z}$. Thus Q is integer valued. The time-periodic part $\phi(t)$ of the phase is found by

$$\phi(t) = \frac{\mathcal{A}(t)}{2\hbar} + \Xi(t) + \phi_0, \tag{4.75}$$

where

$$\mathcal{A}(t) = \int_0^t dt'\ [A(t') - (1/T)\int_0^T dt''\ A(t'')], \tag{4.76a}$$

$$\Xi(t) = \int_0^t dt' \left[\frac{Q\omega}{2} - \frac{d}{dt'}\frac{\text{Im }\log u(t')}{2}\right] \tag{4.76b}$$

and ϕ_0 is an arbitrary phase. Note that for each time t the phase $\phi(t)$ as defined in Eq. (4.75) is real. Since $\Xi(t)$ is defined such that it is time-periodic $\Xi(T) = \Xi(0)$ it is easily shown that also $\phi(t)$ is time periodic. Further, Eqns. (4.73) and (4.75) remain invariant under the shift of the Floquet Brillouin zone of the parameters of the Floquet-Bogoliubov equation according to $\epsilon \to \epsilon - m\hbar\omega$, $u(t) \to u(t)e^{im\omega t}$, $v(t) \to v(t)e^{im\omega t}$.

With this thoughts the proof is finished. We have indeed managed to find a state which simultaneously obeys the definition of a vacuum state given by Eq. (4.66) and solves the Floquet equation with Hamiltonian (4.33). This is a key result, as it serves as the base case for the inductive generation of the quasienergy spectrum in sec. (4.3.2). If the Floquet vacuum state (4.65) exists, the whole quasienergy spectrum can be found with the Floquet-Bogoliubov transformation.

4.4. Solution Method of the Floquet-Bogoliubov Equations: Stability and Instability Regions

In this section a numerical procure for finding the parameters $u(t)$, $v(t)$ and the quasienergy ϵ of the Bogoliubov quasiparticles is presented. At first, Eq. (4.38) is Fourier transformed. Like in chapter 2,

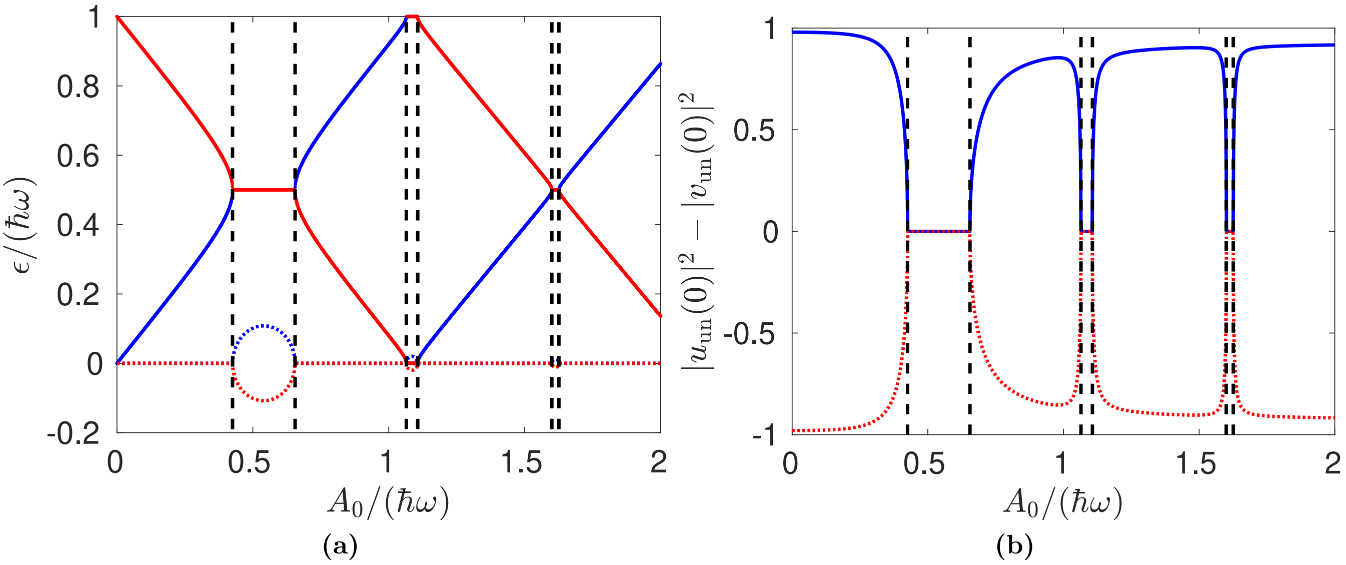

Figure 4.2.: (a) Real part (solid) and imaginary part (dotted) of the quasienergies ϵ calculated by Eq. (4.77). (b) Canonical condition $|u_{\rm un}(0)|^2 - |v_{\rm un}(0)|^2$ of the unnormalized Bogoliubov parameters at initial time $t = 0$. Black dashed lines mark the border of the instability regions. The blue solution obeys $|u_{\rm un}(0)|^2 - |v_{\rm un}(0)|^2 > 0$ in the stability regions and Im $\epsilon > 0$ in the instability regions, while the red solution has correspondingly $|u_{\rm un}(0)|^2 - |v_{\rm un}(0)|^2 < 0$ and Im $\epsilon < 0$. The parameters are $A(t) = A_0$ and $B(t) = B_0 + 2B_1 \cos(\omega t)$ with $B_0 = B_1 = 0.2\ A_0$.

the Fourier transform of a time-periodic quantity $x(t)$ is defined as $x^{(n)} = (1/T) \int_0^T dt\ e^{in\omega t} x(t),\ n \in \mathbb{Z}$. Using the Fourier transformation, Eq. (4.38) can be written as an eigenvalue equation of the Floquet matrix, c.f. Eqns. (2.18) and (2.19):

$$\sum_{l=-\infty}^{\infty} \begin{pmatrix} -A^{(n-l)} & B^{(n-l)} \\ -B^{(n-l)} & A^{(n-l)} \end{pmatrix} \begin{pmatrix} u^{(l)} \\ v^{(l)} \end{pmatrix} - n\hbar\omega \begin{pmatrix} u^{(n)} \\ v^{(n)} \end{pmatrix} = -\epsilon \begin{pmatrix} u^{(n)} \\ v^{(n)} \end{pmatrix}. \tag{4.77}$$

The solution of Eq. (4.77) yields the Fourier coefficients of the parameters of the Floquet-Bogoliubov transformation as well as the negative quasienergies of the Bogoliubov quasiparticles. For a numerical solution, Eq. (4.77) is truncated in Fourier space following the general procedure described in Subec. (2.2.1). Note that Eq. (4.77) describes a non-hermitian eigenvalue problem, a theory of non-hermitian Floquet Hamiltonians is presented in Appendix C. For this setting it is important to note that a Floquet solution of the form (2.7) is still possible in the most cases, but the quasienergies may become complex. However, the Floquet Brillouin zone structure $\epsilon_{\alpha,m} = \epsilon_\alpha + m\hbar\omega$ is still valid. As Eq. (4.38) describes a two-level system, there are two quasienergies in each Floquet Brillouin zone. We choose the interval $[0, \omega[$ as first Floquet Brillouin zone.

In Fig. 4.2 (a) the quasienergies in the first Floquet Brillouin zone, found by the numeric solution of Eq. (4.77), are shown. There are regions where both quasienergies are real. In these regions there are two solutions, one with a positive and one with a negative slope. A real quasienergy yields Floquet states with a motion that is bounded for all times as $|e^{-i\epsilon t/\hbar}| = 1$. Thus a solution with a real quasienergy is termed as stable solution, the parameter region with stable solutions is called stability region. In the other parameter regions, the real part of both quasienergies equals $n\hbar\omega/2,\ n \in \mathbb{Z}$ while the imaginary part is non-zero. There is one solution with positive and one with negative imaginary part. The Floquet dynamics of these solutions is characterized by the complex exponential function $e^{-i\epsilon t/\hbar} = e^{-i\text{Re }\epsilon t/\hbar} \times e^{\text{Im }\epsilon t/\hbar}$. The solution with a quasienergy with negative imaginary part corresponds to an exponentially decaying solution while the amplitude of the solution with positive imaginary part increases exponentially. This exponential increase of the amplitude over time corresponds to the behavior of an unstable solution [194, 195]. Thus, the regions with complex quasienergies are termed as instability regions. Note that at the boundary of stability and instability regions where the quasienergy equals an integer multiple of $\hbar\omega/2$ solely one periodic solution may exist, c.f. Ince's theorem for the Mathieu equation [196, 197]. Since these special solutions only occur at a null set in parameter space, a detailed discussion is left to future works.

In order to choose which of the two solutions in the first Floquet Brillouin zone is used as parameters in the Floquet-Bogoliubov transformation, we calculate for both solutions the canonical constraint $|u_{\text{un}}(0)|^2 - |v_{\text{un}}(0)|^2$ for the unnormalized Bogoliubov parameters at initial time. These unnormalized parameters are called unnormalized, as $|u_{\text{un}}(0)|^2 - |v_{\text{un}}(0)|^2$ is not normalized to plus or minus one. The numerical solution of Eq. (4.77) yields the unnormalized parameters as intrinsic result, since the numerical eigenvalue solver normalizes the states such that $(1/T)\int_0^T dt\ [|u_{\text{un}}(t)|^2 + |v_{\text{un}}(t)|^2] = 1$. In Fig. 4.2 (b) the canonic constraint $|u_{\text{un}}(0)|^2 - |v_{\text{un}}(0)|^2$ of the unnormalized Bogoliubov parameters at initial time is shown. In the stability region there exists a solution with $|u_{\text{un}}(0)|^2 - |v_{\text{un}}(0)|^2 > 0$ and a solution with $|u_{\text{un}}(0)|^2 - |v_{\text{un}}(0)|^2 < 0$ while in the instability region it holds that $|u_{\text{un}}(0)|^2 - |v_{\text{un}}(0)|^2 = 0$. Numeric values of $|u_{\text{un}}(0)|^2 - |v_{\text{un}}(0)|^2$ with modulus below a certain threshold are treated as zero by the numerical procedure.

We first discuss the stability regions. In order to find parameters of the Floquet-Bogoliubov equation that fulfill condition (4.39), the solution with $|u_{\text{un}}(0)|^2 - |v_{\text{un}}(0)|^2 > 0$ is chosen and the parameters are normalized according to

$$u(t) = u_{\text{un}}(t)/\sqrt{|u_{\text{un}}(0)|^2 - |v_{\text{un}}(0)|^2},\ v(t) = v_{\text{un}}(t)/\sqrt{|u_{\text{un}}(0)|^2 - |v_{\text{un}}(0)|^2}. \tag{4.78}$$

The paramters in Eq. (4.78) obey $|u(0)|^2 - |v(0)|^2 = 1$, but is this condition fulfilled for all times as required by Eq. (4.39)? In order to find out, the derivative $\frac{d}{dt}[|u(t)|^2 - |v(t)|^2]$ is calculated, which yields with the use of Eq. (4.38) the following differential equation

$$\frac{d}{dt}[|u(t)|^2 - |v(t)|^2] = 2\frac{\text{Im }\ \epsilon}{\hbar}[|u(t)|^2 - |v(t)|^2]. \tag{4.79}$$

In the stability regions the imaginary part of the quasienergies vanishes $\text{Im }\ \epsilon = 0$, such that with Eq. (4.79) it follows that $|u(t)|^2 - |v(t)|^2$ is constant in time. As a result Eq. (4.39) is fulfilled for all times. We found a valid Floquet-Bogoliubov transformation in the stability regions and are able to calculate properties of the Floquet-Bogoliubov eigenstates.

In the instability regions the situation is different. Here $|u(0)|^2 - |v(0)|^2 = 0$, with Eq. (4.79) it follows with Eq. (4.79) that $|u(t)|^2 - |v(t)|^2 = 0$ for all times. Thus in the instability regions both solutions do not fulfill Eq. (4.39). As a result the Bogoliubov operators defined by Eq. (4.34) do not obey bosonic commutation relations and the vacuum state defined by Eq. (4.65) does not exist.

In the next section physically relevant expectation values are calculated using the Floquet-Bogoliubov transformation. In addition, we give physical insight in the occurrence of the instability regions.

4.5. Expectation Values and Stability Charts

In this subsection expectation values are calculated and stability charts are presented. In particular, we are interested in the density of excited states of the Floquet vacuum state

$$n(t) = \langle \phi_0(t) | b^\dagger b | \phi_0(t) \rangle, \tag{4.80}$$

with $|\phi_0(t)\rangle$ as in Eq. (4.65). Since our theory involved both Heisenberg and Schrödinger picture, in the following we show that Eq. (4.80) can be evaluated in both pictures equally.

The first way starts with transforming Eq. (4.80) to Heisenberg picture

$$n(t) = \langle \tilde{0} | b_{\mathrm{H}}^\dagger(t) b_{\mathrm{H}}(t) | \tilde{0} \rangle. \tag{4.81}$$

Equation (4.81) is evalutated further using Eq. (4.40) and the canonic commutation relation of the β_{H} / $\beta_{\mathrm{H}}^\dagger$ operators. As result we get

$$n(t) = |v(t)|^2. \tag{4.82}$$

The second way evaluates Eq. (4.80) in Schödinger picture with the explicit form of the Floquet vacuum state given by Eq. (4.65). With the definition $F(t) = -v(t)/[2u(t)]$ and the fact that $[b^\dagger b, \exp[-F(t) b^\dagger b^\dagger]] = -2F(t) b^\dagger b^\dagger \exp[-F(t) b^\dagger b^\dagger]$, Eq. (4.80) becomes

$$n(t) = \frac{1}{|u(t)|} \langle 0 | \exp[-F^*(t) bb][-2F(t)] b^\dagger b^\dagger \exp[-F(t) b^\dagger b^\dagger] | 0 \rangle \tag{4.83}$$

Equation (4.83) is further simplified by noting that $[-2F(t)] b^\dagger b^\dagger \exp[-F(t) b^\dagger b^\dagger] = 2F(t) \frac{\partial}{\partial F} \exp[-F(t) b^\dagger b^\dagger]$. With $\langle 0 | \exp[-F^*(t) bb] \exp[-F(t) b^\dagger b^\dagger] | 0 \rangle = 1/\sqrt{1 - 4F^*(t) F(t)}$ it follows

$$n(t) = \frac{2F(t)}{|u(t)|} \frac{\partial}{\partial F} \left(\frac{1}{\sqrt{1 - 4F(t) F^*(t)}} \right). \tag{4.84}$$

By performing the derivative in Eq. (4.84), Eq. (4.82) is found as a result. This shows that the expectation value (4.80) can be evaluated both in Heisenberg and Schrödinger picture and that the two methods indeed yield the same result.

Another quantity of interest is the expectation value of the Hamiltonian

$$E(t) = \langle \phi_0(t) | H(t) | \phi_0(t) \rangle. \tag{4.85}$$

The observable (4.85) measures the energy of the Floquet vacuum state. In comparison to the quasienergy E_0, which determines the linear phase evolution, the expectation value Eq. (4.85) measures the physical energy. Due to the time dependence in the system the energy expectation value

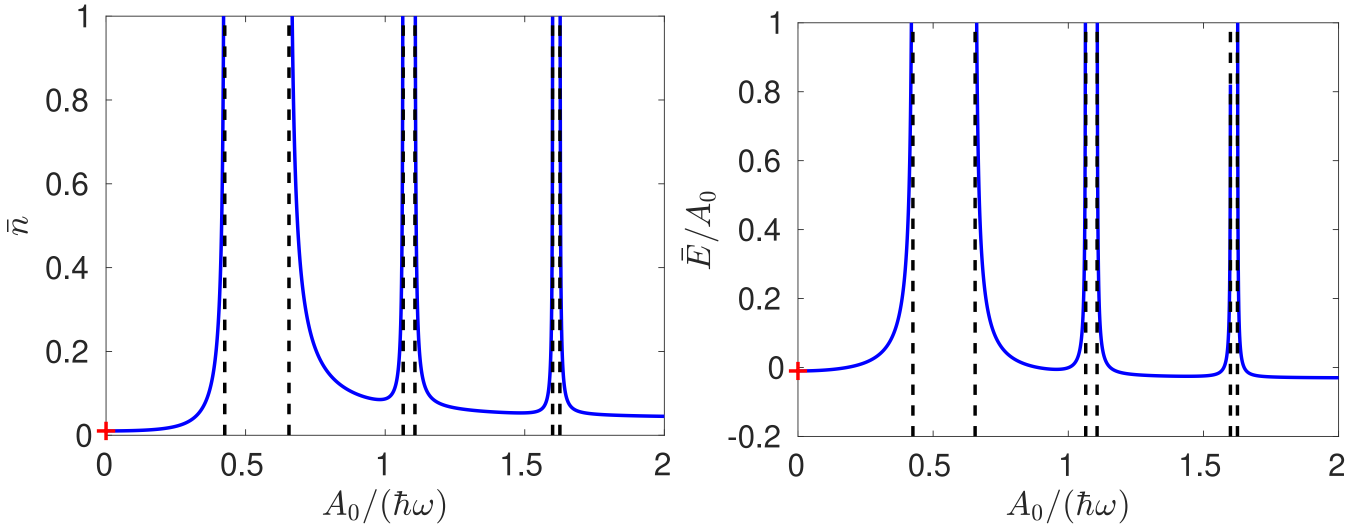

(a) **(b)**

Figure 4.3.: (a) Time average of the density of excitations $\bar{n}$, (b) Time average of the energy expectation value of the Floquet vacuum state $\bar{E}$. The parameters are $A(t) = A_0$ and $B(t) = B_0 + 2B_1 \cos(\omega t)$ with $B_0 = B_1 = 0.2\ A_0$. Black dashed lines mark the border of the instability regions, the red cross marks the static limits.

(4.85) is also time dependent. For finding an explicit formula, Eq. (4.85) is transformed into the Heisenberg picture and evaluated using Eq. (4.40). This calculation yields

$$E(t) = A(t)|v(t)|^2 - \frac{B(t)}{2}[u(t)v^*(t) + v(t)u^*(t)]. \tag{4.86}$$

In the following we denote time-averaged quantities by a bar $\bar{x} = (1/T)\int_0^T dt\ x(t)$ and use the Fourier coefficient notation of Eq. (4.18). In Fig. 4.3 the time-averaged quantities $\bar{n}$ and $\bar{E}$ are shown. At small $A_0/(\hbar\omega)$ the value of $\bar{n}$ and $\bar{E}$ converges to the static limit. This is directly visible, as the case $A_0/(\hbar\omega) \to 0$ corresponds to the high frequency limit, in which the effective Hamiltonian can be approximated by a high frequency expansion, such as Eq. (2.15a). With Eq. (2.15a) the effective Hamiltonian is in zeroth order given by the zeroth Fourier component of the Hamiltonian (4.33), which corresponds to the undriven part of Hamiltonian. Thus, the limit of $A_0/(\hbar\omega) \to 0$, under the assumption that $y = B_0/A_0$ is constant as in Fig. 4.3, can be found with the static case: The average number of excitation goes to $\bar{n} \to (1 - \sqrt{1-y^2})/(2\sqrt{1-y^2})$ and the average energy is given by $\bar{E}/A_0 \to (\sqrt{1-y^2} - 1)/2$. Near the instability regions a totally different behavior is visible, here both $\bar{n}$ and $\bar{E}$ show divergences. This gives physical insight why the Floquet-Bogoliubov state does not exist inside the instability regions: When approaching an instability region both average density of excitations and average energy of the Floquet vacuum state diverges. In the ultimate limit the Floquet vacuum state would thus correspond to a state of infinite energy, which is of course not physically realizable. In addition, the average number of bosonic excitations diverges. We will find that the instability regions are linked to the parametric excitation of pairs of bosons, which is generated by the time-dependent $b^\dagger b^\dagger$ term in the Hamiltonian. A possible Floquet state that is describing this process would consist of an infinite amount of bosons, as indicated by the divergence in $\bar{n}$. This again signalizes that a Floquet solution is unphysical in the instability regions. However,

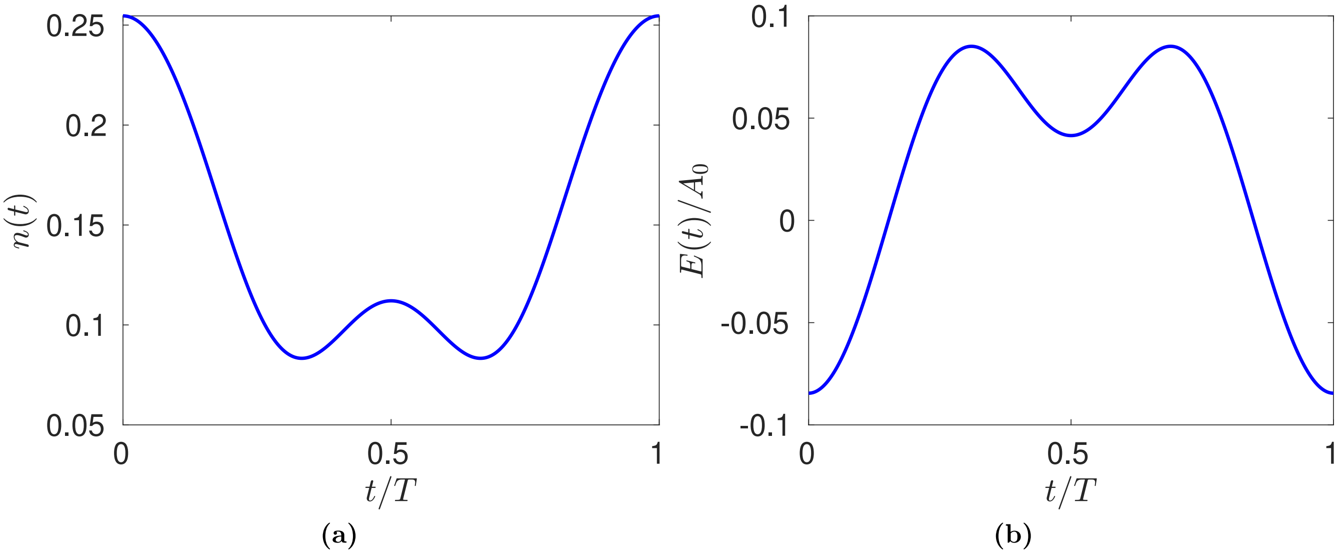

(a) **(b)**

Figure 4.4.: Time dependence of (a): $n(t)$, (b): $E(t)$ for $A(t)/(\hbar\omega) = 0.8$ and $B(t) = 0.2\ A_0 \times (1 + 2\cos(\omega t))$.

it will be shown in Sec. 4.6 that with proper regularization it is possible to find the Floquet vacuum state inside the instability regions.

Figure 4.4 depicts the time-dependent quantities $n(t)$ and $E(t)$. Note, that both expectation values are time-periodic with the same period as the vacuum Floquet mode $|\phi_0(t)\rangle$, thus we restrict to show the results for one period only. Both expectation values oscillate around their average, while the largest contribution is given by the first harmonic. As both expectation values are given by a non-linear function of the Bogoliubov parameters $u(t)$ and $v(t)$, also higher harmonics are visible in Fig. 4.4. Note that the negative energies in Eq. (4.4) come in due to a negative ground state energy, as in Eq. (4.31).

Figure 4.5 displays the quasienergy of the Floquet-Bogoliubov quasiparticles and the average density of excited states $\bar{n}$ in dependence of B_0. The quasienergy shows a behavior similar to the ones of the static Bogoliubov particles that is displayed in Fig. 4.1 (a), but the curve in the driven case is fitted into the first Floquet Brillouin zone. In Fig. 4.5 two instability regions can be spotted. The instability region near $B_0/A_0 \approx 0.6$ is induced by the periodic drive, the region for $B_0/A_0 >\approx 0.8$ corresponds to the case $B_0/A_0 > 1$ in the static solution, where the Bogoliubov transformation fails to diagonalize the Hamiltonian. This demonstrates that the periodic drive can also shift the boundaries of instability regions.

In order to get a deeper physical understanding of the occurrence of the instability regions that are induced by the time-periodic drive, we appeal to special parameters that allow to strictly relate the physics of the instability regions to a parametric resonance occurring in the Mathieu equation.

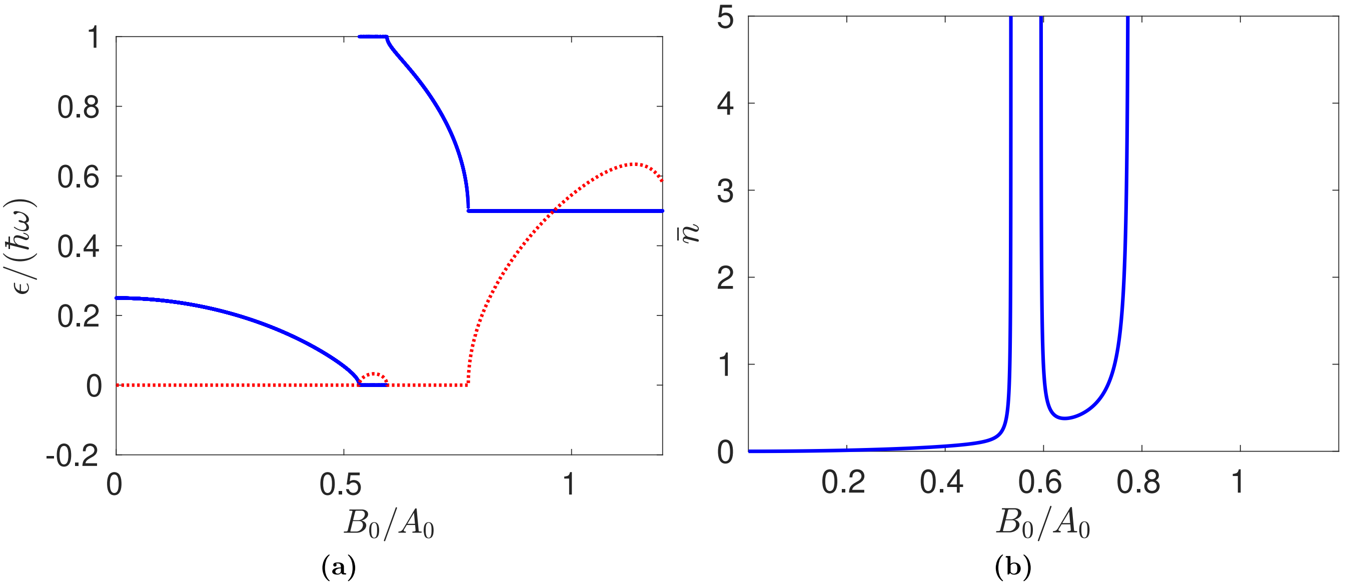

Figure 4.5.: (a): Real (blue) and imaginary (red) part of the quasienergy of the Floquet-Bogoliubov particles, (b): time average of the density of excitations with the parameters $A(t) = A_0$, $B(t) = B_0 + 0.2\ B_0 \cos(\omega t)$ and $\hbar\omega = 0.8\ A_0$. In the instability regions the solution with positive imaginary part is chosen.

For this we assume that both $A(t)$ and $B(t)$ are driven sinusoidally with the same strength A_{AC}:

$$A(t) = A_0 + A_{\text{AC}} \cos(\omega t), \tag{4.87a}$$

$$B(t) = B_0 + A_{\text{AC}} \cos(\omega t). \tag{4.87b}$$

Similar to Ref. [104], we introduce new transformation parameters $\tilde{u}(t) = e^{-i\epsilon t/\hbar} u(t)$, $\tilde{v}(t) = e^{-i\epsilon t/\hbar} v(t)$ that obey the following equations of motion

$$i\hbar \frac{d}{dt} \tilde{u}(t) = -A(t)\tilde{u}(t) + B(t)\tilde{v}(t), \tag{4.88a}$$

$$i\hbar \frac{d}{dt} \tilde{v}(t) = A(t)\tilde{v}(t) - B(t)\tilde{u}(t). \tag{4.88b}$$

The variables $f_\pm(t) = \tilde{u}(t) + \tilde{v}(t)$ are introduced. Due to the fact that $A(t) - B(t) = A_0 - B_0$ is constant in time, the time-dependence of $f_-(t)$ is determined by a Mathieu equation

$$\ddot{f}_-(t) + \frac{E_{\text{st}}^2}{\hbar^2} \left[1 + \frac{2A_{\text{AC}}}{A_0 + B_0} \cos(\omega t) \right] f_-(t) = 0, \tag{4.89}$$

where $E_{\text{st}} = \sqrt{A_0^2 - B_0^2}$ is the eigenenergy of the static Bogoliubov particles. The other variable $f_+(t)$ is determined by $i\hbar \dot{f}_-(t) = (A_0 - B_0) f_+(t)$. An analytical Floquet solution can be generated from Eq. (4.89) with a method developed by our collaborator S. Fazzini. The general solution of Eq. (4.89) is given by [104]:

$$f_-(t) = c_1 \mathcal{C}(a, p, \tau) + c_2 \mathcal{S}(a, p, \tau) \tag{4.90}$$

with the parameters

$$a = \frac{4E_{\text{st}}^2}{\hbar^2\omega^2},\ p = -\frac{4A_{\text{AC}}E_{\text{st}}^2}{\hbar^2\omega^2(A_0+B_0)},\ \tau = \frac{\omega t}{2}. \tag{4.91}$$

In Eq. (4.90), $\mathcal{C}(a,p,\tau)$ and $\mathcal{S}(a,p,\tau)$ are even and odd Mathieu functions that are normalized such that $\mathcal{C}(a,p,0) = \mathcal{S}(a,p,\pi) = 1$ while c_1, c_2 are parameters that are completely determined by requiring that the solution is of Floquet form (2.7) and the canonic condition Eq. (4.39) is fulfilled [104]. The parameter ϵ is determined the formula [104]

$$\epsilon = \hbar \times \arccos[\mathcal{C}(a,p,\pi)]/T. \tag{4.92}$$

Equation (4.92) allows for the analytic calculation of the quasienergies in the special case of the driving scheme Eq. (4.87). This is an remarkable result, as we will see later that it can be used to find an analytic solution of a periodically driven many-body problem [104].

In the following we focus on the stability of the solution. With Eq. (4.89) stability and instability regions are determined by the famous stability charts of the Mathieu equation [194,195]. This is an important result, since it allows to relate the instability regions that are induced by the drive to the well-known phenomenon of a parametric resonance in a mathematically concise way. Further physical understanding can be gained in the case of weak driving where it is known that the Mathieu equation shows a parametric resonance if the following condition holds [194]

$$\frac{E_{\text{st}}}{\hbar\omega} = \frac{n}{2},\ n \in \mathbb{N}. \tag{4.93}$$

In the setting of Hamiltonian (4.33) condition (4.93) corresponds to the parametric excitation of a pair of bosons by n quanta of the drive. This process is induced by a time-dependent parameter in the off-diagonal term $b^\dagger b^\dagger + bb$.

In Fig. 4.6 (a) the stability chart is shown for the case of $B_0 = 0$. Here it holds that $E_{\text{st}} = A_0$, for small A_{AC}/A_0 the instability tongues reach the x axis at integer multiples of $A_0/(2\hbar\omega)$ as predicted by Eq. (4.93). For increasing driving strength A_{AC} the instability regions become broader such that they dominate for large values of A_{AC}/A_0. However, in the high frequency limit $A_0/(\hbar\omega) \ll 1$ the system remains stable even for large A_{AC}/A_0. Figure 4.6 (b) shows the case of a non-vanishing B_0 with a weak driving strength A_{AC}. The condition of the parametric resonance Eq. (4.93) determines a family of curves in the B_0-A_0 plane

$$\frac{B_0}{\hbar\omega} = \sqrt{\left(\frac{A_0}{\hbar\omega}\right)^2 - \frac{n^2}{4}}, n \in \mathbb{N}. \tag{4.94}$$

The course of the instability regions in Fig. 4.6 (b) is for small B_0/A_0 in good agreement with the curves defined in Eq. (4.94). For larger B_0/A_0 the curves lie for the resonances with $n > 1$ outside the instability regions, but they are still together within a reasonable range. This visually demonstrates that the physics of the instability regions is governed by the parametric excitation of pairs of bosons. The small shift of instability regions and Eq. (4.94) for larger B_0/A_0 is interpreted as the dressing of the boson energy in Eq. (4.93), in analogy to the Floquet-Feshbach resonance theory, where the resonance position shifts due to a dressing of the bound state by the periodic drive. The broadening

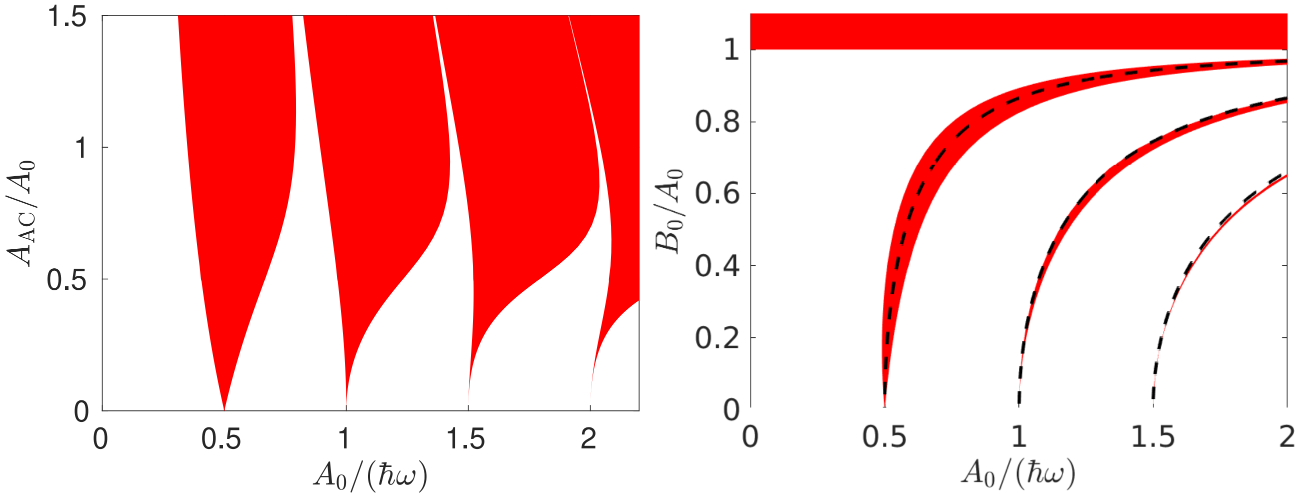

(a) **(b)**

Figure 4.6.: Stability chart with parameters according to Eq. (4.87) calculated with the numerical procedure described in Sec. 4.4. (a) $B_0 = 0$, (b) $A_{\mathrm{AC}} = 0.5\ B_0$. With areas mark stability regions, red areas mark the instability regions. Black dashed lines mark the condition (4.93).

of the instability regions with increasing B_0 is related to the fact that the driving strength A_{AC} is increases with B_0. For increasing n the instability regions get thinner. This behavior is generic since in general processes that involve a higher number of drive quanta are weaker than the corresponding first order transitions. For values above $B_0/A_0 = 1$ also no Floquet-Bogoliubov solution exists. This behavior corresponds to the static case Eq (4.19), where the same condition determines whether a Bogoliubov solution exists or not.

Figure 4.7 shows stability charts for a general harmonic driving of the parameters $A(t)$, $B(t)$. In Fig. 4.7 (a), the case where only $B(t)$ is modulated sinusoidally, is displayed. We choose $A(t) = A_0$ and $B(t) = B_0(1 + 2\cos(\omega t))$. This choice includes the case that is shown in Figs. 4.2 and 4.3. At small fractions B_0/A_0 there are stable solutions for nearly all values of $A_0/(\hbar\omega)$. Tongues of instability regions reach the A_0-axis at integer multiples of $A_0/(2\hbar\omega)$ as predicted by Eq. (4.93). For increasing ratio B_0/A_0 the instability regions broaden and are shifted to larger A_0. At a large B_0/A_0 the instability regions extend to a vast parameter region. Only in the high-frequency limit $A_0/(\hbar\omega) \to 0$ the system remains stable if $B_0 < A_0$. In the opposite case $A_0 < B_0$ the system is unstable for $A_0/(\hbar\omega) \to 0$. This behavior is directly linked to that static case Eq. (4.19), where for $A_0 < B_0$ that Bogoliubov transformation fails to diagonalize the Hamiltonian.

In Fig. 4.7 (b) $A(t)$ is modulated time-periodically according to $A(t) = A_0 + 2A_1\cos(\omega t)$ while B is kept constant at $B(t) = 0.4\ A_0$. Here a completely different structure of the instability regions compared to Fig. 4.7 (a) is visible, which raises multiple questions. First one may ask why a parametric resonance is possible at all, since $B(t)$ is not time-dependent. Second, it is of interest to find an explanation of the location of the instability regions for the examined parameter range. Third it

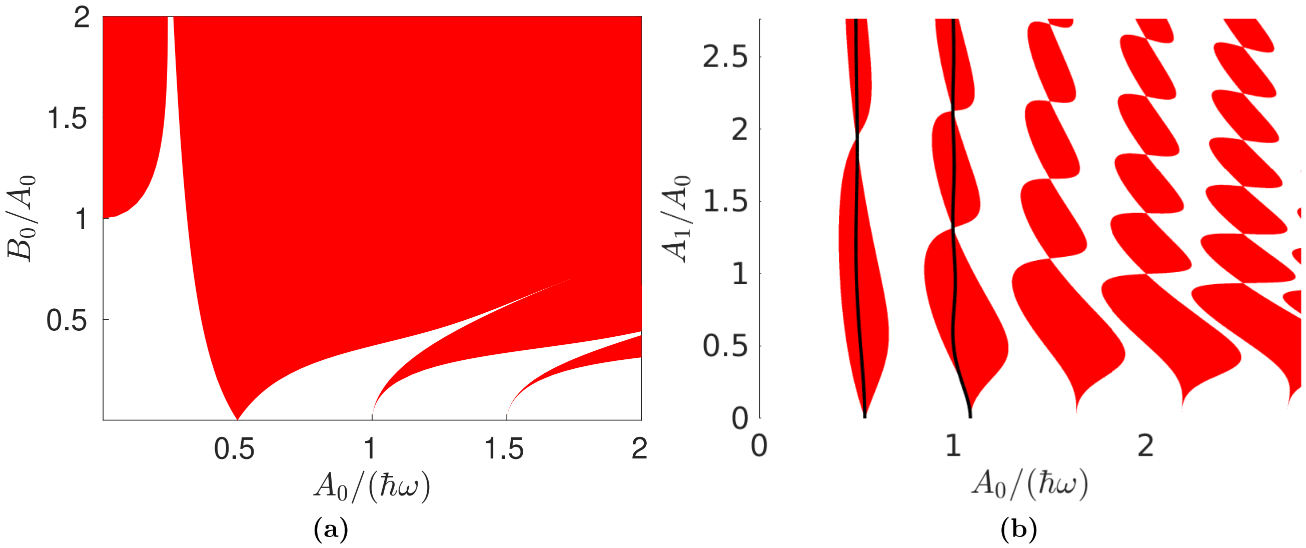

Figure 4.7.: Stability chart for (a) $A(t) = A_0$, $B(t) = B_0[1 + 2\cos(\omega t)]$, (b) $A(t) = A_0 + 2A_1\cos(\omega t)$, $B(t) = 0.4\,A_0$ calculated with the numerical procedure described in Sec. 4.4. Instability regions in red, stability regions in white. In black the condition $2E_{\text{eff}} = n\hbar\omega,\ n = 1, 2$ is shown.

is not clear why there the instability regions do not look like tongues but rather as lines of islands.

In order to answer these questions we perform the time-dependent gauge transformation

$$Q(t) = \exp[-iA_1\sin(\omega t)(b^\dagger b + bb^\dagger)], \tag{4.95}$$

which rotates Hamiltonian (4.33) to a frame in which the time-dependence of $A(t)$ is removed. In appendix E it is shown that Eq. (4.95) leads to the transformed Hamiltonian

$$\tilde{H} = A_0 b^\dagger b + \frac{B_0}{2}\left(\sum_{n=-\infty}^{\infty} \mathcal{J}_n[4A_1/(\hbar\omega)]e^{in\omega t}b^\dagger b^\dagger + h.c.\right) - \frac{2A_1\cos(\omega t)}{2}, \tag{4.96}$$

where $h.c.$ denotes the hermitian conjugate and $\mathcal{J}_n(x)$ the Bessel functions of the first kind. With the Eq. (4.96) we are able to answer all above questions. In the rotating frame it can be seen directly that the sinusoidal drive of $A(t)$ induces a time dependence in the off-diagonal part $b^\dagger b^\dagger + bb$ provided that $B_0 \neq 0$. Since the parametric excitation is traced back to a time-dependence in $B(t)$, this allows to explain why instability regions can be seen in Fig. 4.7 (b) at all. Further, the course of the instability regions can be made visible with Eq. (4.96). Performing the high-frequency expansion Eq. (2.15a) in zeroth order the drive renormalizes the energy of a Bogoliubov quasiparticle to

$$E_{\text{eff}} = \sqrt{A_0^2 - B_0^2\mathcal{J}_0^2[4A_1/(\hbar\omega)]}. \tag{4.97}$$

The black lines in Fig. (4.7) corresponds to the parametric excitation of bosons with the renormalized energy $2E_{\text{eff}} = n\hbar\omega,\ n = 1, 2$ and resemble quite accurate the actual course of the instability regions.

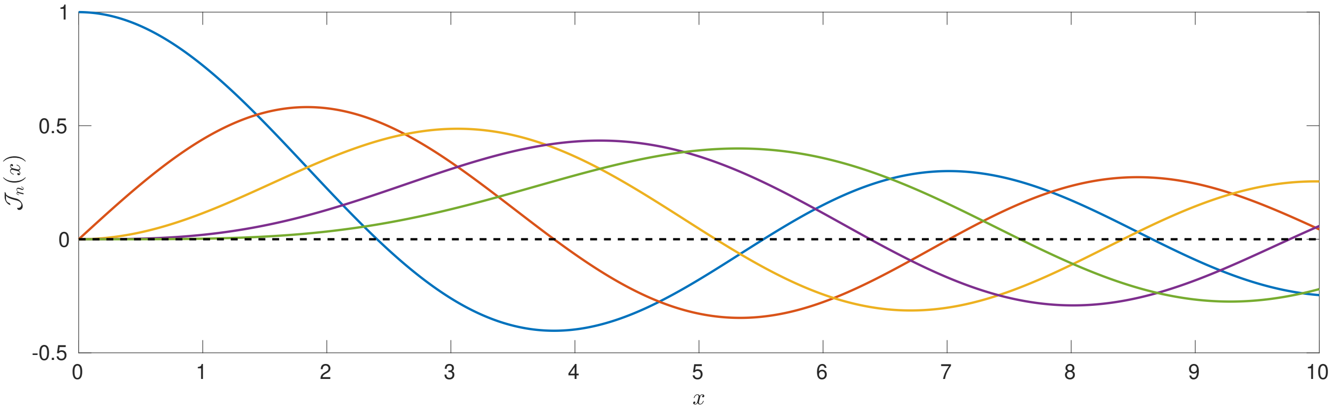

Figure 4.8.: Bessel functions of first kind $\mathcal{J}_n(x)$ in dependence of x: $\mathcal{J}_0(x)$ blue, $\mathcal{J}_1(x)$ red, $\mathcal{J}_2(x)$ yellow, $\mathcal{J}_3(x)$ purple, $\mathcal{J}_4(x)$ green. A black dashed line marks $y = 0$.

It is remarkable that even for parameters where the instability regions contract to a single point Eq. (4.97) serves as a good description. The fact that for large A_1/A_0 the instability islands are centered at $2A_0/(\hbar\omega) = n,\ n \in \mathbb{N}$ can be explained with the behavior of the Bessel function $\mathcal{J}_0(x)$ for large arguments. As shown in Fig. 4.8 the overall amplitude of the Bessel functions decays, while the ultimate limit $x \to \infty$ the Bessel function $\mathcal{J}_0(x)$ converges to zero. Thus, for large A_1/A_0 Eq. (4.97) converges to $E_{\text{eff}} \approx A_0$, such that the parametric resonance occurs at $2A_0/(\hbar\omega) = n,\ n \in \mathbb{N}$. Last but not least, the contraction of the instability regions to a single point can also be explained with the behavior of the Bessel functions. As shown in Fig. 4.8, the Bessel functions obey an oscillatory behavior that allows for the existence of zeros. For example, the location of the contraction point of the instability regions for the parametric resonance with $n = 1$ can be predicted by the zero of the first Bessel function $\mathcal{J}_1[4A_1/(\hbar\omega)] = 0$. This implies with $\mathcal{J}_1(x) = 0 \Leftrightarrow x = 0, \pm 3.83, \ldots$ a value of $A_1/A_0 \approx 1.91$ which fits quite well to Fig. 4.7 (b). For the discussion of other contraction points it might be necessary to further include the higher harmonics in Eq. (4.96). Having all these points in mind we conclude that Fig. 4.7 (b) contains rich Floquet physics, since the drive both induces parametric resonances and renormalizes the parameters such as the effective energy of the Bogoliubov particles Eq. (4.97) in the sense of Floquet engineering.

4.6. Regularization of Diverging Expectation Values by a Finite Lifetime

In the previous section it is found that the average density of excitations diverges in the instability regions. Here we discuss how these divergences can be regularized by introducing a finite lifetime of the original bosons. This lifetime τ_0 is introduced into Hamiltonian (4.33) as a time-independent imaginary part of $A(t)$:

$$\text{Im}\ A(t) = -\frac{\hbar}{\tau_0}. \tag{4.98}$$

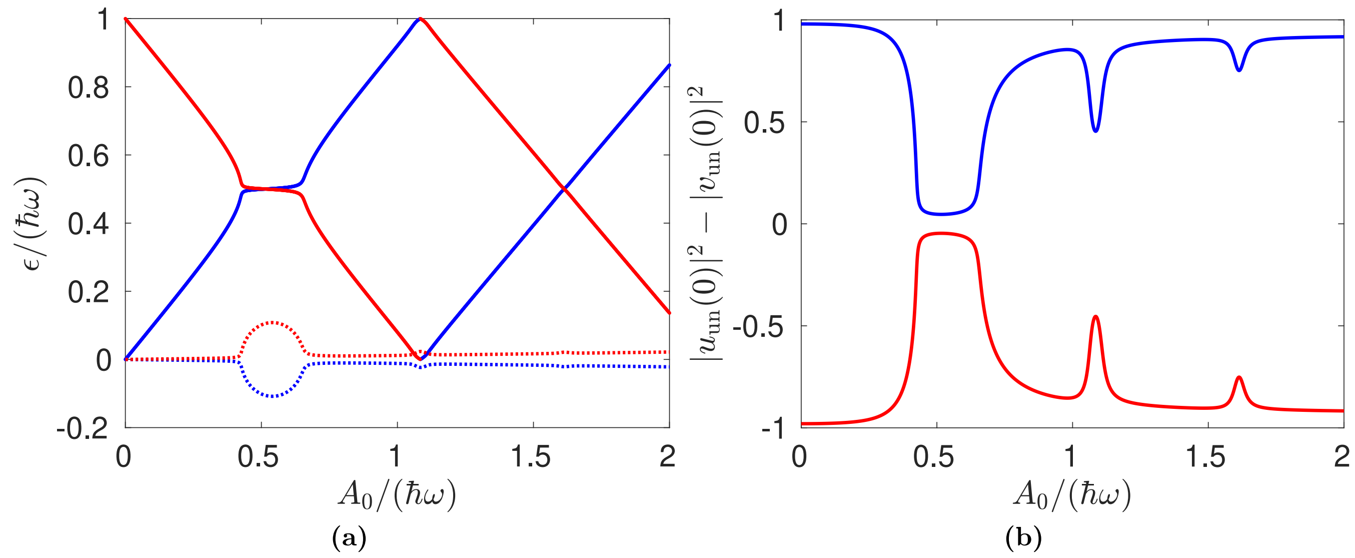

Figure 4.9.: Real part (solid) and imaginary part (dotted) of the quasienergies ϵ calculated by Eq. (4.77) with finite imaginary part $\hbar\tau_0 A_0 = 10^2$. (b) Canonic condition $|u_{\rm un}(0)|^2 - |v_{\rm un}(0)|^2$ of the unnormalized Bogoliubov parameters at initial time $t = 0$. The blue / red solution obey $|u_{\rm un}(0)|^2 - |v_{\rm un}(0)|^2 > 0$ / < 0. The parameters are $A(t) = A_0 - i\hbar/\tau_0$, $B(t) = 0.2\ A_0 + 0.4\ A_0 \cos(\omega t)$.

In the limit of $\tau_0 \to \infty$ the case that is discussed in the previous section is recovered. A finite lifetime τ_0 implies that Hamiltonian (4.33) becomes non-hermitian. Since it is involved to find a general solution of the non-hermitian problem and only expectation values of the Floquet vacuum state are of interest, we will here specialize on the Floquet vacuum state Eq. (4.65). It is easily verified that with finite τ_0 the Floquet vacuum state $|\phi_0(t)\rangle$ is still given by Eq. (4.65) and solves the Floquet equation $[H(t) - i\hbar\partial_t]|\phi_0(t)\rangle = E_0|\phi_0(t)\rangle$ with the quasienergy given by Eq. (4.73) and the phase given by Eq. (4.75), provided that the parameters $u(t)$, $v(t)$ obey Eq. (4.38) with a complex $A(t)$ with imaginary part given by Eq. (4.98). Condition Eq. (4.66) is unaffected at finite lifetime τ_0.

For the further discussion, the behavior of Eq. (4.38) is of relevance. In Fig. 4.9 (a) the quasienergies ϵ, that are found by the numerical solution of Eq. (4.77), are shown. A solution with positive slope of the real part and a solution with a negative exists. In the stability regions the finite lifetime has little effect, but in the instability regions it unpins the real part of ϵ from the value $n\hbar\omega/2$, $n \in \mathbb{Z}$ while the imaginary part of ϵ still shows finite values. The value of $|u_{\rm un}(0)|^2 - |v_{\rm un}(0)|^2$, i.e. the canonical constraint with parameters before the numerical normalization procedure, is displayed in Fig. 4.9 (b). Here a new behavior is present: Instead of having $|u_{\rm un}(0)|^2 - |v_{\rm un}(0)|^2 = 0$ in the instability regions, the numerical investigation reveals that the value of $|u_{\rm un}(0)|^2 - |v_{\rm un}(0)|^2$ never vanishes for any finite τ_0. This is the key result, since it allows to normalize $u(t)$ and $v(t)$ for each parameter value such that we now find a solution also in the instability regions. In the following the solution with $|u_{\rm un}(0)|^2 - |v_{\rm un}(0)|^2 > 0$ is chosen and the parameters are normalized according to Eq. (4.78). This finally normalizes the Floquet vacuum state such that $\langle\phi_0(t_0)|\phi_0(t_0)\rangle = 1$ where t_0 denotes the initial time. Note that due to the non-hermiticity of the Hamiltonian $H(t)$ the norm of the Floquet

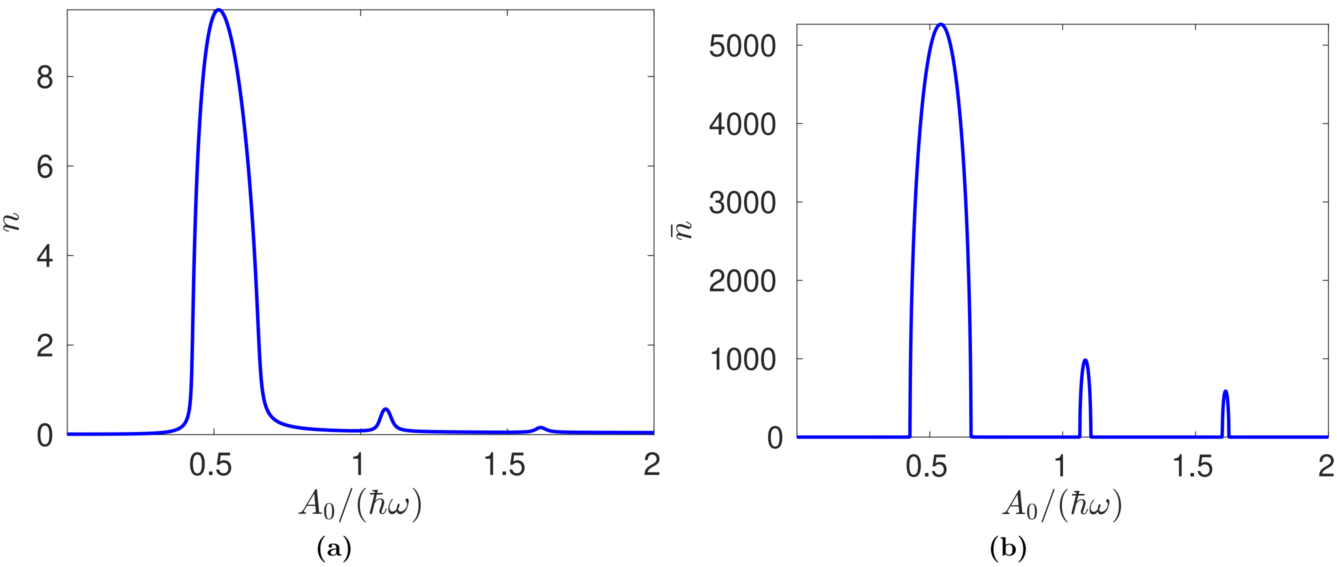

Figure 4.10.: Time-averaged number of excited states $\bar{n}$ with the parameters $A(t) = A_0 - i\hbar/\tau_0$, $B(t) = 0.2\ A_0 + 0.4\ A_0 \cos(\omega t)$ with (a) $\hbar/\tau_0 = 10^{-2}A_0$ and (b) $\hbar/\tau_0 = 10^{-5}A_0$.

vacuum state may be time-dependent [193, 198]. Let us here summarize the important points: Since the condition $|u(t)|^2 - |v(t)|^2 \neq 0$ holds for all parameter values with finite τ_0, we find that the Floquet vacuum state exists in both the stability and the instability regions. This is remarkable, as it enables to calculate expectation values of the Floquet vacuum state for general parameters. We will see that this procedure allows to define a Floquet steady state for the driven Tomonaga-Luttinger liquid at all. A more detailed analysis of the non-hermitian problem using biorthogonal quantum mechanics will be useful [98, 193], but exceeds the scope of this thesis.

The time average of the density of excitations is calculated with the use of Eq. (4.80) while the results are shown in Fig. 4.10. The divergences appearing for $\bar{n}$ in the undamped case turn here into large maxima. This shows that the Floquet vacuum state contains a finite number of excitations such that we are able to regularize the infinities occurring in the undamped case $\tau_0 = \infty$. As a key result we can now calculate expectation values in the whole parameter range. The height of the maxima in $\bar{n}$ increases with the lifetime τ_0 of the particles. In the limit of an infinite long lifetime $\tau_0 \to \infty$ the height of the maxima diverges. The maximum with lowest $A_0/(\hbar\omega)$ dominates all others, since it corresponds to the parametric excitation of pairs of bosons with one drive quantum. The more drive quanta are involved into a parametric resonance, the weaker is the response of the system. The finite height of the maximum of $\bar{n}$ is physically interpreted as an interplay of parametric excitation due to the drive and the losses induced by a finite boson lifetime which make the occupation of a highly excited state unfavorable.

In Fig. 4.11 the height of the first maximum, i.e. the one with the lowest value of $A_0/(\hbar\omega)$, is shown for a driving scheme of the form $A(t) = A_0 - i\hbar/\tau_0$, $B(t) = B_1[1 + 2\cos(\omega t)]$ with different parameter values in dependence of $B_1\tau_0/\hbar$. For a vast parameter range a linear dependence of the height of the first maximum on the variable $B_1\tau_0/\hbar$ is visible. This demonstrates that the height

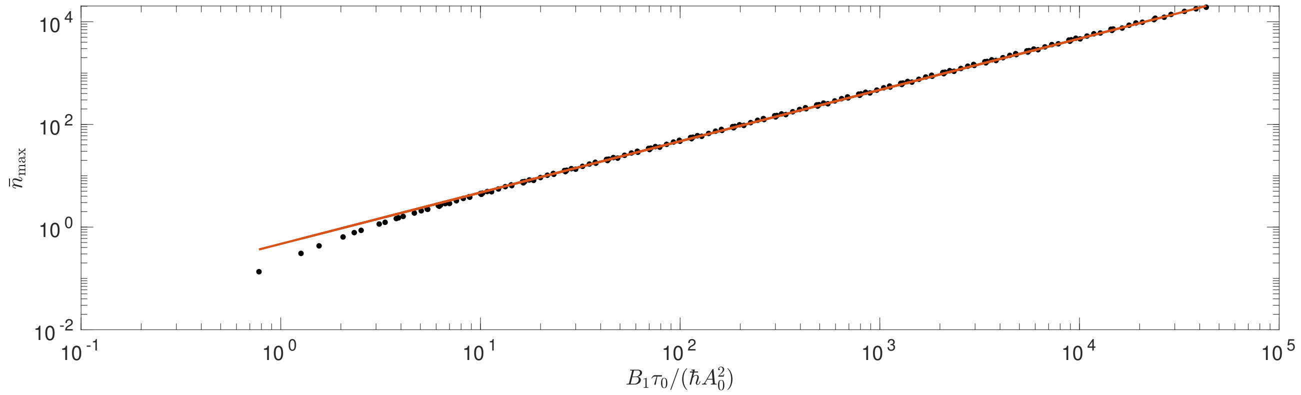

Figure 4.11.: Height of the first maximum plotted in dependence of $B_1\tau_0/\hbar$ given by black dots. With a numerical method the height of the first maxima is found for the driving scheme $A(t) = A_0 - i\hbar/\tau_0$, $B(t) = B_1[1 + 2\cos(\omega t)]$. The value of $\hbar\tau_0 A_0$ is chosen between 10^1 and 10^5, the value of B_1/A_0 between 0 and 0.7. The method uses an grid with adaptive step size such that the maxima are correctly resolved. The red line shows a fit with the function $y = 0.4707 \times B_1\tau_0/\hbar$.

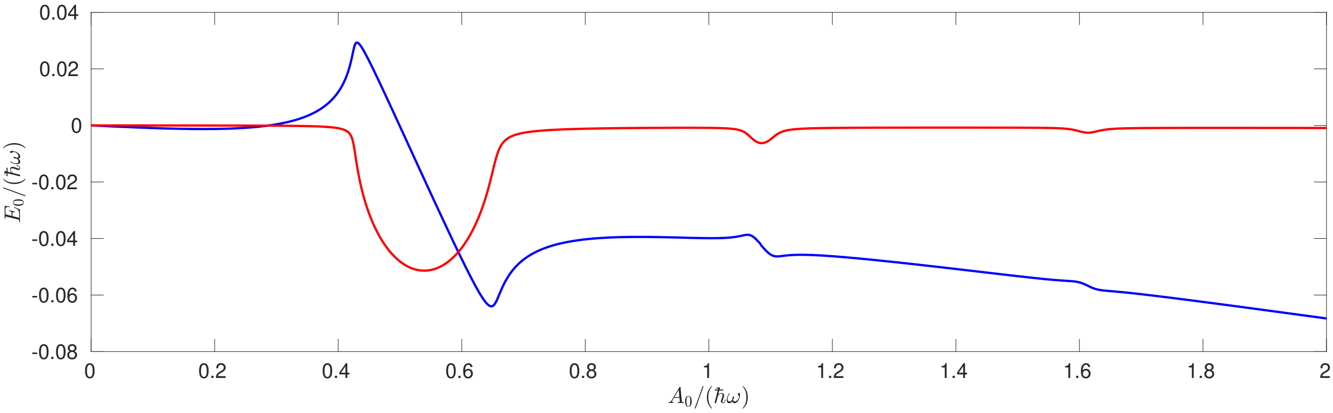

Figure 4.12.: Real (blue) and imaginary (red) part of the quasienergy E_0 of the Floquet vacuum state for the parameters of Fig. 4.9.

of the maximum can be tuned with the product of driving strength B_1 and boson lifetime τ_0 while both larger lifetime τ_0 and larger driving B_1 leads to a larger value of the maximum. In the first case the damping is minimized while the second case more energy is imparted into the system. Note that for small values of $B_1\tau_0/\hbar$ the system deviates from the linear dependence.

Up to now we calculated the time-average of the expectation value (4.80) using the time-periodic Floquet modes. As seen in Fig. 4.12, the quasienergy E_0 of the Floquet vacuum state becomes complex. The negative imaginary part of E_0 leads to an overall exponential decay of the wave function. This decay can be understood with Eq. (4.98), which implies that the dynamic phase $e^{-in\mathrm{Re}(A_0)t/\hbar}e^{-nt/\tau_0}$ of the states $|n\rangle = (b^\dagger)^n|0\rangle/\sqrt{n!}$ acquires an additional exponential decay with a lifetime given by $n\tau_0$. Thus, higher excited states are damped out fast. Such a situation assumes that the wave function leaves the considered harmonic oscillator mode and decays into a bath.

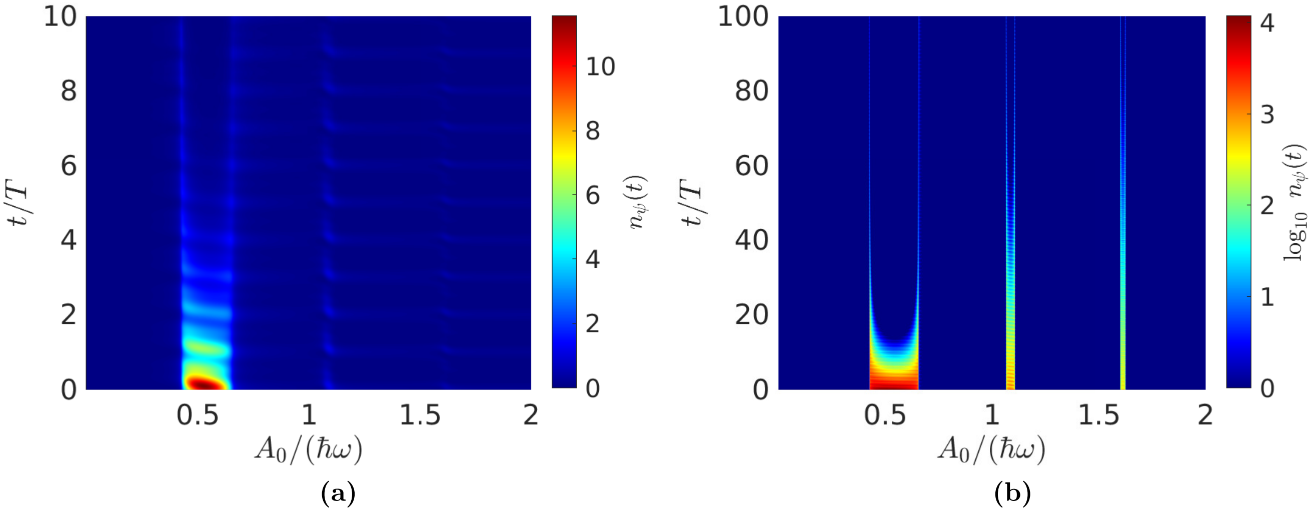

Figure 4.13.: Density of excitations $n_\psi(t)$ in dependence of A_0 with the parameters $A(t) = A_0 - i\hbar/\tau_0$, $B(t) = A_0(0.2+0.4\cos(\omega t))$. (a) shows $n_\psi(t)$ for $\hbar/\tau_0 = 10^{-2}\ A_0$, (b) shows $\log_{10}\ n_\psi(t)$ for $\hbar/\tau_0 = 10^{-5}\ A_0$. The color axis in (b) is limited to values of $1 \leq \log_{10}\ n_\psi(t)$.

In the following we take such a situation into account in our theory and calculate the expectation value of the Floquet vacuum state $|\psi_0(t)\rangle = e^{-iE_0t/\hbar}|\phi_0(t)\rangle$:

$$n_\psi(t) = \langle\psi_0(t)|b^\dagger b|\psi_0(t)\rangle = e^{2\mathrm{Im}\ E_0t/\hbar}\langle\phi_0(t)|b^\dagger b|\phi_0(t)\rangle. \tag{4.99}$$

The results of Eq. (4.99) are compared to a time-evolution of the non-hermitian Schrödinger equation. Finally, we construct from the results an interpretation in which the norm of the wave function does not decay and relate it to the results of Eq. (4.80).

Values for $n_\psi(t)$ are shown in Fig. 4.13 for two different boson lifetimes. At $t = 0$ there are large maxima as displayed in Fig. 4.10. As time evolves, these maxima decay, since the imaginary part of the quasienergy E_0 has a pronounced modulus in the instability regions. At late times, the values of $n_\psi(t)$ for parameters that lie at the border of the instability regions dominate. These solutions have little decay due to an almost vanishing imaginary part of the quasienergy E_0 while the expectation value $n_\psi(t)$ is still large. This result is clearly visible in Fig. 4.13 (b) where the density of excitations in the bulk of the instability regions decays in about 10 driving periods while at the border of the instability regions $n_\psi(t)$ remains high after even 100 periods.

At this point, we give a deeper interpretation how the finite lifetime as introduced in Eq. (4.98) influences the physics. For this task it is useful investigate the time-evolution of a quantum state and relate it to the Floquet steady states. We prepare the system at initial time in the vacuum state $|\psi(t=0)\rangle = |0\rangle$ of the b operator and calculate the time evolution by solving the Schrödinger equation numerically. In order to do so, the boson Hilbert space is cut off, such that $(b^\dagger)^{100} = 0$. The parameters are chosen to lie inside an instability region. Figure 4.14 (a) shows the time evolution of the number of excitations $|\langle n|\psi(t)\rangle|^2$, with $|n\rangle = (b^\dagger)^n|0\rangle/\sqrt{n!}$. Having the full probability at

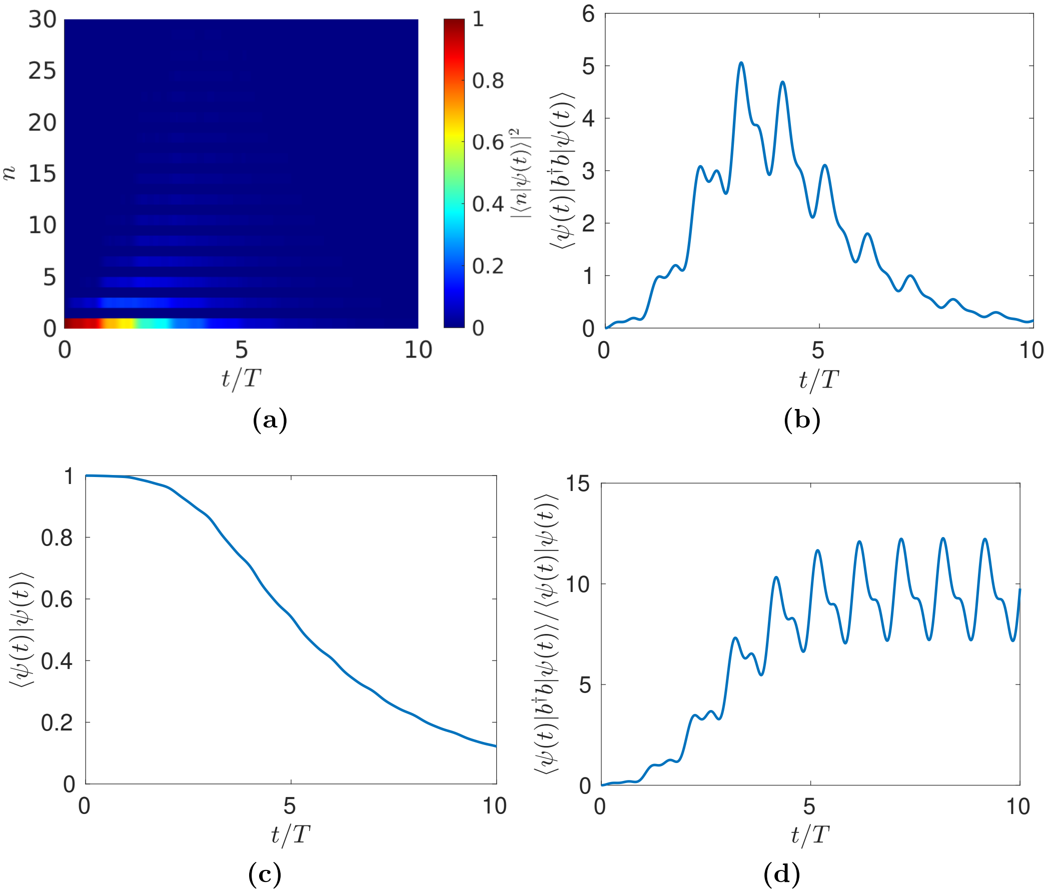

(a) **(b)**

(c) **(d)**

Figure 4.14.: Time evolution of the state $|\psi(t)\rangle$ with initial condition $|\psi(0)\rangle = |0\rangle$, where $b|0\rangle = 0$, for the parameters $A(t) = A_0 - i\hbar/\tau_0$, $B(t) = A_0(0.2 + 0.4\cos(\omega t))$ with $A_0 = 0.5\hbar\omega$ and $\hbar/\tau_0 = 10^{-2}\ A_0$. This configuration lies in the first instability region, c.f. Fig. 4.9 (a). (a) shows the time evolution of the number of excitations $|\langle n|\psi(t)\rangle|^2$ in color code, (b) the time-dependent expectation value of the number of excitations, (c) norm of the time-evolved state, (d) expectation value divided by the norm.

$n = 0$ at initial time, for small times the next higher states are excited. This process can be seen as the parametric excitation of boson pairs, since only states with odd n are populated. As time evolves, states with higher number n are occupied. This is reflected in the time-dependence of the expectation value $\langle\psi(t)|b^\dagger b|\psi(t)\rangle$ as shown in Fig. 4.14 (b), which drastically increases in the first few periods. At this point the finite lifetime τ_0 enters the game: The damping factor of state $|n\rangle$ is given by $n\gamma$, such that the higher excited states are damped out fast. This is seen in the decrease of the norm in Fig. 4.14 (c). As a result, also the expectation value of the number of excitations decreases in time and follows an exponential decay that is superimposed by a periodic modulation. This is exactly the behavior that is also seen for the expectation value in Floquet vacuum state in Fig. 4.13. We thus conclude that the Floquet vacuum state describes the decrease of the density due to the finite lifetime of the particles. For larger lifetime τ_0 the maximum of the expectation value $\langle\psi(t)|b^\dagger b|\psi(t)\rangle$ increases and is reached at later times.

It is of interest to also discuss the case where instead of the wave function, the number of excitations decays. In order to achieve this in our model, we divide in a plain calculation the expectation value by the norm of the state at each time $\tilde{n}(t) = \langle\psi(t)|b^\dagger b|\psi(t)\rangle/\langle\psi(t)|\psi(t)\rangle$ [199]. This corresponds to a redefinition of the quantum mechanical probability distribution at each time, such that effectively the norm of the state stays constant. A more sophisticated result is expected to be found within the formalism of biorthogonal quantum mechanics [193] or a microscopic description of the decay, that might also inculcate stochastic terms which especially become relevant for short lifetimes τ_0 [199]. However, for long lifetimes τ_0, the system is well-described by a non-hermitian Hamiltonian for relatively long timescales [199–201]. Before results are shown, we motivate why dividing by the norm in $\tilde{n}(t)$ describes exactly a decay of the excitation. We calculate the normalized expectation value $\langle\tilde{A}\rangle = \langle\psi(t)|A|\psi(t)\rangle/\langle\psi(t)|\psi(t)\rangle$ of an operator A with the wave function

$$|\psi(t)\rangle = e^{-iE_0t}a_0|0\rangle + e^{-i(E_0+n\epsilon)t}e^{-n\gamma t}a_n|n\rangle. \tag{4.100}$$

The calculation yields

$$\langle\tilde{A}\rangle = \frac{\langle 0|A|0\rangle|a_0|^2 + \langle n|A|n\rangle|a_n|^2e^{-2n\gamma t} + e^{-n\gamma t}2\text{Re}\left(\langle n|A|0\rangle a_n^* a_0 e^{in\epsilon t}\right)}{|a_0|^2 + |a_n|^2e^{-2n\gamma t}}. \tag{4.101}$$

Assuming $|a_0|^2 + |a_n|^2 = 1$, Eq. (4.101) decays from $\langle\tilde{A}\rangle(t=0) = \langle 0|A|0\rangle|a_0|^2 + \langle n|A|n\rangle|a_n|^2 + 2\text{Re}\left(\langle n|A|0\rangle a_n^* a_0\right)$ at $t = 0$ to $\lim_{t\to\infty}\langle\tilde{A}\rangle(t) = \langle 0|A|0\rangle$. This shows, that in the long-time limit all excitations decay and the expectation value of the vacuum state is recovered, while the quantum probability is at each time normalized to one. In Fig. 4.14 (d) the expectation value $\tilde{n}(t)$, found with the results displayed in Fig. 4.14 (a-c), is shown. At late times $\tilde{n}(t)$ has a time-periodic behavior. This is expected for the expectation value of a Floquet-steady state, c.f. Fig. 4.4. We emphasize that this is an interesting result, since it shows that the combination of decay and parametric driving results in a time-periodic expectation value that oscillates around a finite value. The average value of the expectation value is roughly given by the value that is expected from the Floquet-Bogoliubov calculation, see Fig. 4.10 (a). This gives the interpretation that the expectation value of the Floquet mode Eq. (4.80), without taking the damping by the complex quasienergy into account, describes the average number of excitations that are reached in a model where the number of excitations, and not the wave function itself, are damped.

As an overall result, this consideration results in the statement that a finite particle lifetime induces finite amount of excitations in the instability regions that is seen in large but finite maxima in the expectation value of the density of excited states.

4.7. Floquet-Steady States of the Tomonaga-Luttinger Liquid

After having introduced the Floquet-Bogoliubov transformation for a single bosonic mode, we are going to use this result for the discussion of the steady states of the time-periodically driven Tomonaga-Luttinger liquid, following Ref. [104]. In Subsec. 4.7.1 the Floquet-Bogoliubov transformation is written in the notation of the Tomonaga-Luttinger liquid theory and the unitary transformation found in Ref. [104] is presented. Subsection 4.7.2 contains the implications of the periodic driving on the physics of the Tomonaga-Luttinger liquid. As prominent result the formation of a standing-wave pattern is reported. We contextualize our result with the current literature and point out the implications for ultracold gas experiments.

4.7.1. Floquet-Bogoliubov Solution and Transformation to Floquet Frame

The results of the Floquet-Bogoliubov transformation are used in order to characterize Floquet steady state solutions in the periodically driven Tomonaga-Luttinger Liquid with parameters chosen to describe the Lieb-Liniger model. In this setting, the coefficients A and B are proportional to a wavenumber q as given by Eq. (4.17). Periodic time-dependence is described by time-periodic parameters $g_2(t)$ and $g_4(t)$, as discussed in Sec. 4.1. Following Ref. [104] it is assumed that the system is driven such that $g_2(t) = g_4(t)$ varied sinusoidally

$$2g_2(t) = 2g_4(t) = \bar{\rho} + \rho\cos(\omega t). \tag{4.102}$$

Note that $-1/2 < g_2(t) = g_4(t) < 0$ for the Lieb-Liniger model. Together with Eq. (4.17) this constraint implies that $A_0 > 0$ while $A_1 < 0$, $B(t) < 0$. Since this case cannot be recasted with the above shown figures, we will in the following show results for the periodically driven Tomonaga-Luttinger liquid as a special case. Based on the knowledge of the previous sections, a Floquet-Bogoliubov transformation for Hamiltonian (4.16) is found by

$$\beta_{q,\pm}(t) = u_q(t)b_{q,\pm} \pm v_q(t)b^\dagger_{q,\pm}, \tag{4.103}$$

where $u_{q,\pm}(t)$ and $v_{q,\pm}(t)$ solve the Floquet-Bogoliubov equation (4.38) with $A = A_q$ and $B = \pm B_q$ as defined in Eq. (4.17). For both $\beta_{q,\pm}$ we find the same quasienergy ϵ_q. This allows to rotate the basis

$$\beta_{q,\mathrm{L}} = \frac{1}{\sqrt{2}}(\beta_{q,+} + \beta_{q,-}),\ \beta_{q,\mathrm{R}} = \frac{1}{\sqrt{2}}(\beta_{q,+} - \beta_{q,-}). \tag{4.104}$$

Using Eq. (4.15), the $\beta_{q,\mathrm{L/R}}$ operators can be expressed in the form that is also found in Ref. [104]:

$$\beta_{q,\mathrm{L/R}}(t) = u_q(t)b_{q,L/R} + v_q(t)b^\dagger_{q,R/L}. \tag{4.105}$$

The Floquet vacuum state of the mode q of Hamiltonian (4.14) can be calculated by $|\phi_{q,0}(t)\rangle = |\phi_{q,0,+}(t)\rangle|\phi_{q,0,-}(t)\rangle$, where $|\phi_{q,0,\pm}(t)\rangle$ is the vacuum state with respect to the $\beta_{q,\pm}(t)$ operators as defined in Eq. (4.65). With this, the vacuum state reads

$$|\phi_{q,0}(t)\rangle = \frac{e^{i\mathcal{A}_q(t)}/\hbar}{u_q(t)} \exp\left[-\frac{v_q(t)}{u_q(t)} b^\dagger_{q,\mathrm{L}} b^\dagger_{q,\mathrm{R}}\right]|0\rangle, \tag{4.106}$$

with $b_{q,\mathrm{L}}|0\rangle = b_{q,\mathrm{R}}|0\rangle = 0$ and $\mathcal{A}_q(t) = \int_0^t dt'\ [A_q(t') - (1/T)\int_0^T dt''\ A_q(t'')]$, and obeys $\beta_{q,\mathrm{L/R}}|\phi_{q,0}(t)\rangle = 0$. The corresponding quasienergy reads

$$E_0 = \epsilon - \frac{1}{T}\int_0^T dt\ A(t). \tag{4.107}$$

For parameter regions where the Floquet vacuum state (4.106) exists, the whole spectrum is given by the Floquet modes

$$|\phi_{q,n,m}(t)\rangle = \frac{1}{\sqrt{n!m!}}\left[\beta^{\dagger}_{q,L}(t)\right]^{n}\left[\beta^{\dagger}_{q,R}(t)\right]^{m}|\phi_{q,0}(t)\rangle, \tag{4.108}$$

while the quasienergies are found by

$$\epsilon_{n,m} = (n+m)\epsilon + E_0,\ \ n,m\in\mathbb{N}_0. \tag{4.109}$$

This shows that the Floquet-Bogoliubov transformation enables us to find steady state solutions in a quantum many body setting.

This full solution of the Floquet-Bogoliubov transformation even allows to explicitly find a time-dependent unitary transformation $U_{q,\mathrm{P}}(t)$ that transforms Hamiltonian (4.14) to the Floquet frame in the sense of Eq. (2.3). A detailed discussion of the far-from trivial derivation of $U_{q,\mathrm{P}}(t)$ is given in Refs. [104, 202], in the following we present the major results of this calculation. As a prerequisite for writing down $U_{q,\mathrm{P}}(t)$, we give the Hamilton operator in terms of the generators of a SU(1,1) algebra

$$H_q = \hbar v_{\mathrm{F}} q(1+g_4)2J_{q,0} + \hbar v_{\mathrm{F}} g_2 q(J_{q,+}+J_{q,-}), \tag{4.110}$$

where an additional time-dependent constant is dropped in Eq. (4.110). The explicit form of the generators of the SU(1,1) algebra is given by $2J_{q,0} = b^{\dagger}_{q,\mathrm{L}}b_{q,L} + b_{q,R}b^{\dagger}_{q,R}$ and $J_{q,+} = J^{\dagger}_{q,-} = b^{\dagger}_{q,\mathrm{L}}b^{\dagger}_{q,\mathrm{R}}$ [203–205]. The transformation $U_{q,\mathrm{P}}(t)$ leads to an effective Hamiltonian in diagonal form

$$\tilde{H}_{q,\mathrm{eff}} = \epsilon_q 2J_{q,0}, \tag{4.111}$$

which is a remarkable step [104, 202]. The explicit form of $U_{q,\mathrm{P}}(t)$ that achieves all of this is given by [104]

$$U_{q,\mathrm{P}}(t) = e^{i\theta_q(r)J_{q,0}}e^{r_q(t)(J_{q,+}-J_{q,-})}e^{-i\phi_q(t)J_{q,0}}. \tag{4.112}$$

The parameters $\theta(t)$, $r(t)$, $\phi(t)$ of the transformation (4.112) are determined by the results of the Floquet-Bogoliubov transformation [104, 202]

$$u_q(t) = e^{i[\theta_q(t)-\phi_q(t)]/2}\cosh[r_q(t)], \tag{4.113a}$$

$$v_q(t) = e^{i[\phi_q(t)+\theta_q(t)]/2}\sinh[r_q(t)]. \tag{4.113b}$$

In combination with the analytic approach of Eq. (4.90) that is valid for the driving scheme eq.(4.102), one is now able to find an analytical expression of the time-dependent transformation to Floquet frame $U_{q,\mathrm{P}}(t)$ in a quantum many-body system. This is a key result, since it is far from trivial to obtain such a transformation at all. We further emphasize that the deviation of Eq. (4.112) can be done without going to the Floquet space [202]. Note that $U_{q,\mathrm{P}}(t)$ has not to be confused with the time-evolution operator $U(t,t')$.

4.7.2. Results of the Floquet Analysis

Using the Floquet-Bogoliubov transformation we are able to analyze the possible Floquet steady states of the time-periodically driven Tomonaga-Luttinger liquid. Figure 4.15 (a) shows the quasi-

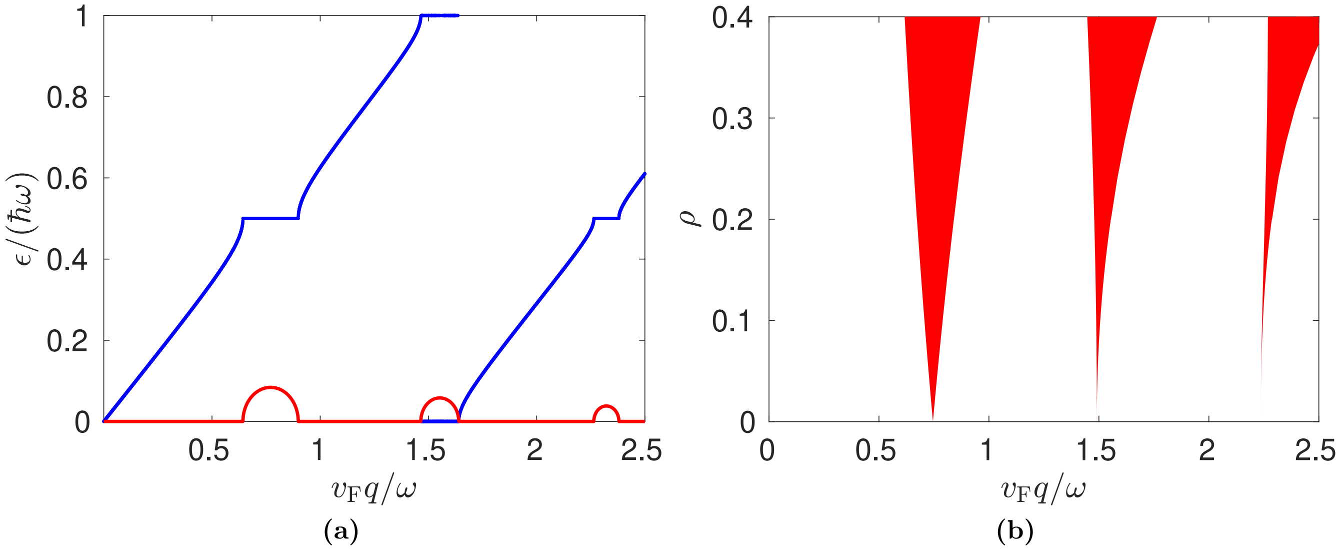

Figure 4.15.: (a) Real (blue) and imaginary (red) part of the quasienergy of the Floquet-Bogoliubov particles for $\bar{\rho} = -0.4$ and $\rho = 0.3$. (b) Stability chart for $\bar{\rho} = -0.4$, red areas mark the instability regions, white the stability regions.

energy of the Floquet-Bogoliubov particles in dependence of the dimensionless momenta $v_{\mathrm{F}}q/(\hbar\omega)$. The behavior is similar to Fig. 4.2. The quasienergy is real and shows an almost linear slope until it reaches a instability region where it acquires a non-vanishing imaginary part. This shows that also in the Floquet steady state solution of the periodically driven Luttinger Liquid instability regions exist. In Fig. 4.15 (b) the stability chart of the harmonically driven Lieb Liniger model is shown for $\bar{\rho} = 0.4$. Also here instability tongues run parallel to the y-axis, the thickness of each instability region increases with ρ. This corresponds to the argument that the larger the driving strength the more energy is introduced to the system which shows up in a stronger instability. The values where the instability regions reach the x-axis are determined by condition (4.93). Applied to the concrete setting of a periodically driven Tomonaga-Luttinger liquid this condition is written as

$$2\frac{v_{\mathrm{F}}q_n}{\omega}\sqrt{1+\bar{\rho}} = n, \;\; n \in \mathbb{N}. \tag{4.114}$$

Similar to the discussion of Eq. (4.93), Eq. (4.114) corresponds to the physical process of the parametric excitations of two bosons with energy $\hbar v_{\mathrm{F}} q\sqrt{1+\bar{\rho}}$. Here, both right and left movers are excited. Eq. 4.114 allows to define the resonant wave vectors, at which the parametric resonance occurs

$$q_n = n\omega/(2v_{\mathrm{F}}\sqrt{1+\bar{\rho}}), \tag{4.115}$$

Equation (4.115) shows that the resonant wave vector is proportional to the ratio of driving frequency and Fermi velocity.

A more general driving scheme leads to similar results. For example, we consider a driving with the second harmonic

$$2g_2(t) = 2g_4(t) = \bar{\rho} + \rho\cos(\omega t) + \rho_2\cos(2\omega t). \tag{4.116}$$

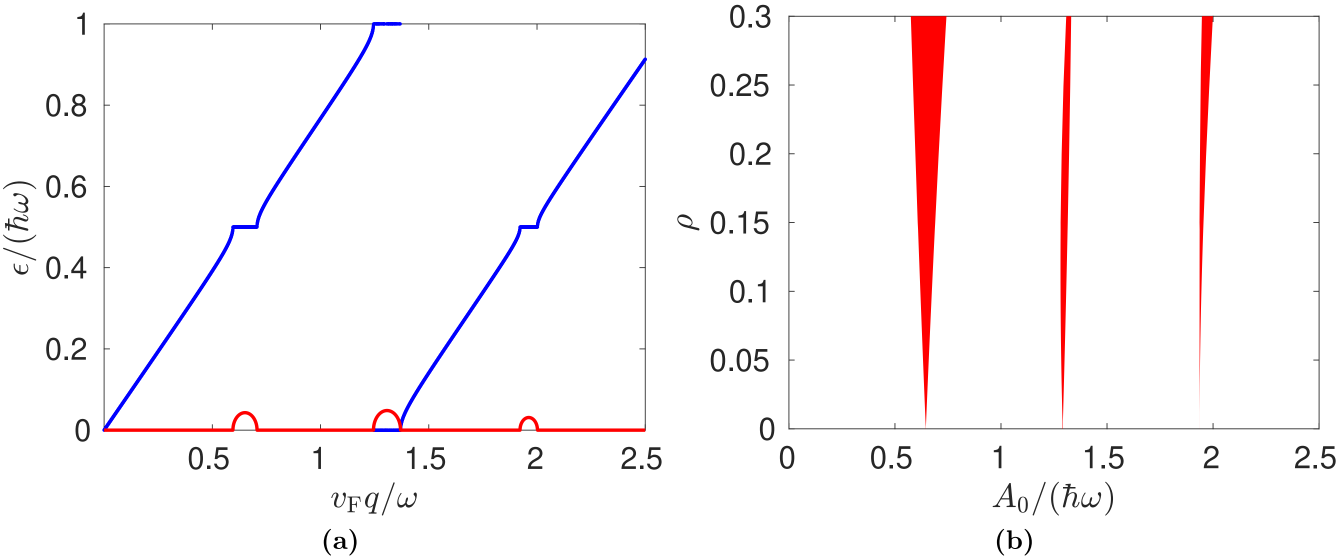

Figure 4.16.: (a) Real (blue) and imaginary (red) part of the quasienergy of the Floquet-Bogoliubov particles for $\bar{\rho} = -0.4$, $\rho = 0.3$ and $\rho_2 = 0.1$ (b) Stability chart for $\bar{\rho} = -0.4$ and $\rho_2 = \rho/3$, red areas mark the instability regions, white the stability regions.

The quasienergies are shown in Fig. 4.16 (a), the behavior is similar to the harmonically driven case. In Fig. 4.16 (b) the stability chart for $\bar{\rho} = -0.4$ and $\rho_2 = \rho/3$ is displayed. Also here instability regions are visible. This behavior is expected, since the occurrence of a parametric resonance in a Floquet system is in analogy to the occurrence of a band gap in a band structure calculation [104]. Ref. [100] finds the band structure of a 1D cosine lattice in terms of Mathieu functions, in analogy to the analytic solution for a special case of the Floquet Bogoliubov transformation. As for generic space-periodic potentials band gaps are expected to occur, it is self-evident that the occurrence of the instability regions in the Floquet-Bogoliubov transformation is also generic.

Next, we are interested in calculating the number of excitations by the expectation value

$$n_q(t) = \langle \phi_{q,0}(t) | b^{\dagger}_{q,L/R} b_{q,\mathrm{L/R}} | \phi_{q,0}(t) \rangle. \tag{4.117}$$

In Fig. 4.17 (a) the time average $\bar{n}_q$ is shown for different values of the driving strength ρ. For $v_{\mathrm{F}}q/\omega \to 0$ the corresponding static limit is recovered. Similar to Fig. 4.3, the expectation value $\bar{n}_q$ diverges in the instability regions. This is showing that the average number of excitations in the Floquet steady state increases when approaching the instability regions. As shown in Sec. 4.6, a finite lifetime of the original bosonic operators turns a divergence appearing in the average number of excitations to an overwhelming maximum. In the Tomonaga-Luttinger liquid theory a finite lifetime of the bosonic operators is related to damping due to additional higher order terms of the bosonic operators [104, 163]. These higher order terms can come in due to a more detailed description of the underlying physical model that goes beyond Eq. (4.6). Thus the lifetime depends on microscopic details of the considered model. Here, we do not account for all the microscopic details and introduce in a pioneering calculation the lifetime similar to Eq. (4.98) as an imaginary part Im $A_q = -i\hbar/\tau_q$ that leads to a decay of the excitations, while τ_q is assumed to be inverse proportional to $v_{\mathrm{F}}q$. Further

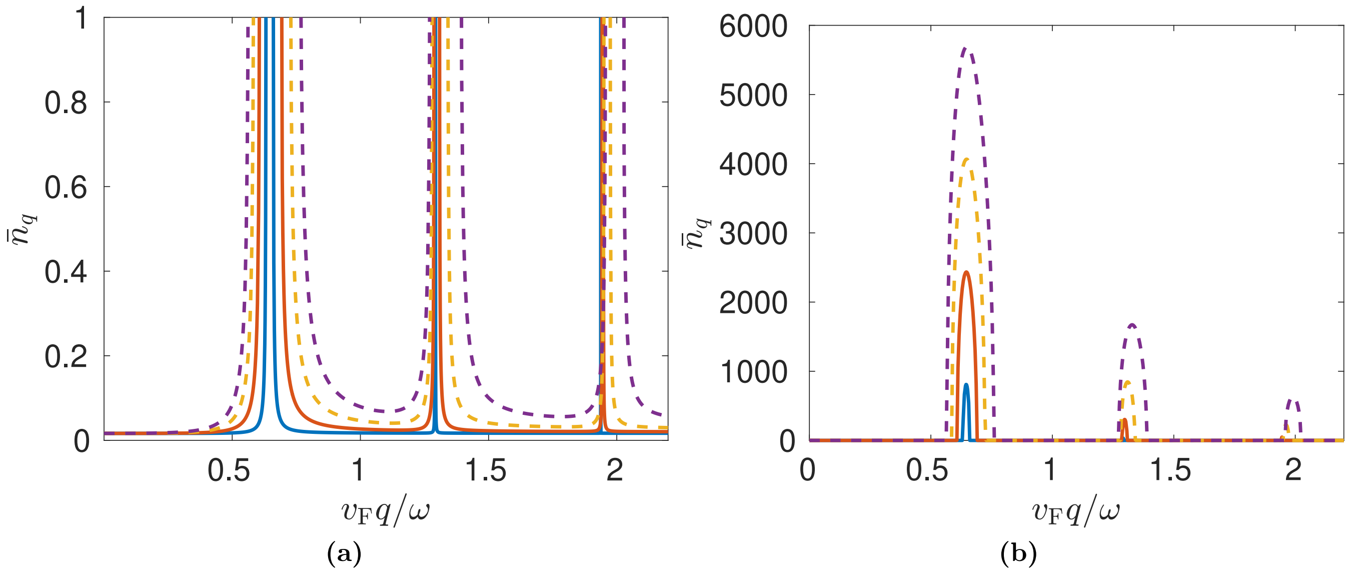

(a) **(b)**

Figure 4.17.: Time-averaged number of excited states $\bar{n}_q$ for $\bar{\rho} = -0.4$ with (a) infinite boson lifetime, (b) with an finite lifetime of $\hbar/\tau_0 = 10^5\ v_\mathrm{F}q$. The blue curve corresponds to $\rho = 0.05$, the red to $\rho = 0.15$, the yellow to $\rho = 0.25$ and the purple to $\rho = 0.35$.

calculations might take possible non-linearities of the theory into account [165,185] or elaborate the microscopic description of the coupling to a reservoir [199]. In Fig. 4.17 (b) the results are shown for a finite damping of $\hbar/\tau_q = 10^5\ \hbar v_\mathrm{F}q$. As expected, the divergences turn into dominating but finite maxima. The results of section 4.6 directly apply to this case showing that the height of the maxima can be tuned by the product $\rho\tau_0$. We emphasize that by this we have managed to calculate a Floquet steady state in an interacting quantum many-body system, which is a remarkable result.

In order to discuss the physical behavior of the driven Tomonaga-Luttinger Liquid it is important to note that the description of the correlation by Hamiltonian (4.14) breaks down for large q [104]. This motivates to define a cutoff q_c, below which the correlations are given by the Tomonaga-Luttinger Liquid [188]. Using a Fermi velocity that is rescaled by $\sqrt{1+\bar{\rho}}$ it is estimated in our case to $q_\mathrm{c} \approx v_\mathrm{F}m\sqrt{1+\bar{\rho}}/2$ [104,188].

For large driving frequencies all resonant wave vectors (4.115) lie above the cut-off q_c, such that in the physical relevant region of momentum space no parametric resonances occur. Since for $q \to 0$ the static case is recovered within the Floquet-Bogoliubov approach, the famous asymptotic power law correlations Eqns. (4.9) and (4.10) are again found. At finite distances, the Floquet-Bogoliubov result differs from the static one, which will lead to corrections of the correlation functions.

If the driving frequency is lowered, multiple resonant wave vectors q_n might lie below q_c. In this case the time-periodic drive leads to the parametric excitation of modes with resonant wave vectors q_n. The resonant wave vectors dominate the density-density correlation function, which shows a long range order of the form [104, 202]

$$\langle \rho(x)\rho(y)\rangle \propto \cos[q_n(x-y)]. \tag{4.118}$$

This signals that the time-periodic drive induces standing density waves with resonant wave vectors q_n. This is a notably different behavior compared to the static case. The occurrence of a density wave is a key result of this investigation since it demonstrates the effects of resonances in Floquet physics and can be measurable in an ultracold gas experiment. In order to give actual numbers the parameters of a one-dimensional ^{87}Rb gas from Ref. [183] are considered, following Ref. [104]. With a density of $\rho_0 = 6.2 \times 10^6/\mathrm{m}$, $\gamma = mg/(\hbar^2\rho_0) \approx 0.6$ and by driving the confinement with a frequency of $\omega = 2 \times \pi$ 500 Hz it follows that the wavelength of the standing wave corresponding to the first resonant wave vector is $\lambda_1 = 2\pi/q_1 \approx 14$ μm. Note that this physics is below the cutoff of $\omega_\mathrm{c} = v_\mathrm{F}\sqrt{1+\bar{\rho}}q_\mathrm{c} \approx 2\pi \times 1.4$ kHz. The standing density wave can be observed with common experimental techniques [3].

We found that the time-periodic drive induces a standing density-wave pattern with wave vectors that are determined by the condition of a parametric resonance. At this place we make an insertion and discuss the literature on parametrical pattern formation in fluids. A special group of a surface wave excitations of a fluid are the so called Faraday waves. The name goes back to an analysis of M. Faraday himself in which a fluid in a receptacle is shaken in vertical direction [1]. As a result, standing wave patterns that arise from parametric resonance have been observed on the surface of the fluid. At this place we emphasize that the properties of a Faraday wave and a parametrically excited pattern in general, mainly depend on the properties of the fluid and the external drive [6, 206, 207], while the density pattern oscillates with half the driving frequency [2, 6, 206–209]. This distinguishes the parametrically excited standing waves from resonantly excited eigenmodes, e.g. the modes of a membrane, which oscillate with the same frequency as the drive. The wave vector a of Faraday wave is determined by a condition of parametric resonance in the hydrodynamic description of fluids [2, 6, 206, 208] and depends on the driving frequency. The pattern formation, and especially the formation of Faraday waves, in a parametrically driven Bose-Einstein condensate has been discussed in Refs. [76–78, 206] within the Gross-Pitaevskii mean field description. The time dependence can be either introduced by a time-dependent potential or by making the interparticle interaction, that enters the the mean field description by a non-linear term, time dependent. Ref. [206] discusses Faraday waves in a periodically modulated Bose-Einstein condensate by relating the dynamics to a Mathieu-type equation, the wave vector of the density pattern is given by the strongest instability. Ref. [2] observed the occurrence of Faraday waves in an ultracold gas experiment with a Bose-Einstein condensate of ^{87}Rb atoms. It was found that both the time-periodic modulation of the transverse confinement and the oscillation of the transverse breathing mode leads to the pattern formation in the longitudinal direction. Ref. [2] measured that the wavelength of the pattern depends on the driving frequency.

In our research standing density waves are predicted if the driving frequency is below the cutoff ω_c. In accordance to the literature we find that the wavelength of these resonant waves is inverse proportional to the driving frequency $\lambda \propto \omega^{-1}$ and the generation of these density waves is related to a parametric resonance that occurs in the instability regions. Thus, the standing density wave patterns that we found in the driven Tomonaga-Luttinger Liquid have properties that are also found for Faraday waves, see the discussion above. What makes our research special is the fact that the density wave pattern are induced intrinsically by the periodic modulation of interaction strength, and no vibration of a receptacle is needed, as it is done for example in Faraday's experiment [1]. Further, our result goes beyond the mean field descriptions, such as in Ref. [76], since we analyze the density wave patterns in the Tomonaga-Luttinger liquid model, a field theory that is capable of describing strongly correlated one-dimensional quantum many-body systems. Thus we are able to analyze the parametric density wave excitations in strongly correlated quantum systems. This paves the way for further investigations. Ref. [6] observed Faraday wave patterns in a one-dimensional ultracold quantum gas with periodic modulation. If the frequency is lowered, the ultracold gas shows a granulated density that cannot be described by a mean field theory. In our theory multiple resonant wave vectors emerge if the frequency is lowered. A future analysis would clarify if the resulting real space density distribution of our model fits to the grains observed in Ref. [6].

When lowering the driving frequency even further, more and more resonant wave vectors enter the area in which the Tomonaga-Luttinger liquid describes the physics of the model. Ref. [210] found parametric instabilities in a time-periodically driven Bose-Hubbard model and interprets them as the initial stage of heating. Since in our model the parametric instabilities dominate the physics for low driving frequencies, we predict that in this case the system will heat up and show a large number of excitations.

Note that a trapping potential does not alter the physics much as long as the local density approximation is valid [104]. One prediction of the local density approximation is that the density $\rho_0(x,t)$ decreases when leaving the center of the trapping potential [183, 211]. As the Fermi velocity $v_{\mathrm{F}} = \pi\rho_0/m$ is proportional to the density and gives the characteristic energy scale of our system we are able to reach the different regimes that are discussed above within a experimental setup. As one goes nearer to the center of the trap, the lower is the rescaled driving frequency and the larger the wavelength of a possible parametrically excited density wave.

4.8. Conclusion and Outlook

In this chapter we generalized the concept of the Bogoliubov transformation to periodically driven Hamiltonians that are quadratic in bosonic operators. This is achieved by introducing time-dependent parameters in the Bogoliubov transformation, which results in operators that describe Floquet-Bogoliubov quasiparticles. Similar to the static case we are able to calculate the quasienergies of these quasiparticles and the parameters of the transformation by an eigenvalue equation. It turns out that two cases are distinguished: In the stability regions the quasienergy of the Floquet-Bogoliubov particle is real and the full spectrum can be generated using the transformation. In the instability regions the quasienergies become complex while the real part is pinned to integer multiples of half the driving frequency. In this case no Floquet-Bogoliubov solution is possible. This fact is made more visible when calculating the average number of excitations which diverges in the instability regions and relates the instabilities to the parametric generation of pairs of bosons. This is the key result, since it shows that the parametric resonance has a major implication to the physical behavior of the system. Introducing a finite lifetime for the bosons, we are still able to find a Floquet vacuum state and the above discussed divergences are regularized to finite but dominating peaks. This is a remarkable result, it shows that a damped system has a finite response to the time-periodic drive.

When applying the theory to actual physical systems, it is of further research interest to discuss an accurate microscopic description of the mechanisms that introduce the damping. Ref. [210] found that in a periodically driven Bose-Hubbard system parametric resonances can be suppressed when coupling it to a reservoir, such that a stable steady state can be reached. The coupling of a time-independent Tomonaga-Luttinger liquid to a reservoir is discussed in Ref. [212]. It is of further interest how the interplay between the periodic drive and the dissipative dynamics influences the occurrence of parametric resonances and thus the properties of possible steady states of the Floquet system in detail. Such a calculation must take into account fluctuating terms that come in due to the microscopic description of the dissipation, such that the mathematical description might become more involved. On the other hand, non-linearities in the description of the considered physical system could also stabilize the motion [165]. A numerical investigation reveals that the solutions of the classical Mathieu equation can be stabilized by introducing non-linear terms. Also in the Tomonaga-Luttinger liquid theory higher order terms may appear which could stabilize the system. In the Tomonaga-Luttinger liquid theory these non-linearities couple modes with different wavenumber which makes the solution of a Hamiltonian including higher order terms much more involved compared to the solution of a Hamiltonian that is quadratic in bosonic operators.

In Fig. 4.7 (b) we found that for a special driving scheme the instability regions contract to a single point at a finite driving strength. There we expect the parametric resonances to be strongly, or even completely, suppressed. It would be of interest to relate this results to the results of Ref. [83], where with the use of an exact space-time mapping the complete suppression of heating in a periodically driven quantum many-body system with a thoroughly chosen driving scheme is found.

Another way of future research is to generalize the Floquet-Bogoliubov transformation to a finite number of bosonic modes and to find a similar transformation in the fermionic case. For fermions we expect avoided crossings instead of parametric resonances. With a fermionic version of the Floquet-Bogoliubov transformation the steady states of a periodically driven superconductor can be investigated. Interesting physics, such as the Floquet engineering of a p-wave superconductor [213] and topologically protected Floquet Majorana edge modes [214, 215] has been observed in these models.

In order to demonstrate the physical properties of the Floquet steady state solutions, we applied the Floquet-Bogoliubov transformation to a periodically driven Tomonaga-Luttinger liquid using which the low energy excitations of a Lieb-Liniger model can be described. A finite lifetime in the Tomonaga-Luttinger description enables us to find a Floquet steady state solution in a periodically driven quantum many-body system, which is a remarkable result.

It turns out that the physical behavior of the periodically driven Lieb-Liniger model depends on the proportion of the driving frequency and a cutoff frequency. The cutoff frequency defines an energy scale below which the system can be described by the Tomonage-Luttinger Liquid theory. If the driving frequency is larger than the cutoff, no parametric resonances occur and the asymptotic limit of the correlation functions is given by the corresponding static case. If the driving frequency is lower than the cutoff, parametric resonances occur. In this regime the correlation functions are given by standing density waves with resonant wave vectors that are determined by the condition of a parametric resonance. This is the key result of this chapter, since the occurrence of the density wave is directly related to the results of the Floquet analysis. This result indeed shows that the parametric resonances have a intriguing implication on the physics of the system.

5. Dissipation Engineered Direction-Dependent Filter for Hamiltonian Quantum Ratchets

In this chapter we combine the one-dimensional setting from Ch. 4 with a scattering problem, as discussed for the 3D case in Ch. 3. The goal is to design a time-dependent, dissipative impurity that acts as a direction-dependent filter. The special feature of the model of this chapter is that the bulk part of the system is not static, as in Ch. 3, but is a Hamiltonian ratchet that is driven with the same frequency as the impurity.

The ratchet effect enables to convert an unbiased fluctuating force into directed motion [216–220]. A basis for the ratchet effect to occur is the breaking of certain space- and time-reversal symmetries [219, 221–224]. A commonplace example of this effect is the ratchet and pawl. As sketched in Fig. 5.1, the pawl allows to rotate a gear in forward, i.e. mathematical positive, direction but prevents rotary motion in backward direction. The asymmetric shape of the gear and the mounting of the pawl breaks the relevant symmetries. The discussion of the ratchet effect goes back to the work of Smoluchowski [225] and was later popularized by Feynman [226]. In recent literature, the ratchet effect has been proposed at the nanoscale as e.g. Brownian motors or nanomachines and has been observed in various experimental settings: A prominent example is the biological cell motion, where Ref. [227] demonstrates the rectification of motion by asymmetrically shaped micropatterns. Light-induced unidirectional rotation of molecules was discussed in Ref. [228]. Other realizations of ratchets are made in semiconductor heterostructures [229], terahertz irradiated graphene [217], waveguide arrays [98, 230, 231] and ultracold quantum gases [219, 224, 232].

There is a differentiation between classical and quantum ratchets [218, 233, 234]. A prominent effect appearing in quantum ratchets is the reversal of the directed current due to quantum tunneling [233]. Another differentiation is made in dissipative and Hamiltonian ratchets. Dissipative ratchets operate with thermal fluctuations or quantum fluctuations or frictional force [106, 218, 221, 234]. In dissipative quantum ratchets the fluctuations are introduced by coupling the system to a bath [218, 234]. In contrast, Hamiltonian ratchets work in the absence of any dissipative or stochastic force [219, 235] and rely on the coherence of quantum transport. An example of an Hamiltonian ratchet is the Thouless pump [236], where a the parameters of a special lattice Hamiltonian are driven adiabatically on a cycle. The drive breaks the relevant space-time symmetries and leads to a quantized current which is related to a nontrivial topological structure. In contrast, there are Hamiltonian ratchets which operate at non-adiabatic driving frequencies, where the Hamiltonian preserves all relevant

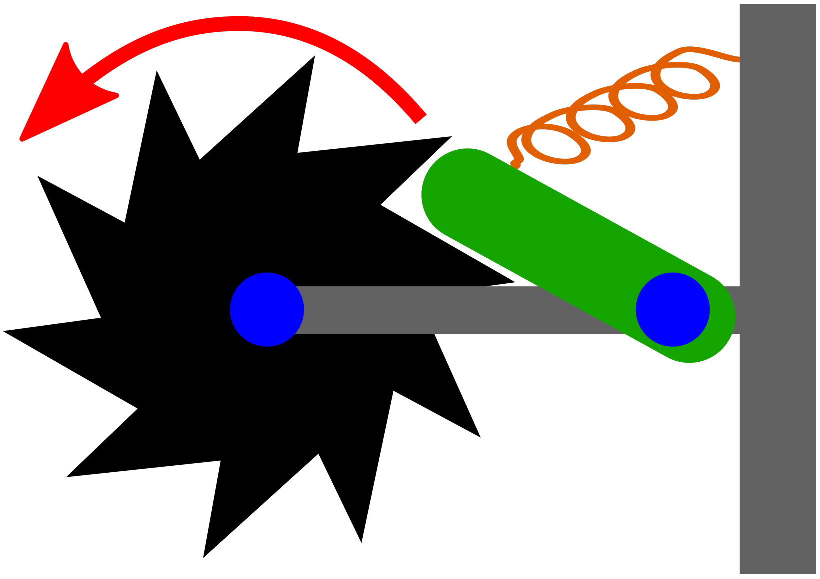

Figure 5.1.: Sketch of ratchet and pawl. A gear (black) is mounted on a base (grey). The pawl (green) is spring-loaded (orange) and only allows the rotation of the gear in forward direction (indicated by a red arrow).

symmetries and, in principle, allows for transport in both directions [219, 222, 223, 232, 234]. In this case, directed transport depends sensitively on the initial state. If the state is chosen such that mostly Bloch states with positive or negative group velocity are excited, a finite current is possible in this systems.

Our research, which is presented in Ref. [216], focuses on a Hamiltonian quantum ratchet that is inspired by the conditions of a waveguide experiment. Thus, at first an introduction to waveguide experiments is done in Sec. 5.1. In Sec. 5.2 the ratchet scheme, which is mathematically described by a Su-Schrieffer-Heeger model with time-periodic coupling constants, is introduced. The band structure of the model and its transport properties are investigated in collaboration with Z. Fedorova from the University of Bonn. In contrast to Thouless pumping, in our ratchet model quantized transport is possible at non-adiabatic conditions, i.e. at a finite driving period, which is much easier to realize in an experiment [216]. We will find out that the driving frequencies at which quantized transport is possible, are given by a resonance condition. This will demonstrate the importance of resonances to this chapter. Ref. [98] observed directed transport at non-adiabatic driving frequencies in a setup that is described by a non-hermitian ratchet model. However, the non-hermiticity introduces damping, such that the particle transport decays after a few driving periods. In our Hamiltonian ratchet model no damping is present. This leads to transport over longer distances compared to Ref. [98]. But also our Hamiltonian ratchet model suffers from a disadvantage: The directed transport strongly depends on the initial state. If it is not possible to choose the initial state, directed transport might not be observed. In order to circumvent this issue a direction-dependent filter, which is based on the properties of the waveguide experiment of Z. Fedorova from the University of Bonn, is introduced. The filter is realized as a dissipative, time-dependent impurity that damps out particles moving in one direction while it does not affect the current in the other direction. Section 5.3 is devoted to the introduction of the direction-dependent filter. The theoretical investigation is made with the

Floquet S-matrix theory, which is formulated in Sec. 5.4 for the relevant case of a non-hermitian, time-periodic impurity operator. The analysis of the direction-dependent filter is provided in Sec. 5.5. At last, the results of the waveguide experiment, conducted by Z. Fedorova from the university of Bonn, are presented in Sec. 5.6. The experiment successfully proves the working principle of both ratchet and direction-dependent filter.

5.1. Introduction to Waveguide Experiments

The introduction to waveguide experiments is placed at first, since the conditions of such an experiment motivate the choice of the lattice model of a ratchet that will be investigated throughout this chapter. Subsec. 5.1.1 describes how Schrödinger wave mechanics is simulated with optical waveguide arrays. The central result is an equation that relates the electric field distribution in the arrays to a tight-binding description, a well-know concept of solid state physics. In Subsec. 5.1.2 the experimental realization of the Hamiltonian ratchet and the direction-dependent filter in coupled dielectric-loaded surface plasmon-polariton waveguide array (DLSPPWs) is presented. A more detailed discussion is found in Ref. [237]. The experiment was conducted and analyzed by Z. Fedorova from the University of Bonn.

5.1.1. Simulation of Schrödinger Equation with Waveguide Arrays

The reader is introduced in the working principle of waveguide arrays as a simulator for the time-dependent Schrödinger equation. A waveguide is a structure that guides electromagnetic waves along a designated direction. For the sake of simplicity we focus on dielectric waveguides which operate at optical frequencies. As sketched in Fig. 5.2, they are made up of a core with a material having a higher refractive index than the material surrounding it [85]. This choice of the refractive indices induces total reflection on the interface, as a result the light is guided inside the waveguide along propagation direction, which corresponds to z direction in Fig. 5.2. The transversal profile of the waveguide lays in the $x-y$ plane. Light propagation along z direction is described by the paraxial Helmholtz equation [85, 86, 238]

$$i\frac{\partial\psi(x,y,z)}{\partial z} = -\frac{1}{2k_{\text{eff}}}\left[\left(\frac{\partial^2}{\partial x^2}+\frac{\partial^2}{\partial y^2}\right)+k_{\text{eff}}^2\frac{n^2(x,y)-n_{\text{eff}}^2}{n_{\text{eff}}^2}\right]\psi(x,y,z). \tag{5.1}$$

Here $n(x,y)$ is the refractive index profile of the waveguide and $\psi(x,y,t)$ is the envelope of the electric field distribution $E(x,y,z,t) = \psi(x,y,z)e^{i(k_{\text{eff}}z-\omega t)}$ propagating in the waveguide. The material surrounding the waveguide has a refractive index of n_0, so that propagation inside the waveguide is with a wave vector of $k_{\text{eff}} = k_0 n_{\text{eff}}$, where the effective refractive index n_{eff} obeys $n_0 < n_{\text{eff}}$, for details see Ref. [85]. Here k_0 denotes the wave vector in vacuum. The paraxial Helmholtz equation (5.1) is in close analogy to the Schrödinger equation of a single particle

$$i\frac{\partial}{\partial t}\psi(x,y,z) = \left[-\frac{1}{2m}\left(\frac{\partial^2}{\partial x^2}+\frac{\partial^2}{\partial y^2}\right)+V(x,y)\right]\psi(x,y,z). \tag{5.2}$$

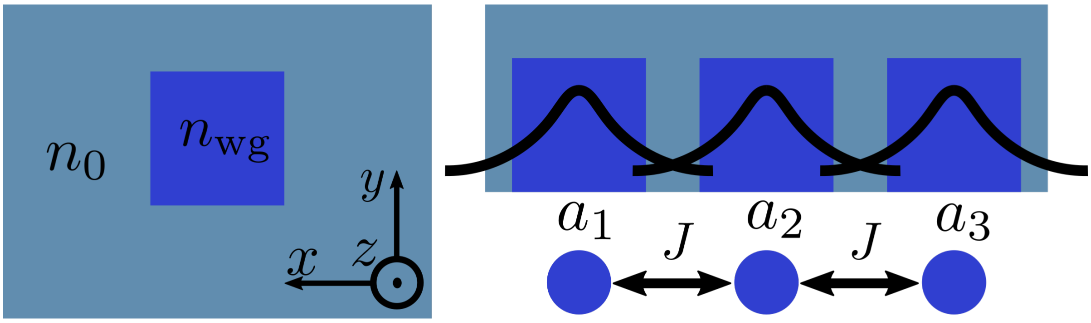

Figure 5.2.: Left: Sketch of the transverse profile of a waveguide. The core material has the refractive index n_{wg} while its surrounding is made up of a material with refractive index n_0. In the lower right corner a coordinate system is shown, the z direction points into the paper plane. Top right: Array of three coupled waveguides operating in the single mode regime. Bottom right: Tight-binding model corresponding to this configuration. The mode profile is sketched by black curves, each mode populated with the amplitude a_i. The non-vanishing overlap of the modes can induce nearest-neighbor coupling J in the tight-binding description.

The propagation distance z in a waveguide experiment corresponds to time in the Schrödinger equation, the mass is given by $m = k_{\mathrm{eff}}$ and the single particle potential corresponds to

$$V(x, y) = \frac{k_{\mathrm{eff}}}{2} \frac{n_{\mathrm{eff}}^2 - n(x, y)^2}{n_{\mathrm{eff}}^2}. \tag{5.3}$$

For example, the potential corresponding to Fig. 5.2 is a box potential that has the value of $V(x, y) = \frac{k_{\mathrm{eff}}}{2} \frac{n_0^2 - n_{\mathrm{wg}}^2}{n_0^2}$ inside the waveguide profile while it is zero outside. Now we come to the important point to make: The analogy between Schrödinger equation (5.2) and paraxial Helmholtz equation (5.1) allows to simulate single particle quantum dynamics with waveguides. This is seen by the fact that the propagation of light along the z direction corresponds to the time-evolution of a quantum state. In analogy to eigenstates in quantum mechanics, the eigenmodes of the waveguide consist of a field distribution that is up to a linear phase evolution constant along the z direction.

More interesting than a single waveguide is an array of coupled waveguides, as sketched in Fig. 5.2. In the following each waveguide is assumed to operate in the single mode regime, where a_j denotes the amplitude of the mode in the jth waveguide. Similar to the tight-binding method in solid state physics a lattice Schrödinger equation for the a_j can be derived [85, 237]:

$$i \frac{da_j}{dz} = J_{j,j-1} a_{j-1} + J_{j,j+1} a_{j+1} + V_j a_j \tag{5.4}$$

In Eq. (5.4) $J_{j,l}$ denotes the coupling constant between the waveguides j and l, where $J_{j,l} = J_{l,j}^*$. The coupling constants are determined by the size of the overlap of the eigenmodes in the two neighboring waveguides and the strength of the coupling constants decreases with the distance between two waveguides [85, 237]. In Eq. (5.4) we assumed that only the nearest neighbor coupling is non vanishing. On each waveguide there can be an additional local potential V_j, which can be tuned by the value of the refractive index of the waveguide core and the cross section of the waveguide [85].

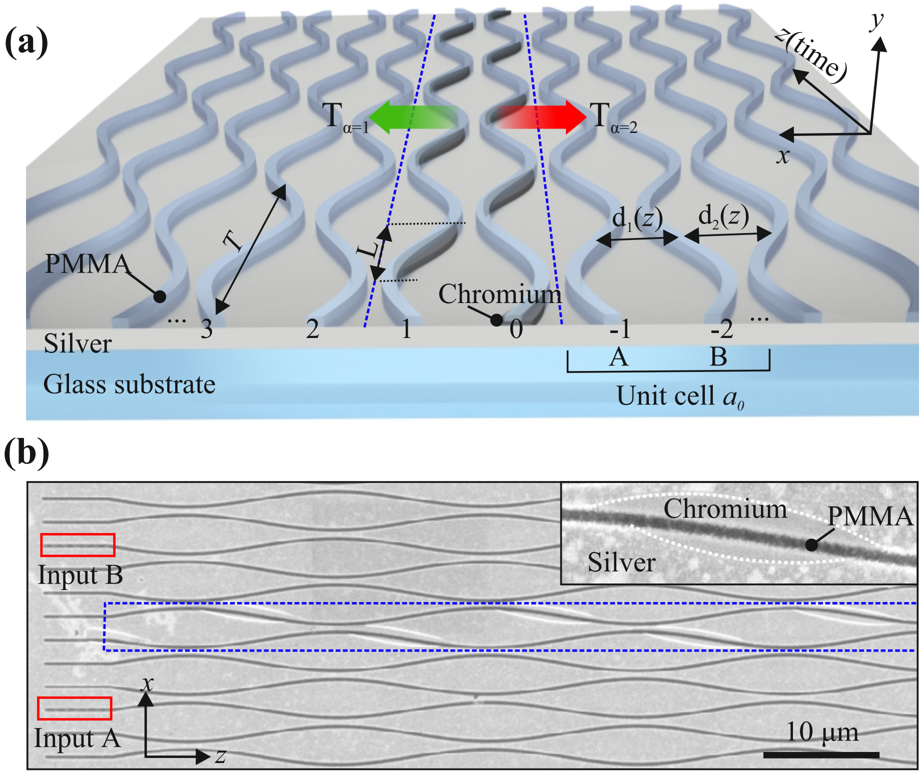

Figure 5.3.: Figure created by Z. Fedorova from the University of Bonn and published in [216]. (a) sketch of a plasmon-polariton waveguide array with the dissipative impurity on the central waveguides. Relevant parameters are visualized, the direction with high transmission is marked by a green array, the one with low by a red arrow. (b) scanning electron micrograph of a sample. Input A and B are marked by red boxes, blue dotted lines mark the dissipative region. The top right corner provides a magnified view on the chromium stripe that induces dissipation in the experiment.

Floquet systems can be realized by changing the configuration of the waveguides periodically in propagation distance z [85, 216]. For example the location of the waveguides can be shifted sinusoidally along z direction. A periodic z dependence of the waveguide configuration leads in Eq. (5.4) to model parameters that depend periodically on z, $J_{j,l} \to J_{j,l}(z)$, $V_j \to V_j(z)$ that induce Floquet dynamics.

5.1.2. Surface Plasmon-Polariton Waveguide Array Experiment

Surface plasmon polaritons are the collective oscillatory excitation of electromagnetic field and conducting electrons at the interface of a dielectric and a metal [237]. As sketched in Fig. 5.3, plasmon polaritons can be guided in waveguide structures. The samples fabricated by Z. Fedorova from the

University of Bonn consist of a glass substrate with a silver layer on top. The waveguides are made up of the dielectric material poly-methyl-methylacrylate and have a higher refractive index than the surrounding air. This leads to a confinement of the surface plasmon polaritons to the waveguides similar to the case of dielectric waveguides discussed above [237]. The waveguides are designed such that they operate in the single mode regime [216, 237]. An array of such plasmon-polariton waveguides simulates a tight-binding lattice as in Eq. (5.4) [216]. As a measurement technique a method called leakage radiation microscopy is applied [237]. It obtains the full intensity distribution of the surface plasmon polaritons in real or momentum space, for details see Refs. [216, 237]. In addition, the output intensity of surface plasmon polaritons that traveled through the sample can be measured [216].

5.2. Hamiltonian Quantum Ratchet

Based on the experimental conditions that are discussed above, we introduce a Hamiltonian quantum ratchet that is given by a periodically driven Su-Schrieffer-Heeger model (SSH model) in Subsec. 5.2.1. It is examined how a time-periodic modulation of the coupling constants induces directed motion. Since the time-dependence of the coupling constants, that are given by the conditions of the waveguide experiment, leads to a rather involved theoretical discussion, we introduce a second driving scheme that is much simpler to handle mathematically, but still grasps the relevant physics. We first stick to this second driving scheme, for which we find a resonance condition that calculates the driving frequencies at which ratchet transport with the velocity of one unit cell per driving period is possible. In Subsec. 5.2.2 the Floquet-Bloch theory is introduced, using which quasienergy band structures are calculated in order to further characterize the transport properties of the ratchet model. A symmetry discussion is done in Subsec. 5.2.3. With the knowledge of the Floquet-Bloch theory and the symmetry discussion the transport rectification is analyzed in Subsec. 5.2.4, where we report that transport with the velocity of one unit cell per driving period is related to the closing of the bulk gap. Subsec. 5.2.5 finds a condition for the closing of the bulk gap that is valid for a whole class of driving schemes of the coupling constants. In particular, this condition proves that transport with the velocity of one unit cell per driving period is also possible in the experimentally motivated driving scheme. The closed bulk gap is further related to a nontrivial topology. In Subsec. 5.2.6 we apply all this knowledge to the discussion of the ratchet model with the experimentally motivated driving scheme of the coupling constants.

5.2.1. Lattice Model

The aim is to motivate a lattice model that describes the conditions of the experimental sample shown in Fig. 5.3, where the waveguides are periodically curved in z. This periodic modulation mimics Floquet dynamics, since the nearest neighbor coupling constants of the surface plasmon-polariton waveguide experiment behave as

$$J(z) \propto e^{-ad(z)}, \tag{5.5}$$

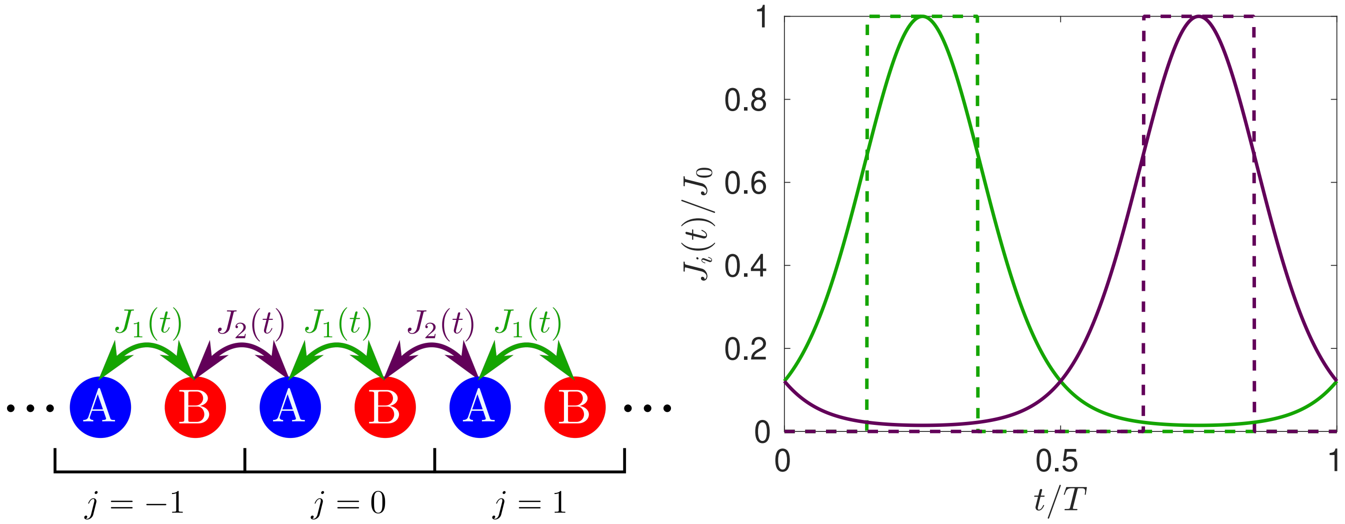

(a) **(b)**

Figure 5.4.: (a) Sketch of the SSH model with time-periodic coupling constants $J_i(t)$, $i = 1, 2$, the unit cells are labeled by j. (b) Coupling constants $J_1(t)$ (green) and $J_2(t)$ (purple) for the disconnected dimer model (dashed) and the experimentally motivated scheme (solid) with the parameters $J = J_0$, $t_1 = 0.15\ T$, $\delta t = 0.2\ T$ and $\lambda = 2.11$.

where $d(z)$ is the z dependent center-to-center distance of neighboring waveguides [237] and a is a constant. As sketched in Fig. 5.3, neighboring waveguides are modulated out of phase. As a result, the configuration of Fig. 5.3 is described by a lattice model with a bipartite unit cell and staggered coupling constants between the lattice sites, which is known as SSH-model. The model is visualized in Fig. 5.4 (a) and described by the following Hamiltonian [239]:

$$H_{\text{bulk}}(t) = \sum_j J_1(t) c^\dagger_{j,\text{A}} c_{j,\text{B}} + J_2(t) c^\dagger_{j,\text{B}} c_{j+1,\text{A}} + h.c.\ . \tag{5.6}$$

In Eq. (5.6), $c^\dagger_{j,\gamma}$ / $c_{j,\gamma}$, $\gamma = \text{A}, \text{B}$ are the creation / annihilation operators for site γ in unit cell j and $h.c.$ denotes the hermitian conjugate. Further, the z-dependence is replaced in Eq. (5.6) by a time-dependence due to the analogy between Schrödinger equation (5.2) and the paraxial Helmholtz equation (5.1).

The antipodal variation of the waveguides changes the center-to-center distance $d(z)$ sinusoidally. This leads in combination with Eq. (5.5) to the concrete form of the coupling constants that describes the waveguide experiment

$$J_1(t) = J_0 e^{-\lambda[1-\sin(\omega t)]},\ J_2(t) = J_1(t - T/2). \tag{5.7}$$

The variable J_0 quantifies the maximum while the parameter $\lambda = 2.11$ is determined experimentally [216]. The hopping amplitudes $J_i(t)$, $i = 1, 2$ are time-periodic with period $T = 2\pi/\omega$. As shown in Fig. 5.4 (b), it holds that $J_1(t) > J_2(t)$ in the first half period, while the situation is inverted in the second half. Note, that there is no additional on site potential V_j in spite of the periodic bending of the waveguides [216].

Throughout this chapter, the experimentally motivated driving scheme Eq. (5.7) will lead to equations that cannot be solved analytically. This is due to the rather involved mathematical expression in Eq. (5.7). The goal is therefore to investigate Hamiltonian (5.6) with coupling constants that have a much simpler time-dependence. This is achieved by assuming a step-function-like behavior which leads to the disconnected dimer driving scheme

$$J_1(t) = \begin{cases} J, & t \in \cup_{n\in\mathbb{Z}}[t_1, t_1+\delta t[+nT \\ 0, & \text{otherwise} \end{cases}, \tag{5.8a}$$

$$J_2(t) = \begin{cases} J, & t \in \cup_{n\in\mathbb{Z}}[t_1, t_1+\delta t[+T/2+nT \\ 0, & \text{otherwise} \end{cases}. \tag{5.8b}$$

Here, J parameterizes the strength of the coupling, the other parameters require $\delta t > 0$ and $t_1 + \delta t < T/2$. The coupling constants defined via Eq. (5.8) are visualized by the dashed lines in Fig. 5.4 (b) which is showing their step-function like behavior that mimics the dynamics of Eq. (5.7). In the first half of the period there is a time interval where $J_1(t)$ differs from zero, while in the second half $J_2(t)$ is non zero for a certain time period. As the name "disconnected dimer model" suggests, the driving scheme (5.8) couples maximally two lattice sites at once, such that the lattice is made up of either uncoupled single sites or disconnected dimers. Note that the coupling constants as defined in Eq. (5.8) are time-periodic with period T.

Both driving schemes Eq. (5.7) and (5.8) are designed to construct a Hamiltonian ratchet. In the following, we introduce the working principle of the ratchet model based on a discussion in the disconnected dimer scheme (5.8). For a single particle wave function $|\psi(t)\rangle = \sum_j(\psi_j^{\mathrm{A}}(t)c_{j,\mathrm{A}}^\dagger + \psi_j^{\mathrm{B}}(t)c_{j,\mathrm{B}}^\dagger)|0\rangle$ the Schrödinger equation reads

$$i\hbar\partial_t\psi_j^{\mathrm{A}}(t) = J_1(t)\psi_j^{\mathrm{B}}(t) + J_2(t)\psi_{j-1}^{\mathrm{B}}(t), \tag{5.9a}$$

$$i\hbar\partial_t\psi_j^{\mathrm{B}}(t) = J_1(t)\psi_j^{\mathrm{A}}(t) + J_2(t)\psi_{j+1}^{\mathrm{A}}(t). \tag{5.9b}$$

As initial condition for the ratchet a single site of sublattice A is excited

$$\psi_j^\gamma(t=0) = \delta_{\gamma,\mathrm{A}}\delta_{j,l}, \tag{5.10}$$

with $l \in \mathbb{Z}$. This configuration can be reached in the waveguide experiment, where a single waveguide is excited by shining a laser beam onto a grating coupler, for details see Ref. [216]. Now we take a look on the dynamics. For $0 < t < t_1$ nothing happens, as there is no coupling between the sites. If $t_1 < t < t_1 + \delta t$, the site labeled by (l, A) couples via $J_1(t)$ to site (l, B). The Schrödinger equation (5.9) reads for $t_1 < t < t_1 + \delta t$:

$$i\hbar\partial_t\psi_j^{\mathrm{A}}(t) = J\psi_j^{\mathrm{B}}(t), \tag{5.11a}$$

$$i\hbar\partial_t\psi_j^{\mathrm{B}}(t) = J\psi_j^{\mathrm{A}}(t). \tag{5.11b}$$

Equation (5.11) describes a static two-level system, whose solution with initial conditions (5.10) performs Rabi oscillations between the two sublattices

$$\psi_l^{\mathrm{A}}(t) = \cos[J(t-t_1)/\hbar], \tag{5.12a}$$

$$\psi_l^{\mathrm{B}}(t) = -i\sin[J(t-t_1)/\hbar]. \tag{5.12b}$$

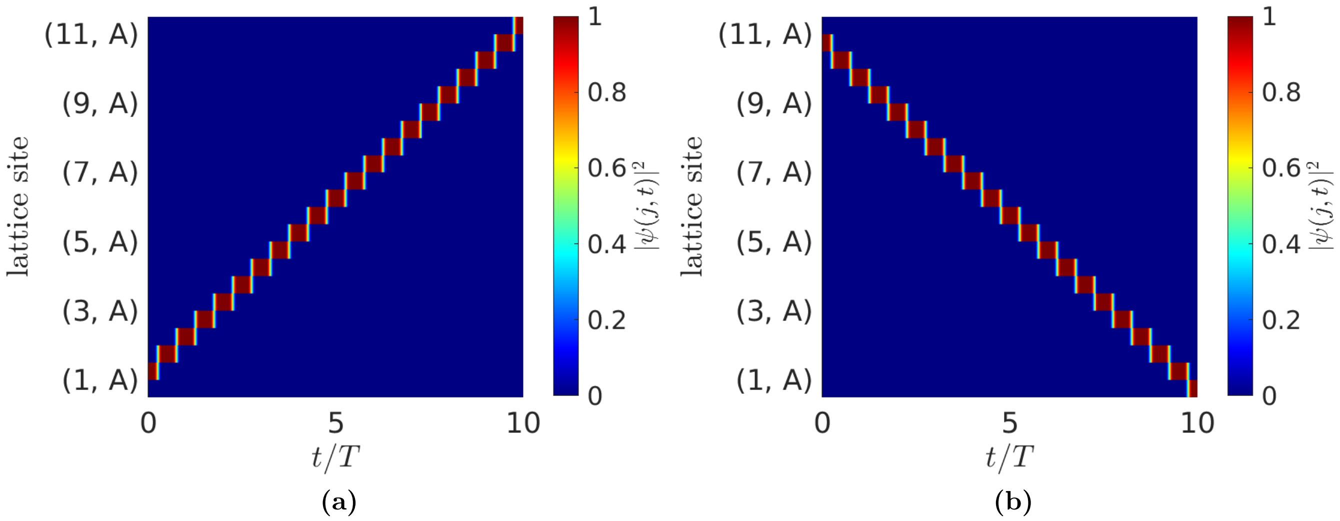

(a) **(b)**

Figure 5.5.: Simulation of a right-moving (a) and left-moving state (b) of the SSH-ratchet model with the disconnected dimer driving scheme with parameters $\delta t = 0.2T$, $J = \hbar\pi/(2\delta t)$, such that condition Eq. (5.13) is fulfilled.

Now we come to the key effect that is responsible for the ratchet transport. If the product $J\delta t$ is chosen such that the cosine is one ans the sine vanishes, the wave function can be fully transferred from sublattice A to B. The condition for that to occur reads

$$\frac{J\delta t}{\hbar} = \pi/2 + n\pi, \; n \in \mathbb{N}_0. \tag{5.13}$$

Equation (5.13) can be seen as a resonance condition, where the periodic drive is in resonance with the frequency of the Rabi oscillations. For the following discussion it is assumed that condition (5.13) is met. In the interval $t_2 < t < t_2 + \delta t$ the coupling constant $J_2(t)$ is nonzero, connecting sites (l, B) and $(l+1, \mathrm{A})$. As $J_2(t) = J_1(t - T/2)$, the wave function is coherently transferred back to sublattice A, but moved one unit cell to the right

$$\psi_j^\gamma(t = T) = \delta_{\gamma,\mathrm{A}}\delta_{j,l+1}. \tag{5.14}$$

Equation (5.14) prominently shows the working principle of the ratchet, as directed transport is possible with the velocity of one unit cell per driving period. Since it will turn out that this is the largest transport possible in this particular ratchet model, and further that the transport is dispersionless, we refer to this as the case of ideal transport.

In Figure 5.5 (a) the discussed directed transport is visualized, a quantum particle is transported dispersionless with a positive group velocity. What happens if initially a lattice site on sublattice B is excited? This is shown in Fig. 5.5 (b). Here dispersionless transport with the velocity of one unit cell per driving period is possible in negative direction. This signals that the direction of transport can be chosen by the initial conditions.

The qualitative behavior of the ratchet model significantly depends on the details of the periodic driving. As prominent case, the parameters can also be tuned such that in Eq. (5.12) the cosine vanishes and the sine equals one. In this case the condition

$$J\delta t/\hbar = n\pi,\ n \in \mathbb{N} \tag{5.15}$$

holds, the state performs full Rabi oscillations between the sublattices during the time intervals of active coupling constants. As a result, the state resides after one driving period at the same site as it was before

$$\psi_j^\gamma(t=T) = \delta_{\gamma,\mathrm{A}}\delta_{j,l}. \tag{5.16}$$

Here no transport is possible. This high tunability of the transport properties will turn out as the key feature of the SSH ratchet model.

Conditions (5.13) and (5.15) can be solved for the driving frequency in order to predict the frequencies ω_n^{id} / ω_n^{ab} where transport is ideal / absent:

$$\hbar\omega_n^{\mathrm{id}} = \frac{4J\delta\xi}{1+2n},\ n \in \mathbb{N}_0, \tag{5.17a}$$

$$\hbar\omega_n^{\mathrm{ab}} = \frac{4J\delta\xi}{2+2n},\ n \in \mathbb{N}_0, \tag{5.17b}$$

with $\delta\xi = \delta t/T$. Eqns. (5.17) are of central importance. They exactly determine the driving frequencies at which the ratchet dynamics is most interesting, e.g. where the ideal transport shown in Fig. 5.5 is possible. The frequencies defined in Eq. (5.17) solely depend on the product of the coupling strength and the fraction of the driving period where the hopping is active. For $n \to \infty$ the frequencies of Eq. (5.17) converge to zero and become more dense, while neither ideal transport nor absence of transport is possible for $\omega > \omega_0^{\mathrm{id}}$. Eqns. (5.17) are seen as resonance conditions, where the driving frequency is on resonance with the Rabi oscillation between the sublattices and thus demonstrate the prominent impact of resonant driving.

5.2.2. Floquet-Bloch Analysis

Floquet-Bloch Theory

For time-periodic quantum systems Floquet theory can be applied in order to find eigenfunctions in terms of Floquet states. Similarly, for spatially periodic Hamiltonians the solution is given by Bloch waves [240]. If a Hamiltonian is both periodic in space and time $H(r,t) = H(r+a,t) = H(r,t+T)$, with a as the lattice constant, the combination of Floquet and Bloch theory ensures the existence of the so-called Floquet-Bloch states [100, 241]:

$$\psi_{k,\alpha,m}(r,t) = e^{i(kr-\epsilon_{k,\alpha,m}t/\hbar)}\phi_{k,\alpha,m}(r,t). \tag{5.18}$$

The function $\phi(k,\alpha,m)$ is periodic in space and time, i.e $\phi_{k,\alpha,m}(r,t) = \phi_{k,\alpha,m}(r+a,t) = \phi_{k,\alpha,m}(r,t+T)$. Here $k \in [-\pi,\pi[$ labels the quasimomentum in the first Brillouin zone, α the Floquet band and m the Floquet Brillouin zone, cf. Ch. 2. In the case of the lattice model given by Eq. (5.6), the Floquet-Bloch states are found by the following procedure: We start by defining the operators ψ_j by

$$\psi_j = \begin{pmatrix} c_{j,\mathrm{A}} \\ c_{j,\mathrm{B}} \end{pmatrix}. \tag{5.19}$$

With Eq. (5.19) Hamiltonian (5.6) is expressed as

$$H_{\mathrm{bulk}}(t) = \sum_j \psi_j^\dagger \begin{pmatrix} 0 & J_1(t) \\ J_1(t) & 0 \end{pmatrix} \psi_j + \psi_j^\dagger \begin{pmatrix} 0 & 0 \\ J_2(t) & 0 \end{pmatrix} \psi_{j+1} + \psi_{j+1}^\dagger \begin{pmatrix} 0 & J_2(t) \\ 0 & 0 \end{pmatrix} \psi_j. \tag{5.20}$$

Equation (5.20) expresses the ratchet model as a tight-binding model with the nearest neighbor hopping only, but has a matrix valued internal structure that corresponds to the structure of the unit cells. Hamiltonian (5.20) can be brought to Fourier representation by the transformation

$$\psi_k = \frac{1}{\sqrt{N_0}} \sum_j e^{-ikj} \psi_j, \tag{5.21}$$

with N_0 being the number of unit cells. Note that with the definition of the Fourier transform in Eq. (5.21) we choose the units such that the length of the unit cell is set to one. The Fourier representation of Hamiltonian (5.20) reads

$$H_{\mathrm{bulk}}(t) = \sum_k \psi_k^\dagger H_k(t) \psi_k, \tag{5.22}$$

where the time-periodic Bloch Hamiltonian is given by

$$H_k(t) = \begin{pmatrix} 0 & J_1(t) + J_2(t)e^{-ik} \\ J_1(t) + J_2(t)e^{ik} & 0 \end{pmatrix}. \tag{5.23}$$

Similar to the discussion of static lattice Hamiltonians, our problem becomes diagonal in quasimomentum k. The Floquet-Bloch states are found by solving the Floquet equation related to Eq. (5.23):

$$(\hat{H}_k - i\hbar\hat{\partial}_t)|\phi_{k,\alpha,m}\rangle\rangle = \epsilon_{k,\alpha,m}|\phi_{k,\alpha,m}\rangle\rangle. \tag{5.24}$$

Here the Floquet-Bloch modes $|\phi_{k,\alpha,m}\rangle\rangle$ and the operators are written in the abstract Floquet representation discussed in Ch. 2, e.g. $(t|\langle r|\phi_{k,\alpha,m}\rangle\rangle = \phi_{k,\alpha,m}(r,t)$. The quasienergies $\epsilon_{k,\alpha,m}$ define a bandstructure in Floquet space and allow for a systematic analysis. Since the model (5.6) has a two-site unit cell, there are two quasienergy bands in each Floquet-Brillouin zone. If possible, the quasienergy bands are labeled such that the band with $\alpha = 1$ corresponds to states with positive group velocity, while $\alpha = 2$ is related to a negative group velocity. Eq. (5.24) is solved numerically by a truncation to an eigenvalue equation of a finite size, following the method described in Subsec. 2.2.1.

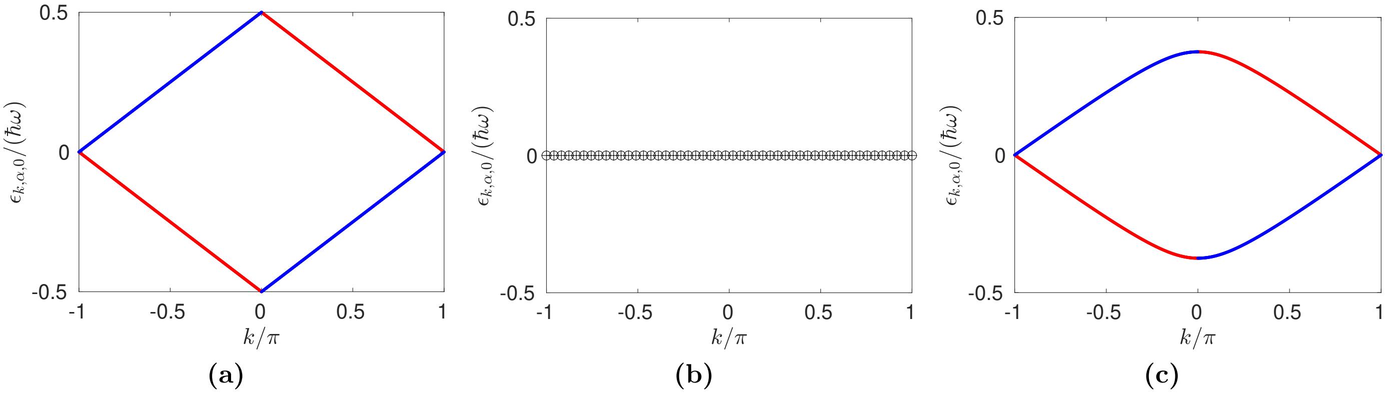

(a) (b) (c)

Figure 5.6.: Quasienergy band structure of the disconnected dimer model with $\delta t = T/4$ and (a) $\hbar\omega = J$, (b) $\hbar\omega = J/2$, (c) $\hbar\omega = 4J/5$, calculated by numerically solving Eq. (5.24). The bands with positive group velocity is marked in blue, the ones with negative in red and the bands with vanishing group velocity in black.

Floquet-Bloch Analysis of the Disconnected Dimer Model

We perform a systematic analysis of the quasienergy bands of the driven SSH ratchet model (5.6) in the case of the disconnected dimer driving scheme Eq. (5.8). Figure 5.6 shows that the form of the band structure significantly depends on the driving frequency ω. This enables to tune the bands from a perfect linear with a group velocity of one unit cell per driving period to completely flat. In the following the understanding of this high tunability is deepened by analytical arguments.

Let us start with the perfectly linear bands with finite group velocity shown in Fig. 5.6 (a), where the driving frequency is chosen such that condition (5.17a) is met. In this case the band structure is found analytically by calculating the time evolution of a state $|\psi_k(t)\rangle = \sum_{\gamma=\mathrm{A,B}} \psi_{k,\gamma}(t) c^\dagger_{k,\gamma}|0\rangle$ with the Bloch Hamiltonian (5.23) in Fourier space. As initial condition $\psi_{k,\gamma}(t=0) = \delta_{\gamma,\mathrm{A}}$ is chosen. It turns out that besides a Rabi oscillation $H_k(t)$ induces a momentum-dependent phase in the time evolved state. After one driving period t the state reproduces itself up to a phase factor

$$\psi_{k,\gamma}(t=T) = \delta_{\gamma,\mathrm{A}} \times (-1)e^{-ik}, \tag{5.25}$$

a behavior that Floquet states are known for, cf. Eq. (2.7). Comparing Eq. (5.25) to Eq. (2.12), the quasienergy band is found to be

$$\epsilon_{k,\alpha=1,m}/\hbar = \frac{w}{2\pi}k - \frac{\omega}{2} + m\omega,\ m \in \mathbb{Z}. \tag{5.26}$$

Equation (5.26) displays the perfectly linear slope of the quasienergy band mathematically. The group velocity is defined by

$$v_{k,\alpha} = \frac{1}{\hbar}\frac{\partial \epsilon_{k,\alpha,m}}{\partial k}. \tag{5.27}$$

The Floquet-Bloch states in the band with $\alpha = 1$ have a positive group velocity and thus are right movers. With the band structure of Eq. (5.26) the directed transport shown in Fig. 5.5 can be explained on a more formal level. A Fourier analysis shows that the excitation of a single lattice site such as in Eq. (5.10) coincides to an uniformly populated right moving band. The velocity of the wave packet is given by the average over the first Brillouin zone $\bar{v}_\alpha = 1/(2\pi)\int_{-\pi}^{\pi} dk v_{k,\alpha}$. With Eq. (5.26) we have

$$\bar{v}_1 = \frac{1}{T}. \tag{5.28}$$

This shows that the averaged group velocity $\bar{v}_1$ is positive and that the state moves at the speed of one unit cell per driving period, the same we found out in the real space discussion of Subsec. 5.2.1.

A similar calculation finds that a state with $\psi_{k,\gamma}(t=0) = \delta_{\gamma,\mathrm{B}}$ corresponds to a Floquet-Bloch state with the quasienergy band

$$\epsilon_{k,\alpha=2,m}/\hbar = -\frac{w}{2\pi}k + \frac{\omega}{2} + m\omega,\ m \in \mathbb{Z}, \tag{5.29}$$

where the direction of transport is exactly inverted. Here the linear slope is negative and the states are left movers.

In Fig. 5.6 (b) the driving frequency is lowered to the half of Fig. 5.6 (a). In this case the corresponding quasienergy bands are flat

$$\epsilon_{k,\alpha,m}/\hbar = m\omega, \tag{5.30}$$

and transport is absent.

In Fig. 5.6 (c) the band structure is calculated numerically for a driving frequency that does not meet Eqns. (5.17). The bands are neither perfectly linear nor completely flat, but are curved with a finite band gap at $k = 0$. Phenomenologically, the physical cause of this gap can be made visible by the time-evolution of the states in real space. If condition Eq. (5.15) is not met, the Rabi oscillation of the state is such that both sublattices are populated. As a result, a portion of the state travels to the right, while another portion is transported to the left. If this picture is transferred into Fourier space, it corresponds to a coupling of left and right moving Floquet-Bloch states which is in turn related to a hybridization of the quasienergy bands and a finite band gap.

In the following a deeper understanding of this effect is provided. Instead of changing the driving frequency away from Eq. (5.17a), an increase or decrease of the coupling constant J is assumed. The Hamiltonian is written as $H(t) = H_{\mathrm{Ideal}}(t) + H_{\mathrm{Pert}}(t)$. The explicit form of both $H_{\mathrm{Ideal}}(t)$ and $H_{\mathrm{Pert}}(t)$ is given by the SSH ratchet model (5.20) with the disconnected dimer driving scheme (5.8) as coupling constant. The values of δt and t_1 are chosen to be the same for both $H_{\mathrm{Ideal}}(t)$ and $H_{\mathrm{Pert}}(t)$, only the value of the coupling constants J differs. The value of J of $H_{\mathrm{Ideal}}(t)$ is tuned in such a way that the transport is ideal, while $H_{\mathrm{Pert}}(t)$ is assumed to be a small perturbation. The Floquet modes solving the Floquet equation of the unperturbed Hamiltonian $H_{\mathrm{Ideal}}(t)$ are denoted as $|\phi^{\mathrm{id}}_{k,\alpha,m}\rangle\rangle$, their mathematical form can be found with the earlier discussion in this section. In order to calculate the band structure of the total Hamiltonian $H(t) = H_{\mathrm{Ideal}}(t) + H_{\mathrm{Pert}}(t)$ an expansion in the unperturbed basis $|\phi^{\mathrm{id}}_{k,\alpha,m}\rangle\rangle$ is performed in Floquet space:

$$\langle\langle\phi^{\mathrm{id}}_{k,\alpha,m}|\hat{H}|\phi^{\mathrm{id}}_{k,\beta,n}\rangle\rangle = \epsilon_{k,\alpha,m}\delta_{\alpha,\beta}\delta_{n,m} + \langle\langle\phi^{\mathrm{id}}_{k,\alpha,m}|\hat{H}_{\mathrm{Pert}}|\phi^{\mathrm{id}}_{k,\beta,n}\rangle\rangle. \tag{5.31}$$

Since the $\hat{H}_{\mathrm{Pert}}$ is periodic in real space, the matrix elements of $\hat{H}_{\mathrm{Pert}}$ are diagonal in quasimomentum k. A full solution of Eq. (5.31) is possible, but rather exhaustive to elaborate. At weak driving, however, only the two quasienergy bands that come close to each other are relevant. In this limit it can be decided whether there is an avoided crossing or not by investigating the matrix elements of the perturbative part in Eq. (5.31). The relevant matrix element is the one that couples two crossing bands with different group velocity. By calculating its size we can explain, why there is an avoided crossing at $k = 0$ and a crossing at $k = \pm\pi$. The matrix element is explicitly given by the integral

$$\langle\langle \phi^{\mathrm{id}}_{k,\alpha=1,m} | \hat{H}_{\mathrm{Pert}} | \phi^{\mathrm{id}}_{k,\beta=2,n} \rangle\rangle \propto (1+e^{-ik}) \int_{t_1}^{t_1+\delta t} dt\ \sin^2[J(t-t_1)/\hbar] + (1+e^{ik}) \int_{t_1}^{t_1+\delta t} dt\ \cos^2[J(t-t_1)/\hbar], \tag{5.32}$$

where we inserted the explicit form of the Floquet-Bloch states, where n and m are chosen such that the respective crossing / avoided crossing is reached. In Eq. (5.32) it is directly visible that for $k = 0$ the matrix element $\langle\langle \phi^{\mathrm{id}}_{k,\alpha,m} | \hat{H}_{\mathrm{Pert}} | \phi^{\mathrm{id}}_{k,\beta,n} \rangle\rangle$ is finite while it vanishes for $k = \pi$. This behavior explains mathematically why there is a crossing of the quasienergy bands at $k = 0$ and an avoided crossing at $k = \pi$.

5.2.3. Discrete Symmetries of the Ratchet Model

Before a detailed analysis the transport rectification is given, the discrete symmetries of our model are elaborated for a deeper understanding of the ratchet and the directional filter, that will be proposed in a later section. The well-known Altland-Zirnbauer symmetry classes [242, 243] can be generalized to time-periodically driven single particle Hamiltonians [244]. First, discrete symmetries are defined in terms of Floquet-Bloch Hamiltonians and then the implications of these symmetries on the quasienergy spectrum and the Floquet states are pointed out. Finally, the symmetries in our SSH ratchet model Eq. (5.20) are discussed.

In the following particle-hole, time-reversal, and chiral symmetry are defined for Floquet-Bloch Hamiltonians $H_k(t)$ in d spatial dimensions $k \in \mathbb{R}^d$, $d \in \mathbb{N}_0$ [244].

Particle-Hole Symmetry

If particle-hole symmetry is present, there exists an operator $\mathbb{P} = \mathcal{K}P$, with $\mathcal{K}$ as the complex conjugation and P as a unitary operator, which acts on the Bloch-Hamiltonian as follows [244]

$$P H_k(t) P^{-1} = -H^*_{-k}(t). \tag{5.33}$$

Here * denotes the complex conjugation. What are the consequences of Eq. (5.33) on the quasienergies and the Floquet modes? In order to figure this out the Floquet equation is investigated

$$\left(P H_k(t) P^{-1} - i\hbar \frac{\partial}{\partial t} \right) P |\phi_k(t)\rangle = \epsilon_k P |\phi_k(t)\rangle, \tag{5.34}$$

where we apply the transformation P from the left. A possible band index α as well as the Floquet Brillouin zone index m are dropped. The Floquet-Bloch Hamiltonian can be transformed with Eq. (5.33), such that we are left with the Floquet equation at $-k$:

$$\left(H_{-k}(t) - i\hbar\frac{\partial}{\partial t}\right)(P|\phi_k(t)\rangle)^* = -\epsilon_k(P|\phi_k(t)\rangle)^*. \tag{5.35}$$

With Eq. (5.35) the following relation for the quasienergies are made

$$\epsilon_{-k} = -\epsilon_k.$$

This says that in the presence of particle-hole symmetry the quasienergy bands are anti-symmetric with respect to k. The Floquet modes fulfill

$$|\phi_{-k}(t)\rangle = (P|\phi_k(t)\rangle)^* \tag{5.36}$$

in the presence of particle-hole symmetry. Eq. (5.36) can be written in terms of Fourier components as

$$|\phi_k^{(n)}\rangle = (P|\phi_k^{(-n)}\rangle)^*. \tag{5.37}$$

Time-Reversal Symmetry

If the Floquet-Bloch Hamiltonian is time-reversal symmetric, there exists an operator $\mathcal{T} = \mathcal{K}\theta$, where θ is unitary, and a number $\xi \in \mathbb{R}$ such that [244]

$$\theta H_k(\xi T + t)\theta^{-1} = H_{-k}^*(\xi T - t). \tag{5.38}$$

Similar to the considerations for the particle-hole symmetry one finds that the time-reversal symmetry implies the quasienergies to be symmetric in k:

$$\epsilon_{-k} = \epsilon_k. \tag{5.39}$$

The Floquet modes fulfill

$$|\phi_{-k}(t)\rangle = (\theta|\phi_k(2\xi T - t)\rangle)^*. \tag{5.40}$$

Here the Floquet mode is mirrored in time around the point $2\xi T$, and the operator θ is applied to it. Eq. (5.40) can be expressed in terms of Fourier modes by

$$|\phi_{-k}^{(n)}\rangle = e^{i4\pi\xi n}(\theta|\phi_k^{(n)}\rangle)^* \tag{5.41}$$

Chiral Symmetry

A Floquet-Bloch Hamiltonian has chiral symmetry if there exists an unitary operator C such that

$$CH_k(\xi T + t)C^{-1} = -H_k(\xi T - t) \tag{5.42}$$

is fulfilled with $\xi \in \mathbb{R}$. If both particle-hole and time-reversal symmetry are present, it follows that $C = P\theta$. Using chiral symmetry we can assign each Floquet mode a chiral symmetric partner [239], whose properties are indicated with a bar. The quasienergies of the partnered Floquet modes have opposite sign

$$\bar{\epsilon}_k = -\epsilon_k, \tag{5.43}$$

while partnered Floquet modes are related by

$$|\bar{\phi}_k(t)\rangle = C|\phi_k(2\xi T - t)\rangle. \tag{5.44}$$

Equation (5.44) reads in terms of Fourier components as

$$|\bar{\phi}_k^{(n)}\rangle = e^{i4\pi\xi n} C|\phi_k^{(n)}\rangle. \tag{5.45}$$

Symmetry Classification of the SSH Ratchet Model

The Floquet-Bloch Hamiltonian (5.23) of the periodically driven SSH ratchet shows all three aforementioned symmetries with the operators $P = \sigma_z$, where σ_z is a Pauli-Matrix, $\theta = \mathbb{I}_{2\times 2}$ is the 2×2 identity matrix and $C = P\theta$. For the disconnected dimer model Eq. (5.8) the condition $\xi T = t_1 + \delta t/2$ determines the parameter ξ that is in the definition of the time-reversal symmetry. Note that also the experimentally motivated driving scheme (5.7) obeys all aformentined symmetries, here it holds that $\xi = 1/4$. In summary, the driven SSH ratchet model lies in the Altland-Zirnbauer class BDI [242,244].

Particle-hole symmetry guarantees that the quasienergy bands are anti-symmetric with respect to $k = 0$ and the density $n_{k,\alpha,m}(\gamma, t) = |\phi_{k,\alpha,m}(\gamma, t)|^2$, $\gamma = \mathrm{A/B}$, is symmetric in k at each time t. Time-reversal symmetry has two consequences: For each mode with quasienergy $\epsilon_{k,\alpha,m}$ there exists a mode with the same quasienergy, but opposite propagtion direction $\epsilon_{k,\alpha,m} = \epsilon_{-k,\beta\neq\alpha,m}$. Using condition (5.40) with the experimentally relevant case of $\xi = 1/4$ the densities are related by $n_{k,\alpha,m}(\gamma, t) = n_{-k,\beta\neq\alpha,m}(\gamma, T/2 - t)$. If the Floquet-Bloch states perform sublattice oscillations, the above relation of the densities implies that the oscillation of left and right movers is antipodal. The chiral symmetry leads to relations that are a combination of the above two: The quasienergies lie symmetric around zero $\epsilon_{k,\alpha,m} = -\epsilon_{k,\beta\neq\alpha,m}$ and also the density of those states are related by $n_{k,\alpha,m}(t, \gamma) = n_{k,\beta\neq\alpha,m}(T/2 - t, \gamma)$.

5.2.4. Rectification of Transport in a Hamiltonian Quantum Ratchet

This subsection is devoted to the deeper analysis of the transport rectification induced by the ratchet effect. As a central quantity the average group velocity of a wave packet is introduced. A systematic analysis of the average group velocity and the resulting particle transport for a large parameter range is performed in the case of the disconnected dimer model.

Relation of Asymptotic Current to Average Group Velocity

Directed particle transport is possible in a Hamiltonian quantum ratchet and can be measured by the current that runs through the system. References [222–224, 245] quantify the asymptotic current transported in the ratchet by a time-averaged expectation value of the momentum operator

$$J = \lim_{t\to\infty} \frac{1}{t-t_0} \int_{t_0}^{t} dt' \langle \psi(t') | P | \psi(t') \rangle. \tag{5.46}$$

Here, P denotes the momentum operator and $|\psi(t)\rangle$ is the time-dependent wave function of the system which is evolved from an arbitrary state $|\psi(t_0)\rangle = |\psi_0\rangle$ at an initial time t_0. Following the argumentation of Refs. [222–224, 245], we assume a particle in a lattice potential as a model system

$$H(r,t) = \frac{P^2}{2m_{\mathrm{P}}} + U(r,t), \tag{5.47}$$

where m_{P} is the particle mass and the space- and time periodic potential is given by $U(r,t) = U(r+a,t) = U(r,t+T)$ with unit cell a and period T. Since Hamiltonian (5.47) is periodic in both space and time, a solution via Floquet-Bloch theory is possible [223, 224]. The resulting Floquet modes $|\phi_{k,\alpha,m}(t)\rangle$ are labeled by quasimomentum k, band index α and Floquet Brillouin zone index m. The time-evolution of an arbitrary state $|\psi(t)\rangle$ is found with Eq. (2.9) by

$$|\psi(t)\rangle = \sum_{k,\alpha} A_{k,\alpha} e^{-i\epsilon_{k,\alpha,0}t/\hbar} |\phi_{k,\alpha,0}(t)\rangle, \tag{5.48}$$

where the coefficients $A_{k,\alpha}$ are determined by the projection of the initial state to the Floquet modes

$$A_{k,\alpha} = \langle \phi_{k,\alpha,0}(t_0) | \psi(t_0) \rangle. \tag{5.49}$$

The normalization of the state (5.48) requires

$$\sum_{k,\alpha} |A_{k,\alpha}|^2 = 1. \tag{5.50}$$

Using $\langle \phi_{q,\beta,0}(t) | P | \phi_{k,\alpha,0}(t) \rangle = \delta_{k,q}\delta_{\alpha,\beta} \frac{\partial \epsilon_{k,\alpha,0}}{\partial k} m/\hbar$ [224], the asymptotic current is given by $J = \frac{m}{\hbar} \sum_{k,\alpha} |A_{k,\alpha}|^2 \frac{\partial \epsilon_{k,\alpha,0}}{\partial k}$ [222, 223, 245]. Dividing by the particle mass yields the average group velocity

$$\bar{v}_{\mathrm{g}} = \sum_{k,\alpha} |A_{k,\alpha}|^2 v_{k,\alpha}, \tag{5.51}$$

with $v_{k,\alpha}$ as defined in Eq. (5.27). With Eq. (5.51) $\bar{v}_{\mathrm{g}}$ is given by an average of the group velocity $v_{k,\alpha}$ weighted by the distribution $|A_{k,\alpha}|^2$, which in turn is defined by the initial state. The average group velocity is the central quantity that will be considered as a measure of particle transport in the following. The better a ratchet works, the larger is the particle transport, which is measured by $\bar{v}_{\mathrm{g}}$. The above calculation shows that the average group velocity is not a conceptual construct, but can be related to experimental situations where a time-evolution of a quantum state is observed. At last, note that Ref. [217] relates the average group velocity to an electric current in a setup similar to ours.

The previous calculation found a formula for the average group velocity for the case that a real space representation Eq. (5.47) of the model is possible. In the following we derive Eq. (5.51) within the tight-binding description. On a lattice model, an average group velocity is defined by introducing a group velocity operator v_{g} on the basis of the Floquet-Bloch states $|\phi_{k,\alpha,m}\rangle\rangle$:

$$v_{\mathrm{g}}|\phi_{k,\alpha,m}(t)\rangle = v_{k,\alpha}|\phi_{k,\alpha,m}(t)\rangle, \tag{5.52}$$

with the group velocity $v_{k,\alpha}$ defined in Eq. (5.27). The average group velocity is calculated by the expectation value of the group velocity operator

$$\bar{v}_{\mathrm{g}} = \langle\psi(t)|v_{\mathrm{g}}|\psi(t)\rangle, \tag{5.53}$$

where $|\psi(t)\rangle$ is a wave packet given by Eq. (5.48). Using the orthonormality of the Floquet modes Eq. (2.41), Eq. (5.53) transforms into Eq. (5.51), the result we obtained by looking at the asymptotic current. This shows that the same expression for average group velocity (5.51) is found with both calculations.

Transport in a Hamiltonian Quantum Ratchet, Case Study of the Disconnected Dimer Scheme

Equation (5.51) shows that in a Hamiltonian quantum ratchet the direction and the magnitude of particle transport strongly depends on the initial state. Consider now a general two-band ratchet model fulfilling time-reversal symmetry, such as the SSH ratchet model of Eq. (5.6). Time-reversal symmetry implies that the group velocities of the two bands are anti-symmetric in quasimomentum

$$v_{k,\alpha} = -v_{-k,\beta\neq\alpha}. \tag{5.54}$$

Using Eq. (5.54) the averaged group velocity is expressed as

$$\bar{v}_{\mathrm{g}} = \sum_k v_{k,\alpha}(|A_{k,1}|^2 - |A_{-k,2}|^2). \tag{5.55}$$

Equation (5.55) makes directly visible that for creating a directed current it is central to populate the two bands unequally. The extreme example of an asymmetric distribution is to populate the right movers only

$$A_{k,\alpha} = \frac{\delta_{\alpha,1}}{\sqrt{N_0}}. \tag{5.56}$$

Figure 5.7 (a) shows the average group velocity for a uniform population of the right moving band in case of the disconnected dimer driving scheme. The average group velocity performs an oscillating behavior between ideal transport $\bar{v}_{\mathrm{g}}T = 1$ and absence of transport $\bar{v}_{\mathrm{g}}T = 0$. This demonstrates the key feature of the SSH ratchets model (5.6), namely, the high tunablility of the particle transport. The frequencies of ideal transport and absence of transport are correctly predicted by Eqns. (5.17).

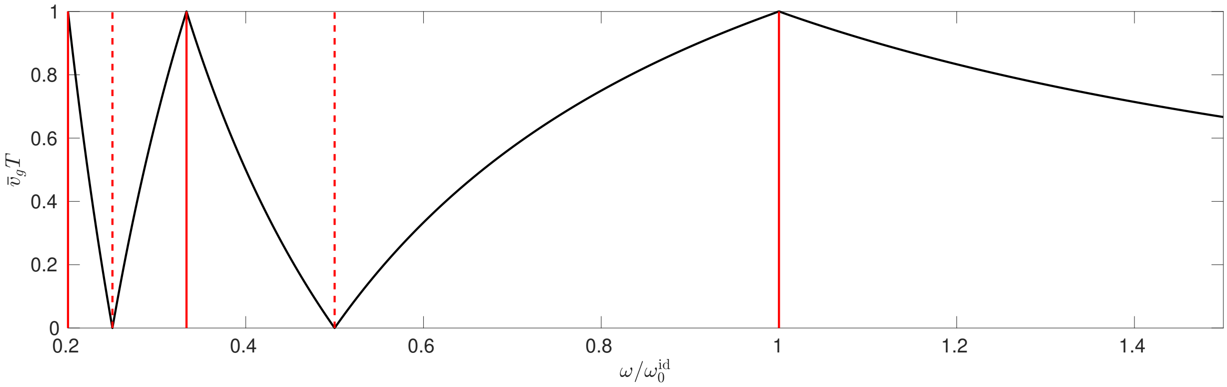

(a)

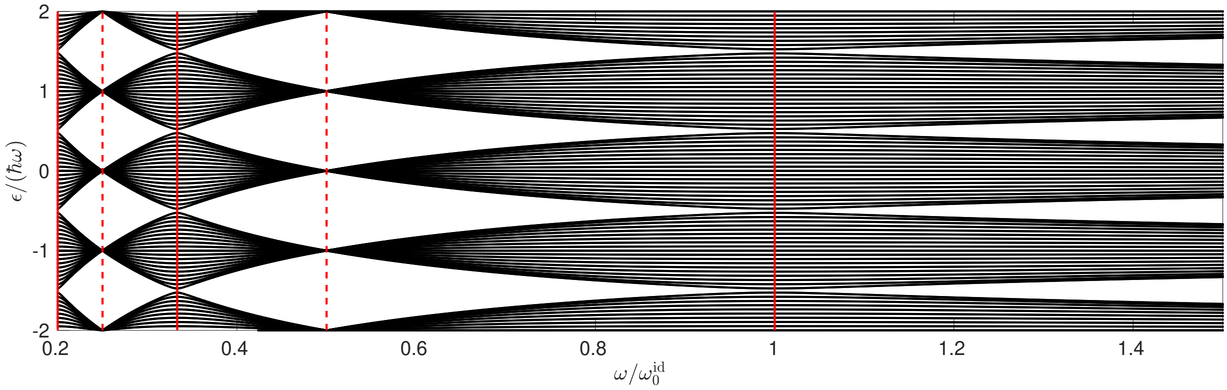

(b)

Figure 5.7.: Results for the disconnected dimer model with $\delta t = 0.2\ T$ and $J = \hbar\omega_0^{\mathrm{id}} 5/4$. (a) averaged group velocity $\bar{v}_{\mathrm{g}}$ in dependence of the driving frequency, (b) quasienergy spectrum in dependence of the driving frequency. Red solid lines mark the position of ideal transport predicted by Eq. (5.17a), red dashed lines the frequencies of absence of transport predicted by Eq. (5.17b).

In Fig. 5.7 (b) the quasienergy band structure is shown. It directly links the quantized transport to the closing of the bulk gap, while flat bands imply a vanishing group velocity. For a band with solely positive group velocity and uniform population of the form (5.56), the average group velocity is directly linked to the size of the band gap by

$$\bar{v}_{\mathrm{g}} = \frac{1}{2\pi\hbar}\left(\lim_{k\to 0^-} \epsilon_{k,1,0} - \lim_{k\to 0^+} \epsilon_{k,1,0}\right). \tag{5.57}$$

If the band gap closes, Eq. (5.57) direclty predicts that there is particle transport with $\bar{v}_g = 1/T$.

In the high frequency limit $\omega_0^{\mathrm{id}} \ll \omega$ neither ideal transport nor complete absence of transport is possible. Calculating the effective Hamiltonian up to first order using Eq. (2.15a) reveals that the effective model is given by Eq. (5.6) with time-independent effective coupling constants $J_i = J_{\mathrm{eff}},\ i = 1, 2$. A formula for J_{eff} will be given in Eq. (5.64). In the high frequency regime the transport is ballistic and the ratchet effect is absent.

At last, it is discussed how the initial state influences the ratchet transport. We consider the disconnected dimer model at a driving frequency given by Eq. (5.17a) and a population of the bands given by

$$A_{k,1} = \frac{\cos(\theta)}{\sqrt{N_0}},\ A_{k,2} = \frac{\sin(\theta)}{\sqrt{N_0}}, \tag{5.58}$$

with $\theta \in [0, \pi]$. A population as in Eq. (5.58) is achieved by exciting neighboring lattice sites in real space with different intensities. If $\theta = 0$, only the right movers are populated while $\theta = \pi$ corresponds to an uniform population of the left movers. For $\theta = \pi/4$ both bands are populated equally. The average group velocity for the distribution (5.58) is calculated in the case of linear bands with the use of Eqns. (5.26), (5.27) and (5.57) to

$$\bar{v}_g T = \cos(2\theta). \tag{5.59}$$

This shows that both direction and magnitude of the transport depend on the angle θ and thus on the initial population of the two sublattices. For a distribution that populates both sites equally, which is described by $\theta = \pi/4$, the average group velocity vanishes and thus transport is absent in this case even for linear quasienergy bands.

5.2.5. Helical Bands and Relation to Topology

In the case where the gap of the quasienergy band structure is closed, the bands are helical in the Floquet-Bloch Brillouin zone. The term helical means that the bands wind around the Floquet-Bloch Brillouin zone. In this subsection a general condition for the occurrence of a closed band gap is derived which is related to helical bands. A topological invariant is introduced that characterizes this helicity.

Condition of a Closed Band Gap at $\mathbf{k = 0}$

The final goal of this part is to generalize the conditions (5.17) found for the disconnected dimer scheme to time-dependent coupling constants of a general form, including the experimentally motivated scheme (5.7). In order to achieve this, an analytical expression of the quasienergy at $k = 0, \pi$ is derived in the following. For a general time-periodic driving scheme $J_i(t) = J_i(t+T)$ the Schrödinger equation for the Floquet-Bloch waves reads at $k = 0, \pi$:

$$i\partial_t \psi_{k,\mathrm{A}} = f_k(t)\psi_{k,\mathrm{B}}, \tag{5.60a}$$

$$i\partial_t \psi_{k,\mathrm{B}} = f_k(t)\psi_{k,\mathrm{A}}, \tag{5.60b}$$

where $\hbar f_k(t) = J_1(t) + J_2(t)e^{-ik}$. The special cases $k = 0, \pi$ are chosen such that the hamiltonian matrix governing the dynamics of Eq. (5.60) solely has real entries. In this case an analytic solution of Eq. (5.60) is found by

$$\begin{aligned}\psi_{k,\mathrm{A}}(t) &= c_1 \exp\left[i\int_0^t dt' f_k(t')\right] + c_2 \exp\left[-i\int_0^t dt' f_k(t')\right], && (5.61\mathrm{a})\\ \psi_{k,\mathrm{B}}(t) &= -c_1 \exp\left[i\int_0^t dt' f_k(t')\right] + c_2 \exp\left[-i\int_0^t dt' f_k(t')\right], && (5.61\mathrm{b})\end{aligned}$$

valid for $k = 0, \pi$. For the calculation of the Floquet spectrum it is important to note that the wave function at $t = 0$ is related to the coefficients by $\psi_{k,\mathrm{A}}(0) = c_1 + c_2$, $\psi_{k,\mathrm{B}}(0) = c_2 - c_1$. The quasienergies are extracted from the eigenvalue equation of the time-evolution operator $U_k(T, 0)$ in the sense of Eq. (2.12):

$$\begin{pmatrix} \cos[i\int_0^T dt f_k(t)] & -i\sin[i\int_0^T dt f_k(t)] \\ -i\sin[i\int_0^T dt f_k(t)] & \cos[i\int_0^T dt f_k(t)] \end{pmatrix} \begin{pmatrix} \psi_{k,\mathrm{A}}(0) \\ \psi_{k,\mathrm{B}}(0) \end{pmatrix} = e^{-i\epsilon_{k,\alpha,m}T/\hbar} \begin{pmatrix} \psi_{k,\mathrm{A}}(0) \\ \psi_{k,\mathrm{B}}(0) \end{pmatrix}, \ k = 0, \pi. \quad (5.62)$$

The quasienergies are then given by the time average of the function $f_k(t)$:

$$\epsilon_{k,\pm,m} = \pm\frac{1}{T}\int_0^T dt f_k(t) + m\hbar\omega, \ k = 0, \pi, \ m \in \mathbb{Z}. \quad (5.63)$$

This is a remarkable result, since it yields an analytical understanding of the quasienergies at $k = 0, \pi$ and is valid for a general real valued, time-periodic driving scheme $J_i(t)$, $i = 1, 2$ which is capable of being integrated. As Eq. (5.63) only calculates the quasienergies at the two points $k = 0, \pi$ in k-space, we are not able to label them via the group velocity and introduce a ±-notation as labeling.

In the following we restrict to a driving scheme where the time average of both coupling constants is equal. This holds in particular for the experimentally motivated driving scheme (5.7). If both coupling constants have an equal time average, an effective coupling constant can be defined as the time average

$$J_{\text{eff}} = \frac{1}{T}\int_0^T dt J_i(t), \ i = 1, 2, \quad (5.64)$$

using which the quasienergies at $k = 0$ read

$$\epsilon_{k=0,\pm,m} = \pm 2J_{\text{eff}} + m\hbar\omega, \ m \in \mathbb{Z}. \quad (5.65)$$

At $k = \pi$ the time average is taken over the difference $f_{k=\pi}(t) = J_1(t) - J_2(t)$ such that the integral in Eq. (5.63) vanishes. The quasienergies at $k = \pi$ are thus given by an integer multiple of $\hbar\omega$:

$$\epsilon_{k=\pi,\pm,m} = m\hbar\omega, \ m \in \mathbb{Z}. \quad (5.66)$$

In the following we find a condition for a closed band gap, provided that the driving scheme obeys the following assumptions: First, the time average of both hopping constants should be equal. This implies with Eq. (5.65) that the quasienergies at $k = 0$ are symmetric around $\epsilon = 0$. Equation (5.66) says that the quasienergies at $k = \pm\pi$ reside in all cases at zero. Thus, a possible opening and closing of a band gap cannot be at $\epsilon = 0$. Second, the driving scheme is assumed such that $|\epsilon_{k,1,0} - \epsilon_{k,2,0}|$ is maximal at $k = 0$, provided that at least one of the quasienergy bands is in the neighborhood of the edge of the first Floquet Brillouin zone at $\epsilon = \pm\hbar\omega/2$. Physically speaking, it is assumed that if the band gap closes, then it closes at $k = 0$. Since the quasienergies at $k = 0$ are symmetric around ϵ, this closing of the band gap is at the edge of the first Floquet-Brillouin zone at $\epsilon = \pm\hbar\omega/2$. Both the disconnected dimer and experimentally motivated driving scheme obey these conditions, c.f. Fig. 5.6 (a) and Fig. (5.9) (a). Under this circumstances, the closing of the bulk gap can be predicted with Eq. (5.65) by assuming $\epsilon_{k=0,+,m'} = \hbar\omega/2 + m'\hbar\omega,\ m' \in \mathbb{Z}$. This incarnates into the equation

$$2J_{\text{eff}} = \frac{\hbar\omega}{2} + n\hbar\omega,\ n \in \mathbb{N}_0, \tag{5.67}$$

which generalizes Eq. (5.13) found for the disconnected dimer model. The main difference to Eq. (5.13) is that in Eq. (5.67) the coupling constant is not required to have a step-function-like behavior, so that the product of coupling strength times duration of active coupling is generalized to an integral. Equation (5.67) is solved for the driving frequency to

$$\hbar\omega_n^{\text{id}} = \frac{4J_{\text{eff}}}{1+2n},\ n \in \mathbb{N}_0,\ i = 1, 2. \tag{5.68}$$

This equation generalizes Eq. (5.17a) and predicts the driving frequencies at which the band gap closes. It is remarkable, that this prediction is possible for relatively general driving schemes, which simply have to fulfill the assumptions mentioned above. Thus, Eq. (5.68) is of central relevance of this chapter. In particular, Eq. (5.68) will predict the driving frequencies at which the experimentally motivated driving scheme hosts ideal transport. This makes Eq. (5.68) a generalization of Eq. (5.17a) found in the case of the disconnected dimer driving scheme. Note the interesting point that the ω_n^{id} solely depend on the time average of the coupling constant $J_i(t),\ i = 1, 2$. The quantity n can be interpreted in analogy to the disconnected dimer model as the number of full Rabi-cycles the system undergoes before it performs the transfer of the state between the two sublattices.

Alike to the case of a closed gap, a condition for a maximal bulk gap, i.e. a collapse of the quasienergy bands to $\epsilon = 0$, at $k = 0$ is found by assuming $\epsilon_{k=0,\pm,m'} = m'\hbar\omega$, which results in

$$\hbar\omega_n^{\text{ab}} = \frac{4J_{\text{eff}}}{2+2n},\ n \in \mathbb{N}_0. \tag{5.69}$$

This consideration is valid for general driving schemes where both coupling constants are required to have an equal time average, but the implications are weaker that the ones made in the discussion of Eq. (5.68). In Fig. 5.9 (b) the quasienergy bands of the experimentally motivated driving scheme at a driving frequency of $\omega = \omega_0^{\text{ab}}$ is shown, where it can be seen that at $k = 0$ the quasienergies $\epsilon_{k,\alpha,0}$ are indeed zero, but the quasienergy bands are not completely flat, like it is found in the disconnected dimer model. Nevertheless, Eq. (5.69) is interpreted as a generalization of Eq. (5.17b), since it will turn out that Eq. (5.69) roughly predicts the driving frequencies where the transport is minimal in a SSH ratchet model with experimentally motivated driving scheme.

Helical Bands and their Relation to Topology

The relation of a closed gap to quasienergy bands that are helical in the Floquet-Bloch Brillouin zone is discussed. Consider therefore Fig. 5.8 (a), where the band structure in the case of the disconnected dimer model is shown for a finite gap. Since the Floquet-Bloch Brillouin zone structure is both periodic in quasimomentum and quasienergy, the points on the lines with $k = \pm\pi$ and $\epsilon = \pm\hbar\omega/2$ are equivalent to each other. Thus the first Floquet Brillouin zone is topologically equivalent to a torus, which we parameterize in the following

$$x = [R + r\cos(k)]\cos(\epsilon T), \tag{5.70a}$$

$$y = [R + r\cos(k)]\sin(\epsilon T), \tag{5.70b}$$

$$z = r\sin(k). \tag{5.70c}$$

Here R is the distance of the center of the torus to the central line of the tube, while r denotes the radius of the tube itself. A rotation along the axis of revolution of the torus is described by ϵT, while k gives a rotation around the tube. As seen in Fig. 5.8 (b), for a finite band gap the quasienergy bands wind around the tube, but they do not wind around the free space in the center of the torus. Figure 5.8 (c) shows the case for perfect linear bands. Here the Floquet-Bloch bands wind around the first Floquet-Bloch Brillouin zone and are thus regarded as helical. This behavior is directly visible in the torus representation of Fig. 5.8 (d), where each Floquet-Floquet Bloch band winds around the free space in the center of the torus. In case of the experimentally motivated driving scheme Eq. (5.63) shows that at $k = \pm\pi$ the quasienergies in the first Floquet Brillouin zone are pinned to zero, while at $k = 0$ they are located at the upper and lower edge at $\pm\hbar\omega/2$. In addition to that, the numerical analysis yields that the quasienergy bands behave similar to the ones of the disconnected dimer model, if Eq. (5.68) holds, c.f. Fig. 5.9 (a). In summary we find that the quasienergy bands of the experimentally motivated driving scheme are helical if condition (5.68) holds.

The helical bands are related to a nontrivial topology [246]. With the visual representation of the quasienergy bands on the torus this becomes clear, since one curve winds around the center of the torus while the other does not. Mathematically speaking the curve in Fig. 5.8 (d) is homotopic to a different element of the fundamental group of the torus than the curve shown in Fig. 5.8 (b) [247]. For the time-periodically driven SSH-ratchet, the topological invariant can be determined with the one-cycle time-evolution operator in momentum space $U_k(T,0)$ [73, 246]. In the case of the disconnected dimer model the one-cycle evolution operator reads $U(T,0) = -e^{-ik\sigma_z}$. It commutes with σ_z and thus preserves the sublattice symmetry.If such a sublattice symmetry is present, $U_k(T,0)$ decomposes into two irreducible blocks and the Floquet winding number is defined as topological invariant for each block by [246]

$$\nu_\beta = \frac{1}{2\pi i}\int_{-\pi}^{\pi} dk \mathrm{Tr}[U_k^\beta(T,0)\partial_k U_k^\beta(T,0)^\dagger] = \frac{1}{\hbar\omega}\int_{-\pi}^{\pi} dk\partial_k\epsilon_{k,\beta,0}. \tag{5.71}$$

Here $U_k^\beta(T,0)$ denotes the projection of $U(T,0)$ to block $\beta = 1,2$. For the disconnected dimer model these blocks are just the $U_{1,1}(T,0)$ and $U_{2,2}(T,0)$ component. In the case of perfect linear bands it follows that

$$\nu_\beta = \begin{cases} 1, \ \beta = 1, \\ -1, \ \beta = 2 \end{cases}, \tag{5.72}$$

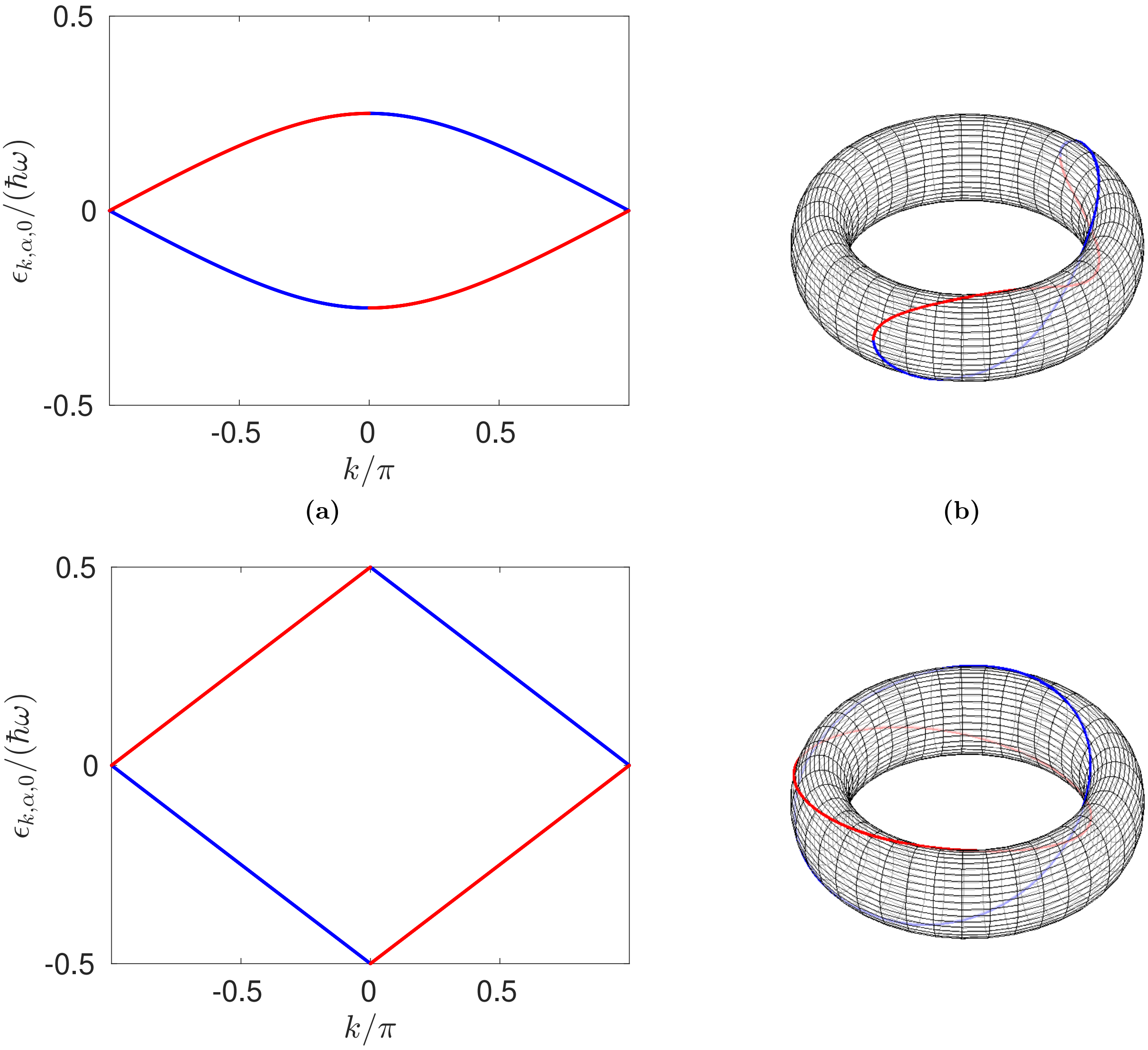

(a) **(b)**

(c) **(d)**

Figure 5.8.: Band structure of the disconnected dimer scheme for $\delta t = T/4$ and (a) $\hbar\omega = 2J/3$ (c) $\hbar\omega = J$. (b,d) representation of the first Floquet Brillouin zone on a torus, the colored parts of (a) and (b), (c) and (d) correspond to each other.

showing that the Floquet winding number indeed measures the winding of the helical quasienergy bands in the Floquet-Bloch Brillouin zone.

The helical bands are stable against perturbations that preserve the sublattice symmetry in the effective Hamiltonian. Unlike to common phenomena in topological systems, such as the edge states in the static SSH-model [239], this symmetry is easily broken and the quasienergy bands loose their helicity if one of the system parameters is slightly detuned from a value at which helical bands occur. This is seen by the fact that by driving the system away from condition (5.13) the bands hybridize and the quasienergy bands are not helical anymore.

Equation (5.71) directly relates the topological invariant to the average group velocity Eq. (5.51) in the case of a uniformly filled quasienergy band. This emphasizes that the particle transport with the velocity of one unit cell per driving period is quantized in our SSH ratchet model.

5.2.6. Analysis of the Experimentally Motivated Driving Scheme

We use the knowledge from the previous subsections in order to analyze the ratchet effect in the experimentally motivated driving scheme.

Floquet-Bloch Analysis

In Fig. 5.9 the results of the Floquet-Bloch analysis of the experimentally motivated driving scheme (5.7) are shown. As predicted by Eqns. (5.68) and (5.69), there are driving frequencies where the system has helical quasienergy bands which are almost linear, and frequencies where the bands are almost flat. Also dispersive bands with a finite band gap exist. Figure 5.9 (a) shows the case of almost linear quasienergy bands at $\hbar\omega = 1.195\ J_0$, which equals to Eq. (5.68) in the case of $n = 0$. Here the band gap is closed and the bands are helical in the Floquet-Brillouin zone. The dynamics of the corresponding Floquet-Bloch states is visualized in Fig. 5.9 (b). Here, almost perfect sublattice oscillations of the states are visible. The difference to the disconnected dimer model, where the quasienergy bands are linear and the states perform full sublattice oscillations, is directly visible in the lattice simulation shown in Fig. 5.9 (c). The simulated right moving wave packet slightly broadens, which is related to a dispersion relation that is not exactly linear in quasimomentum k. The barely visible non-linearity of the quasienergy bands can be explained by the fact that in the experimentally motivated driving scheme the coupling constants never vanish, i.e. there always remains a dispersive element in the motion.

A similar consideration as above explains why the quasienergy bands in Fig. 5.9 (d), which is made for $\hbar\omega = 0.597\ J_0$ corresponding to Eq. (5.69) with $n = 0$, cannot be totally flat. The corresponding Floquet-Bloch states in Fig. 5.9 (e) show a deformed sublattice oscillation. In the real space simulation in Fig. 5.9 (f) the wave function is in a localized oscillatory motion. Also here the non-linear behavior of the quasienergy bands as a function of quasimomentum k induces a slight spreading of

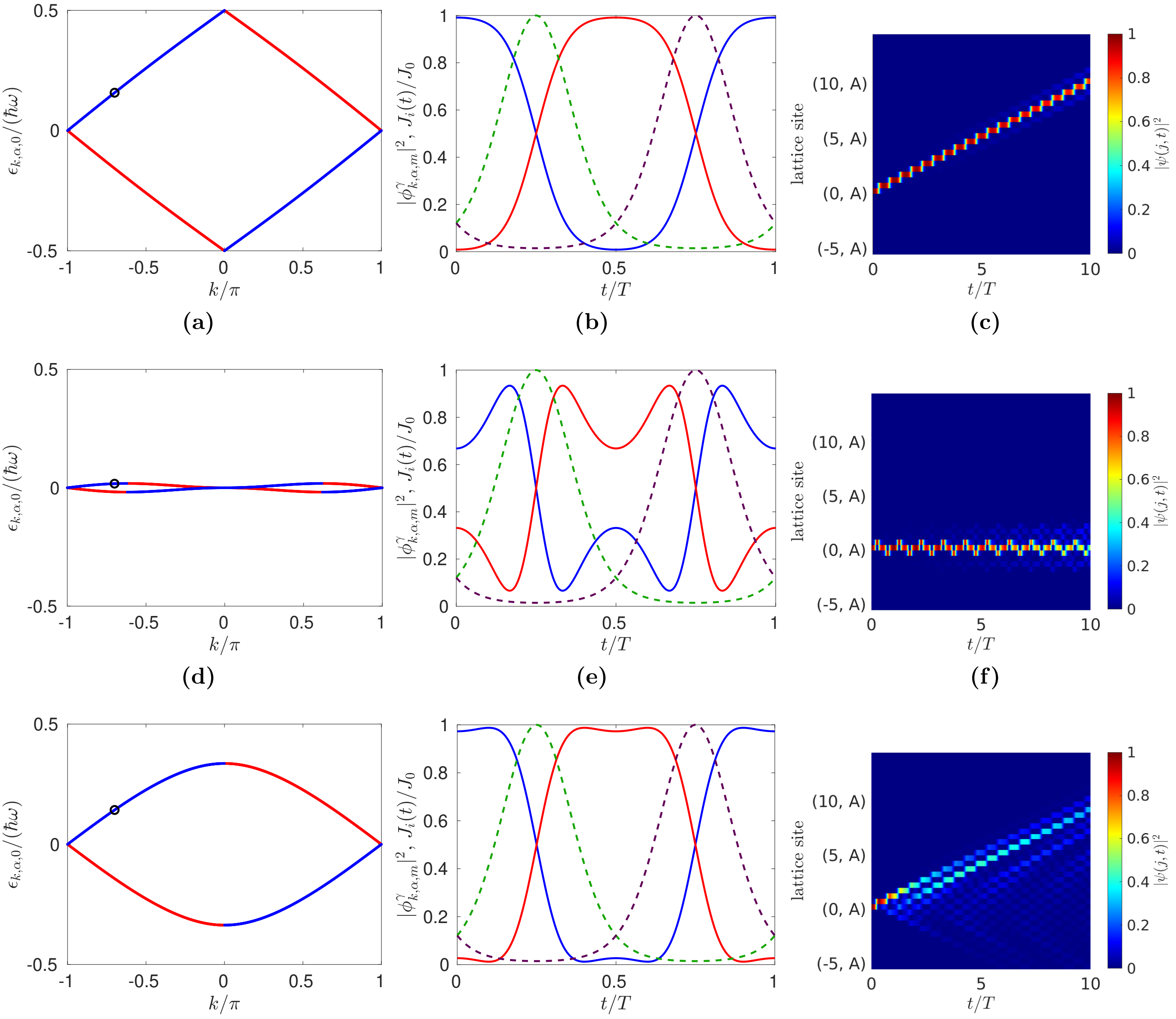

(g) **(h)** **(i)**

Figure 5.9.: Numerically calculated quasienergy bands (a,d,g), Floquet-Bloch states (b,e,h) and simulation of the lattice dynamics (c,f,i) of the ratchet with the experimentally motivated driving scheme Eq. (5.7). As initial condition for the simulations a single site on sublattice A is excited. In panels (a,b,c) $\hbar\omega = \hbar\omega_0^{\text{id}} \approx 1.195\ J_0$, in (d,e,f) $\hbar\omega = \hbar\omega_0^{\text{ab}} \approx 0.597\ J_0$ and in (g,h,i) $\hbar\omega = 0.9\ J_0$. In (a,d,g) are states with positive group velocity are marked blue, states with negative are marked red. In (b,e,h) is the density of a Floquet-Bloch state on sublattice A given in blue, on B in red, $J_1(t)$ in green dashed, $J_2(t)$ in purple dashed. The parameters for (b,e,h) are marked by a black circle in (a,d,g). The initial state in (c,f,i) is an excitation of the site $(0, \text{A})$ only.

the localized state.

Fig. 5.9 (g) shows the case of a driving frequency away from the case of almost linear or almost flat bands. Here the quasienergy bands are curved, a finite band gap is visible. Similar to the disconnected dimer model, the bands hybridize at $k = 0$. The Floquet-Bloch states displayed in Fig. 5.9 (h) perform sublattice oscillations with slight imperfections compared to Fig. 5.9 (b). The corresponding simulation of a wave packet in real space is shown in Fig. 5.9 (i), here the directed motion in positive direction is washed out. This is due to the following two effects. First, the influence of the finite dispersion of the band structure is visible, second, in this case also the left-moving states are excited.

In the surface plasmon-polariton waveguide array experiments conducted by Z. Fedorova from the University of Bonn a single site is excited and directed transport is observed [216,237]. It is therefore of interest to investigate the average group velocity for the experimentally motivated driving scheme (5.7) if a single lattice site is excited.

Rectification of Transport

Fig. 5.10 (a) shows the average group velocity $\bar{v}_{\mathrm{g}}$ for the driving scheme (5.7) with the assumption that a single site of sublattice A is initially excited. Also here the group velocity follows an oscillatory behavior. The location of the maxima of $\bar{v}_{\mathrm{g}}$ can be predicted with a good accuracy by Eq. (5.68) and goes hand in hand with a closing of the bulk gap as shown in Fig. 5.10 (b). However, the optimal transport of $\bar{v}_{\mathrm{g}}T = 1$ cannot be reached. This is explained with the aid of Fig. 5.10 (c) and (d) showing the modulus squared of $A_{k,1} = \langle\phi_{k,1,0}(0)|\psi(0)\rangle$ and $A_{k,2} = \langle\phi_{k,2,0}(0)|\psi(0)\rangle$, respectively. In contrast to the disconnected dimer model, the Floquet-Bloch states do not perform full oscillations between the two sublattices even for an ideal driving frequency $\omega = \omega_n^{\mathrm{id}}$, as seen in Fig. 5.9 (b). Thus, the overlap $A_{k,1}$ is close to one, but in any case a bit smaller than one. When performing the average over the group velocity, this leads to a value that is slightly reduced from $\bar{v}_{\mathrm{g}} = 1/T$. As seen in Fig. 5.10 (b), there are no frequencies where the quasienergy bands are completely flat. Despite these peculiarities, Eq. (5.69) gives a quite good approximation for the frequency with minimal bandwidth and the point where the average group velocity vanishes. At last, note the discontinuity in the $A_{k,\alpha}$ coefficients shown in Fig. 5.10 (c) and (d). This comes about the labeling of the quasienergy bands by their respective group velocity and has no physical impact. As shown in Fig. 5.9 (d), the band structure of the experimentally motivated driving scheme develops two maxima at $k \approx \pm\pi/2$ if ω is close to a point of almost flat bands. This implies that right movers turn into left movers and vice versa for a certain range of k values. Despite the change of the group velocity, the sublattice dynamics stays nearly the same. Thus, there are Floquet-Bloch states with a negative group velocity, but a major population of sublattice A at initial times. This implies the interesting effect that the average group velocity can become negative, as displayed in Fig. 5.10 (a).

Also in the experimentally motivated driving scheme the transport properties depend on the initial state as given by Eq. (5.55). It would be beneficial to avoid this dependence of the ratchet transport

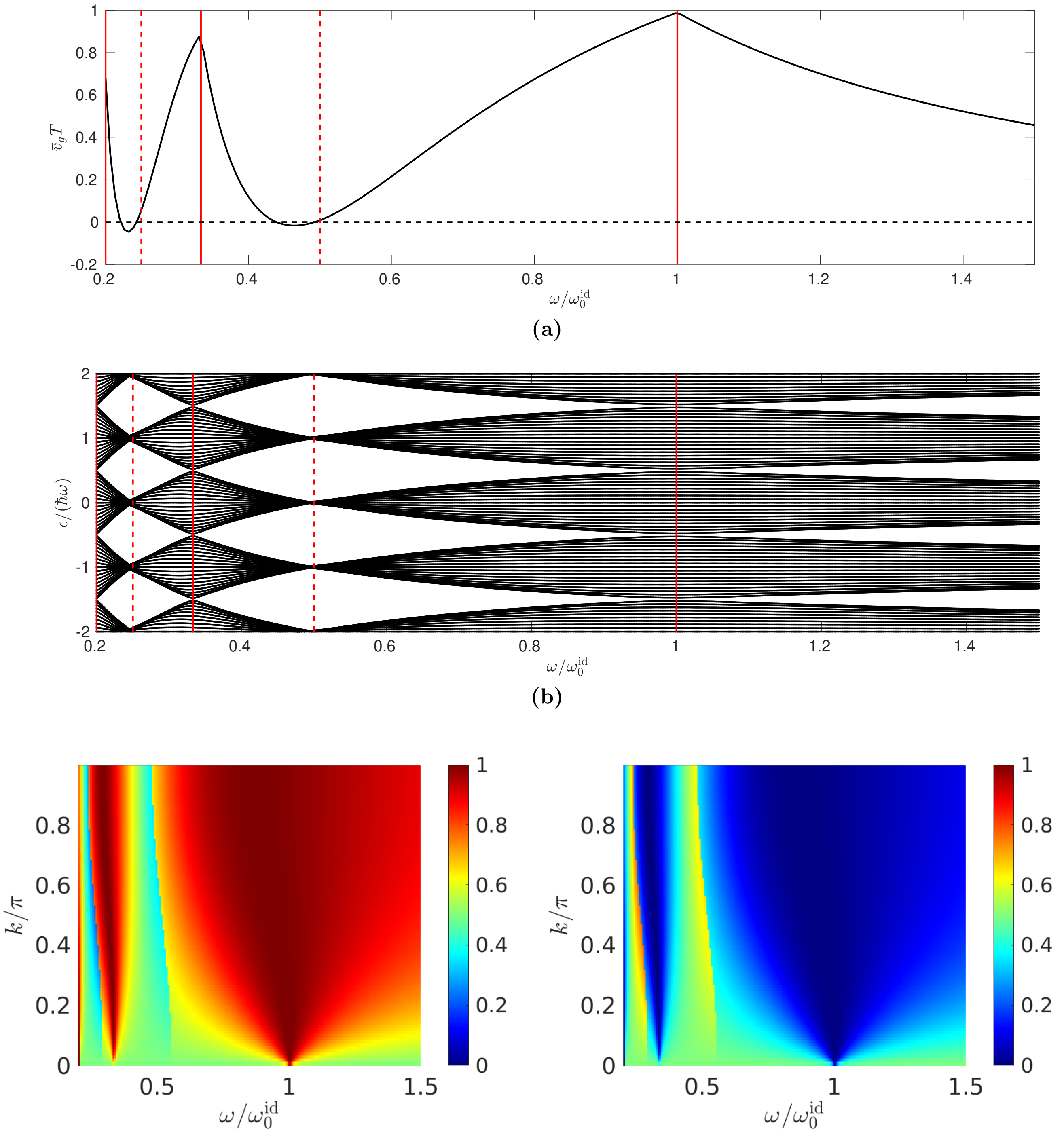

(a)

(b)

(c)

(d)

Figure 5.10.: (a) Average group velocity in dependence of the driving frequency for the experimentally motivated driving scheme (black), (b) quasienergy spectrum in dependence of the driving frequency. Red solid lines mark the position of ideal transport predicted by Eq. (5.68), red dashed lines the frequencies of absence of transport predicted by Eq. (5.69). Color plot of the squared absolute value of the coefficient $A_{k,1} = \langle \phi_{k,1,0}(0)|\psi(0)\rangle$ (c) and $A_{k,2} = \langle \phi_{k,2,0}(0)|\psi(0)\rangle$ (d).

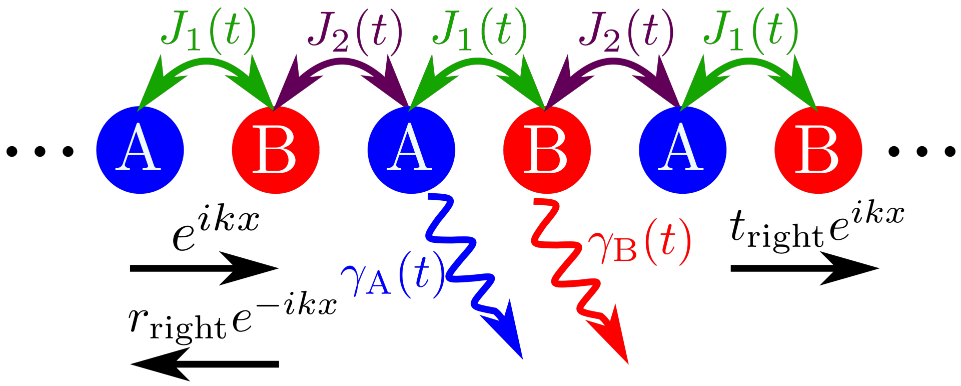

Figure 5.11.: Sketch of the direction-dependent filter in a bipartite lattice model: Time periodic loss applied to two central lattice sites is marked by oscillating lines. A particle sketched as a plane wave impinges upon the dissipative region, resulting in a transmitted and reflected wave. $J_{\text{A/B}}(t)$ denote the time-dependent coupling constants, $\gamma_{\text{A/B}}(t)$ the decay rates. t_{right} is the transmission amplitude of a right moving particle, r_{right} the reflection amplitude.

on the initial state and to design a system that induces a non-vanishing current intrinsically. This is done by introducing a direction-dependent filter in the next section.

5.3. Introducing a Direction-Dependent Filter

In Sec. 5.2 a Hamiltonian quantum ratchet based on a periodically driven SSH model was introduced. Quantized directional transport was found for special driving frequencies, however, direction and magnitude of the particle current strongly depends on the initial state. This is unfortunate for experiments with no or little control over the initial state. Due to the presence of time-reversal symmetry the average current vanishes for distributions that populate both sublattices equally. This motivates our goal to make the system intrinsically non-reciprocal, such that transport can be observed without a special preparation of the initial state. In order to achieve this goal, a direction-dependent filter is introduced that filters out states moving in the left direction while the ones moving to the right remain unimpaired. The filter is implemented by a dissipative, time-periodic impurity. The resulting direction dependent transport is based on the breaking of time-reversal symmetry due to the dissipative nature of the filer. In this section the working principle of the filter is discussed in the case of the disconnected dimer driving scheme, where asymmetric transmission coefficients are found by an analytical discussion. For the experimentally motivated driving scheme no analytical solution is possible. For tackling this problem we introduce the Floquet S-matrix method in Sec. 5.4. With the Floquet S-matrix theory a full analysis of the direction-dependent filter is done in Sec. 5.5.

The direction-dependent filter is realized by time-periodic dissipation on the sites in a single unit cell, based on the considerations of collaborator Z. Fedorova from University of Bonn. The Hamiltonian

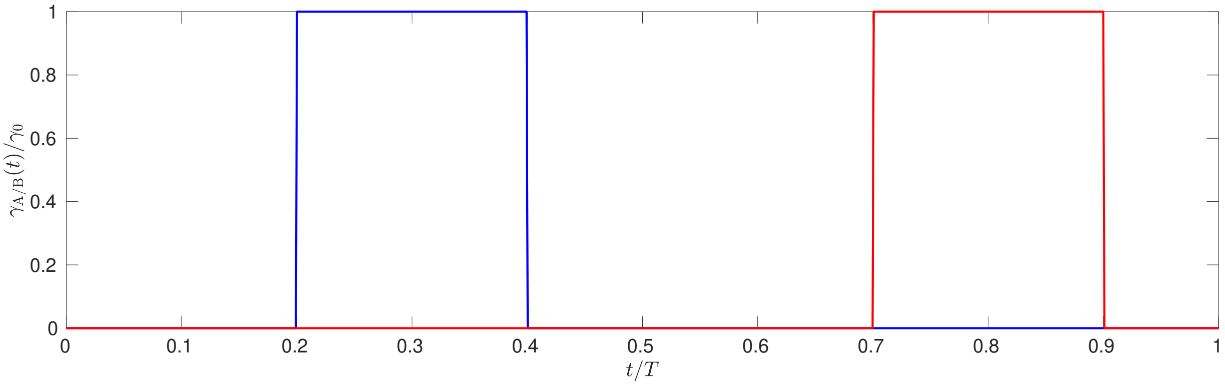

Figure 5.12.: Time dependent decays rate $\gamma_{\mathrm{A}}(t)$ (blue) and $\gamma_{\mathrm{B}}(t)$ (red) for $\varphi = 0.2 \times 2\pi$ and $L_t = 0.2\ T$.

is the sum of the bulk Hamiltonian H_{bulk} given by Eq. (5.6) and the impurity operator $V(t)$:

$$H(t) = H_{\mathrm{bulk}}(t) + V(t), \tag{5.73a}$$
$$V(t) = -i\gamma_{\mathrm{A}}(t)c^{\dagger}_{0,\mathrm{A}}c_{0,\mathrm{A}} - i\gamma_{\mathrm{B}}(t)c^{\dagger}_{0,\mathrm{B}}c_{0,\mathrm{B}}. \tag{5.73b}$$

The dissipation is described by the time-dependent decay rates $\gamma_{\mathrm{A/B}}(t)$ defining a non-hermitian impurity operator $V(t)$. This approach is sufficient in order to describe losses in the surface plasmon-polariton waveguide experiment [237, 248, 249], in which the dissipative impurity is realized by chromium stripes that are positioned periodically along z-direction below the two central waveguides. Chromium induces strong losses while keeping real part of the refractive index almost unchanged [237]. In the analogy of paraxial Helmholtz and Schrödinger equation, the effect of chromium is well described by the decay rates (5.74) acting as an imaginary part of a potential [216, 237, 248, 249]. The finite length of the chromium stripes is modeled by the step-function like behavior of the decay rates [237]

$$\gamma_{\mathrm{A}}(t) = \gamma_0\theta[-\cos(\omega t + \varphi) - \cos(\pi L_t/T)], \tag{5.74a}$$
$$\gamma_{\mathrm{B}}(t) = \gamma_{\mathrm{A}}(t - T/2). \tag{5.74b}$$

Here $\theta(x)$ denotes the heaviside function. The decay rates are time periodic with the same period T as the bulk Hamiltonian, $\gamma_{\mathrm{A/B}}(t + T) = \gamma_{\mathrm{A/B}}(t)$. The concrete form of $\gamma_{\mathrm{A/B}}(t)$ is displayed in Fig. 5.12, it corresponds to a function which takes constant value γ_0 inside an interval and is zero at all other times inside a driving period. In the waveguide experiment, the strength of the dissipation is fixed to $\gamma_0 = 1.5\ J_0$ [216]. The parameter L_t gives the length of the interval with finite dissipation on each sublattice within one driving period, while φ determines the location of the lossy interval within one driving period. At $\varphi = 0$ the lossy interval is centered around $t = T/2$ on sublattice A, a positive φ shifts the center to the smaller times.

We have introduced the time-dependent dissipative impurity. But how does it act as a direction-dependent filter? First, note that the non-hermiticity of $V(t)$ breaks the time-reversal symmetry which in principle allows for a finite current in the system. In order to understand this filtering effect in a more detailed way, a simple calculation within the disconnected dimer driving scheme (5.8) is presented. We choose $\varphi = 0$, such that the loss is centered around $t = T/2$ on sublattice

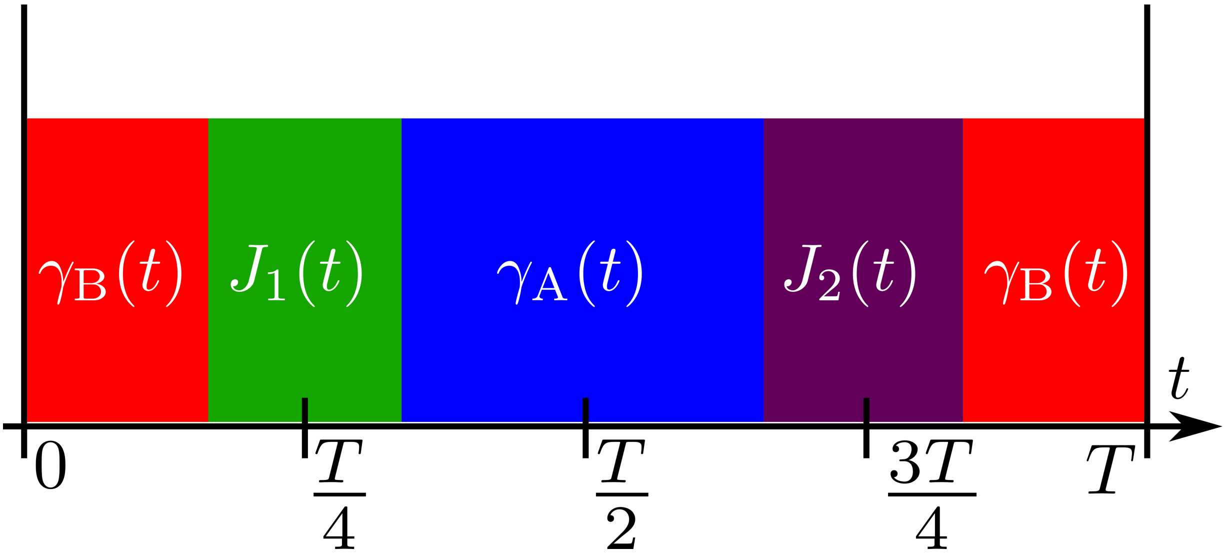

Figure 5.13.: Sketch of one cycle of the disconnect dimer scheme with dissipative impurity. The time-interval within each driving period where a certain quantity is non-zero is marked by a colored rectangle which is labeled by the corresponding quantity.

A and at $t = T$ on sublattice B. The disconnected dimer coupling constants (5.8) are chosen with $\delta t = T/2 - L_t$, $t_1 = T/4 - \delta t/2$ and J is tuned such that the condition of ideal transport (5.68) is fulfilled. This situation is visualized in Fig. 5.13, where the parameters are chosen such that one cycle is partitioned in intervals where either one hopping constant or one decay rate is non-zero. The strength of the decay γ_0 and the duration of the loss L_t remain as free parameters.

Consider now a state that initially was located on a site on sublattice A left of the impurity, i.e. a state moving to the right without any dispersion. Following the discussion of Subsec. 5.2.1, the particle enters the dissipative region on the site $(0, \mathrm{A})$ at time $t = -L_t/2$. As shown in Fig. 5.13, there is no dissipation on this site for the times $-L_t/2 < t < L_t/2$. Then a full Rabi transition to the neighboring site on sublattice B is performed. For $(T/2 - L_t/2) < t < (T/2 + L_t/2)$ the dissipation is on site $(0, \mathrm{A})$, but the state sits on site $(0, \mathrm{B})$. After a second Rabi cycle it leaves the dissipative region unimpaired. The transmission of a right moving state through the dissipative impurity is therefore

$$T_{\alpha=1} = 1. \tag{5.75}$$

For a left moving state this situation is different. It enters the dissipative region on site $(0, \mathrm{B})$ at time $t = -L_t/2$ and stays on this site until $t = L_t/2$. During this time interval, dissipation is active and the amplitude of the state gets damped $\psi_{0,\mathrm{B}}(t = L_t/2) = e^{-\gamma_0 L_t}\psi_{0,\mathrm{B}}(t = -L_t/2)$. After a Rabi transition to site $(0, \mathrm{A})$, the decay rate $\gamma_\mathrm{A}(t)$ is active for $(T/2 - L_t/2) < t < (T/2 + L_t/2)$ and the state is damped a second time. When leaving the dissipative region, the amplitude of a left moving state is damped, which reflects in a transmission coefficient of

$$T_{\alpha=2} = \exp(-4\gamma_0 L_t). \tag{5.76}$$

The left movers are thus exponentially damped, while the strength of the suppression depends on the product of decay rate γ_0 and the length of the interval with finite loss L_t.

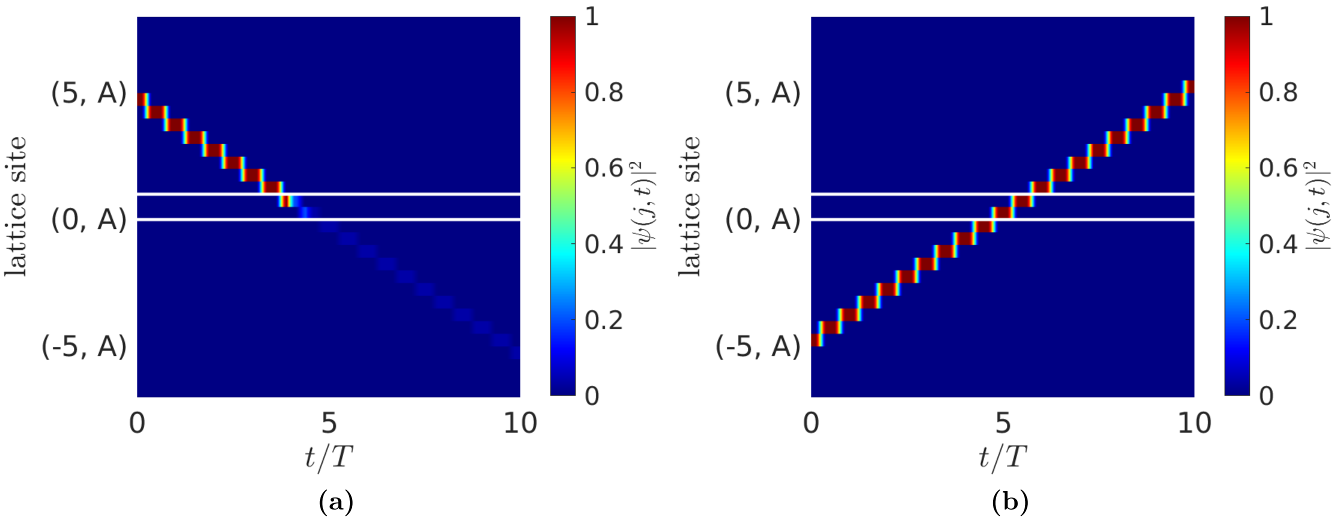

(a)

(b)

Figure 5.14.: Simulation of the dissipative filter for $L_t = 0.2\ T$, $\gamma_0 = J/4$ and the disconnected dimer driving scheme with parameters $\delta t = 0.3\ T$ and $J = 6\hbar\omega/5$, such that the ideal transport is possible. White lines mark the region of the impurity. (a) Left moving state, (b) right moving state.

This short discussion shows that a time-dependent dissipative impurity allows for directional dependent transmission. We have created a direction-dependent filter which leaves the right moving states unimpaired while filtering out the left moving states by damping their wave function exponentially. This impressive effect is visualized by Fig. 5.14. Note that there is in both cases no reflection $R_{\alpha=1,2} = 0$.

For the experimentally motivated driving scheme (5.7), however, no such simple discussion is possible. The main reason for this is the presence of dispersion even in the case of helical bands, i.e. the bands are not perfectly linear. This leads in any case to a spreading of a wave packet which makes an analytical discussion impossible. In order to still be able to analyze the properties of the filter, we use the well-known S-matrix theory in order to calculate transmission coefficients of left and right moving states. The S-matrix theory has the further advantage that momentum resolved quantities can be calculated. This is of importance for the case of driving frequencies that are away from Eq. (5.68). In the following section we generalize the commonly used S-matrix theory such that it is able to describe scattering properties in our periodically driven SSH ratchet model with a dissipative, time-periodic impurity.

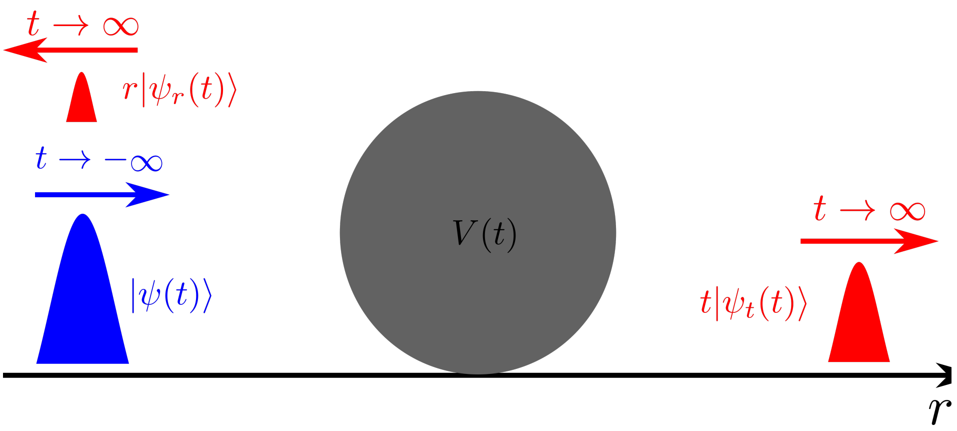

Figure 5.15.: Sketch of the setting of Floquet S-matrix theory in one dimension. In the remote past a wave packet $|\psi(t)\rangle$ travels through space, while the dynamics is given by the bulk Hamiltonian $H_0(t)$. At $t \approx 0$ the packet impinges upon the impurity and is scattered at late times into a transmitted part $t|\psi_t\rangle$ and reflected part $r|\psi_r\rangle$. The transmission / reflection amplitude is denoted by t / r.

5.4. Floquet S-Matrix Theory

The S-matrix theory is a well-known method for investigating the scattering by various types of potentials [113]. Here we apply the theory to a one-dimensional scattering problem, as visualized in Fig. 5.15. Consider a particle scattered by a possibly time-dependent potential. At times before the scattering process occurred it is described by a wave packet being far away from the impurity. When the particle impinges upon the impurity, the actual dynamics may be involved to describe. Nevertheless, at times far after the scattering event, the wave function of the particle divides into a transmitted part on the right of the impurity and a reflected part on the left. The S-matrix theory enables to calculate the proportion of transmitted and reflected parts of the wave function and allows to find the transmission and reflection coefficients. In order to calculate the transport properties of the direction-dependent filter, this section introduces a formal scattering theory for describing the scattering of states Floquet-Bloch states by a time-periodic, non-hermitian potential $V(t)$. We emphasize that this theory solves two nontrivial tasks that do not occur in the common formulation of a S-matrix theory [99, 118, 250]. First, we consider a case where the bulk part of the Hamiltonian is driven periodically, second, the impurity operator is non-hermitian and time-dependent.

5.4.1. Floquet Lippmann-Schwinger Equation

As a prerequisite of the definition of the S matrix, a Floquet Lippmann-Schwinger equation is derived in the case of a time-periodic, dissipative impurity. It turns out that some arguments of the following discussion in the Floquet case are similar to the time-independent case. If possible, we will therefore do the connection to the time-independent case, but we will also point out what concepts are new due to the presence of periodic driving and dissipation.

Starting point is a discussion of the overall Hamiltonian

$$H(t) = H_0(t) + V(t), \tag{5.77}$$

where $H_0(t)$ is the bulk or free Hamiltonian, and $V(t)$ is the scattering potential, which is also named as impurity operator. The bulk Hamiltonian is considered to be hermitian, while $V(t)$ is a non-hermitian time-dependent operator with the same driving period as the bulk Hamiltonian $H_0(t)$. Unlike to Refs. [99, 250–255], which all contain a formal scattering theory for time-periodic scattering potentials, we explicitly include in our theory the case where both bulk and impurity operator are time-periodic. This is motivated by the fact that the SSH-ratchet, which sets up the bulk in our model, is time-dependent. A set of basis states $|\phi_a^{(0)}(t)\rangle$ is given by the solution of the Floquet equation of the bulk [256]

$$\left(H_0(t) - i\hbar\frac{\partial}{\partial t}\right)|\phi_a^{(0)}(t)\rangle = \epsilon_a|\phi_a^{(0)}(t)\rangle. \tag{5.78}$$

These states are assumed to be free states forming a continuous spectrum. The multiindex a can contain both continuous and discrete quantum numbers. For the Hamiltonian quantum ratchet Eq. (5.6) it holds that $a = (k, \alpha, m)$, with k as the quasi momentum, α as the band label and m as the Floquet Brillouin-zone index.

The scattering states $|\psi_a(t)\rangle = e^{-i\epsilon_a t/\hbar}|\phi_a(t)\rangle$ are defined by their related Floquet modes which solve the Floquet equation of the full Hamiltonian $H(t) = H_0(t) + V(t)$:

$$\left(H(t) - i\hbar\frac{\partial}{\partial t}\right)|\phi_a(t)\rangle = \epsilon_a|\phi_a(t)\rangle. \tag{5.79}$$

It is assumed that the spectrum of Eq. (5.79) contains a continuous spectrum and may, in addition, have a discrete spectrum. Possible wave functions related to the discrete spectrum are bound states while the continuous spectrum is composed of scattering states. The impurity operator $V(t)$ is assumed to be local in real space [254], in a sense that $V(t)$ is such that the continuous spectrum of the scattering states $|\psi_a(t)\rangle$ does not differ from the spectrum of the free states $|\psi_a^{(0)}(t)\rangle$ [119]. This allows to choose a labeling such that a free Floquet mode $|\phi_a^{(0)}(t)\rangle$ with quantum number a has the same quasienergy as the scattering state $|\phi_a(t)\rangle$ with the same quantum number. The non-hermiticity of the impurity potential is reflected in the fact that the $|\phi_a(t)\rangle$ states do not form an orthonormal basis [98, 193]. However, we will not need the orthonormality of $|\phi_a(t)\rangle$ in the discussion of this subsection.

For a complete classification of the scattering properties of the scattering states $|\phi_a(t)\rangle$ it is important to relate them to the free states. In order to do so, a wave packet $|\psi(t)\rangle$ is considered. As sketched in Fig. 5.15 in the setting of one dimension, the packet can be scattered by the impurity potential $V(t)$. As typical for scattering theory, it is assumed that in the remote past the wave packet is sufficiently away from the impurity such that it is not affected by the potential. This motivates to define the "in" states by [118]:

$$|\psi_{\text{in}}(t)\rangle = \lim_{\tau\to-\infty} U_0(t, \tau)|\psi(\tau)\rangle, \tag{5.80}$$

where $U_0(t,\tau)$ is the time-evolution operator with respect to the free Hamiltonian $H_0(t)$. The state $|\psi_{\text{in}}(t)\rangle$ is equal to the wave packet $|\psi(t)\rangle$ in the remote past, but it evolves with the free Hamiltonian and thus stays unaffected by the impurity at all times. Conversely, by setting the mathematical structure of $|\psi_{\text{in}}(t)\rangle$, the initial conditions of the scattering process are defined by Eq. (5.80). Here we follow Ref. [118] and assume that $|\psi_{\text{in}}(t)\rangle$ is a wave packet centered around a quantum number a. Such a packet is denoted by $|\psi_a^{\text{wp}}(t)\rangle$. It is furthermore assumed that the $|\psi_a^{\text{wp}}(t)\rangle$ states span the complete space of the continuous spectrum [118]. With Eq. (5.80) the freely evolving wave packet $|\psi_{\text{in}}(t)\rangle = |\psi_a^{\text{wp}}(t)\rangle$ is related to the scattered packet $|\psi(t)\rangle = |\psi_a^{\text{sc}}(t)\rangle$ by

$$|\psi_a^{\text{wp}}(t)\rangle = \lim_{\tau\to-\infty} U_0(t,\tau)U(\tau,t)|\psi_a^{\text{sc}}(t)\rangle. \tag{5.81}$$

Here $U(t,\tau)$ is the time-evolution operator with respect to the full non-hermitian Hamiltonian $H(t)$ [98,257,258]. Performing the limit that the wave packet $|\psi_a^{\text{wp}}(t)\rangle$ gets infinitely sharp in quasienergy, Eq. (5.81) can be formulated in terms of Floquet states with energy ϵ_a [118,119]

$$|\psi_a^{(0)}(t)\rangle = \lim_{\tau\to-\infty} U_0(t,\tau)U(\tau,t)|\psi_a(t)\rangle. \tag{5.82}$$

Up to now the reasoning was similar to the case of a Lippmann Schwinger equation with time-independent Hamiltonian such as in Refs. [118,119], but in the next step the Floquet calculation differs. The identity $U(t,\tau) = \int_{-nT}^{T-nT} dt'\delta(t'-\tau)e^{i\epsilon_a(t'-\tau)}U(t,t'),\ \tau\in[-nT,t-nT[,\ n\in\mathbb{Z}$ is inserted into Eq. (5.82), which results in the intermediate step

$$|\psi_a^{(0)}(t)\rangle = \lim_{\tau\to-\infty}\int_{0-nT}^{T-nT} dt'\ U_0(t,\tau)\delta(\tau-t')e^{i\epsilon_a(t'-\tau)}U(t',t)|\psi_a(t)\rangle. \tag{5.83}$$

Here n is chosen such that τ lies in the interval of integration, i.e. n goes to infinity. We now want to express Eq. (5.83) in term of Floquet modes. The complex exponential that has been introduced into Eq. (5.83), is such that all terms that depend on the intermediate time t' cancel out. With the identities (2.42), (2.21), $U(t,t')|\psi_a(t')\rangle = |\psi_a(t)\rangle$ and the definition $\Delta t = \tau - t$ we find

$$|\phi_a^{(0)}(t)\rangle = \lim_{\Delta t\to-\infty}\sum_b e^{-i\Delta t(\epsilon_a-\epsilon_b)}|\phi_b^{(0)}(t)\rangle\frac{1}{T}\int_0^T dt'\ \langle\phi_b^0(t')|\phi_a(t')\rangle. \tag{5.84}$$

The limit $\Delta t\to-\infty$ is performed using the identity [119]

$$\lim_{t\to-\infty} f(t) = \lim_{\eta\to0^+}\eta\int_{-\infty}^{0} dt\ e^{\eta t}f(t). \tag{5.85}$$

If the limit for a function $f(t)$ exists, Eq. (5.85) is an alternative way for calculating it. For functions where the ordinary limit does not exist, such as it is the case for the complex exponential $e^{i\Delta t(\epsilon_a-\epsilon_b)}$, Eq. (5.85) can serve as a way of calculating this limit. With this it holds that

$$\lim_{\eta\to0^+}\eta\int_{-\infty}^{0} dt\ e^{\eta t}e^{-it(\epsilon_a-\epsilon_b)} = \frac{i0^+}{\epsilon_a-\epsilon_b+i0^+}, \tag{5.86}$$

where 0^+ stands for a small positive number of which the limit to zero is implicitly taken [118,119]. In Eq. (5.84) an arbitrary, but finite time t was chosen. The time dependence in Eq. (5.84) can thus be translated to a notation in Floquet space by using Eqns. (2.20c), (2.23) and (2.25). With $\hat{H}_0^{\mathrm{F}} = \sum_a \epsilon_a |\phi_a^{(0)}\rangle\rangle\langle\langle\phi_a^{(0)}|$ the Floquet-space version of Eq. (5.84) reads

$$|\phi_a^{(0)}\rangle\rangle = \frac{i0^+}{\epsilon_a - \hat{H}_0^{\mathrm{F}} + i0^+}|\phi_a\rangle\rangle. \tag{5.87}$$

Equation (5.87) is remarkable, as it constitutes a step needed for deriving the time-independent Lippmann-Schwinger equation [119], but formulated in Floquet space. It implies that the Floquet Lippmann-Schwinger theory is a well-known time-independent Lippmann-Schwinger theory in Floquet space. The Floquet Lippmann-Schwinger equation reads

$$|\phi_a^+\rangle\rangle = |\phi_a^{(0)}\rangle\rangle + \hat{G}_0^+(\epsilon_a)\hat{V}|\phi_a^+\rangle\rangle, \tag{5.88}$$

where the retarded Greens function in Floquet space is introduced by

$$\hat{G}_0^+(\epsilon_a) = \frac{1}{\epsilon_a - \hat{H}_0^{\mathrm{F}} + i0^+}. \tag{5.89}$$

The notation $|\phi_a^+\rangle\rangle$ denotes the Floquet scattering solutions that solve the Lippmann-Schwinger equation with retarded Greens function.

Similar to the "in" states, the "out" states are defined via [118]

$$|\psi_{\mathrm{out}}(t)\rangle = \lim_{\tau\to\infty} U_0(t,\tau)|\psi(\tau)\rangle. \tag{5.90}$$

Equation (5.90) sets the boundary conditions such that the scattered particle is in the remote future in a controlled wave packet state, an assumption which is not easy to realize in an experiment. Nevertheless, using it one can derive a Lippmann-Schwinger equation

$$|\phi_a^-\rangle\rangle = |\phi_a^0\rangle\rangle + \hat{G}_0^-(\epsilon_a)\hat{V}|\phi_a^-\rangle\rangle, \tag{5.91}$$

with the advanced Greens function

$$\hat{G}_0^-(\epsilon_a) = \frac{1}{\epsilon_a - \hat{H}_0^{\mathrm{F}} - i0^+}. \tag{5.92}$$

The Floquet Lippmann-Schwinger equation enables a systematic calculation of the scattering states $|\phi_a^\pm\rangle\rangle$ which have the correct boundary conditions in a sense that they coincide either at infinite early or late times with the free states. As seen in Eqns. (5.88) and (5.91), the boundary conditions at infinite early and late times are reflected in the choice of either the retarded or advanced Greens function, while the inhomogeneity is given in both cases by the free state $|\phi_a^{(0)}\rangle\rangle$. It is easily verified that the solution of the Floquet Lippmann-Schwinger equations (5.88) and (5.91) solve the Floquet-equation (5.79). At last, note that the formal solution of the Floquet Lippmann Schwinger equation is given by

$$|\phi_a^\pm\rangle\rangle = |\phi_a^{(0)}\rangle\rangle + \hat{G}^\pm(\epsilon_a)\hat{V}|\phi_a^{(0)}\rangle\rangle \tag{5.93}$$

with the Greens function of the full Hamiltonian

$$\hat{G}^\pm(\epsilon_a) = (\epsilon_a - \hat{H}_0^{\mathrm{F}} + \hat{V} \pm i0^+)^{-1}. \tag{5.94}$$

5.4.2. Møller Wave Operators and Floquet S Matrix for a Non-Hermitian Impurity

The solution of the Floquet Lippmann-Schwinger equation characterizes the scattering process and can be used in order to calculate the so called scattering matrix (S matrix). In the following we define the S matrix by relating it to the overlap of the scattering states with a freely evolving state at infinite late times, a quantity that characterizes the scattering process [99, 118, 119, 250]. For example, in the one-dimensional case a relation between the S matrix and the transmission coefficients is found.

Before the S matrix can be introduced, operators that relate the "in" and "out" states to the state of a scattered particle are defined via [118]

$$
\begin{aligned}
|\psi(t)\rangle &= \Omega^{+}|\psi_{\mathrm{in}}(t)\rangle, && (5.95a)\\
|\psi(t)\rangle &= \Omega^{-}|\psi_{\mathrm{out}}(t)\rangle. && (5.95b)
\end{aligned}
$$

These operators are called Møller wave operators. Similar to the discussion in the previous subsection, the wave packet is contracted to a single state $|\psi_a^{\pm}(t)\rangle = \Omega^{\pm}|\psi_a^{(0)}(t)\rangle$. This defines the Møller wave operators in Floquet space

$$
\hat{\Omega}^{\pm} = \sum_a |\phi_a^{\pm}\rangle\rangle\langle\langle\phi_a^{(0)}|. \tag{5.96}
$$

Note that this result is similar to that what is found in Ref. [118] for the static case. For a hermitian impurity, the Møller wave operators obey $(\hat{\Omega}^{\pm})^{\dagger}\hat{\Omega}^{\pm} = 1$, in the non-hermitian case this equation is not fulfilled due to the fact that the scattering states $|\phi_a^{\pm}\rangle\rangle$ do not form an orthonormal basis. This issue is resolved with the use of biorthogonal Floquet theory, which is introduced in App. C. The adjoint scattering states are defined as Floquet eigenfunctions of the hermitian adjoint of the full Hamiltonian

$$
[H^{\dagger}(t) - i\hbar\partial_t]|\bar{\phi}_a(t)\rangle = \epsilon_a|\bar{\phi}_a(t)\rangle, \tag{5.97}
$$

where $V(t)$ is again assumed to be local such that the continuous spectrum of the adjoint scattering states coincides with the one of the free states $|\phi_a^{(0)}(t)\rangle$ and is thus real valued. With the results of Subsec. 5.4.1 the adjoint Møller wave operators are defined by

$$
\hat{\bar{\Omega}}^{\pm} = \sum_a |\bar{\phi}_a^{\pm}\rangle\rangle\langle\langle\phi_a^{(0)}|. \tag{5.98}
$$

Note that for the hermitian case the adjoint operators Eq. (5.98) coincide with Eq. (5.96). The Møller wave operators and their adjoint fulfill the condition

$$
(\hat{\bar{\Omega}}^{\pm})^{\dagger}\hat{\Omega}^{\pm} = 1. \tag{5.99}
$$

due to the biorthogonality of the Floquet scattering states $|\phi_a^{\pm}\rangle\rangle$ and the adjoint basis $|\bar{\phi}_a^{\pm}\rangle\rangle$. Combining both Eqns. (5.95) with the use of Eq. (5.99), the "out" states are related to the "in" states by

$$
|\psi_{\mathrm{out}}(t)\rangle = (\bar{\Omega}^{-})^{\dagger}\Omega^{+}|\psi_{\mathrm{in}}(t)\rangle. \tag{5.100}
$$

This result is of relevance for the subsequent discussion.

For defining the S matrix, the following thoughts are made [118]: Consider a particle in a scattering state $|\psi(t)\rangle$, that in the remote past started in a wave packet state of the form $|\psi_b^{\mathrm{wp}}(t)\rangle$. How large is the overlap of the scattering state $|\psi(t)\rangle$ with the wave packet state $|\psi_a^{\mathrm{wp}}(t)\rangle$ at infinite late times? In order to answer this question, a short calculation is performed following Ref. [118]:

$$\lim_{t\to\infty}\langle\psi_a^{\mathrm{wp}}(t)|\psi(t)\rangle = \lim_{t\to\infty}\langle\psi_a^{\mathrm{wp}}(t)|\psi_{\mathrm{out}}(t)\rangle = \lim_{t\to\infty}\langle\psi_a^{\mathrm{wp}}(t)|(\bar{\Omega}^-)^\dagger\Omega^+|\psi_b^{\mathrm{wp}}(t)\rangle \tag{5.101}$$

In the first step Eq. (5.90) is applied, while the second step uses the relation of "in" and "out" states, Eq. (5.100), together with the assumption that at initial time the system is in the state $|\psi_b^{\mathrm{wp}}(t)\rangle$. In the limit that the wave packets are contracted to zero width, Eq. (5.101) makes the statement that the quantum mechanical amplitude, that the state $|\phi_b^{(0)}\rangle\rangle$ scatters into the state $|\phi_a^{(0)}\rangle\rangle$, is given by

$$\langle\langle\phi_a^{(0)}|(\hat{\bar{\Omega}}^-)^\dagger\hat{\Omega}^+|\phi_b^{(0)}\rangle\rangle = \langle\langle\phi_a^{(0)}|\hat{S}|\phi_b^{(0)}\rangle\rangle = S_{a,b} \tag{5.102}$$

With Eq. (5.102) the Floquet S-matrix for scattering by a non-hermitian impurity is defined by $\hat{S} = (\hat{\bar{\Omega}}^-)^\dagger\hat{\Omega}^+$ and the matrix elements of the Floquet S matrix with respect to the free basis are denoted by $S_{a,b}$. Equation (5.102) is central to this section, since it defines the quantum mechanical amplitudes for a scattering process from state $|\phi_b^{(0)}\rangle\rangle$ to state $|\phi_a^{(0)}\rangle\rangle$. The beauty of the S matrix is that with it the outcome of a scattering experiment can be calculated with a simple expectation value. Due to the non-hermiticity of the impurity operator, the adjoint Møller wave operator appears in Eq. (5.102).

For practical reasons it is of favor to find a formula for the matrix elements of the S matrix Eq. (5.102) without the use of the Møller wave operators. Generalizing the result of Ref. [119], this is done in the following by applying the adjoint of Eq. (5.93) to the difference of retarded and advanced adjoint solution

$$|\bar{\phi}_a^-\rangle\rangle - |\bar{\phi}_a^+\rangle\rangle = [\hat{\bar{G}}^-(\epsilon_a) - \hat{\bar{G}}^+(\epsilon_a)]\hat{V}^\dagger|\phi_a^{(0)}\rangle\rangle. \tag{5.103}$$

In Eq. (5.103) the adjoint Greens function is given by $\hat{\bar{G}}^\pm(\epsilon_a) = (\epsilon_a - \hat{H}_0^{\mathrm{F}} + \hat{V}^\dagger \pm i0^+)^{-1}$. In order to continue, note that the matrix elements of the Floquet S matrix are also given by $S_{a,b} = \langle\langle\bar{\phi}_a^-|\phi_b^+\rangle\rangle$. This motivates to multiply in Eq. (5.103) with $\langle\langle\phi_b^+|$ and then do a complex conjugation

$$S_{a,b} - \delta_{a,b} = \langle\langle\phi_a^{(0)}|\hat{V}[\hat{\bar{G}}^-(\epsilon_a) - \hat{\bar{G}}^+(\epsilon_a)]^\dagger|\phi_b^+\rangle\rangle. \tag{5.104}$$

The Kronecker delta on the left comes in due to the biorthogonality of the Floquet states $|\phi_a^+\rangle\rangle$ and the adjoint basis $|\bar{\phi}_a^+\rangle\rangle$. In case that a contains continuous indices, the Kronecker delta turns into a Dirac delta function for the continuous indices. For example, for our ratchet model it holds $\delta_{a,b} = \delta_{(k,\alpha,m),(q,\beta,n)} = \delta(k-q)\delta_{\alpha,\beta}\delta_{m,n}$. Finally, the adjoint Greens functions are evaluated using that the state $|\phi_b^+\rangle\rangle$ is at quasienergy ϵ_b:

$$[\hat{\bar{G}}^-(\epsilon_a) - \hat{\bar{G}}^+(\epsilon_a)]^\dagger|\phi_b^+\rangle\rangle = \lim_{\eta\to 0^+}\frac{-2i\eta}{(\epsilon_a-\epsilon_b)^2+\eta^2}|\phi_b^+\rangle\rangle \tag{5.105}$$

Inserting $\lim_{\eta\to 0^+} -2i\eta/[(\epsilon_a-\epsilon_b)^2+\eta^2] = -2\pi i\delta(\epsilon_a-\epsilon_b)$ [119] and $|\phi_b^+\rangle\rangle = \hat{\Omega}^+|\phi_b^{(0)}\rangle\rangle$ into Eq. (5.104), the following expression of the matrix elements $S_{a,b}$ is found

$$S_{a,b} = \delta_{a,b} - 2\pi i\delta(\epsilon_a-\epsilon_b)T_{a,b}, \tag{5.106}$$

which is a central result. In Eq. (5.106) $T_{a,b} = \langle\langle \phi_a^{(0)} | \hat{V}\hat{\Omega}^+ | \phi_b^{(0)} \rangle\rangle$ are the matrix elements of the Floquet T matrix

$$\hat{T} = \hat{V}\hat{\Omega}^+. \tag{5.107}$$

The first term in Eq. (5.106) describes the matrix element of the identity matrix, while the second term is related to the scattering process. The Dirac delta function ensures the conservation of quasienergy and is weighted by the matrix elements of the Floquet T matrix. Eq. (5.106) is impressive, since it describes the scattering by a non-hermitian impurity operators without the need of the adjoint basis. Further, it is of relevance to this chapter, since the matrix elements of the Floquet T matrix $T_{a,b}$ are accessible. A self-consistency equation for the matrix elements $T_{a,b}$ is found by multiplying $\langle\langle \phi_b^{(0)} | \hat{V}$ to the left of Eq. (5.88). Since Eq. (5.107) implies $T_{a,b} = \langle\langle \phi_a^{(0)} | \hat{V} | \phi_b^+ \rangle\rangle$, the self-consistency equation for the $T_{a,b}$ reads

$$T_{a,b} = V_{a,b} + \sum_c \frac{V_{a,c}}{\epsilon_b - \epsilon_c + i0^+} T_{c,b}. \tag{5.108}$$

Equation (5.108) is of importance to this thesis, since it enables the direct calculation of the matrix elements of the Floquet T matrix without any additional steps. If the matrix elements $T_{a,b}$ are known, the Floquet S matrix can be calculated by Eq. (5.106). With the use of the Floquet S matrix other scattering properties, such as the transmission coefficients, are found. In case of our time-periodic SSH ratchet model (5.20), Eq. (5.108) is expanded in the Floquet-Bloch basis $|\phi_a^{(0)}\rangle\rangle = |\phi_{k,\alpha,m}^{(0)}\rangle\rangle$, as defined in Eq. (5.24), in order to obtain a self-consistency equation for the matrix elements $T_{(q,\beta,n),(k,\alpha,m)} = \langle\langle \phi_{q,\beta,n}^{(0)} | \hat{T} | \phi_{k,\alpha,m}^{(0)} \rangle\rangle$:

$$T_{(q,\beta,n),(k,\alpha,m)} = V_{(q,\beta,n),(k,\alpha,m)} + \sum_{\delta,l} \int_{-\pi}^{\pi} dp \frac{V_{(q,\beta,n),(p,\delta,l)}}{\epsilon_{k,\alpha,m} - \epsilon_{p,\delta,l} + i0^+} T_{(p,\delta,l),(k,\alpha,m)}. \tag{5.109}$$

The integral in Eq. (5.109) is split in a principal value and resonant contributions using the distributional identity $1/(x + i0^+) = \mathrm{P.V.}1/x - i\pi\delta(x)$ following the procedure of Ref. [259]. Here *P.V.* denotes the principal value.

At last, a deeper look is taken on the Floquet Brillouin zone structure of the Floquet S matrix. Consider similar to the SSH ratchet model the case where the quantum number is given by a triple consisting of the quasimomentum k, band index within one Floquet Brillouin zone α and Floquet Brillouin zone index m. The quasienergy conserving Dirac delta function in Eq. (5.106) only allows non-vanishing Floquet S matrix elements within one Floquet Brillouin zone, that means that there are no transitions between different Floquet Brillouin zones. With the Floquet Brillouin zone structure of the scattering states $|\phi_{k,\alpha,m}^{\pm}\rangle\rangle$ it can be shown that the matrix elements repeat themselves in each Floquet Brillouin zone $S_{(q,\beta,m),(k,\alpha,m)} = S_{(q,\beta,0),(k,\alpha,0)}$. Thus it is sufficient to determine the S matrix in one Floquet Brillouin zone in order to have knowledge about the S matrix in the whole Floquet Hilbert space.

5.4.3. Finding Transmission and Reflection Coefficients with the Floquet S Matrix

In this work we are interested in applying the Floquet S-matrix theory to scattering problems in one dimension. The central quantity to look at are transmission and reflection coefficients that describe the probability for a quantum particle to be transmitted through the impurity or the probability of reflection, respectively. In order to clarify how these quantities are calculated with the S-matrix theory, we consider the simplest case of one-dimensional scattering, namly the scattering by a time-independent impurity potential. For a position x far away from the impurity position at $x = 0$, the scattering wave function can be generically parameterized by a superposition of plane waves

$$\psi_a(x) = \begin{cases} \frac{1}{\sqrt{2\pi}} e^{ik_a x} + \frac{r}{\sqrt{2\pi}} e^{-ik_a x}, \ x < 0, \\ \frac{t}{\sqrt{2\pi}} e^{ik_a x}, x > 0. \end{cases} \tag{5.110}$$

Here, t / r is the transmission / reflection amplitude, using which the transmission / reflection coefficients are given in this simple case by $T = |t|^2$, $R = |r|^2$, respectively. In the language of the Floquet S-matrix theory, these amplitudes are found with the overlap of a free state with the scattering state at infinite late times. In order to see this argument, consider the transmission coefficient defined in Eq. (5.110), which can be calculated by

$$t\delta(k - q) = \int_{-\infty}^{\infty} dx \, t \frac{e^{i(k-q)x}}{2\pi}, \tag{5.111}$$

i.e. by the scalar product of a plane wave with amplitude t and the free state $e^{iqx}/\sqrt{2\pi}$. In analogy to Eq. (5.111), the identity $\delta(f(x)) = \sum_{x_0, \ f(x_0=0)} \delta(x - x_0)/|f'(x = x_0)|$ is used in order to express the matrix elements of the Floquet S-matrix Eq. (5.106) solely in terms of delta functions in k:

$$S_{(q,\beta,0),(k,\alpha,0)} = \delta(k - q)\delta_{\alpha,\beta} - \sum_{k_\beta} \frac{2\pi i}{|v_{k_\beta,\beta}|} \delta(q - k_\beta) T_{(k_\beta,\beta,0),(k,\alpha,0)}. \tag{5.112}$$

In Eq. (5.112) it is assumed that the multiindex is of the form $a = (k, \alpha, m)$, with k as quasimomentum, α as band index and m as Floquet-Brillouin zone index. The k_β in Eq. (5.112) are given by the conservation of quasienergy $\epsilon_{k_\beta,\beta,0} - \epsilon_{k,\alpha,0} = 0$. Assuming that the group velocity $v_{k,\alpha,0}$ of the incoming wave is positive, the transmission and reflection amplitudes read with Eq. (5.112) in analogy to Eq. (5.111) [260, 261]:

$$t_{\alpha,\beta}(k, k_\beta) = \delta_{\alpha,\beta} - \frac{2\pi i}{|v_{k_\beta,\beta}|} T_{(k_\beta,\beta,0),(k,\alpha,0)}, \text{ for } k_\beta \text{ with } v_{k_\beta,\beta} > 0, \tag{5.113a}$$

$$r_{\alpha,\beta}(k, k_\beta) = -\frac{2\pi i}{|v_{k_\beta,\beta}|} T_{(k_\beta,\beta,0),(k,\alpha,0)}, \text{ for } k_\beta \text{ with } v_{k_\beta,\beta} < 0. \tag{5.113b}$$

Transmission and reflection amplitudes are parameterized by the momentum of the incoming wave k, the band α of the incoming wave as well as band β and momentum k_β of the outgoing wave. The sign of the group velocity $v_{k_\beta,\beta}$ decides whether a state with quasimomentum k_β contributes to either transmission or reflection amplitude. If $v_{k_\beta,\beta} > 0$, the probability current assigned to this state flows in positive direction and is thus related to the transmitted part of the scattering wave function. Vice versa, terms with $v_{k_\beta,\beta} < 0$ contribute to the reflection. Equation (5.113) tells us that transmission and reflection amplitudes are fully determined if the matrix elements of the Floquet T matrix and the group velocities are known. Similar to the Floquet scattering in three dimensions discussed in chapter 3, the bands α can be seen as channels from and to which a particle can scatter. In the following we assume that there is in each channel at most one k_β with positive group velocity and at most one with negative group velocity. If k_β exists in channel β, the channel β is said to be open, otherwise it is closed. Momentum-dependent transmission and reflection coefficients are found in the Floquet case by dividing the modulus of scattered and incoming current [159,262]. The coefficients read

$$T_{k,\alpha} = \sum_{\substack{\beta \text{ open} \\ v_{k_\beta,\beta}>0}} \frac{|v_{k_\beta,\beta}|}{|v_{k,\alpha}|} |t_{\alpha,\beta}(k,k_\beta)|^2, \tag{5.114a}$$

$$R_{k,\alpha} = \sum_{\substack{\beta \text{ open} \\ v_{k_\beta,\beta}<0}} \frac{|v_{k_\beta,\beta}|}{|v_{k,\alpha}|} |r_{\alpha,\beta}(k,k_\beta)|^2, \tag{5.114b}$$

where the summation goes over all open channels. Note, that definitions analog to Eq. (5.113) and Eq. (5.114) can be made for an initial state with negative group velocity.

In the case of our ratchet model Eq. (5.20), the transport properties of a wave packet are also of relevance. For a given initial state $|\psi_0\rangle$, Eq. (2.9) dictates that the weight of each Floquet state is found by $A_{k,\alpha} = \langle \phi^{(0)}_{k,\alpha,0}(t_0)|\psi_0\rangle$. In the following it is assumed that only Floquet-Bloch states with either positive or negative group velocity are excited. In the case that only one channel contributes in Eq. (5.114), averaged transmission and reflection coefficients are defined by

$$\bar{T} = \sum_{k,\alpha} T_{k,\alpha}|A_{k,\alpha}|^2, \tag{5.115a}$$

$$\bar{R} = \sum_{k,\alpha} R_{k,\alpha}|A_{k,\alpha}|^2, \tag{5.115b}$$

where the sum in Eq. (5.115) goes over all states with either positive or negative group velocity. Equation (5.115a) is found by calculating the norm of the state $|\psi(t)\rangle = \sum_{k,\alpha} t_{k,\alpha} A_{k,\alpha} e^{-i\epsilon_{k,\alpha,0}t/\hbar}|\phi^{(0)}_{k,\alpha,0}(t)\rangle$, where $|\phi^{(0)}_{k,\alpha,0}(t)\rangle$ are the Floquet-Bloch modes given by the solution of Eq. (5.24). A similar calculation can be done for Eq. (5.115b).

After having introduced the general expressions for transmission and reflection amplitude within the Floquet S-matrix theory, we specialize to the case of the driven SSH ratchet (5.20). Here, only two quasienergy bands reside inside each Floquet Brillouin zone. If we are not too close to a point of almost flat bands, each channel only allows for either a single transmitted or a single reflected wave. Since the impurity operator oscillates with the same frequency than the bulk, the quasienergy conserving delta function in the Floquet S matrix Eq. (5.106) restricts the scattered wave to channels inside the first Floquet Brillouin zone. Thus, the Floquet S matrix is in this case effectively a

2×2-matrix, where with Eqns. (5.112) and (5.113) the non-singular parts at $\epsilon_{k,\alpha,0}$ read

$$\tilde{S}(k) = \begin{pmatrix} t_{\alpha=1,\beta=1}(k,k) & r_{\alpha=2,\beta=1}(-k,k) \\ r_{\alpha=1,\beta=2}(k,-k) & t_{\alpha=2,\beta=2}(-k,-k) \end{pmatrix}. \tag{5.116}$$

The transmission and reflection amplitudes define the matrix elements in Eq. (5.116). The corresponding coefficients are given by $T_{k,\alpha} = |t_{\alpha,\alpha}(k,k)|^2$ and $R_{k,\alpha} = |r_{\alpha,\beta\neq\alpha}(k,-k)|^2$. Band averaged transmission and reflection coefficients are defined using Eq. (5.115) by

$$T_\alpha = \frac{1}{N_0}\sum_k T_{k,\alpha}, \tag{5.117a}$$

$$R_\alpha = \frac{1}{N_0}\sum_k R_{k,\alpha}, \tag{5.117b}$$

where N_0 is the number of unit cells. The band averaged quantities will be used in the further discussion. They are of relevance, since the excitation of a single lattice site corresponds to an almost uniform population of one quasienergy band at the ideal driving frequencies. Furthermore, it turns out that at ideal conditions the dependence of the transmission and reflection coefficients on k is barely visible, so that in many cases only little information is lost by the average.

5.4.4. Numerical Method for Calculating the Floquet T Matrix

Due to the complexity of the problem we have to apply numerical methods in order to find the transmission and reflection coefficients. The way to go is to solve the self-consistency equation of the Floquet T matrix (5.109), specialized to the filter model Eq. (5.73), numerically. With the numerical result the transmission and reflection amplitudes are calculated with Eqns. (5.113). For the numeric solution of Eq. (5.109) at first a cutoff in Floquet space m_{co} is introduced, such that the T-matrix $T_{(q,\beta,n),(k,\alpha,m)}$ is considered to be nonzero only for $|n|, |m| \leq m_{\text{co}}$. The cutoff m_{co} is chosen large enough in order to guarantee that the result has converged, it is typically chosen to be of the order of 10. Momentum space is discretized by using the grid $k_n = -\pi + 2\pi/(N_k-1)n,\ n = 0, ..., N_k - 1$, which is chosen such that it is symmetric around $k = 0$. This simplifies the procedure, since, if a quasi momentum k is an element of the grid, then $-k$ is as well. The quasienergies fulfill $\epsilon_{k,\alpha,0} = \epsilon_{-k,\beta\neq\alpha,0}$, which is the condition of quasienergy conservation in the Floquet S matrix (5.106). Thus transmission and reflection can be calculated using the elements of the T matrix within the grid points k_n, and no extrapolation is needed. In the end, the self-consistency equation (5.109) is approximated by the following inhomogeneous linear system

$$\begin{aligned} T_{(k_i,\beta,n),(k_j,\alpha,m)} = {} & V_{(k_i,\beta,n),(k_j,\alpha,m)} + \sum_{r,\delta,l} \Delta k \frac{P.V}{\epsilon_{k_j,\alpha,m} - \epsilon_{k_r,\delta,l}} V_{(k_i,\beta,n),(k_r,\delta,l)} T_{(k_r,\delta,l),(k_j,\alpha,m)} \\ & - \frac{i\pi}{|v_{k_n,\alpha}|}\big[V_{(k_i,\beta,n),(k_j,\alpha,m)} T_{(k_j,\alpha,m),(k_j,\alpha,m)} + V_{(k_i,\beta,n),(-k_j,\delta\neq\alpha,m)} T_{(-k_j,\delta\neq\alpha,m),(k_j,\alpha,m)}\big]. \end{aligned} \tag{5.118}$$

In Eq. (5.118) Δk is the step size of the grid k_i in quasimomentum space and $\frac{P.V}{x}$ is defined such that $\frac{P.V}{x} = 1/x$ for $x \neq 0$ and $\frac{P.V}{x} = 0$ for $x = 0$ in order to approximate the principal value in the numerical calculation. We used $1/(x+i0^+) = \text{P.V.}1/x - i\pi\delta(x)$ in order to separate in principal value and resonant part, while an occurring energy dependent delta function can be explicitly evaluated due to the choice of the grid in k-space having the property that the Dirac delta function only peaks at k-values that lie inside the grid. For calculating the quasienergies $\epsilon_{k_i,\alpha,m}$ and the matrix elements $V_{(k_i,\beta,n),(k_j,\alpha,m)}$, the Floquet-Bloch equation Eq. (5.24) is numerically solved within the k grid. For given multiindex $(k_j, \alpha, m = 0)$ of the incoming wave, Eq. (5.118) translates to a set of linear equations for the vector $\mathbf{T}_{k_i,\beta,n} = T_{(k_i,\beta,n),(k_j,\alpha,m=0)}$, which is solved with common numerical methods.

In order to obtain more accurate results, the transmission and reflection coefficients calculated by the numerics are extrapolated to infinitely many grid points in k-space $N_k \to \infty$. This routine is performed by calculating the transmission and reflection coefficients for different values of N_k, which typically range from $80 < N_k < 200$. Since the different grids in quasi momentum can be incommensurate with each other, some results have to be extrapolated to the grid in k-space that is used for the final result. At each final grid point the data are interpolated by a polynomial in $1/N_k$. The extrapolation of this polynomial to $1/N_k = 0$ yields the desired limit $N_k \to \infty$ of transmission and reflection coefficients. However, this method leads to unreliable results near $k = \pm\pi$, as there the two bands are degenerate. Also the hybridization of the bands at $k \approx 0$ can cause this numerical method to fail, as the group velocity drops to zero at this point. Nevertheless, in the case of helical bulk bands, both transmission and reflection coefficients only depend weakly on quasimomentum k and the above discussed extrapolation method is used in order to increase the accuracy of the numerically calculated transmission and reflection coefficients.

5.5. Analysis of the Direction-Dependent Filter

In this section the properties of the direction-dependent filter are analyzed thoroughly. In Subsec. 5.5.1 the working principle of the direction-dependent filter is formulated within the language of the Floquet S-matrix theory. A Floquet S-matrix analysis of the direction-dependent filter is performed in Subsec. 5.5.2, while Subsec. 5.5.3 reports on direction dependent reflection.

5.5.1. Understanding the Direction-Dependent Filter within Floquet S-Matrix Theory

Here a deeper understanding of the direction-dependent filter is provided in the language of the Floquet S-matrix theory. The central quantity to look at are the matrix elements of the impurity operator in the Floquet-Bloch basis

$$V_{(q,\beta,n),(k,\alpha,m)} = \frac{1}{T}\int_0^T dt \langle \phi^{(0)}_{q,\beta,n}(t)|V(t)|\phi^{(0)}_{k,\alpha,m}(t)\rangle. \tag{5.119}$$

As defined by Eq. (2.45), they are given by the time average of the matrix elements of the impurity operator $V(t)$ and the Floquet-Bloch states $|\phi^{(0)}_{k,\alpha,m}(t)\rangle$ calculated with Eq. (5.24). Applying Floquet

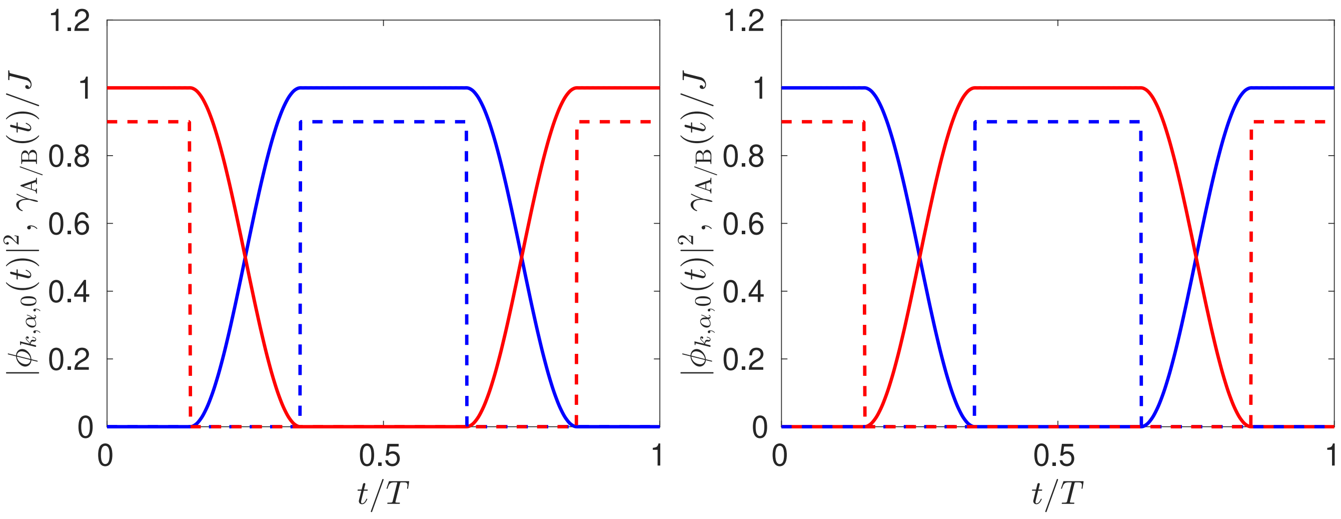

(a) **(b)**

Figure 5.16.: Density of the Floquet-Bloch states on sublattice A (blue solid) and sublattice B (red solid), decay rate on sublattice A (blue dashed) and sublattice B (red dashed) in case of the disconnected dimer model for (a) left-moving state at $k = -\pi/2$, (b) right moving state at $k = \pi/2$. Parameters: $\hbar\omega = 0.8\ J$, $\delta t = 0.2\ T$, $\gamma_0 = 0.9\ J$, $\varphi = 0$, $L_t = 0.3\ T$.

S-matrix theory to the SSH ratchet model, the matrix elements diagonal in the quasienergy band index $\alpha = \beta$ determine the magnitude of the transmission coefficients, while the matrix elements coupling different bands $\alpha \neq \beta$ are related to the reflection coefficients.

For a simple discussion, the disconnected dimer model in the case of perfect linear bands is considered. The Floquet-Bloch states perform full sublattice oscillations during each driving period. In Fig. 5.16 the Floquet-Bloch states and the time-dependent loss rates are depicted. As discussed in Subsec. 5.2.3, time-reversal symmetry guarantees that the sublattice oscillation of right and left movers is antipodal. As a result, the dissipation can be chosen at space-times where, for example, the density of a left moving state is large and the density of a right moving state vanishes. This situation is visible in Fig. 5.16, where a left moving state has a substantial overlap with the time-dependent decay rates, while the overlap of a right moving state with the dissipation is zero. This leads with Eq. (5.119) to finite matrix elements for the left movers and vanishing ones for the right movers. As a result the right movers are transmitted with unit probability, while the left movers are affected by the dissipative impurity potential and thus damped. The matrix elements coupling left and right movers are zero in this case $V_{(q,\beta,0),(k,\alpha\neq\beta,0)} = 0$. This implies that all reflection coefficients are vanishing. Since for the case of helical bands the Floquet-Bloch states are independent of quasimomentum k, the above discussion holds at each k and it is sufficient to look at band averaged transmission and reflection coefficients as defined in Eq. (5.117). We expect for the experimentally motivated driving scheme a qualitatively similar behavior, since Figs. 5.16 and 5.17 are similar to each other.

Within the Floquet S-matrix theory we can see why the non-hermiticity of the impurity is nec-

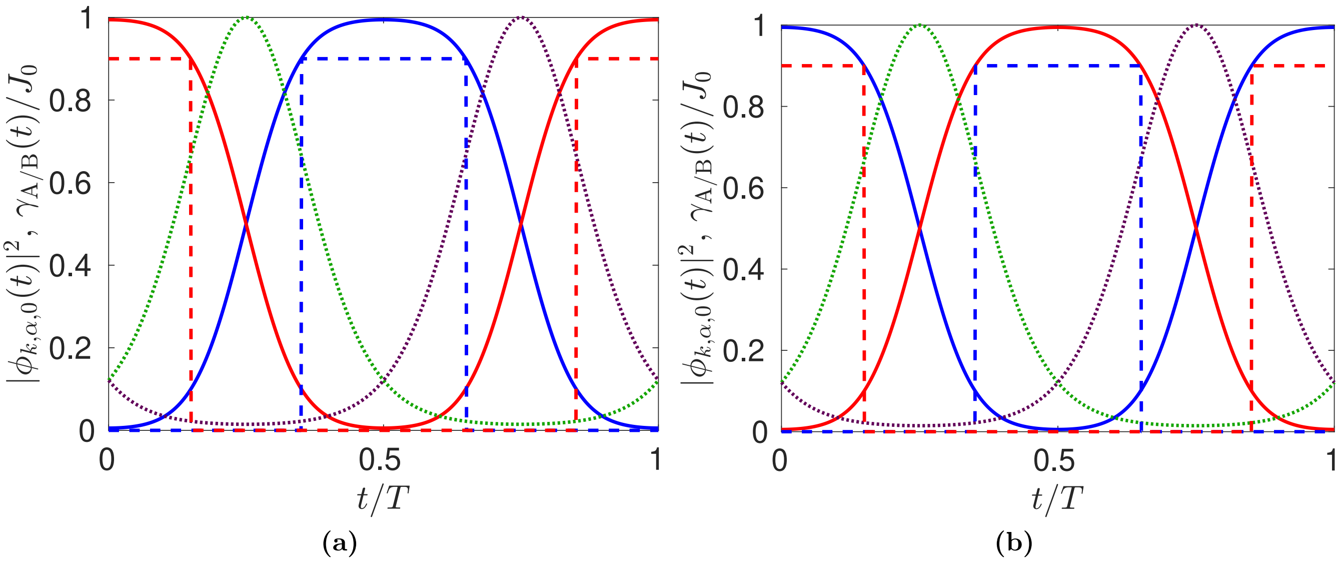

(a) **(b)**

Figure 5.17.: Density of the Floquet-Bloch states on sublattice A (blue solid) and sublattice B (red solid), decay rate on sublattice A (blue dashed) and sublattice B (red dashed) in case of the experimentally motivated driving scheme for (a) left-moving state at $k = -\pi/2$, (b) right moving state at $k = \pi/2$. Parameters: $\hbar\omega = \hbar\omega_0^{\mathrm{id}} = 1.1948\ J_0$, $\gamma_0 = 0.9\ J$, $\varphi = 0$, $L_t = 0.3\ T$. Green dashed $J_1(t)$, purple dashed $J_2(t)$.

essary to achieve direction dependent transport. Consider now the case of a hermitian impurity operator. In this case the Floquet S matrix is unitary [118, 250]. For the SSH ratchet, the S matrix then is a unitary 2×2 matrix. The general structure of unitary 2×2 matrices implies that the transmission and reflection coefficients at equal quasienergy are equal

$$T_{k,1} = T_{-k,2},\ \ R_{k,1} = R_{-k,2}. \tag{5.120}$$

When averaged over a full band, as it is done in our case, the transmission / reflection of right and left movers are the same

$$T_1 = T_2,\ \ R_1 = R_2. \tag{5.121}$$

This implies the absence of direction-dependent transport in the case of uniformly populated bands for a hermitian impurity operator. It follows that the non-hermiticity of the impurity operator is a key feature in order to achieve direction dependent transport as observed in our case.

We introduced the direction-dependent filter and discussed its working principle on a prototype case. In the next section we ask the question, how the direction-dependent transport depends on system parameters such as the strength of the decay γ_0, the duration of the losses L_t, the driving frequency ω and the center of the dissipative region controlled by φ.

5.5.2. Floquet S-Matrix Analysis of the Direction-Dependent Filter

Dependence on Dissipation Strength and Duration

At first, the dependence of the transmission coefficients on the dissipation strength γ_0 and duration L_t is investigated. The bulk ratchet is assumed to be driven with ω_0^{id}, such that the bands are helical and particle transport is possible with the velocity of one unit cell per driving period, while we choose for the impurity $\varphi = 0$. In Sec. 5.3 this case is discussed for the disconnected dimer model in order to create a direction-dependent filter. Figure 5.17 shows the dynamics of the Floquet-Bloch states in the case of the experimentally motivated driving scheme (5.7) together with the temporal form of decay rates and coupling constants. The dynamics of Floquet-Bloch states and decay rate allows direction-dependent filtering: The dissipation is timed such that the overlap with the density of a left moving state is large, while it is small for a right moving state.

Here we specialize in the case of the experimentally motivated driving scheme and appeal to Floquet S-matrix theory in order to numerically calculate transmission and reflection coefficients. The results for the disconnected dimer model have already been found by Eqns. (5.75) / (5.76). Figure 5.18 (a,b) shows the band averaged transmission coefficient of right / left movers obtained using Eq. (5.117) in dependence of the driving strength γ_0 and duration L_t at $\varphi = 0$. The transmission of the right movers is at unity for vanishing L_t and γ_0, while at small, but finite parameters it remains on a plateau of large transmission $T_1 = \mathcal{O}(1)$. As for the experimentally motivated driving scheme the sublattice oscillation is not separated in time from the intervals with finite decay, c.f. Fig. 5.17, the right movers are also affected by the dissipation, such that T_1 is a bit smaller than one for finite parameters. The transmission of the left moving states decays fast to smaller values if γ_0 or L_t is increased. This implies that in a vast parameter region there is a pronounced direction dependent transport $T_2 \ll T_1$. In particular if $0.1 < L_t/T < 0.3$ and $\gamma_0 > J_0$ the transmission coefficient of the right movers is near unity, while a left mover can be transmitted with a probability below 10^{-2}, such that we conclude to have designed a filter that works in a wide parameter region. In Fig. 5.18 (c) the ratio T_1/T_2 is shown. This ratio quantifies the selectivity of the filter and exceeds in the shown parameter range the value of $T_1/T_2 > 10^3$ while keeping T_1 of the order of 1.

As a function of L_t, the ratio T_1/T_2 has a maximum at a finite duration L_t, and drops again for larger L_t. This is related to a steep decrease of T_1 at $L_t \approx 0.4\ T$ which comes from the fact that at these large values of L_t the dissipative region does not fit into the sublattice oscillation of the Floquet-Bloch states. As a result both right and left movers are damped. In Fig. 5.18 (d) the reflection coefficient R_1 is displayed, which is, in difference to the disconnected dimer model, non-zero. Nevertheless, in the parameter region where our system works most optimal as a direction-dependent filter the transmission coefficient is close to zero if compared to the size of T_1. Note that both reflection coefficients are equal $R_1 = R_2$.

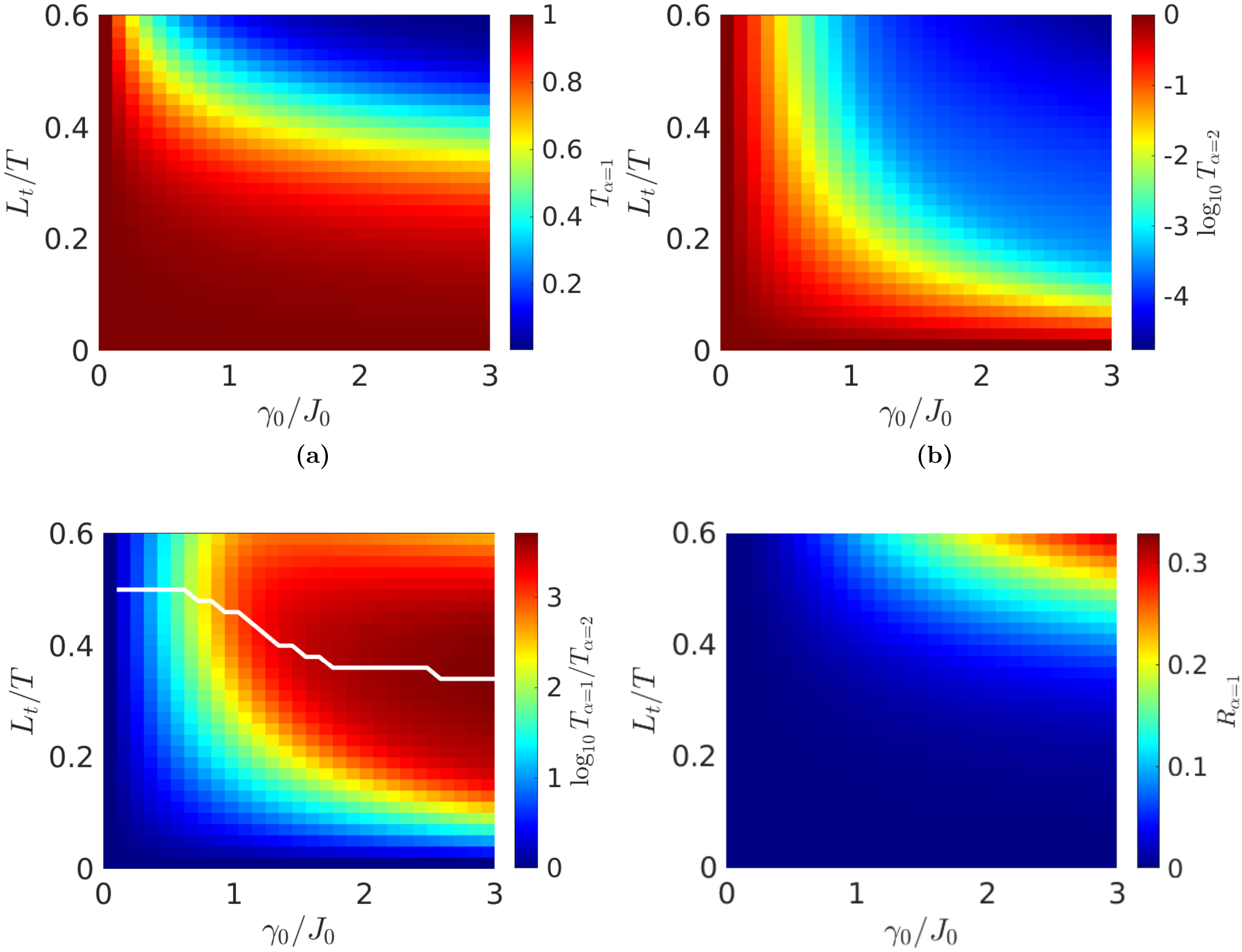

(a) (b)

(c) (d)

Figure 5.18.: Transmission of (a) right and (b) left movers in dependence of the dissipation strength γ_0 and duration of the dissipation L_t. (c) Decade logarithm of the ratio T_1/T_2, the white line marks the function $\max_{L_t}(T_1/T_2)(\gamma_0)$. (d) Reflection coefficients $R_1 = R_2$. Figures (a-d) are made using the experimentally motivated driving scheme for $\hbar\omega = \hbar\omega_0^{\mathrm{id}} = 1.195\ J_0$.

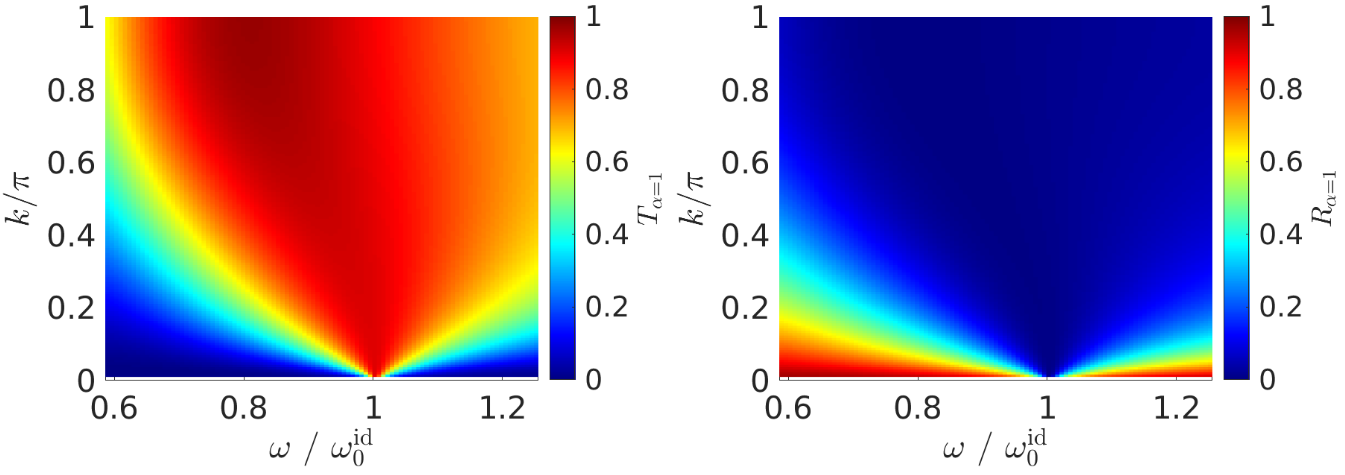

(a) **(b)**

Figure 5.19.: Transmission (a) and reflection (b) of right movers for the experimentally motivated driving scheme with parameters $L = 0.25\ T$, $\varphi = 0$ and $\gamma_0 = 1.5\ J_0$.

Dependence on the Driving Frequency: Creating a Velocity Filter

In the case of helical Floquet-Bloch bands we saw that the dissipative impurity acts as a direction-dependent filter. But what happens if one goes away from this ideal case by tuning the driving frequency to other values than ω_0^{id}?

The question is answered by Fig. 5.19, where transmission and reflection coefficient of the right movers are shown in color code in dependence of quasimomentum k and driving frequency ω in the case of the experimentally motivated driving scheme. The coefficients are symmetric in k, so we restrict to showing them for $k > 0$ only. At $\omega = \omega_0^{\mathrm{id}}$ the transmission coefficient T_1 is homogeneous and close to one, while the reflection is near zero at each k. Shifting the driving frequency away from $\omega = \omega_0^{\mathrm{id}}$, the value of T_1 drops to lower values in the vicinity of $k = 0$, while the reflection coefficient peaks at $k = 0$. The further ω is away from ω_0^{id}, the wider are the areas of small transmission and non-zero values of the reflection coefficient. The numerical analysis shows that the transmission coefficient of the left movers is smaller than 10^{-1} in the examined parameter range. In summary, we find that the direction-dependent filter operates optimal at $\omega = \omega_0^{\mathrm{id}}$ with minimally damped right movers and almost vanishing reflection coefficients.

The fact that transmission drops near $k = 0$ can be explained by the hybridization of the quasienergy bands, that mixes left and right movers near $k = 0$, cf. Subsec. 5.2.2. As discussed in Subsec. 5.2.2, this hybridization leads to a reduced amplitude of the Rabi oscillation of the Floquet-Bloch states. As a result, both right and left movers are affected by the dissipation for quasimomenta k in the region of the hybridization. This leads to a drop of the transmission coefficient at the corresponding values of k. In a similar vein the reflection coefficient peaks at $k = 0$ when moving away from the ideal driving frequency ω_0^{id}. This is explained by the fact that the hybridized states lead to finite

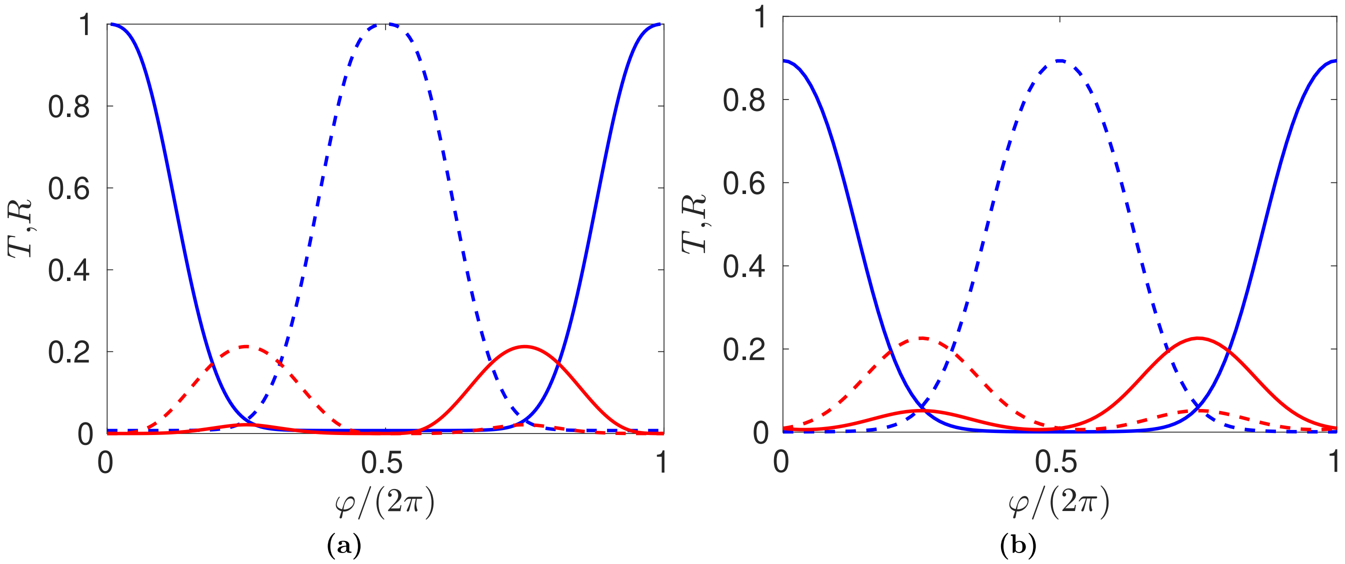

Figure 5.20.: Transmission coefficient of right movers (blue solid) and left movers (blue dashed), reflection coefficient of right movers (red solid) and left movers (red dashed) with $\omega = \omega_0^{\mathrm{id}}$ and $L_t = 0.25\ T$. (a) Disconnected Dimer driving scheme with $\delta t = 0.25\ T$, (b) Experimentally motivated driving scheme.

matrix elements $V_{(k,1,n),(q,2,m)}$ coupling the different channels, which in turn implies a non-vanishing reflection coefficient.

The dependence of the transmission and reflection coefficients shown in Fig. 5.19 on k can be used in order to create a velocity-dependent filter. The Floquet-Bloch states with a relatively slow group velocity are located near $k = 0$ and correlate with a smaller transmission coefficient. This implies that away from ideal driving the driven impurity works as a velocity-dependent filter that reflects and dissipates the slow moving parts of a wave packet.

Dependence on Temporal Location of the Dissipation

In this part we ask the question what happens if the interval of active dissipation is shifted against the coupling constants in time. This is achieved by changing the parameter φ, as defined in Eq. (5.74). Here it is assumed that the system is driven at the ideal driving frequency ω_0^{id}, such that the bands are helical. Figure 5.20 shows the resulting transmission and reflection coefficients for both the disconnected dimer and the experimentally motivated driving scheme. Both plots show that the maxima of the transmission coefficients are reached at $\varphi = 0, \pi$, confirming that we chose φ for an optimal direction-dependent filter in the previous section. At $\varphi = 0$ the left movers are filtered out, at $\varphi = \pi$ the right movers are dissipated. While for the disconnected dimer driving scheme a maximal transmission of $T_{1/2} = 1$ can be achieved, this is not the case for the experimentally motivated scheme. The reason for this effect is that in the case of the experimentally motivated driving scheme the coupling constants never vanish, such that the dissipation always affects both

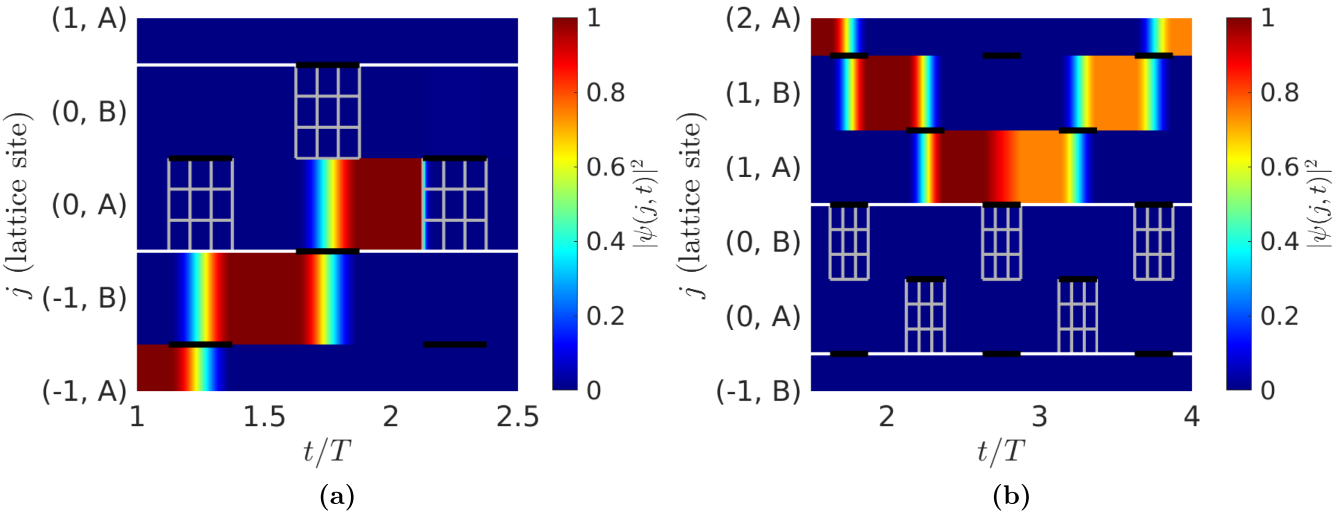

Figure 5.21.: Simulations in the disconnected dimer model with $\hbar\omega = J$, $\delta t = T/4$ such that optimal transport is possible. The impurity parameters are $\gamma_0 = 10\ J$, $\varphi = \pi/2$ and $L_t = T/4$. The probability density of the wave function is given in color code. White lines border the dissipative region, while space times with finite dissipation are marked by gray meshes. Black lines give active coupling constants. (a) right moving state, (b) left moving state.

right and left movers. Away from $\varphi = 0, \pi$ the ratio T_1/T_2, T_2/T_1 decreases in a similar way in both considered driving schemes. If the dissipation is active at times where the Floquet-Bloch states perform the sublattice oscillations, both sublattices are occupied by the Floquet-Bloch states and both left and right movers are affected by the dissipation almost equally.

The reflection coefficients peak at $\varphi = \pi/4, 3\pi/4$. Here the dissipation is centered around the time where the states populate both sublattices equally within a Rabi oscillation. This implies large matrix elements $V_{(k,1,m),(q,2,n)}$ and strong coupling between the channels, which in turn is reflected in the peak of the reflection coefficients. Remarkably, the reflection coefficients are not symmetric around $\varphi = \pi/2$. This interesting feature allows for direction-dependent reflection and is discussed in the next subsection.

5.5.3. Direction-Dependent Reflection

In Fig. 5.20 an asymmetry of the reflection coefficients can be observed. This feature is termed as direction-dependent reflection, since the size of the reflection coefficient depends on the direction of the particle. Figure 5.21 visualizes this effect by showing two different scenarios in the case of $\varphi = \pi/2$ and using the disconnected dimer scheme (5.8): In Fig. 5.21 (a) a right moving wave packet is impinging on the impurity, in Fig. 5.21 (b) a left moving packet is coming. While the right moving packet is damped, leading to both vanishing transmission and reflection, the left moving packet is partially reflected by the dissipative impurity.

In order to quantify this effect, a discussion based on an analytical calculation is provided in the case of the disconnected dimer model. For simplicity we choose $\varphi = \pi/2$ and assume that the hopping strength and the decay rate activate and deactivate at the same times by choosing the parameters $\delta t = L_\mathrm{T}, t_1 = T/4 - \delta t/2$. As shown in Fig. 5.21 (a), this choice implies that the sublattice oscillations are timed such that a right moving wave packet enters the lattice sites of the dissipative impurity without being immediately affected by the dissipation. Inside the impurity the coupling constant and the decay rates are active at the same time. The equations of motion with active hopping and decay rate $\gamma_\mathrm{A}(t)$ read

$$\begin{aligned} i\hbar\partial_t\psi_{0,\mathrm{A}}(t) &= J\psi_{0,\mathrm{B}}(t) - i\gamma_0\psi_{0,\mathrm{A}}(t), & \text{(5.122a)} \\ i\hbar\partial_t\psi_{0,\mathrm{B}}(t) &= J\psi_{0,\mathrm{A}}(t), & \text{(5.122b)} \end{aligned}$$

while the initial conditions are in the case of a right mover $\psi_{0,\mathrm{A}}(t_1) = 1, \psi_{0,\mathrm{B}}(t_1) = 0$. The portion of the wave function that remains on site $(0, \mathrm{A})$ after the decay rate is turned off will move to the left and becomes the reflected part of the wave packet. Using model (5.122) this part becomes

$$\begin{aligned} \psi_{0,\mathrm{A}}(t_1 + L_t) = \frac{1}{2\sqrt{\gamma_0^2 - 4J^2}} \Big[&(\gamma_0 + \sqrt{\gamma_0^2 - 4J^2}) e^{-(\sqrt{\gamma_0^2 - 4J^2}) L_t/(2\hbar)} \\ &+ (\sqrt{\gamma_0^2 - 4J^2} - \gamma_0) e^{-(\gamma_0 - \sqrt{\gamma_0^2 - 4J^2}) L_t/(2\hbar)} \Big] \end{aligned} \tag{5.123}$$

showing that the particle gets damped before it can perform the sublattice oscillation inside the dissipative region. Performing the limit of large γ_0 we arrive by using $\sqrt{\gamma_0^2 - 4J^2} = 2\gamma_0 - 2J^2/\gamma_0 + \mathcal{O}(1/\gamma_0^2)$ at a simplified expression

$$\psi_{0,\mathrm{A}}(t_1 + L_t) \approx e^{-\gamma_0 L_t/\hbar} + \frac{J^2}{\gamma_0^2} e^{-J^2 L_t/(\hbar\gamma_0)}. \tag{5.124}$$

We neglect possible contributions that stem from a similar effect from the site $(0, B)$, since these contributions are exponentially damped compared to the result in Eq. (5.124). The reflection coefficient is given by the modulus squared $R_1 = |\psi_{0,\mathrm{A}}(t_1 + L_\mathrm{T})|^2$. For infinite large γ_0 the reflection coefficient of the right movers R_1 goes to zero.

In Fig. 5.21 (b) a left mover is considered. Here the coupling constant that enables the sublattice oscillation from outside to inside the impurity is in time with the decay rate of the adjacent impurity site. This situation is described by the following equations of motion

$$\begin{aligned} i\hbar\partial_t\psi_{1,\mathrm{A}}(t) &= J\psi_{0,\mathrm{B}}(t), & \text{(5.125a)} \\ i\hbar\partial_t\psi_{0,\mathrm{B}}(t) &= J\psi_{1,\mathrm{A}}(t) - i\gamma_0\psi_{0,\mathrm{B}}(t), & \text{(5.125b)} \end{aligned}$$

with the initial conditions $\psi_{1,\mathrm{A}}(T/2 + t_1) = 1, \psi_{0,\mathrm{B}}(T/2 + t_1) = 0$. A strong decay rate γ_0 in Eq. (5.125) leads to a detuning of the Rabi frequency of the sublattice oscillation, c.f. the exponent in Eq. (5.123). As a result, a major portion of the state stays outside the dissipative region, the

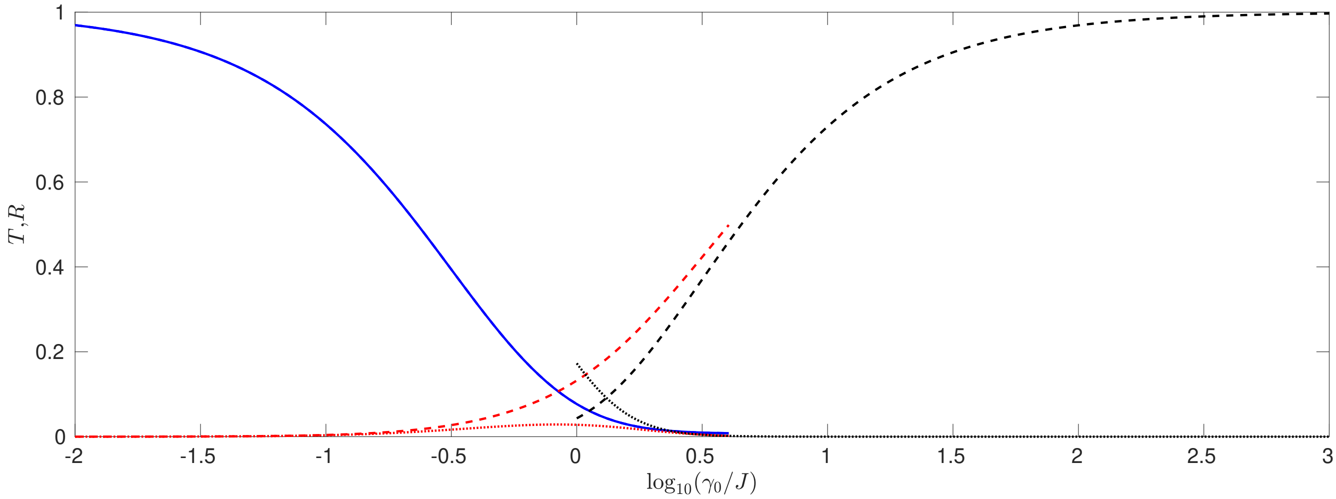

Figure 5.22.: Transmission (blue $T_1 = T_2$) and reflection (red dotted R_1, red dashed R_2) coefficients for the disconnected dimer model with $\hbar\omega = J$, $\delta t = T/4$, $L_t = T/4$, $\phi = \pi/2$. The black dotted R_1 with Eq. (5.124), black dashed R_2 with Eq. (5.126).

little portion that gets inside is damped and will be neglected in the further calculation. The portion that stays outside the dissipative region becomes a right moving state in the next cycle of the drive and is thus the reflected part of the wave packet. With a calculation similar to the one of the right movers, the reflection coefficient of the left movers is found in the limit of large γ_0 to be equal to

$$R_2 \approx e^{-2J^2 L_t/(\hbar\gamma_0)}. \tag{5.126}$$

For sufficiently large dissipation strength, the reflection coefficient for a left mover is of the order of one.

In Fig. 5.22 the formulas (5.124) and (5.126) are compared to the results of the Floquet S-matrix theory for the disconnected dimer model. It holds that at small γ_0 both transmission coefficients are near one and the reflection coefficients are close to zero and equal to each other. The transmission coefficients decline to $T_\alpha \to 0$ for $\gamma_0 \to \infty$ and $\alpha = 1, 2$. For $\gamma_0 > 0$ the reflection coefficients differ significantly from each other. For $\gamma_0 \to \infty$ the right movers are totally absorbed while the reflection coefficient of the left movers R_2 is substantially larger than R_1. The results of the Floquet S-matrix theory are shown up to $\log_{10}(\gamma_0/J) = 0.6$, both curves of numerical data and analytical approximation adapt to each other at that point. For larger γ_0 the Floquet S-matrix yields unreliable results for given parameters. For $\gamma_0 \to \infty$ the right movers are totally absorbed $R_1 \to 0$, while the left movers are reflected with unit probability $R_2 \to 1$.

5.6. Results of the Waveguide Experiment

In this subsection the results of the waveguide experiment performed by Z. Fedorova from University of Bonn are presented.

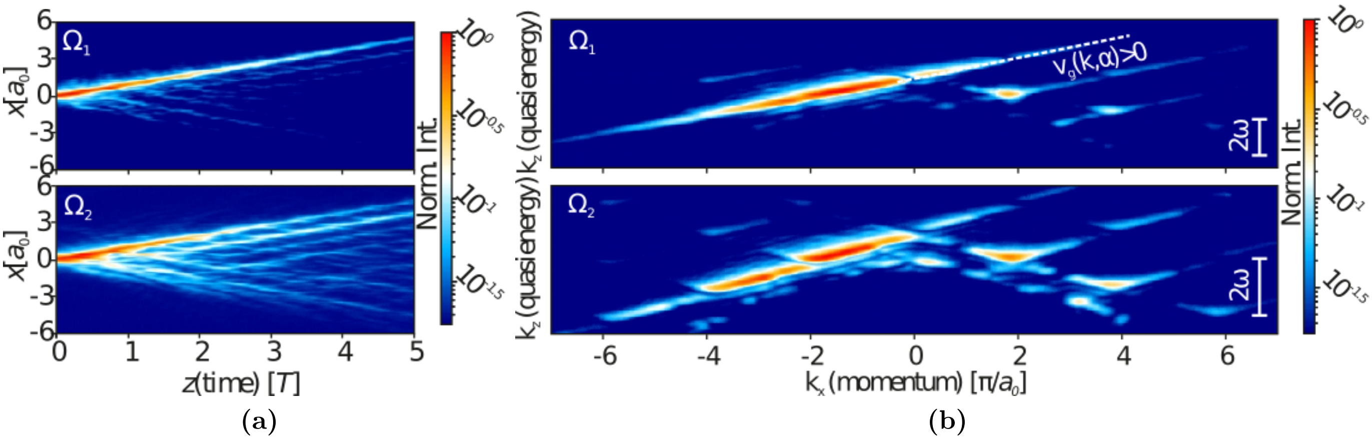

Figure 5.23.: Figure created by Z. Fedorova from University of Bonn and published in Ref. [216]. (a) Real space surface plasmon-polariton intensity distribution, (b) Fourier space surface plasmon-polariton intensity distribution in color code for driving frequencies Ω_1 coresponding to ω_0^{id} and Ω_2 larger than ω_0^{id}.

At first, directed transport in the Hamiltonian ratchet is characterized. In order to do so, a single waveguide is excited by shining a laser beam onto a grating coupler, for details see Ref. [216]. This configuration corresponds in analogy to quantum mechanics to an initial state located at a single lattice site. Figure 5.23 (a) shows the resulting real space intensity distribution measured by leakage radiation microscopy, while Fig. 5.23 (b) displays the corresponding quantities in Fourier space. For the driving frequency Ω_1, that corresponds to ω_0^{id} in the experiment, ratchet transport is almost perfect. Note that in the experiment the driving frequency has the unit of an inverse length, for better distinction to actual frequencies we use the symbol Ω. The intensity of the surface plasmon-polaritons is transported almost dispersionless with positive velocity, while only little intensity decays into the $-x$ direction. The corresponding figure in Fourier space shows linear quasienergy bands with almost vanishing band gaps. The fact that the slope of most bands is positive confirms that in a high proportion Floquet-Bloch states with positive group velocity are excited. The lower figures show the case of the driving frequency Ω_2 that is substantially higher than Ω_1. Here the ratchet effect is less pronounced compared to Ω_1, the transport is more dispersive and there is a substantial transport in $-x$ direction. This agrees with the results found by the theoretical investigation in Subsec. 5.2.4. The corresponding quasienergy bands are shown in Fig. 5.23 (b). Here both right and left movers are populated, while band gaps are clearly visible in the spectrum.

In order to investigate the direction-dependent filter, the parameters of the waveguides on the sample are chosen such that optimal bulk transport is possible, including a the driving frequency of $\omega \approx \omega_0^{\mathrm{id}}$. This can be seen in Fig. 5.24 by the almost dispersionless directed propagation of the state in real space.

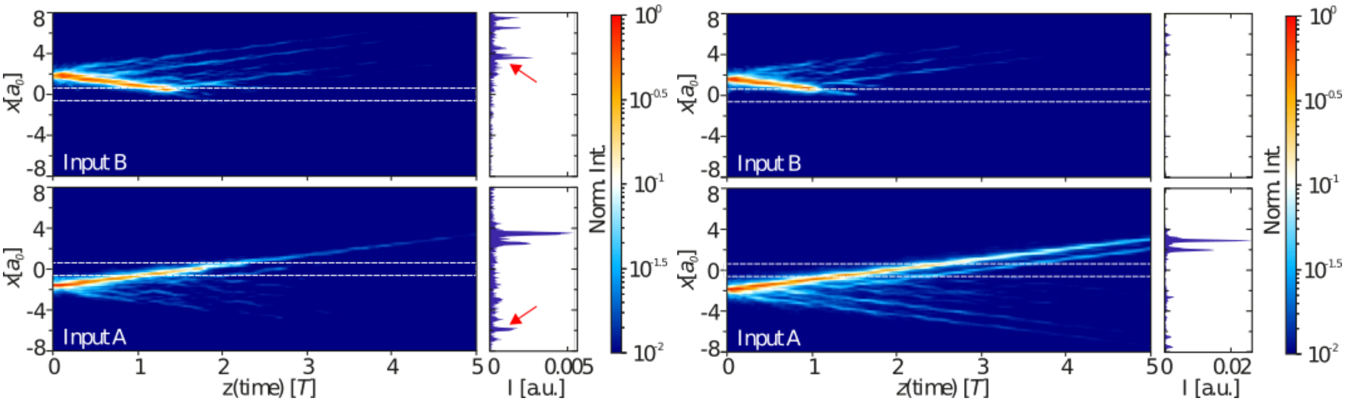

(a) **(b)**

Figure 5.24.: Figure created by Z. Fedorova from University of Bonn and published in Ref. [216]. Real space surface plasmon-polariton intensity distribution in color code, white lines mark the dissipative region. The parameters are chosen such that maximal ratchet transport is possible and that the dissipative impurity acts as an direction-dependent filter. Surface plasmon polaritons are excited at input A (x<0) and input B (x>0), while x denotes the transverse position on the sample in units of the unit cell $a_0 \approx 4\ \mu m$. The plots on the right side display the intensity distribution after the propagation through the sample at $z = 5\ T$, red arrows mark reflected waves. The impurity parameters are $\gamma_0 \approx 1.5\ J_0$, $\varphi \approx 0$. The length of the chromium stripes inside the dissipative region is (a) $L_t = 0.3\ T$, (b) $L_t = 0.15\ T$.

The results shown Fig. 5.24 verify that the dissipative impurity acts as a direction-dependent filter. While the surface plasmon polaritons that travel with positive velocity can pass the impurity only with little decay, the states moving with a negative velocity are almost completely dissipated by the impurity. This is an ample result, since it demonstrates that such a filter can be really built. The sample shown in Fig. 5.24 (a) is made with $L_t = 0.3\ T$, the one of Fig. 5.24 (b) is designed with $L_t = 0.15\,T$. In both cases the transmission of the left movers is below the noise level $T_2 < 10^{-2}$, while for the parameters of Fig. 5.24 (a) $T_1 \approx 0.53$ and for the parameters of Fig. 5.24 (b) $T \approx 0.92$ was measured [216]. This again confirms that the proposed driving scheme of the impurity parameters works as an excellent direction-dependent filter. As predicted by the Floquet S-matrix analysis the transmission coefficient of the right movers T_1 slightly decreases with increasing loss duration L_t.

5.7. Conclusion and Outlook

In this chapter the realization of a Hamiltonian quantum ratchet based on a time-periodically driven SSH model is proposed. The model is inspired by the conditions of the surface plasmon-polariton waveguide array experiment. Directed transport with the velocity of one unit cell per driving period is possible at certain driving frequencies, which obey a resonance condition. This situation is much easier to realize in an experiment compared to adiabatic Thouless pumping [236, 237]. In contrast to other realizations of a Hamiltonian ratchet [219, 232], a maximal current can be reached with a relatively simple initial state distribution. In addition, it is discovered that the band structure and the magnitude of transport is highly tunable. By adjusting the driving frequency a configuration with helical quasienergy bands can be reached. This helicity is related to quantized transport of one unit cell per driving period. But also driving frequencies with flat bands are possible. Here, transport is absent. This high tunability of the quasienergy band structure is what makes the model interesting for future investigations.

The transport in a Hamiltonian quantum ratchet significantly depends on the initial state. In order to overcome this limitation, a direction-dependent filter is introduced. The filter is realized by time-dependent dissipation placed on a few central lattice sites and filters out the states moving in negative direction while leaving the ones moving in positive direction almost unimpaired. This result implies that it is possible to create a Hamiltonian ratchet that intrinsically allows for a directed current independent of the initial state, as all states contributing to a current in negative direction are damped out by the filter. We investigate the direction-dependent filter using Floquet S-matrix theory which we originally derive for a time-periodic, dissipative impurity operator, as it is required by this setting. As a key result direction-dependent transmission coefficients are observed. There is a vast region of parameters where a left moving state is filtered out almost completely while the transmission of a right mover is of close to one.

Both ratchet and filter are realized by the surface plasmon-polariton waveguide array experiment, where the ratchet effect is observed by measuring directed transport. As prominent result, the direction-dependent filter is found to work as proposed in the waveguide experiment: The right movers are transmitted with almost no losses, while the transmission of the left movers is below noise level.

For future research activities it might be of interest to realize both ratchet scheme and dissipative filter with ultracold atoms in an optical lattice. The bipartite unit cell can be realized with an optical superlattice and time dependent coupling constants by a periodic modulation of a phase difference [263]. Ref. [263] realized a Touless pump based on the Rice-Mele model with ultracold fermions. The Rice-Mele model differs from the SSH model by an additional staggered on-site potential. It remains a future task to either get rid of this additional potential in order to realize the time-dependent SSH model in an ultracold gas experiment, or to extend the theory of the Hamiltonian ratchet to a fast Thouless pump. The direction-dependent filter is achieved by applying time dependent losses on a few lattice sites. This might be realized for example by shining an electron beam onto the ultracold atoms, as discussed in Ref. [264]. For realizing a filter, the electron beam should be focused one a single or a few lattice sites. In order to describe the ultracold gas realization of the direction-dependent filter theoretically, a more sophisticated description of the dissipation compared to the simple decay rates used in this work has to be considered. One way to do so is to describe the dissipation by a Lindblad approach, which may include new effects such as the dephasing of a state [199]. However, the description of open Floquet systems is a nontrivial task [265, 266], such that a future investigation might additionally develop new tools for the theoretical investigation of a wide class of models.

6. Conclusion of the Thesis and Outlook

We conclude on the main points of this thesis and give a brief outlook on further research topics.

Motivated by the relevance to ultracold gas experiments, we investigate in Ch. 3 Feshbach resonances within the framework of scattering theory. As a main result, we relate scattering resonances, that are induced by the time-periodic driving of a pseudo potential, to the physics of a Feshbach resonance in the Floquet Hilbert space. Using the Floquet-Feshbach resonance theory we find that the shape of these resonances is given by a simple formula. This proves that the periodic drive can tune the scattering length to arbitrary positive and negative values. Further, we calculate the resonance parameters such as position and width, and show that they depend on the details of the periodic drive, while the atom loss remains comparably small.

The Floquet-Feshbach resonance theory is a powerful tool for understanding and calculating the resonance properties in periodically driven impurity systems. Future works apply this formalism to other situations, such as radial potentials with finite range, the tunneling through a periodically driven barrier in one dimension, or even impurity problems in a quantum many-body system.

In a further part, we investigate a periodically driven multi-channel model of atom scattering. Floquet-Feshbach resonances, which give rise to finite atom loss, emerge in this model. An inelastic rate coefficient that is asymmetric around the resonance position is directly linked to scattering in the Floquet Hilbert space. This is an important result, since this asymmetry in the rate coefficient, serving as a probe of Floquet physics, can be measured by inelastic loss spectroscopy [18, 29]. Our multi-channel model serves as prototype of a further discussion about the influence of strong time-periodic fields on ultracold atom scattering.

Chapter 4 stays in the field of ultracold quantum gases and investigates the periodic driving of the interaction strength in a one-dimensional ultracold bosonic gas. In comparison to Ch. 3, our interest lies explicitly in analyzing a quantum many-body system, and we consider driving frequencies that are adiabatic on the energy scales of the scattering problem of Ch. 3. As a central result, we observe that the drive induces a standing wave pattern in the density-density correlation function of the ultracold gas. The origin of this pattern is revealed within the Tomonaga-Luttinger description of the underlying model. There it is found that the periodic drive generates density waves at wave vectors that obey the condition of a parametric resonance.

A parametric resonance is in general associated with an exponential increase of a physical quantity in time, such that the drive resonantly imparts energy into the system. This is in contrast to the nature of the Feshbach resonance, which is based on a quantum mechanical interference effect leading to a sharp change of the scattering phase shift. However, the two above discussed resonance phenomena have in common that they appear in the case that two energies come close to each other. A Feshbach resonance emerges if the energy of a bound state equals the energy of the scattering state, while a parametric resonance in the Tomonaga-Luttinger description is given by the condition that an integer multiple of drive quanta has the same energy as a pair of bosonic particles. Further, in both cases the system shows a pronounced response at resonance. At the position of a Feshbach resonance the scattering length diverges, while at a parametric resonance the Floquet steady state solution of the driven Tomonaga-Luttinger Liquid model shows a prominent peak in the presence of damping. This again demonstrates that a resonance is related to an enhanced response of the system to an external influence, which fits to the introduction of the term "resonance" in Ch. 1.

Mathematically, we find the Floquet steady states of the periodically driven Tomonaga-Luttinger Liquid by introducing the Floquet-Bogoliubov theory. With this theory we generalize the well-known Bogoliubov transformation to periodically driven Hamiltonians and thus find a framework that is capable of calculating Floquet steady states in quantum many-body systems.

The Floquet-Bogoliubov theory has been applied in Refs. [181, 267, 268] to the case of magnonic excitations in magnetic materials that are subject to a time-periodic magnetic field. Further works might generalize the Floquet-Bogoliubov theory to fermionic models or investigate, how possible non-linearities in a theory influence the parametrically induced density-wave patterns. It is also of interest to couple the system to a bath and investigate if this configuration can stabilize the dynamics without destroying the nontrivial Floquet-induced correlations.

In Ch. 5 we consider a periodically driven Su-Schrieffer-Heeger model, which is based on the conditions of a surface plasmon-polariton waveguide array experiment. The periodic drive is designed to make the system act as a Hamiltonian ratchet. We find that there are driving frequencies which are resonant with the sublattice oscillations of the Floquet-Bloch states. As a result, at these resonant frequencies ratchet transport is possible with the velocity of one unit cell per driving period, which is the maximum that can be achieved within this model. This behavior fits into the phenomenology of a resonance, in this case the velocity is the quantity that is maximal at a resonant frequency. The major drawback of our ratchet model is that the current depends on the initial state. In order to remove this dependence on the initial state, the direction-dependent filter is introduced as a time-periodic, dissipative impurity. We emphasize that we derive for the theoretical analysis of this model an S-matrix theory that deals with the combination of a non-hermitian, time-periodic impurity and a bulk, that is driven with the same frequency as the impurity. The findings of the S-matrix analysis agree with the results of the plasmon-polariton waveguide experiment.

A future way of research would be to apply the filter in ultracold gas experiments. Here, a description of the dissipation that goes beyond decay rates is necessary, it will be an interesting task to describe such a dissipation theoretically.

Bibliography

[1] M. Faraday, *XVII. On a peculiar class of acoustical figures; and on certain forms assumed by groups of particles upon vibrating elastic surfaces*, Philosophical Transactions of the Royal Society of London **121**, 299 (1831).

[2] P. Engels, C. Atherton, and M. A. Hoefer, *Observation of Faraday Waves in a Bose-Einstein Condensate*, Phys. Rev. Lett. **98**, 095301 (2007).

[3] I. Bloch, J. Dalibard, and W. Zwerger, *Many-body physics with ultracold gases*, Rev. Mod. Phys. **80**, 885 (2008).

[4] M. C. Rechtsman, J. M. Zeuner, Y. Plotnik, Y. Lumer, D. Podolsky, F. Dreisow, S. Nolte, M. Segev, and A. Szameit, *Photonic Floquet topological insulators*, Nature **496**, 196 (2013).

[5] M. Aidelsburger, M. Atala, M. Lohse, J. T. Barreiro, B. Paredes, and I. Bloch, *Realization of the Hofstadter Hamiltonian with Ultracold Atoms in Optical Lattices*, Phys. Rev. Lett. **111**, 185301 (2013).

[6] J. H. V. Nguyen, M. C. Tsatsos, D. Luo, A. U. J. Lode, G. D. Telles, V. S. Bagnato, and R. G. Hulet, *Parametric Excitation of a Bose-Einstein Condensate: From Faraday Waves to Granulation*, Phys. Rev. X **9**, 011052 (2019).

[7] L. W. Clark, A. Gaj, L. Feng, and C. Chin, *Collective emission of matter-wave jets from driven Bose–Einstein condensates*, Nature **551**, 356 (2017).

[8] H. J. Korsch, *Mathematische Ergänzungen zur Einführung in die Physik*, Binomi Verlag (2007).

[9] A. E. Miroshnichenko, S. Flach, and Y. S. Kivshar, *Fano resonances in nanoscale structures*, Rev. Mod. Phys. **82**, 2257 (2010).

[10] Y. S. Joe, A. M. Satanin, and C. S. Kim, *Classical analogy of Fano resonances*, Physica Scripta **74** 2, 259 (2006).

[11] U. Fano, *Effects of Configuration Interaction on Intensities and Phase Shifts*, Phys. Rev. **124**, 1866 (1961).

[12] U. Fano, *Sullo spettro di assorbimento dei gas nobili presso il limite dello spettro d'arco*, Nuovo Cimento **12**, 154 (1935).

[13] U. Fano, G. Pupillo, A. Zannoni, and C. W. Clark, *On the absorption spectrum of noble gases at the arc spectrum limit*, J. Res. Natl. Inst. Stand. Technol. **110**, 583–587 (2005).

[14] H. Feshbach, *Unified theory of nuclear reactions*, Ann. Phys. (New York) **5** (4), 357 390 (1958).

[15] K. Aoki, H. Yamawaki, and M. Sakashita, *Observation of Fano Interference in High-Pressure Ice VII*, Phys. Rev. Lett. **76**, 784 (1996).

[16] L. Armstrong, C. E. Theodosiou, and M. J. Wall, *Interference between radiative emission and autoionization in the decay of excited states of atoms*, Phys. Rev. A **18**, 2538 (1978).

[17] A. E. Miroshnichenko and Y. S. Kivshar, *Engineering Fano resonances in discrete arrays*, Phys. Rev. E **72**, 056611 (2005).

[18] C. Chin, R. Grimm, P. Julienne, and E. Tiesinga, *Feshbach resonances in ultracold gases*, Rev. Mod. Phys. **82**, 1225 (2010).

[19] R. E. March, *An Introduction to Quadrupole Ion Trap Mass Spectrometry*, Jour. Mass. Spec. **32**, 351 (1997).

[20] W. Paul, *Electromagnetic Traps for Charged and Neutral Particles (Nobel Lecture)*, Angewandte Chemie International Edition in English **29** 7, 739 (1990).

[21] C. J. Pethick and H. Smith, *Bose-Einstein Condensation in Dilute Gases*, Cambridge University Press, 2. edition (2008).

[22] H. J. Metcalf and P. van der Straten, *Laser Cooling and Trapping*, Springer New York (1999).

[23] W. Ketterle and N. V. Druten, *Evaporative Cooling of Trapped Atoms*, volume 37 of *Advances In Atomic, Molecular, and Optical Physics*, 181–236, Academic Press (1996).

[24] S. Bose, *Quantentheorie des einatomigen idealen Gases*, Zweite Abhandlung, Z. Physik **26**, 178 (1924).

[25] A. Einstein, *Quantentheorie des einatomigen idealen Gases. Zweite Abhandlung (Quantum theory of monatomic ideal gases, part two), Sitzber*, Kgl. Preuss. Akad. Wiss **1** 3 (1925).

[26] M. H. Anderson, J. R. Ensher, M. R. Matthews, C. E. Wieman, and E. A. Cornell, *Observation of Bose-Einstein Condensation in a Dilute Atomic Vapor*, Science **269** 522, 198 (1995).

[27] K. B. Davis, M. O. Mewes, M. R. Andrews, N. J. van Druten, D. S. Durfee, D. M. Kurn, and

W. Ketterle, *Bose-Einstein Condensation in a Gas of Sodium Atoms*, Phys. Rev. Lett. **75**, 3969 (1995).

[28] L. P. Pitaevskij and S. Stringari, *Bose-Einstein condensation and superfluidity*, International series of monographs on physics 164, Clarendon Press (2016).

[29] S. Inouye, M. R. Andrews, J. Stenger, H.-J. Miesner, D. M. Stamper-Kurn, and W. Ketterle, *Observation of Feshbach resonances in a Bose-Einstein condensate*, Nature **392**, 151 (1998).

[30] V. Vuletić, A. J. Kerman, C. Chin, and S. Chu, *Observation of Low-Field Feshbach Resonances in Collisions of Cesium Atoms*, Phys. Rev. Lett. **82**, 1406 (1999).

[31] S. L. Cornish, N. R. Claussen, J. L. Roberts, E. A. Cornell, and C. E. Wieman, *Stable* ^{85}Rb *Bose-Einstein Condensates with Widely Tunable Interactions*, Phys. Rev. Lett. **85**, 1795 (2000).

[32] T. Weber, J. Herbig, M. Mark, H.-C. Nägerl, and R. Grimm, *Bose-Einstein Condensation of Cesium*, Science **299**, 232 (2003).

[33] G. Roati, M. Zaccanti, C. D'Errico, J. Catani, M. Modugno, A. Simoni, M. Inguscio, and G. Modugno, ^{39}K *Bose-Einstein Condensate with Tunable Interactions*, Phys. Rev. Lett. **99**, 010403 (2007).

[34] T. Lahaye, T. Koch, B. Fröhlich, M. Fattori, J. Metz, A. Griesmaier, S. Giovanazzi, and T. Pfau, *Strong dipolar effects in a quantum ferrofluid*, Nature **448**, 672 (2007).

[35] B. DeMarco, J. L. Bohn, J. P. Burke, M. Holland, and D. S. Jin, *Measurement of p-Wave Threshold Law Using Evaporatively Cooled Fermionic Atoms*, Phys. Rev. Lett. **82**, 4208 (1999).

[36] F. Schreck, L. Khaykovich, K. L. Corwin, G. Ferrari, T. Bourdel, J. Cubizolles, and C. Salomon, *Quasipure Bose-Einstein Condensate Immersed in a Fermi Sea*, Phys. Rev. Lett. **87**, 080403 (2001).

[37] M. Greiner, C. A. Regal, and D. S. Jin, *Emergence of a molecular Bose–Einstein condensate from a Fermi gas*, Nature **426**, 537 (2003).

[38] M. W. Zwierlein, J. R. Abo-Shaeer, A. Schirotzek, C. H. Schunck, and W. Ketterle, *Vortices and superfluidity in a strongly interacting Fermi gas*, Nature **435**, 1047 (2005).

[39] T. Bourdel, L. Khaykovich, J. Cubizolles, J. Zhang, F. Chevy, M. Teichmann, L. Tarruell, S. J. J. M. F. Kokkelmans, and C. Salomon, *Experimental Study of the BEC-BCS Crossover Region in Lithium 6*, Phys. Rev. Lett. **93**, 050401 (2004).

[40] I. Bloch, *Ultracold quantum gases in optical lattices*, Nat. Phys. **1**, 23 (2005).

[41] I. Bloch, J. Dalibard, and S. Nascimbène, *Quantum simulations with ultracold quantum gases*, Nat. Phys. **8**, 267 (2012).

[42] E. Altman, E. Demler, and M. D. Lukin, *Probing many-body states of ultracold atoms via noise correlations*, Phys. Rev. A **70**, 013603 (2004).

[43] H. Ott, *Single atom detection in ultracold quantum gases: a review of current progress*, Rep. Prog. Phys. **79** 5, 054401 (2016).

[44] J. F. Sherson, C. Weitenberg, M. Endres, M. Cheneau, I. Bloch, and S. Kuhr, *Single-atom-resolved fluorescence imaging of an atomic Mott insulator*, Nature **467**, 68 (2010).

[45] D. Jaksch, C. Bruder, J. I. Cirac, C. W. Gardiner, and P. Zoller, *Cold Bosonic Atoms in Optical Lattices*, Phys. Rev. Lett. **81**, 3108 (1998).

[46] M. Greiner, O. Mandel, T. Esslinger, T. Hänsch, and I. Bloch, *Quantum phase transition from a superfluid to a Mott insulator in a gas of ultracold atoms*, Nature **415**, 39 (2002).

[47] T. Stöferle, H. Moritz, C. Schori, M. Köhl, and T. Esslinger, *Transition from a Strongly Interacting 1D Superfluid to a Mott Insulator*, Phys. Rev. Lett. **92**, 130403 (2004).

[48] I. B. Spielman, W. D. Phillips, and J. V. Porto, *Mott-Insulator Transition in a Two-Dimensional Atomic Bose Gas*, Phys. Rev. Lett. **98**, 080404 (2007).

[49] I. B. Spielman, W. D. Phillips, and J. V. Porto, *Condensate Fraction in a 2D Bose Gas Measured across the Mott-Insulator Transition*, Phys. Rev. Lett. **100**, 120402 (2008).

[50] A. Takamoto, F. Hong, R. Higashi, and H. Katori, *An optical lattice clock*, Nature **435**, 321 (2005).

[51] B. Santra, C. Baals, R. Labouvie, A. B. Bhattacherjee, A. Pelster, and H. Ott, *Measuring finite-range phase coherence in an optical lattice using Talbot interferometry*, Nature **8**, 15601 (2017).

[52] L. Tarruell, D. Greif, T. Uehlinger, G. Jotzu, and T. Esslinger, *Creating, moving and merging Dirac points with a Fermi gas in a tunable honeycomb lattice*, Nature **483**, 302 (2012).

[53] R. Jördens, N. Strohmaier, K. Günter, H. Moritz, and T. Esslinger, *A Mott insulator of fermionic atoms in an optical lattice*, Nature **455**, 204 (2008).

[54] B. Paredes, A. Widera, V. Murg, O. Mandel, S. Fölling, I. Cirac, G. V. Shlyapnikov, T. W. Hänsch, and I. Bloch, *Tonks–Girardeau gas of ultracold atoms in an optical lattice*, Nature **429**, 277 (2004).

[55] F. D. M. Haldane, *Effective Harmonic-Fluid Approach to Low-Energy Properties of One-Dimensional Quantum Fluids*, Phys. Rev. Lett. **47**, 1840 (1981).

[56] M. A. Cazalilla, R. Citro, T. Giamarchi, E. Orignac, and M. Rigol, *One dimensional bosons: From condensed matter systems to ultracold gases*, Rev. Mod. Phys. **83**, 1405 (2011).

[57] E. H. Lieb, *Exact Analysis of an Interacting Bose Gas. II. The Excitation Spectrum*, Phys. Rev. **130**, 1616 (1963).

[58] E. H. Lieb and W. Liniger, *Exact Analysis of an Interacting Bose Gas. I. The General Solution and the Ground State*, Phys. Rev. **130**, 1605 (1963).

[59] P. Belén, A. Widera, V. Murg, O. Mandel, S. Fölling, I. Cirac, G. V. Shlyapnikov, T. W. Hänsch, and I. Bloch, *Tonks–Girardeau gas of ultracold atoms in an optical lattice*, Nature **429**, 277 (2004).

[60] A. Vogler, R. Labouvie, G. Barontini, S. Eggert, V. Guarrera, and H. Ott, *Dimensional Phase Transition from an Array of 1D Luttinger Liquids to a 3D Bose-Einstein Condensate*, Phys. Rev. Lett. **113**, 215301 (2014).

[61] T. Kinoshita, T. Wenger, and D. S. Weiss, *Observation of a One-Dimensional Tonks-Girardeau Gas*, Science **305**, 1125 (2004).

[62] Dunlap, D. H. and Kenkre, V. M., *Dynamic localization of a charged particle moving under the influence of an electric field*, Phys. Rev. B **34** 6, 3625 (1986).

[63] A. Eckardt, *Colloquium: Atomic quantum gases in periodically driven optical lattices*, Rev. Mod. Phys. **89** 1, 1 (2017).

[64] H. Lignier, C. Sias, D. Ciampini, Y. Singh, A. Zenesini, O. Morsch, and E. Arimondo, *Dynamical Control of Matter-Wave Tunneling in Periodic Potentials*, Phys. Rev. Lett. **99**, 220403 (2007).

[65] A. Eckardt, C. Weiss, and M. Holthaus, *Superfluid-Insulator Transition in a Periodically Driven Optical Lattice*, Phys. Rev. Lett. **95**, 260404 (2005).

[66] A. Eckardt and M. Holthaus, *AC-induced superfluidity*, Europhys. Lett. **80** 5, 50004 (2007).

[67] A. Zenesini, H. Lignier, D. Ciampini, O. Morsch, and E. Arimondo, *Coherent Control of Dressed Matter Waves*, Phys. Rev. Lett. **102**, 100403 (2009).

[68] V. V. Ivanov, A. Alberti, M. Schioppo, G. Ferrari, M. Artoni, M. L. Chiofalo, and G. M. Tino, *Coherent Delocalization of Atomic Wave Packets in Driven Lattice Potentials*, Phys. Rev. Lett. **100**, 043602 (2008).

[69] C. Sias, H. Lignier, Y. P. Singh, A. Zenesini, D. Ciampini, O. Morsch, and E. Arimondo, *Observation of Photon-Assisted Tunneling in Optical Lattices*, Phys. Rev. Lett. **100**, 040404 (2008).

[70] J. Struck, C. Ölschläger, M. Weinberg, P. Hauke, J. Simonet, A. Eckardt, M. Lewenstein, K. Sengstock, and P. Windpassinger, *Tunable Gauge Potential for Neutral and Spinless Particles in Driven Optical Lattices*, Phys. Rev. Lett. **108**, 225304 (2012).

[71] N. Fläschner, D. Vogel, M. Tarnowski, B. S. Rem, D. S. Lühmann, M. Heyl, J. C. Budich, L. Mathey, K. Sengstock, and C. Weitenberg, *Observation of dynamical vortices after quenches in a system with topology*, Nat. Phys. **14**, 1 (2017).

[72] M. S. Rudner, N. H. Lindner, E. Berg, and M. Levin, *Anomalous Edge States and the Bulk-Edge Correspondence for Periodically Driven Two-Dimensional Systems*, Phys. Rev. X **3**, 031005 (2013).

[73] T. Kitagawa, E. Berg, M. Rudner, and E. Demler, *Topological characterization of periodically driven quantum systems*, Phys. Rev. B **82**, 235114 (2010).

[74] K. Wintersperger, C. Braun, F. N. Ünal, A. Eckardt, M. D. Liberto, N. Goldman, I. Bloch, and M. Aidelsburger, *Realization of an anomalous Floquet topological system with ultracold atoms*, Nat. Phys. **16**, 1058 (2020).

[75] S. E. Pollack, D. Dries, R. G. Hulet, K. M. F. Magalhães, E. A. L. Henn, E. R. F. Ramos, M. A. Caracanhas, and V. S. Bagnato, *Collective excitation of a Bose-Einstein condensate by modulation of the atomic scattering length*, Phys. Rev. A **81**, 053627 (2010).

[76] K. Staliunas, S. Longhi, and G. J. de Valcárcel, *Faraday Patterns in Bose-Einstein Condensates*, Phys. Rev. Lett. **89**, 210406 (2002).

[77] A. I. Nicolin, R. Carretero-González, and P. G. Kevrekidis, *Faraday waves in Bose-Einstein condensates*, Phys. Rev. A **76**, 063609 (2007).

[78] A. Balaz, R. Paun, A. I. Nicolin, S. Balasubramanian, and R. Ramaswamy, *Faraday waves in collisionally inhomogeneous Bose-Einstein condensates*, Phys. Rev. A **89**, 023609 (2014).

[79] T. Bilitewski and N. R. Cooper, *Scattering theory for Floquet-Bloch states*, Phys. Rev. A **91**, 033601 (2015).

[80] M. Bukov, M. Heyl, D. A. Huse, and A. Polkovnikov, *Heating and many-body resonances in a periodically driven two-band system*, Phys. Rev. B **93**, 155132 (2016).

[81] D. A. Abanin, W. De Roeck, W. W. Ho, and F. m. c. Huveneers, *Effective Hamiltonians,*

prethermalization, and slow energy absorption in periodically driven many-body systems, Phys. Rev. B **95**, 014112 (2017).

[82] M. Reitter, J. Näger, K. Wintersperger, C. Sträter, I. Bloch, A. Eckardt, and U. Schneider, *Interaction Dependent Heating and Atom Loss in a Periodically Driven Optical Lattice*, Phys. Rev. Lett. **119**, 200402 (2017).

[83] E. Wamba, A. Pelster, and J. R. Anglin, *Mapping as a probe for heating suppression in periodically driven quantum many-body systems*, arXiv:2108.07171 (2021).

[84] L. Lu, J. Joannopoulos, and M. Soljačić, *Topological photonics*, Nat. Phot. **8**, 821 (2014).

[85] C. Jörg, *Interfaces and defects in topological model systems of 3D micro-printed waveguides*, Ph.D. thesis, Technischen Universität Kaiserslautern (2019).

[86] C. Jörg, Erste Schritte in Richtung optischer topologischer Isolatoren durch direktes Laserschreiben, Diploma Thesis, TU Kaiserslautern (2015).

[87] C. Jörg, F. Letscher, M. Fleischhauer, and G. von Freymann, *Dynamic defects in photonic Floquet topological insulators*, N. J. P. **19**, 083003 (2017).

[88] I. L. Garanovich, S. Longhi, A. A. Sukhorukov, and Y. S. Kivshar, *Light propagation and localization in modulated photonic lattices and waveguides*, Phys. Rep. **518** (1), 1 (2012), light propagation and localization in modulated photonic lattices and waveguides.

[89] S. Longhi, M. Marangoni, M. Lobino, R. Ramponi, P. Laporta, E. Cianci, and V. Foglietti, *Observation of Dynamic Localization in Periodically Curved Waveguide Arrays*, Phys. Rev. Lett. **96**, 243901 (2006).

[90] L. J. Maczewsky, M. Heinrich, M. Kremer, S. K. Ivanov, M. Ehrhardt, F. Martinez, Y. V. Kartashov, V. V. Konotop, L. Torner, D. Bauer, and A. Szameit, *Nonlinearity-induced photonic topological insulator*, Science **370** 6517, 701 (2020).

[91] Z. Fedorova (Cherpakova), C. Jörg, C. Dauer, F. Letscher, M. Fleischhauer, S. Eggert, S. Linden, and G. von Freymann, *Limits of topological protection under local periodic driving*, Light Sci. & Appl. **8** 63 (2019).

[92] O. Balabanov and H. Johannesson, *Robustness of symmetry-protected topological states against time-periodic perturbations*, Phys. Rev. B **96**, 035149 (2017).

[93] L. Feng, R. El-Ganainy, and L. Ge, *Non-Hermitian photonics based on parity–time symmetry*, Nat. Phot. **11**, 752 (2017).

[94] S. Longhi, *Parity-time symmetry meets photonics: A new twist in non-Hermitian optics*, Europhys. Lett. **120** 6, 64001 (2017).

[95] W. D. Heiss, *Exceptional points of non-Hermitian operators*, J. Phys. A: Math. Gen. **37**, 2455 (2004).

[96] X. Zhang and J. Gong, *Non-Hermitian Floquet topological phases: Exceptional points, coalescent edge modes, and the skin effect*, Phys. Rev. B **101**, 045415 (2020).

[97] S. Longhi, D. Gatti, and G. Della Valle, *Non-Hermitian transparency and one-way transport in low-dimensional lattices by an imaginary gauge field*, Phys. Rev. B **92**, 094204 (2015).

[98] Z. Fedorova, H. Qiu, S. Linden, and J. Kroha, *Observation of topological transport quantization by dissipation in fast Thouless pumps*, Nat. Comm. **11** 1, 3758 (2020).

[99] D. H. Smith, *Inducing Resonant Interactions in Ultracold Atoms with a Modulated Magnetic Field*, Phys. Rev. Lett **115** 19, 193002 (2015).

[100] M. Holthaus, *Floquet engineering with quasienergy bands of periodically driven optical lattices*, J. Phys. B **49** 1, 013001 (2016).

[101] G. Floquet, *Sur les équations différentielles linéaires à coefficients périodiques*, Annales scientifiques de l´École Normale Supérieure **12**, 47 (1883).

[102] N. Goldman and J. Dalibard, *Periodically driven quantum systems: Effective Hamiltonians and engineered gauge fields*, Phys. Rev. X **4** 3, 1 (2014).

[103] S. Rahav, I. Gilary, and S. Fishman, *Effective Hamiltonians for periodically driven systems*, Phys. Rev. A **68**, 013820 (2003).

[104] S. Fazzini, P. Chudzinski, C. Dauer, I. Schneider, and S. Eggert, *Nonequilibrium Floquet Steady States of Time-Periodic Driven Luttinger Liquids*, Phys. Rev. Lett. **126**, 243401 (2021).

[105] F. Gesztesy and H. Mitter, *A note on quasi-periodic states*, J. Phys. A: Math. Gen. **14** 4, L79 (1981).

[106] P. Hänggi and F. Marchesoni, *Artificial Brownian motors: Controlling transport on the nanoscale*, Rev. Mod. Phys. **81**, 387 (2009).

[107] J. Cayssol, B. Dóra, F. Simon, and R. Moessner, *Floquet topological insulators*, Phys. Status Solidi RRL **7** 1-2, 101 (2013).

[108] M. Grifoni and P. Hänggi, *Driven quantum tunneling*, Phys. Rep. **304** 5, 229 (1998).

[109] J. H. Shirley, *Solution of the Schrödinger Equation with a Hamiltonian Periodic in Time*, Phys. Rev. **138**, B979 (1965).

[110] M. Rodriguez-Vega, M. Lentz, and B. Seradjeh, *Floquet perturbation theory: formalism and application to low-frequency limit*, New. J. Phys. **20**, 093022 (2018).

[111] H. Sambe, *Steady states and quasienergies of a quantum-mechanical system in an oscillating field*, Phys. Rev. A **7** 6, 2203 (1973).

[112] R. Shankar, *Principles of Quantum Mechanics*, Springer US, 2. edition (2008).

[113] H. Friedrich, *Scattering Theory*, Springer Berlin Heidelberg (2015).

[114] H. Feshbach, *A unified theory of nuclear reactions. II*, Ann. Phys. (New York) **19** (2), 287 (1962).

[115] T. L. Nicholson, S. Blatt, B. J. Bloom, J. R. Williams, J. W. Thomsen, J. Ye, and P. S. Julienne, *Optical Feshbach resonances: Field-dressed theory and comparison with experiments*, Phys. Rev. A **92**, 022709 (2015).

[116] A. G. Sykes, H. Landa, and D. S. Petrov, *Two- and three-body problem with Floquet-driven zero-range interactions*, Phys. Rev. A **95**, 062705 (2017).

[117] C. Dauer, Tuning of Scattering Properties by Periodic Modulation, Diploma Thesis, TU Kaiserslautern (2018).

[118] R. Newton, *Scattering theory of waves and particles*, International series in pure and applied physics, McGraw-Hill (1966).

[119] C. Timm, *Quantentheorie 2*, TU Dresden, Institut für Theoretische Physik (2015), abgerufen am 11.08.2021, 13:10.

[120] NIST Digital Library of Mathematical Functions, http://dlmf.nist.gov/, Release 1.1.4 of 2022-01-15, f. W. J. Olver, A. B. Olde Daalhuis, D. W. Lozier, B. I. Schneider, R. F. Boisvert, C. W. Clark, B. R. Miller, B. V. Saunders, H. S. Cohl, and M. A. McClain, eds.

[121] A. Pelster, *Bose-Einstein-Kondensation*, Universität Duisburg-Essen, http://users.physik.fu-berlin.de/ pelster/Vorlesungen/WS1213/bec.pdf (2004).

[122] M. D. Frye and J. M. Hutson, *Characterizing Feshbach resonances in ultracold scattering calculations*, Phys. Rev. A **96**, 042705 (2017).

[123] R. Stock, A. Silberfarb, E. L. Bolda, and I. H. Deutsch, *Generalized Pseudopotentials for Higher Partial Wave Scattering*, Phys. Rev. Lett. **94**, 023202 (2005).

[124] K. Huang and C. N. Yang, *Quantum-Mechanical Many-Body Problem with Hard-Sphere Interaction*, Phys. Rev. **105**, 767 (1957).

[125] G. Breit, *The Scattering of Slow Neutrons by Bound Protons. I. Methods of Calculation*, Phys. Rev. **71**, 215 (1947).

[126] R. Duine and H. Stoof, *Atom–molecule coherence in Bose gases*, Phys. Rep. **396** 3, 115 (2004).

[127] E. Timmermans, P. Tommasini, M. Hussein, and A. Kerman, *Feshbach resonances in atomic Bose–Einstein condensates*, Phys. Rep. **315** 1, 199 (1999).

[128] E. A. Donley, N. R. Claussen, S. L. Cornish, J. L. Roberts, E. A. Cornell, and C. E. Wieman, *Dynamics of collapsing and exploding Bose–Einstein condensates.*, Nature **412**, 295–299 (2001).

[129] J. L. Roberts, N. R. Claussen, S. L. Cornish, E. A. Donley, E. A. Cornell, and C. E. Wieman, *Controlled Collapse of a Bose-Einstein Condensate*, Phys. Rev. Lett. **86**, 4211 (2001).

[130] T. Kraemer, J. Herbig, M. Mark, T. Weber, C. Chin, H.-C. Nägerl, and R. Grimm, *Optimized production of a cesium Bose–Einstein condensate*, Appl. Phys. B **79**, 1013 (2004).

[131] T. Lahaye, J. Metz, B. Fröhlich, T. Koch, M. Meister, A. Griesmaier, T. Pfau, H. Saito, Y. Kawaguchi, and M. Ueda, *d-Wave Collapse and Explosion of a Dipolar Bose-Einstein Condensate*, Phys. Rev. Lett. **101**, 080401 (2008).

[132] P. Courteille, R. S. Freeland, D. J. Heinzen, F. A. van Abeelen, and B. J. Verhaar, *Observation of a Feshbach Resonance in Cold Atom Scattering*, Phys. Rev. Lett. **81**, 69 (1998).

[133] B. Bransden and C. Joachain, *Physics of Atoms and Molecules*, Pearson Education, Prentice Hall (2003).

[134] M. Stoll and T. Köhler, *Production of three-body Efimov molecules in an optical lattice*, Phys. Rev. A **72**, 022714 (2005).

[135] P. O. Fedichev, Y. Kagan, G. V. Shlyapnikov, and J. T. M. Walraven, *Influence of Nearly Resonant Light on the Scattering Length in Low-Temperature Atomic Gases*, Phys. Rev. Lett. **77**, 2913 (1996).

[136] G. Thalhammer, M. Theis, K. Winkler, R. Grimm, and J. H. Denschlag, *Inducing an optical Feshbach resonance via stimulated Raman coupling*, Phys. Rev. A **71**, 033403 (2005).

[137] O. Thomas, C. Lippe, T. Eichert, and H. Ott, *Experimental realization of a Rydberg optical Feshbach resonance in a quantum many-body system*, Nat. Comm. **9**, 2238 (2018).

[138] T. V. Tscherbul, T. Calarco, I. Lesanovsky, R. V. Krems, A. Dalgarno, and J. Schmiedmayer, *rf-field-induced Feshbach resonances*, Phys. Rev. A **81**, 050701 (2010).

[139] A. M. Kaufman, R. P. Anderson, T. M. Hanna, E. Tiesinga, P. S. Julienne, and D. S. Hall, *Radio-frequency dressing of multiple Feshbach resonances*, Phys. Rev. A **80**, 050701 (2009).

[140] S. V. Alyabyshev, T. V. Tscherbul, and R. V. Krems, *Microwave-laser-field modification of molecular collisions at low temperatures*, Phys. Rev. A **79**, 060703 (2009).

[141] D. J. Papoular, G. V. Shlyapnikov, and J. Dalibard, *Microwave-induced Fano-Feshbach resonances*, Phys. Rev. A **81**, 041603 (2010).

[142] T. M. Hanna, E. Tiesinga, and P. S. Julienne, *Creation and manipulation of Feshbach resonances with radiofrequency radiation*, New J. Phys. **12**, 083031 (2010).

[143] D. J. Owens, T. Xie, and J. M. Hutson, *Creating Feshbach resonances for ultracold molecule formation with radio-frequency fields*, Phys. Rev. A **94**, 023619 (2016).

[144] Y. Ding, J. P. D'Incao, and C. H. Greene, *Effective control of cold collisions with radio-frequency fields*, Phys. Rev. A **95**, 022709 (2017).

[145] P. Zhang, P. Naidon, and M. Ueda, *Independent Control of Scattering Lengths in Multicomponent Quantum Gases*, Phys. Rev. Lett. **103**, 133202 (2009).

[146] M. Abramowitz and I. A. Stegun (editors), *Handbook of Mathematical Functions with Formulas, Graphs, and Mathematical Tables*, New York: Dover, 9th printing edition (1972).

[147] C. Simmendinger, A. Wunderlin, and A. Pelster, *Analytical approach for the Floquet theory of delay differential equations*, Phys. Rev. E **59**, 5344 (1999).

[148] D. Martinez, *Floquet theory and continued fractions for harmonically driven systems*, Ph.D. thesis, The University of Texas, Austin (2003).

[149] H. S. Wall, *Analytic Theory of Continued Fractions.*, Dover Books on Mathematics, Dover Publications (2018).

[150] C. Brezinski, *History of Continnued Fractions and Padé Approximations*, Springer-Verlag Berlin Heidelberg (1991).

[151] A. M. Ishkhanyan, *Exact solution of the Schrödinger equation for the inverse square root potential* $V_0/\sqrt{x}$, Europhys. Lett. **112** 1, 10006 (2015).

[152] R. A. Rowlands, M. L. Gonzalez-Martinez, and J. M. Hutson, *Ultracold collisions in magnetic fields: reducing inelastic cross sections near Feshbach resonances*, arXiv:0707.4397 (2007).

[153] J. M. Hutson, *Feshbach resonances in ultracold atomic and molecular collisions: threshold behaviour and suppression of poles in scattering lengths*, New. J. Phys. **9** (5, 152 (2007).

[154] *Workgroup of A. Widera, Private Communications (2018).*

[155] F. Schmidt, D. Mayer, Q. Bouton, D. Adam, T. Lausch, J. Nettersheim, E. Tiemann, and A. Widera, *Tailored Single-Atom Collisions at Ultralow Energies*, Phys. Rev. Lett. **122**, 013401 (2019).

[156] K. Baumann, N. Q. Burdick, M. Lu, and B. L. Lev, *Observation of low-field Fano-Feshbach resonances in ultracold gases of dysprosium*, Phys. Rev. A **89**, 020701 (2014).

[157] C. Dauer, *Private Notes on a Floquet-Feshbach Resonance Theory for a General Radial Symmetric Scattering Potential*, (2021).

[158] C. Dauer, *Private Notes on a Floquet-Fano Resonance Theory for 1D Tunneling throgh a periodically driven Impurity*, (2022).

[159] S. A. Reyes, D. Thuberg, D. Pérez, C. Dauer, and S. Eggert, *Transport through an AC-driven impurity: Fano interference and bound states in the continuum*, New J. Phys. **19**, 043029 (2017).

[160] F. Hübner, C. Dauer, S. Eggert, C. Kollath, and A. Sheikhan, *Floquet-engineered pair and single particle filter in the Fermi Hubbard model*, arXiv:2112.07964 (2021).

[161] H. Friedrich and D. Wintgen, *Interfering resonances and bound states in the continuum*, Phys. Rev. A **32**, 3231 (1985).

[162] M. P. A. Fisher, P. B. Weichman, G. Grinstein, and D. S. Fisher, *Boson localization and the superfluid-insulator transition*, Phys. Rev. B **40**, 546 (1989).

[163] T. Giamarchi, *Quantum Physics in One Dimension*, Oxford University Press, Oxford (2004).

[164] F. D. M. Haldane, *Luttinger liquid theory of one-dimensional quantum fluids. I. Properties of the Luttinger model and their extension to the general 1D interacting spinless Fermi gas*, J. Phys. C: Solid State Phys. **14** 19, 2585 (1981).

[165] Y. Kagan and L. A. Manakova, *Parametric generation of density and spin modes with formation of stationary condensed states in ultracold two-component quasi-one-dimensional Fermi gases*, Phys. Rev. A **80**, 023625 (2009).

[166] M. Bukov and M. Heyl, *Parametric instability in periodically driven Luttinger liquids*, Phys. Rev. B **86**, 054304 (2012).

[167] S. Pielawa, *Interference of parametrically driven one-dimensional ultracold gases*, Phys. Rev. A **83**, 013628 (2011).

[168] C. D. Graf, G. Weick, and E. Mariani, *Parametric resonance and spin-charge separation in 1D fermionic systems*, Europhys. Lett. **89** 4, 40005 (2010).

[169] J.-S. Bernier, R. Citro, C. Kollath, and E. Orignac, *Correlation Dynamics During a Slow Interaction Quench in a One-Dimensional Bose Gas*, Phys. Rev. Lett. **112**, 065301 (2014).

[170] P. Chudzinski and D. Schuricht, *Time evolution during and after finite-time quantum quenches in Luttinger liquids*, Phys. Rev. B **94**, 075129 (2016).

[171] N. N. Bogoliubov, *A New Method in the Theory of Superconductivity. I*, JETP **7** 1, 41 (1958).

[172] N. N. Bogoliubov, *On the theory of superfluidity*, J. Phys (USSR) **11**, 77 (1947).

[173] W. Witschel, *On the general linear (Bogoliubov-) transformation for bosons*, Z Physik B **21**, 313 (1975).

[174] G. D. Mahan, *Condensed Matter in a Nutshell*, Princeton University Press (2011).

[175] M. Takahashi, *Modified spin-wave theory of a square-lattice antiferromagnet*, Phys. Rev. B **40**, 2494 (1989).

[176] R. Kubo, *The Spin-Wave Theory of Antiferromagnetics*, Phys. Rev. **87**, 568 (1952).

[177] A. Kreisel, F. Sauli, L. Bartosch, and P. Kopietz, *Microscopic spin-wave theory for yttrium-iron garnet films*, Eur. Phys. J. B **71** 59 (2009).

[178] M. R. Andrews, D. M. Kurn, H.-J. Miesner, D. S. Durfee, C. G. Townsend, S. Inouye, and W. Ketterle, *Propagation of Sound in a Bose-Einstein Condensate*, Phys. Rev. Lett. **79**, 553 (1997).

[179] M. R. Andrews, D. M. Stamper-Kurn, H.-J. Miesner, D. S. Durfee, C. G. Townsend, S. Inouye, and W. Ketterle, *Erratum: Propagation of Sound in a Bose-Einstein Condensate [Phys. Rev. Lett. 79, 553 (1997)]*, Phys. Rev. Lett. **80**, 2967 (1998).

[180] S. W. Hawking, *Particle creation by black holes*, Comm. Mat. Phys. **43**, 199 (1975).

[181] A. Becker, Magnonen Transport mit periodisch getriebener Barriere, Bachelor Thesis, TU Kaiserslautern (2019).

[182] K. Jachymski, F. Meinert, H. Veksler, P. S. Julienne, and S. Fishman, *Ultracold atoms in*

quasi-one-dimensional traps: A step beyond the Lieb-Liniger model, Phys. Rev. A **95**, 052703 (2017).

[183] A. Vogler, R. Labouvie, F. Stubenrauch, G. Barontini, V. Guarrera, and H. Ott, *Thermodynamics of strongly correlated one-dimensional Bose gases*, Phys. Rev. A **88**, 031603 (2013).

[184] M. Olshanii, *Atomic Scattering in the Presence of an External Confinement and a Gas of Impenetrable Bosons*, Phys. Rev. Lett. **81**, 938 (1998).

[185] S. Eggert, *One-dimensional quantum wires: A pedestrian approach to bosonization*, arXiv:0708.0003 (2007).

[186] J. von Delft and H. Schoeller, *Bosonization for beginners — refermionization for experts*, Ann. Phys. **7**, 225 (1998).

[187] D. C. Mattis and E. H. Lieb, *Exact Solution of a Many-Fermion System and Its Associated Boson Field*, J. Math. Phys. **6** 2, 304 (1965).

[188] M. A. Cazalilla, *Bosonizing one-dimensional cold atomic gases*, J. Phys. B: At. Mol. Opt. Phys. **37** 7, S1 (2004).

[189] A. Messiah, *Quantenmechanik, Band 1*, Walter de Gruyter: Berlin, New York, 1 edition (1976).

[190] J. Garcia and R. Rossignoli, *Spectrum and normal modes of non-Hermitian quadratic boson operators*, Phys. Rev. A **96**, 062130 (2017).

[191] T. R. Moussa, Floquet-Theorie in Luttinger Flüssigkeiten, Bachelor Thesis, TU Kaiserslautern (2019).

[192] V. P. Flynn, E. Cobanera, and L. Viola, *Deconstructing effective non-Hermitian dynamics in quadratic bosonic Hamiltonians*, New J. Phys. **22**, 083004 (2020).

[193] D. C. Brody, *Biorthogonal quantum mechanics*, J. Phys. A: Math. Theor. **47** 3, 035305 (2013).

[194] I. Kovacic, R. Rand, and S. Mohamed Sah, *Mathieu's Equation and Its Generalizations: Overview of Stability Charts and Their Features*, Appl. Mech. Rev. **70** 2 (2018), 020802.

[195] M. J. O. Strutt, *Lamésche- und Mathieusche- und verwandte Funktionen in der Physik und Technik*, Chelsea Publishing Company, New York (1967), (reprint).

[196] F. M. Arscott, *Periodic Differential Equations*, Pergamon Press Oxford (1964), an introduction to Mathieu, Lamë, and allied functions.

[197] M. Giessen, *Private Discussion* (2022).

[198] H.-Y. Wang, X.-M. Zhao, L. Zhuang, and W.-M. Liu, *Non-Floquet engineering in periodically driven non-Hermitian systems*, arXiv:2105.10980 (2021).

[199] H. Carmichael, *An Open Systems Approach to Quantum Optics*, Springer, Berlin, Heidelberg, 1 edition (1991).

[200] S. Dürr, J. J. García-Ripoll, N. Syassen, D. M. Bauer, M. Lettner, J. I. Cirac, and G. Rempe, *Lieb-Liniger model of a dissipation-induced Tonks-Girardeau gas*, Phys. Rev. A **79**, 023614 (2009).

[201] X. Niu, J. Li, S. L. Wu, and X. X. Yi, *Effect of quantum jumps on non-Hermitian system*, arXiv:2202.1259v1 (2022).

[202] S. Fazzini, P. Chudzinski, C. Dauer, I. Schneider, and S. Eggert, *Supplementary Material of Nonequilibrium Floquet Steady States of Time-Periodic Driven Luttinger Liquids*, Phys. Rev. Lett. **126**, 243401 (2021).

[203] D. R. Truax, *Baker-Campbell-Hausdorff relations and unitarity of SU(2) and SU(1,1) squeeze operators*, Phys. Rev. D **31**, 1988 (1985).

[204] H. Ui, *Boson Bogolyubov Transformation and the SU(1, 1) Group*, Progress of Theoretical Physics **44** 3, 703 (1970).

[205] J. Shen, H. Zhu, and P. Chen, *Exact solutions and geometric phase factor of time-dependent three-generator quantum systems*, Eur. Phys. J. D **23**, 305 (2003).

[206] A. I. Nicolin, *Resonant wave formation in Bose-Einstein condensates*, Phys. Rev. E **84**, 056202 (2011).

[207] D. Binks and W. van de Water, *Nonlinear Pattern Formation of Faraday Waves*, Phys. Rev. Lett. **78**, 4043 (1997).

[208] P. H. Wright and J. R. Saylor, *Patterning of particulate films using Faraday waves*, Review of Scientific Instruments **74** 9, 4063 (2003).

[209] B. Christiansen, P. Alstrøm, and M. T. Levinsen, *Ordered capillary-wave states: Quasicrystals, hexagons, and radial waves*, Phys. Rev. Lett. **68**, 2157 (1992).

[210] K. Iwahori and N. Kawakami, *Stabilization of prethermal Floquet steady states in a periodically driven dissipative Bose-Hubbard model*, Phys. Rev. A **95**, 043621 (2017).

[211] K. V. Kheruntsyan, D. M. Gangardt, P. D. Drummond, and G. V. Shlyapnikov, *Finite-temperature correlations and density profiles of an inhomogeneous interacting one-dimensional Bose gas*, Phys. Rev. A **71**, 053615 (2005).

[212] A. H. Castro Neto, C. de C. Chamon, and C. Nayak, *Open Luttinger Liquids*, Phys. Rev. Lett. **79**, 4629 (1997).

[213] Z.-Z. Li, C.-H. Lam, and J. Q. You, *Floquet engineering of long-range p-wave superconductivity: Beyond the high-frequency limit*, Phys. Rev. B **96**, 155438 (2017).

[214] X. Yang, B. Huang, and Z. Wang, *Floquet Topological Superfluid and Majorana Zero Modes in Two-Dimensional Periodically Driven Fermi Systems*, Sci. Rep. **8**, 2243 (2018).

[215] L. Lepori, D. Giuliano, and S. Paganelli, *Edge insulating topological phases in a two-dimensional superconductor with long-range pairing*, Phys. Rev. B **97**, 041109 (2018).

[216] Z. Fedorova, C. Dauer, A. Sidorenko, S. Eggert, J. Kroha, and S. Linden, *Dissipation engineered directional filter for quantum ratchets*, Phys. Rev. Research **3**, 013260 (2021).

[217] C. Drexler, S. A. Tarasenko, P. Olbrich, J. Karch, M. Hirmer, F. Müller, M. Gmitra, J. Fabian, R. Yakimova, S. Lara-Avila, S. Kubatkin, M. Wang, R. Vajtai, P. M. Ajayan, J. Kono, and S. D. Ganichev, *Magnetic quantum ratchet effect in graphene*, Nat. Nanotechnol. **8**, 107 (2013).

[218] G. G. Carlo, G. Benenti, G. Casati, and D. L. Shepelyansky, *Quantum Ratchets in Dissipative Chaotic Systems*, Phys. Rev. Lett. **94**, 164101 (2005).

[219] T. Salger, S. Kling, T. Hecking, C. Geckeler, L. Morales-Molina, and M. Weitz, *Directed Transport of Atoms in a Hamiltonian Quantum Ratchet*, Science **326**, 1241 (2009).

[220] S. Denisov, S. Kohler, and P. Hänggi, *Underdamped quantum ratchets*, Europhys. Lett. **85** 4, 40003 (2009).

[221] S. Flach, O. Yevtushenko, and Y. Zolotaryuk, *Directed Current due to Broken Time-Space Symmetry*, Phys. Rev. Lett. **84**, 2358 (2000).

[222] Denisov, S., Morales-Molina, L., and Flach, S., *Quantum resonances and rectification in ac-driven ratchets*, Eur. Phys. Lett. **79** 1, 10007 (2007).

[223] S. Denisov, L. Morales-Molina, S. Flach, and P. Hänggi, *Periodically driven quantum ratchets: Symmetries and resonances*, Phys. Rev. A **75**, 063424 (2007).

[224] F. Zhan, S. Denisov, A. V. Ponomarev, and P. Hänggi, *Quantum ratchet transport with minimal dispersion rate*, Phys. Rev. A **84**, 043617 (2011).

[225] M. S. Smoluchowski, *Experimentell nachweisbare, der üblichen Thermodynamik widersprechende Molekularphänomene*, Pisma Mariana Smoluchowskiego **2**, 226 (1927).

[226] R. P. Feynman, R. B. Leighton, M. L. Sands, and M. Gottlieb, *The Feynman lectures on physics*, volume 1, California Institute of Technology (2013).

[227] G. Mahmud, C. Campbell, K. Bishop, Y. K. anf Oleg Chaga, S. Soh, S. Huda, K. Kandere-Grzybowska, and B. A. Grzybowski, *Directing cell motions on micropatterned ratchets*, Nat. Phys. **5**, 696 (2009).

[228] N. Koumura, R. Zijlstra, R. van Delden, N. Harada, and B. Feringa, *Light-driven monodirectional molecular rotor*, Nature **401**, 152 (1999).

[229] H. Linke, T. E. Humphrey, A. Löfgren, A. O. Sushkov, R. Newbury, R. P. Taylor, and P. Omling, *Experimental Tunneling Ratchets*, Science **286**, 2314 (1999).

[230] F. Dreisow, Y. V. Kartashov, M. Heinrich, V. A. Vysloukh, A. Tünnermann, S. Nolte, L. Torner, S. Longhi, and A. Szameit, *Spatial light rectification in an optical waveguide lattice*, Europhys. Lett. **101** 4, 44002 (2013).

[231] S. Longhi, *Rectification of light refraction in curved waveguide arrays*, Opt. Lett. **34** 4, 458 (2009).

[232] J. Ni, S. Dadras, W. K. Lam, R. K. Shrestha, M. Sadgrove, S. Wimberger, and G. S. Summy, *Hamiltonian Ratchets with Ultra-Cold Atoms*, Ann. Phys. **529**, 1600335 (2017).

[233] P. Reimann, M. Grifoni, and P. Hänggi, *Quantum Ratchets*, Phys. Rev. Lett. **79**, 10 (1997).

[234] I. Goychuk and P. Hänggi, *Minimal Quantum Brownian Rectifiers*, The Journal of Physical Chemistry B **105** 28, 6642 (2001).

[235] S. Denisov, S. Flach, and P. Hänggi, *Tunable transport with broken space–time symmetries*, Phys. Rep. **538** 3, 77 (2014).

[236] D. J. Thouless, *Quantization of particle transport*, Phys. Rev. B **27**, 6083 (1983).

[237] Z. Fedorova, *Simulation of time-periodic and topological tight-binding systems with plasmonic waveguide arrays*, Ph.D. thesis, University of Bonn (2021).

[238] A. Szameit and S. Nolte, *Discrete optics in femtosecond-laser-written photonic structures*, J. Phys. B: At. Mol. Opt. Phys. **43** 16, 163001 (2010).

[239] J. K. Asbóth, L. Oroszlány, and A. Pályi, *A Short Course on Topological Insulators*, Springer International Publishing (2016).

[240] M. N. D. Ashcroft, Neil W., *Solid state physics*, Cengage Learning (2008).

[241] A. Gómez-León and G. Platero, *Floquet-Bloch Theory and Topology in Periodically Driven Lattices*, Phys. Rev. Lett. **110**, 200403 (2013).

[242] A. Altland and M. R. Zirnbauer, *Nonstandard symmetry classes in mesoscopic normal-superconducting hybrid structures*, Phys. Rev. B **55**, 1142 (1997).

[243] M. R. Zirnbauer, *Riemannian symmetric superspaces and their origin in random-matrix theory*, J. Math. Phys. **37** 10, 4986 (1996).

[244] R. Roy and F. Harper, *Periodic table for Floquet topological insulators*, Phys. Rev. B **96**, 155118 (2017).

[245] T. Wulf, C. Petri, B. Liebchen, and P. Schmelcher, *Symmetries and transport in site-dependent driven quantum lattices*, Phys. Rev. E **90**, 042913 (2014).

[246] J. C. Budich, Y. Hu, and P. Zoller, *Helical Floquet Channels in 1D Lattices*, Phys. Rev. Lett. **118**, 105302 (2017).

[247] T. Richmond, *General Topology: An Introduction*, De Gruyter (2020).

[248] A. Guo, G. J. Salamo, D. Duchesne, R. Morandotti, M. Volatier-Ravat, V. Aimez, G. A. Siviloglou, and D. N. Christodoulides, *Observation of $\mathcal{PT}$-Symmetry Breaking in Complex Optical Potentials*, Phys. Rev. Lett. **103**, 093902 (2009).

[249] W. Song, W. Sun, C. Chen, Q. Song, S. Xiao, S. Zhu, and T. Li, *Breakup and Recovery of Topological Zero Modes in Finite Non-Hermitian Optical Lattices*, Phys. Rev. Lett. **123**, 165701 (2019).

[250] M. Moskalets and M. Büttiker, *Floquet scattering theory of quantum pumps*, Phys. Rev. B **66**, 205320 (2002).

[251] H. Li, T. Kottos, and B. Shapiro, *Floquet-Network Theory of Nonreciprocal Transport*, Phys. Rev. Applied **9**, 044031 (2018).

[252] H. Li, B. Shapiro, and T. Kottos, *Floquet scattering theory based on effective Hamiltonians of driven systems*, Phys. Rev. B **98**, 121101 (2018).

[253] T. Millack, *T-matrix and K-matrix Floquet theory for atoms in strong laser fields*, J. Phys. B: At. Mol. Opt. Phys. **23** 11, 1693 (1990).

[254] U. Peskin and N. Moiseyev, *Time-independent scattering theory for time-periodic Hamiltonians: Formulation and complex-scaling calculations of above-threshold-ionization spectra*, Phys. Rev. A **49**, 3712 (1994).

[255] M. Henseler, T. Dittrich, and K. Richter, *Classical and quantum periodically driven scattering in one dimension*, Phys. Rev. E **64**, 046218 (2001).

[256] K. Brandner, *Coherent Transport in Periodically Driven Mesoscopic Conductors: From Scattering Amplitudes to Quantum Thermodynamics*, Zeitschrift für Naturforschung A **75** 5, 483 (2020).

[257] X.-C. Gao, J.-B. Xu, and T.-Z. Qian, *Invariants and geometric phase for systems with non-Hermitian time-dependent Hamiltonians*, Phys. Rev. A **46**, 3626 (1992).

[258] C. F. de Morisson Faria and A. Fring, *Time evolution of non-Hermitian Hamiltonian systems*, J. Phys. A: Math. Gen. **39** (29), 9269 (2006).

[259] T. Mongan, *Note on the numerical solution of the LippmannSschwinger equation*, Nuovo Cimento B **63**, 539 (1969).

[260] A. F. Sadreev and I. Rotter, *S-matrix theory for transmission through billiards in tight-binding approach*, J. Phys. A: Math. Gen. **36** 45, 11413 (2003).

[261] Y. Avishai and Y. B. Band, *One-dimensional density of states and the phase of the transmission amplitude*, Phys. Rev. B **32**, 2674 (1985).

[262] W. Li and L. E. Reichl, *Floquet scattering through a time-periodic potential*, Phys. Rev. B **60**, 15732 (1999).

[263] S. Nakajima, T. Tomita, S. Taie, T. Ichinose, H. Ozawa, L. Wang, M. Troyer, and Y. Takahashi, *Topological Thouless pumping of ultracold fermions*, Nat. Phys. **12**, 296 (2016).

[264] G. Barontini, R. Labouvie, F. Stubenrauch, A. Vogler, V. Guarrera, and H. Ott, *Controlling the Dynamics of an Open Many-Body Quantum System with Localized Dissipation*, Phys. Rev. Lett. **110**, 035302 (2013).

[265] A. Schnell, A. Eckardt, and S. Denisov, *Is there a Floquet Lindbladian?*, Phys. Rev. B **101**, 100301 (2020).

[266] S. Kohler, T. Dittrich, and P. Hänggi, *Floquet-Markovian description of the parametrically driven, dissipative harmonic quantum oscillator*, Phys. Rev. E **55**, 300 (1997).

[267] L. Schwarz, Spinwellen in periodischen Magnetfeldern, Bachelor Thesis, TU Kaiserslautern (2021).

[268] P. Jung, Magnonen in zeitlich periodischen Feldern, Bachelor Thesis, TU Kaiserslautern (2021).

Appendices

A. Relating a Recursion Relation to a Continued Fraction

In this appendix it is shown that the ratio of recursion coefficients can be calculated by a continued fraction. Consider a general, tridiagonal recursion relation

$$A_n x_n + B_n x_{n+1} + C_n x_{n-1} = h_n, n \in \mathbb{Z} \tag{A.1}$$

with the boundary conditions $\lim_{n\to\pm\infty} x_n = 0$ and inhomogeneity h_n with $h_n = 0 \; \forall n \geq -1$. Equation (A.1) resembles the case of Eq. (3.82). Here, we specialize to the positive indices and aim to compute the ratio x_0/x_{-1}. For a inhomogeneity h_n, that also vanishes for large negative indices, a similar discussion is possible for the negative indices. We define the fraction

$$f_n = \frac{x_{n-1}}{x_n}. \tag{A.2}$$

Dividing recursion (A.1) by x_n we arrive at the following equation for the f_n:

$$f_n = b_n + \frac{a_{n+1}}{f_{n+1}}. \tag{A.3}$$

with $b_n = -A_n/C_n$, $a_{n+1} = -B_n/C_n$. With this definition we formulate the following theorem.

Theorem 1

If Eq. (A.3) is fulfilled for each $n \in \mathbb{N}_0$, the following relation holds

$$f_0 = b_0 + \cfrac{a_1}{b_1 + \cfrac{a_2}{\ddots b_n + \frac{a_{n+1}}{f_{n+1}}}}. \tag{A.4}$$

Proof of Theorem 1

The proof goes via mathematical induction. In the base case of $n = 0$, Eq. (A.4) equals Eq. (A.3) for the case $n = 0$, and thus Eq. (A.4) holds true. The induction step follows directly from inserting Eq. (A.3) into Eq. (A.4) and using the fact that this procedure is consistent with the structure of a continued fraction.

Performing the limit $n \to \infty$ of Eq. (A.4), which is assumed to exist, we can express f_0 by an infinite continued fraction

$$f_0 = b_0 + \cfrac{a_1}{b_1 + \cfrac{a_2}{b_2 + \cfrac{a_3}{\ddots}}}. \tag{A.5}$$

B. Floquet-Feshbach Resonance Theory for Multi-Channel Models

In this appendix we give a derivation of Eq. (3.236). The first step is to write down an equation for the Floquet bound states of the model Eq. (3.217). In analogy to Sec. 3.8, this is achieved by truncating Eq. (3.233) to the closed channels only. Introducing the multiindex $a = (\mu_a, n_a)$ and the notation $V_{a,b} = \langle\langle \mu_a, n_a|\hat{A}|\mu_b, n_b\rangle\rangle$, this equation can be written as

$$(\hat{\mathbb{I}} + \hat{V} i \hat{K}_\alpha)\mathbf{D}^\alpha = \mathbf{0}, \text{ for closed channels only} \tag{B.1}$$

where the wave function in the closed channels is given by $R_{\alpha,a}(r) = -iD_a^\alpha e^{ik_{\alpha,a}r}/(k_{\alpha,a}r)$ and $(\hat{K}_\alpha)_{a,a} = k_{\alpha,a} = \sqrt{E_\alpha - E_a - E_{\sigma_0,n_0}}$ as purely imaginary number. We again emphasize that Eq. (B.1) is truncated to the closed channels only. Similar to Eq. (3.111), the normalization of the bound state is incarnated into the condition

$$1 = \sum_{a,\ k_a^2<0} \frac{|D_a^\alpha|^2}{2ik_{\alpha,a}^3}. \tag{B.2}$$

Equations (B.1) and (B.2) are solved numerically and yield the vector $\mathbf{D}^\alpha$ as well as the quasienergies E_α of the bound state.

We now want to solve the Floquet equation of the full coupled channel model while assuming that the wave function in the closed channels is proportional to the one of a single bound state $|\phi_\alpha\rangle\rangle$

$$|\phi_{\text{closed channels}}\rangle\rangle = A_\alpha|\phi_\alpha\rangle\rangle. \tag{B.3}$$

The entrance channel is labeled by $a_{\text{in}} = (\mu_{\text{in}}, n_{\text{in}})$ and contains the wave function

$$R_{a_{\text{in}}} = \frac{\sin(kr)}{kr} + f\frac{e^{ikr}}{r}. \tag{B.4}$$

The wave function in the inelastic channels is given by

$$R_a(r) = -iB_a\frac{e^{ik_ar}}{k_ar}, \tag{B.5}$$

where the k_a are determined by Eq. (3.231).

The equivalent to Eq. (3.195) reads in the Floquet multichannel calculation

$$(E_\alpha - \epsilon)A_\alpha = -\sum_{a,k_a^2<0} D_a^\alpha V_{a,a_{\text{in}}}(1 + ikf) - \sum_{\substack{a,k_a^2<0,\\ b,k_b^2>0}} D_a^\alpha V_{a,b}B_b. \tag{B.6}$$

For the entrance channel we find

$$f + V_{a_{\rm in},a_{\rm in}}(1+ikf) + \sum_{b,k_b^2>0} V_{a_{\rm in},b}, D_b + \sum_{b,k_b^2<0} V_{a_{\rm in},b} D_b = 0. \tag{B.7}$$

while it holds for the inelastic channels that

$$B_a = \sum_{a',\ k_{a'}^2>0} \Lambda_{a,a'} \left(\sum_{b,\ k_b^2<0} V_{a',b} D_b + V_{a',a_{\rm in}}(1+ikf) \right) \tag{B.8}$$

with the matrix $\Lambda_{a,b}$ defined by $\sum_{b,k_b^2>0} \Lambda_{a,b}(i\delta_{b,c}/k_b - V_{b,c}) = 1,\ a,b,c$ as indices of open channels. Inserting Eq. (B.8) into Eq. (B.6) and then finally in Eq. (B.7) an expression of the energy dependent scattering length in the entrance channel is found

$$a_{\rm E} = a_{\rm bg} - \frac{\Xi_\alpha}{E_\alpha + \delta E_\alpha + i\gamma_\alpha - \epsilon} + a_{\rm non-res} \tag{B.9}$$

In Eq. (B.9), the shift δE_α is found as real part and the loss coefficient γ_α is imaginary part of the quantity

$$\delta E_\alpha + i\gamma_\alpha = \sum_{\substack{a,k_a^2<0,\\ b,k_b^2>0,\\ a',k_{a'}^2>0,\\ b',k_{b'}^2<0}} D_a^\alpha V_{a,b} \Lambda_{b,a'} V_{a',b'} D_{b'}^\alpha. \tag{B.10}$$

The variable Ξ_α determines the width of the resonance and is given by

$$\begin{aligned} \Xi_\alpha = & \left(\sum_{\substack{b,\ k_b^2>0,\\ a',\ k_{a'}^2>0\\ b,\ k_b^2<0}} V_{a_{\rm in},b} \Lambda_{b,a'} V_{a',b} D_b^\alpha + \sum_{b,\ k_b^2>0} V_{a_{\rm in},b} D_b^\alpha \right) \\ & \times \left(\sum_{\substack{a,\ k_a^2<0,\\ b,\ k_b^2>0,\\ a',\ k_{a'}^2>0}} D_a^\alpha V_{a,b} \Lambda_{b,a'} V_{a',a_{\rm in}} + \sum_{a,\ k_a^2<0} D_a^\alpha V_{a,a_{\rm in}} \right). \end{aligned} \tag{B.11}$$

The non-resonant part of the scattering length is determined by

$$a_{\rm non-res} = \sum_{\substack{b,\ k_b^2>0,\\ a',\ k_{a'}^2>0}} V_{a_{\rm in},b} \Lambda_{b,a'} V_{a',a_{\rm in}}. \tag{B.12}$$

The position of the resonance δ_α at zero energy is found by the condition

$$E_\alpha(\delta_\alpha) + \delta E_\alpha(\delta_\alpha) = 0. \tag{B.13}$$

Similar to Eq. (3.206) an additional energy shift δE_α is present. With this Eq. (B.9) can be easily reduced to the scattering length (3.236). We emphasize that the physical interpretation of the quantities in Eq. (B.9) is analog to Eq. (3.204).

C. Non-Hermitian Floquet Theory

In this appendix a Floquet theory for a non-hermitian Hamiltonian $H(t)$ is presented. Since Floquet theory has been introduced to a set of linear ordinary differential equations with periodic coefficients [101], it can be readily generalized to non-hermitian Hamiltonians in the quantum mechanical setting [98]. The Floquet states are still of the form

$$|\psi_\alpha(t)\rangle = e^{-i\epsilon_\alpha t/\hbar}|\phi_\alpha(t)\rangle, \tag{C.1}$$

but the quasienergy ϵ_α is in general complex. It is seen in Eq. (C.1) that the Floquet-Brillouin zone structure still valid as defined in Eq. (2.8). In Eq. (C.1) and in the following, α labels a state within one Floquet-Brillouin zone, while m serves as Floquet-Brillouin zone index. The notation in Floquet space as defined in Sec. 2.2.2 also holds for the non-hermitian case. With the definition of the Floquet Hamiltonian $\mathcal{H}(t) = H(t) - i\hbar\partial_t$ and the notation of Subsec. 2.2.2 the Floquet equation reads

$$\hat{\mathcal{H}}|\phi_{\alpha,m}\rangle\rangle = \epsilon_{\alpha,m}|\phi_{\alpha,m}\rangle\rangle. \tag{C.2}$$

Equation (C.2) looks exactly as in the hermtian case, but the eigenstates $|\phi_{\alpha,m}\rangle\rangle$ are in general not orthogonal. This is seen by the following relation

$$\langle\langle\phi_{\alpha,m}|\phi_{\beta,n}\rangle\rangle = \frac{\langle\langle\phi_{\alpha,m}|(\hat{\mathcal{H}} - \hat{\mathcal{H}}^\dagger)|\phi_{\beta,n}\rangle\rangle}{\epsilon_{\beta,n} - \epsilon^*_{\alpha,m}}, \tag{C.3}$$

where it is assumed that $\epsilon^*_{\alpha,m} \neq \epsilon_{\beta,n}$. In the hermitian case the right hand side of Eq. (C.3) is zero such that the orthogonality of the $|\phi_{\alpha,m}\rangle\rangle$ states follows. In the non-hermitian case, however, $\hat{\mathcal{H}} \neq \hat{\mathcal{H}}^\dagger$ such that in general the right hand side of Eq. (C.3) as an expectation value of a non-vanishing operator can become non-zero. This indicates that the states $|\phi_{\alpha,m}\rangle\rangle$ are non-orthogonal. This issue is resolved by introducing biorthogonal quantum mechanics [98, 193]. The key is to define a basis of the Hermitian adjoint Hamiltonian

$$\hat{\mathcal{H}}^\dagger|\chi_{\alpha,m}\rangle\rangle = h_{\alpha,m}|\chi_{\alpha,m}\rangle\rangle. \tag{C.4}$$

In the following we assume that both $|\phi_{\alpha,n}\rangle\rangle$ and $|\chi_{\alpha,n}\rangle\rangle$ form a basis. In this case we can label the states such that [193]

$$\epsilon_{\alpha,n} = h^*_{\alpha,n}, \tag{C.5}$$

while the states $|\phi_{\beta,n}\rangle\rangle$ and the adjoint states $|\chi_{\alpha,m}\rangle\rangle$ obey biorthonormality [98, 193]

$$\langle\langle\chi_{\alpha,m}|\phi_{\beta,n}\rangle\rangle = \delta_{\alpha,\beta}\delta_{n,m} \tag{C.6}$$

and a biorthonormal completeness relation

$$\sum_{\alpha,m} |\phi_{\alpha,m}\rangle\rangle\langle\langle\chi_{\alpha,m}| = \mathbb{I}_{\mathcal{F}}. \tag{C.7}$$

Following Ref. [193], the expectation value of an operator $A(t)$ is the system is in a Floquet state is defined as

$$\langle A(t)\rangle_\alpha = \langle\chi_{\alpha,0}(t)|A(t)|\phi_{\alpha,0}(t)\rangle. \tag{C.8}$$

Similar to Eq. (2.43) we find that

$$\sum_{\alpha} |\phi_{\alpha,0}(t)\rangle\langle\chi_{\alpha,0}(t)| = \mathbb{I}_{\mathcal{R}}. \tag{C.9}$$

Using Eq. (C.9), any state $|\psi_0\rangle$ can be expanded in the $|\phi_{\alpha,n}\rangle\rangle$ basis

$$|\psi_0\rangle = \sum_{\alpha} c_\alpha |\phi_{\alpha,0}(t_0)\rangle, \tag{C.10}$$

while t_0 is assumed as initial time. Using Eqns. (C.1) and (C.10), the time-evolution operator for a time-evolution with respect to $H(t)$ calculates to

$$U(t,t_0) = \sum_{\alpha} e^{-i\epsilon_{\alpha,0}(t-t_0)/\hbar} |\phi_{\alpha,0}(t)\rangle\langle\chi_{\alpha,0}(t_0)|, \tag{C.11}$$

which looks similar to Eq. (2.9) that has been derived for the hermitian case. The key difference is that in Eq. (C.11) we project at initial time with the adjoint basis.

D. Inductive Generation of the Floquet-Bogoliubov Spectrum

Here we prove via mathematical induction that the quasienergies and the Floquet modes of Hamiltonian (4.33) are found by Eqns. (4.53) and (4.54). Furthermore we prove that the Floquet modes form a basis. The base case is shown in Sec. 4.3.3, where the existence of the Floquet vacuum state is proven and its quasienergy is found.

For the induction step we use the result of Eq. (4.52), from which follows that if $|\phi_n(t)\rangle$ is a Floquet state, also $|\phi_{n+1}(t)\rangle$ is and that the quasienergy is indeed given by Eq. (4.53).

For showing that $|\phi_{n+1}(t)\rangle$ is normalized to one, we assume that $|\phi_n(t)\rangle$ is normalized to one. Note that in Sec. 4.2 is is shown that the Floquet vacuum state is properly normalized. For performing the induction step we use

$$\beta^\dagger(t)|\phi_n(t)\rangle = \sqrt{n+1}|\phi_{n+1}(t)\rangle. \tag{D.1}$$

With $[\beta(t), [\beta^\dagger(t)]^n] = n[\beta^\dagger(t)]^{n-1}$ it follows that

$$\beta(t)|\phi_n(t)\rangle = \sqrt{n}|\phi_{n-1}(t)\rangle. \tag{D.2}$$

Using Eqns. (D.1) and (D.2) it can be found that the two states have equal norm

$$\langle\phi_{n+1}(t)|\phi_{n+1}(t)\rangle = \langle\phi_n(t)|\phi_n(t)\rangle, \tag{D.3}$$

which implies $\langle\phi_{n+1}(t)|\phi_{n+1}(t)\rangle = 1$. For showing that to states with different index are orthogonal, the following inner product is calculated

$$\langle\phi_n(t)|\phi_j(t)\rangle = \langle\phi_0(t)|\frac{[\beta(t)]^n[\beta^\dagger(t)]^j}{\sqrt{n!j!}}|\phi_0(t)\rangle, \tag{D.4}$$

with $j < n$. With the iterativ evaluation of pairs of operators $\beta(t)\beta^\dagger(t)$, Eq. (D.4) is simplified to

$$\langle\phi_n(t)|\phi_j(t)\rangle = (\Pi_{l=1}^{j})\langle\phi_0(t)|[\beta(t)]^{n-j}|\phi_0(t)\rangle. \tag{D.5}$$

Using the condition (4.50) of the Floquet vacuum state, Eq. (D.5) implies that two distinct Floquet states are orthonormal

$$\langle\phi_n(t)|\phi_j(t)\rangle = 0. \tag{D.6}$$

In summary, we have shown that the Floquet modes given by Eq. (4.33) are orthonormal. As the Floquet modes (4.33) can be mapped by a unitary transformation to a static eigenbasis, c.f. Eq. (4.58), we found all Floquet modes within one Floquet Brillouin zone by Eq. (4.33). Solutions from other Floquet Brillouin zones can be reached via transformation (2.8). This shows that the that the Floquet modes given by Eq. (4.33) form an orthonormal basis.

E. Transformation to Rotating Frame in Floquet-Bogoliubov Transformation

In this appendix it is shown how Hamiltonian (4.33) with parameters

$$A(t) = A_0 + 2A_1 \cos(\omega t),\ B(t) = B_0 \tag{E.1}$$

can be transformed to Eq. (4.96) with the time-dependent transformation Eq. (4.95). Starting point is to express the Hamiltonian (4.33) in terms of the generators $J_0,\ J_\pm$ of the SU(1,1) algebra which obey the following commutation relations

$$[J_0, J_\pm] = \pm J_\pm,\ [J_+, J_-] = -2J_0. \tag{E.2}$$

A representation of the SU(1,1) algebra is given by

$$J_0 = \frac{b^\dagger b + bb^\dagger}{4},\ J_+ = \frac{b^\dagger b^\dagger}{2},\ J_- = \frac{bb}{2}. \tag{E.3}$$

With Eq. (E.3) Hamiltonian (4.33) can be written as

$$H(t) = 2A(t)J_0 + B(J_+ + J_-) - \frac{A(t)}{2}. \tag{E.4}$$

The transformation Eq. (4.95) is expressed in terms of the SU(1,1) algebra as

$$Q(t) = \exp[-i4A_1/(\hbar\omega)\sin(\omega t)J_0], \tag{E.5}$$

while the transformed Hamiltonian is found by the formula

$$\tilde{H}(t) = Q^\dagger(t)H(t)Q(t) - i\hbar Q^\dagger(t)\partial_t Q(t). \tag{E.6}$$

The transformation $Q(t)$ is chosen such that the time-dependent part of $A(t)$ cancels out in Eq. (E.6). For finding $\tilde{H}(t)$ the following relation is used [202]

$$e^{izJ_0}(J_+ + J_-)e^{-izJ_0} = e^{iz}J_+ + e^{-iz}J_-,\ z \in \mathbb{R}. \tag{E.7}$$

In combination with the Jacobi-Anger decomposition $e^{ix\sin(\theta)} = \sum_{n=-\infty}^{\infty} \mathcal{J}_n(x)e^{in\theta}$, Eq. (4.96) is derived as result.

Curriculum Vitae

Personal Information

University address	Department of Physics, University of Kaiserslautern, 67633 Kaiserslautern, Germany
Electronic address	cdauer@physik.uni-kl.de
Date and place of birth	December 3, 1993, in 76829 Landau, Germany
Nationality	German

Education

2018 - 2022	PhD student at University of Kaiserslautern, Supervisor: Prof. Dr. Sebastian Eggert
2013 - 2018	Diploma studies in Physics at University of Kaiserslautern, Diploma thesis: "Tuning of Scattering Properties by Periodic Modulation", Supervisor: Prof. Dr. Sebastian Eggert
2004 - 2013	Abitur at Trifels Gymnasium Annweiler, 76857 Annweiler am Trifels

List of Publications

- F. Hübner, C. Dauer, S. Eggert, C. Kollath, and A. Sheikhan: Floquet-engineered pair and single particle filter in the Fermi Hubbard model, arXiv:2112.07964 (arXiv preprint)
- S. Fazzini, P. Chudzinski, C. Dauer, I. Schneider, and S. Eggert, Non-equilibrium Floquet steady states of time-periodic driven Luttinger liquids, Phys. Rev. Lett. **126**, 243401 (2021)
- Z. Fedorova*, C. Dauer*, A. Sidorenko, S. Eggert, J. Kroha, and S. Linden: Dissipation engineered directional filter for quantum ratchets, Phys. Rev. Research **3**, 013260 (2021)
  * *equally contributed*
- Z. Fedorova (Cherpakova)*, C. Jörg*, C. Dauer, F. Letscher, M. Fleischhauer, S. Eggert, S. Linden, and G. v. Freymann: Limits of topological protection under local periodic driving, Light: Science & Applications **8**, 63 (2019)
  * *equally contributed*
- S. A. Reyes, D. Thuberg, D. Pérez, C. Dauer, and S. Eggert: Transport through an AC driven impurity: Fano interference and bound states in the continuum, New J. Phys. **19**, 043029 (2017).

Selected Schools and Conferences

Burgbrohl, Germany: 08/2018	SFB/TR 49 and SFB/TR185 International School on Linear Response and Nonequilibrium Dynamics of Quantum Many-Body Systems (poster): *Tuning of Scattering by Periodic Modulation*
Bad Neuenahr, Germany: 03/2019	3rd International Symposium of the SFB/TR 49 on "Novel states in correlated condensed matter – from model systems to real materials" (poster): *Tuning of Scattering by Periodic Modulation*
Virtual Space: 06/2020	DAMOP Virtual Meeting 2020 (talk): *Engineering Feshbach Resonances by Time-Periodic Driving*
Virtual Space: 03/2021	APS Virtual March Meeting 2021 (two talks): *Theory of Resonances in Floquet Scattering*, *Direction Depended Transport in a Hamiltonian Ratchet induced by a time-dependent Dissipative Impurity*

Acknowledgment

At this point I say thanks to all people who were important during my time as a PhD student. I show my gratitude to Sebastian Eggert for supervising me and for enabling me to work as a researcher in his group. I appreciate all the inspiring discussions I had with him and am thankful for the knowledge I gained during my time as a PhD student. Further thanks go to Prof. James Anglin for his attentions to my work.

I thank Serena Fazzini for the fruitful collaboration and the wealth of discussions we had about physics. I also enjoyed to do research with Imke Schneider, André Becker and Piotr Chudzinski.

I enjoyed the physical and non-physical conversations with Aslam Parvej. Thanks go to Martin Bonkhoff, who was my colleague during a long period and always had time for a sophisticated discussion. I appreciated the discussions with Simon Jäger and Mathis Giessen, where I gained new knowledge about physics and the presenting of my own theories. I value the interlocution with Kevin Jägering and appreciate that I could pelt him with questions about the IT. I thank Flavia Braga Ramos for her uncomplicated relief. Thanks go to Marina Frey and Silvia Opperskalski. I enjoined multiple fruitful discussions with Enrico Stein and Maximilian Kiefer-Emmanouilidis and thank Steffen Plunder for advice concerning the supercomputer. I thank all my colleagues for the support and the friendly atmosphere.

I appreciated to work with Axel Pelster and am thankful for his support during my time as a PhD student. Special thanks go to Christina Jörg and Zlata Fedorova, which whom I had very fruitful collaboration. It was a great fun to develop new theoretical models that can directly be realized in their experiments. I gained a lot from the discussions during these collaborations. I further enjoyed the collaboration with Julian Schulz, Friedrich Hübner, Ameneh Sheikhan, Prof. Georg von Freymann, Prof. Stefan Linden, Prof. Johann Kroha, Prof. Michael Fleischhauer and Prof. Corinna Kollath. It is important to mention that the CRC "OSCAR" gave the framework for these collaborations and I enjoyed compelling discussions with my colleagues during the retreats.

I thank Prof. Artur Widera, Prof. Herwig Ott and Thomas Niederprüm for the interest in my work and I learned a lot during multiple conversations.

I show a huge gratitude to the hospitality of Prof. Antun Balaz during my visit in Belgrade.

Last but not least I thank my wife Katharina for always being on my side, and my parents and the whole family for the never ending support.